

Sheffield Hallam University

Study of the physical properties of a novel lithium aluminosilicate dental glass-ceramic

AL-JLAIHAWI, Zaid Ghalib Abdul-kadhim

Available from the Sheffield Hallam University Research Archive (SHURA) at:

<http://shura.shu.ac.uk/28655/>

A Sheffield Hallam University thesis

This thesis is protected by copyright which belongs to the author.

The content must not be changed in any way or sold commercially in any format or medium without the formal permission of the author.

When referring to this work, full bibliographic details including the author, title, awarding institution and date of the thesis must be given.

Please visit <http://shura.shu.ac.uk/28655/> and <http://shura.shu.ac.uk/information.html> for further details about copyright and re-use permissions.

Study of the Physical Properties of a Novel Lithium Aluminosilicate Dental Glass-ceramic

Zaid Ghalib Abdul-kadhim Al-Jlaihawi

A thesis submitted in partial fulfilment of the requirements of

Sheffield Hallam University

for the degree of Doctor of Philosophy

August 2020

DECLARATION

I hereby declare that:

1. I have not been enrolled for another award of the University, or other academic or professional organisation, whilst undertaking my research degree.
2. None of the material contained in the thesis has been used in any other submission for an academic award.
3. I am aware of and understand the University's policy on plagiarism and certify that this thesis is my own work. The use of all published or other sources of material consulted have been properly and fully acknowledged.
4. The work undertaken towards the thesis has been conducted in accordance with the SHU Principles of Integrity in Research and the SHU Research Ethics Policy.
5. The word count of the thesis is 55,000.

| | |
|------------------------|---|
| Name | <i>Zaid Ghalib Abdul-kadhim Al-Jlaihawi</i> |
| Date | <i>August 2020</i> |
| Award | <i>PhD</i> |
| Faculty | <i>Materials & Engineering Research Institute</i> |
| Director(s) of Studies | <i>Professor Antonio Feteira</i> |

DEDICATION

To my father (*Ghalib*) who is a gift from Allah, my mother (*Rabab*) who is a pure blessing, my dear uncle (*Najeh*) and my late aunt (*Buthaina*) may Allah have mercy upon her.

To my lovely wife (*Zahraa*) with beautiful daughters (*Noor*, *Zainab* and *Tuqa*) who supported me throughout my life and PhD journey.

To my wonderful brothers (*Fahad*, *Shahad* and *Ali*) and dear sister (*Zahraa*).

This achievement is a small gift for all of you.

Zaid Al-jlaihawi

Acknowledgement

First and foremost, I would like to express my sincere gratitude to my main supervisor **Professor Antonio M. Feteira** for the unremitting support of my PhD study and related researches, for his patience, insightful vision and senior knowledge and my second supervisor **Dr Evangelos Kordatos**, for his insightful comments and encouragement. Their advices and suggestions were a key support me in my entire journey towards PhD and writing of this thesis.

Here, I must record my sincere thanks to my sponsor, the Ministry of Higher Education and Scientific Research (MOHESR) in Iraq and the Iraqi Cultural Attaché in London for their sponsor morally and financially during my PhD research. Grateful thanks to the University of Kufa, the faculty of engineering and the department of mechanical engineering for the continuing support during my study. The same thank also goes to Sheffield Hallam University.

At Sheffield Hallam University, I would like to thank laboratory staff Dr Tony Bell, Mr Paul Allender and Miss Deeba Zahoor, further MERI staff Rachael Toogood, Gail Hallewell, Corrie Houton, Clare Mills Roberts and Amy McNally for the stimulating discussions, for the days we were working together before deadlines, and for all the time we have had in the last four years.

I am so thankful for my dear colleagues for making study life interesting during the five years together; Ali Al-Jawdah, Ali Ghanim Al-Rubaye, Burak Yahya Kadem, Hisham Abu-Ali, Khalid Rmaydh, Muhaed Alali, Murtadha Kareem, Hadi Al-Sagur and Yaqub Rahaq.

Finally, I would like to extend my sincere thanks to dear friends Mr Hayder Abueless and the neighbour Erkan Yildiz for helping and making life easier during my study.

Abstract

The aim of this study is to simultaneously establish the processability and physical properties of Lithium aluminosilicate-based (LAS) glass for dental restorations. An eventual outcome is the production of glass-ceramic matching both the aesthetics and mechanical properties of natural tooth. The two LAS-based glass compositions, refer to as LAS1 glass and LAS2 glass, are investigated using Inductively Coupled Plasma Optical Emission Spectroscopy (ICP-OES), Differential Scanning Calorimetry (DSC), X-ray Diffraction (XRD), Raman Spectroscopy (RS), Ultrasonic Testing (UT), Vickers Hardness and three-point bending flexural testing. ICP-OES analyses reveal LAS1 glass and LAS2 glass to be compositionally similar, however LAS2 glass contains traces of vanadium. XRD analyses reveal the presence of Li_3PO_4 and Li_2SiO_3 crystals in LAS1 glass, which apparently are not detected in LAS2 glass, however RS analyses obviously show vestiges of these phases in LAS2 glass. DSC reveals LAS1 glass and LAS2 glass to exhibit similar thermal behaviour. LAS1 glass shows a glass transition temperature of $\sim 500^\circ\text{C}$, two major thermal exothermic events at 615°C and 705°C , which are followed by two minor thermal exothermic events at 750°C and 790°C , and finally a major endothermic event at 910°C . Based on *In-situ* XRD analyses carried out between 540°C to 790°C , the first exothermic event centred at $\sim 615^\circ\text{C}$ can be associated with the successive crystallisation of Li_2SiO_3 , $\text{Li}_{0.25}\text{Al}_{0.25}\text{Si}_{0.75}\text{O}_2$ and $\text{LiAlSi}_4\text{O}_{10}$, whereas the second peak centred at $\sim 705^\circ\text{C}$ can be associated with the crystallisation of $\text{LiAlSi}_2\text{O}_6$ and $\text{Li}_2\text{Si}_2\text{O}_5$. Similar results are obtained for isothermal treatments of 30 minutes in the temperature range of 610°C and 870°C , as shown by combined *ex-situ* by XRD and RS analyses. The incorporation of a nucleation step of 300 minutes at 550°C , reduces the crystallisation temperature of $\text{LiAlSi}_4\text{O}_{10}$ and $\text{Li}_{0.25}\text{Al}_{0.25}\text{Si}_{0.75}\text{O}_2$ by $\sim 20^\circ\text{C}$, but also leads to increase of the crystallite sizes. Following this initial evaluation of the impact of isothermal heat treatments, other heat treatments are strategically carried out at temperatures below and above the exothermic events in order to evaluate again their impact on both phase assemblage and physical properties, such as hardness, elastic modulus, fracture toughness and colour. Hence, based on the DSC data, nucleation is carried out at a temperature of 550°C for 300 minutes, and crystallisations are carried out at 670°C , 780°C , 800°C , 830°C and 850°C , for different time lengths. XRD results reveal $\text{LiAlSi}_2\text{O}_6$ to be the dominant crystalline phase, followed by $\text{Li}_2\text{Si}_2\text{O}_5$ and Li_2SiO_3 for both LAS1 glass and LAS2 glass. Both LAS1 and LAS2 glass-ceramics exhibit high values of mechanical properties when the heat treatment is at 550°C for 300min, 780°C for 120min and $830^\circ\text{C}-850^\circ\text{C}$ for 120 min. Moreover, LAS1 glass and LAS2 glass heat treated above 770°C are both aesthetically suitable for dental restorations. Regarding the LAS1 glass, the colour is white, whereas LAS2 glass colour is identical to several standard shades including D2, C1 and B2, depending on the heat treatment temperature.

Abbreviations and nomenclature lists

| Nomenclature abbreviations list | | Nomenclature list | |
|---------------------------------|---|-------------------|---|
| LAS1 glass | First composition of Lithium aluminosilicate | δ | Delta |
| LAS2 glass | Second composition of Lithium aluminosilicate | β | Beta |
| CAD | Computer Aided Design | A_u | Gold |
| CAM | Computer Aided Manufacture | Ar | Argon |
| DSC | Differential scanning calorimetry | He | Helium |
| SEM | Scanning electron microscopy | T_N | Nucleation temperature |
| DSC | Differential scanning calorimetry | T_C | Crystallization temperature |
| XRD | X-ray diffraction | T_P | Peak Crystallization temperature |
| LS | Lithium disilicate | T_G | Crystal growth temperature |
| CAS | Calcium aluminosilicate | T_g | Glass transition temperature |
| ZAS | Zinc aluminosilicate | T_m | Melting temperature |
| MAS | Magnesium aluminosilicate | T_o | Freezing temperature |
| LAS | Lithium aluminosilicate | T_f | Onset crystallization temperature |
| PSZ | Partially Stabilized Zirconia | t_n | Nucleation hold time |
| CIE | Commission Internationale de l'Eclairage | t_p | Crystallization hold time |
| CIE L* | Lightness | λ | Wavelength |
| CIE a* | Green-red colour | n | Planes of atoms |
| CIE b* | Blue-yellow colour | W | Thermodynamic barrier to nucleation |
| XRD | X-ray diffraction | ΔG_D | Kinetic barrier to nucleation |
| UV-V | Ultraviolet-visible | G_S | Gibbs free energy per unit volume of solid |
| Exo | Exothermic reactions | G_L | Gibbs free energy per unit volume of liquid |
| Endo | Endothermic reactions | E_a | Activation energy |
| LP | Li_3PO_4 phase | R | Universal gas constant |
| LS1 | Li_2SiO_3 phase | V_c | Compression wave velocity (Ultrasound speed) |
| LS2 | $Li_2Si_2O_5$ phase | ρ | Density of material |
| LAS1 | $LiAlSi_4O_{10}$ phase | E | Young's modulus of elasticity (Elastic modulus) |
| LAS2 | $Li_{0.25}Al_{0.25}Si_{0.75}O_2$ phase | v | Poisson's ratio |
| LAS3 | $LiAlSi_2O_6$ phase | P | Force applied by the indenter |
| ICP-OES | Inductively coupled plasma- Optical Emission Spectroscopy | d | Two diagonals of the rhomb impression |
| | | Hv | Vickers hardness |

Contents

| | |
|---|-----------|
| ABSTRACT | V |
| CHAPTER ONE: INTRODUCTION..... | 1 |
| 1.1 Context of project | 1 |
| 1.2 Aim of project..... | 2 |
| 1.3 Objectives of project | 2 |
| 1.4 Outline of the thesis..... | 3 |
| CHAPTER TWO: LITERATURE REVIEW AND PRIOR STUDIES..... | 4 |
| 2.1 Biomaterials..... | 4 |
| 2.2 Bioceramics definition and classification | 5 |
| 2.3 Natural tooth | 5 |
| 2.3.1 Microstructure of natural tooth | 5 |
| 2.3.2 Appearance of natural teeth | 7 |
| 2.3.3 Mechanical properties of natural teeth | 7 |
| 2.4 Required Characteristics in Dental Ceramics | 8 |
| 2.4.1 Biocompatibility..... | 8 |
| 2.4.2 Chemical durability..... | 8 |
| 2.4.3 Aesthetics | 9 |
| 2.4.3.1 Translucency and opalescence | 9 |
| 2.4.3.2 Translucency and opalescence of dental ceramics..... | 10 |
| 2.4.3.3 Colour | 10 |
| 2.4.3.4 History of Newtonian Light Experiment | 10 |
| 2.4.3.5 Visual Detectors in the Retina | 11 |
| 2.4.4 Mechanical properties..... | 14 |
| 2.5 Theory on glass and glass ceramics..... | 15 |
| 2.5.1 Glass | 15 |
| 2.5.2 Glass ceramics | 18 |
| 2.6 The formation and heat treatment of glass ceramics | 18 |
| 2.6.1 Nucleation process | 20 |
| 2.6.1.1 Homogeneous nucleation..... | 21 |
| 2.6.1.2 Heterogeneous nucleation | 24 |
| 2.6.2 Crystals growth process..... | 26 |
| 2.6.3 Determination activation energy | 27 |
| 2.6.3.1 Kissinger method | 28 |
| 2.6.3.2 Modified Kissinger method..... | 29 |
| 2.6.3.3 Ozawa method..... | 30 |
| 2.7 Dental glasses and glass-ceramics..... | 30 |
| 2.8 Dental glass ceramics | 32 |
| 2.8.1 Lithium disilicate glass ceramics..... | 32 |
| 2.8.2 Lithium aluminosilicate glass ceramics..... | 33 |

| | |
|--|-----------|
| 2.9 Prior studies on Lithium disilicate and lithium aluminosilicate-based Glass-ceramics | 35 |
| 2.9.1 Lithium disilicate glass ceramics..... | 37 |
| 2.9.2 Lithium aluminosilicate (LAS) glass ceramics..... | 39 |
| 2.10 Effect of V₂O₅ and CeO₂ as colouring oxides on Li-Si glass-ceramics | 42 |
| 2.11 Commercial lithium disilicate-based glass-ceramics: IPS e.max®, Vita Suprinity and Celtra Duo .. | 43 |
| CHAPTER THREE: EXPERIMENTAL TECHNIQUES | 45 |
| Introduction | 45 |
| 3.1 Non-destructive characterization methods..... | 46 |
| 3.1.1 Chemical, structural, mechanical, and optical characterizations | 46 |
| 3.1.1.1 X-rays fluorescence spectroscopy (XRF)..... | 46 |
| 3.1.1.2 X-ray diffraction (XRD)..... | 47 |
| 3.1.1.3 Raman Spectroscopy (RS)..... | 49 |
| 3.1.1.3.1 Raman Spectroscopy (RS) principle | 49 |
| 3.1.1.3.2 Raman spectra of phosphate, lithium disilicate and lithium aluminosilicate phases | 51 |
| 3.1.1.4 Ultrasonic Testing (UT) | 52 |
| 3.1.1.4.1 Ultrasound waves generation..... | 52 |
| 3.1.1.4.2 Ultrasound waves | 53 |
| 3.1.1.5 Vickers Hardness | 56 |
| 3.1.1.6 Scanning Electron microscopy (SEM) | 56 |
| 3.1.1.7 Ultraviolet-visible spectroscopy | 58 |
| 3.1.1.8 Colorimetry..... | 59 |
| 3.1.1.9 Principles of colour measurement | 60 |
| I. Direct transmittance of light | 60 |
| II. Translucency parameter (TP) | 60 |
| III. Opalescence parameter (OP) | 61 |
| IV. Contrast ratio (CR)..... | 61 |
| 3.2 Destructive Methods..... | 61 |
| 3.2.1 Thermal, structural and chemical characterizations | 61 |
| 3.2.1.1 Differential scanning calorimetry (DSC) | 61 |
| 3.2.1.2 Inductively coupled plasma-Optical Emission Spectroscopy (ICP-OES)..... | 62 |
| 3.2.1.2.1 Inductively coupled plasma formation | 63 |
| 3.2.1.2.2 ICP-OES operating procedure | 63 |
| 3.2.2 Mechanical characterization..... | 64 |
| 3.2.2.1 Fracture Toughness by Vickers Indentation Fracture (VIF) | 64 |
| 3.2.2.2 Three-point flexural test..... | 65 |
| CHAPTER FOUR: MATERIALS AND RESEARCH METHODOLOGY | 69 |
| Introduction | 69 |
| 4.1 Materials | 70 |
| 4.1.1 Preparation of powder samples for XRF, DSC and ICP-OES | 70 |
| 4.2 Heat treatment | 71 |
| 4.2.1 Heat treatment design | 71 |
| 4.2.2 Heat treatment Process..... | 74 |
| 4.3 Characterisation of bulk glass and glass-ceramics system..... | 75 |
| 4.3.1 Sample preparation and XRF analyses | 75 |

| | |
|---|------------|
| 4.3.2 DSC analyses | 75 |
| 4.3.3 Inductively Coupled Plasma Optical Emission Spectroscopy (ICP-OES) sample preparation | 76 |
| 4.3.4 XRD analyses..... | 76 |
| 4.3.4.1 Room-temperature XRD analyses..... | 76 |
| 4.3.4.2 In-situ XRD analyses..... | 77 |
| 4.3.5 Raman spectroscopy | 77 |
| 4.3.6 Scanning Electrons Microscopy (SEM) sample preparation | 77 |
| 4.3.7 Ultrasound testing (UT) | 78 |
| 4.3.7.1 Sample preparation for UT | 78 |
| 4.3.7.2 UT Procedure | 79 |
| 4.4 Characterisation of the optical properties..... | 80 |
| 4.4.1 UV-visible spectroscopy | 80 |
| 4.4.2 Colorimetry..... | 81 |
| 4.5 Characterisation of mechanical properties of glass and glass-ceramics..... | 83 |
| 4.5.1 Hardness Test Procedure..... | 83 |
| 4.5.2 Fracture Toughness by Vickers Indentation Fracture (VIF) method..... | 84 |
| 4.5.3 Three-point bending..... | 85 |
| 4.5.3.1 Specimen preparation for three-point bending testing | 85 |
| 4.5.3.2 Three-point bending Test Procedure..... | 86 |
| CHAPTER FIVE: PROCESSING AND CHARACTERISATION OF THE LAS1 GLASS | 87 |
| Introduction | 87 |
| 5.1 Differential Scanning Calorimetry (DSC) Analyses | 87 |
| 5.1.1 DSC analyses of the as-cast LAS1 glass composition | 87 |
| 5.1.2 Impact of the heating rate on the thermal behaviour of LAS1 glass | 90 |
| 5.1.3 Thermal behaviour of LAS1 glass nucleated 550°C for 300 min measured at different heating rates..... | 91 |
| 5.1.4 Impact of the nucleation holding time on the thermal behaviour of LAS1 glass | 92 |
| 5.1.5 Thermal behaviour of LAS1 glass subjected to prior isothermal heat treatments..... | 93 |
| 5.2 Determination of Activation Energies | 95 |
| 5.2.1 Kissinger's method | 95 |
| 5.2.2 Modified Kissinger's method..... | 97 |
| 5.2.3 Ozawa's method..... | 99 |
| 5.3 In-situ high-temperature XRD patterns of LAS1 as-cast glass..... | 100 |
| 5.4 Ex-situ X- ray diffraction of LAS1 glass | 105 |
| 5.4.1 Phase assemblage after isothermal heat treatments at 550°C for different times | 105 |
| 5.4.2 Phase assemblage after heat treatment for 30 min in the 610°C to 870°C temperature range | 106 |
| 5.4.3 Phase assemblage after nucleation at 550°C for 300 min followed by heat treatments for 30 min in the 630°C to 870°C temperature range..... | 109 |
| 5.4.4 Crystallization pathway at 670°C..... | 111 |
| 5.4.5 Median crystallite size evolution for Li ₂ SiO ₃ heat treated at 670°C | 113 |
| 5.4.6 Crystallite size evolution for LiAlSi ₂ O ₆ | 115 |
| 5.4.7 LiAlSi ₂ O ₆ /Li ₂ Si ₂ O ₅ ratio between 730°C and 850°C | 116 |
| 5.5 Raman spectroscopy of LAS1 glass..... | 117 |
| 5.5.1 Impact of time on the nucleation at 550°C | 118 |
| 5.5.2 Raman spectra for LAS1 glass heat treated for 30 minutes in 610°C to 870°C temperature range | 120 |
| 5.5.3 Raman spectra for LAS1 glass nucleated at 550°C for 30 minutes and then heat treated for 30 minutes in 630°C to 870°C temperature range | 122 |

| | |
|--|------------|
| 5.5.4 Isothermal heat treatment at 670°C for different holding time | 124 |
| 5.6 Mechanical properties of LAS1 glass..... | 126 |
| 5.6.1 Elastic modulus..... | 126 |
| 5.6.1.1 Elastic modulus after isothermal heat treatments at 550°C for different holding times ... | 126 |
| 5.6.1.2 Elastic modulus after heat treatment for 30 min in the 630°C to 870°C temperature range | 127 |
| 5.6.1.3 Elastic modulus after nucleation at 550°C for 300 min followed by heat treatment for 30 min in the 630°C to 870°C temperature range | 128 |
| 5.6.2 Hardness..... | 129 |
| 5.6.2.1 Hardness after isothermal heat treatments at 550°C for different holding times | 130 |
| 5.6.2.2 Hardness after heat treatment for 30 min in the 630°C to 870°C temperature range | 131 |
| 5.6.2.3 Hardness after nucleation at 550°C for 300 min followed by heat treatment for 30 min in the 630°C to 870°C temperature range | 132 |
| 5.6.3 Fracture Toughness | 133 |
| 5.6.3.1 Fracture toughness after isothermal heat treatments at 550°C for different holding times | 134 |
| 5.6.3.2 Fracture toughness after heat treatment for 30 min in the 630°C to 870°C temperature range..... | 135 |
| 5.6.3.3 Fracture toughness after nucleation at 550°C for 300 min followed by heat treatment for 30 min in the 630°C to 870°C temperature range | 136 |
| 5.7 Optical properties of LAS1 glass..... | 137 |
| 5.7.1 L*a*b* values after isothermal heat treatments at 550°C for different holding times | 137 |
| 5.7.2 Colour evolution upon heat treatment for 30 min in the 630°C to 870°C temperature range.. | 138 |
| 5.7.2.1 L*a*b* values | 138 |
| 5.7.2.2 Colour matching with the VITA Classical shade guide standard | 140 |
| 5.7.3 Colour evolution after nucleation at 550°C for 300 minutes followed by heat treatment for 30 minutes in the 630°C to 870°C temperature range..... | 141 |
| 5.7.3.1 L*a*b* values | 141 |
| 5.7.3.2 Colour matching with the VITA Classical shade guide standard | 142 |
| 5.8 Phase assemblage, mechanical and optical properties of LAS1 glass following a two-step crystallisation process..... | 143 |
| 5.8.1 Phase assemblage | 143 |
| 5.8.1.1 Phase assemblage for samples nucleated at 550°C for 300 min, followed by a crystallisation step at 670°C and a second crystallisation step at 750°C or 780°C | 144 |
| 5.8.1.2 Phase assemblage for samples with a top crystallisation temperature of 830°C, 850 °C or 870°C | 146 |
| 5.8.1.3 Evolution of the crystallite size for LiAlSi ₂ O ₆ | 148 |
| 5.8.1.4 XRD peak intensity ratio for LiAlSi ₂ O ₆ /Li ₂ Si ₂ O ₅ | 149 |
| 5.8.1.5 Volume fraction of amorphous content | 150 |
| 5.8.2 Mechanical properties..... | 151 |
| 5.8.2.1 Elastic modulus | 151 |
| 5.8.2.2 Hardness | 154 |
| 5.8.2.3 Fracture toughness | 156 |
| 5.8.2.4 Flexural strength..... | 158 |
| 5.8.3 Optical properties..... | 159 |
| 5.8.3.1 colour..... | 159 |
| 5.8.3.2 Optical Transmittance | 163 |
| 5.9 Typical microstructure of nucleated and crystallised samples | 167 |
| 5.10 Transmission Electron Microscopy (TEM)..... | 169 |

CHAPTER SIX: PROCESSING AND CHARACTERISATION OF THE LAS2 GLASS

171

| | |
|--|------------|
| Introduction | 171 |
| 6.1 Differential Scanning Calorimetry (DSC) Analyses | 171 |
| 6.1.1 Impact of the heating rate on the thermal behaviour of LAS2 glass..... | 171 |
| 6.1.2 Thermal behaviour of LAS2 glass nucleated 550°C for 300 min measured at different heating rates..... | 172 |
| 6.1.3 Impact of the nucleation holding time on the thermal behaviour of LAS2 glass | 173 |
| 6.1.4 Thermal behaviour of LAS2 glass subjected to prior isothermal heat treatments..... | 174 |
| 6.2 Activation energy determination..... | 176 |
| 6.2.1 Kissinger's method | 176 |
| 6.2.1 Modified Kissinger's method..... | 178 |
| 6.2.2 Ozawa's method..... | 179 |
| 6.3 In-situ high-temperature XRD patterns of LAS2 as-cast glass..... | 180 |
| 6.4 Ex-situ X- ray diffraction of LAS2 glass | 183 |
| 6.4.1 Phase assemblage after isothermal heat treatments at 550°C for different times | 183 |
| 6.4.2 Phase assemblage after heat treatment for 30 min in the 610°C to 870°C temperature range | 184 |
| 6.4.3 Phase assemblage after nucleation at 550°C for 300 min followed by heat treatments for 30 min in the 630°C to 870°C temperature range..... | 187 |
| 6.4.4 Crystallization pathway at 670°C..... | 189 |
| 6.4.5 Median crystallite size evolution for LiAlSi ₄ O ₁₀ , Li _{0.25} Al _{0.25} Si _{0.75} O ₂ and Li ₂ SiO ₃ heat treated at 670°C | 191 |
| 6.4.6 Evolution of the crystallite size for LiAlSi ₂ O ₆ | 192 |
| 6.4.7 XRD peak intensity ratio for LiAlSi ₂ O ₆ /Li ₂ Si ₂ O ₅ between 730 and 850 °C | 194 |
| 6.5 Raman spectroscopy of LAS2 glass..... | 195 |
| 6.5.1 Impact of time on the nucleation at 550°C | 195 |
| 6.5.2 Raman spectra for LAS2 glass heat treated for 30 minutes in 610°C to 870°C temperature range | 197 |
| 6.5.3 Raman spectra for LAS2 glass nucleated at 550°C for 30 minutes and then heat treated for 30 minutes in 630°C to 870°C temperature range | 197 |
| 6.5.4 Isothermal heat treatment at 670°C for different holding time | 200 |
| 6.6 Mechanical properties of LAS2 glass..... | 200 |
| 6.6.1 Elastic modulus..... | 200 |
| 6.6.1.1 Elastic modulus after isothermal heat treatments at 550°C for different holding times ... | 201 |
| 6.6.1.2 Elastic modulus after heat treatment for 30 min in the 630°C to 870°C temperature range | 201 |
| 6.6.1.3 Elastic modulus after nucleation at 550°C for 300 min followed by heat treatment for 30 min in the 630°C to 870°C temperature range | 203 |
| 6.6.2 Hardness | 204 |
| 6.6.2.1 Hardness after isothermal heat treatments at 550°C for different holding times | 204 |
| 6.6.2.2 Hardness after heat treatment for 30 min in the 630°C to 870°C temperature range | 205 |
| 6.6.2.3 Hardness after nucleation at 550°C for 300 min followed by heat treatment for 30 min in the 630°C to 870°C temperature range | 206 |
| 6.6.3 Fracture Toughness | 207 |
| 6.6.3.1 Fracture toughness after isothermal heat treatments at 550°C for different holding times | 208 |
| 6.6.3.2 Fracture toughness after heat treatment for 30 min in the 630°C to 870°C temperature range | 208 |
| 6.6.3.3 Fracture toughness after nucleation at 550°C for 300 min followed by heat treatment for 30 min in the 630°C to 870°C temperature range | 209 |
| 6.7 Optical properties of LAS2 glass..... | 210 |
| 6.7.1 L*a*b* values after isothermal heat treatments at 550°C for different holding times | 210 |
| 6.7.2 Colour evolution upon heat treatment for 30 min in the 630°C to 870°C temperature range.. | 211 |
| 6.7.2.1 L*a*b* values | 211 |

| | |
|---|------------|
| 6.7.2.2 Colour matching with the VITA Classical shade guide standard | 213 |
| 6.7.3 Colour evolution after nucleation at 550°C for 300 minutes followed by heat treatment for 30 minutes in the 630°C to 870°C temperature range..... | 214 |
| 6.7.3.1 L*a*b* values | 214 |
| 6.7.3.2 Colour matching with the VITA Classical shade guide standard | 215 |
| 6.8 Phase assemblage, mechanical and optical properties of LAS2 glass following a two-step crystallisation process..... | 216 |
| 6.8.1 <i>Ex-situ</i> XRD of heated treated LAS2 glass selected | 217 |
| 6.8.2 Evolution of the crystallite size for LiAlSi ₂ O ₆ | 219 |
| 6.8.3 XRD peak intensity ratio for LiAlSi ₂ O ₆ /Li ₂ Si ₂ O ₅ between 830°C and 850°C | 220 |
| 6.8.4 Mechanical properties..... | 221 |
| 6.8.4.1 Elastic modulus | 221 |
| 6.8.4.2 Hardness | 222 |
| 6.8.4.3 Fracture toughness | 223 |
| 6.8.5 Optical properties..... | 224 |
| 6.8.5.1 Colour | 224 |
| 6.8.5.2 Colour matching against VITA Classical shade guide standard | 225 |
| CHAPTER SEVEN: GENERAL DISCUSSION | 227 |
| 7.1 Glass composition | 227 |
| 7.2 Thermal behaviour and phase assemblages..... | 229 |
| 7.3 Mechanical properties | 233 |
| 7.3.1 Elastic modulus, hardness and fracture toughness | 233 |
| 7.3.2 Flexural strength..... | 234 |
| 7.4 Optical properties | 236 |
| CHAPTER EIGHT: CONCLUSION AND FUTURE WORK..... | 239 |
| 8.1 Conclusion | 239 |
| 8.2 Future Work..... | 240 |
| REFERENCES..... | 241 |

Chapter

1

Introduction

Chapter One: Introduction

1.1 Context of project

Every year millions of individuals undergo dental treatment in order to repair damaged teeth, but also to replace anaesthetic and dysfunctional teeth or simply to restore missing teeth. These interventions are motivated, first by the rehabilitation of the oral functions and then by the improvement of oral aesthetics. Various materials exist that meet the strict constraints in terms of mechanical properties (fracture toughness, flexural strength, and wear resistance), chemical durability in the oral environment and aesthetics (shade, translucency). Moreover, bio-compatibility and bio-functionality are the essential characteristics required for the manufacturing of dental implants [1]. In addition, commercial prosthetic dental materials need to be suitable for computer aided design–computer manufacture (CAD/CAM) technologies [2]. Nowadays, CAD/CAM technology is commonly employed in the fabrication of many dental prosthetic restorations such as crowns, onlays, inlays and veneers, just to name a few. Traditionally, fabrication of these restorations is conducted in a dental laboratory, however lately this can take place next to the dentist's chairside [3]. Importantly, the mechanical performance of dental prostheses results from a combination of factors, including material's intrinsic physical characteristics (such as phase assemblage, microstructure) and the sophistication of the fabrication procedures. Basically, the effectiveness of a dental CAD/CAM system is simultaneously dictated by the precision of the system and the underlying properties of the material [4]. In summary, a material suitable for dental applications needs to exhibit both suitable intrinsic mechanical strength and aesthetics, but also should be amenable to be shaped into the required contour via CAM processes. CAM milling procedures are likely to create undesirable surface defects, which undermine mechanical strength [5]. Thus, achieving the best possible surface finishing is vital, as this will ultimately determine the effectiveness of a dental prosthetic restoration.

Glass-ceramic materials, that are ceramics produced via controlled nucleation and crystallization of glass [6], can interestingly meet all the requirements listed above. Indeed, glass-ceramics and specifically lithium disilicate glass-ceramics have been used for various applications due to their extraordinary aesthetics,

good mechanical properties and ease of modelling into final restoration [7]. Lithium disilicate together with leucite and leucite-apatite, as listed in Table 2. 4, are the most prominent glass-ceramics used in dentistry. In fact, leucite is commonly used for veneering metal alloys and lithium disilicate glass-ceramics are employed in the fabrication of cores. The usefulness of lithium disilicate-based glass-ceramics as a dental material is associated to the ability to tailor its mechanical and aesthetical properties via modification of its composition and microstructure. Moreover, lithium disilicate glass-ceramics exhibit strengths three to four times greater than leucite glass-ceramics [8], in addition to their excellent chemical durability and aesthetics.

1.2 Aim of project

This thesis is focused on two novel compositions of glass-ceramics supplied by an international dental materials company. These two glasses compositions are based on ternary $\text{Li}_2\text{O}-\text{SiO}_2-\text{Al}_2\text{O}_3$ (LAS) system. LAS glass-ceramics can be found in several technological application ranging from cooktop plates to telescope mirrors [9][10]. LAS glass-ceramics are known to exhibit excellent chemical durability and suitable aesthetics for dental restorations; however, these exhibit low-to-moderate mechanical properties. Their flexural strength varies between 100-250 MPa and the fracture toughness is lower than $1.5 \text{ MPa}\sqrt{\text{m}}$ [11]–[13].

The overall aim of this study is to investigate two newly developed LAS-based glass-ceramics, in terms of phase assemblage, mechanical and aesthetics characteristics, and to compare with those of lithium-disilicate glass-ceramics and others. In practice, this study aims at supporting knowledge-transfer into the field of glass-ceramics.

1.3 Objectives of project

The key objectives of this study are as follows:

- Exploration and optimisation of heat treatments, essentially studying the impact of nucleation and crystallisation temperatures on mechanical properties including flexural strength, elastic modulus, hardness, fracture toughness and optical properties including colour and light transmission.

- Establishment of correlations between phase assemblage and mechanical properties, i.e. volume fraction of different crystals embedded in the glassy matrix, type of crystals in terms of crystal structure and composition, their dimensions and spatial distribution.
- Investigation of processing parameters leading to optimised aesthetics, consistent with the VITA classical shade guide, which is widely used in dental clinics.

1.4 Outline of the thesis

This thesis consists of eight chapters; the ***first chapter*** is an introduction setting the context of the thesis. The ***second chapter*** reviews glass-ceramics in the context of dental applications. The ***third chapter*** describes the fundamentals of the techniques employed in this study. The ***fourth chapter*** details the experimental procedures. The ***fifth and six chapter*** provides results and discussion of properties for both types of glass-ceramics used in this study. This chapter compares results with recent related studies. Finally, ***seventh chapter*** presents the general discussion, which is followed by an ***eighth chapter*** that proposes the conclusions and further work.

Chapter | 2 |

Literature Review and Prior Studies

Chapter Two: Literature Review and Prior Studies

2.1 Biomaterials

Biomaterials is an umbrella term which encompasses synthetic or natural materials, such as metals, ceramics, polymers, collagen [14], as shown in Fig. 2. 1. Synthetic biomaterials can be described how do they interact with biological systems and how they are used in the construction of medical devices. Indeed, in the 1986 Proceedings of a Consensus Conference of the European Society for Biomaterials, a biomaterial was defined as "***A nonviable material used in a medical device, intended to interact with biological systems***" [15].

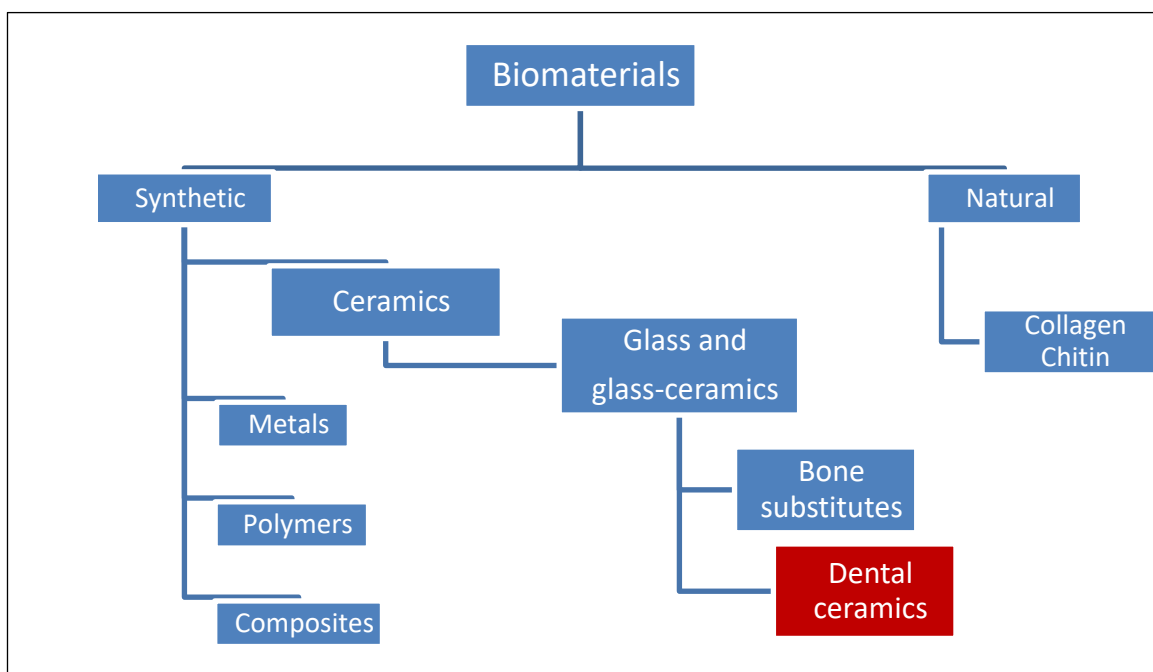


Fig. 2. 1 Classifications of biomaterials [14].

Biomaterials are used widely in medicine, with most common applications being addition of hard tissues to the human body in the form of hip and knee joint prosthesis. Biomaterials are also extensively employed in the field of dentistry; here, biomaterials replace natural tissues such as dentine and enamel. The use of biomaterials has grown considerably over the past twenty years. Recent research conducted on biomaterials showed the significant development in their overall performance, but there is ongoing research to improve the functionality of these materials [3].

2.2 Bioceramics definition and classification

A ceramic is commonly defined as an ‘inorganic, non-metallic material’. Ceramics, when used for biomaterial applications, are referred to as bioceramics. There has been considerable research done on bioceramics, and steady progress has been made on the clinical use of such materials [16], [17]. Bioceramics are used for reconstruction purposes such as for bone replacement. This particular use accounts for a majority of the global biomaterials consumption [3].

Bioceramics are classified into three separate classes as per their tissue response; bio-passive ceramics, bioactive ceramics and bio-resorbable ceramics [17], [18]. The latter two types of bioceramics show interaction with biological tissue [19]. Bio-passive ceramics (also called bioinert ceramics) show no interaction with biological tissues [3], [20] and hence are most suited to fulfil mechanical and aesthetic characteristics. The popularity of dental ceramics is increasing rapidly in the world of bioceramics. These are commonly utilized to replace missing teeth through crown and bridge constructions [21]. In such cases, the mechanical performance of the material and its durability and aesthetics are crucial elements.

2.3 Natural tooth

2.3.1 Microstructure of natural tooth

Natural tooth is basically composed of three parts: crown, root and neck. The latter is the region in-between the crown and the root [22]. The crown is the part visible in the mouth, whereas the root is the part inside the bone socket.

The tooth contains four types of tissue: enamel, dentin, pulp and cementum, as schematically illustrated in Fig. 2. 2 [23], [24]. The external most layer of the tooth is the enamel; it also covers the crown, which is exposed to the oral cavity. Enamel is naturally milky white to light yellow, depending upon the thickness and level of mineralization [25]. The thickness is approximately 2.5 mm [26], and is depicted in Fig. 2. 2. It is widely regarded as the hardest bone of the human body [27] and is brittle due to the high mineral level (~96 wt%), and low of organic content (~4 wt%) [24], [28], [29]. The functionality and strength of the enamel can be attributed to its microstructure, as illustrated in Fig. 2. 2, which prevents crack

Chapter Two: Literature Review and Prior Studies

propagation, stopping it from reaching the dentin-enamel junction, and also preventing delamination of the tissues [25].

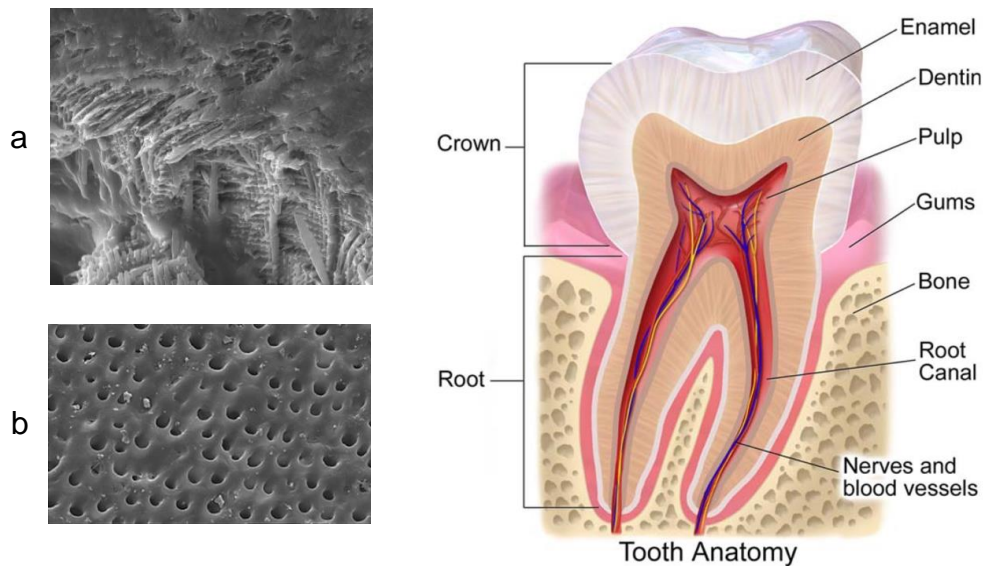


Fig. 2. 2 Sectional view and microstructure of a human tooth [30] [31], a) enamel [25] and b) dentin [32].

Dentin is also a hard tissue, which forms the majority of the tooth and is covered by a layer of enamel and cementum, and it surrounds the pulp; this is depicted in Fig. 2. 2. Dentin in contrast to enamel, grows throughout the life of a human, is responsive to stimuli which occur following tooth decay and abrasion [25]. Fig. 2. 3 displays comparison of a natural tooth with the common dental implant design that consists of a crown which is frequently a glass-ceramic and a screw-shaped implant which is fabricated from titanium [33], [34].

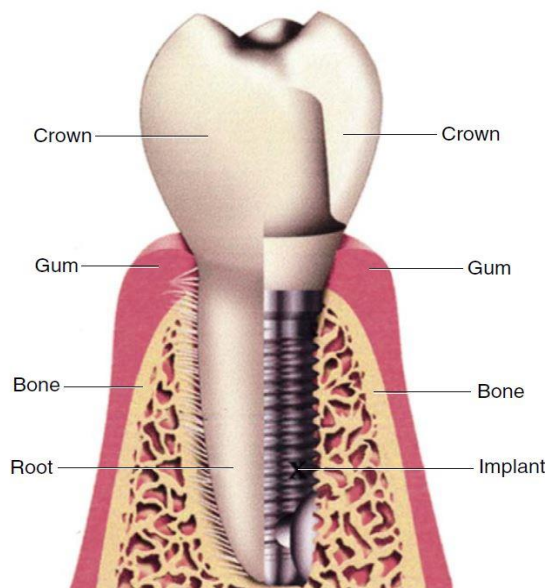


Fig. 2. 3 Comparison of a natural tooth with the dental implant; a crown and screw-shaped implant [35].

2.3.2 Appearance of natural teeth

The colour of the tooth, opacity, opalescence, translucency and metamerism are important in the dentistry [22], [36]. Such optical properties determine the outward appearance of the tooth. Hence, it is a combination of the optical properties of the tooth and the natural structure of the tooth, which determines its colour [25]. As shown above, the dental crown is composed of several layers, enamel, dentin and pulp. When light impinges the tooth, there are three possibilities; the light could get absorbed, reflected or transmitted through the tooth. This could occur in all layers with varying levels of intensity. It is evident that the colour of dentin plays a major role in establishing the colour of the tooth as a whole [25], this is shown in Fig. 2. 4, and according to Bosch et al. [37], dentin is responsible for the colour of the tooth.



Fig. 2. 4 Tooth layers: pulp, dentin and enamel [25].

2.3.3 Mechanical properties of natural teeth

Understanding of the mechanical properties of the natural teeth assists the development of dental materials [25], [38]. Human teeth are capable of withstanding pressures for prolonged periods of time. According to certain studies [17], [31], dentin and enamel should be capable of resisting a pressure of 20 MPa for approximately three thousand times each day. Nevertheless, it is extremely rare to see a complete tooth fracture in practice. The natural enamel is extremely hard and rigid, and similarly, dentin offers high levels of flexibility and toughness

to the tooth. Enamel is approximately five times stronger than dentin. But still, it should offer a level of flexibility to the soft dentin below it. As a result, the enamel is brittle and may break easily in contrast to dentin. This is depicted in Table 2. 1.

Table 2. 1 Summary of the mechanical properties of the natural tooth (enamel and dentin).

| Property | Enamel | Dentin |
|--|--------------------------------|-----------------------------------|
| Density g/cm³ | 2.96-3.02 [25], [39] | 1.29-2.4 [25], [39] |
| Elastic modulus GPa | 48-120 [22], [25], [39] | 16-24 [22], [25], [39] |
| Fracture toughness MPam^{1/2} | 0.6-1.5 [39] | 2.2-3.1 [39] |
| Flexural strength MPa | 60-90 [25] | 245-280 [25] |
| Hardness GPa | 3-6 [22], [25], [39] | 0.13-0.92 [22], [25], [39] |

2.4 Required Characteristics in Dental Ceramics

2.4.1 Biocompatibility

Biocompatibility is defined as the ability of a material to exist and integrate with surrounding living tissues without causing any harm. During the Conference of the European Society for Biomaterials in 1987, the definition was presented as: "***Biocompatibility refers to the ability of a material to perform with an appropriate host response in a specific situation***" [40].

With regard to the use of ceramics in the medical field, its biocompatibility becomes the most important characteristic upon which its application depends [1], [41], [34].

2.4.2 Chemical durability

The durability of materials is defined as the resistance of its surface to corrosion, which includes both physical and chemical changes, which can be induced by interaction with the surrounding environment, such as an aqueous solution of acids, salts, and alkalis, etc. Therefore durability is a property that can be related to four key components; the surface state of the material, its composition, and structure as well as the corrosive nature of the surrounding environment [42], [43].

Impact of glass composition on durability property has been investigated and continues to be under scientific investigations [44]. The chemical durability of glass-ceramic materials arises as a result of several factors, including:

- The ratio of the glass oxides which are added, i.e. the collection and nature of the crystalline phases which are formed.
- Composition of the residual glass phase, which in turn depends on the nature of glass composition and how the heat treatment has been controlled [43], [45].

2.4.3 Aesthetics

The ever-growing demand from patients and doctors alike for more aesthetic designs coupled with the emergence of CAD/CAM caused an increasing demand in the aesthetic development of dental materials over the past two decades [46], [47]. Aesthetics play an important role when establishing the use of bio-ceramic materials [48], this is especially important for dental implants [7], [26], [27] and the replacement of missing teeth [49].

The colour of a restoration should be on par with those structures around it. To develop such a material, the optical materials of the restorative material should be identical to those of natural teeth [16], [21].

An artificial tooth to display similar attributes to a biological tooth would need to reflect, diffuse, absorb and transmit light, which impinges its outer layer [52].

Colour can be categorised by CIE LAB colour system established by the CIE (Commission Internationale de l'Eclairage) [53]. This system is also referred to as the CIE $L^*a^*b^*$, where L^* representing lightness, a^* for green-red and b^* for blue-yellow colour components [54]. Other important factors which determine optical properties include opalescence, fluorescence, surface texture and translucency [54], [55].

2.4.3.1 Translucency and opalescence

The translucency of the material permits light to pass through the object without scattering [56]. Opalescence is the opposite of transparency, which is the prevention of the passage of light though a material or the transmittance is negligible to be considered. In the case of transparent objects, the amount of reflected light is extremely small or insignificant [56]. As an example, glass reflects a maximum of 4% of the light from an object-air interface, whereas it absorbs 1% [3].

2.4.3.2 Translucency and opalescence of dental ceramics

The enamel section of the human tooth is transparent to a considerable degree. Translucency and opalescence are attributes that should be present in dental materials [57], [58]. These are important parameters for assessing the aesthetic aspect of dental materials [58]–[60]. There is a challenge when developing dental ceramics, which are able to possess sufficient mechanical strength whilst maintaining the required optical properties [61].

2.4.3.3 Colour

Colour is the visual perception produced from the stimulation of the light-sensitive receptors of the human retina when light falls upon it. These light-sensitive receptors are referred to as cones [62].

Light can be defined as the range in the electromagnetic spectrum, which can be detected by the human eye. The colour spectrum formed when light passes through a spectrum range from wavelengths of 380 to 760 nm (CIE 1987). Every colour has a unique wavelength value; these values are identical to the values of colours found in the spectrum. As an example, the perception of red colour is produced as a result of the longest wavelength (760 nm), and the shortest wavelength (380 nm) produces the violet light perception [63].

2.4.3.4 History of Newtonian Light Experiment

Newton first conducted experiments using colour in 1671; he discovered that when passing a beam of sunlight through a prism produced a band of colours, which was referred to as a spectrum [64]. This is shown in Fig 2. 5.

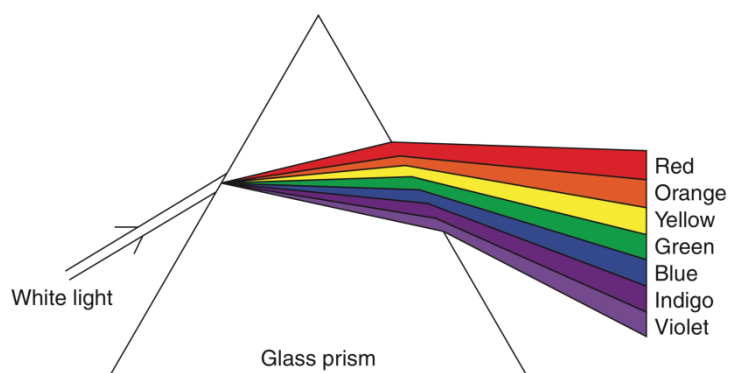


Fig. 2. 5 Newton's prism experiment [65].

He realized that the spectrum consisted of seven different colours which were arranged as red, orange, yellow, green, blue, indigo, and violet, as seen in Fig. 2. 5. He proposed the idea that white light is formed from the overlap of these colours. However, Newton noted that this spectrum was present only in nature but everywhere. In addition, colours could be created from the dilution of other colours by adding white, causing changes to their saturation [63].

2.4.3.5 Visual Detectors in the Retina

The retinal layer of the human eye is responsible for the perception of light and is composed of rods and cones, which acts as photoreceptor cells. These two cells respond differently to different light coordinates arising from a distance [62]. Rods have greater sensitivity and are responsible for vision during the night (or under dim light conditions), cones are responsible for daytime vision [63].

The function of cones is to transmit the signal of the rate of photon absorption; however, it is the wavelength that determines the rate of absorption. The signal which is transmitted from the cones does not include any information on the colour. The sensation of colour is derived from the relative degrees of signals which get filtered through the three detectors and the cone pigments found in the retina [63]. These signals reach the optic nerve, from where it is transmitted to the brain for interpretation to produce colour [65].

There are three different sets of colour-receptive elements in cone cells; these are L-cones which are sensitive to red and long wavelengths (560 nm – 580 nm), M-cones sensitive to green and medium wavelengths (530 nm – 540 nm), S-cones sensitive to blue and short wavelengths (420 nm – 440 nm) [53], this is depicted in Fig. 2. 6.

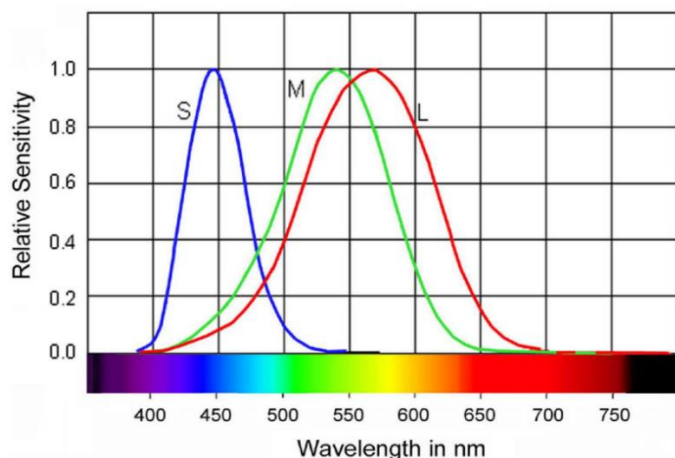


Fig. 2. 6 Relative spectral sensitivities for the three types of cones in a linear scale [63].

The tri-stimulus values RGB are described as the amount of three-color stimuli of the trichromatic system, which is responsible for the colour of the stimulus. The tri-stimulus values are a form of practical measurement to assess the intensity of the light, taking into account the values of the primary colours (red, green and blue) [66].

In 1931, the International Commission on Illumination (CIE) introduced a different system named as CIE XYZ colour space. This colour space was a result of the work done by William David Wright and John Guild in the later part of 1920 [63], [67]. Here, the tristimulus RGB values of colour would be denoted by X, Y, and Z coordinates in CIE XYZ system.

X, Y and Z tristimulus values can be precisely calculated by integrating of the colour stimulus multiplied by the respective colour matching function of the observer over the full visible extend of wavelengths, which is 380 nm to 780 nm [53], as shown in Fig. 2. 7. In the case of objects, with regards to reflection, noticed that the production of the colour stimulus was a result of the absolute spectral reflectance of the object and the relative spectral power of the illuminate, hence, it can be expressed as follows mathematically [68], [69]:

$$X = k \int S(\lambda) \cdot R(\lambda) \cdot \bar{x}(\lambda) d\lambda$$

$$Y = k \int S(\lambda) \cdot R(\lambda) \cdot \bar{y}(\lambda) d\lambda$$

$$Z = k \int S(\lambda) \cdot R(\lambda) \cdot \bar{z}(\lambda) d\lambda$$

Where k constant is selected, $\bar{x}(\lambda)$, $\bar{y}(\lambda)$, $\bar{z}(\lambda)$ represent the respective colour-matching function of the observer, $R(\lambda)$ refers to the absolute reflectance of the object, and $S(\lambda)$ is the spectral power of the illuminating. Therefore, $Y_n = 100$ is the appropriate reference white (CIE Tristimulus Values).

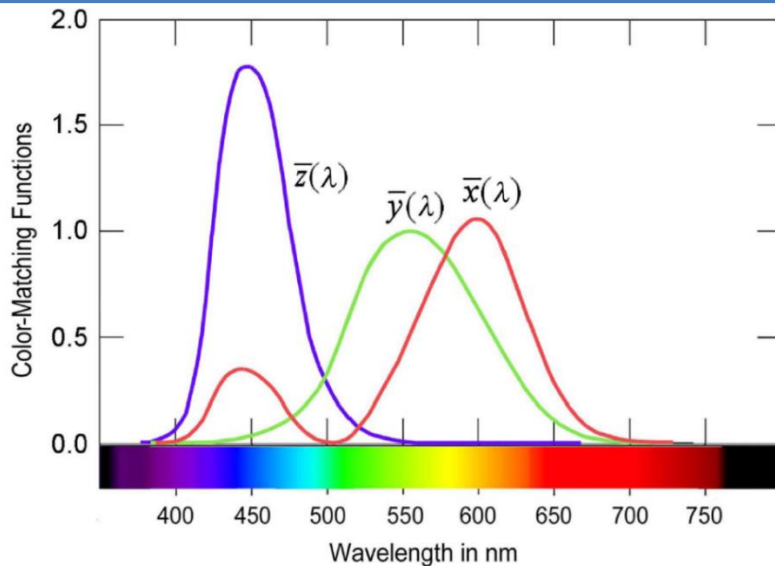


Fig. 2. 7 Three colour-matching function of the observer for a 2° field [63].

The CIE congress in 1976 recommended the use of CIE Lab space for measuring the colour of an object. The newly designed system takes use of color space values from X, Y, Z [53]. This is the commonest space utilized for object color measurements [70] and the most accurate means of representation [71]. This makes it proper in numerous different industries and more efficient than the other colour system such as RGB and CMYK [71].

Three values comprise of the CIE Lab color, these are L, a, and b. L represents the lightness and is 100 for white and 0 for black. a and b represent chromaticity coordinates, positive a [+] for red and negative a [-] for green, positive b for [+] yellow and negative b [-] for blue. The equations for converting between the CIE X, Y, Z system to the CIE L, a, b system are given below [53], [63], [65];

$$L = 116 \left(\frac{Y}{Y_n} \right)^{1/3} - 16 \quad \text{for } \frac{Y}{Y_n} > 0.008856$$

$$L = 903.3 \left(\frac{Y}{Y_n} \right) \quad \text{for } \frac{Y}{Y_n} \leq 0.008856$$

$$a = 500 \left[f \left(\frac{X}{X_n} \right) - f \left(\frac{Y}{Y_n} \right) \right],$$

$$b = 200 \left[f \left(\frac{Y}{Y_n} \right) - f \left(\frac{Z}{Z_n} \right) \right]$$

Values of X_n , Y_n and Z_n are the CIE tristimulus values of the reference white point. Hence, when it is the system under D_{65} (artificial daylight) illuminate

Chapter Two: Literature Review and Prior Studies

condition, the X_n , Y_n and Z_n are 95.053, 100 and 108.9 respectively for 2° field [63], [68], [72], as shown in Fig. 2. 7.

There are numerous studies [72]–[75] which have taken use of the Commission Internationale de l'Eclairage (CIELab) system to assess the colour values for ceramics, which are utilized for dental applications. Standard values of CIELab values for white and black backgrounds are taken as standard backgrounds; this differs as per reference; this is depicted in Table 2. 2.

Table 2. 2 CIELab values of white and black backgrounds.

| References | White background | Black background |
|------------|------------------------------------|------------------------------------|
| [76] | CIE L = 93.2, a = 0.7, b = 1.7 | CIE L = 2.8, a= 0.7, b= 1.9 |
| [77] | CIE L = 96.97, a = -0.14, b = -0.2 | CIE L = 1.43, a = -0.13, b = -0.62 |
| [78] | CIE L = 88.81, a = - 4.98, b=6.09 | CIE, L = 7.61, a = 0.45, b = 2.42 |
| [79] | CIE L = 93.7, a = -0.3, b = 2.9 | CIE L = 9.1, a = -0.2, b = 0.3 |
| [80] | CIE L =88.83, a =-4.95, b =-6.07 | CIE L =7.60, a = 0.45, b = 2.44 |

2.4.4 Mechanical properties

Glass-ceramics are typically hard and stiff but brittle. These properties can be attributed to the special chemical bonds mostly ionic bonds formed through the electrostatic attraction between positive and negative ions found within these materials [81], [82]. Apart from the optical properties of ceramic, such as colour and translucency, it possesses high levels of flexural strength and toughness [81], [83], [84].

According to Arun [85], the mechanical properties of glass-ceramic can be attributed to the crystal size. Hence, glass-ceramics are strong, which can be associated with small crystal size and semi zero-porosity [86], [87].

Glass-ceramics also possess larger fracture toughness when compared to glass, as the path of fracture gets deflected through the crystalline particles, which prevent crack propagation and retard it [88].

If glass-ceramics are to be used in dentistry, they should offer properties such as ideal optical properties, colour, biocompatibility and ease of production. One of the most important factors to be fulfilled is possessing mechanical strength, which is on par with the natural human teeth [9], [89]. In order to accomplish this, there are two approaches, the first approach being regulation of the heat treatment process or secondly to enhance the composition of glass [90]. Since the dental restorative materials are used in load-bearing structures, their mechanical

properties such as strength, toughness and hardness are considered critical for such applications [3]. The mechanical dental strengths are classified using methods in which a force is applied [91].

2.5 Theory on glass and glass ceramics

2.5.1 Glass

Glass was first studied in the 1930s by Tammann and was described as an aggregate material in a vitreous state. This shaped the modern definition of glass as an amorphous or non-crystalline material [92]. The American Society for Testing and Materials (ASTM) provided the most widely accepted definition for glass and stated "***Glass is an inorganic product of fusion which has cooled from a liquid to a rigid condition without crystallising***" [93].

Solid materials can be broadly divided as amorphous (vitreous (glassy), non-crystalline) or crystalline (ordered). However, the smallest basic structure of amorphous glass is similar to the crystalline structure. The only difference is that there is no particular arrangement in the glass. This is shown in Fig. 2. 8.

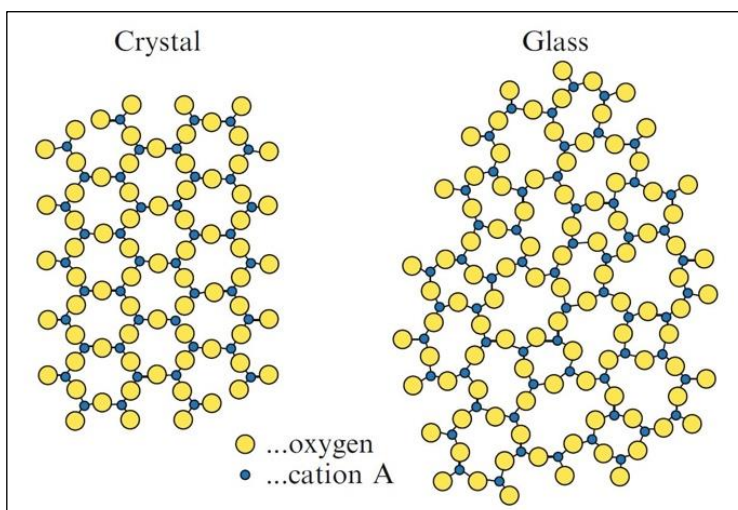


Fig. 2. 8 Structure of glass and glass crystalline ceramic [3].

Formation of glass occurs on rapid cooling from melting. The mobility of the atoms is restricted when cooling rapidly; this causes solidification to occur rather than crystallization, rendering an amorphous structure. The amorphous nature can be recognized from the random distribution of atom distances and bond angles, which develops a non-equilibrium state within the material [94].

Chapter Two: Literature Review and Prior Studies

The structure formed in this manner are thermodynamically unstable, offering the ability to transform into a crystalline structure. In which the ordered crystalline structure requires minimum free energy and is the preferred thermodynamic choice for the system (this will be explained again with crystallization process). During crystallisation there is a discontinuous volume change at a certain temperature. This temperature is referred to as the point of freezing, T_f . However, glass continues to cool below T_f without any discontinuous volume change, resulting in a “supercooled liquid”. After a certain point, the gradient of the volume-temperature curve drops suddenly, resembling the curve for a crystalline material. This is a point that the supercooled liquid becomes a glass, called the glass transition temperature of the materials (T_g), as shown in Fig. 2. 9 [94].

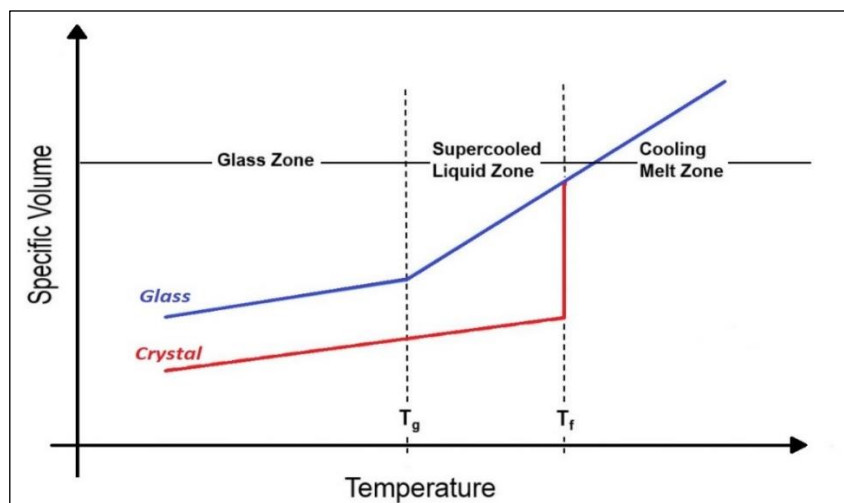


Fig. 2. 9 Behaviour of specific volume with temperature (T_f and T_g points) in the formation of glass solid and crystalline solid [94].

Glass can be produced from melting glass batches at temperatures in the range of 1200– 1600°C [95]–[97]. Subsequently it can be quenched and annealed, as depicted in Fig. 2. 10. Finally, crystallization can be promoted by increasing the temperature to a level, where the atomic kinetic energy is increased.

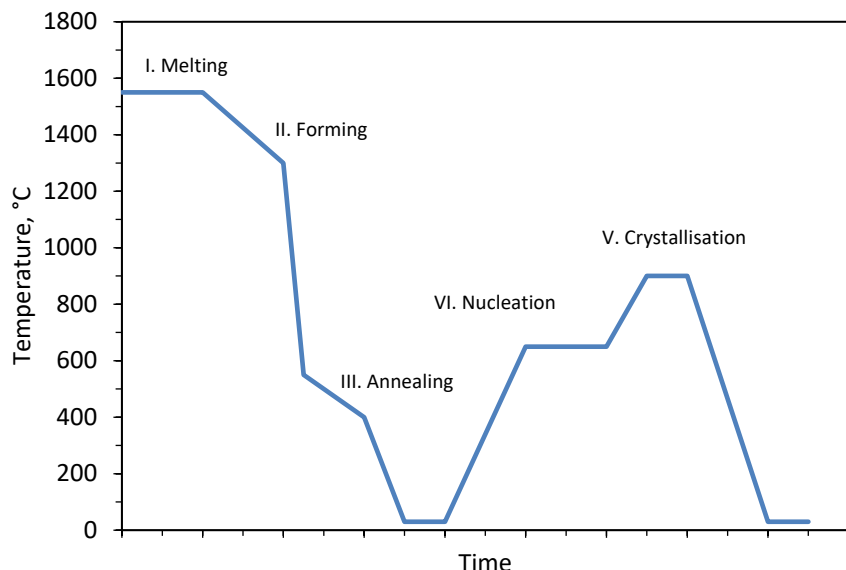


Fig. 2. 10 The stages of formation and processing of glass and glass-ceramics [3].

A glass batch may consist of 5–12 components, but there are only four to six main compounds. The most important compound in glass forming is usually silica. Alumina is not a glass former, but a conditional glass former, as in the presence of other act as a glass former. Alumina is a vital compound in the dental glass industry. This is because of the extreme chemical stability, excellent biocompatibility, resistance to corrosion, resistance to wear, strength and minimal friction [3],[21]. Several other compounds are used in dental glass manufacturing, to enhance the overall properties (refer to Table 2. 3) of the glass-ceramics, such as CeO_2 , Fe_2O_3 and V_2O_5 , which assist in creation of coloured shades [3].

Table 2. 3 Oxides added to the chemical composition of glass and their impact [3], [99].

| Oxides | Chemical name | Utility |
|-------------------------|-------------------|---|
| Al_2O_3 | Alumina | -to enhance chemical solubility |
| CaO | Calcium oxide | -to reduce viscosity -to improve the flow |
| CeO_2 | Cerium (IV) oxide | -used to modify the refractive index -to bestow fluorescence, like to the natural teeth |
| Cs_2O | Caesium oxide | -used to stabilize the residual glass phase -to improve refractive index -to improve translucency -to reduce viscosity |
| Fe_2O_3 | Iron (III) oxide | -to assist just in creating coloured shades |
| K_2O | Potassium oxide | -to reduce viscosity |
| Na_2O | Sodium oxide | -to reduce viscosity |
| NiO | Nickel (II) oxide | -to assist in creating coloured shades |
| P_2O_5 | Phosphorus oxide | -using as a nucleating agent and opacifiers |
| ZrO_2 | Zirconium oxide | |
| TiO_2 | Titanium oxide | |
| SrO | Strontium oxide | -to improve refractive index -to improve translucency |

| | | |
|--------------------------------|--------------------|--|
| Ta ₂ O ₅ | Tantalum oxide | -to modify the refractive index -to enhance the nucleation -to improve chemical solubility |
| V ₂ O ₅ | Vanadium (V) oxide | -to assist in creating coloured shades |
| ZnO | Zinc oxide | -to enhance chemical solubility -to increases the maturing temperature -to produces bright and glossy colours. |

The composition of glass can have a major effect on the biological response, determining if the particular material becomes bioactive, biopassive or bio-resorbable [17], [18]. Glass systems such as Li-Si (LS), Ca-Al-Si (CAS), Zn-Al-Si (ZAS), Mg-Al-Si (MAS) and Li-Al-Si (LAS) are common in numerous applications owing to their favourable properties, mainly in the field of dentistry [98].

2.5.2 Glass ceramics

Glass-ceramics fall under the classification of polycrystalline structural materials [100]. The very first glass-ceramic material classification was developed by Stookey [101]. This has been done by controlled crystallization of an appropriate glass composition. The heat treatment procedure is carefully controlled to obtain the desired properties, morphology, and relative volume of crystalline phases.

Glass-ceramics (heat-treated glass) can reach high crystallinity levels, in the range of 50–90% of the volume fraction. Amorphous vestiges will remain within the ceramic structures [102]. Such vestiges are glassy and, upon completion of crystallization, differ significantly from the parent glass owing to the depletion of ions and the formation of crystal phases in the ceramic [103].

2.6 The formation and heat treatment of glass ceramics

For the production of glass ceramics, glass, once formed, has to undergo changes through two stages known as nucleation and crystal growth (also known as crystallization) [3], [104]. The combination of these two stages gives rise to the process known as the process of heat treatment. Therefore, it is the amount of control applied to the process of heat treatment that plays a key role in the formation of characteristic glass-ceramics [1], [22], [23], [35], and the properties of the ceramics produced can be further enhanced depending on the mineral phases which are developed [6]. The primary factors [3], [107] which need to be controlled during heat treatment include:

- Nucleation temperature.

- Crystallisation temperature.
- Rate of heating.
- Length of the heating time.

From this, it can be understood that the characteristics of the crystalline phases are dependent on the two basic stages of nucleation and crystals growth, as well as the dwelling time to which the ceramic is subjected in those two stages, as shown above in Fig. 2. 9. Glass-ceramics are made of both crystal phases and amorphous vestiges, and it is the volume of the fraction of the amorphous vestiges upon which the strength of the glass-ceramic depends [108]. Lower the amount of the amorphous vestiges, the stronger will be the glass-ceramic. This is the reason glass has to undergo optimum heat treatment, in order to promote the growth of glass crystals within its matrix and to minimize the quantity of amorphous vestiges.

Fig. 2. 11 shows schematically the temperatures at which maximized rates of both nucleation and crystal growth occurs, with the temperatures being indicated as T_N and T_G , respectively. T_c represents the point where the two temperature curves intersect, indicating that there is an overlap area between the nucleation and crystal growth curves. The range of temperatures present within the overlap area indicates those temperatures which can be used for the development of the best quality glass-ceramic material [109].

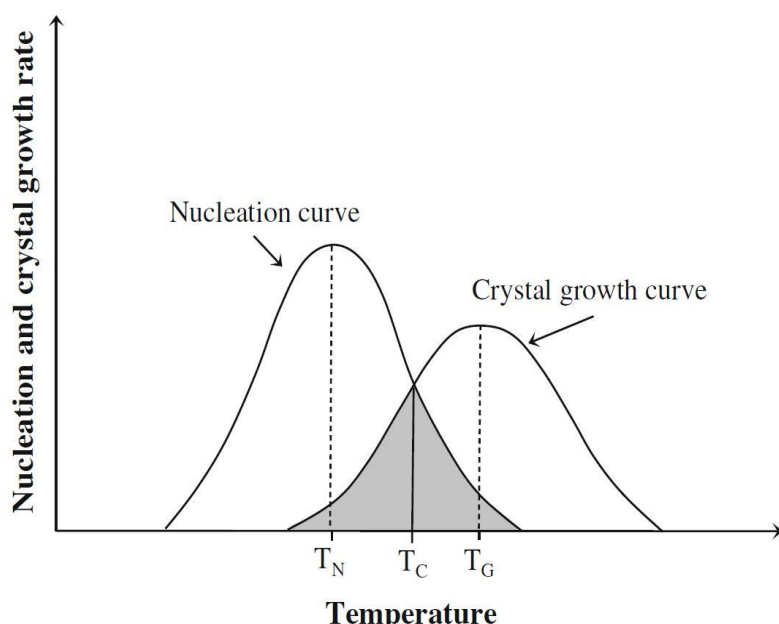


Fig. 2. 11 Relative behaviour of the nucleation and crystal growth rates with temperature [109].

Therefore, it can be understood that when the curves T_N and T_G are further apart, the overlap zone will continue to become smaller, which suggests that in order to manufacture glass-ceramics, it will require a two-stage method which consists of the conventional nucleation and crystal growth stages. In contrast, if the curves T_N and T_G are positioned in close proximity to each other, and the overlap zone is wide, this makes it possible for the glass-ceramics to be produced using a single-stage method, where the process of nucleation and crystal growth takes place simultaneously.

2.6.1 Nucleation process

Nucleation is the process that leads to the formation of nuclei within the glass, which is considered the stepping stone required to promote the process of crystal growth within the glass [87], [100]. Nuclei can be found scattered regularly within the bulk of glass during the process of heat treatment [110], as shown in Fig. 2.12-a.

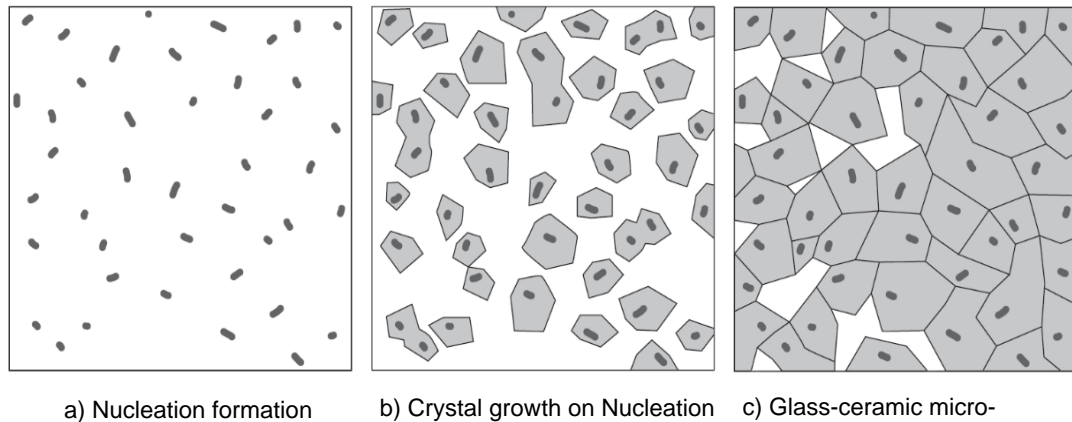


Fig. 2. 12 Transformation from glass to glass-ceramic [6].

Obtaining optimal nucleation of the glass and the development of high-quality glass-ceramics depends on two basic factors, which are [6];

- 1) Choosing a suitable nucleating agent which will help develop the optimal chemical composition of glass.
- 2) Controlling the temperature and holding time that the glass is subjected to during the process of heat treatment.

Chapter Two: Literature Review and Prior Studies

The nucleation temperature (T_N) can be determined when the temperature of the glass (T_g) transitions to above +50°C or up to +100°C for an appropriate length of time in order to obtain major nucleation [6], [111]. Therefore, it is evident that the latter plays an important role in controlling the crystallization of glass-ceramic, which also includes the formation of an extensive order to its atomic structure than amorphous glass. This initial nucleation process helps to promote the formation of a more stable crystalline phase in the glass-ceramic [45].

Nucleation temperature is commonly in the 450– 700°C range and the glass should be processed for a time ranging between 1/2 to 4 hours depending on the glass composition [3], [112]. The process of nucleation is of two types: homogeneous nucleation or heterogeneous nucleation.

2.6.1.1 Homogeneous nucleation

In the case of most glasses, homogeneous nucleation is a stochastic process that occurs when all the nuclei are formed from their molten composition, as a result of which their positions are not required to be in remote boundaries [109], in which the crystals would thereafter grow upon the same these positions [87]. With regard to the process of nucleation, the derivation of a mathematical expression for the nucleation rate begins from the moment where a spherical nucleus is formed. There are two main barriers to the formation of a nucleus, which include:

- Thermodynamic barrier.
 - Kinetic barrier.

The thermodynamic barrier is formed as a result of the change in free energy when a nucleus is created, whereas the kinetic barrier arises as a result of the movement and rearrangement of mass in space, which then allows a particle to develop as a crystal [87]. Both the thermodynamic and kinetic barrier can be incorporated into and described by the equation 2.1 [96]:

$$I \equiv A e^{[-\frac{W + \Delta G_D}{kT}]}$$

Where:

I is the rate of homogenous steady-state nucleation

W is the thermodynamic free-energy barrier to nucleation.

Chapter Two: Literature Review and Prior Studies

ΔG_P is a kinetic barrier to nucleation,

A is a constant.

T is an absolute temperature

K is a Boltzmann constant

Embryo crystals are spontaneously formed when the glass passes through the supercooled stage, after which the nucleation process can proceed in relation to free energy considerations.

The model of the homogeneous nucleation, the thermodynamic barrier to nucleation, can be described by a simple energy balance, where the net change of energy, ΔW , is by equation 2.2:

Where;

G_V is the free energy-change per unit volume by the formation of nuclei,

r is radius of nuclei embryo,

γ is an energy per unit area of the solid/liquid interface.

Basically, the overall free energy of nucleation consists of a volume term and surface term, as shown in equation 2.2. The volume term, $\frac{4}{3}\pi r^3 \cdot (\Delta G_V)$, is dictated by ΔG_V , which corresponds to the change of the Gibbs free energy per unit volume upon the transformation of a unit volume of liquid into a unit volume of the crystal. This is also commonly referred to as the Gibbs free energy of crystallization and it takes negative values below T_m , thereby offering the driving force for crystallization. When the Gibbs free energy ΔG_V is negative, the reaction tends to occur, whereas when it is positive value, the reaction tends not to happen [113]. The surface term, $4\pi r^2 \gamma$, is positive and acts as an obstacle for crystallization. This term is associated with the formation of a solid-liquid interface and the surface tension at this interface [114]. From equation 2.2, it becomes obvious that thermodynamic barrier to nucleation is dependent on r , therefore its maximum value, ΔG^* , can be plotted as shown in Fig. 2. 13, which also shows a critical nuclei radius, r^* .

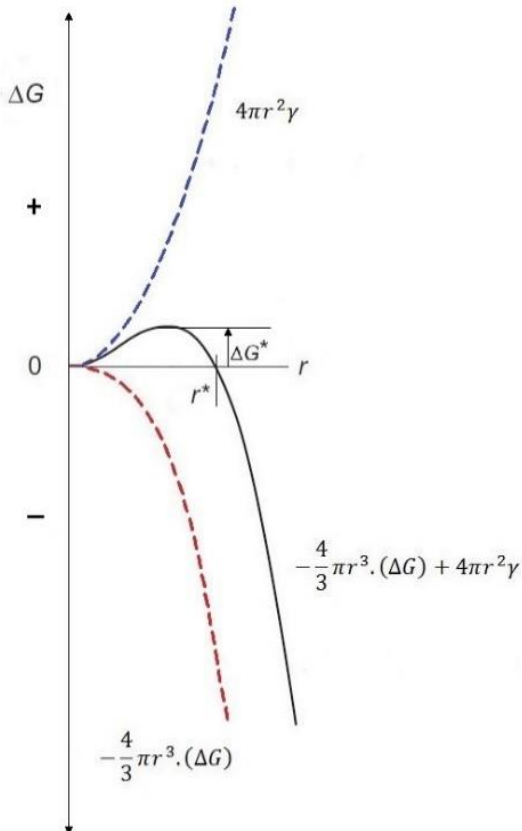


Fig. 2. 13 Change in Gibbs free energy (ΔG), the energy of surface (blue curve) and free energy of volume (red curve), versus the radius of nuclei (r).

Particles below the critical radius (r^*) are called embryos or subcritical particles. They are unstable and eventually dissolve or disintegrate. Particles with radii exceeding r^* are known as supercritical nuclei and will become stable nuclei. The critical radius, r^* , increases with rising temperatures. The critical nuclei radius, r^* , can be obtained by differentiating W with respect to r and setting this differentiation to zero, as follows $\frac{dW}{dr} = 0$ [115].

$$\frac{dW}{dr} = 4\pi r^2 \Delta G_V + 8\pi r \gamma$$

As shown in Fig. 2. 13 the maximum free energy ΔG_{max} is at r^* (a critical radius for nucleation). Thus:

$$\frac{\partial \Delta G}{\partial r} \downarrow_{r=r^*} = 0$$

$$4\pi r^{*2} \Delta G_V + 8\pi r^* \gamma = 0$$

$$r^* \Delta G_V + 2\gamma = 0$$

$$r^* \Delta G_V = -2\gamma$$

$$r^* = \frac{-2\gamma}{\Delta G_V} \quad [115]$$

2.6.1.2 Heterogeneous nucleation

In contrast to homogenous nucleation, heterogeneous nucleation is a process that involves phase boundaries [109] or suitable nucleation spots; such as solid impurities or surface flaws, earlier nucleated phases and interfaces which existed previously [108], [109].

The process of heterogeneous nucleation takes place in sites where the driving forces required for the formation of a new phase are relatively more active than the forces which drive the transformation of the parent phase to a crystal [108].

Fig 2. 14 depicts the pattern of formation of nuclei through the process of heterogeneous nucleation, where the heterogeneous substrate/catalyst is represented by the letter H, the nucleus/ solid by S, the parent phase by L and the contact angle by the symbol θ .

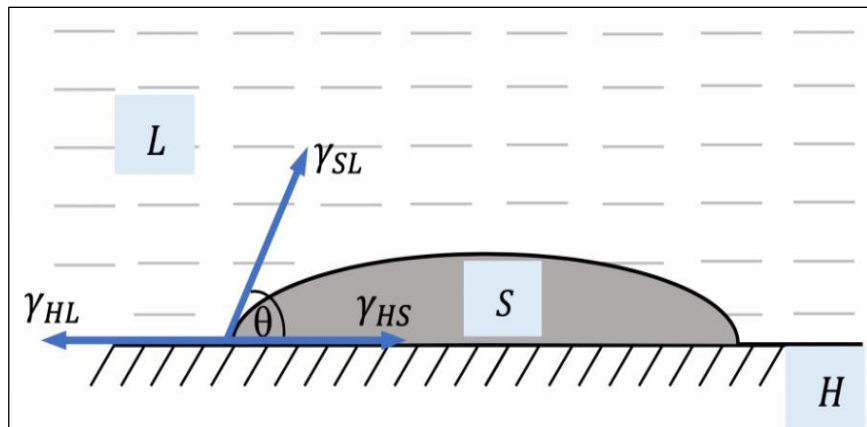


Fig. 2. 14 Heterogeneous nucleation [116].

$$\Delta G_H^* = \Delta G^*.S(\theta)$$

$$S(\theta) = \frac{(2+\cos\theta)(1-\cos\theta)^2}{4} \quad \dots \quad 2.3 [6]$$

Chapter Two: Literature Review and Prior Studies

When the contact angle is maintained at 180° , the substrate's surface (H) does not undergo wetting [116]. Therefore, this can be considered homogenous nucleation. Whereas, when the surface of H has been completely wetted, the contact angle (θ) is close 0° , which then results in the function that is represented in equation 2.3 gradually becoming ≥ 0 , giving rise to a ΔG_H^* which is quite small, resulting in the process of heterogeneous nucleation [117]. Therefore, it can be understood that when the contact angle is less than 180° homogenous nucleation is more likely to occur than heterogeneous nucleation [118].

According to the pattern of formation of nuclei through heterogeneous nucleation in Fig. 2. 14, the balance between the three different interfacial energies for crystal (S), the heterogeneous substrate (H), and liquid/melt (L) determine the efficiency of the nucleating agent. Therefore, the interface energy of the heterogeneous substrate and melt in this type of nucleation process can be determined by equation 2.4 [114]:

Where:

γ_{HL} is a substrate/catalyst-liquid interface energy,
 γ_{HS} is a substrate/catalyst-nucleus/solid interface energy,
 γ_{SL} is a nucleus/solid-liquid interface energy
 θ is a contact angle.

It was observed that regardless of whether the nucleation occurs in a homogenous or heterogeneous manner, it makes no difference to the critical radius r^* of the nuclei (no change in the size of nuclei) [6]. However, it is evident that the critical Gibbs free energy is affected when the surface undergoes wetting, which acts as the catalyst for heterogeneous nucleation, as shown in Fig. 2. 15. In saying this, we can also determine that the process of heterogeneous nucleation occurs easily compared to homogeneous nucleation as it requires lower levels of Gibbs free energy in comparison to homogeneous nucleation [119]. Hence, heterogeneous nucleation remains the preferred nucleation method in the glass-ceramic making process.

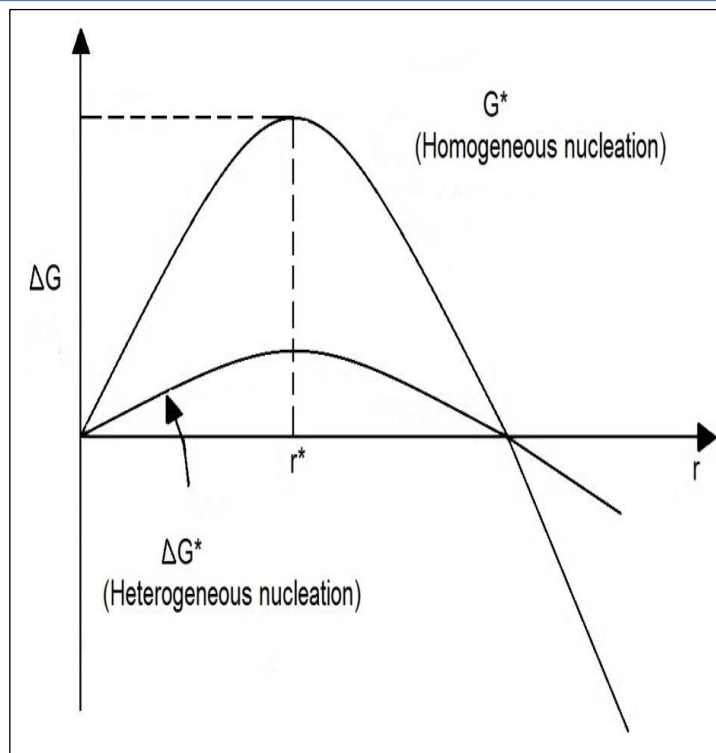


Fig. 2. 15 Difference in Gibbs free energy of homogeneous and heterogeneous nucleation based on the radius of nuclei (r) [120].

2.6.2 Crystals growth process

A nucleated glass is subjected to very high temperatures that exceed the softening point of glass. This process initiates the development of crystals on the nuclei, which have been formed within the nucleated glass during the process of nucleation [3], [121], as shown above in Fig. 2. 12-b and -c. This stage of crystal growing is carried out in temperatures ranging from 700–1,000°C for a period of time, which may range between a few minutes to many hours. The rate at which the growth of the crystals occurs needs to be determined cautiously, because a slow rate may result in deformation within the glass when it undergoes heat treatment. Hence, it is necessary to control this rate in such a manner that we provide adequate time to achieve the perfect growth of crystals while ensuring no deformation occurs within the glass. Therefore, it is understood that a rate of 3–5°C/min is the most favourable in order to make sure that no deformation occurs to the body of the glass [122], [123], and bringing about a decrease in the slumping of the vestige glass [124]. Where Beall G. H. [125] stated that the low rate of the crystal growth resulted in minimizing the grain size.

2.6.3 Determination activation energy

Activation energy is defined as the minimum energy which is required to promote atoms or molecules to a state where they will be able to undergo chemical transformation [126]. In 1864, Cato Guldberg and Peter Waage published the law of mass action, which describes the chemical reaction as being an equilibrium [127]. 15 years later, they published a well-known description of this law, which was defined as the rate of a reaction, which explained that a rate constant is proportionate to and consistent with the concentration of the stoichiometric reactants. This concept went on to determine that the rate of reaction [$d\alpha/dt$] proportionate to the function of the amount of reactant $f(\alpha)$ and the rate constant $k(T)$, in this equation [128];

$$\frac{d\alpha}{dt} = k(T)f(\alpha) \dots \quad 2-5$$

The kinetic factors have the characteristic ability to predict performance under different conditions of temperature and time. In 1889, Svante Arrhenius described how the reaction rate varies with temperature using the following equation [128];

$$k(T) = A \exp\left(\frac{-E_a}{RT}\right) \quad \dots \quad 2-6$$

Where;

A = the pre-exponential factor.

E_a = the activation energy (J/mole)

R = the universal gas constant (J. mole/K)

When the equation 2-5 and equation 2-6 are combined into a single equation, we can obtain the general rate equation [129];

$$\frac{d\alpha}{dt} = f(\alpha)A \exp\left(\frac{-E_a}{RT}\right)$$

Based on this initial concept of the rate equation, many methods (equations) have since then been derived, in order to help to determine the thermal behaviour of materials, the most important of them being the 'Kissinger's' method and 'Ozawa's' method.

2.6.3.1 Kissinger method

Kissinger's and Ozawa's methods are used for the estimation of the kinetic factors of materials using the thermal analysis. These two methods are based on a set of DTA or DSC experiments taken at different heating rates. Kissinger suggested that the activation energy of a first-order process can be estimated from the changes of the temperature peaks which can be coupled with the heating rates using DSC as follows [130];

$$\ln\left(\frac{\beta}{T_p^2}\right) = \frac{-E_a}{RT_p} + constant$$

$$\ln\left(\frac{\beta}{T_n^2}\right) = \left[\frac{-E_a}{R}\right] \frac{1}{T_p} + \text{constant} \dots \quad 2-7$$

Using $[1000/T_p]$ in the x-axis versus $[\ln(\beta/T_p^2)]$ in the y-axis, the pattern is plotted based on the heating rate (α) and the peak temperature, T_p . The slope of the straight line that results from the plotted data is equal to $[-E_a/R]$ according to Kissinger equation 2-7 [128]. An example is a method by which R. Wurth et al [131] estimated the activation energy for a lithium alumino-silicate glass system. They made use of the Kissinger model to determine the kinetic energy of crystallization using differential scanning calorimetry (DSC), as shown in Fig. 2.

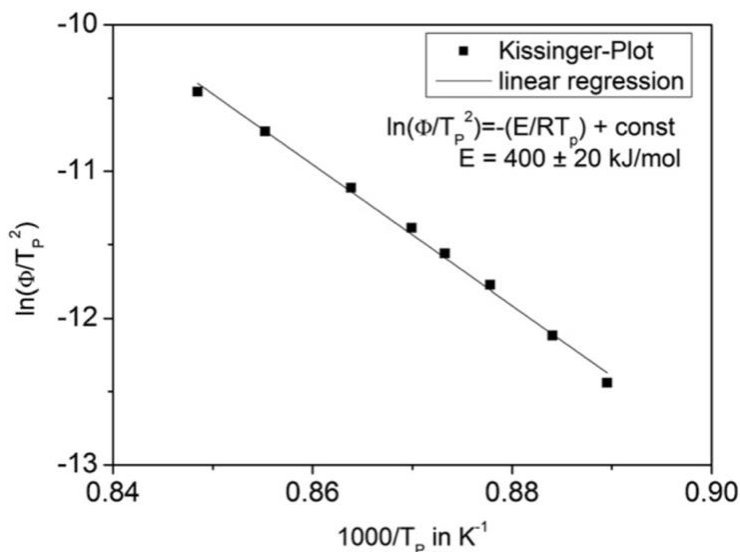


Fig. 2. 16 Kissinger model utilized to estimate the activation energy of crystallization for Li-Al-Si glass system [131].

2.6.3.2 Modified Kissinger method

In the years that followed, several changes have been made to both the common methods of Kissinger and Ozawa in order to take into account the kinetic energy of crystallisation and obtain a more significant activation energy value. According to several studies [132]–[136], it has been recommended that the calculation of activation energies should be carried out by using the modified Kissinger method, which was proposed by Matusita and Sakka [135].

Thus, the modified Kissinger method is based on the equation 2-7, as follows 2-8.

$$\ln\left(\frac{\beta^n}{T_p^2}\right) = \left[m \frac{-E_a}{R}\right] \frac{1}{T_p} + constant \dots \quad 2-8$$

Here, n and m are considered as Avrami numbers (the numerical constants), which are dependent on the crystallization characteristics. Here $n=m=1$ indicates 1D, surface crystallisation, while $n=m=2$ is indicative of planar surface nucleation. However, $n=m=3$ indicates bulk nucleation from a constant number of nuclei and 3D growth [135], [137], [138]. This modified method aims to obtain a better estimation of the activation energies. An example is a method by which R. Wurth et al [131] estimated the activation energy for a lithium alumino-silicate glass system. They made use of the Modified Kissinger model to determine the kinetic energy of crystallization using differential scanning calorimetry (DSC), as shown in Fig. 2. 17.

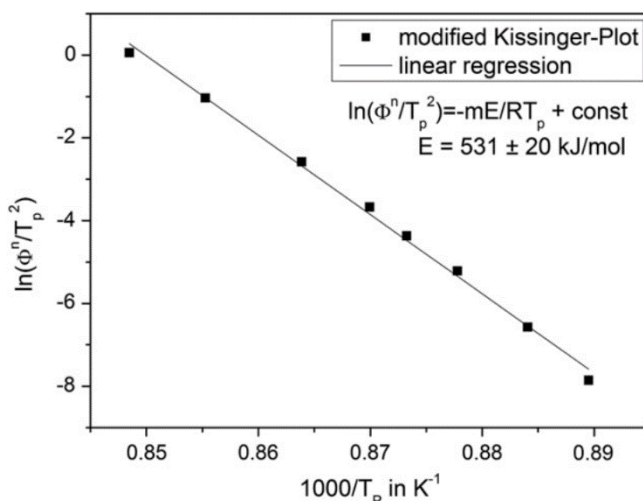


Fig. 2. 17 Modified Kissinger model utilized to estimate the activation energy of crystallization for Li-Al-Si glass system [131].

2.6.3.3 Ozawa method

The Ozawa equation also depends on temperature peaks and heating rates; however, its formula is different from Kissinger's equation, in the following manner [139];

$$\ln(\beta) = \frac{-E_a}{RT_p} + constant$$

Ozawa's pattern is also plotted by using $[1000/T_p]$ in the x-axis versus $[\ln(\beta)]$ in y-axis. The slope of the straight line that resulted from the plotted data is equal to $[-E_a/R]$ according to the Ozawa equation 2-9 [140]. Kangguo Cheng [141] determined the energy of the crystallization for the $\text{Li}_2\text{O}-\text{Al}_2\text{O}_3-\text{SiO}_2$ glass system using the Ozawa method, as shown in Fig. 2. 18.

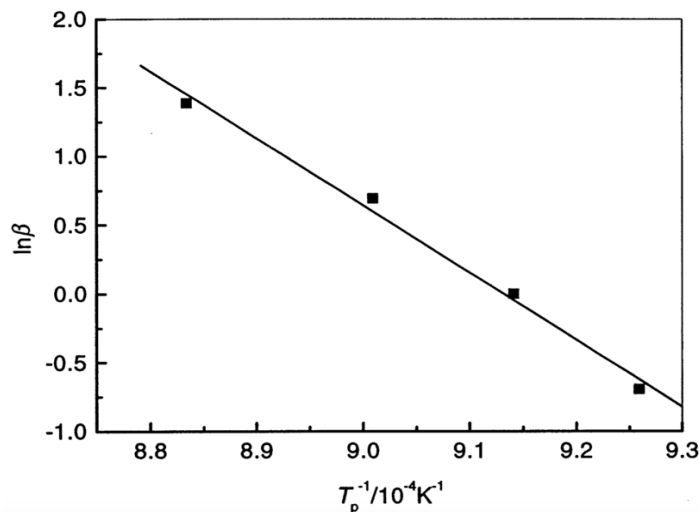


Fig. 2. 18 Ozawa model utilized to estimate the activation energy of crystallization for $\text{Li}_2\text{O}-\text{Al}_2\text{O}_3-\text{SiO}_2$ glass system [141].

2.7 Dental glasses and glass-ceramics

Dental ceramics can be divided into different types of materials, such as feldspathic porcelains, aluminous porcelains, leucite re-enforced porcelains, glass-infiltrated alumina, glass-ceramics, and infiltrated spinel [3], [111]. Table 2. 4 shows the results of the mechanical and physical properties of these different types, which resulted from studies carried out over the past three decades.

Chapter Two: Literature Review and Prior Studies

Table 2. 4 Summary of the physical and mechanical properties of different types of commercially available dental ceramics and glass-ceramics.

| Glass ceramics | Crystalline Phase | Flexural strength (MPa) | Fracture toughness (MPa.m ^{1/2}) | Hardness (GPa) | Elastic modulus (GPa) |
|---|---|--|--|--------------------------------------|----------------------------------|
| Feldspathic porcelain | | 60–103 [111] [142], [143] | 0.92–1.26 [111][142][56] | 6–6.4 [111][56], [142] | 68–70 [111][56], [142] |
| Reinforced feldspathic porcelain (Aluminous, leucite) | Alumina, leucite | 120–150 [111][144][142] | 1.3–1.5 [111][142] | 5.6–9.3 [111][142][144][145] | 70 [111][144] |
| Fluormica glass ceramic | K ₂ Mg ₅ Si ₈ O ₂₀ F ₄ | 150 [111] | 1.4 - 1.5 [111] | 0.362 (Knoop) [111] | 70.3 [111] |
| Leucite glass ceramic | KAlSi ₂ O ₆ | 160 [111] | 1.3 [111] | 6.2 (Vickers) [111] | 65 [111] |
| Lithium disilicate glass-ceramic | Li ₂ Si ₂ O ₅ | 256–400 [111][142][56] | 2.25 - 2.75 [111] | 5.8 (Vickers) [111] | 95 [111] |
| Fluorapatite glass-ceramic | Ca ₅ (PO ₄) ₃ F | 60–252 [111][21][146] | 0.6 [111] [21] | 5.4–9.2 (Vickers) [111] [146] | 45 [111] [21] |
| Glass-infiltrated spinel | MgAl ₂ O ₄ | 291–400 [111][147] | 1.79–2.7 [111][148] | 11 [111][148] | 185–212 [111][148] |
| Glass-infiltrated alumina | Al ₂ O ₃ | 340–560 [111][147], [149]–[152] | 2.89–5.9 [111][148], [150] | 12.3 [111][148], [151] | 271–280 [111][148], [151] |
| Glass-infiltrated zirconia | ZrO ₂ | 236–600 [111][150], [153] | 3.1–4.6 [111][153] | 59 [111][150] | 258 [111] |
| Pure alumina (corundum) | Al ₂ O ₃ | 220–700 [111] | 4.5 [111] | 12 [111] | 270 [111] |

2.8 Dental glass ceramics

Glass-ceramics are appropriate in applications which great tensile strength is not required. However, glass-ceramics have been identified to have characteristics such as excellent low thermal expansion coefficient, chemical resistance, high thermal conductivity, great transparency, high Young modulus, low density, excellent surface smoothness, high levels of stability at high temperatures. They are convenient materials for coating metal seals, fireplace windows, bearings, magnets, telescope mirrors, engine components, transducers, capacitors, valves, chemical process equipment, substrates, super cutting tools and conductors [6]. Over three decades, glass-ceramics have undergone several improvements with regard to their mechanical properties, which have been the reason they are also used the field of dentistry. The glass-ceramics used in the field of dentistry can be classified according to their use as follows: bridges, tooth replacement appliances, space maintainers, splints, partial crowns, crowns, dentures, teeth, posts, jackets, onlays, inlays, facing, facets, veneers, implants, cylinders, connectors and abutments [3], [111], [154]. They can also be classified according to the process they are manufactured, such as sintering, machining, casting, and CAD-CAM.

2.8.1 Lithium disilicate glass ceramics

Lithium disilicate glass-ceramics are known for their high mechanical flexural strength that may reach up to 400 MPa [97]. They are fabricated from two major components: Li_2O and SiO_2 . The lithium-disilicate phase, $\text{Li}_2\text{Si}_2\text{O}_5$, in the Li-Si system, melts approximately at a temperature of 1,033°C, this is shown in Fig. 2. 19.

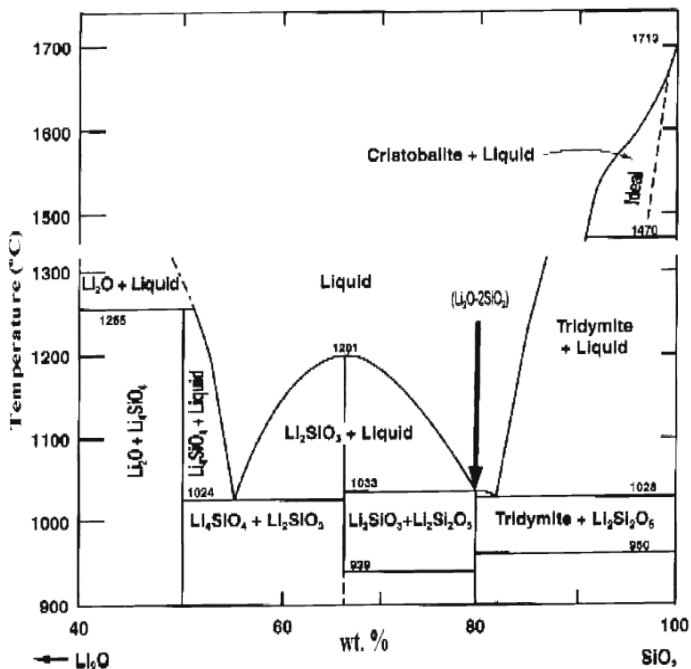


Fig. 2. 19 The phase Li_2O - SiO_2 diagram [97].

Lithium disilicate glass-ceramics consist of a large volume fraction of fine rod-like $\text{Li}_2\text{Si}_2\text{O}_5$ crystals reaching up to 70% [111]. Additionally, during the process of crystallization, small amounts of Lithium metasilicate (Li_2SiO_3) and lithium orthophosphate (Li_3PO_4) crystals are produced [95], this would vary depending upon the glass composition. Li_2SiO_3 crystallization occurs at a much lower temperature as a metastable phase. Crystallization of Li_2SiO_3 occurs earlier than $\text{Li}_2\text{Si}_2\text{O}_5$; however the relative amount of Li_2SiO_3 is minute and with increasing temperature may disappear [3]. Crystallization varies upon the initial composition of glass and the temperature. Other chemical ingredients can be added in order to enhance properties such as Al_2O_3 and ZnO for the chemical solubility, as listed in Table 2. 3.

2.8.2 Lithium aluminosilicate glass ceramics

Lithium aluminosilicate is also a form of glass-ceramic material which is produced from the Li-Al-Si oxides system. This material is recognized for its unique features such as favourable optical properties, high mechanical strength, minimal to zero thermal expansion coefficient [106], chemical stability, biological properties and excellent optical properties [155][156], all these properties render the material suitable for a wide range of uses [156]–[158]. These superior properties can be attributed to the high precipitation of crystals [10]. The crystallization phases in

this type of glass-ceramics are predominantly β -quartz and β -spodumene (β - $\text{LiAlSi}_2\text{O}_6$) [10], [157], [159]. In order to obtain a full understanding of the ternary phases in Li_2O - Al_2O_3 - SiO_2 system refer to Fig. 2. 20, which depicts the phase diagram. β -quartz is formed at $\leq 900^\circ\text{C}$, whereas the irreversible formation of β -spodumene occurs when heated at a temperature between 900 and 1000°C [159].

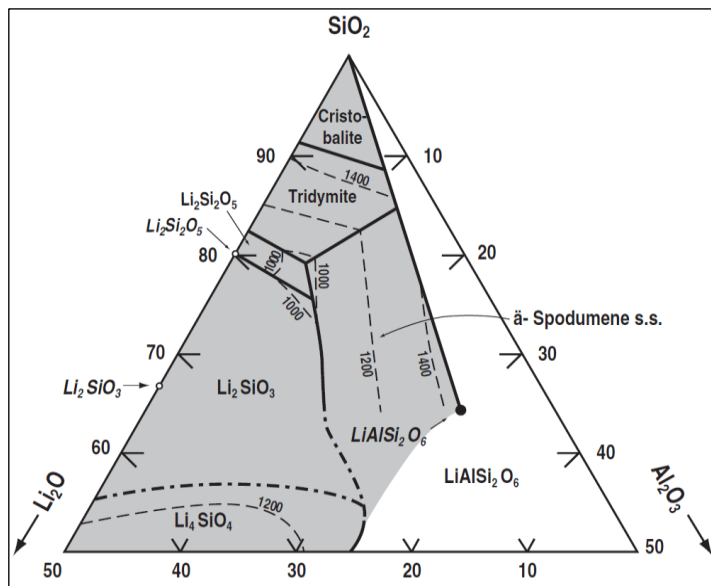


Fig. 2. 20 Phase diagram of LAS glass ceramics system [6].

Ross et al. [160] studied the lithium mobility in Al-Si-O glasses, in fully polymerized glasses with a constant Li/Al ratio equal to 1 and depolymerized glasses with $\text{Li}/\text{Al} > 1$ with a fixed amount of lithium (labelled DG1, DG2 and DG3 in Fig 2. 21). They re-iterated that analogues of the polymerized glasses, indicated in Fig. 2. 21 occur in nature as eucryptite (LiAlSiO_4), spodumene ($\text{LiAlSi}_2\text{O}_6$) and petalite ($\text{LiAlSi}_4\text{O}_{10}$) and $\text{LiAlSi}_3\text{O}_8$, which is a lithium analogue of albite ($\text{NaAlSi}_3\text{O}_8$).

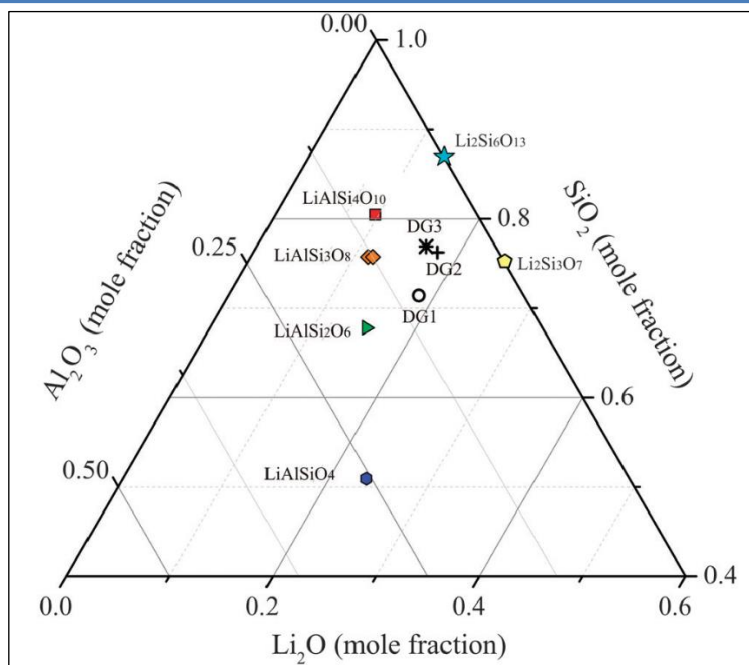


Fig. 2. 21 Phases with $\text{Li}/\text{Al}=1$ in the partial Li_2O - Al_2O_3 - SiO_2 ternary phase diagram [160].

2.9 Prior studies on Lithium disilicate and lithium aluminosilicate-based Glass-ceramics

This particular section presents prior investigations of glass-ceramics based on both lithium disilicate and lithium aluminosilicate phases coupled with the glass ceramic of this study which is based on lithium disilicate, strengthened lithium aluminosilicate and the other phases, as presented in Table 2. 5. Chemical glass compositions for typical lithium-based glass ceramics are listed in Table 2. 6, whereas the mechanical properties of selected systems are listed in Table 2. 7.

Table 2. 5 Phases of LAS1 glass used in this study and respective temperatures range based on In-situ high-temperature X-ray diffraction.

| Phases | Symbol of phase | Temperature range |
|---|-----------------|-------------------|
| Li_2SiO_3 Lithium metasilicate | LS1 | 570–790°C |
| $\text{LiAlSi}_4\text{O}_{10}$ Petalite, Monoclinic | LAS1 | 590–690°C |
| $\text{Li}_{0.25}\text{Al}_{0.25}\text{Si}_{0.75}\text{O}_2$ Lithium orthoclase | LAS2 | 640–710°C |
| $\text{Li}_2\text{Si}_2\text{O}_5$ Lithium disilicate | LS2 | 690–790°C |
| $\text{LiAlSi}_2\text{O}_6$ Lithium aluminosilicate | LAS3 | 680–790°C |

Chapter Two: Literature Review and Prior Studies

Table 2. 6 Chemical compositions of Li-based glass-ceramics prior to heat treatment.

| Elements oxides→ | SiO ₂ | Al ₂ O ₃ | Li ₂ O | CaO | ZnO | MgO | CeO ₂ | BaO | B ₂ O ₃ | K ₂ O | Na ₂ O | NiO | TiO ₂ | P ₂ O ₅ | ZrO ₂ | V ₂ O ₅ |
|--------------------------------------|------------------|--------------------------------|-------------------|------|------|------|------------------|-----|-------------------------------|------------------|-------------------|-----|------------------|-------------------------------|------------------|-------------------------------|
| Lithium disilicate↓ | | | | | | | | | | | | | | | | |
| 1 Y. IQBAL et al. [161] | 80.08 | | 19.91 | | | | | | | | | | | 0 | | |
| | 77.85 | | 19.36 | | | | | | | | | | | 2.79 | | |
| | 75.70 | | 18.82 | | | | | | | | | | | 5.47 | | |
| | 69.68 | | 17.33 | | | | | | | | | | | 12.99 | | |
| 2 W. Holand et al [121] | 70.64 | 3.38 | 14.68 | | | | 1.88 | | | 3.09 | | | | 3.21 | 3 | 0.12 |
| | 71.27 | 3.40 | 14.81 | | | | 1.89 | | | 3.11 | | | | 2.38 | 3.02 | 0.12 |
| | 71.8 | 3.43 | 14.92 | | | | 1.91 | | | 3.14 | | | | 1.63 | 3.05 | 0.12 |
| | 73 | 3.49 | 15.16 | | | | 1.94 | | | 3.19 | | | | 0 | 3.10 | 0.12 |
| 3 X. Zheng et al. [162] | 66.7 | | 33.3 | | | | | | | | | | | | | |
| | 62 | | 31 | 1 | 2 | | | | | 3 | | | | 1 | | |
| | 62 | | 30 | 1 | 2 | | | | | 3 | | | | 2 | | |
| | 62 | | 30 | 1 | 2 | | | | | 3 | | | | 4 | | |
| 4 Wang et al. (2010) [163] | 66.4 | 1.8 | 27.5 | | | | | | | 1.8 | | | | 0.5 | 1.4 | |
| | 66.0 | 1.8 | 27.4 | | | | | | | 1.8 | | | | 1.0 | 1.4 | |
| | 65.6 | 1.8 | 27.3 | | | | | | | 1.8 | | | | 1.5 | 1.4 | |
| | 65.2 | 1.8 | 27.2 | | | | | | | 1.8 | | | | 2.0 | 1.4 | |
| 5 Huang, et al. [164] (mole%) | 100 | | 41.6 | 3 | | | | | | | | | | 2.3 | 1.3 | |
| 6 Huang et al. [165] (mole%) | 100 | 2 | 40 | | | | | | | | | | | 2.8 | 0.4 | |
| 7 Zhang et al. [166] | 65 | 2.2 | 27.5 | | | | | | | 2.3 | | | | 1 | 2 | |
| Lithium aluminosilicate↓ | | | | | | | | | | | | | | | | |
| 8 Guo et al. [167] | 67 | 19.5 | 4 | | 0.7 | 0.6 | | 0.4 | | | 1 | | | 2.5 | 0.5 | 2 |
| | 67 | 19.5 | 4 | | 0.7 | 0.6 | | 0.4 | | | 1 | | | 2.2 | 0.5 | 1.8 |
| 9 A. Arvind et al. [168] | 71.7 | 7.1 | 10.6 | | | | | | 3.2 | 4.9 | | | | 2.25 | | |
| | | | | | | | | | | | | | | 1.25 | 1.25 | |
| 10 Hu et al. [106] | 57.60 | 25.30 | 4.00 | | 1.00 | 1.00 | | | | | | | | 1.00 | 8.10 | 2.00 |
| | 57.00 | 25.00 | 4.00 | | 1.00 | 1.00 | | | | | | | | 2.00 | 8.00 | 2.00 |
| | 56.30 | 24.80 | 4.00 | | 1.00 | 1.00 | | | | | | | | 3.00 | 7.90 | 2.00 |
| | 55.80 | 24.50 | 3.90 | | 1.00 | 1.00 | | | | | | | | 4.00 | 7.80 | 2.00 |
| | 56.70 | 24.94 | 4.00 | | 1.00 | 1.00 | | | | | | | | 2.36 | 8.00 | 2.00 |
| 11 Laczka M. et al. [10] | 66 | 10.5 | 10.5 | 2.45 | | | 1.5 | | | 0.5 | 3 | | | 4.5 | 0.5 | 0.55 |
| 12 Łaczka K. el al. [169] | 66.3 | 10.2 | 12.1 | 1.46 | | | 1.5 | | | 0.53 | 2.59 | | | 4.28 | 0.56 | 0.04 |

Chapter Two: Literature Review and Prior Studies

Table 2. 7 The mechanical properties of previous studies on LS and LAS glass-ceramics .

| | Vickers Hardness (GPa) | Flexural strength (MPa) | Elastic modulus (GPa) | Fracture toughness MPa.m ^{1/2} |
|---------------------------------------|------------------------|-------------------------|-----------------------|---|
| Wang et al. 2010 [163] ^y | | 310 | | |
| Huang et al. 2013 [164] ^y | 7.83±0.2 | 439±93 | | 1.29±0.07 |
| Zhang, et al. 2013 [165] ^y | 8.4±0.1 | 307±16 | | 1.23 |
| Lien et al. 2015 [170] ^y | 8.2±0.1 | 367 ± 43.3 | 99.0 ± 1.29 | |
| Li et al. 2016 [171] ^y | 9.07±0.13 | 370±36 | 117.66±.96 | |
| Laczka et al. 2014 [10] ^z | | ~400 | | |

y-indicates Lithium disilicate glass-ceramics, the main phase $\text{Li}_2\text{Si}_2\text{O}_5$.
z-indicates Lithium aluminosilicate glass-ceramics, the main phase $\text{LiAlSi}_2\text{O}_6$.

2.9.1 Lithium disilicate glass ceramics

Y. Iqbal et al. (1999) [161] investigated the effect of minute quantities of phosphorus pentoxide (P_2O_5) as nucleation agent on the overall process of crystallization in lithium disilicate glass, Table 2. 6-1. They observed that amorphous lithium phosphate forms for ≤ 2.79 wt% P_2O_5 , whereas of crystalline Li_3PO_4 is present for $x \geq 5.47$ wt% P_2O_5 . This strongly suggests that Li_3PO_4 crystals are sites for heterogeneous nucleation of stable $\text{Li}_2\text{Si}_2\text{O}_5$ crystals.

Similarly, W. Höland el al. (2006) [121] studied the evolution of crystalline phases in a multicomponent lithium-disilicate glass system, with changing P_2O_5 content (0, 1.63, 2.38 and 3.21 wt%) to control the bulk crystallization of $\text{Li}_2\text{Si}_2\text{O}_5$, Table 2. 6-2. W. Höland el al. found out that the P_2O_5 content has a strong effect on the thermal behaviour, with the composition with 3.21 wt% P_2O_5 showing two exothermic peaks at 672°C and 834°C, whereas the other glasses with lower P_2O_5 exhibiting only one exothermic peak. According to Höland et al., lithium metasilicate formation can take place at low temperatures (550–750°C). This is the predominant phase in pre-crystallized samples, which enhances the strength of machining blocks and act as an initiator for the subsequent crystallization process of $\text{Li}_2\text{Si}_2\text{O}_5$ crystals [170]. Höland et. al. also revealed that when heat treatment is done at temperature ranging from 780–820°C, it causes the Li_2SiO_3 phase to be converted to $\text{Li}_2\text{Si}_2\text{O}_5$, producing a glass-ceramic possessing extremely high levels of flexural strength in the range of 726 ± 63 MPa.

Both X. Zheng et al. (2008) [162] and Wang et al. (2010) [163] also studied the effect of varying P_2O_5 content in lithium disilicate glass-ceramics compositions, as shown in Table 2. 6-3, 4. According to Wang et al. (2010) findings, Li_2SiO_3 is

Chapter Two: Literature Review and Prior Studies

the primary crystalline phase forming during the pre-crystallization step (636–748°C for 1hour). Lithium disilicate ($\text{Li}_2\text{Si}_2\text{O}_5$) appears in a post-crystallization step of 810-848 °C for 1 hour. This controlled crystallization process produces a lithium disilicate glass–ceramic with flexural strength 310 MPa with suitable translucency characteristics. Huang et al. 2013 [164] analysed the lithium-disilicate glass-ceramic considering the different glass compositions given in Table 2. 6-5. Huang et al. [164] employed annealing profiles as follows; first stage (530°C/90 min), second stage (620-675°C/15-120 min), third stage (780-800°C/ 30min) and fourth stage (850°C /30min). They recorded the greatest flexural strength of 439 ± 93 MPa coupled with a Vickers hardness of 7.83 ± 0.2 GPa following the heating profile 530°C/90 min→ 674°C/ 30min, but lowest fracture toughness of $0.93 \text{ MPa.m}^{1/2}$. Though the fracture toughness improved marginally from 0.93 to a value of $1.29 \text{ MPa.m}^{1/2}$ following the heating of glass to 530°C/90 min→ 674°C/30 min→ 780°C/ 30min→ 850°C/30 min, there was a reduction in the flexural strength and Vickers hardness to 371 ± 49 MPa and 6.39 ± 0.25 GPa, respectively.

Huang et al. 2013 [165] obtained a glass-ceramics derived from a composition which is similar to the glass composition discovered by W. Höland el al. [121], as depicted in Table 2. 6-6 and subjecting them of temperatures of 1500°C for duration of three hours. Huang et al. [165] used annealing profiles, as seen in Table 2. 8; to produce a glass ceramic having flexural strength of merely 246–307 MPa, but in contrast, the Vickers hardness was much greater at 7.9–8.4 GPa.

Table 2. 8 Heat treatment temperature profiles [165].

| | Samples | Annealing profiles | | Flexural strength MPa |
|-------|---------|--|---------------------|-----------------------|
| Set 1 | S1 | 520°C/10 min 620°C/20 min 740°C/20 min | 770°C/20 min | 246 ± 11 |
| | S2 | | 790°C/20 min | 282 ± 32 |
| | S3 | | 820°C/20 min | 283 ± 34 |
| | S4 | | 850°C/20 min | 307 ± 16 |
| Set 2 | M1 | 740°C/20 min | 770°C/20 min | |
| | M2 | | 770°C/60 min | |
| | M3 | | 770°C/150 min | |

The flexural strength was about 246 ± 11 MPa by following a S1 heat treatment profile. A maximum flexural strength of 307 ± 16 MPa is obtained for S4 profile, as shown in Table 2. 8. XRD analysis of Huang et al. showed that the main phase

at low temperatures was Li_2SiO_3 , whereas LiSi_2O_5 was dominant at 790°C, which is accompanied by disappearance of Li_2SiO_3 . Zhang et al. 2014 [166] studied lithium-disilicate glass-ceramics with the compositions listed in Table 2. 6-7. A huge loss in strength when samples were subjected to longer holding times. In the other hand, the flexural strength reaches the highest value of about 392 ± 27 MPa for a 650°C/6h → 830°C/3h sample, while the lowest value flexural strength was 242 ± 31 MPa for a 650°C/72h → 830°C/3h sample. However, there was a significant improvement for all samples after third stage heat treatment (650°C/3-72h → 830 °C/3h → 550 °C/3h) of value flexural strength from 562 MPa to 611 MPa.

Both Lien et al. 2015 [170] and Li et al. 2016 [171] employed a glass-ceramic with uniform composition well-known as IPS e.max Press (Ivoclar Vivadent), as an original material. Lien et al. 2015 [170] measured the highest flexural strength of 367 ± 43.3 MPa, for a heat treatment done at 820–840 °C for 14 min. This is accompanied increase of hardness to 8.2 ± 0.1 GPa and elastic modulus to 99.0 ± 1.29 GPa. Li et al. 2016 [171] employed a simple heating schedule, following a continuous first stage at 610°C/1h and second stage at 755 °C/8h, 799 °C/4h, 843°C/2h, 900°C/1h. The highest elastic modulus of 117.66 ± 0.96 GPa accompanied by a highest Vickers hardness and flexural strength of 9.07 ± 0.13 GPa and 370 ± 36 MPa, respectively, was obtained after subjecting the glass to 610°C/1 h and 799°C/4h.

2.9.2 Lithium aluminosilicate (LAS) glass ceramics

Guo et al. (2006) [167] analysed the effect of TiO_2 , ZrO_2 , P_2O_5 and/or F as nucleating agents for lithium aluminosilicate (LAS) glass-ceramics compositions shown in Table 2. 6-8. They discovered that the addition of P_2O_5 and F on the LAS glass which undergoes crystallization, permits the alteration of crystallization kinetic parameters. A. Arvind et al. (2008) [168] developed two new lithium aluminosilicate glass compositions which are shown in Table 2. 6-9. They found that the presence of TiO_2 with P_2O_5 impacts phase formation and morphology by a slight increase in the temperature of peak crystallization. In addition, they speculated that TiO_2 crystallites serves to form lithium-titanate that acts as a site for heterogeneous nucleation. This mitigates the crystallization of quartz and promotes the crystallization of cristobalite. Additional studies of LAS glass-ceramics were also done by Hu et al. 2009 [106], who studied the influence of

Chapter Two: Literature Review and Prior Studies

ZrO_2 and TiO_2 as nucleating agents. Through the course of their research, they studied different LAS compositions, which are noted in Table 2. 6-10. They found that when TiO_2 is used as a nucleating agent it may cause a reduction in the Vickers hardness, fracture toughness and flexural strength. They concluded the ideal concentration of TiO_2 to be 2.36%.

Laczka M. et al. (2014) [10] studied the LAS glass ceramics composition listed in Table 2. 6-11. They used ZrO_2 and P_2O_5 were used as nucleating agents. According to their DTA data, the glass transition temperature (T_g) is $\sim 490^\circ\text{C}$. Moreover, they observed two notable exothermic peaks, one at approximately 630°C and other at 729°C , plus two other minor peaks at 770°C and 846°C . Łaczka K. el al. (2014) [169] also investigated the thermal characterisation of LAS glass-ceramics with the chemical composition, shown in Table 2. 6-12. According to the particular DTA for that study, 495°C was found to be the transition temperature (T_g) of glass. Again, there were two significant exothermic peaks, one at $\sim 627^\circ\text{C}$ and the other at 720°C , and two other small exothermic peaks at 771°C and 847°C , as shown in Fig. 2. 22.

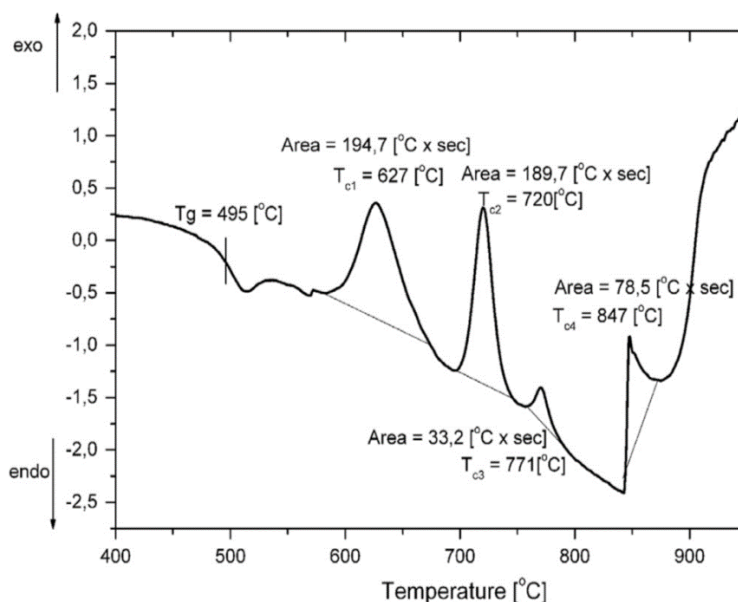


Fig. 2. 22 DTA thermogram shows endothermic and exothermic reactions of the LAS glass used in the study [169].

Laczka M. et al. [10] developed unique heating treatment (nucleation and crystallization) profiles for this LAS glass-ceramic system based on the DTA data; and those are listed in Table 2. 9.

Chapter Two: Literature Review and Prior Studies

Table 2. 9 Heat treatment profiles of investigated glass samples.

| Profile 1 | Profile 2 | Profile 3 | Profile 4 | Profile 5 |
|------------|----------------------------|--|--|--|
| Nucleation | Nucleation/ 630°C/30min | Nucleation /630°C/30min /730°C/30min | Nucleation /630°C/30min /730°C/30min /770°C/30min | Nucleation /630°C/30min /730°C/30min /770°C/30min /850°C/30min |

Laczka M. et al. discovered a progressive increase in the flexural strength from a value of 185 MPa for nucleation to 280-310 MPa for profile 2 and 3, reaching a maximum of~ 400 MPa for profile 5. Assessment of the XRD data showed samples from profile 1 and profile 2 had no LiAlSi₂O₆. This phase starts developing at 730°C/30 min. The 5% Li₂SiO₃ found in the nucleated sample increased to 12% at 630°C/30 min, as shown in Fig. 2. 23.

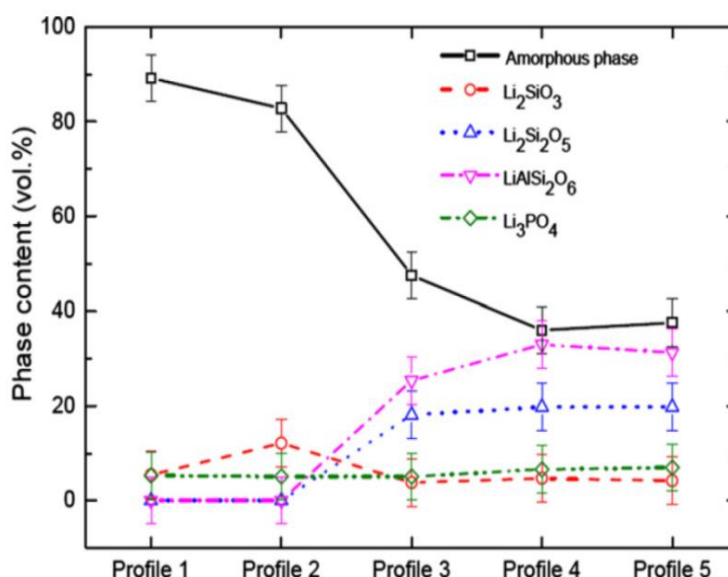


Fig. 2. 23 Volumetric phase content of the heat-treated samples [10].

Lower content of Li₂SiO₃ was observed for profiles 3, 4 and 5, however Li₂Si₂O₅ and LiAlSi₂O₆ contents were seen to increase sharply, reaching a maximum proportion for profile 5. Therefore, it can be stated that Li₂Si₂O₅ and LiAlSi₂O₆ crystals develop from 730 to 850 °C. Łaczka K. el al. [169] discovered that Li₂Si₂O₅ and LiAlSi₂O₆ crystals started developing at a temperature of 720°C to a level intensity of 23% just within 5 mins and slowly increased with increased annealing times. It was also reported that Li₂SiO₃ is the first crystalline phase to appear during heating at 630°C after 5 min. Interestingly, the petalite type structure (LiAlSi₄O₁₀) appeared at 720°C after 5 min and then disappeared at 720°C after 30 min.

2.10 Effect of V₂O₅ and CeO₂ as colouring oxides on Li-Si glass-ceramics

Certain oxides are incorporated into dental glass manufacturing to produce different shades of colour, these oxides include Fe₂O₃, NiO, Co₃O₄, Fe₂O₃, V₂O₅, CeO₂, etc. Generally, these compounds are included into the base glass mixture [172]. Numerous studies [173]–[175] were conducted to assess the effect of oxide colouring agents on optical properties shown by glass. There has been recent research conducted to assess the use of colouring agents such as MnO₂ [176], [177], Cr₂O₃ [178] and, V₂O₅ and CeO₂ [179], [180] in lithium based glass-ceramics. Gaddam A. et. al. (2014) [176] conducted experiments to analyse the effect of 0, 0.5, 1.00 and 2.00 mole% MnO₂ within Li₂O–K₂O–Al₂O₃–SiO₂ glass system. According to their findings, there was a redox equilibrium of Mn²⁺/Mn³⁺ with predominance of Mn³⁺, which caused the development of a purple colour in glass. Additional studies were conducted by Molla A. R. et al (2012) [177] to analyze the optical properties shown by transparent MnO₂ doped Li-Si based glass–ceramics (SiO₂:70.64, K₂O:3.09, Li₂O:14.68, Al₂O₃:3.38, P₂O₅:3.21, ZrO₂:3.00, CeO₂:1.88, MnO₂:0.12, 1.00, 3.00, 5.00 w%) prepared through controlled crystallization methods. It was observed that increasing the non-bridging oxidants along with the rise of Mn content minimises of the optical band gap. Rukmani S. J. et al (2007) [179] to analyse after effects from the addition of colouring oxides include CeO₂, V₂O₅, and MnO₂ to the Li-disilicate glasses produced by Ivoclar. It was concluded that CeO₂, V₂O₅, and MnO₂ are potentially likely to remain in residual glassy phase of the glass ceramics. This is highlighted by the higher effect seen for V₂O₅, and MnO₂ in glass-ceramic samples compared to that of glass. Kim D. et al (2020) [180] proceeded to analyse the effect of V₂O₅ colouring on two Li-disilicate glass-ceramics systems by maintaining definitive concentrations of V₂O₅, SiO₂, Li₂O, and P₂O₅ at the following values from 0.5, 65.92, 27.58, to 1.5 mol%, respectively, while simultaneously altering the ratio of ZnO/K₂O and Al₂O₃/K₂O from 0.5 to 2. It was found that all the glasses had a green-like colour which can be attributed to the presence of V⁺⁵ ions. Variation of the level of V⁺⁴, V⁺³ and V⁺⁵ caused an alteration in the colour from light-green to a violet, greenish, bluish and brownish hues of glass ceramic, as depicted in Fig. 2. 24. It was seen that following crystallization at greater temperatures, majority of the vanadium ions were scattered within the vestigial glassy matrix in an inhomogeneous manner. Additionally, minute amounts of V⁺⁵ ions were doped

into the crystalline phase which developed a greenish colour. This is vastly important for dental use.



Fig. 2. 24 Photographs of glass and glass-ceramics samples [180].

2.11 Commercial lithium disilicate-based glass-ceramics: IPS e.max®, Vita Suprinity and Celtra Duo

In 2006, Ivoclar Vivadent AG, Liechtenstein, introduced the IPS e.max® CAD, a lithium disilicate-based glass-ceramic CAD/CAM block for fabrication of dental prosthetic restorations such as crowns, veneers, inlays and onlays. Such blocks are supplied in a pre-crystallized state encompassing lithium metasilicate. Their colour varies between blue and bluish grey to white, which is associated compositional variations. In this intermediary machinable stage, the biaxial flexural strength of this material is $\sim 130 \pm 30$ MPa, the Vickers hardness is around 5400 ± 200 MPa, whereas its fracture toughness is $\sim 0.9\text{--}1.25$ MPa. $\sqrt{\text{m}}$. Following milling this can be crystallized in about 25 minutes at 840°C. Upon heat-treatment, the microstructure will mainly encompass lithium disilicate crystals, which will impart the final mechanical properties, such as a biaxial flexural strength of $\sim 360 \pm 60$ MPa, a Vickers hardness of $\sim 5800 \pm 200$ MPa and a fracture toughness of $\sim 2.0\text{--}2.5$ MPa $\sqrt{\text{m}}$. These properties are combined with appropriate optical attributes, such as translucency and shade. According to Ivoclar the compositional range of this material is as follows: 11.0–19.0 wt.% Li₂O, 57.0–80.0 wt.% SiO₂, 0.0–11.0 wt.% P₂O₅, 0.0–13.0 wt.% K₂O, 0.0–8.0 wt.% ZrO₂, 0.0–8.0 wt.% ZnO, 0.0–5.0 wt.% Al₂O₃, 0.0–5.0 wt.% MgO, and 0.0–8.0 wt.% colouring oxides. P₂O₅ acts as a heterogeneous nucleating agent that

Chapter Two: Literature Review and Prior Studies

encourages volume nucleation of the lithium silicate-based phases [6]. Two newly fabricated zirconia-reinforced lithium silicate-based CAD/CAM blocks have been commercialised under the tradename of VITA Suprinity and Celtra Duo. Lithium disilicate ($\text{Li}_2\text{Si}_2\text{O}_5$) and lithium metasilicate (Li_2SiO_3) are the main phases in both [181]. Li_2SiO_3 phase size seems to have grown larger in Celtra Duo reaching $\sim 1 \mu\text{m}$, which is only $\sim 0.5 \mu\text{m}$ in Suprinity [181]. This difference can be associated with the differing glass composition and different thermal treatment parameters such as temperature and time. VITA Suprinity and Celtra Duo offered a high level of flexural strength, ranging between 370 and 420 MPa [182]–[185].

Chapter

| 3 |

Experimental Techniques

Chapter Three: Experimental Techniques

Introduction

This chapter describes the basics of the experimental techniques employed in this study. Basically, it covers two major categories of characterisation methods: non-destructive and destructive, as illustrated in Fig. 3. 1.

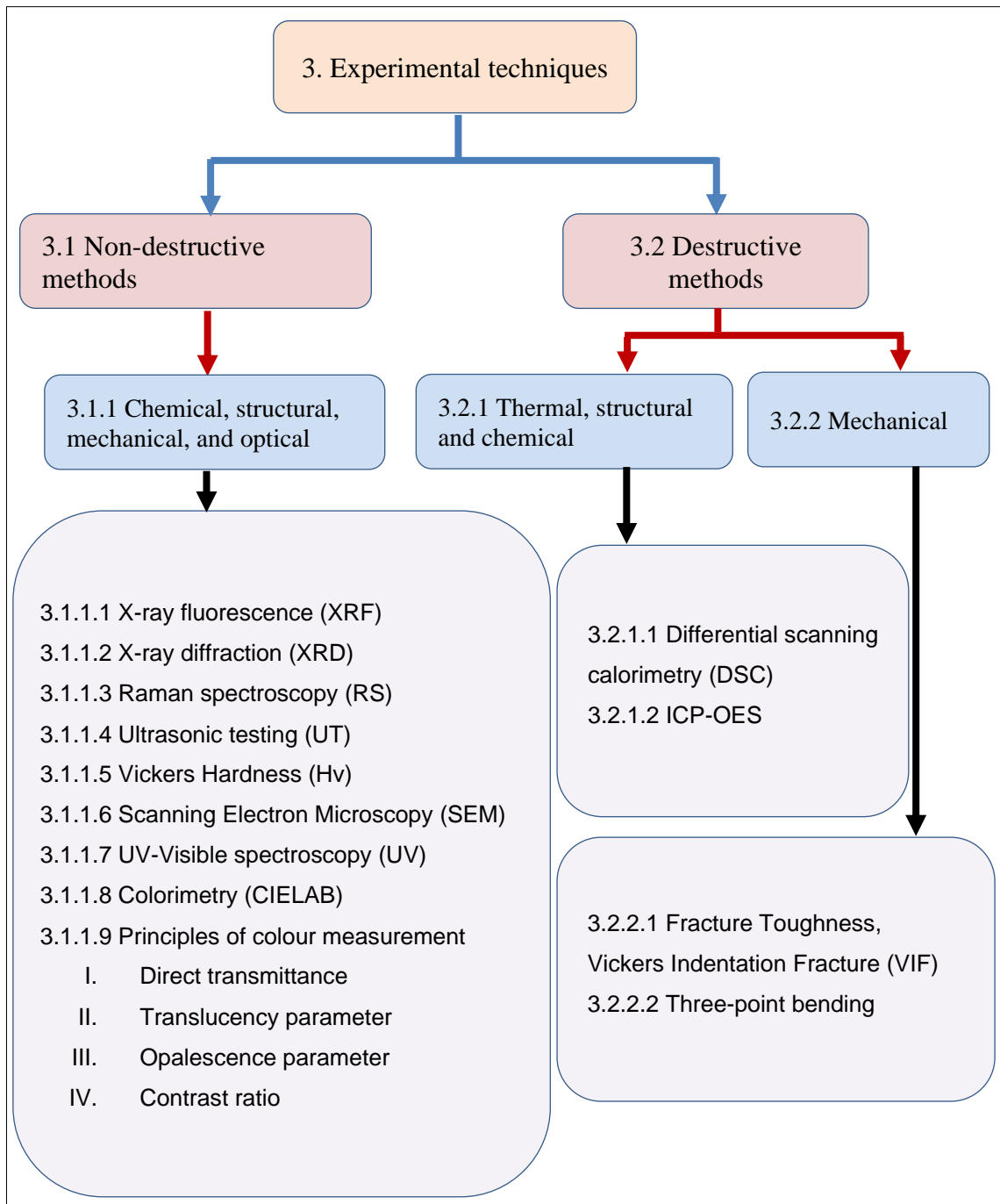


Fig. 3. 1 Diagram summarising the experimental techniques used in this study.

3.1 Non-destructive characterization methods

According to the American Society of Non-destructive Testing (ASNT) [186], non-destructive examination (NDE) is the examination of an object with technology that does not affect the object's future usefulness [186]. For example, this can be achieved using X-rays, ultrasound probes, electron beams and light.

3.1.1 Chemical, structural, mechanical, and optical characterizations

3.1.1.1 X-rays fluorescence spectroscopy (XRF)

X-rays fluorescence spectroscopy (XRF) is a technique that has ability to analyse and determine the bulk elemental composition of a range of materials. XRF instruments are composed of two key components: an x-ray tube and a detector. Primary X-rays emitted from the X-ray tube, are filtered and directed onto the surface of the sample to be characterised. When this X-ray beam strikes the atoms of the sample it will produce secondary X-rays (or X-ray fluorescence), which are collected and processed by a detector. The principle of this technique lies on the measurement of the energy of the secondary x-rays. Basically, a stable atom consists of a nucleus and electrons orbiting in quantic levels of energy, which are specific for each element. When a high energy x-ray beam strikes an atom, it disorders its equilibrium, by ejecting electrons and leaving behind electron holes. This leaves the atom unstable. To return stability, an electron in a higher energy levels may fall into the electron hole. As result of the difference of energy between these two levels, the energy excess is emitted in the form of secondary x-rays [187], as illustrated in Fig. 3. 2.

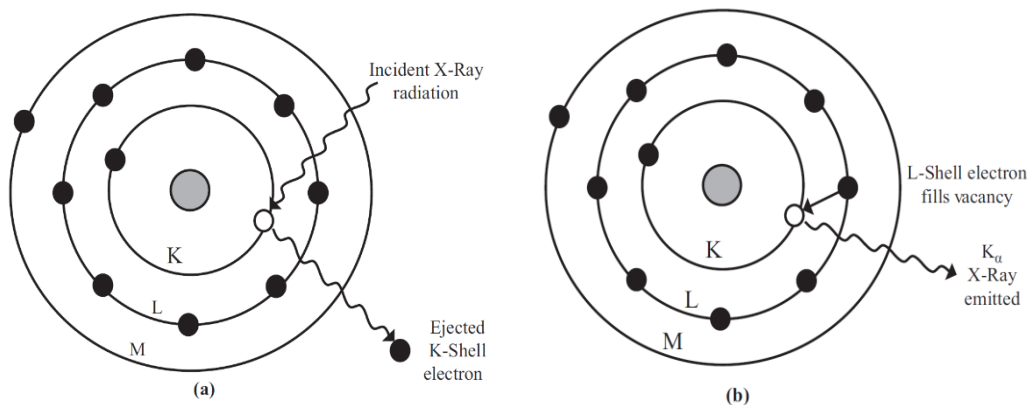


Fig. 3. 2 Schematic representation of X-ray fluorescence. (a) Electron ejection (b) X-ray emission [187].

Every single element has a characteristic set of electronic energy levels, thereby it will produce a characteristic X-ray spectrum, which can be analysed by either measuring the energies of the photons using an energy dispersive detector or by sorting the wavelengths using a wavelength dispersive detector. Hence, XRF can be employed as a qualitative technique, but also as quantitative one, through the calculation of the radiation intensity ratios associated with different elements [187].

3.1.1.2 X-ray diffraction (XRD)

XRD is a non-destructive testing method which allows the determination of the structure of crystalline phases, but also provides the ability to examine phase purity, thereby it can be employed for quantitative phase analyses. The principle of the XRD is based on the diffraction of X-rays by a periodic arrangement of atomic planes and energy-resolved detection of the diffracted signal [188]. X-rays are high energy electromagnetic radiation which energies ranging from approximately 100 eV to 200 keV. Thus they are positioned in the electromagnetic spectrum, between γ -rays and ultraviolet (UV) [189], as shown in Fig. 3 .3.

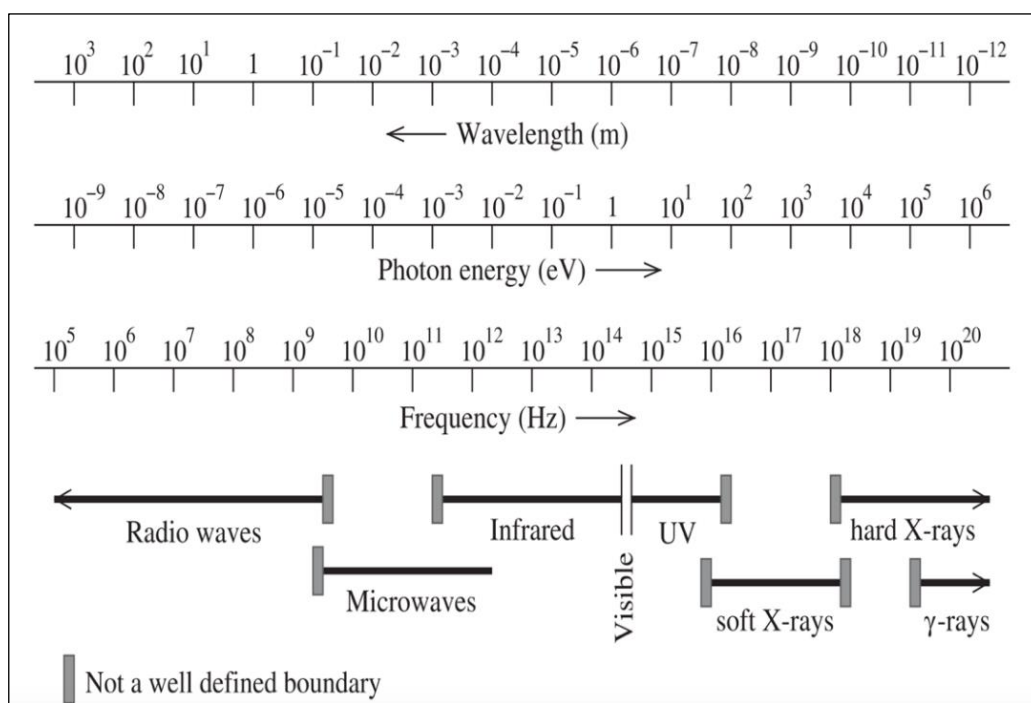


Fig. 3. 3 Electromagnetic spectrum with their frequencies and wavelengths ranges [190].

X-rays are produced by a so-called X-ray tube. This is a vacuum tube incorporating a cathode (filament) and an anode (target). The cathode emits electrons that are accelerated a high velocity towards the anode. X-rays are emitted when high-speed electrons strike the metal target, as shown in Fig. 3. 4.

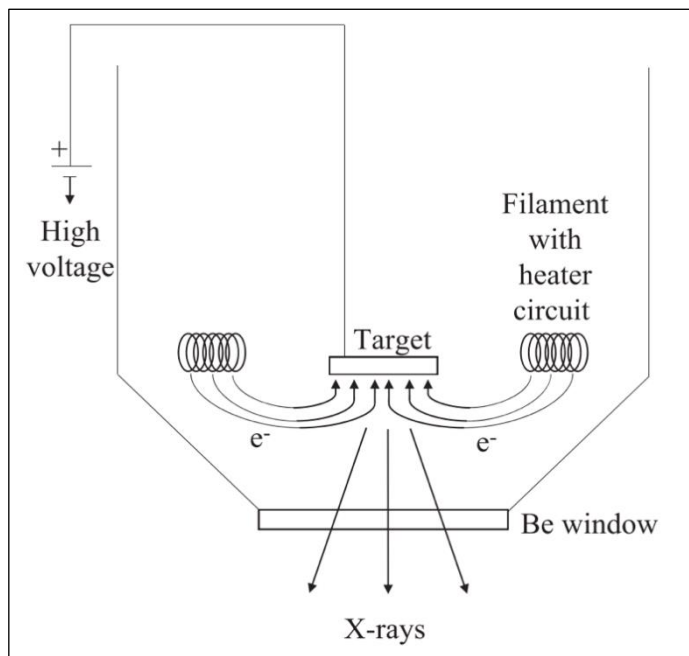


Fig. 3. 4 Schematic representation of a X-ray tube [187].

When X-ray photons exit the X-ray tube and hit the surface of sample to be investigated, an elastic scattering and Rayleigh scattering take place between the photons and the surrounded electrons of the nuclei. As a result, the X-ray photons that impinge on all atoms and are scattered in all directions. The output consists of two types of radiations resulting from constructive and destructive interferences. In constructive interference, the scattered wave retains its phase relationship with the source wave. This characteristic diffraction phenomenon is employed to investigate the crystal structure of materials [188].

Moreover, this phenomenon depends on the wavelength of X-rays, λ , and the angle of the incoming X-rays with the lattice planes, θ , and the interplanar distance, d_{hkl} , as shown in Fig. 3. 5. This principle was first proposed by W.L. Bragg [191], who derived equation 3.1, later known as Bragg's law.

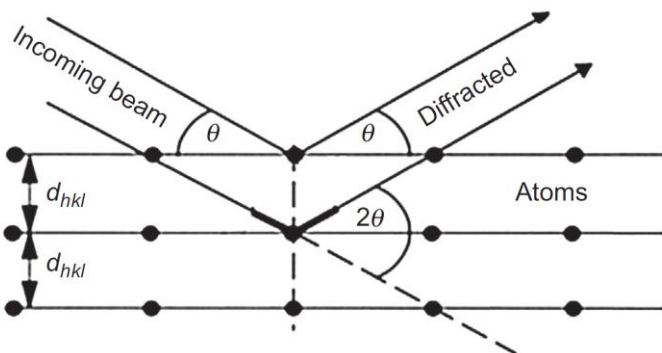


Fig. 3.5 Geometrical condition for diffraction from lattice planes [188]

Where;

$$n = 1$$

λ = X-ray wavelength

d_{hkl} = interplanar distance

θ = X-ray beam angle

3.1.1.3 Raman Spectroscopy (RS)

3.1.1.3.1 Raman Spectroscopy (RS) principle

Raman Spectroscopy (RS) is a non-destructive analysis technique that gives detailed information about chemical structure, phase assemblage and crystallinity. It can be used to carry out qualitative and/or quantitative analysis on a sample. RS is based on light (usually from a laser) interaction with the chemical bonds of molecule or the phonons of a solid. When monochromatic light illuminates a specimen, two forms of light scattering occurs; elastic scattering called "Rayleigh scattering" and inelastic scattering called "Raman scattering". The latter accounts for about 1% of total scattered intensity at frequencies different from the incident frequency [192]. Depending on the frequency of the scattered photon, the Raman scatter wavelength can be shifted either up or down. Consequently, Raman scattering can be divided into Stokes lines when energy is absorbed and anti-Stokes lines when energy is released, as shown in Fig. 3. 6.

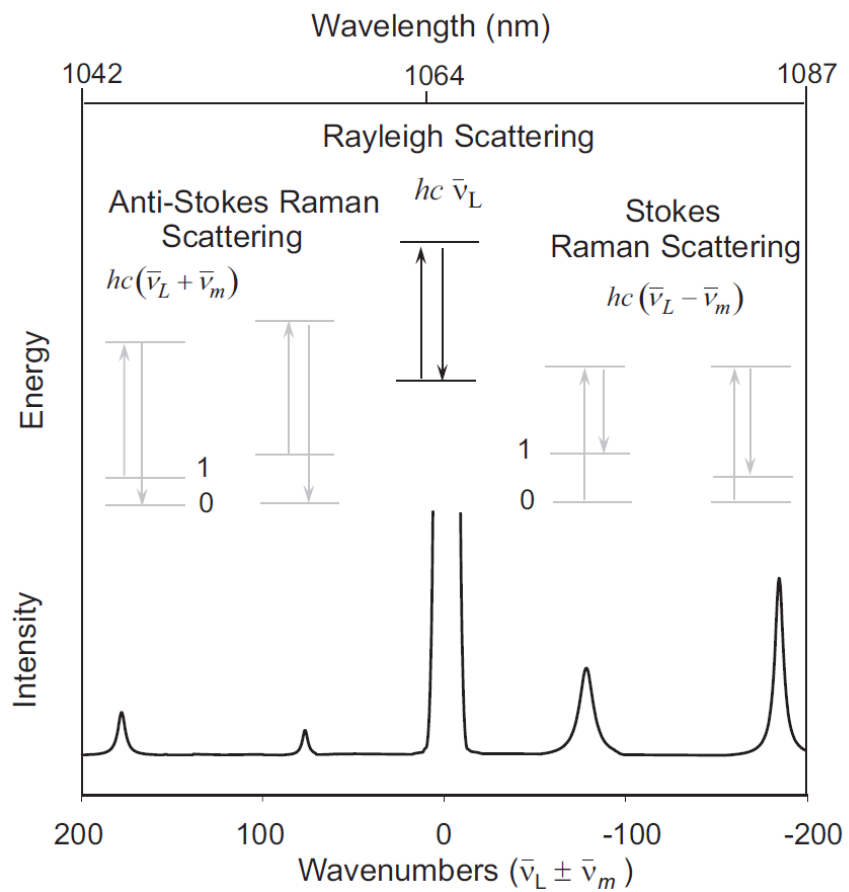


Fig. 3. 6 Schematic illustration of Rayleigh, Stokes and anti-Stokes Raman scattering [193].

The laser light is steered by numbers of mirrors onto the surface of the sample. The back-scattered radiation is collected and returned by a filter, which removes the Rayleigh scattering and enables the detection of the weak Raman signal, up to 50 cm^{-1} above the laser frequency. Then, different wavelengths are guided through a rotating diffraction grid and their intensities measured by charge-coupled device (CCD) detector [194], as shown in Fig. 3. 7.

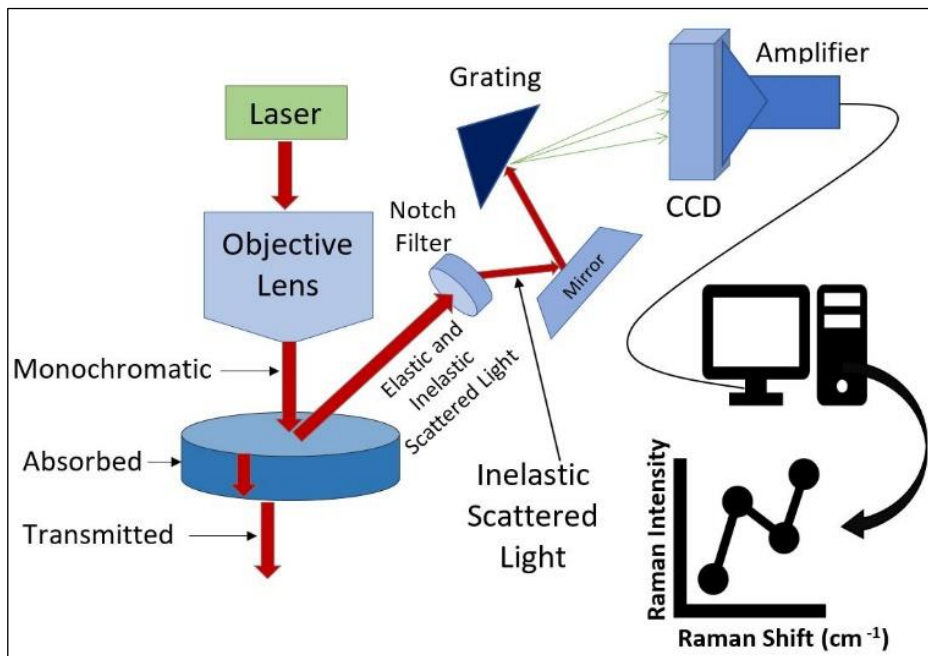


Fig. 3. 7 Schematic representation of a Raman spectrometer.

3.1.1.3.2 Raman spectra of phosphate, lithium disilicate and lithium aluminosilicate phases

A summary of the Raman band assignments for phosphate, lithium disilicate and lithium aluminosilicate phases is given in Table 3. 1. This was done by the identification of these in the literature data covering a wide range of phosphate, lithium di-silicate and lithium aluminosilicate glasses. Knowledge of the Raman modes helps to identify phases in multiphasic silicate glass ceramics.

Table 3. 1 Raman band positions identified from this study and band assignments taken from literature.

| Bands range | Bands assignment | References |
|---------------------------------------|---|---------------------|
| 300-400 cm ⁻¹ | O-P-O bending motions | [195], [196] |
| 350-650 cm ⁻¹ | bending vibrations of Si-O and Al-O bonds related to the aluminosilicate network | [196]–[198] |
| 650-800 cm ⁻¹ | (P-O-P) symmetric stretching of the bridging oxygen | [195], [199], [200] |
| 950-1200 cm ⁻¹ | Si-O-Si, Si-O-Al asymmetric stretching vibrations and symmetric Si-O- stretching vibrations | [195], [201]–[206] |
| 1050-1100 cm ⁻¹ | lithium di-silicate ($\text{Li}_2\text{Si}_2\text{O}_5$) | [195], [207] |
| 492 cm ⁻¹ | lithium aluminosilicate $\text{LiAlSi}_2\text{O}_6$ | [208], [209] |
| 338, 432, 490, 584 cm ⁻¹ | | [160] |
| 782, 947, 1060, 1174 cm ⁻¹ | | |

3.1.1.4 Ultrasonic Testing (UT)

Ultrasonic testing (UT) is a non-destructive technique that enables the measurement of physical properties (such as elastic modulus) and allows the determination of micro-defects, via the measurement of the propagation of ultrasonic waves through the material under test.

Generally, ultrasound energy can be defined as acoustic energy in form of waves above 20,000 Hz (above the human hearing range). Ultrasonic waves can propagate in different media including gas, fluids, and solids but not in vacuum. Thus, ultrasonic waves are widely applied in several different fields, including medicine (ultrasound imaging), non-destructive testing of structures and materials (to estimate damage and detect invisible flaws). The speed of ultrasonic waves varies depending on the type of the medium that they propagate through. For example, the ultrasound speed in the air is about 340 m/s, in water about 1530 m/s and in iron as high as about 5,850 m/s [210].

This clearly shows that ultrasonic waves propagate faster within solids, than liquids and gases. According to the propagation pattern, ultrasonic waves can be classified as compression (longitudinal) waves, the shear (transversal) waves and the surface (Rayleigh) waves [211]. In gas and fluid media only longitudinal waves propagate, while in solids both longitudinal waves and transverse waves propagate, as well as surface waves [212].

3.1.1.4.1 Ultrasound waves generation

The ultrasonic waves can be generated and received by piezoelectric transducers. A piezoelectric crystal within the transducer carries out the conversion of electrical energy into mechanical energy (and vice versa). Basically, when this crystal is exposed to an electrical pulse it results in the generation of ultrasonic waves. The crystal will convert the returning ultrasonic vibrations into electrical energy producing a voltage [213], [214].

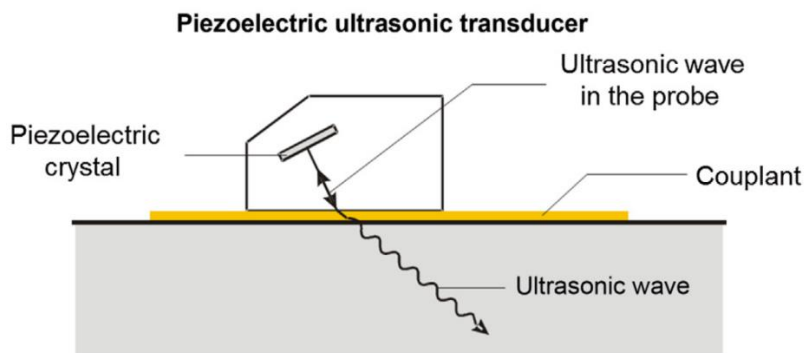


Fig. 3. 8 Principles of piezoelectric ultrasonic transducer [211].

Sound energy, particularly at the ultrasonic frequencies, are ineffectively transmitted through air. Any air gap between the test sample and the transducer hinders an efficient transmission of sound energy. Hence, couplants are used to facilitate the transmission of sound energy between the transducer and the test sample [215], as shown in Fig. 3. 8.

3.1.1.4.2 Ultrasound waves

Longitudinal waves propagate in the direction of the particle movement as shown in Fig. 3. 9 for the propagation of the ultrasonic wave along a thin rode axis. The periodic particle displacements are in the same direction as the wave propagation [211].

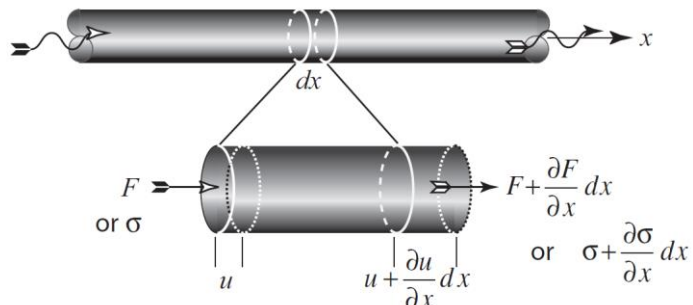


Fig. 3. 9 The propagation of Ultrasonic longitudinal wave (compressional wave) within a long thin rod [211].

The imbalance of forces (stresses) which are acting on the volume $A dx = V$ is resulting from the movement of particle.

$$\left(\sigma + \frac{\partial \sigma}{\partial x} dx \right) - \sigma = \frac{\partial \sigma}{\partial x} dx \text{ (Not stress)}$$

$$F_{imbalance} = \left(\frac{\partial \sigma}{\partial x} dx \right) A$$

By applying Newton's second law of motion, $F = m(\partial v_{\text{particle}} / \partial t)$ which indicates that a motion results from an imbalance in force. Therefore, the force imbalance could be substituted for Newton's second law of motion yields.

$$\left(\frac{\partial \sigma}{\partial x} dx \right) A = m \left(\frac{\partial v_{particle}}{\partial t} \right)$$

$$= \rho(dx A) \left(\frac{\partial}{\partial t} \frac{\partial u_x}{\partial t} \right) \dots \quad 3.2 [211]$$

$$\frac{\partial \sigma}{\partial x} = \rho(dx A) \left(\frac{\partial}{\partial t} \frac{\partial u_x}{\partial t} \right) \frac{1}{dx A}$$

$$\frac{\partial \sigma}{\partial x} = \rho \left(\frac{\partial^2 u_x}{\partial t^2} \right) \dots \quad 3.3 [211]$$

Where, ρ is the density of the material.

Here no Poisson's ratio impacts due to utilising a long thin rod with a stress-free surface. Therefore,

$$\sigma = E\varepsilon$$

$$\varepsilon = \frac{\Delta l \text{ (change in length)}}{l_o \text{ (original length)}}$$

$$= \frac{\left(u_x + \frac{\partial u_x}{\partial x} dx \right) - u_x}{dx}$$

$$\varepsilon = \frac{\partial u_x}{\partial x} \text{ (in axial strain)} \dots \quad 3.4 [211]$$

E Elastic modulus (Young's Modulus) was constant for uniaxial stress-strain (engineering elastic) [211].

Substituting Eq. (3.4) into Eq. (3.2), we get

$$\frac{\partial \sigma}{\partial x} = E \frac{\partial u_x}{\partial x} = E \frac{\partial}{\partial t} \frac{\partial u_x}{\partial t} = \rho \frac{\partial^2 u_x}{\partial t^2}$$

$$\frac{\partial^2 u_x}{dx^2} = \frac{\rho}{E} \frac{\partial^2 u_x}{dt^2} \dots \quad 3.5 [211]$$

Basically, the longitudinal wave is travelling as harmonic longitudinal wave. So, the wave function is

$$u(xt) = u_0 \cos(\omega t - kx)$$

$$u(xt) = u_0 e^{j(\omega t - kx)}$$

Uses the second partial differential with respect to displacement and time, the exponential formats are:

$$\frac{\partial^2 u}{\partial x^2} = -k^2 u_0 e^{j(\omega t - kx)} \quad \text{or} \quad \frac{1}{-k^2} \frac{\partial^2 u}{\partial x^2} = u(xt)$$

$$\frac{\partial^2 u}{\partial t^2} = -\omega^2 u_0 e^{j(\omega t - kx)} \quad \text{or} \quad \frac{1}{-\omega^2} \frac{\partial^2 u}{\partial t^2} = u(xt)$$

Now, these two differential equations could rearrange and be equating and gives;

$$\frac{\partial^2 u}{\partial x^2} = - \frac{k^2}{\omega^2} \frac{\partial^2 u}{\partial t^2} = \frac{1}{-v^2} \frac{\partial^2 u}{\partial x^2} = k^2 u(xt)$$

$$\frac{\partial^2 u}{\partial x^2} = \frac{1}{v^2} \frac{\partial^2 u}{\partial t^2} = 0 \dots \quad 3.6 [211]$$

Equation (3.6) appears as the linear equation for 1-D (x), where k considers the angular spatial frequency (wavenumber) and $v = \omega/k$ represents the phase velocity.

Therefore, the phase velocity of a one-dimension longitudinal wave in an isotropic, homogeneous medium (Substitute equation. 3.5 for equation. 3.6) gives:

$$V = \sqrt{E/\rho}$$

Consequently, the phase velocity (compression wave velocity) is computed only via the elastic properties and the density of the material. Thus, the longitudinal (compressional) wave velocity of one-dimensional $V = \sqrt{E/\rho}$ should be adjusted to comprise the changes of volume (volumetric changes) that appear in bulk materials: [216], we get;

$$V_c = \sqrt{\frac{E(1-v)}{\rho(1+v)(1-2v)}}$$

Where,

V_c Compression wave velocity, Ultrasound speed m/s.

ρ Density of material, kg/m³

E Young's modulus of elasticity (Elastic modulus), GPa.

v Poisson's ratio.

3.1.1.5 Vickers Hardness

The hardness of material can be determined by many methods including the Mohs, Vickers and Knoop methods. The Vickers indentation hardness method is often employed to measure the hardness of glass-ceramics. In this method, a diamond indenter installed in a hardness tester is used to create square pyramidal-shaped indentations, as shown in Fig. 3. 10. By measuring the diagonals of the indentation, the micro-hardness can be computed using the equation 3.7 [217];

$$HV = 1.854 P/d^2 \dots \quad 3.7$$

Where,

P = the force applied by the indenter in Newton (N)

d = the two diagonals of the rhomb impression d_1 and d_2 in micrometres (μm)

HV = Vickers hardness

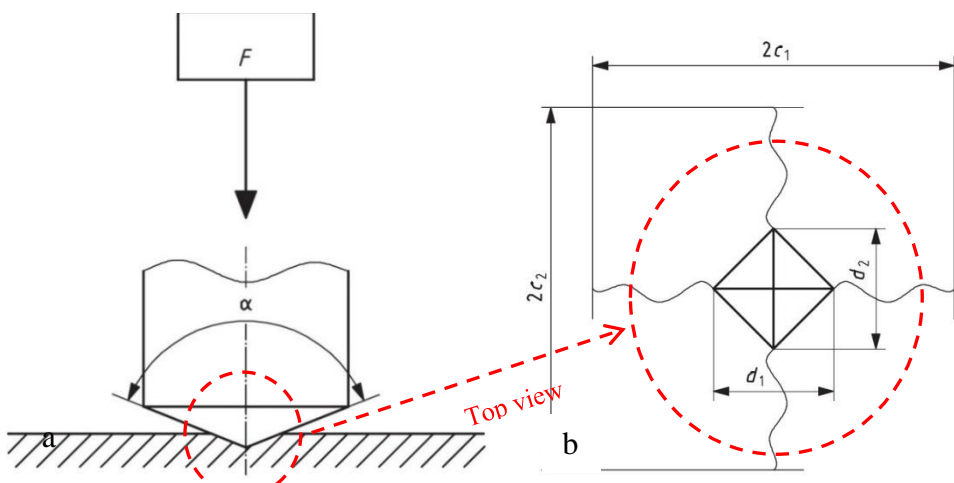


Fig. 3. 10 a) A Vickers indenter b) a Vickers indentation [217].

The surface finishing of the specimen plays an essential role in the micro-hardness measurement and until today, no precise method exists for determining the materials micro-hardness. Therefore, the measurements of hardness are executed by the comparison of the surfaces finished in same conditions with the same load and measuring method [217].

3.1.1.6 Scanning Electron microscopy (SEM)

Scanning electron microscopy (SEM) uses electrons to form an image [218]–[221]. Basically, an SEM creates images via the interaction of a scanning electron

beam with the sample's surface. A highly focused beam of electrons (primary beam) hits the surface of the sample inside a vacuum chamber. Upon hitting the surface of the sample, the primary electrons will generate several signals, including backscattered electron (BSE), secondary electrons (SE), Auger electrons and X-rays, as shown in Fig. 3. 11 [219], [220] [222]–[226]. SE emerge from near the surface resulting from inelastic interactions with the sample and are used to topography, whereas BSE emerge further down resulting from elastic interactions. BSE are sensitive to atomic number; therefore, they are used to create images containing compositional contrast [227].

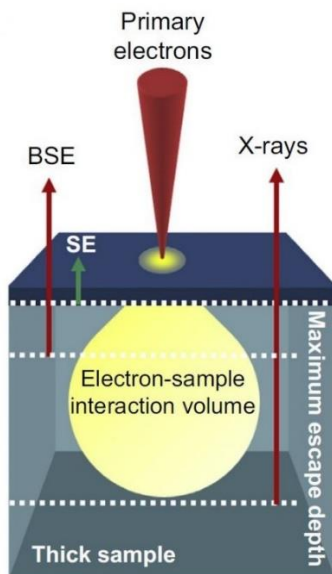


Fig. 3. 11 Schematic representation of the interaction of a primary electron beam with a sample, giving rise to BSE, SE and X-rays [227].

The typical layout of an SEM is illustrated in shown in Fig. 3. 12.

- 1- The electron gun on top (electron source and accelerating anode) that aims to accelerate electrons from 1 to 30 KV [223], [225].
- 2- The set of electromagnetic lenses consisting of two condenser lenses, objective lens and scanning coils. These electromagnetic lenses focus and control beam astigmatism, and drive the beam over sample's surface to form images [222].
- 3- A motorised stage inside a vacuum chamber [228].
- 4- Three sets of detectors (SE detector, BSE detector and X-rays detector) to collect interaction signals between the primary beam and the sample [227].

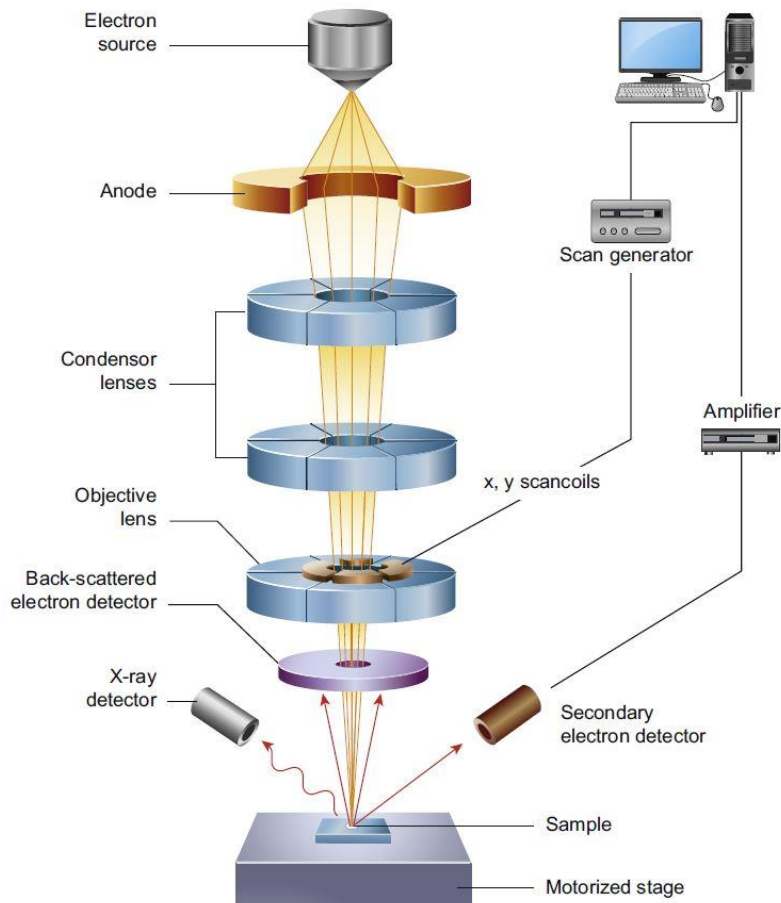


Fig. 3. 12 Components of SEM microscope: an electron gun, the electromagnetic lenses and the sets of detectors [227].

Magnification can reach 500,000 or higher. This allows that the microstructure of material to be investigated at different length scales [227].

3.1.1.7 Ultraviolet-visible spectroscopy

Ultraviolet-visible (UV) spectroscopy can be employed to measure the absorption or reflectance of a material using monochromatic light in the visible and adjacent UV range. Basically, UV measurements fall onto three subregions of electromagnetic spectrum, as shown in Table 3. 2.

Table 3. 2 Wavelength ranges for different spectral regions within electromagnetic spectrum.

| Spectral region | wavelength |
|-----------------|---------------|
| ultraviolet | 185 - 400 nm |
| visible | 400 - 700 nm |
| infrared | 700 - 1100 nm |

The transmission of light as illustrated in Fig. 3.13, can be employed to calculate the Transmittance, T, using the Beer-Lambert equation (the equation 3.8) [65];

$$I = I_0 e^{-\alpha l} \dots \quad \dots \quad 3.8$$

where I is the intensity of transmitted light and I_o is the intensity of incident light, thickness of the absorbing layer l , an absorption coefficient of the substance α . Basically, transmittance is the ratio of I/I_o

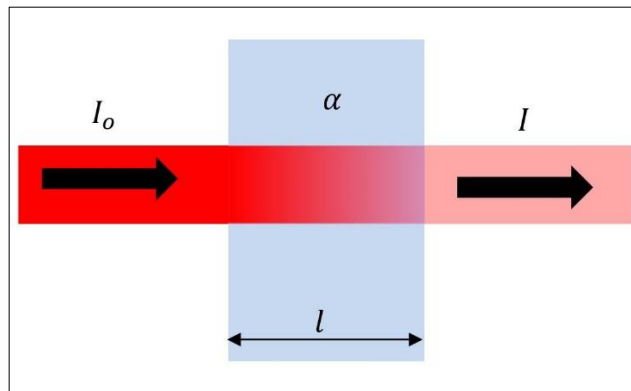


Fig. 3. 13 Beer-Lambert absorption of light [65].

3.1.1.8 Colorimetry

Colorimetry is based on principles of the human colour perception, i.e. it emulates the process that human eye perceives colour. Hence, a colorimeter uses an internal light source that illuminates the object's surface, as illustrated in Fig. 3.14.

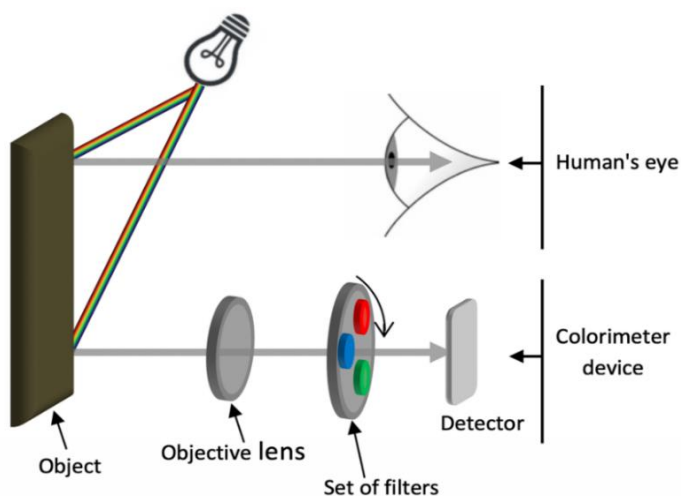


Fig. 3. 14 Schematic representation illustrating the colorimetry principle.

Reflected light comes back to the device, and passes through three filters: red, green, and blue. A detector quantifies the amount of light emerging from each filter, as shown in Fig. 3. 15. These filters extract tri-stimulus (RGB) values that

match how human eye perceives colour. Subsequently the RGB tri-stimulus values can be converted to CIE-XYZ and/or then CIE-LAB colour spaces.

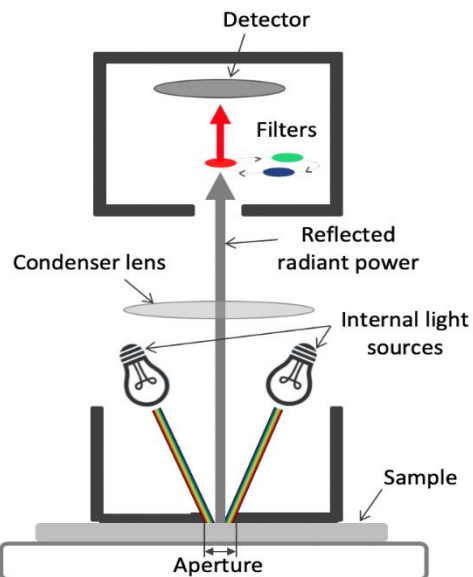


Fig. 3. 15 Schematic representation of the operation of a colorimeter.

3.1.1.9 Principles of colour measurement

Colour measurement is of paramount importance in dental restoration. Many recent studies use methods to quantify the direct transmittance of light, the translucency parameter (TP), the opalescence parameter (OP) and the contrast ratio (CR) [52], [76]–[78], [229]–[234].

I. Direct transmittance of light

The direct transmittance of light can be measured by ultraviolet-visible (UV-V) spectroscopy, see section 3.1.1.7. Measurements refer to the percentage of transmission (%T) between ~400 nm - 780 nm.

II. Translucency parameter (TP)

A colorimeter can be used to record the CIELAB coordinates (L^* , a^* and b^*), using white and black backgrounds. The values of the translucency parameter (TP) can be determined, according to the equation 3.10 [36], [230]:

Where the subscripts W and B indicate white and black backgrounds, respectively. A high TP value indicates high translucency [36].

III. Opalescence parameter (OP)

The values of a and b colour coordinates can be measured using a colorimeter against black and white backgrounds. The opalescence parameter (OP), can be calculated using the equation 3.11 [57], [73], [235], [236];

IV. Contrast ratio (CR)

The contrast ratio (CR), can be calculated using the equation 3.12 [54], [237], [238];

Basically, it defines the illuminance ratio (Y) of the test required material when it is located on a black background (Y_B) to the illuminance of the same material when it is located over a white background (Y_w). Hence, the contrast ratio (CR) value ranges from 0.00 for transparent material to 1.00 for a totally opaque material [36], [54].

3.2 Destructive Methods

3.2.1 Thermal, structural and chemical characterizations

3.2.1.1 Differential scanning calorimetry (DSC)

Differential scanning calorimetry (DSC) is technique employed to investigate the thermal behaviour of the materials. In the context of the present work, DSC is employed to determine the glass transition, nucleation, crystallization and melting events [3][96]. In theory, DSC analysis can be used to design the optimal heat treatment schedule to transform a glass into a glass-ceramic [96]. A DSC trace is a diagram that represents the amount of heat required to increase the temperature of the sample and a reference, usually alumina. Alumina constitutes as inert material without phases changes with increasing temperature, with a well define heat capacity. Basically, the operation of DSC is two main types; heat flux

and power compensated. The latter is operated when the sample and reference are heated up in separate furnace, the amount power desired for both at the same temperature is being the measured quantity. Whereas, the heat flux DSC is practically similar to the differential thermal analysis (DTA), can be measured by the difference in temperature between the sample examined and a reference sample during heating up. Unlike in the power compensated, both samples are heated in the same furnace and using a thermally conductive disc is to ensure a good heat flow. In DTA, the sample and reference are not necessarily kept in thermal contact, however, are still within the same furnace. The reference sample (usually is being Alumina) should be thermally inert over the heating range to assure that the temperature difference is incoming from the sample examined. Hence, this difference heat flux shows as peak and depending upon being of the heat required (either more or less), determining endothermic or exothermic [239], as shown in Fig. 3. 16. DSC experiment has been carried out on the glass and heated glass samples used in this study.

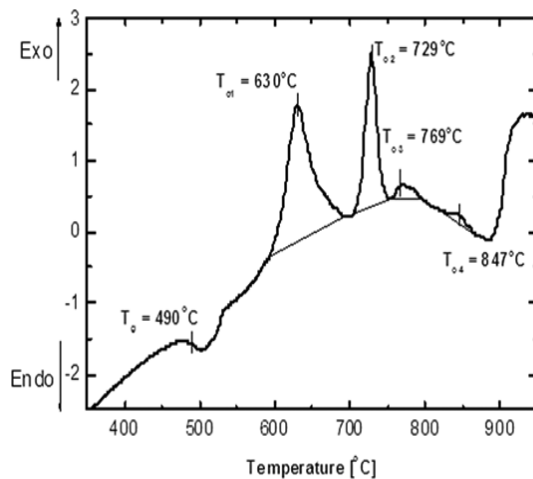


Fig. 3. 16 DTA curve pattern of $\text{Li}_2\text{O}-\text{Al}_2\text{O}_3-\text{SiO}_2$ glass system [10].

The formation and development of glass-ceramics is essentially dependent on the thermal behaviour of the glasses. Hence, the optimised features of glass-ceramics depend on heat treatments based on the differential thermal analysis (DSC/DTA) experiments.

3.2.1.2 Inductively coupled plasma-Optical Emission Spectroscopy (ICP-OES)

Inductively coupled plasma optical emission spectroscopy (ICP-OES) is a technique that offers the ability to precisely identify and quantify the elements present in a sample. The OES uses the visible and part of the ultraviolet regions

of the electromagnetic spectrum, between 130 nm and up to around 800 nm. Therefore, it can analyse a wide range of elements from lithium to uranium. Moreover, ICP-OES shows high accuracy, high precision and low detection limits. An ICP-OES instrument consists basically of two components, an inductively coupled plasma and an optical-emission spectrometer [240].

3.2.1.2.1 Inductively coupled plasma formation

Inductively coupled plasma can be produced by coupling the energy of a radio frequency (RF) generator into a suitable plasma gas. An electromagnetic field is generated by applying a high-power RF signal to a load coil, which positioned around the quartz torch designed to configure the plasma, as illustrated in Fig. 3. 17. Initially, a few seed electrons are generated by the spark of a Tesla coil and coupling with the flowing plasma support gas in the vicinity of the load coil results in ionizing of the flowing gas. These ions are accelerated by the electromagnetic RF field that produces adequate energy to ionize more support gas atoms and to create the ionized medium of the plasma. This results in a significant temperature increase and creates additional electrons. This cascading process generates and sustains the plasma. As a result, a steady state is formed at a high electron density which called plasma and its position is in the torch top as an intensive bright and shaped of fireball, as shown in Fig. 3. 17. Argon (Ar) is used as primary plasma gas with a secondary plasma gas Helium (He) [241]. The main function of ICP source is to excite atoms of the elements present [240].

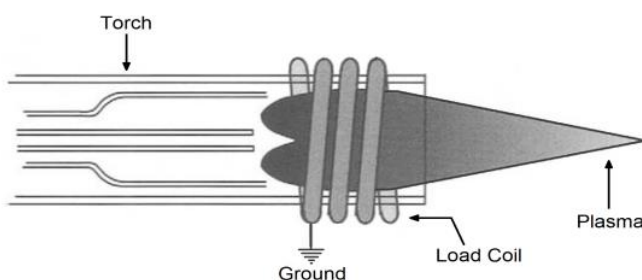


Fig. 3. 17 Schematic representation ICP source [241].

3.2.1.2.2 ICP-OES operating procedure

The sample is pumped from a vial into a nebulizer where it is mixed with argon gas to form an aerosol, this aerosol passes through the cooled spray chamber to remove larger droplets and gaining the fine aerosol which is pushed into the

central channel of the plasma. The aerosol droplets are dried as they travel through a high-temperature argon plasma which is 7000 - 10000°C, then decomposed and atomized. The purpose of this is to create free atoms and excites them to a higher state. When these exciting atoms come back down to the ground state, in this case, they emit light characteristic of the element being tested. A sample with different elements will emit light of different wavelengths. Hence, the emitted light passes through lenses and into a spectrometer. A diffraction grating and prisms in the spectrometer separate the incoming light into specific wavelengths. At the end of the spectrometer, there is a detector that can be measured the wavelength to determine the type of element and the intensity of light for each wavelength to determine how much of each element [240].

3.2.2 Mechanical characterization

3.2.2.1 Fracture Toughness by Vickers Indentation Fracture (VIF)

A high fracture toughness is an essential property for dental ceramics. Several methods are used to provide a good estimate of the fracture toughness.

Since ceramics are brittle materials, the conventional fracture toughness methods are the most difficult methods in terms of their implementation. Therefore, the indentation fracture toughness method using a Vickers Hardness tester emerges as an alternative method. This method is based on the measurement of cracks created during the Vickers Hardness test. For the application of this method, the surface of the sample needs to show a good finishing ($1 \mu\text{m}$ surface finish) in order to be able to visibly determine the cracks. An indentation is made under suitable force to secure that an adequate crack pattern is achieved. The technique demands that all cracks initiate at the corners of the indentation and the appearance of only radial cracks. These radial cracks are measured by the optical microscopy [3]. Researchers have used several equations to assess the fracture toughness. Some of these equations, 3.14 [6], 15 [242] and 16 [243], aimed to estimate the fracture toughness of materials by measuring cracks generated from a Vickers hardness indents [242], as shown in Fig. 3. 18. These selection formulas are listed in the below equations;

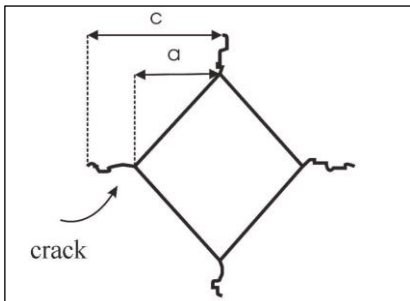


Fig. 3. 18 Vickers indentation spot [244].

Where;

K_{IC} = Fracture toughness

P = The indentation load in Newton

c = The radial crack length in meters.

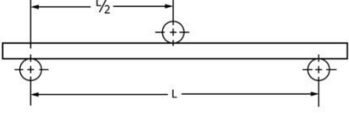
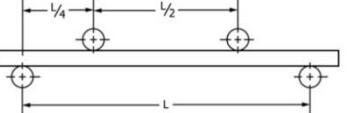
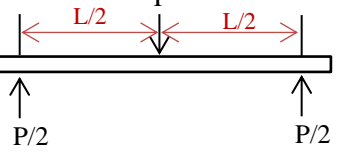
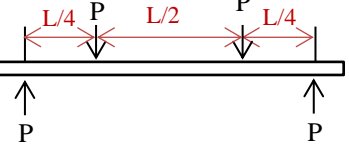
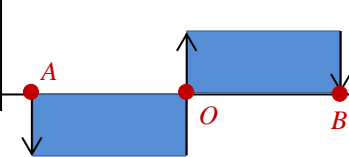
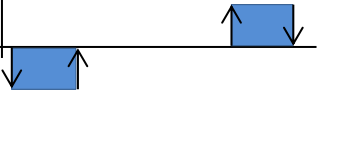
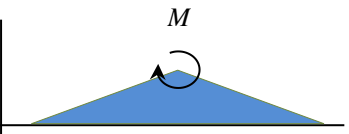
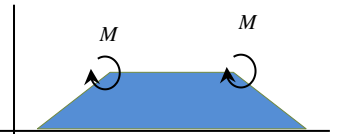
E = The modulus of elasticity for glass ceramic

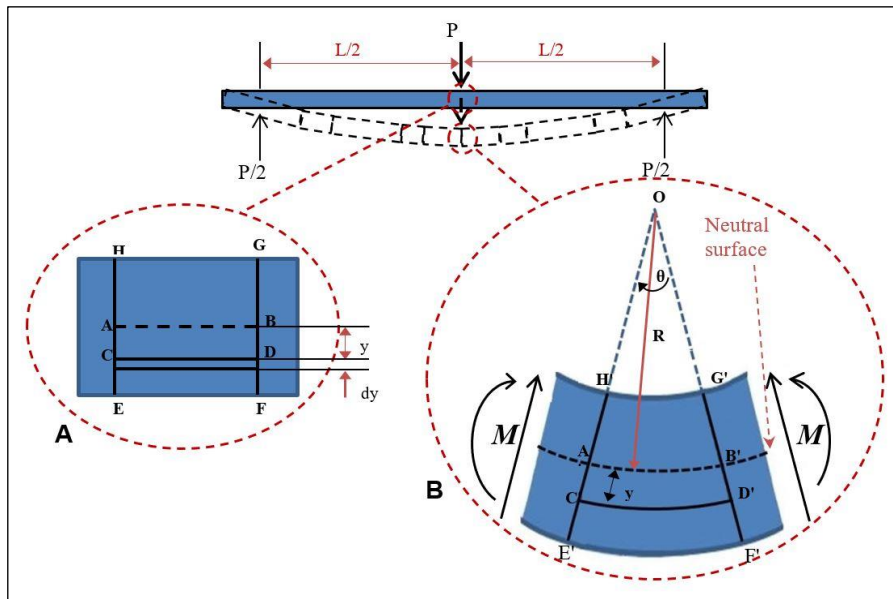
H_V = The Vickers hardness of glass ceramic

3.2.2.2 Three-point flexural test

Flexural strength testing is a technique which aims at measuring the tensile strength of brittle materials such as glasses and ceramics [245]. A simple beam is subjected to a bending load/moment until its breaks. So, the flexural strength could define as the material's ability to resist deformation under a bending load/moment. ISO 6872 [246] defines flexural strength as a measure of the ultimate strength of the materials (a specified beam) in the bending conditions. According to ISO 6872 [246], the flexural strength can be measured by three methods; three-point bending, four-point bending, and biaxial flexure (piston-on-three-ball). The bending flexural test whether three-point or four-point provides properties such as modulus of elasticity in bending, flexural strain and flexural stress of the materials. The three-point flexural test and the four-point flexural test are totally analogous, however the main difference being the positioning of loads. For three-point, the force applied is located at the middle of the beam between two support bearings. While for four-point, the beam is loaded at two positions between two support bearings, as shown in Table 3. 3. This fourth bearing provides a larger portion of the beam to the maximum stress. As oppose, in the three-point bending that is only under the central bearing. Therefore, the assessments or values for the flexural strength which is calculated by three-point bending will be remarkably higher than those by four-point bending [247].

Table 3. 3 Details on the three-point bending and four-point bending methods [248].

| | three-point bending | four-point bending |
|------------------------|--|--|
| Loading method |  |  |
| Free body diagram |  |  |
| Bending force diagram |  |  |
| Bending moment diagram |  |  |


 Fig. 3. 19 A) A beam initially unstressed, B) beam subjected to pure bending moment (M) [249].

The flexural stress for three-point bending can be calculated using a simple theory of elastic bending cases. According to the simple bending theory, we can consider that the beam is initially unstressed, as shown Fig. 3.19-A. Then, the beam is subjected to bending moment, as shown in Fig 3.19-B. Consequently,

Chapter Three: Experimental Techniques

this bending moment (B.M.) is subjected to the top of the beam which results in compression and the bottom to tension. Consider the AB length in the beam section at unstressed and distance y from the neutral axis. Then when the column bends, this will stretch to be A'B' and C'D' [249].

$$\text{Strain in fibre } AB = \frac{\text{extension}}{\text{original length}} = \frac{A'B' - AB}{AB}$$

From Fig. 3.19, $CD = C'D' \xrightarrow{N.A.\text{ is unstressed}} \therefore AB = CD$ [249].

\therefore length of arc = arc radius * angle subtend by the arc at the centre

$$\therefore A'B' = R * \theta \rightarrow A'B' = \theta R$$

$$C'D' (= AB) = (R + y) * \theta \rightarrow C'D' = \theta(R + y)$$

Thus,

$$\text{Strain in fibre } AB = \frac{\text{extension}}{\text{original length}} = \frac{A'B' - AB}{AB}$$

$$\text{Strain} = \frac{C'D' - A'B'}{A'B'} = \frac{(R+y)\theta - R\theta}{R\theta} = \frac{R\theta + y\theta - R\theta}{R\theta} = \frac{y\theta}{R\theta} = \frac{y}{R}$$

However,

$$Young's\; modulus\; "E" = \frac{Stress\; "\sigma"}{Strain\; "\varepsilon"}$$

$$\text{Strain} = \frac{\sigma}{E} = \frac{y}{R} \rightarrow \sigma = \frac{Ey}{R}. \quad \dots \quad 3.18 [249]$$

\therefore the strip is of area δA the force on the strip is

$$F = \sigma \delta A = \frac{Ey}{R} \delta A$$

This is a moment about the Neutral axis of (x y both terms)

$$Fy = \frac{E}{B} y^2 \delta A$$

The total moment for the whole cross-section is

$$M = \sum \frac{E}{R} y^2 \delta A = \frac{E}{R} \sum y^2 \delta A$$

The $\sum y^2 \delta A$ is second moment area (I) of certain cross-section;

From equation 3.18 could be obtained $R = \frac{Ey}{\sigma}$ and substituting in 3.19 which is given by [249], [250];

$$M = \frac{E}{Ey} I \rightarrow M = \frac{\sigma}{y} I$$

$$\sigma = \frac{My}{l} \dots \quad 3.20 [249]$$

From the free body diagram of three-point bending;

$$M_{max} = \frac{P L}{22} \rightarrow M = \frac{PL}{4}$$

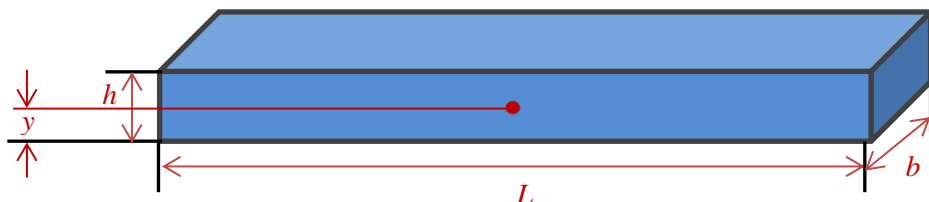


Fig. 3. 20 The Standard Specimen for three-point bending test.

$M = \frac{PL}{4}$ is the bending moment at the area of interest (N.m).

$y = \frac{h}{2}$ is distance at the maximum stress from the Neutral Axis (N.A.) (m).

$I = \frac{bh^3}{12}$ is second moment area about the N.A for a rectangular section sample (m^4), as shown in Fig. 3. 20.

Substituting these three conditions in the equation 3.20 and therefore the stress of a beam in three-point flexure is given by [246], [248];

$$\sigma = \frac{P \frac{L}{4} \frac{h}{2}}{bh^3} = \frac{3PL}{2bh^2}$$

Where;

σ = stress, in (MPa).

P= applied (breaking) load, in (N).

L = span of the beam between the supports, in (mm).

b = width of the specimen, in (mm).

b = width of the specimen, in (mm);

Chapter | 4 |

Materials and Research Methodology

Chapter Four: Materials and Research Methodology

Introduction

This chapter is focused on the materials and research methodology, including all the experimental procedures employed in this study, as outlined in Fig. 4. 1. Hence, this chapter comprises details on the experimental procedures used to: (i) investigate the thermal properties of two glasses with compositions in the LiO₂-Al₂O₃-SiO₂ (LAS) system, (ii) to characterise phase assemblage resulting from heat treatment and (iii) to investigate the mechanical and aesthetic properties.

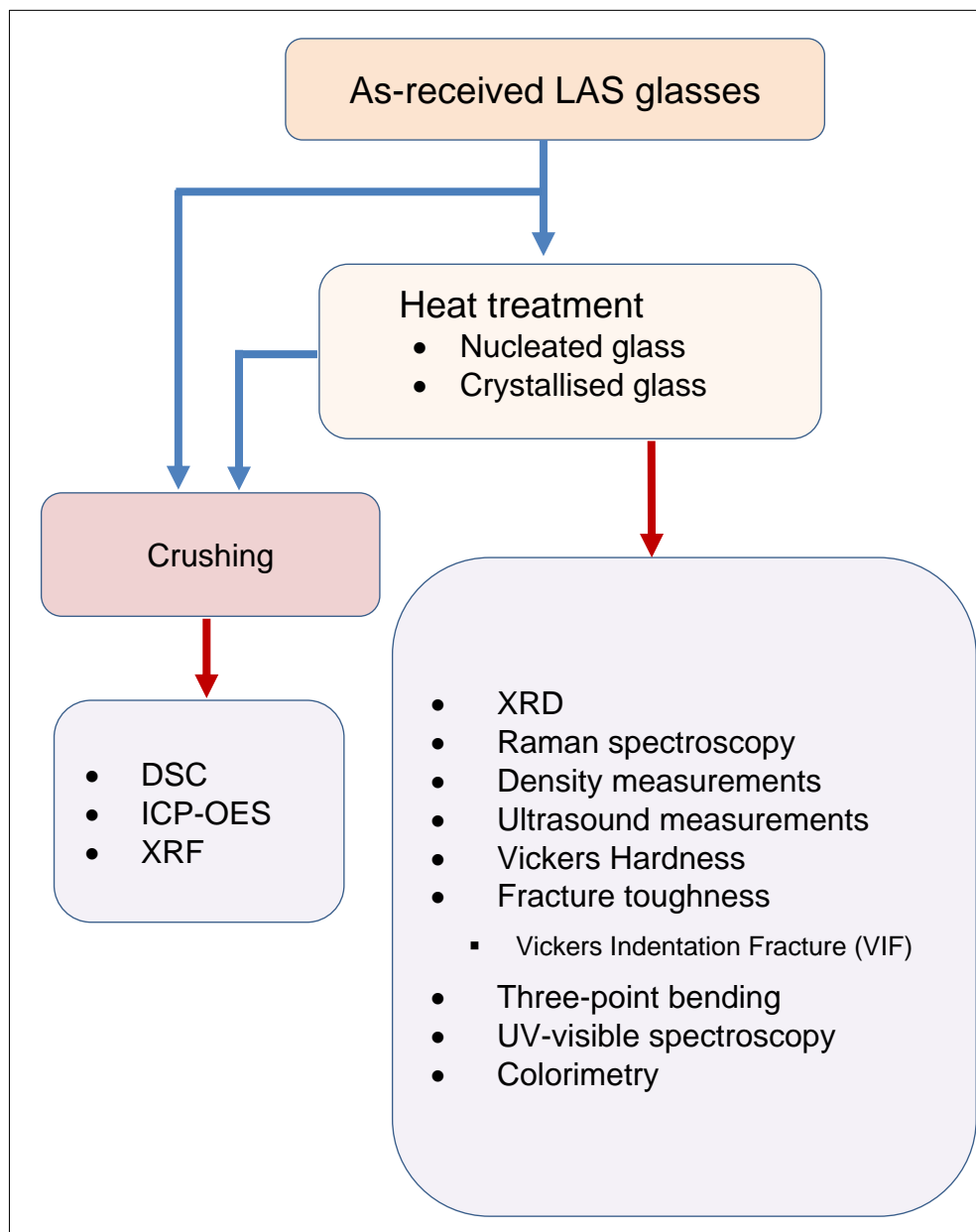


Fig. 4. 1 Flow diagram summarising the experimental methodology.

4.1 Materials

The materials investigated in this study are two glasses with compositions in the $\text{LiO}_2\text{-Al}_2\text{O}_3\text{-SiO}_2$ (LAS) system, hereafter referred to as LAS1 glass and LAS2 glass. Samples consisted of blocks of approximately $18 \times 14 \times 12 \text{ mm}^3$, which were supplied by an international biomaterials company. Both glasses are transparent, however LAS2 glass has a lightly yellow tint, as shown in Fig. 4. 2.

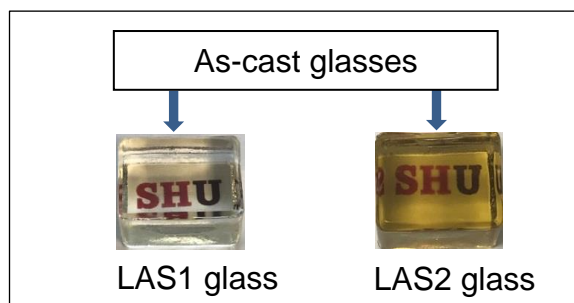


Fig. 4. 2 Glass blocks of LAS1 and LAS2.

4.1.1 Preparation of powder samples for XRF, DSC and ICP-OES

The glass blocks were pulverised using a vibratory disc mill RS 200, in order to prepare fine glass powders suitable for XRF, DSC and ICP-OES analyses. A glass block was placed inside a steel grinding set, which was then firmly attached to the vibration plate of the mill. The grinding speed was set at 700 rpm for the duration of 1 minute. Finely milled powders were obtained under these milling conditions, which were subsequently used for compositional analysis by ICP-OES and XRF. The results of these analyses for LAS1 glass and LAS2 glass powders are listed in Table 4. 1.

Table 4. 1 Chemical composition of both as-received glass blocks.

| Compounds ↓ | Formula ↓ | Chemical composition | |
|---------------------------|-------------------------|----------------------|------------------|
| | | LAS1 Glass (wt%) | LAS2 Glass (wt%) |
| Lithium oxide | Li_2O | 10.55 | 10.14 |
| Silicon dioxide (silica) | SiO_2 | 62.37 | 62.45 |
| Aluminium oxide (alumina) | Al_2O_3 | 11.92 | 11.83 |
| Phosphorous pentoxide | P_2O_5 | 4.09 | 4.03 |
| Zirconium oxide | ZrO_2 | 0.69 | 0.68 |
| Titanium oxide | TiO_2 | 0.03 | 0.02 |
| Sodium oxide | Na_2O | 4.16 | 4.12 |
| Potassium oxide | K_2O | 0.91 | 0.91 |
| Cerium oxide | CeO_2 | 1.18 | 1.17 |

| | | | |
|--------------------|--------------------------------|------------|------------|
| Vanadium pentoxide | V ₂ O ₅ | - | 0.41 |
| Cobalt oxide | CoO | 0.07 | 0.10 |
| Terbium oxide | Tb ₂ O ₃ | 1.28 | 1.28 |
| Calcium oxide | CaO | 2.22 | 2.14 |
| Tungsten oxide | WO ₃ | 0.53 | 0.72 |
| SUM | | 100 | 100 |

LAS1 glass and LAS2 glass exhibit similar compositions, with the exception to V₂O₅, which is well known to give the yellow appearance [3], observed in Fig. 4. 2 for LAS2 glass. ICP-OES and XRF data can be found in Appendix 1.

4.2 Heat treatment

4.2.1 Heat treatment design

Differential scanning calorimetry (DSC) analyses were employed to evaluate the thermal behaviour of both LAS1 and LAS2 glasses. Initial tests were carried from room temperature to melting using a heating rate of 5°C/min. These were employed to determine the temperatures of thermal events such as glass transition temperature, crystallisation phenomena and/or phase transitions, and melting temperature. Subsequently, different heating rates were employed to estimate the activation energies associated to those phenomena.

Following the preliminary evaluation of the thermal characteristics of LAS1 and LAS2 glasses, two different sets of heat-treatments based on those characteristics were carried out. The first set of experiments consisted of an isothermal heat-treatment at 550°C (the chosen nucleation temperature based on the initial DSC results) for periods of time ranging from 0 to 3000 minutes, as listed in Table 4. 2. The second set of experiments consisted of non-isothermal heat-treatments for 30 minutes in the 610 – 870 °C temperature range, as listed in Table. 4. 3, and of isothermal heat-treatment at 550°C for 300 min followed by non-isothermal heat-treatments for 30 min in the 630 – 870 °C temperature range, as listed in Table 4. 4. The latter were aimed at investigating the impact of the nucleation on the crystallisation process.

Chapter Four: Materials and Research Methodology

Table 4. 2 Isothermal heat-treatments at a nucleation temperature of 550°C.

| Sample | Heat-treatment |
|--------|---------------------------------|
| A1 | As-received glasses |
| A2 | 550°C $\xrightarrow{30min}$ ↓ |
| A3 | 550°C $\xrightarrow{150min}$ ↓ |
| A4 | 550°C $\xrightarrow{300min}$ ↓ |
| A5 | 550°C $\xrightarrow{3000min}$ ↓ |

Table 4. 3 Non-isothermal heat-treatment for 30 minutes in the 610 – 870 °C temperature range.

| | Heat-treatment | |
|--------|----------------|--------------------------------------|
| Sample | Heating rate | Maximum temperature and holding time |
| B1 | 5°C/min | 610°C $\xrightarrow{30min}$ ↓ |
| B2 | | 630°C $\xrightarrow{30min}$ ↓ |
| B3 | | 650°C $\xrightarrow{30min}$ ↓ |
| B4 | | 670°C $\xrightarrow{30min}$ ↓ |
| B5 | | 690°C $\xrightarrow{30min}$ ↓ |
| B6 | | 710°C $\xrightarrow{30min}$ ↓ |
| B7 | | 730°C $\xrightarrow{30min}$ ↓ |
| B8 | | 750°C $\xrightarrow{30min}$ ↓ |
| B9 | | 770°C $\xrightarrow{30min}$ ↓ |
| B10 | | 790°C $\xrightarrow{30min}$ ↓ |
| B11 | | 810°C $\xrightarrow{30min}$ ↓ |
| B12 | | 830°C $\xrightarrow{30min}$ ↓ |
| B13 | | 850°C $\xrightarrow{30min}$ ↓ |
| B14 | | 870°C $\xrightarrow{30min}$ ↓ |

Table 4. 4 Isothermal heat-treatment at 550°C for 300 minutes followed by non-isothermal heat-treatment for 30 minutes in the 630 – 870 °C temperature range.

| | Heat-treatment | |
|--------|--|--------------------------------------|
| Sample | Nucleation temperature and holding time | Maximum temperature and holding time |
| B1 | $550^{\circ}\text{C} \xrightarrow{300min}$ | 630°C $\xrightarrow{30min}$ ↓ |
| B2 | | 650°C $\xrightarrow{30min}$ ↓ |
| B3 | | 670°C $\xrightarrow{30min}$ ↓ |
| B4 | | 690°C $\xrightarrow{30min}$ ↓ |
| B5 | | 710°C $\xrightarrow{30min}$ ↓ |
| B6 | | 730°C $\xrightarrow{30min}$ ↓ |
| B7 | | 750°C $\xrightarrow{30min}$ ↓ |
| B8 | | 770°C $\xrightarrow{30min}$ ↓ |
| B9 | | 790°C $\xrightarrow{30min}$ ↓ |

| | | |
|-----|--|-------------------------------|
| B10 | | 810°C $\xrightarrow{30min}$ ↓ |
| B11 | | 830°C $\xrightarrow{30min}$ ↓ |
| B12 | | 850°C $\xrightarrow{30min}$ ↓ |
| B13 | | 870°C $\xrightarrow{30min}$ ↓ |

A final set of heat-treatments were carried out at temperatures below and above the major thermal events detected from the DSC analyses, as listed in Table 4. 5.

Table 4. 5 Heat-treatment profiles based on DSC thermal events.

| Sample | Sequence of maximum temperatures and holding time | | | | | | |
|--------|---|-------|--------|--------|--------|--------|-------|
| | 550°C | 670°C | 750°C | 780°C | 800°C | 830°C | 850°C |
| G1 | -0- | -0- | -0- | 120min | | | |
| | → | → | → | →↓ | | | |
| G2 | 30min | -0- | -0- | 120min | | | |
| | → | → | → | →↓ | | | |
| G3 | 30min | -0- | -0- | -0- | 120min | | |
| | → | → | → | → | →↓ | | |
| G4 | 300min | 30min | 030min | | | | |
| | → | → | →↓ | | | | |
| G5 | 300min | 30min | 090min | | | | |
| | → | → | →↓ | | | | |
| G6 | 300min | 30min | 120min | | | | |
| | → | → | →↓ | | | | |
| G7 | 300min | 30min | -0- | 030min | | | |
| | → | → | → | →↓ | | | |
| G8 | 300min | 30min | -0- | 090min | | | |
| | → | → | → | →↓ | | | |
| G9 | 300min | 30min | -0- | 120min | | | |
| | → | → | → | →↓ | | | |
| G10 | 300min | 90min | | | | | |
| | → | →↓ | | | | | |
| G11 | 300min | 90min | 30min | | | | |
| | → | → | →↓ | | | | |
| G12 | 300min | 90min | 90min | | | | |
| | → | → | →↓ | | | | |
| G13 | 300min | 90min | -0- | 30min | | | |
| | → | → | → | →↓ | | | |
| G14 | 300min | 90min | -0- | 90min | | | |
| | → | → | → | →↓ | | | |
| G15 | 300min | -0- | -0- | 30min | | | |
| | → | → | → | →↓ | | | |
| G16 | 300min | -0- | -0- | 60min | | | |
| | → | → | → | →↓ | | | |
| G17 | 300min | -0- | -0- | 90min | | | |
| | → | → | → | →↓ | | | |
| G18 | 300min | -0- | -0- | 120min | | | |
| | → | → | → | →↓ | | | |
| G19 | 300min | -0- | -0- | -0- | 30min | | |
| | → | → | → | → | →↓ | | |
| G20 | 300min | -0- | -0- | -0- | 120min | | |
| | → | → | → | → | →↓ | | |
| G21 | 300min | -0- | -0- | -0- | -0- | 120min | |
| | → | → | → | → | → | →↓ | |
| G22 | 300min | -0- | -0- | 120min | -0- | 30min | |
| | → | → | → | → | → | →↓ | |
| G23 | 300min | -0- | -0- | 120min | -0- | 90min | |
| | → | → | → | → | → | →↓ | |
| G24 | 300min | -0- | -0- | 120min | -0- | 120min | |
| | → | → | → | → | → | →↓ | |
| G25 | 300min | -0- | -0- | 120min | -0- | -0- | 30min |
| | → | → | → | → | → | → | →↓ |
| G26 | 300min | -0- | -0- | 120min | -0- | -0- | 90min |
| | → | → | → | → | → | → | →↓ |

| | | | | | | | |
|------------|---------|-------|-----|--------|-------|-------|--------|
| G27 | 300min | -0- | -0- | 120min | -0- | -0- | 120min |
| G28 | 300min | 90min | -0- | -0- | -0- | 90min | ↓ |
| G29 | 3000min | -0- | -0- | 120min | ↓ | | |
| G30 | 3000min | 90min | -0- | -0- | 90min | ↓ | |

Note: all heat treatment profiles above are carried out for LAS1 glass, however, the heat treatment profiles, **bold line**, are for LAS2 glass.

Basically, all aforementioned heat-treatment profiles were intended to assess the impact of nucleation and crystallisation on both the mechanical and optical properties of this novel LAS-based glass-ceramic system. Samples resulting from these four sets of heat-treatments were therefore analysed by following the methodology summarised in Fig. 4. 1 and the results for LAS1 and LAS2 glasses, are presented in chapters 5 and 6, respectively.

4.2.2 Heat treatment Process

The glass blocks were placed into an Al_2O_3 crucible as shown in Fig. 4. 3 (a), pushed into the hot zone of the tube furnace (Fig. 4. 3 (b), (c)). A K-type thermocouple placed inside the crucible near the glass blocks was used to feedback the temperature to the furnace's controller as shown in Fig. 4. 3 (c). Finally, two thermal insulating covers were placed at both ends of the furnace, as shown in Fig. 4. 3 (b). The temperature profiles listed in Tables 4. 2-5 were programmed into an Eurotherm controller.

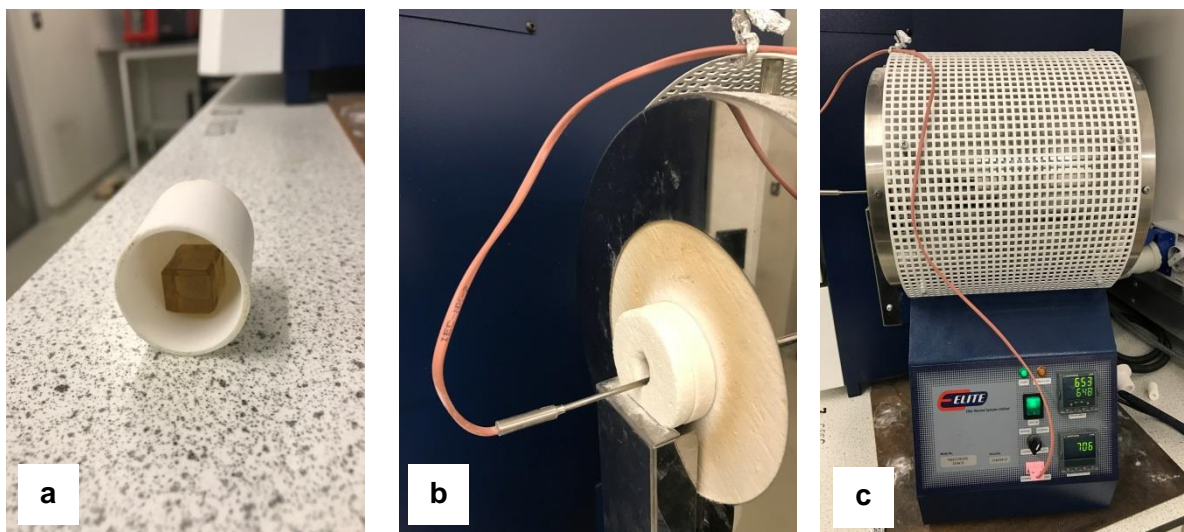


Fig. 4. 3 (a) Glass block inside Al_2O_3 crucible, (b) insulating covers and (c) the tube furnace, thermocouple and controllers.

4.3 Characterisation of bulk glass and glass-ceramics system

4.3.1 Sample preparation and XRF analyses

Approximately 1 gram of finely milled glass powder was mixed in a Platinum crucible with approximately 10 gram of Lithium Tetraborate flux (doped with 0.5% Lithium Iodide to stop the fused beads cracking). A Claisse LeNeo fused bead maker was used to heat up the platinum crucible to 1065°C, this melted the flux and the glass powder dissolved in the molten flux. This molten mixture was poured from the crucible into a casting mould, which cooled to form a flat disc-shaped fused bead. XRF spectra were measured using the PANalytical MagiX PRO spectrometer PW2440, which uses a Rh anode as a source of X-rays.

4.3.2 DSC analyses

Differential scanning calorimetry analyses for glass and heat-treated glass were acquired using the TA Instruments SDT-Q600 Simultaneous TGA / DSC (Fig. 4. 4) in Department of Materials Science and Engineering at the University of Sheffield.



Fig. 4. 4 TGA / DSC TA Instruments SDT-Q600.

Measurements were carried out from room-temperature to 1100°C, using heating rates of 5, 10, 15 and 20 °C/min. Alumina crucibles were used as reference and for the sample, as illustrated in Fig. 4. 5. Both empty crucibles were tarred for zero as the weighting calibration and then ~ 20 - 40 mg of powder sample was placed onto the sample crucible, while another empty alumina crucible and used

as a reference crucible. Finally, data were analysed using the TA instruments Universal Analysis 2000 software. DSC analyses were carried out to determine thermal events such as glass transition temperature (T_g), crystallisation and phase transition temperatures and melting temperature.

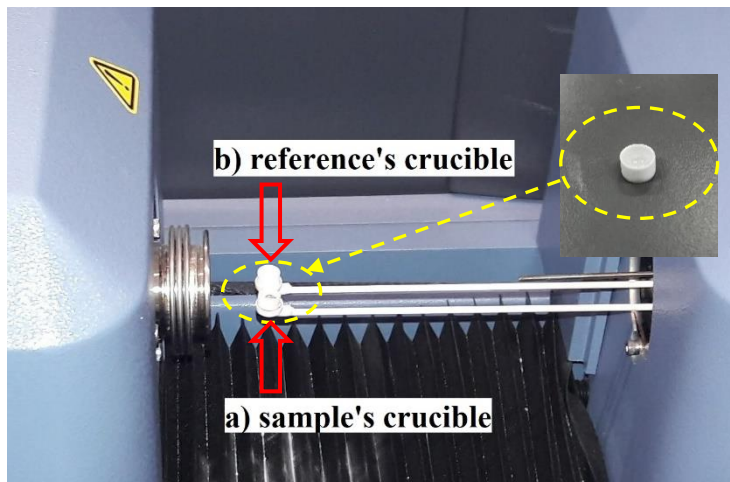


Fig. 4. 5 DSC (a) sample (b) reference crucibles.

4.3.3 Inductively Coupled Plasma Optical Emission Spectroscopy (ICP-OES) sample preparation

The finely milled glass powder was digested in an aqua-regia/HF acid mixture at 150°C. The sample was analysed by using a calibrated ICP-OES spectrometer (Spectro-Ciros-Vision) for ~ 70 elements.

4.3.4 XRD analyses

4.3.4.1 Room-temperature XRD analyses

XRD data were collected from polished and unpolished glass and glass-ceramic blocks using a multi-purpose sample stage. The height of stage was set according to the sample size. XRD patterns were collected at room-temperature using a PANalytical Empyrean diffractometer equipped with Co radiation, $\text{K}\alpha$ wavelength $\lambda = 1.78901 \text{ k-alpha1}$, $\lambda = .\text{k-alpha2} 1.79290$ radiation and an iron beta-filter. Data was acquired in the 2Θ range 5° to 130° using a step size of 0.01313° 2Θ and a time per step of 79.050s. Finally, phase identification was done using the International Centre for Diffraction Data (ICDD database).

4.3.4.2 In-situ XRD analyses

In-situ high temperatures XRD measurements were carried out on a Philips X'Pert PW3020 diffractometer equipped with CuK α radiation, wavelength $\lambda=1.540598 \text{ k-alpha1}$, $\lambda=1.544426 \text{ k-alpha2}$ operated using a current of 40 mA, a voltage 40 kV. Data was acquired using a step size of 0.0131303 2 Θ and time per step of 97.92 seconds.

4.3.5 Raman spectroscopy

Depolarised Raman spectra for polished and unpolished glass and glass-ceramic blocks were collected in backscattering geometry using a Thermo Scientific DXR2 spectrometer equipped with an optical microscope, Fig. 4. 6, and a 520 nm laser. A magnification of 10x was employed.



Fig. 4. 6 Raman microscope Thermo Scientific DXR2.

4.3.6 Scanning Electrons Microscopy (SEM) sample preparation

Selected heat-treated samples were etched with a 3% HF solution for 15 sec at British Glass and then to increase the conductivity of the surface and inhibit charging they were gold coated using a Quorum Q300T-T turbo-pumped coating system, as illustrated in Fig. 4. 7. This instrument allows the deposition of layers between 2 nm - 80 nm.



Fig. 4. 7 Quorum Q300T-T turbo-pumped coating system.

The surfaces of heat-treated glass samples were examined using a FEI Quanta 650 SEM equipped with EDS (Oxford Instruments), Fig. 4. 8, operated with an acceleration voltage of 20 kV.



Fig. 4. 8 SEM instrument FEI Quanta 650 and EDS (Oxford Instruments).

4.3.7 Ultrasound testing (UT)

4.3.7.1 Sample preparation for UT

For enhanced ultrasonic coupling, the samples were prepared as follows. First, blocks were ground to minimize surface protuberances. This process was carried out using abrasive SiC papers with successively finer particle sizes until an even surface was obtained for subsequent polishing. Initial grinding was carried out with a nominal P120 grit with an average particle size of 125 µm, whereas final grinding was performed with P1200 grit with an average particle size of 15.3 µm.

Finally, polishing was employed to remove scratches and grooves on the sample resulting from the grinding process. Diamond paste was employed to attain a 6 μm surface finishing.

4.3.7.2 UT Procedure

The block's thickness was taken at different positions using digital callipers. The average thickness was directly entered into the Olympus UT system. A M109-RM sensor was employed with the UT system, as shown in Fig. 4. 9, which allows to measure compression wave velocity. The Archimedes principle was employed to measure sample's density, as shown in Fig. 4. 10.

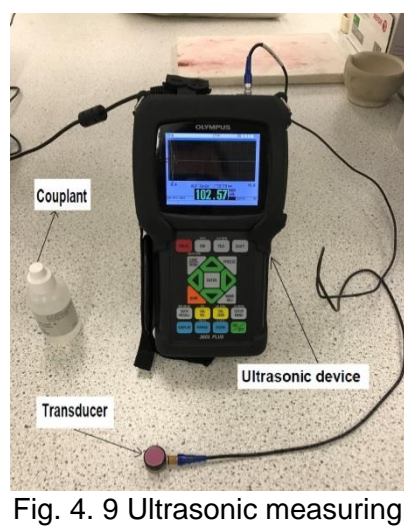


Fig. 4. 9 Ultrasonic measuring device.



Fig. 4. 10 Density measuring device.

A couplant gel (conductive medium) was placed between the sensor surface and the sample's surface in order to transmit directly waves to the specimen, as shown in Fig 4. 11. The sensor and sample are compressed by finger pressure to make sure the waves are travelling directly to the specimen, as shown in Fig 4. 11. Finally, compression wave speed was read.

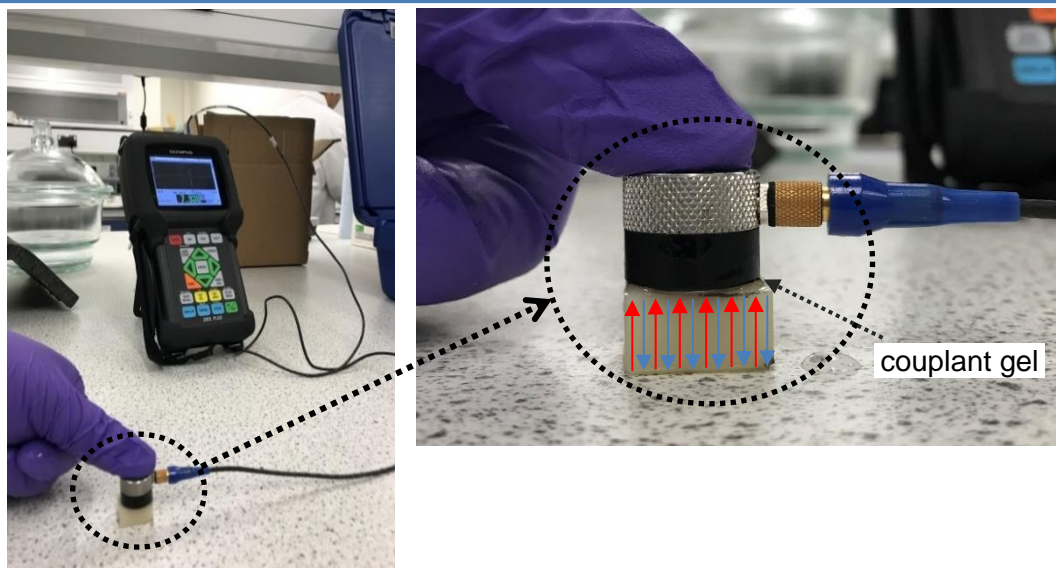


Fig. 4. 11 Ultrasound speed measurement procedure.

Subsequently, the speed of the compression wave together with sample's density was used to compute the sample's modulus of elasticity.

4.4 Characterisation of the optical properties

4.4.1 UV-visible spectroscopy

A Varian Cary 50 scan UV-visible spectrophotometer covering the 200 to 1100 nm spectral region, as illustrated in Fig. 4. 12, was employed in the study to characterise the light transmission through specimens of different thicknesses, which underwent different heat-treatments.

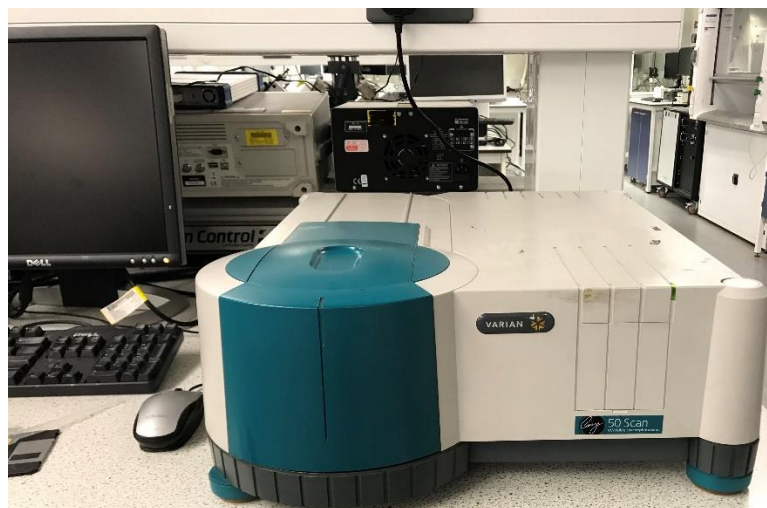


Fig. 4. 12 UV-visible spectrophotometer.

4.4.2 Colorimetry

A portable RM200QC X-Rite spectrophotometer, Fig. 4. 13-a was employed to directly obtain the CIELAB coordinates (L^* , a^* and b^*) from polished heat-treated specimens. The samples were placed under the 4 mm aperture of the portable spectrophotometer, as shown in Fig. 4. 13-b.

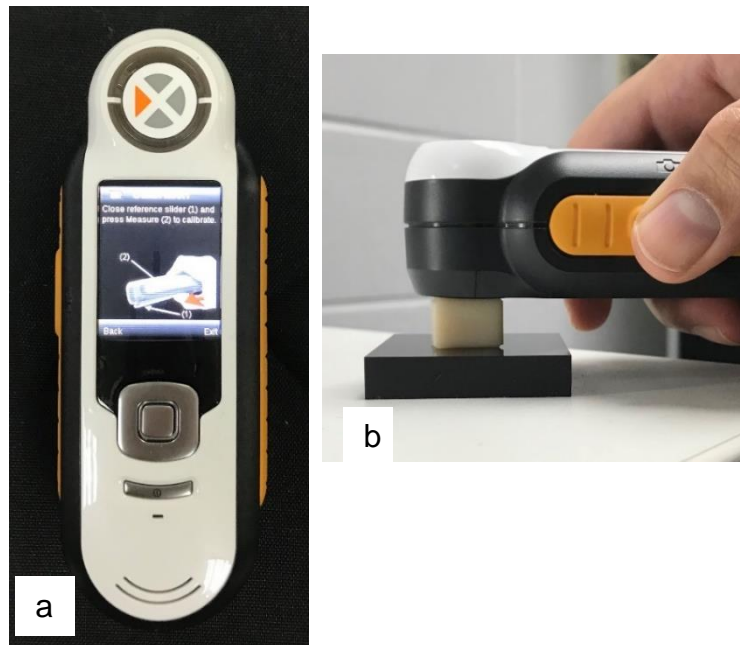


Fig. 4. 13 RM200QC X-Rite spectrophotometer.

Colour parameters were measured according to the CIE D65 Standard illuminate with 2° Standard Observer and determined by recording the colour difference between readings against white ($L^* = 97.89$, $a^* = 0.11$ and $b^* = 0.18$) and black ($L^* = 1.12$, $a^* = 0.12$ and $b^* = 0.48$) standard backgrounds for the same specimen, as depicted in Fig. 4. 14. These white and black are cast acrylic blocks (thickness: 10 mm, length: 50 mm, width: 50 mm). This is agreement with several studies which were mentioned in the literature, in the section 2.4.3.5.

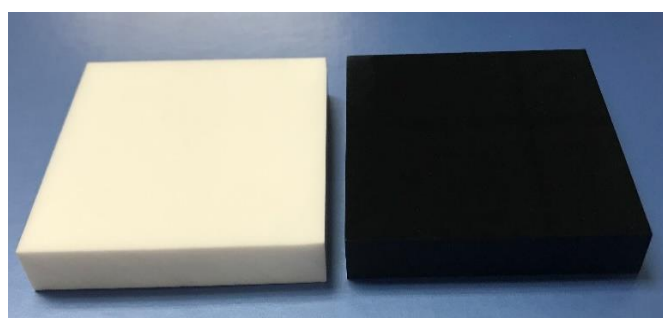


Fig. 4. 14 White and black standard backgrounds made from Cast Acrylic block.

Chapter Four: Materials and Research Methodology

The imaging spectroradiometer also was used to measure the CIELAB coordinates of sixteen shade tabs from the VITAPAN Classical shade guide A [1, 2, 3 and 3.5], B [1, 2, 3 and 4], C [1, 2, 3 and 4] and D [1, 2, 3 and 4] (VITA Zahnfabrik, Bad Säckingen, German), as depicted in Fig. 4. 15.



Fig. 4. 15 VITAPAN® Classical shade guide common which used in dental clinics.

CIE LAB values for the VITAPAN Classical shade guide, are listed in Table 4. 6.

Table 4. 6 CIE LAB values for the VITAPAN Classical shade guide.

| Shade | L | a | b |
|-------|------|------|------|
| A1 | 71.8 | -0.9 | 14.4 |
| A2 | 65.1 | 2.0 | 16.4 |
| A3 | 65.0 | 1.9 | 13.5 |
| A3.5 | 61.1 | 2.1 | 17.3 |
| A4 | 63.5 | 2.6 | 22.6 |
| B1 | 68.6 | -0.1 | 14.9 |
| B2 | 67.7 | 0.9 | 16.2 |
| B3 | 64.0 | 2.6 | 16.6 |
| B4 | 62.7 | 2.5 | 19.6 |
| C1 | 67.7 | 0.3 | 14.1 |
| C2 | 63.3 | 2.0 | 15.1 |
| C3 | 60.9 | 2.2 | 17.1 |
| C4 | 59.8 | 2.5 | 19.5 |
| D2 | 65.6 | 0.8 | 14.7 |
| D3 | 62.3 | 2.1 | 17.2 |
| D4 | 60.6 | 2.5 | 19.5 |

It is worth to mention that although VITAPAN Classical shade guide commonly used in many dental clinics as standard shades, the L*a*b* values maybe vary form between shade guides depending on many factors such as the manufacturer of shade guide, the device spectrometer measurement type, etc.

4.5 Characterisation of mechanical properties of glass and glass-ceramics

4.5.1 Hardness Test Procedure

Samples are prepared prior to be tested by grinding and polishing to a degree that their surfaces are flat and scratch-free, as described in section 4.3.7.1. The hardness tester used was Duramin-40, Struers, as shown in Fig. 4. 16-a. Firstly, the specimen was positioned onto a sample stage which is located directly under the microscope objective, Fig. 4. 16-b. After selecting a spot for indentation, the measurement lines were calibrated through the lens. Subsequently, an indentation was made using a diamond indenter.

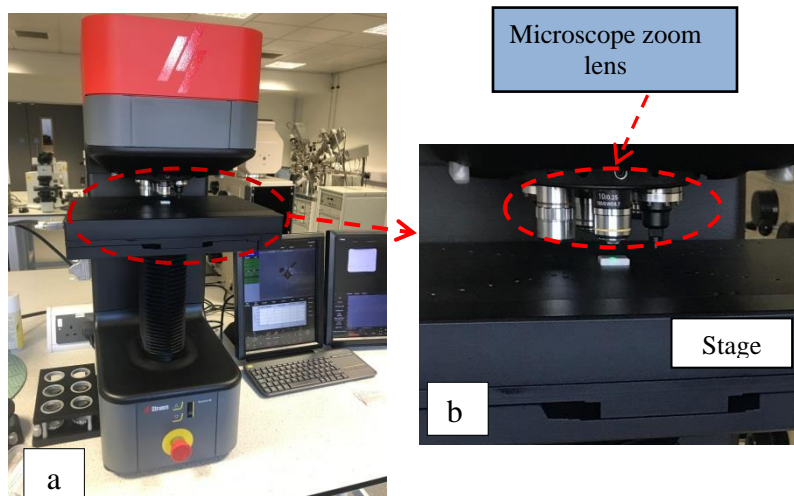


Fig. 4. 16 (a) Duramin 40 Struers Vickers hardness tester (b) objective lens and indenter revolver.

Diamond shaped indents could be found using a 50 X magnification and the diamond diagonals D₁ and D₂ were measured, as illustrated in Fig. 4. 17. Hardness Vickers values were calculated using equation $HV = 1.854 P/d^2$, that depends on loading applied, as discussed in the section 3.1.1.5. Five indentations were obtained for each specimen.

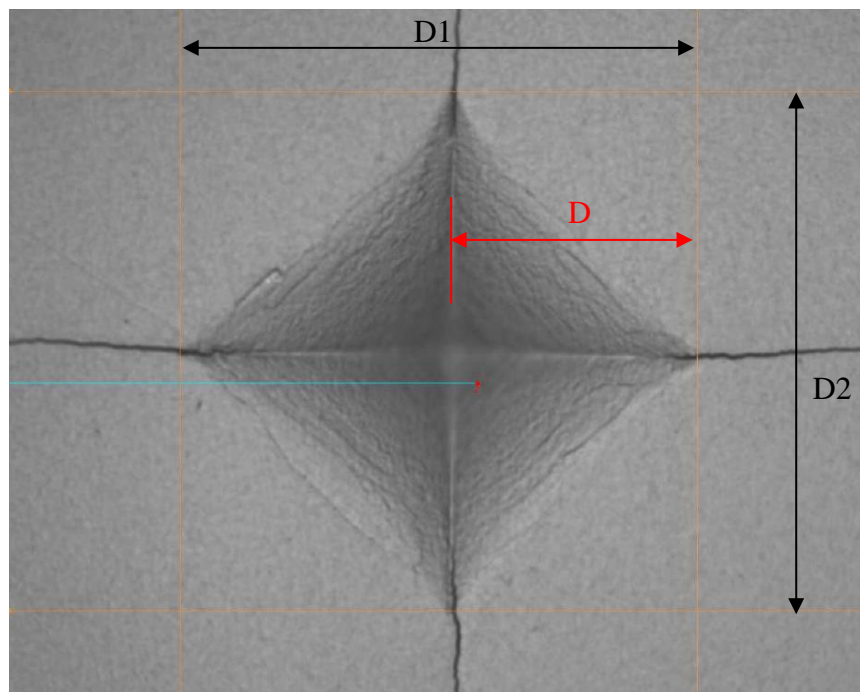


Fig. 4. 17 Typical diamond indentation after hardness test.

4.5.2 Fracture Toughness by Vickers Indentation Fracture (VIF) method

Measurement of the fracture toughness by the VIF method involves measuring the length of the cracks generated via the Vickers hardness test. Following the Vickers hardness test described in section 4.5.1, the microscope of the Duramin-40, Struers instrument was employed to measure the length of the cracks that emanate from the corners of the diamond indentation, as shown in Fig. 4. 18.

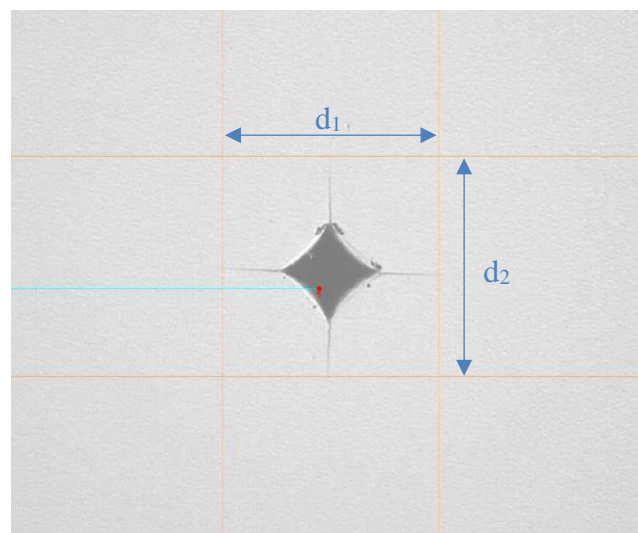


Fig. 4. 18 Determination of the crack lengths.

The instruments software was employed to measure the length of cracks d_1 and d_2 (micrometre), as shown in Fig. 4. 18. Appendix 6 shows the calculation of the fracture toughness by the VIF method.

4.5.3 Three-point bending

4.5.3.1 Specimen preparation for three-point bending testing

Ten bars (~18 mm × ~4 mm × ~3 mm) of selected samples, as shown in Table 4. 7 for LAS1 glass, were cut from heat-treated sample blocks using a Accutom 100, Struers precise cutter, as illustrated in Fig. 4.19. Because glass ceramics are tough materials, the blade speed was set at 2500 rpm and feeding rate at 2.5 mm/min. The specimens were grinded and polished to reduce the thickness from 3 to 2.1 mm, according to ISO 6872 [246]. The final bars, as shown in Table 4. 7, were grinded and polished as described in section 4.3.7.1.



Fig. 4. 19 Accutom-10/100 Struers precision cutter.

Table 4. 7 Selected samples for three-point bending testing.

| Samples | 550°C | 670°C | 750°C | 780°C | 800°C | 830°C | 850°C |
|---------|-------------|------------|---------------|---------------|---------------|-------|-------|
| | 30min → | -0- → | -0- → | -0- → | 120min → ↓ | | |
| | 300min → | 30min → | 030min → ↓ | | | | |
| | 300min → | 30min → | 090min → ↓ | | | | |
| | 300min → | 30min → | -0- → | 030min → ↓ | | | |
| | 300min → | 30min → | -0- → | 090min → ↓ | | | |
| | 300min → | 30min → | -0- → | 120min → ↓ | | | |
| | 300min → | 90min → | -0- → | 090min → ↓ | | | |

| | | | | | | | |
|---|-------------|----------|----------|---------------|----------|---------------|---------------|
|  | 300min → | -0- → | -0- → | 30min → ↓ | | | |
|  | 300min → | -0- → | -0- → | 90min → ↓ | | | |
|  | 300min → | -0- → | -0- → | 120min → ↓ | | | |
|  | 300min → | -0- → | -0- → | 120min → | -0- → | 30min → ↓ | |
|  | 300min → | -0- → | -0- → | 120min → | -0- → | 90min → ↓ | |
|  | 300min → | -0- → | -0- → | 120min → | -0- → | 120min → ↓ | |
|  | 300min → | -0- → | -0- → | 120min → | -0- → | -0- → | 30min → ↓ |
|  | 300min → | -0- → | -0- → | 120min → | -0- → | -0- → | 90min → ↓ |
|  | 300min → | -0- → | -0- → | 120min → | -0- → | -0- → | 120min → ↓ |
|  | 300min → | -0- → | -0- → | 120min → ↓ | | | |

4.5.3.2 Three-point bending Test Procedure

The three-point bending testing was performed using a Instron 3367 universal machine, Fig. 4.20, with a load cell of 500 N. The span length was ~12 mm, and the crosshead movement speed was 0.5 mm/min.

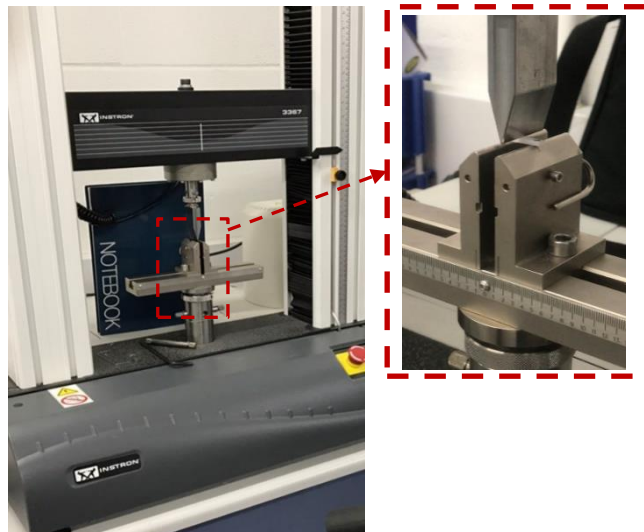


Fig. 4. 20 Instron 3367 universal machine for three-point bending testing.

Chapter

| 5 |

Processing and characterisation
of the LAS1 Glass

Chapter Five: Processing and Characterisation of the LAS1 Glass

Introduction

This chapter reports and discusses the experimental data obtained for the LAS1 glass composition (see Table 4. 1). Basically, the effect of heat treatment on phase assemblage, mechanical and optical properties is presented and discussed. Initially, thermal analyses are employed to gather some insight into the thermodynamics and kinetics of crystallisation, prior to the establishment of specific heat treatment schedules. Subsequently, XRD analysis are employed to associate crystallization and/or phase transformation to the thermal events detected by DSC. Finally, both mechanical and optical properties are correlated to the microstructure and phase assemblage, which are evaluated by combination of XRD, SEM and TEM. The study of the mechanical properties is focussed on the evaluation of elastic modulus, hardness, fracture toughness and flexural strength, whilst the optical characterisation is focussed on both colour evolution and levels of light transmittance.

5.1 Differential Scanning Calorimetry (DSC) Analyses

5.1.1 DSC analyses of the as-cast LAS1 glass composition

Based on the analysis of DSC data, the as-cast LAS1 glass sample was subjected to a two-stage heat treatment process, encompassing a nucleation stage and a crystal growth stage, as detailed in Chapter 3. The establishment of this overall heat treatment process was guided by thermal events detected by DSC experiments, but also by the XRD data presented in sections 5.3 and 5.4, as described below.

Upon heating, the LAS1 glass composition exhibits several exothermic and endothermic events in 400°C - 950°C temperature range. This thermal response can be divided into 3 stages. The first thermal event centered around 498°C, visible within the so-called stage I, is endothermic. Stage II, which extends from 570 to 840 °C is marked by the presence of 4 exothermic events of different magnitudes. Finally, stage III features a large endothermic event.

The glass transition temperature (T_g) can be determined by the onset of the endothermic event in stage I. In practise, a T_g of ~ 498°C is estimated by the intersection of two tangent lines, as illustrated in Fig. 5. 1. This temperature is in

broad agreement with other studies in the literature involving LS- and LAS- based glasses [10], [121], [165], [171], [251].

In principle, the exothermic peaks in stage II can be either ascribed to crystallisation phenomena or phase transitions. For this reason, they need to be interpreted in conjunction with the XRD data in section 5.3. In the literature [10] the first exothermic peak has been associated with the crystallisation of Li_2SiO_3 (lithium metasilicate). This is consistent with the *In-Situ* XRD data shown in Fig. 5. 12. Nevertheless, a closer inspection of this first exothermic peak, reaching a maximum at 615° C, shows a clear asymmetry, which suggests the occurrence of other thermal events just above the temperature of this peak maximum. Based on the *In-Situ* XRD data, shown in Fig. 5. 12, this feature is consistent with the crystallisation of $\text{LiAlSi}_4\text{O}_{10}$ (Petalite) and $\text{Li}_{0.25}\text{Al}_{0.25}\text{Si}_{0.75}\text{O}_2$ (Lithium orthoclase). This contrasts, with the results obtained by [121] for a glass with much lower amount of Al_2O_3 (~ 3 wt%), where both Li_2SiO_3 and $\text{Li}_2\text{Si}_2\text{O}_5$ were reported to appear at 540°C. The second exothermic peak centered at 705°C may appear symmetric, but this thermal event has been associated with the appearance of more than one crystalline phase. Indeed, this exothermic peak has been associated to intensive crystallisation of lithium aluminosilicate, $\text{LiAlSi}_2\text{O}_6$, alongside lithium disilicate, $\text{Li}_2\text{Si}_2\text{O}_5$ [10]. Hölland et al (2006) [121] have reported a substantial increase of $\text{Li}_2\text{Si}_2\text{O}_5$ at ~730 °C. The *In-situ* XRD data shown in Fig. 5. 12, clearly corroborates the appearance of $\text{Li}_2\text{Si}_2\text{O}_5$ and the eventual successive disappearance of Li_2SiO_3 and $\text{Li}_{0.25}\text{Al}_{0.25}\text{Si}_{0.75}\text{O}_2$. The appearance of $\text{Li}_2\text{Si}_2\text{O}_5$ cannot result uniquely from the transformation of Li_2SiO_3 , via a simple $\text{Li}_2\text{SiO}_3 + \text{SiO}_2 \rightarrow \text{Li}_2\text{Si}_2\text{O}_5$, because of the meagre initial content of Li_2SiO_3 . A more complex reaction pattern is occurring, which also involves the presence of a phase that forms a solid solution, as corroborated by continuous shift of some XRD peaks. The two other exothermic peaks are much smaller. Glatz et al (2018) [201] found the formation of Li_3PO_4 (lithium phosphate) at 815°C in a glass also with a much lower Al_2O_3 content. This is in broad agreement with the XRD data for the isothermal treatments shown in Fig. 5. 14. Finally, the melting temperature of LAS1 glass can be determined by the onset of an endothermic event at ~900°C within stage III, as shown in Fig. 5. 1. It is worth to mention that Hölland et al (2006) [121] reported the melting of $\text{Li}_2\text{Si}_2\text{O}_5$ to occur at 950°C, and of Li_2SiO_3 and Li_3PO_4 at 1000°C.

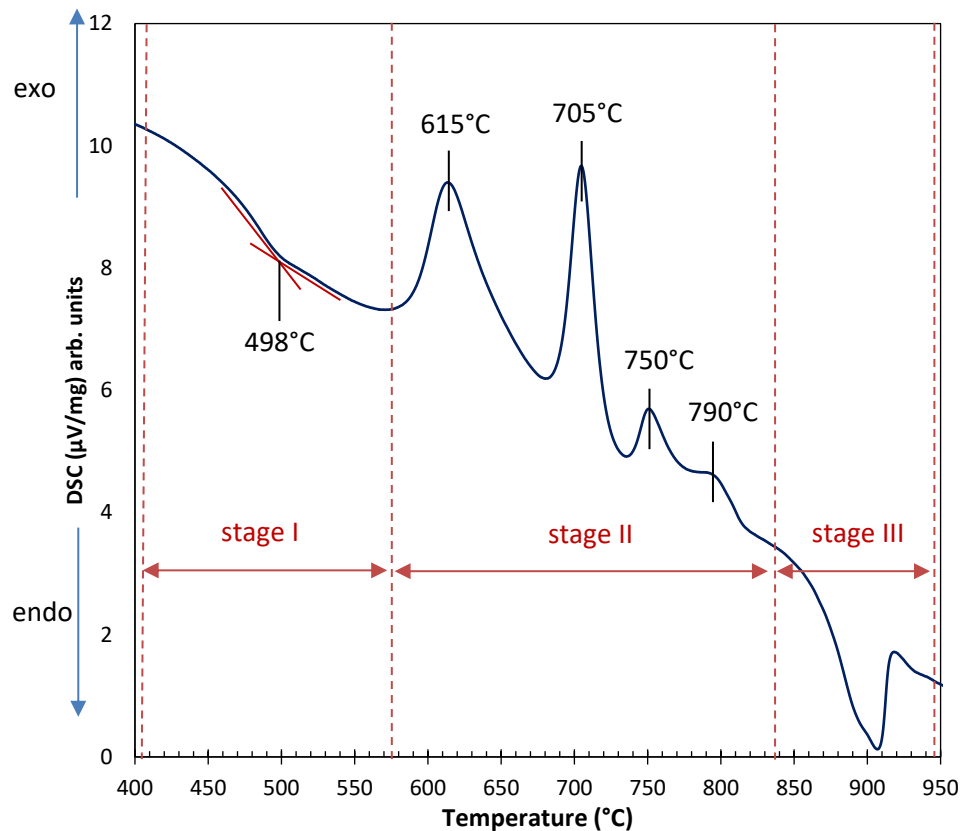


Fig. 5. 1 DSC trace of the as-cast LAS1 glass measured at a heating rate of $5 \text{ }^{\circ}\text{C}/\text{min}$.

In summary, the DSC analysis indicate the initial formation of nuclei occurs above $498\text{ }^{\circ}\text{C}$, because nucleation is an endothermic process. On the other hand, the subsequent exothermic events are mainly associated with the crystallization of different phases, which were identified by XRD analysis presented and discussed later in section 5.3.

In practical terms, it is often accepted that a processing nucleation temperature should be chosen between T_g and the initial point of crystallisation [45]. In the present study, a nucleation temperature of $550\text{ }^{\circ}\text{C}$ was selected and four different crystallisation temperatures at $670\text{ }^{\circ}\text{C}$, $780\text{ }^{\circ}\text{C}$, $830\text{ }^{\circ}\text{C}$ and $850\text{ }^{\circ}\text{C}$ were used to investigate the impact of heat treatment on phase assemblage, mechanical and optical properties. Those crystallisation temperatures fall at temperatures either lower or higher than the main exothermic events observed in the DSC thermogram.

5.1.2 Impact of the heating rate on the thermal behaviour of LAS1 glass

DSC experiments were carried out at heating rates of 5, 10, 15 and 20 °C/min up to a maximum temperature of 950°C and the results are shown in Fig. 5. 2. See Appendix 2.

It clearly observed that T_g slightly shifts up from 498°C to 503°C, 511°C and 515°C with increasing heating rates of 5, 10, 15 and 20°C/min, respectively. The thermogram also shows that all exothermic peaks shift to higher temperatures with increasing heating rates, as indicated by the dashed lines. For example, at a heating rate of 5 °C/min, the first and second exothermic peaks feature at 615°C and 706°C, respectively, whereas at a heating rate 20 °C/min those peaks appear at 657°C and 746°C. These data are useful to calculate the activation energies associated with each thermal event, as shown in section 5.2. Finally, it is worth to mention that melting is marked by at least two processes.

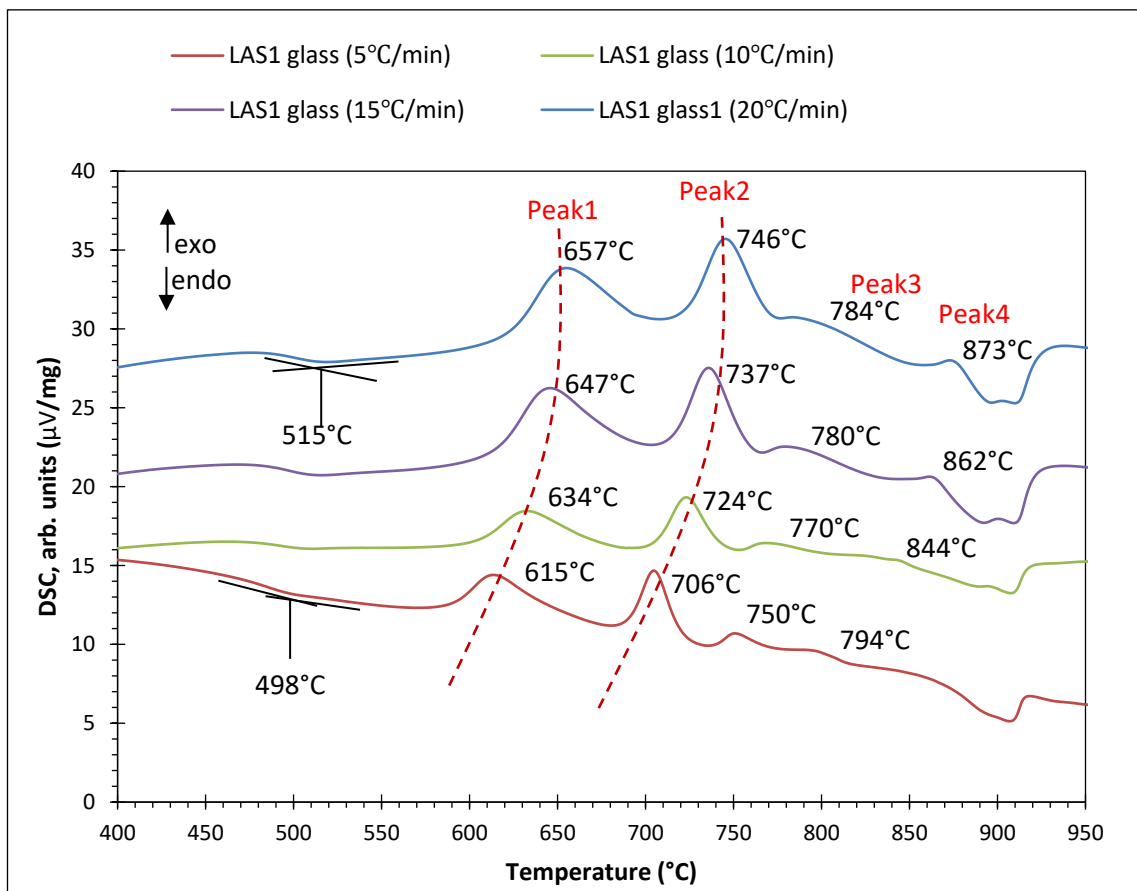


Fig. 5. 2 DSC traces of LAS1 glass measured at different heating rates.

5.1.3 Thermal behaviour of LAS1 glass nucleated 550°C for 300 min measured at different heating rates

In section 5.1, it was established that 550°C would be employed as the nucleation temperature. XRD analysis for isothermal heat treatments at 550°C, presented in section 5.4.1, show the appearance of Li_2SiO_3 and Li_3PO_4 , which after 300 minutes appear to reach a stable level. Hence, an evaluation of the thermal behaviour of LAS1 glass nucleated at 550°C for 300 min measured at different heating rates of 5, 10, 15 and 20 °C/min may offer some further insight into the crystallisation behaviour and in particular the energies of crystallisation. Fig. 5. 3 shows the results of this experiment. The near disappearance of the first exothermic peak that in as-cast LAS1 glass features at 615°C, Fig. 5. 3, is probably the most striking effect. In section 5.1.1, this peak was associated to the crystallisation of Li_2SiO_3 followed by the appearance of $\text{LiAlSi}_4\text{O}_{10}$ and $\text{Li}_{0.25}\text{Al}_{0.25}\text{Si}_{0.75}\text{O}_2$. Comparing XRD data for LAS1 glass heat treated at 650°C for 30 minutes, Fig. 5. 14, with LAS1 glass heat treated 550°C for 300 min followed by 650°C for 30 minutes, Fig. 5. 15, the impact of the nucleation becomes clear. Basically, the crystallisation of $\text{LiAlSi}_4\text{O}_{10}$ and $\text{Li}_{0.25}\text{Al}_{0.25}\text{Si}_{0.75}\text{O}_2$ occurs at lower temperatures in nucleated samples.

The second exothermic peak becomes the most prominent thermal event, which features at 690°C, 705°C, 714°C and 722°C for heating rates of 5, 10 15 and 20 °C/min, respectively. In comparison, with as-cast LAS1 glass, Fig. 5. 2, those peaks appear at lower temperatures, impacting the activation energies as shown in section 5.2.

The third exothermic event featuring at 729°C, 740°C, 764°C and 751°C for heating rates 5, 10, 15 and 20 °C/min respectively, increases in intensity and gradually merges with the second exothermic event, with increasing heating rates.

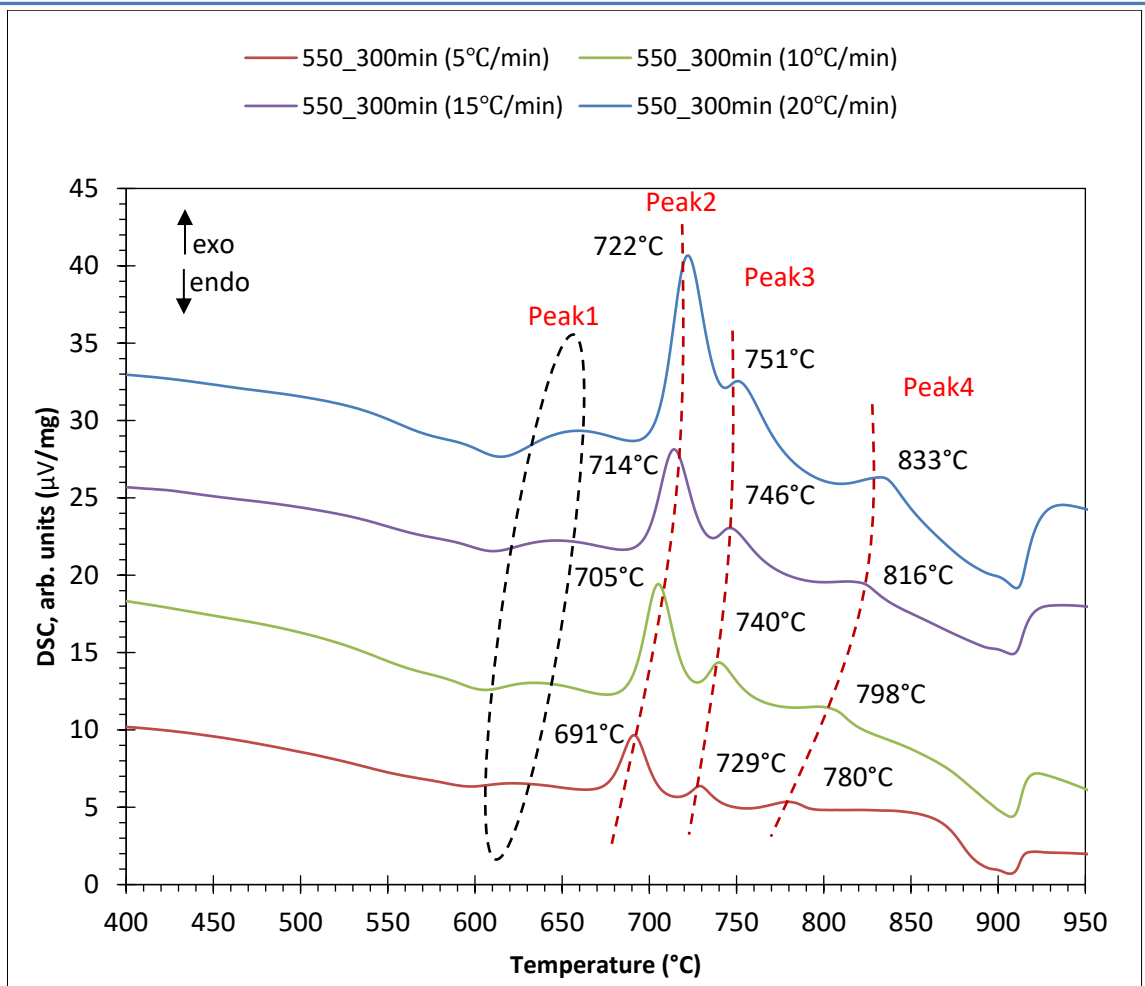


Fig. 5. 3 DSC traces of LAS1 glass nucleated at 550°C for 300 min using different heating rates.

5.1.4 Impact of the nucleation holding time on the thermal behaviour of LAS1 glass

The impact of the holding times (0, 30, 150 and 300 min) at the nucleation temperature of 550°C on the thermal behaviour of LAS1 glass was also evaluated by DSC experiments carried out at heating rate of 5 °C/min up to a maximum temperature of 950°C. The results for these experiments are presented in Fig. 5. 4. The glass transition temperature appears to increase to 540°C, which further corroborates the choice of the nucleation temperature. In agreement with results in section 5.1.2 and 5.1.3, the first exothermic peak at 615°C for as-cast glass becomes weaker and slightly shifts to higher temperatures with increasing holding times. Hardly any difference is detected between holding times of 150 min and 300 min, which evidences that a nucleation time 300 min sufficient to reach a stable level of precipitation of Li₂SiO₃ and Li₃PO₄. This result is in broad agreement with the XRD analysis for isothermal heat treatments at 550°C presented in Fig. 5. 13, in section 5.4.1. The other thermal events shifted slightly

towards lower temperatures as indicated by the dashed lines. For example, the second exothermic event, related to the LiAlSi₂O₆ and Li₂Si₂O₅ as discussed in the section 5.1.1, slightly shifts from 705°C, 695°C, 694°C to 693°C with an increasing nucleation times 30, 150 and 300 min, respectively. Interestingly, the relative intensity of the exothermic events also remained fairly unaltered, in contrast with the impact of heating rates as shown in Fig. 5. 2 and 5. 3. This suggests that some of the crystallisation process take place in short periods of time. A case exemplifying this high kinetics is given in Fig. 5. 18.

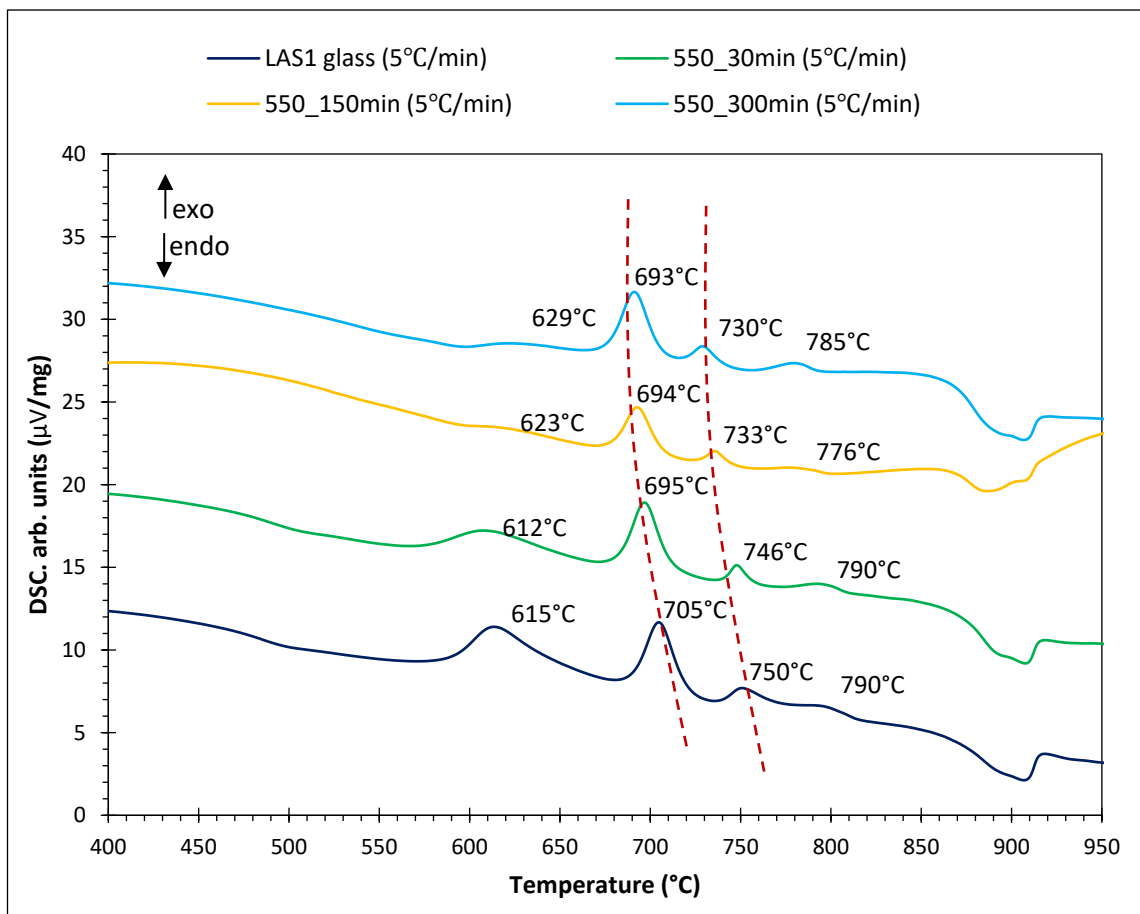


Fig. 5. 4 DSC traces for as-cast LAS1 glass and nucleated at different holding times.

5.1.5 Thermal behaviour of LAS1 glass subjected to prior isothermal heat treatments

The thermal behaviour of LAS1 glass specimens isothermally heat treated at 650, 670, 690, 710 and 730 °C for 30 min (which covers the temperature range of the two major thermal events exhibited by the as-cast LAS1 glass), was carried out to further characterise the crystallisation pattern. In addition, specimens nucleated at 550°C for 300 min and followed by heat treatment at 690, 710 and

730 °C for 30 min were also studied. DSC experiments were carried out at heating rate 5 °C/min up to a maximum temperature of 950°C for the all samples and the findings are shown in Fig. 5. 2. In comparison with the as-cast glass, the first exothermic peak is absent in all heat treated specimens, which provides a strong evidence for the rapid and complete crystallisation of the phases associated with that thermal event, which based on XRD analysis, Fig. 5. 12, is associated to the crystallisation of Li_2SiO_3 , but also to crystallisation of $\text{LiAlSi}_4\text{O}_{10}$ and $\text{Li}_{0.25}\text{Al}_{0.25}\text{Si}_{0.75}\text{O}_2$. The specimen heat treated at 650°C for 30 min, still exhibits a remarkable exothermic event at 690°C, which in the glass appears at 705°C. Based on the In-Situ XRD data, shown in Fig. 5. 12, this exothermic event is consistent with the crystallisation of $\text{Li}_2\text{Si}_2\text{O}_5$ alongside $\text{LiAlSi}_2\text{O}_6$. A small exothermic peak is still present at 740°C, therefore they should not be associated to any reactions/transformations involving the phases crystallised during the first thermal event. This peak only disappears from the traces of the specimens heat treated above 710°C, which then may be linked to reactions/transformation of the phases associated with the exothermic event visible at 705°C in the as-cast glass. Interestingly, no more thermal events, apart from melting, are detected for specimens heat treated above 710°C, independently of nucleation. This is in broad agreement with Table 5. 2 in section 5.3, which shows that no major phase crystallises above 690°C. Schematic DSC data are shown in Appendix 2.

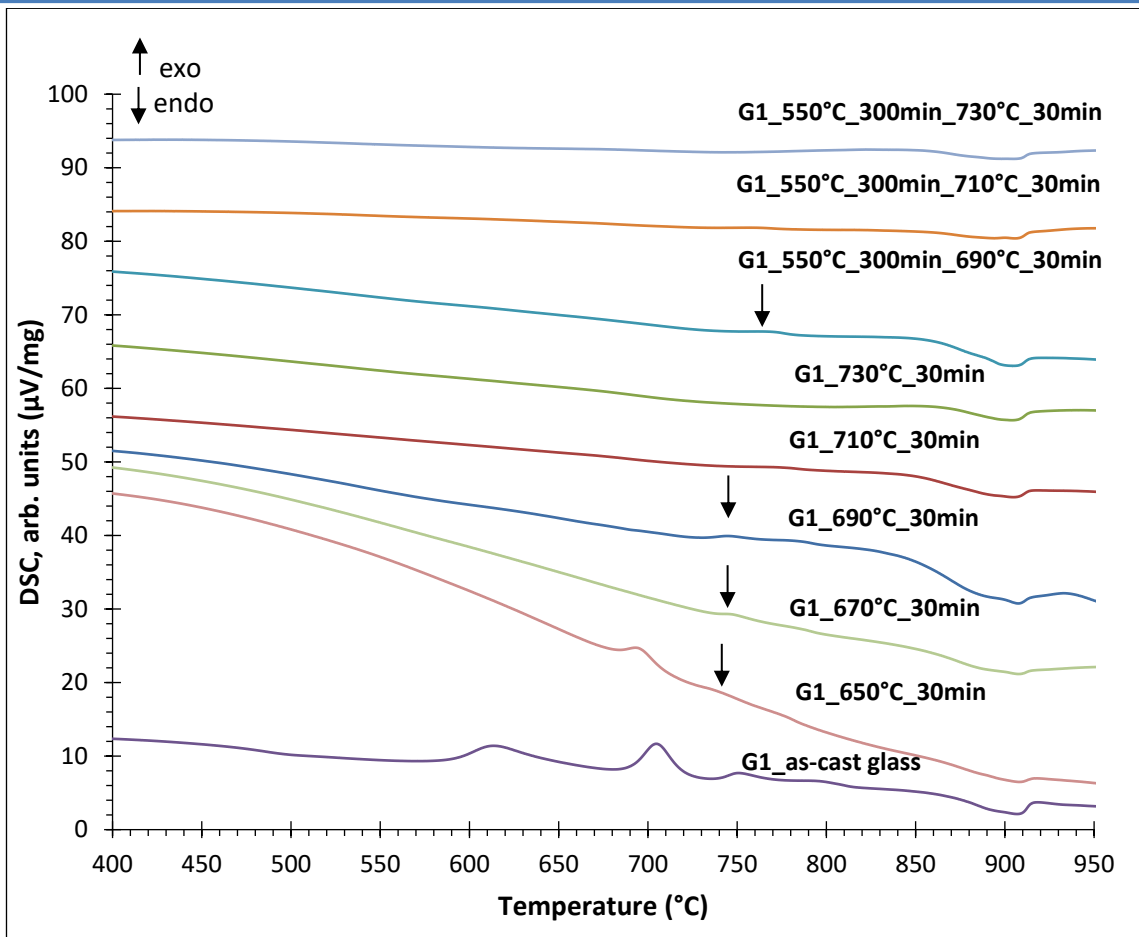


Fig. 5.5 DSC for as-cast and nucleated LAS1 glass heat treated at different temperatures.

5.2 Determination of Activation Energies

Activation energy, E_a , is the minimum energy (kinetic barrier) required for crystal growth. Several models exist to estimate E_a , which rely on the evaluation of the thermal behaviour using different heating rates. Hereafter, three commonly accepted models for the determination of E_a will be employed; the Kissinger's method [170], [252], the modified Kissinger's method proposed by Matusita and Saka [132], [253], and the Ozawa method [139], [254]. These methods were employed using the DSC experiments which have been presented in section 2.6.3, where LAS1 glass and glass nucleated at 550°C for 300 min were studied using heating rates of 5, 10, 15 and 20 °C/min.

5.2.1 Kissinger's method

A detailed description of the Kissinger method can be found in the section 2.6.3.1. Basically, E_a can be estimated from the slope of $[\ln(\beta/T_p^2)]$ in function of $[1000/T_p]$, which represents $[-E_a/R]$, where R is the gas constant, as shown in

Fig. 5. 6 for the successive four exothermic events observed in Fig. 5. 2. Similarly, Fig. 5. 7 shows the estimates of E_a for the thermal events observed in Fig. 5. 3 for the nucleated glass. The peak associated with the successive crystallisation of Li_2SiO_3 , $\text{LiAlSi}_4\text{O}_{10}$ and $\text{Li}_{0.25}\text{Al}_{0.25}\text{Si}_{0.75}\text{O}_2$ has an activation energy of 212 kJ/mole. The peak associated with the crystallisation of $\text{LiAlSi}_2\text{O}_6$ and $\text{Li}_2\text{Si}_2\text{O}_5$ has an activation energy of 270 kJ/mole. These values support a relatively good ability for crystallisation when compared with other glasses, where E_a can be often greater than 400 kJ/mole. The third thermal event has the highest E_a , which maybe lead to a small crystallisation/transformation, which is consistent with the small peak intensity.

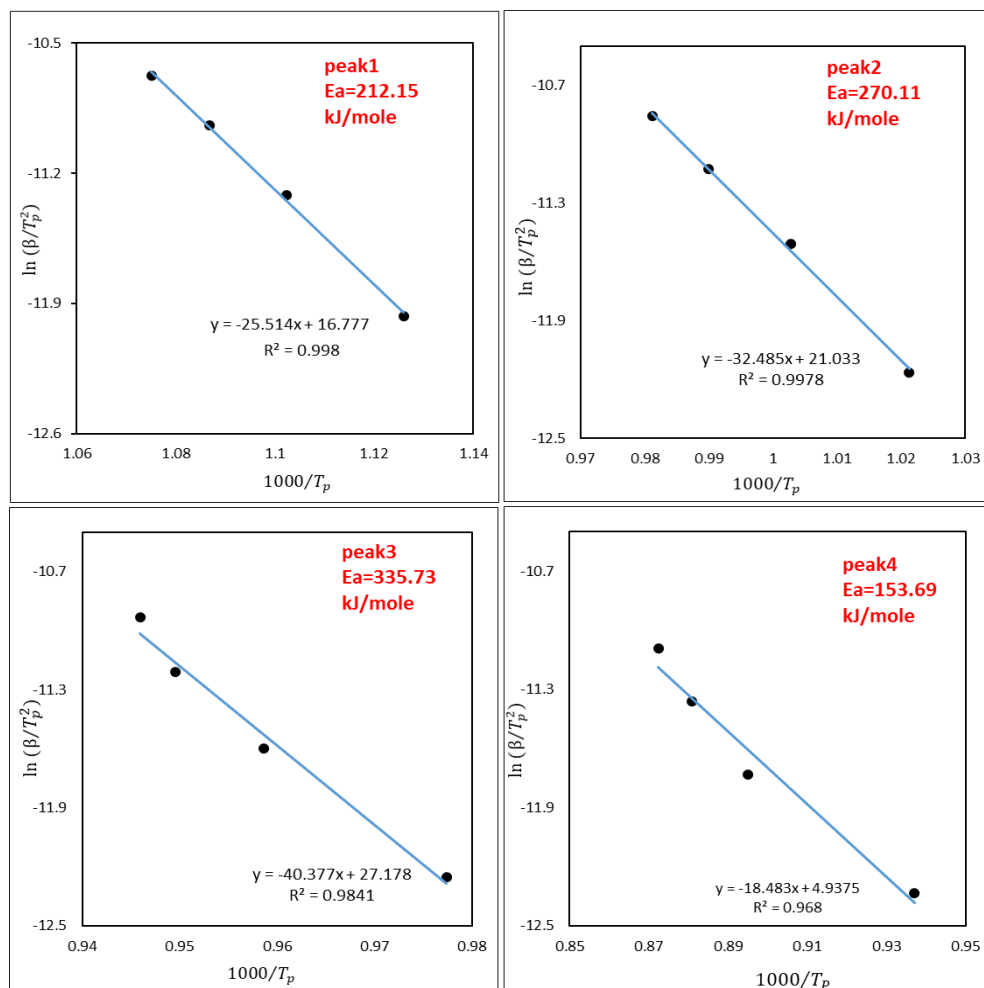


Fig. 5. 6 Kissinger plots used to estimate the activation energy for the crystallization processes in as-cast LAS1 glass.

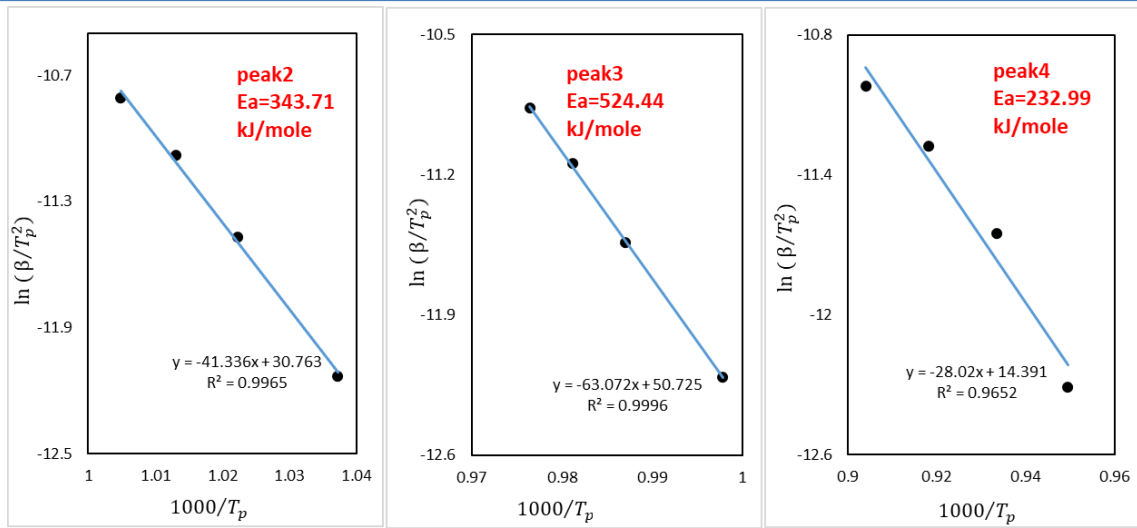


Fig. 5. 7 Kissinger plots used to estimate the activation energy for crystallization processes in LAS1 glass nucleated at 550°C/300min.

5.2.2 Modified Kissinger's method

The modified Kissinger's method was proposed by Matusita and Saka [132], [253] and it is detailed in the section 2.6.3.2. In this case, a plot is constructed as $[\ln(\beta^n/T_p^2)]$ in function of $[1000/T_p]$, where again the slope represents $[-mE_a/R]$ as shown in Fig. 5. 8 and Fig. 5. 9 for the as-cast class and nucleated LAS1 glass, respectively. Here, it is used $n=m=3$ which indicates 3D, bulk nucleation, as described in detail in the section 2.6.3.2.

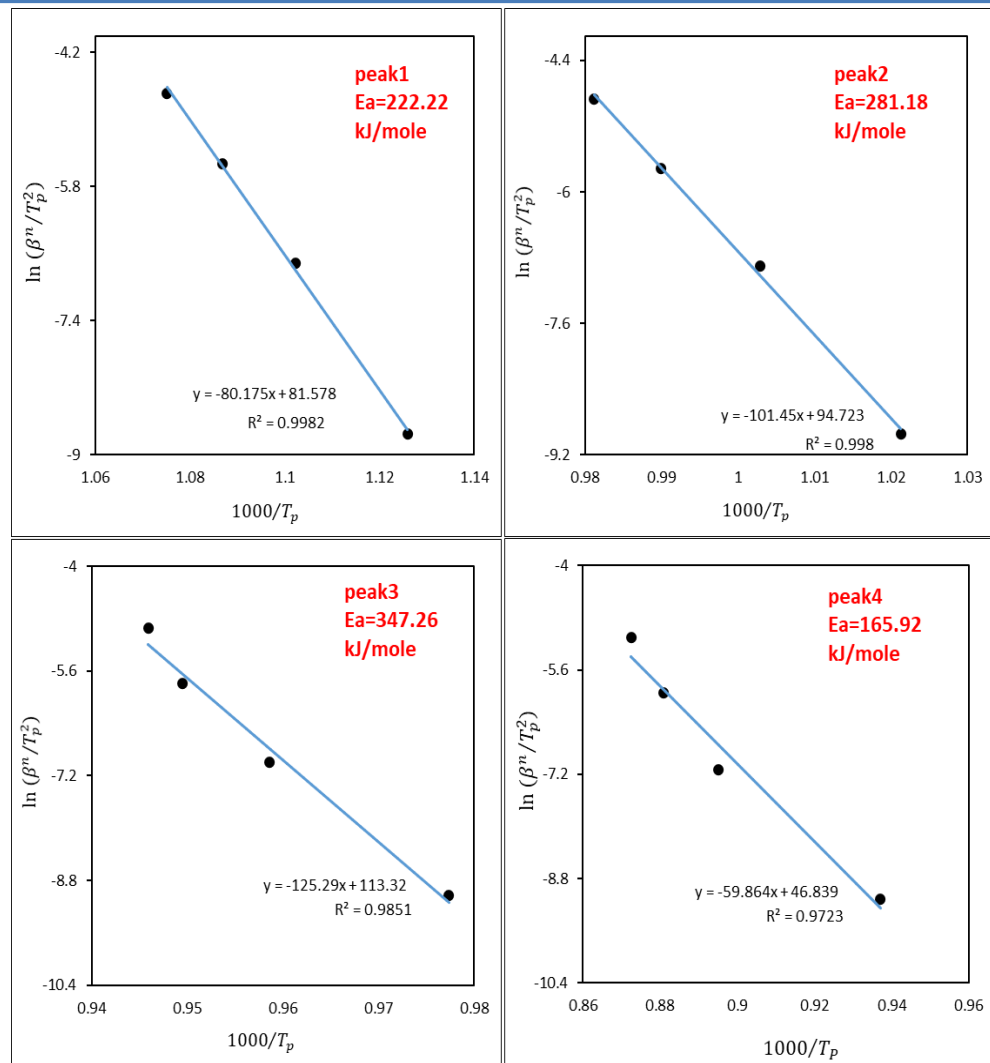


Fig. 5. 8 Modified Kissinger's plots used to estimate the activation energy for the crystallization processes in as-cast LAS1 glass.

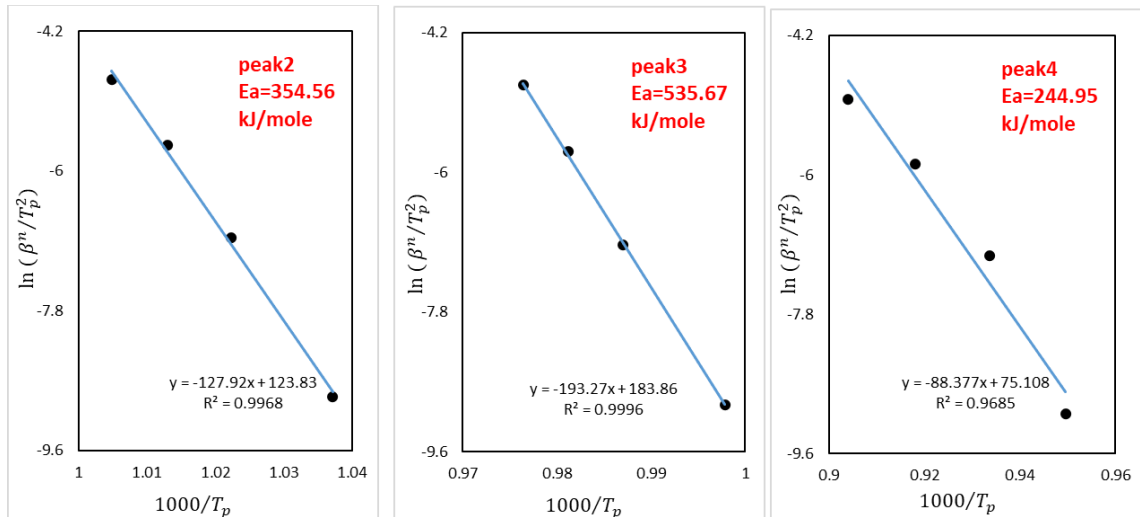


Fig. 5. 9 Modified Kissinger's plots used to estimate the activation energy for crystallization processes in LAS1 glass nucleated at 550°C/300min.

5.2.3 Ozawa's method

Ozawa's method can be employed to determine E_a , as described in the section 2.6.3.3, by plotting $[1000/T_p]$ in function of $[\ln(\beta)]$. The results for the as-cast and the nucleated LAS1 glass are illustrated in Fig. 5. 10 and 5. 11, respectively.

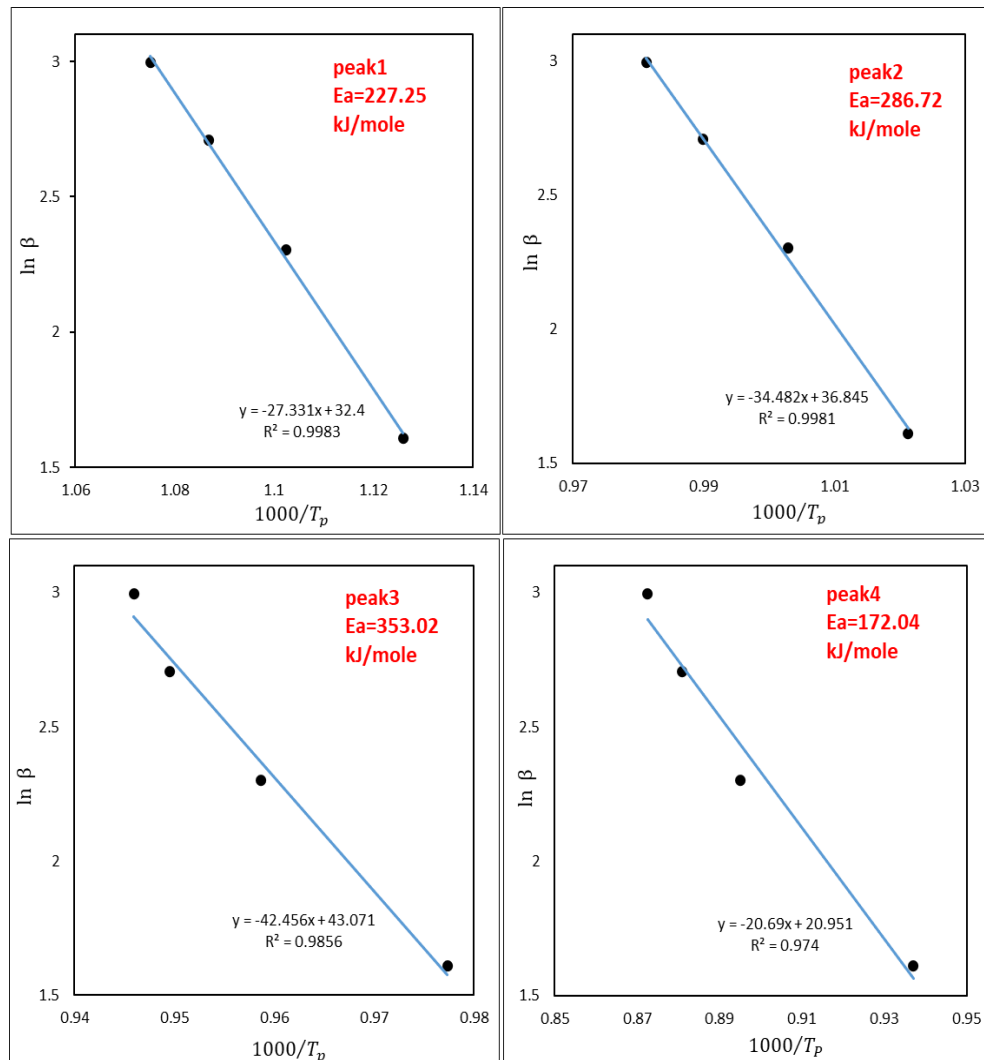


Fig. 5. 10 Ozawa plots used to estimate the activation energy for the crystallization processes in as-cast LAS1 glass.

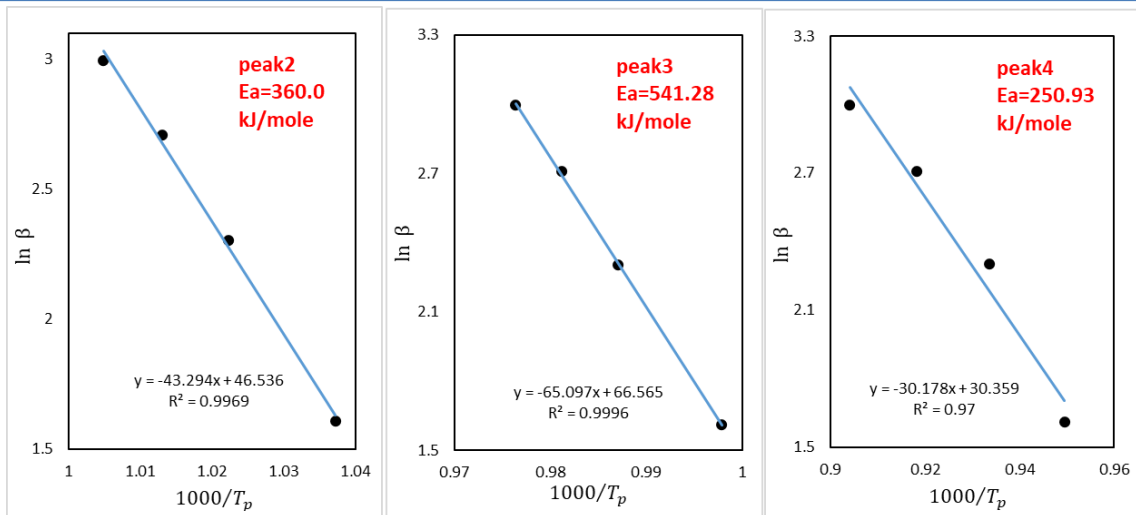


Fig. 5. 11 Ozawa plots used to estimate the activation energy for crystallization processes in LAS1 glass nucleated at 550°C/300min.

A similar trend in the values of E_a is obtained for all the three methods, as shown by the values listed in Table. 5. 1. It is clear that the event associated with peak 3, shows comparatively the highest E_a , which is commensurate with a higher barrier to crystallisation/transformation. In contrast, peak 4 exhibits the lowest E_a , thereby it should be an easier process to occur.

Table. 5. 1 Activation energies for crystallisation processes in as-cast and nucleated LAS1 glass. (units: kJ/mole).

| | LAS1 glass | | | | Nucleated glass 550°C/300min | | | |
|---------------------------|------------|--------|--------|--------|---------------------------------|---------------|---------------|---------------|
| | Peak1 | Peak2 | Peak3 | Peak4 | Peak1 | Peak2 | Peak3 | Peak4 |
| Kissinger method | 212.15 | 270.11 | 335.73 | 153.69 | - | 343.71 | 524.44 | 232.99 |
| Modified Kissinger method | 222.22 | 281.18 | 347.26 | 165.92 | - | 354.56 | 535.67 | 244.95 |
| Ozawa method | 227.25 | 228.72 | 353.02 | 172.04 | - | 360.0 | 541.28 | 250.93 |

5.3 In-situ high-temperature XRD patterns of LAS1 as-cast glass

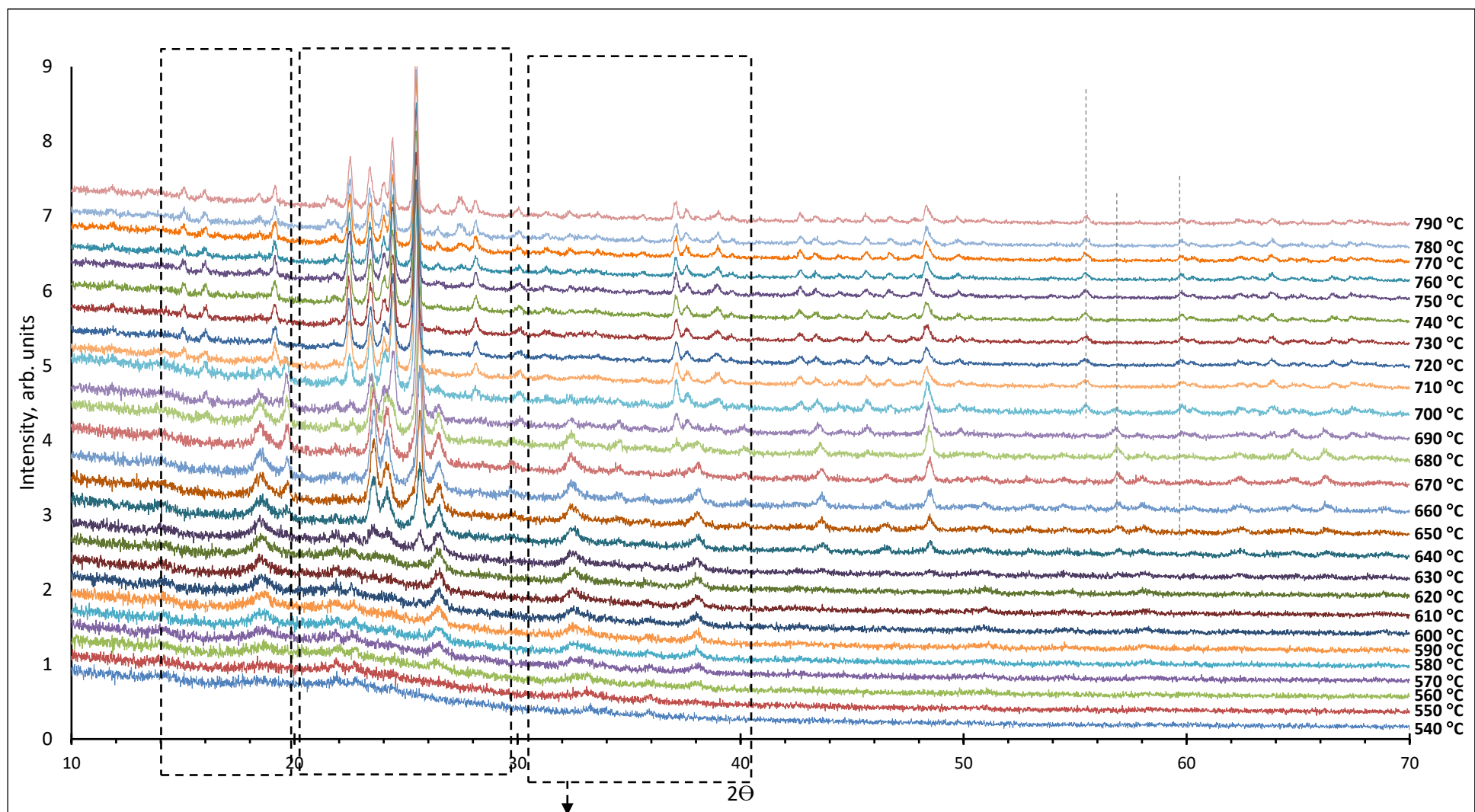
DSC investigations in section 5.1.1 showed the occurrence of multiple thermal events that may be associated to either crystallisation or structural phase transitions. As previously mentioned, *In-situ* high temperature XRD is a powerful technique to gather a deeper insight into the thermal behaviour of LAS1 glass and to investigate the complex crystallisation process of this lithium aluminosilicate-based glass. Hence, *In-situ* high temperature X-ray diffraction between 10° to 70° 2θ was carried out in the temperature range 540°C - 790°C at 10°C steps, with a heating rate 5 °C/min, using a Philips X'Pert PW3020 diffractometer. The results are as illustrated in Fig. 5. 12, see Appendix 3. There

was no distinctive change or shift in the diffraction patterns from 540°C to 560°C. Based on the DSC traces, shown in Fig. 5. 1, this is consistent with small endothermic event before step of the major thermal exothermic event. At 560°C, LiAlSi₄O₁₀ (04-013-7666) and Li₂SiO₃ (00-029-0829) phases appear as indicated in Fig. 5. 12 by peaks at 18.6° and 26.4° 2θ, respectively. This is undoubtedly consistent with the onset of first major thermal exothermic event in DSC trace shown in Fig. 5. 1. At 630°C, LiAlSi₄O₁₀ (04-013-7666) and Li_{0.25}Al_{0.25}Si_{0.75}O₂ (04-018-8284) phases appear as indicated by the peaks at 23.8°, 24.5° and 25.68° 2θ. Again, this is consistent with major thermal exothermic event in the DSC trace, shown in Fig. 5. 1. The *in-Situ* XRD data shown between 690°C-700°C clearly corroborates the appearance of LiAlSi₂O₆ (04-020-3038) as indicated by peaks at 23.5°, 19.7° and 28° 2θ. Between 690°C-700°C, the shift from 25.68° to 25.57° 2θ for the peak associated with main phase is consistent with solid solution between Li_{0.25}Al_{0.25}Si_{0.75}O₂ and LiAlSi₂O₆. Barbieri et al (1997) [159] suggested that above 700°C, Li⁺ and Al³⁺ can stuff disorder β-quartz close to Li_xAl_xSi_{3-x}O₆ forming a complete solid solution between Li_{0.25}Al_{0.25}Si_{0.75}O₂ and LiAlSi₂O₆. On the other hand, the LiAlSi₄O₁₀ phase disappears, and Li₂Si₂O₅ emerges as a new phase as indicated by peaks at 24.44°, 24.04° and 23.4° 2θ. Interestingly, the peak at 19.7° 2θ associated with Li_{0.25}Al_{0.25}Si_{0.75}O₂ disappears at 710°C, but a new peak associated with LiAlSi₂O₆ emerges at 19.23° 2θ. This also corresponds to DSC trace in the second peak that ends at 730°C. However, the other new phase emerges that located at 2θ: 27.5° at 770°C, which is consistent with second minor thermal exothermic events in the DSC pattern. Table 5. 2 summarises the phases appearing on heating and their temperature range of stability. The crystallisation processes occurring in 690°C-730°C temperature range have a significant impact in the mechanical properties, as shown in Fig. 5. 27, 30 and 33. Basically, the elastic modulus increases from 86.5 to 95.8 GPa, the hardness from 6.34 to 6.69 GPa and fracture toughness from 0.67 to 1.15 MPa^{1/2}m. There is also a concomitant modification of the optical properties, as shown in Fig. 5. 36. Basically, the material changes from a semi-transparent glass to a white glass-ceramic.

Chapter Five: Processing and Characterisation of the LAS1 Glass

Table. 5. 2 Phases and respective temperatures range based on *In-situ* high-temperature X-ray diffraction.

| Phases | Symbol of phase | Temperature range |
|--|-----------------|-------------------|
| Li_2SiO_3 Lithium metasilicate 00-029-0829 | LS1 | 570-790°C |
| $\text{LiAlSi}_4\text{O}_{10}$ Petalite, Monoclinic 04-013-7666 | LAS1 | 590-690°C |
| $\text{Li}_{0.25}\text{Al}_{0.25}\text{Si}_{0.75}\text{O}_2$ Lithium orthoclase 04-018-8284 | LAS2 | 640-710°C |
| $\text{Li}_2\text{Si}_2\text{O}_5$ Lithium disilicate 04-009-8780 | LS2 | 690-790°C |
| $\text{LiAlSi}_2\text{O}_6$ Lithium aluminosilicate 04-020-3038 | LAS3 | 680-790°C |



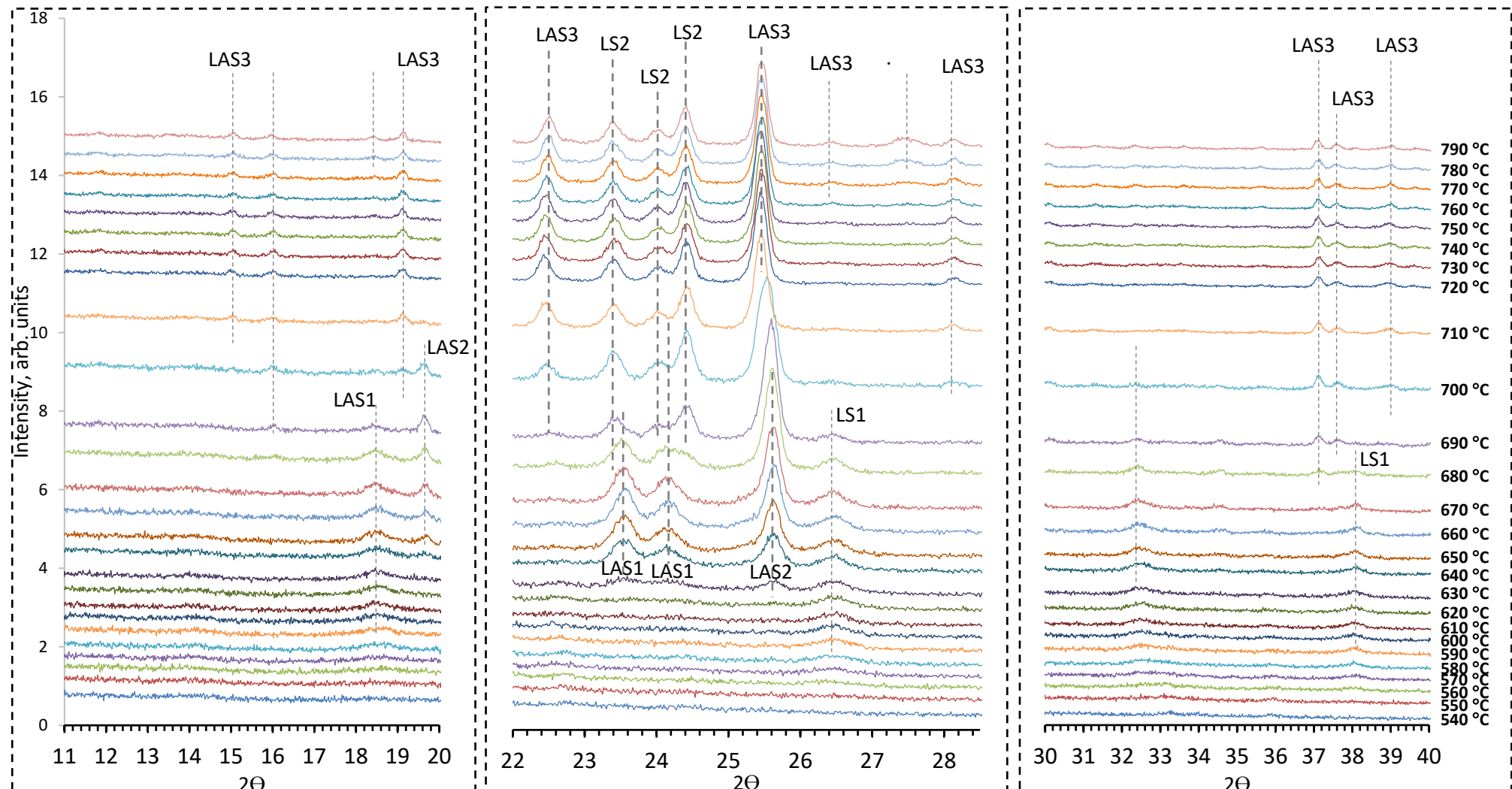


Fig. 5. 12 *In-situ* high-temperature XRD patterns of LAS1 glass heated treated from 540°C to 790°C.

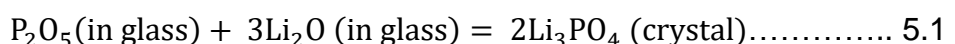
5.4 Ex-situ X-ray diffraction of LAS1 glass

In this section, ex-situ XRD experiments are presented. The results can be grouped into three categories. First, X-ray diffraction as-cast LAS1 glass which undergone isothermal heat treatment at 550°C for different times (0, 30 min, 150 min, 300 and 3000 min). Second, X-ray diffraction for LAS1 glass non-isothermally heat treated in the 610°C to 870°C temperature range for 30 min. Finally, X-ray diffraction for LAS1 glass isothermally heat treated at 550 for 300 min followed by non-isothermal heat treatment in the 630°C to 870°C temperature range for 30 min. *Ex-situ* X-ray patterns are shown in Appendix 3.

5.4.1 Phase assemblage after isothermal heat treatments at 550°C for different times

Ex-situ X-ray diffraction, Fig. 5. 13, for as-cast glass blocks and glass blocks nucleated at 550°C for different holding times: 0, 30, 150, 300 and 3000 min. As it can be seen, the XRD pattern for as-cast glass consists of a broad peak over a whole 2θ range, but with a few but small intensity Bragg peaks. These few peaks are assigned to Li₂SiO₃ and Li₃PO₄. This suggest that the initial sample is mainly an amorphous solid, but it contains some Li₂SiO₃ and Li₃PO₄ crystals, which indicated some devitrification during the preparation of the glass. The X-ray data remains almost unaltered by taking the sample to 550°C, and even after 30 min at this temperature. When the holding time is increased to 150 and 300 min, Bragg peaks assigned to Li₂SiO₃ and Li₃PO₄ increase in intensity. The X-ray data for the glass hold at 550°C for 3000 min shows a minimal increase on the intensity of those peaks. LAS1 glass contains P₂O₅, a well-known nucleating agent, that reduces the growth rate and controls for amorphous phase separation in lithium disilicate-based glasses by reducing the interfacial energy between the nucleus newly formed and the glass matrix residual [121], [162], [165], [255]–[258]. P₂O₅, as nucleating agent, acts as a microphase that induces the formation of a transient phase, Li₃PO₄ phase [161].

Li_3PO_4 crystal nuclei form as P_2O_5 reacts with Li_2O , [257] as shown in equation 5.1.



Based on XRD patterns, the precipitation of Li_3PO_4 gradually increases with increasing nucleation holding time. The precipitation of Li_3PO_4 reaches a near saturation after nucleation at 550°C for 300 min, as shown in Fig. 5. 13.

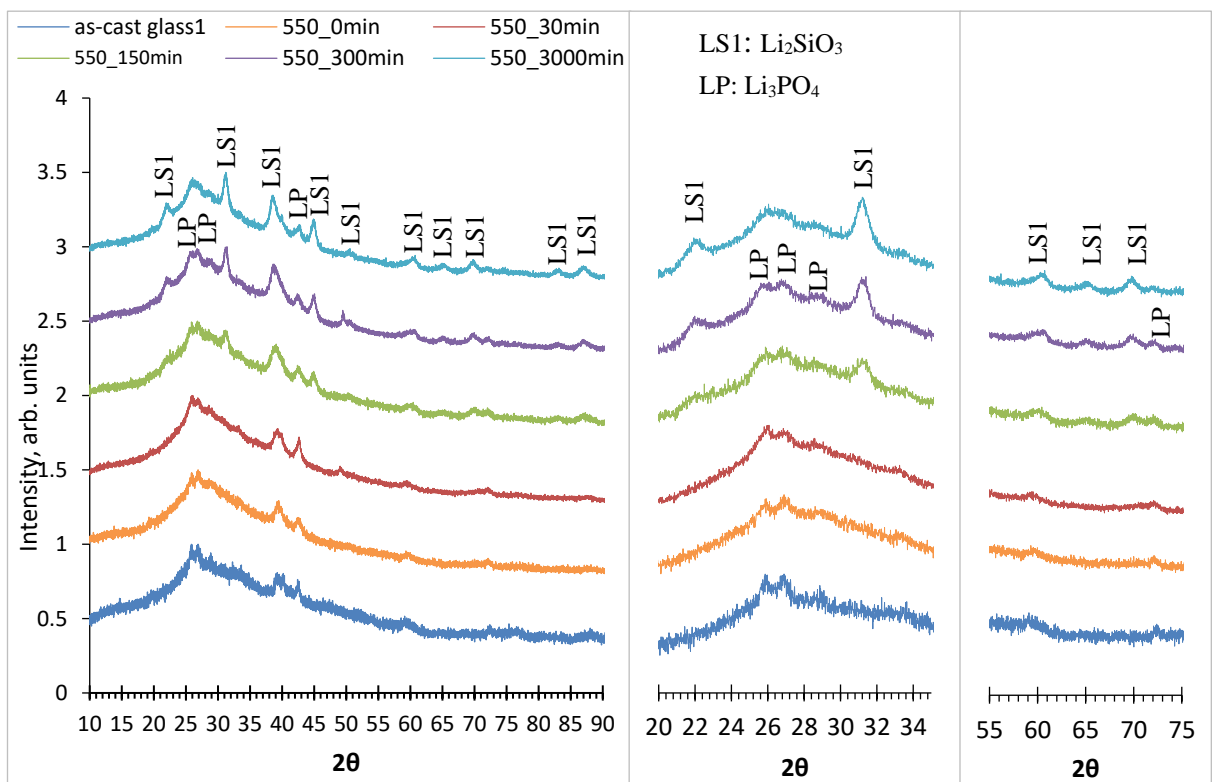
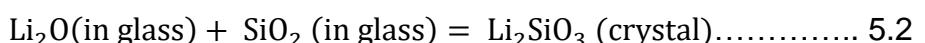


Fig. 5. 13 XRD patterns of isothermal heat treatment at 550°C for different times of as-cast LAS1 glass.

Lithium metasilicate, Li_2SiO_3 , formation mechanism can be expressed by the reaction in equation 5.2;

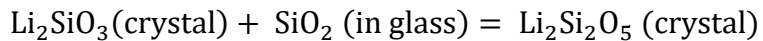


5.4.2 Phase assemblage after heat treatment for 30 min in the 610°C to 870°C temperature range

Based on the *ex-situ* XRD analysis, Li_2SiO_3 and Li_3PO_4 are the crystalline phases present in samples heat treated at 610°C and 630°C for 30 min, as shown in Fig. 5. 14. Samples heat treated at 650°C for 30 min are still rather amorphous which is corroborated by the broad peak and contain mainly Li_2SiO_3 and Li_3PO_4 together with minute amounts of $\text{Li}_{0.25}\text{Al}_{0.25}\text{Si}_{0.75}\text{O}_2$ and $\text{LiAlSi}_4\text{O}_{10}$. This is consistent with the first exothermic peak in DSC trace shown in Fig. 5. 1 and the *in-situ* XRD data in Fig. 5. 12. In contrast, samples heat treated at 670°C are much more crystalline and consist mainly of $\text{Li}_{0.25}\text{Al}_{0.25}\text{Si}_{0.75}\text{O}_2$ and $\text{LiAlSi}_4\text{O}_{10}$, with some residual

Li_2SiO_3 and Li_3PO_4 . The phase assemblage for samples heat treated at 690°C for 30 min is similar. Nevertheless, samples heat treated at 710°C consist mainly of $\text{Li}_{0.25}\text{Al}_{0.25}\text{Si}_{0.75}\text{O}_2$ and $\text{Li}_2\text{Si}_2\text{O}_5$, as indicated by the peak at 29° 2 Θ , a smaller content of $\text{LiAlSi}_4\text{O}_{10}$ and a even smaller amount of $\text{LiAlSi}_2\text{O}_6$. This remarkable change in the phase assemblage is consistent with the occurrence of a sharp exothermic event at 705°C shown in Fig. 5. 1, and it is also in agreement with the *in-situ* X-ray diffraction data shown in 5.12. This is also coincident with modifications to optical properties, shown in Fig. 5. 37. Basically, the material changes from a semi-transparent glass to a white glass-ceramic. Remarkably, $\text{Li}_{0.25}\text{Al}_{0.25}\text{Si}_{0.75}\text{O}_2$ and $\text{LiAlSi}_4\text{O}_{10}$ are no longer observable in samples heat treated at 730°C for 30 min. However, vestiges Li_2SiO_3 and Li_3PO_4 are still present. All remaining samples heat treated at temperatures greater than 730°C consist mainly of $\text{LiAlSi}_2\text{O}_6$ followed by $\text{Li}_2\text{Si}_2\text{O}_5$, plus some vestiges of Li_3PO_4 and Li_2SiO_3 .

Lithium disilicate-based glasses nucleated between 500–600 °C [97], form nuclei suitable for crystallise Li_2SiO_3 crystals. In the present case, the content of Li_2SiO_3 already present in the glass increases with increasing temperature. The appearance of $\text{Li}_2\text{Si}_2\text{O}_5$ may occur via the consumption of Li_2SiO_3 [121], as given below:



Nevertheless, in the present case the crystallisation pattern is more complex because of simultaneous competitive reactions, which lead to the formation of a solid solution between $\text{Li}_{0.25}\text{Al}_{0.25}\text{Si}_{0.75}\text{O}_2$ and $\text{LiAlSi}_2\text{O}_6$ at the same time that $\text{Li}_2\text{Si}_2\text{O}_5$ crystallise.

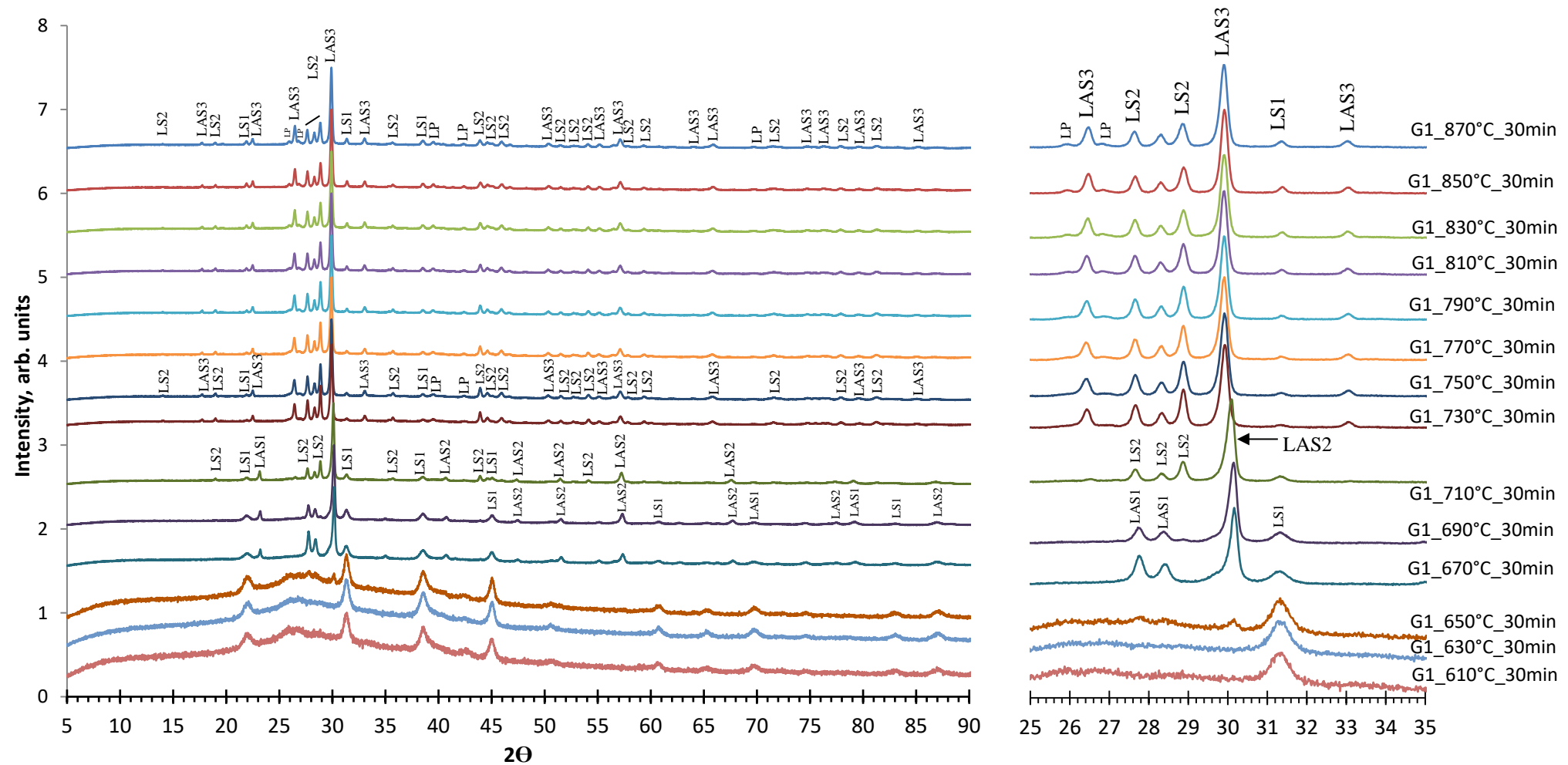


Fig. 5.14 Room-temperature XRD patterns for samples heat treated for 30 min in the 610°C to 870°C temperature range.

5.4.3 Phase assemblage after nucleation at 550°C for 300 min followed by heat treatments for 30 min in the 630°C to 870°C temperature range

The impact of nucleation at 550°C for 300 min on the phase evolution in the 630°C to 870°C was assessed by *ex-situ* XRD analysis of samples heated treated for 30 min, as shown in Fig. 5. 15. These results can be directly compared with those presented in section 5.4.2 for non-nucleated samples. Non-nucleated and nucleated samples heated treated at 630°C have similar phase assemblage, with Li_2SiO_3 and Li_3PO_4 as the main phases. Nevertheless, some differences on the phase assemblage are detected for samples heat treated between 650°C and 710°C, as summarised below:

- The primary phases in the nucleated sample heat treated at 650°C are $\text{Li}_{0.25}\text{Al}_{0.25}\text{Si}_{0.75}\text{O}_2$ and $\text{LiAlSi}_4\text{O}_{10}$, in contrast with the non-nucleated where Li_2SiO_3 and Li_3PO_4 .
- The primary phases in the nucleated sample heat treated at 690°C are $\text{Li}_{0.25}\text{Al}_{0.25}\text{Si}_{0.75}\text{O}_2$, $\text{LiAlSi}_4\text{O}_{10}$, $\text{Li}_2\text{Si}_2\text{O}_5$ and some residual Li_2SiO_3 . In the non-nucleated counterpart, $\text{Li}_2\text{Si}_2\text{O}_5$ is only detected in samples treated at 710°C or above.
- The onset temperature for $\text{Li}_{0.25}\text{Al}_{0.25}\text{Si}_{0.75}\text{O}_2$ and $\text{LiAlSi}_2\text{O}_6$ solid solution formation is also shifted towards lower temperatures in the nucleated sample in comparison with the non-nucleated.

When heat treatment is carried out above 730°C, the phase assemblage is similar in both non-nucleated and nucleated samples, with $\text{LiAlSi}_2\text{O}_6$ as the dominant phase.

The shift towards crystallisation of phases at lower temperatures in the case of nucleated samples is consistent with the DSC data presented in Fig. 5. 2 and 5. 3, for non-nucleated and nucleated LAS1 glass, respectively.

These results suggest that the nucleation stage at 550°C for 300 min plays important role in the subsequent formation of crystalline phases.

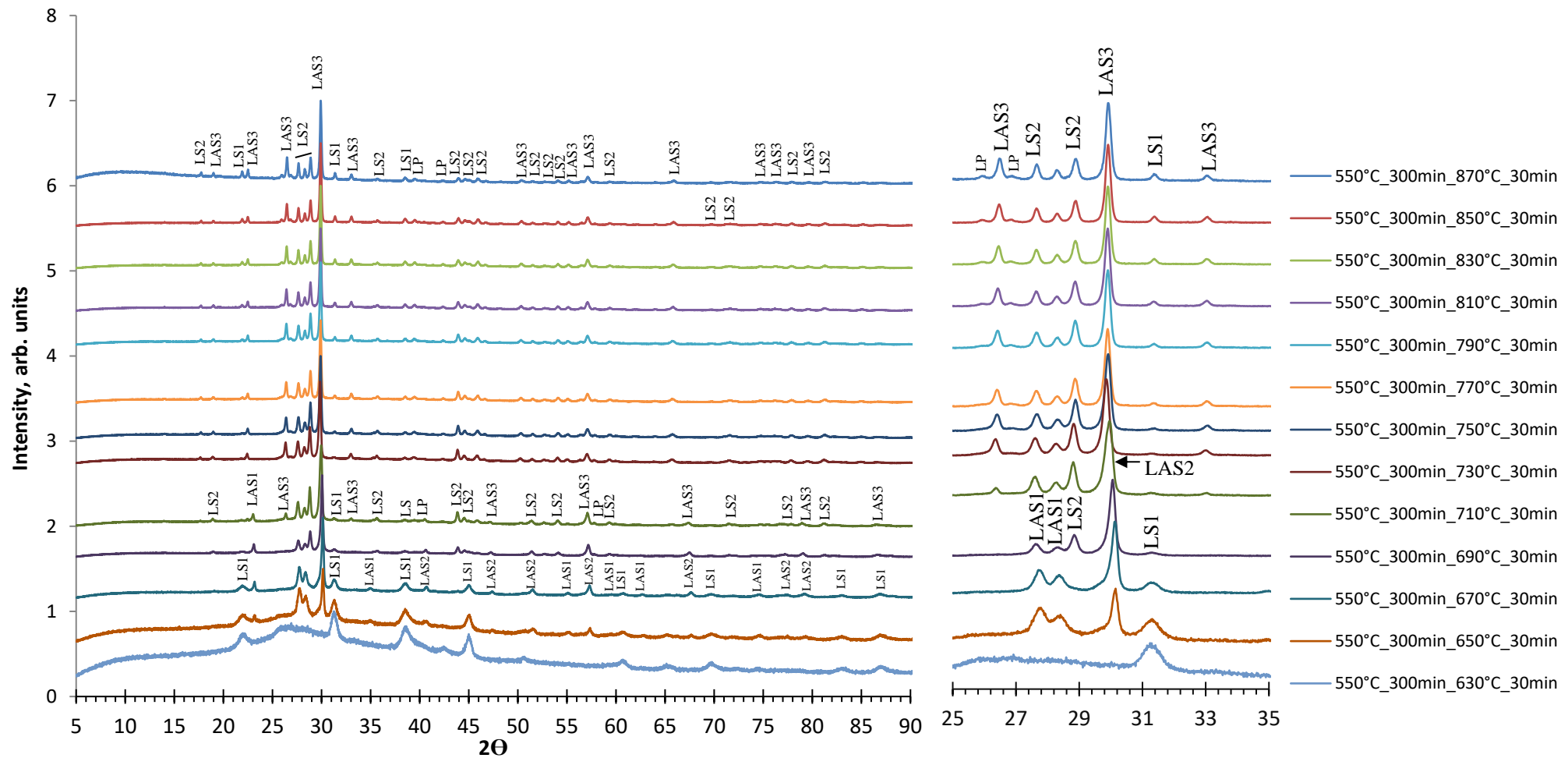


Fig. 5. 15 Room-temperature XRD patterns for samples nucleated at 550 for 300 min followed by heat treatment of 30 min in the 630°C to 870°C temperature range.

5.4.4 Crystallization pathway at 670°C

DSC data in Fig. 5. 1 combined with X-ray diffraction in Fig. 5. 15 suggest the occurrence of a complex crystallisation process around 670°C. Hereafter, the time dependence of the phase assemblage of samples heat treated at 670°C is investigated in order to gather a better understanding of the crystallisation pathway in around this temperature. X-ray diffraction data acquired from samples heat treated for 0, 5, 15, 30, 90 minutes at 670°C are given in Fig. 5. 16.

It can be observed that the initial sample heat treated at 670°C for a zero holding time is mostly amorphous but contains Li_2SiO_3 and Li_3PO_4 . These are the two phases originally present in LAS1 glass blocks, as shown in Fig. 5. 13. After 5 minutes at 670°C, three new peaks appear at 27.7° , 28.4° and 30.1° 2Θ . The latter can be ascribed to $\text{Li}_{0.25}\text{Al}_{0.25}\text{Si}_{0.75}\text{O}_2$, whereas the two first peaks are associated with $\text{LiAlSi}_4\text{O}_{10}$. Nevertheless, Li_2SiO_3 is still the dominant phase. Based on the DSC trace, shown in Fig. 5. 1, this crystallisation of multiple phases is consistent with the asymmetry displayed by the first exothermic peak. This evidences that there are two sub-peaks within the first exothermic peak in the DSC trace.

The $\text{Li}_{0.25}\text{Al}_{0.25}\text{Si}_{0.75}\text{O}_2$ phase becomes the main phase on heating for 15, 30 min and 90 min. Moreover, no apparent changes to the phase assemblage are detected after 30 min at 670°C.

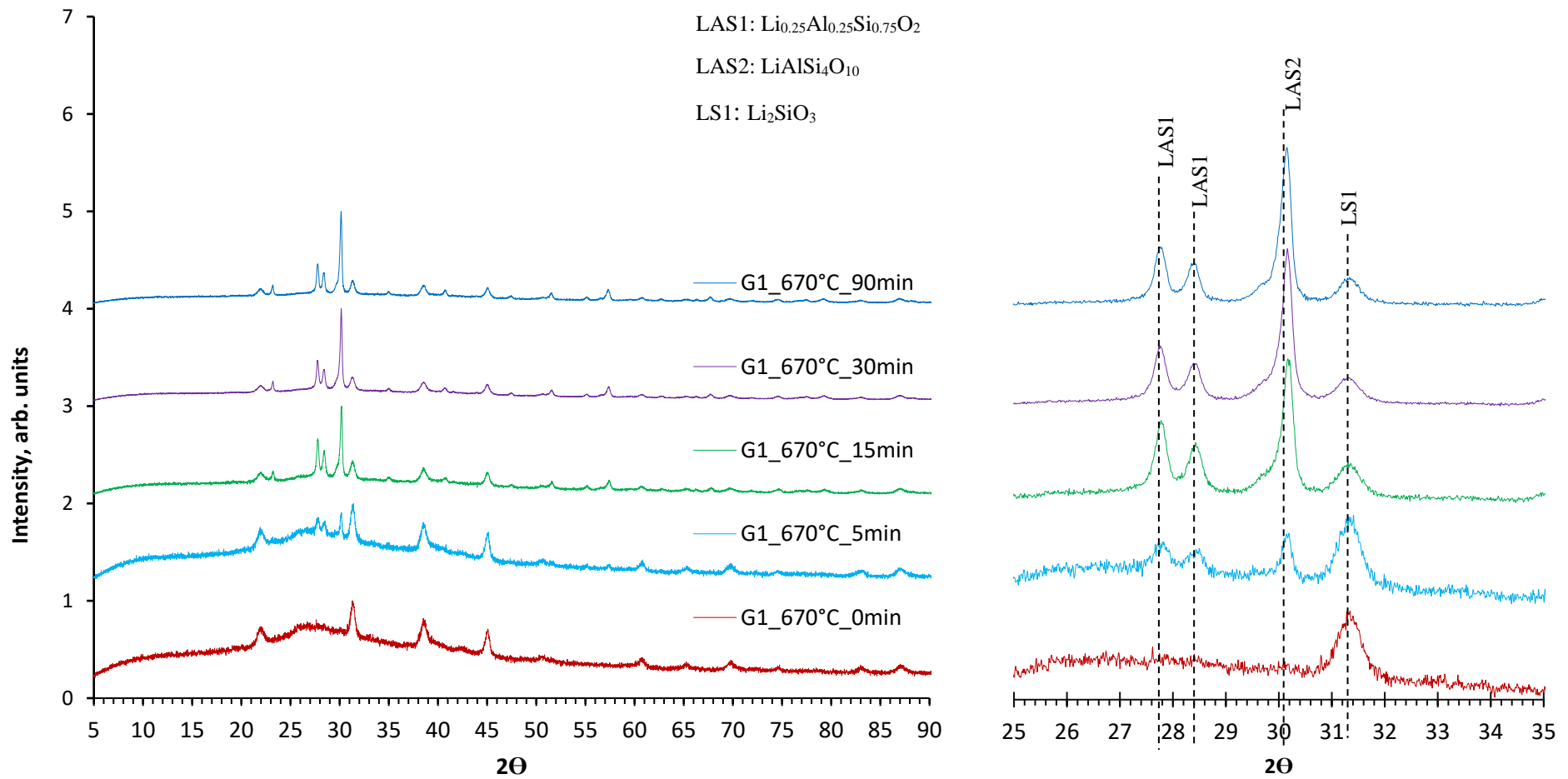


Fig. 5. 16 Room-temperature XRD patterns LAS1 glass heat treated at 670°C for different holding times.

5.4.5 Median crystallite size evolution for Li_2SiO_3 heat treated at 670°C

Many studies involving glass ceramics [124], [259]–[262] have employed the Scherrer equation to obtain crystallite sizes. The Full Width at Half Maximum (FWHM) for the most intense peak ascribed to the Li_2SiO_3 phase is the main variable in the equation 5.3 [263]:

$$\beta = \frac{K\lambda}{FWHM \cos \theta} \dots \quad 5.3$$

Where;

FWHM is the full width at half maximum of the peak.

K is known as the Scherrer constant and is 0.9 [264], [265].

λ is the wavelength.

β is the mean crystallite size.

Fig. 5. 17 shows the evolution of the FWHM for the main Bragg peak $\text{Li}_{0.25}\text{Al}_{0.25}\text{Si}_{0.75}\text{O}_2$ (LAS2) alongside $\text{LiAlSi}_4\text{O}_{10}$ (LAS1) and Li_2SiO_3 (LS1) hold a 670°C for different lengths of time, as illustrated in Fig. 5. 16. Basically, the LAS2 peak gets sharper up 30 minutes holding. Hence, it is found that crystal size of $\text{Li}_{0.25}\text{Al}_{0.25}\text{Si}_{0.75}\text{O}_2$ increases with increasing time, reaching ~ 60 nm after 30 minutes, as shown in Fig. 5. 18. The initial growth rate of LAS2 and LAS1 is ~ 3.44 and 0.21 nm/min, respectively, but for LAS2 after 30 minutes no growth is detected. On the other hand, the crystal size of LS1 remains constant with increasing time reaching ~ 24.02 nm. It is worth mentioning that as for large crystals the equation might not work properly.

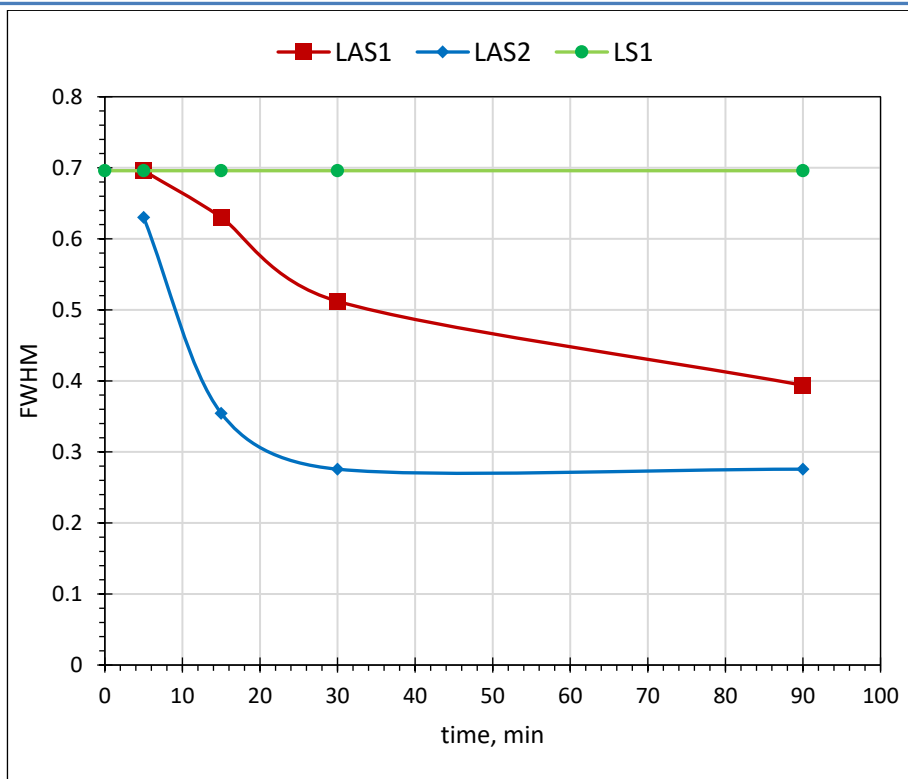


Fig. 5. 17 FWHM of $\text{LiAlSi}_4\text{O}_{10}$ (LAS1), $\text{Li}_{0.25}\text{Al}_{0.25}\text{Si}_{0.75}\text{O}_2$ (LAS2) and Li_2SiO_3 (LS1) upon heating at 670°C.

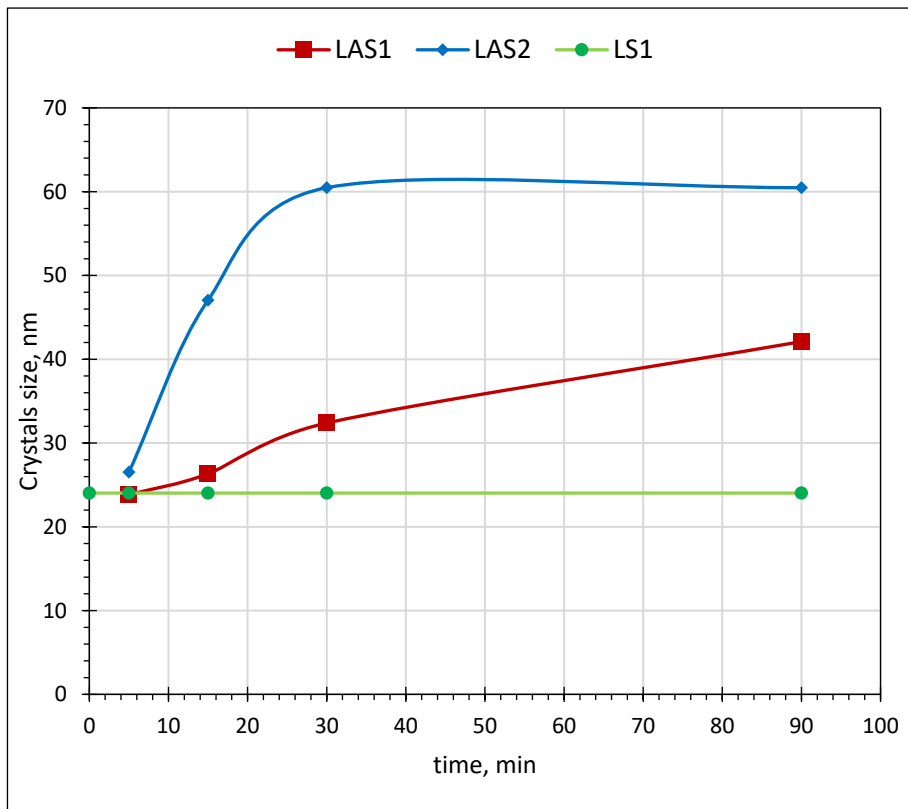


Fig. 5. 18 Time dependence of the median crystallite size of $\text{LiAlSi}_4\text{O}_{10}$ (LAS1), $\text{Li}_{0.25}\text{Al}_{0.25}\text{Si}_{0.75}\text{O}_2$ (LAS2) and Li_2SiO_3 (LS1) upon heating at 670°C.

5.4.6 Crystallite size evolution for LiAlSi₂O₆

Fig. 5. 14 and 15 showed that LiAlSi₂O₆ is the dominant phase in samples heat treated above 730°C. The evolution of FWHM for the LiAlSi₂O₆ Bragg peak located at 29.00°-31° 2θ in terms of heat treatment is illustrated Fig. 5. 19. It is evident that with increasing heat treatment temperature, the peak gets sharper as indicated by the decrease in FWHM. These values can be incorporated in the Scherrer equation to calculate the median crystallite sizes. The results are shown in Fig. 5. 20.

In non-nucleated samples, LiAlSi₂O₆ appears to have a constant crystallite size of ~75 nm. In contrast, in nucleated samples LiAlSi₂O₆ appears to increase size, reaching a maximum of ~90 nm after 30 min at 850°C. This size is in agreement with the SEM images shown in Fig. 5. 56.

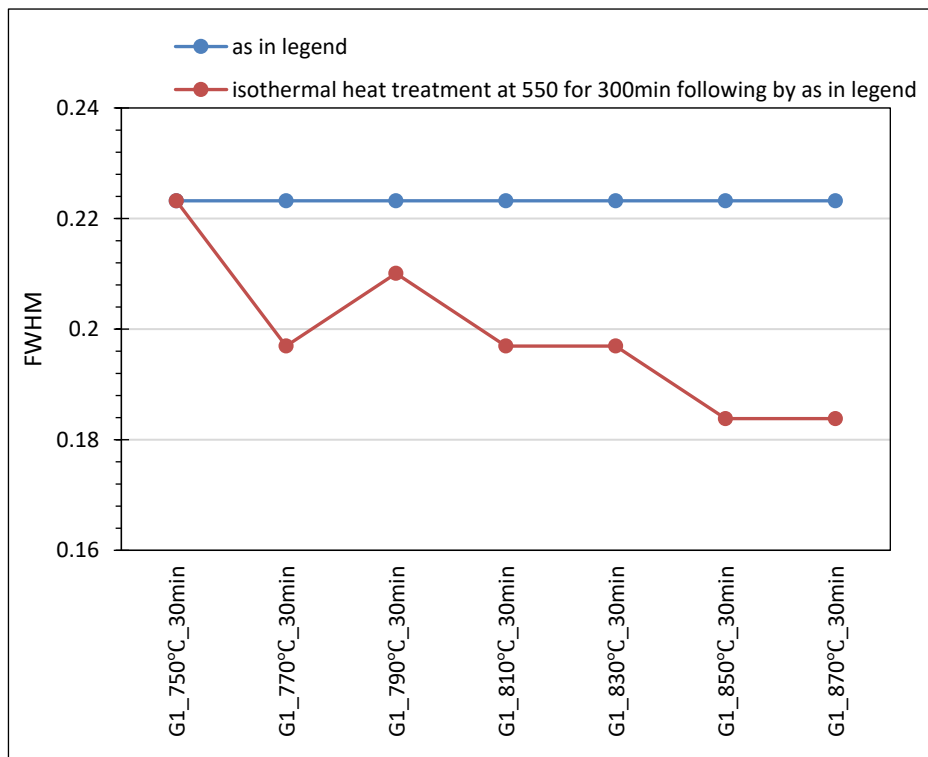


Fig. 5. 19 Evolution of FWHM for the LiAlSi₂O₆ Bragg peak located at 29.00°-31° 2θ in terms of heat treatment.

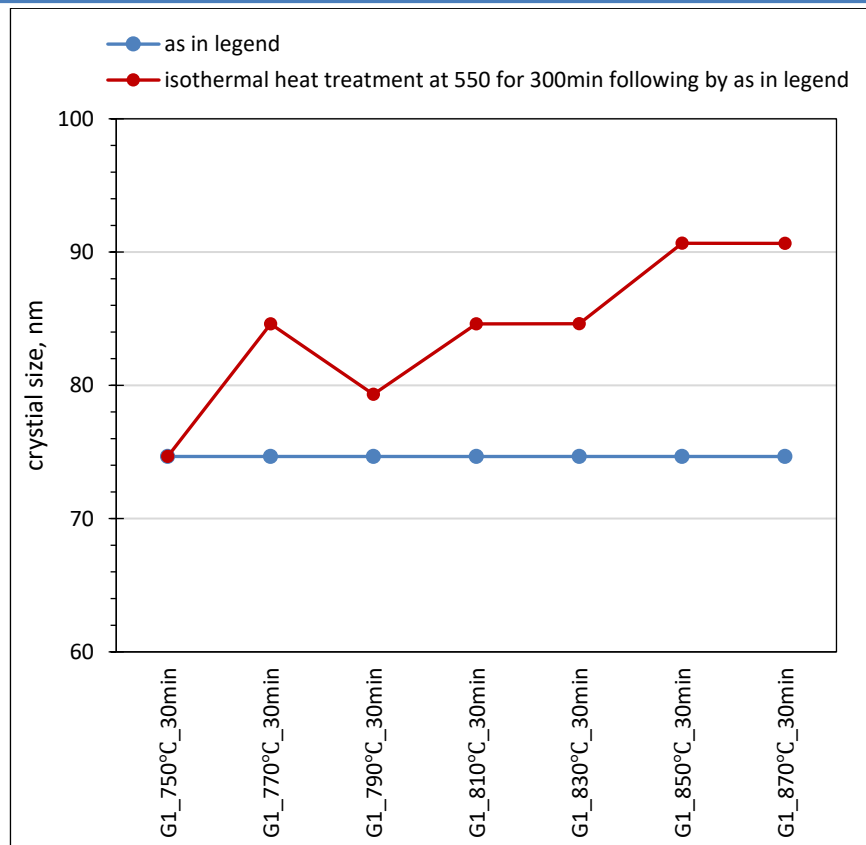


Fig. 5. 20 Median crystallite size of $\text{LiAlSi}_2\text{O}_6$ in function of temperature.

5.4.7 $\text{LiAlSi}_2\text{O}_6/\text{Li}_2\text{Si}_2\text{O}_5$ ratio between 730°C and 850°C

DSC data, Fig. 5. 1, combined with X-ray diffraction data, Fig. 5. 12, show the almost simultaneous crystallisation of $\text{LiAlSi}_2\text{O}_6$ and $\text{Li}_2\text{Si}_2\text{O}_5$ above 700°C . The relative amount of each phase can be estimated by the intensity ratios of the main Bragg peaks associated with each phase, which for $\text{LiAlSi}_2\text{O}_6$ is located at $28.5^\circ - 30^\circ 2\Theta$ and for $\text{Li}_2\text{Si}_2\text{O}_5$ is located at $27.5^\circ - 29.5^\circ 2\Theta$, as shown in Fig. 5. 14 and Fig. 5. 15, for non-nucleated and nucleated, respectively. The ratios are graphically summarized in Fig. 5. 21, for samples heat treated in the $730^\circ\text{C}-870^\circ\text{C}$ temperature.

In general, the ratios show:

- $\text{LiAlSi}_2\text{O}_6$ becomes dominant with increasing temperature.
- Nucleation leads to a larger relative amount of $\text{LiAlSi}_2\text{O}_6$.

A sudden drop in the ratio was observed above 850°C , for nucleated samples, which is not fully understood, but may be linked to approaching the melting temperature.

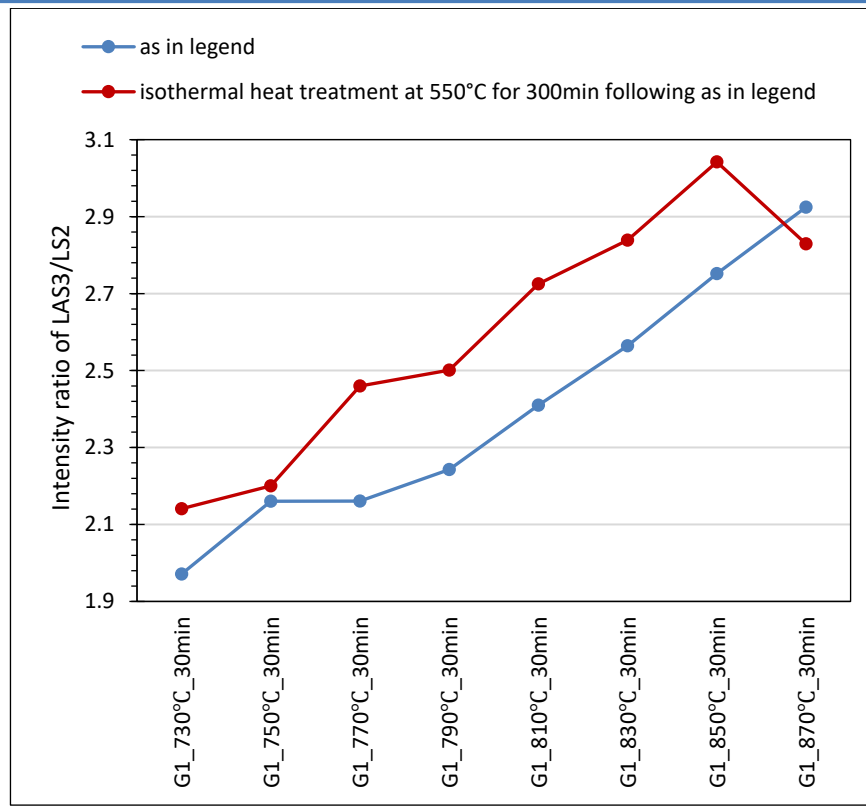


Fig. 5. 21 Intensity ratio of lithium-aluminosilicate (LAS3) and lithium-disilicate (LS2).

5.5 Raman spectroscopy of LAS1 glass

Raman spectroscopy is employed here to further ascertain the nature of the crystals precipitated upon heat treatment. Compared with X-ray diffraction analysis, Raman spectroscopy provides a local probe with better detections limits, therefore it may help provide an earlier detection of a crystallisation process. Raman spectra were acquired from the as-cast, nucleated glass and fully heated treated LAS1 glasses, (glass-ceramics). The main Raman modes were assigned according to data in the literature, as listed in Table 5. 3, and are used as fingerprint for the phase assemblage.

Table. 5. 3 Raman band sites determined from this study and many band assignments according to references.

| Bands observed in this study | Bands observed based on references | Bands assignment | | References |
|---------------------------------|---------------------------------------|------------------|--|--------------|
| 358, 949 cm ⁻¹ | 359, 950 cm ⁻¹ | LP | Li ₃ PO ₄ | [266] |
| 465, 610, 980 cm ⁻¹ | 613, 977 cm ⁻¹ | LS1 | Li ₂ SiO ₃ | [267] |
| | 463 cm ⁻¹ | | | [209] |
| | 607, 979 cm ⁻¹ | | | [201] |
| 488 cm ⁻¹ | 488 cm ⁻¹ | LAS1 | LiAlSi ₄ O ₁₀ | [201], [268] |
| 411, 550, 1109 cm ⁻¹ | 409, 551, 1104 cm ⁻¹ | LS2 | Li ₂ Si ₂ O ₅ | [195], [207] |
| 492 cm ⁻¹ | 492 cm ⁻¹ | LAS3 | LiAlSi ₂ O ₆ | [208], [209] |
| | 338, 432, 490, 584 cm ⁻¹ | | | [160] |
| | 782, 947, 1060, 1174 cm ⁻¹ | | | |

5.5.1 Impact of time on the nucleation at 550°C

The X-ray diffraction data in Fig. 5.13 suggest the as-cast LAS1 glass to contain some Li₃PO₄ and Li₂SiO₃ crystals. Their presence can be confirmed by the presence of some Raman modes specific for each phase. For example, Terry et al 2018 [269] reported bands at 292, 361, 408, 523 (strong), 606 (strongest), 865, 980 (very strong), and 1033 cm⁻¹ for Li₂SiO₃. Due to their intensity, the modes at 606 and 980 cm⁻¹ provide a powerful signal to monitor the presence of Li₂SiO₃. On the other hand, the presence of Li₃PO₄ can be probed by monitoring a mode at 950 cm⁻¹. The Raman spectra shown in Fig. 5. 22, feature bands around 489, 610, 950 and 980 cm⁻¹. The mode at 489 cm⁻¹ may indicate the presence of LiAlSi₄O₁₀, which was not previously identified by the X-ray diffraction data. Hence, the as-cast LAS1 glass contains Li₂SiO₃, Li₃PO₄ and LiAlSi₄O₁₀. With increasing time at 550°C, the mode at 610 cm⁻¹ increases intensity, which corroborates an increase of Li₂SiO₃.

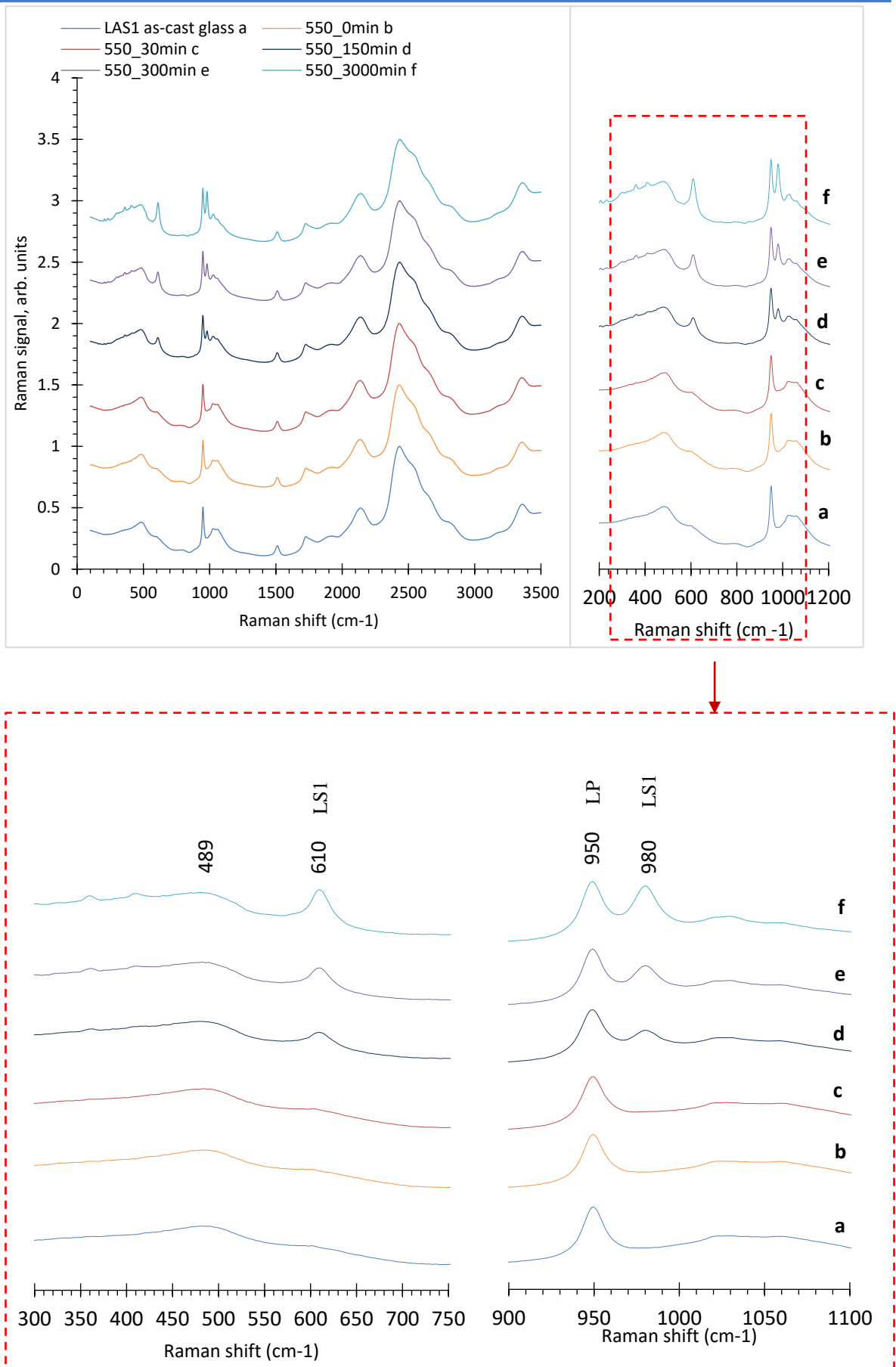


Fig. 5. 22 Raman spectra for as-cast LAS1 glass and heat treated at 550°C for different times.

5.5.2 Raman spectra for LAS1 glass heat treated for 30 minutes in 610°C to 870°C temperature range

Raman spectra shown in Fig. 5. 23, shows that no other phases appear up to 650°C. The band at 949 cm⁻¹ is present from 610°C to 870°C, showing that Li₃PO₄ is always present. The bands at 610 cm⁻¹ and 980 cm⁻¹ are attributed to pure Li₂SiO₃ [267]. There is a mode shift to ~ 608 cm⁻¹ at 670°C, which also coincides with the increase of the ~ 488 cm⁻¹, ascribed to LiAlSi₄O₁₀ crystals [268]. This agrees with the *In-Situ* XRD analysis in this study. Based on DSC trace, in Fig. 5. 1, these phases are associated to the first exothermic peak.

At 690°C, the appearance of new band shows at ~ 411, 550 and 1109 cm⁻¹ corroborate the appearance of Li₂Si₂O₅ [270]. The shift of the 488 cm⁻¹ mode to 492 cm⁻¹ at 730°C is consistent with a solid solution between Li_{0.25}Al_{0.25}Si_{0.75}O₂ and LiAlSi₂O₆. Pure LiAlSi₂O₆ shows a mode at 492 cm⁻¹ [208], [209].

This is consistent with the *In-Situ* XRD data, shown in Fig. 5. 12, and ultimately linked to the second exothermic peak, in DSC trace, Fig. 5. 2. Therefore, this analysis is consistent with the mechanism of crystallization of LAS glass containing phosphate oxide as nucleating agents and can be found in the literature [201], [208], [209].

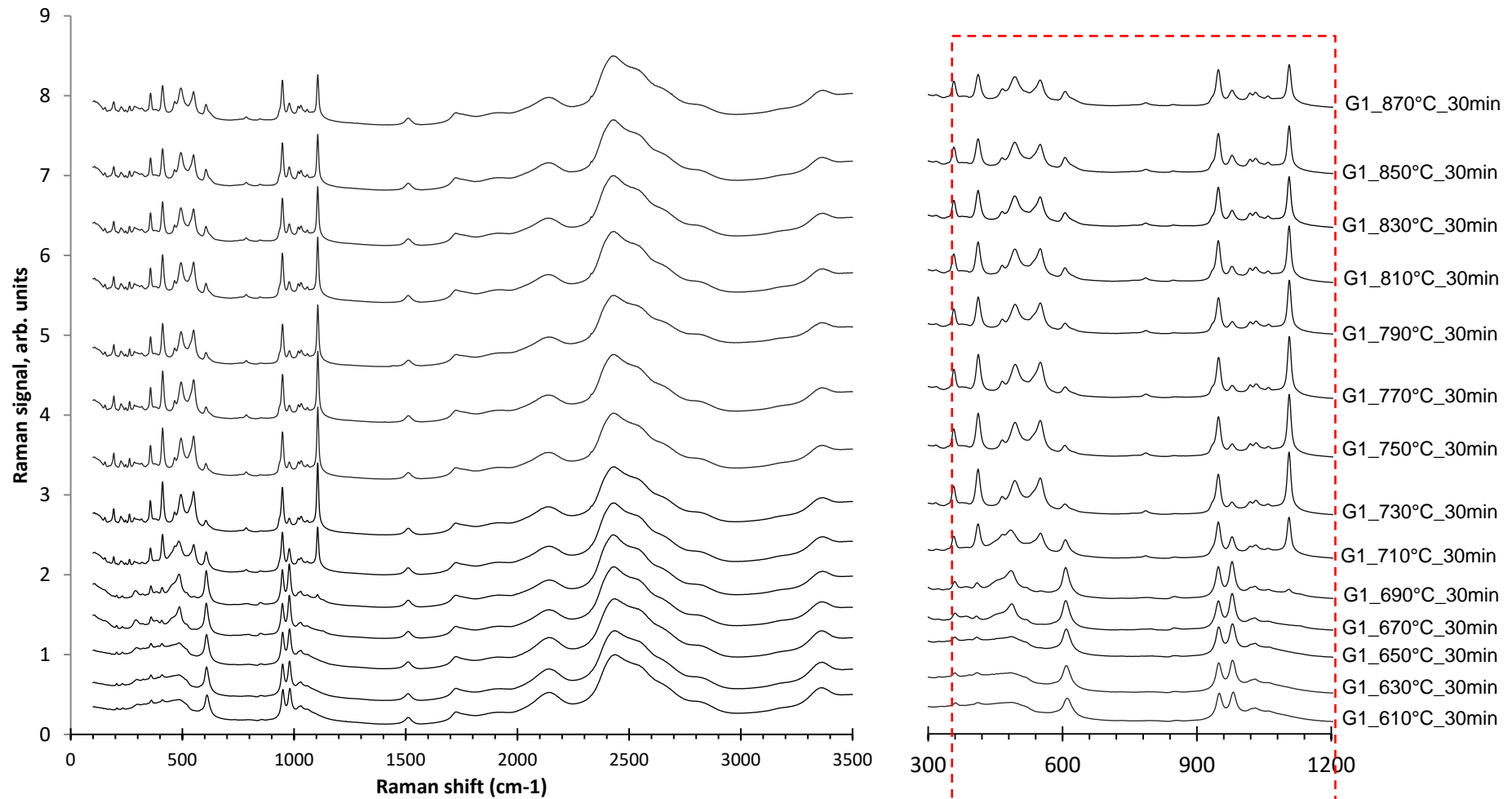


Fig. 5. 23-a Raman spectra for LAS1 glass heat treated for 30 minutes in 610°C to 870°C temperature range.

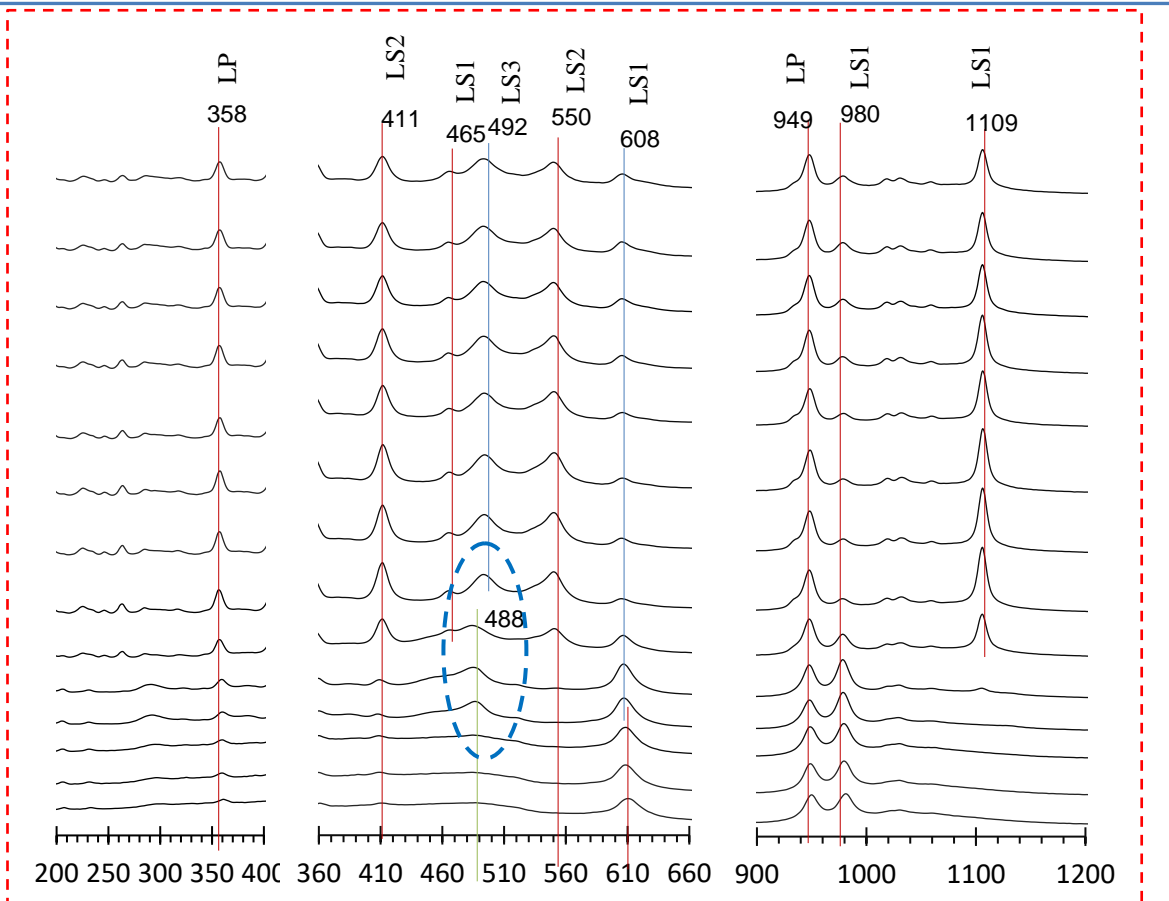


Fig. 5. 23-b Raman spectra for LA1 glass heat treated for 30 minutes in 610°C to 870°C temperature range.

5.5.3 Raman spectra for LAS1 glass nucleated at 550°C for 30 minutes and then heat treated for 30 minutes in 630°C to 870°C temperature range

The Raman bands in Fig. 5. 24 is similarity to Raman bands in Fig. 5. 23 in the section 5.5.2. However, the only difference was at 670°C showing a new band at about 485 cm⁻¹, close to is LiAlSi₄O₁₀ (488 cm⁻¹ in [201], [268]).

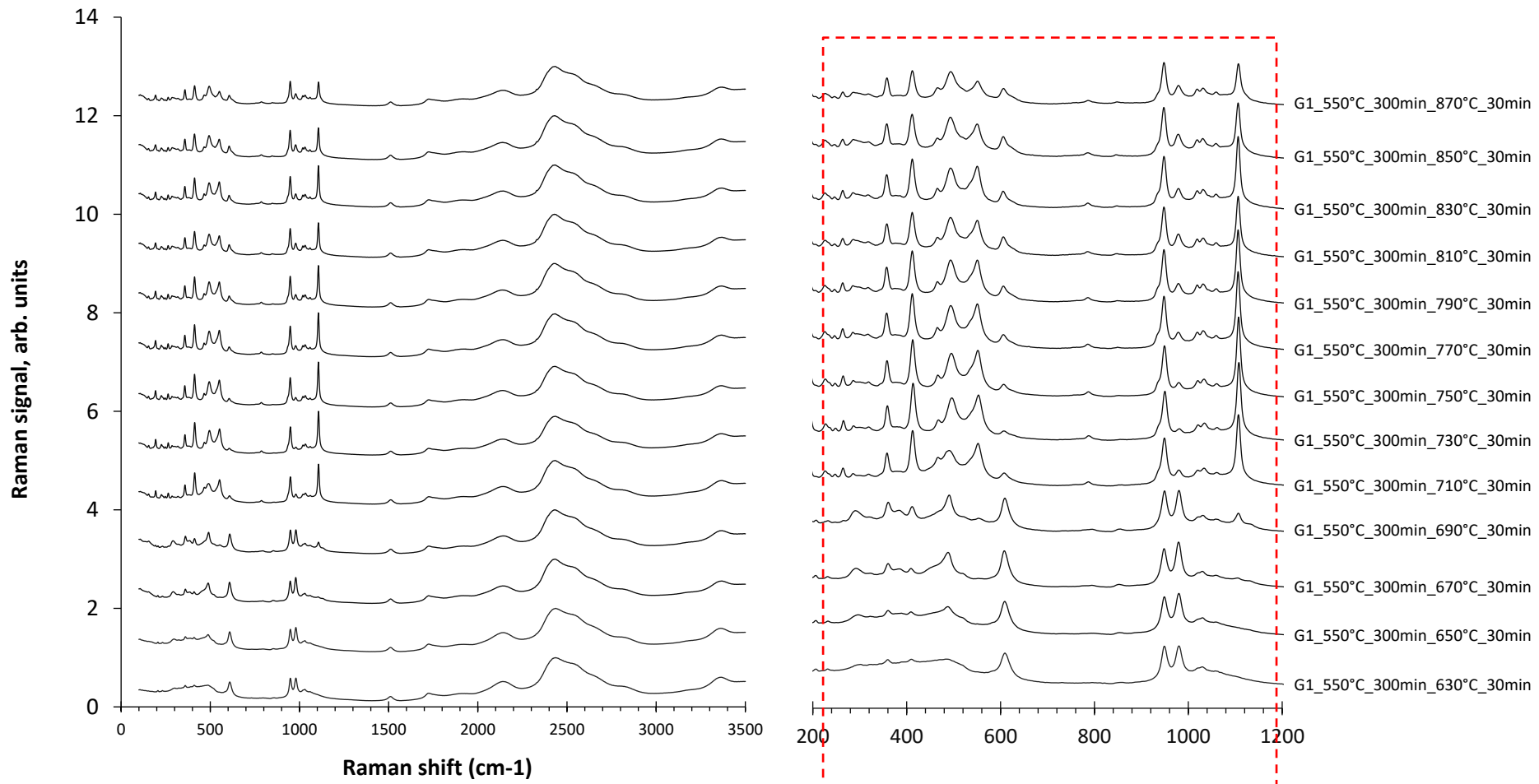


Fig. 5. 24-a Raman spectra for LAS1 glass nucleated at 550 °C for 30 minutes and then heat treated for 30 minutes in 630°C to 870°C temperature range.

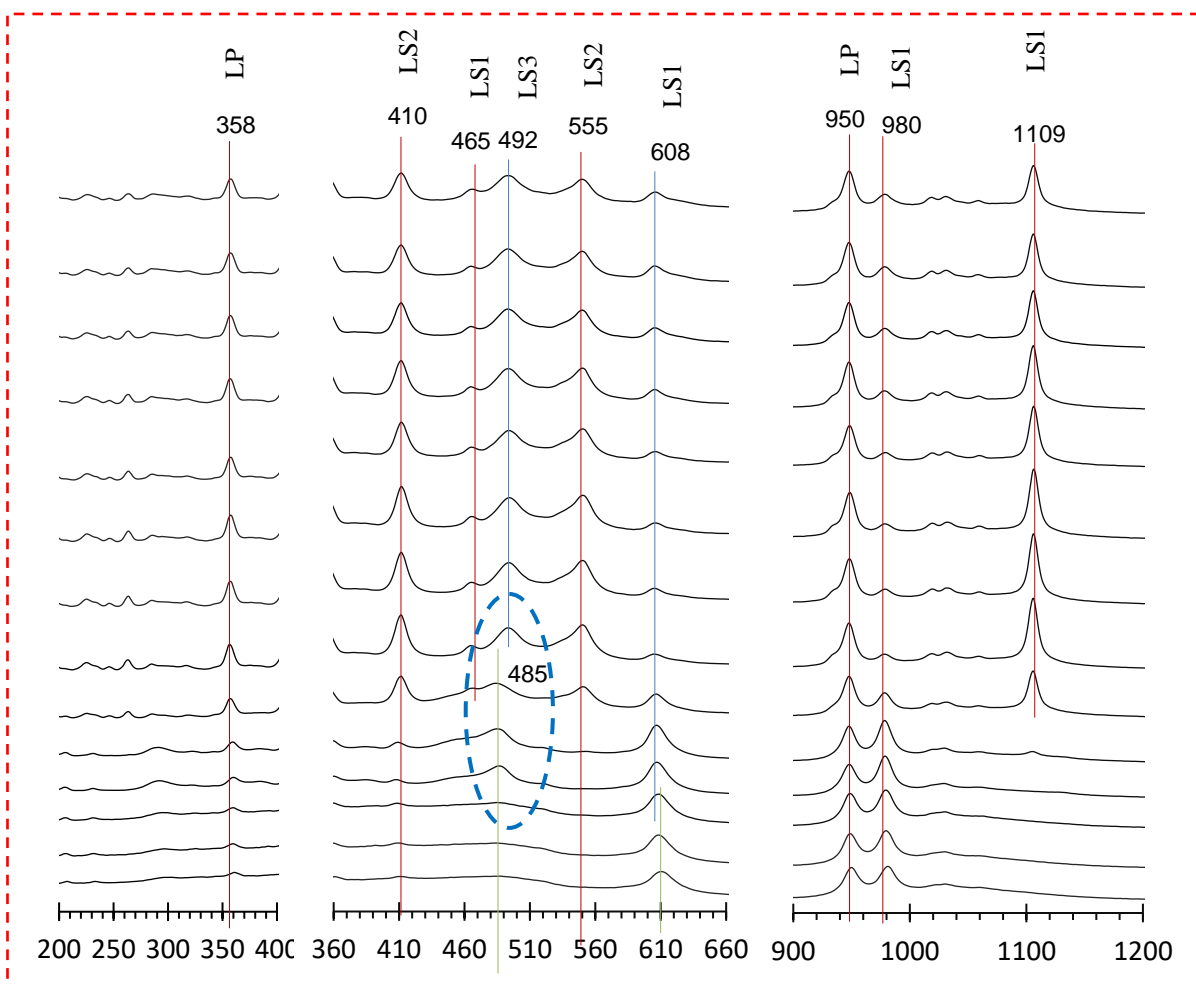


Fig. 5. 24-b Raman spectra for LAS1 glass nucleated at 550°C for 30 minutes and then heat treated for 30 minutes in 630°C to 870°C temperature range.

5.5.4 Isothermal heat treatment at 670°C for different holding time

Based on the Raman spectra, in Fig. 5. 25, many bands for a treatment at 670°C for 0, 5, 15, 30 and 90min are assigned to Li_2SiO_3 and Li_3PO_4 , see the section 5.4.1. Based on the DSC trace, shown in Fig. 5. 1, this is consistent with the first exothermic peak. However, for a treatment at 670°C for 15, 30 and 90min show a new band at about 488 cm^{-1} , this is $\text{LiAlSi}_4\text{O}_{10}$ crystals (488 cm^{-1} in [268]). This evidences that there are two sub-peaks within the first exothermic peak in DSC trace, the first sub-peak is consistent with the crystallisation of Li_2SiO_3 and Li_3PO_4 and the second sub-peak with the crystallisation of $\text{Li}_{0.25}\text{Al}_{0.25}\text{Si}_{0.75}\text{O}_2$ and $\text{LiAlSi}_4\text{O}_{10}$.

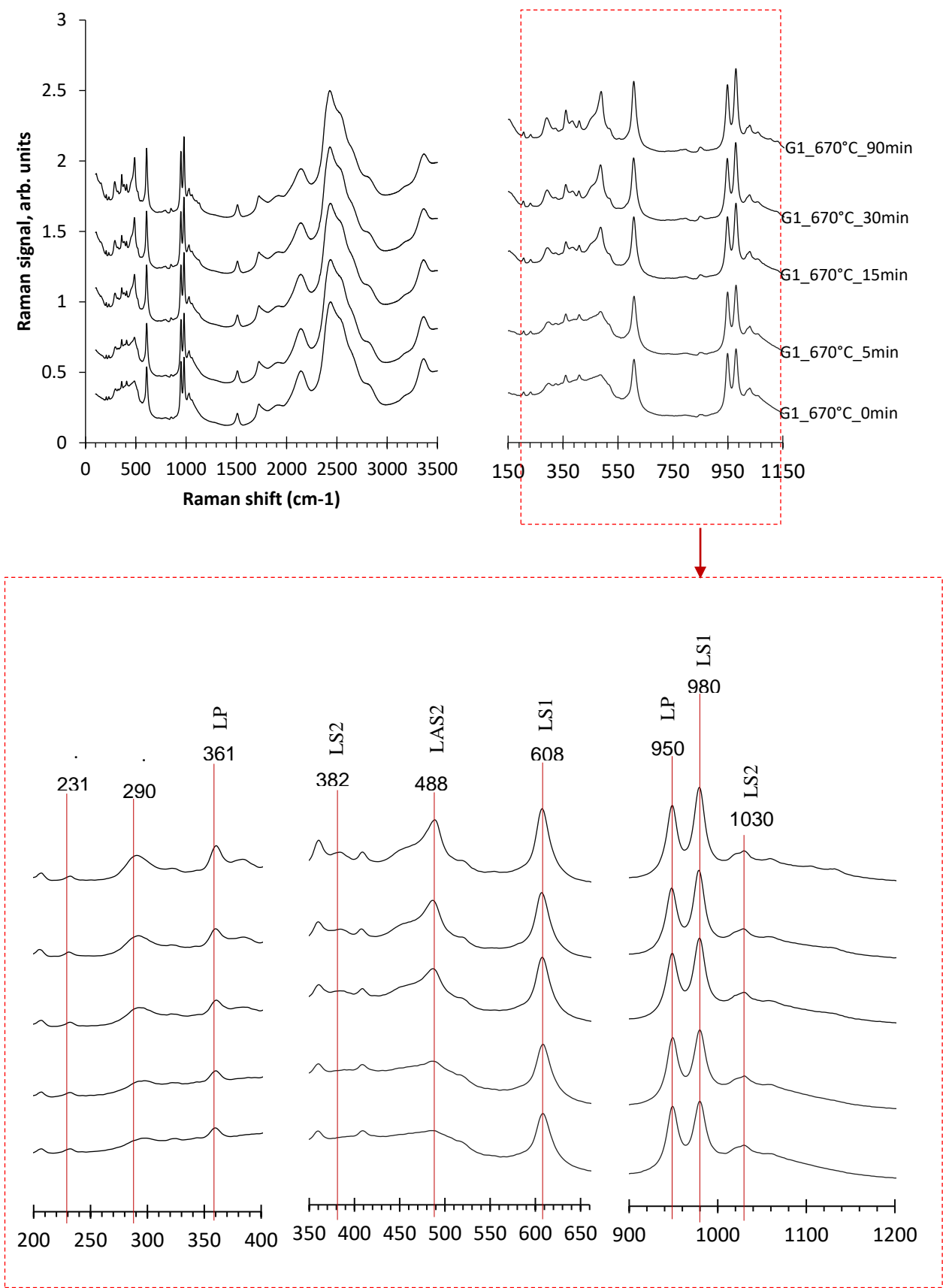


Fig. 5. 25 Raman spectra of isothermal heat treatment of LAS1 as-cast glass at 670°C for different time.

5.6 Mechanical properties of LAS1 glass

5.6.1 Elastic modulus

In this section, elastic modulus values determined by ultrasound measurements as described in literature [181], [211], [215], [216], [271]–[275] are presented. Elastic modulus calculation method by ultrasound speed can be found in Appendix 4.

5.6.1.1 Elastic modulus after isothermal heat treatments at 550°C for different holding times

The as-cast LAS1 glass shows the lowest elastic modulus, E, around 80.77 ± 0.21 GPa. Upon nucleation at 550°C for 30, 150, 300 and 3000 min, E increases to 81.73 ± 0.26 GPa, 82.1 ± 0.1 , 82.8 ± 0.1 GPa and 82.9 ± 0.27 GPa, respectively, as shown in Fig. 5. 26.

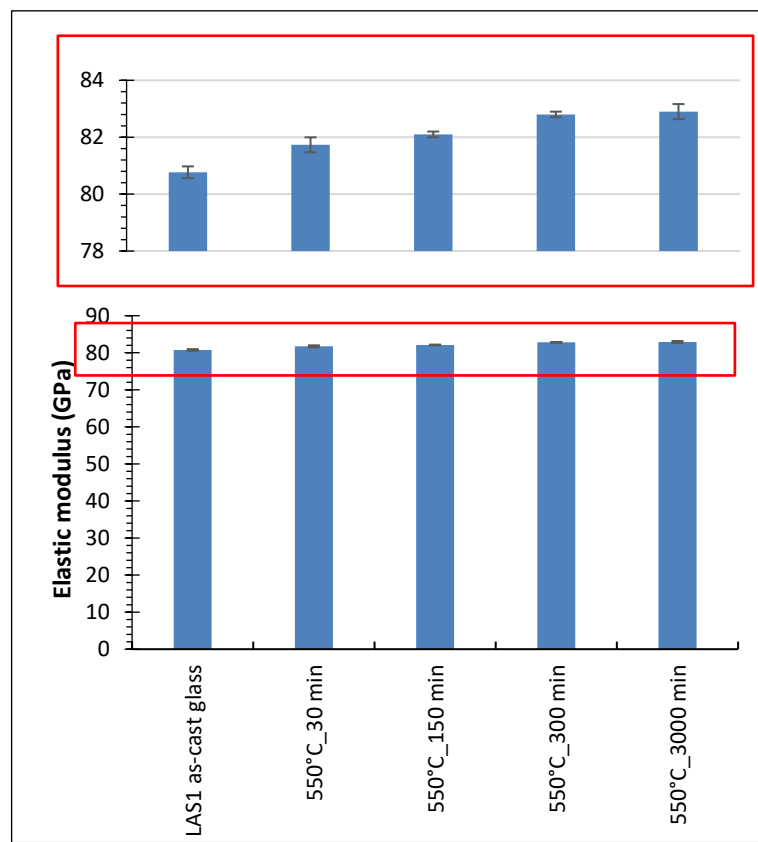


Fig. 5. 26 Elastic modulus after isothermal heat treatments at 550°C for different holding times.

This relatively small enhancement of the elastic modulus with increasing nucleation time is consistent with a limited crystallisation of Li_2SiO_3 and Li_3PO_4 phases, as shown in Fig. 5. 13. These phases promote strength of the glass

structure in comparison with the as-cast glass. Moreover, SEM images in Fig. 5. 55 provide evidence for the appearance of Li_2SiO_3 crystals.

5.6.1.2 Elastic modulus after heat treatment for 30 min in the 630°C to 870°C temperature range

The evolution of elastic modulus for LAS1 glass as a function of the non-isothermal heat treatment is shown in Fig. 5. 27. Samples heat-treated between 630°C and 690°C for 30 min only show a slightly increase of E from $\sim 84.17 \pm 0.55$ to 86.53 ± 0.45 GPa, respectively. Based on the *ex-situ* XRD analysis, Fig. 5. 14, samples heat treated at 630°C for 30 min are still rather amorphous, with a small content of Li_2SiO_3 and Li_3PO_4 . Samples heat treated at 650°C for 30 min, start to show minute amounts of $\text{Li}_{0.25}\text{Al}_{0.25}\text{Si}_{0.75}\text{O}_2$ and $\text{LiAlSi}_4\text{O}_{10}$ alongside Li_2SiO_3 and Li_3PO_4 embedded in a still amorphous matrix. In contrast, samples heat treated at 670°C are much more crystalline and consist mainly of $\text{Li}_{0.25}\text{Al}_{0.25}\text{Si}_{0.75}\text{O}_2$ and $\text{LiAlSi}_4\text{O}_{10}$, with some residual Li_2SiO_3 and Li_3PO_4 . The phase assemblage for samples heat treated at 690°C for 30 min is also similar. Nevertheless, this phase assemblage appears to only have a minor impact on the E values, which reach a maximum of 86.53 ± 0.45 GPa. In contrast, the phase assemblage resulting from heat-treatment at 710°C and 730°C, that is accompanied by the crystallisation of $\text{Li}_2\text{Si}_2\text{O}_5$ and $\text{LiAlSi}_2\text{O}_6$, leads to a considerable increase of E, first to 91.6 ± 0.26 GPa and then to 95.83 ± 0.20 GPa.

The elastic modulus for heat treatments between 750°C and 790°C for 30 min are almost constant in the 95-96 GPa range, however above 790°C there is a slight continuous decrease in E, as illustrated in Fig. 5. 27.

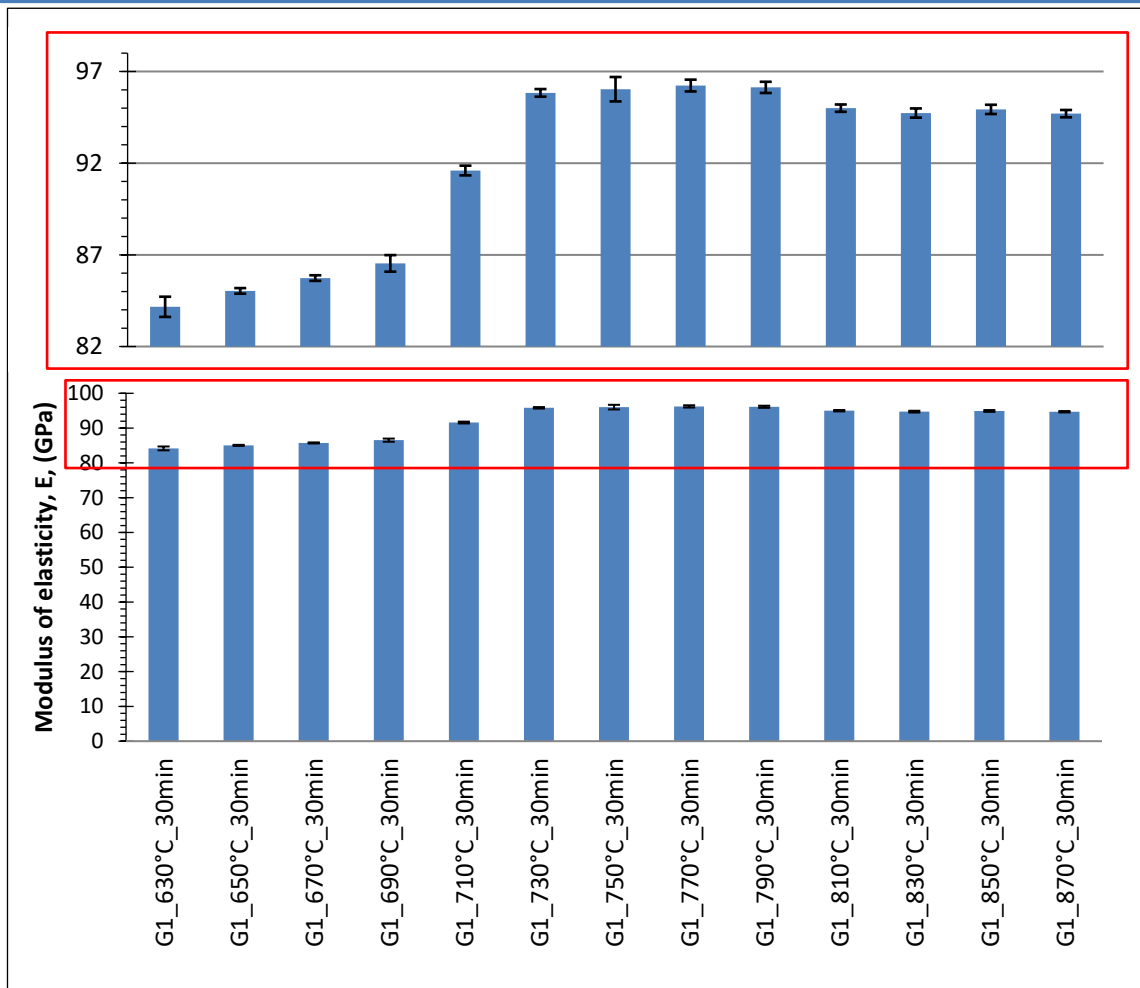


Fig. 5. 27 Elastic modulus after heat treatment for 30 min in the 630°C to 870°C temperature range.

5.6.1.3 Elastic modulus after nucleation at 550°C for 300 min followed by heat treatment for 30 min in the 630°C to 870°C temperature range

The evolution of the elastic modulus of the LAS1 glass as a function of the isothermal heat treatment (nucleation) at 550°C for 300 min followed by heat treatment for 30 min in the 630°C to 870°C temperature range is illustrated in Fig. 5. 28. In comparison with Fig. 5. 27, for non-nucleated samples, it becomes obvious that nucleation leads to an enhancement of E at lower temperatures. This agrees with the fact that crystallisation of $\text{Li}_{0.25}\text{Al}_{0.25}\text{Si}_{0.75}\text{O}_2$, $\text{LiAlSi}_4\text{O}_{10}$, $\text{Li}_2\text{Si}_2\text{O}_5$ and $\text{LiAlSi}_2\text{O}_6$ also occur at lower temperatures in nucleated samples, as shown in Fig. 5. 16. This is especially evident for the nucleated samples heat treated at 690°C for 30 min, which show a E of 93.2 ± 0.1 GPa, compared with 86.53 ± 0.45 GPa for the non-nucleated counterparts.

Similar to the trend observed in Fig. 5. 27, nucleated samples heat treated 730°C for 30 min show the highest E values 97.03 ± 0.12 GPa, due to presence of

$\text{Li}_2\text{Si}_2\text{O}_5$ and $\text{LiAlSi}_2\text{O}_6$ phases. This value is larger than the one observed for non-nucleated.

For samples heat treated above 730°C there is a slight decrease of E, as also observed in the non-nucleated case. This feature is accompanied with the onset of endothermic event at ~ 870°C, that points out towards initial melting.

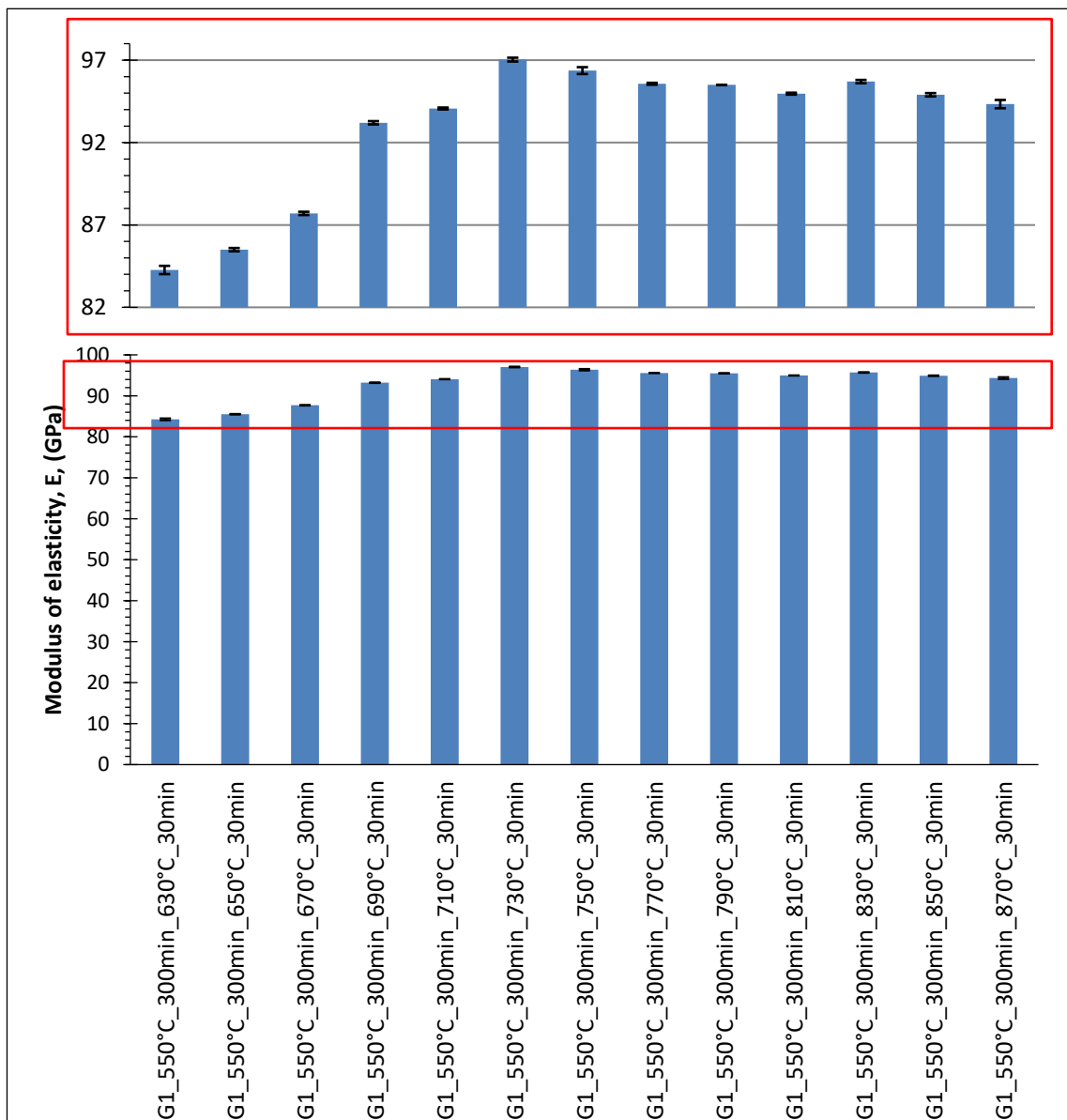


Fig. 5. 28 Elastic modulus after nucleation at 550°C for 300 min followed by heat treatment for 30 min in the 630°C to 870°C temperature.

5.6.2 Hardness

Hardness is defined as the ability of a material to resist scratch or deformation [3], hence, hardness affects ease of cutting, finishing, and polishing blocks in particular these that are made for CAD/CAM processing [56]. Microhardness was

assessed using the Hardness Vickers (H_V) method described in section 3.1.1.5. Harness values for each sample were determined from six different indentations on the sample's surface. See Appendix 5.

5.6.2.1 Hardness after isothermal heat treatments at 550°C for different holding times

The as-cast LAS1 glass shows the lowest $H_V \sim 5.61 \pm 0.15$ GPa. Upon nucleation at 550°C for 30, 150, 300 and 3000 min, H_V increases to 5.98 ± 0.03 GPa, 6.21 ± 0.01 GPa, 6.43 ± 0.11 GPa and 6.64 ± 0.10 GPa, respectively, as shown in Fig. 5. 29. This mirrors the evolution of E as shown in Fig. 5. 26, therefore it may also be correlated to the slight increase in Li_2SiO_3 and Li_3PO_4 content.

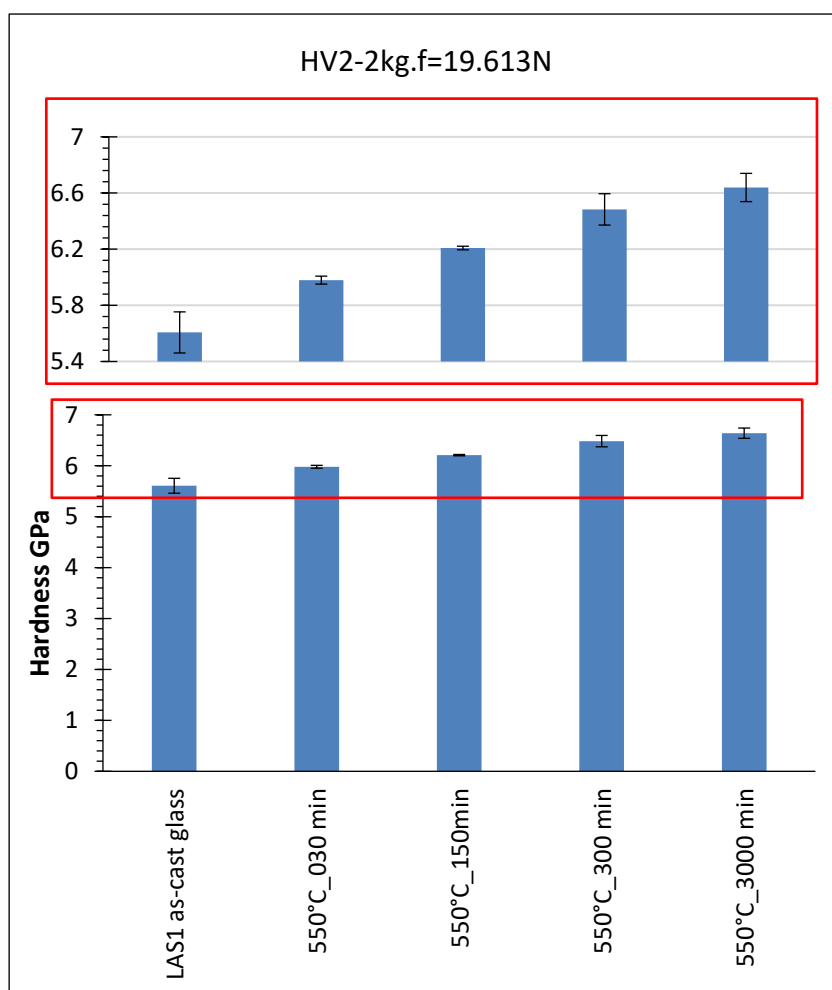


Fig. 5. 29 Hardness after isothermal heat treatments at 550°C for different holding times.

5.6.2.2 Hardness after heat treatment for 30 min in the 630°C to 870°C temperature range

The evolution of hardness, Hv, for LAS1 glass as a function of the non-isothermal heat treatment is shown in Fig. 5. 30. The as-cast glass shows $Hv \sim 5.6 \pm 0.15$ GPa, Fig. 5. 30, which increases to 6.26 ± 0.01 GPa for samples heat-treated at 630°C for 30 min. Those samples are still rather amorphous, with a small content of Li_2SiO_3 and Li_3PO_4 as previously shown in Fig. 5. 14. On the other hand, samples heat treated at 650°C for 30 min, start to show minute amounts of $Li_{0.25}Al_{0.25}Si_{0.75}O_2$ and $LiAlSi_4O_{10}$ alongside Li_2SiO_3 and Li_3PO_4 embedded in a still amorphous matrix. This is accompanied by an increase of Hv to 6.49 ± 0.11 GPa. In contrast, samples heat treated at 670°C, which are more crystalline and consist mainly of $Li_{0.25}Al_{0.25}Si_{0.75}O_2$ and $LiAlSi_4O_{10}$, with some residual Li_2SiO_3 and Li_3PO_4 show a decrease in Hv. The phase assemblage for samples heat treated at 690°C for 30 min is also similar, and interestingly Hv appears to show a larger disparity of values. This heat treatment temperature is close to the onset of a complex crystallisation pathway, leading to the eventual crystallisation of $Li_2Si_2O_5$ and $LiAlSi_2O_6$ above 710°C. It can be speculated that local chemical and phase inhomogeneities can lead to the observed disparity of Hv values. For samples treated between 710 and 770°C, there is an apparent increase in Hv, which can certainly be linked to a larger content of $LiAlSi_2O_6$, as shown by the X-ray diffraction data in Fig. 5. 14. Interestingly, treatments above 770°C for 30min are accompanied by a decrease in Hv, which reaches its lowest value for samples heat treated at 870°C for 30 min. In the other words, the increasing heat treatment temperatures results in decreasing hardness values. A similar high temperature trend was observed for nucleated samples as shown in the next section.

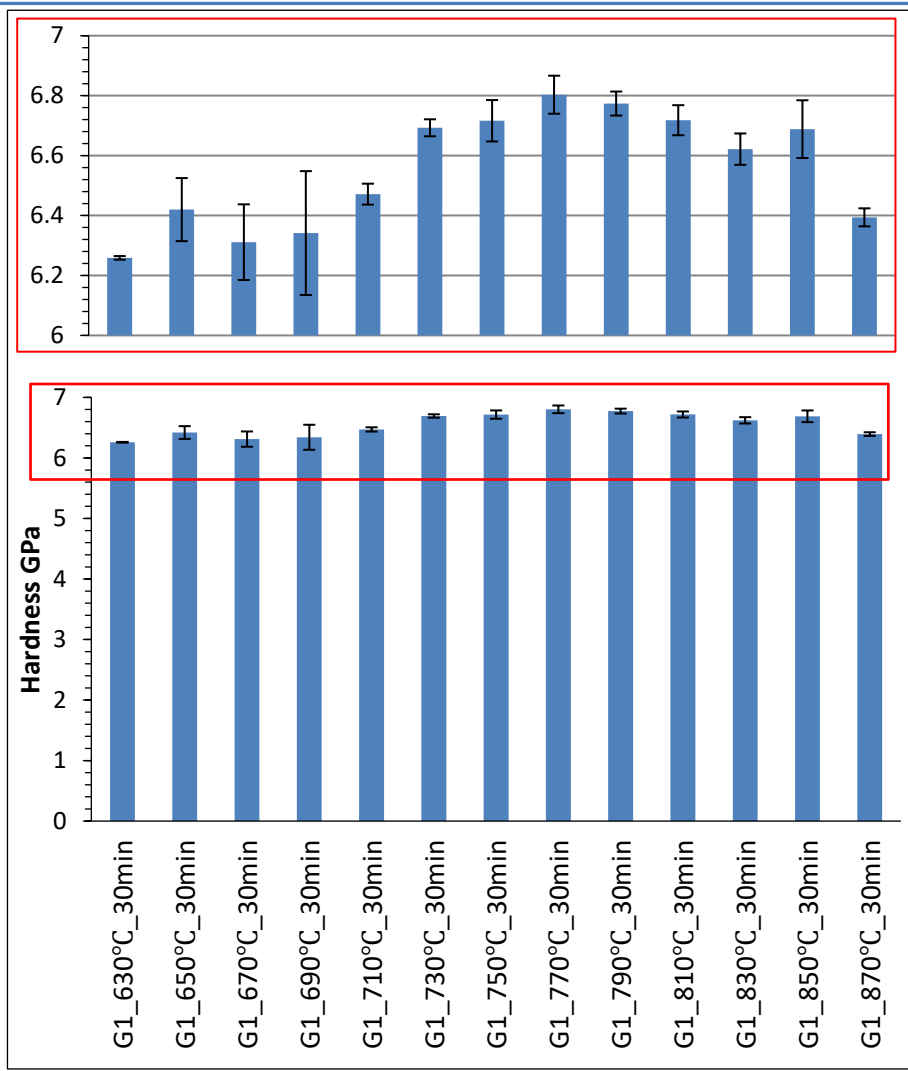


Fig. 5. 30 Hardness after heat treatment for 30 min in the 630°C to 870°C temperature range.

5.6.2.3 Hardness after nucleation at 550°C for 300 min followed by heat treatment for 30 min in the 630°C to 870°C temperature range

The evolution of hardness, H_v , for LAS1 glass as a function of the non-isothermal heat treatment for samples nucleated at 550°C for 300 min is shown in Fig. 5. 31. In terms of H_v values the samples can be divided into two groups. The first group is for samples heat treated below 730°C for 30 min, which show an average H_v smaller than 6.3 GPa. The second group is for samples heat treated for 30 min at 730°C and above, which show an average H_v greater than 6.6 GPa, with the exception of the sample heat treated at 870°C for 30 min.

For first group, average H_v values range from 6.16 to 6.22 GPa, but also show a large disparity of values, which is consistent with a complex crystallisation pathway as shown by the X-ray diffraction data in Fig. 5. 15. Whereas the second group, that has significantly higher H_v , and a smaller dispersion of values is

compatible with the nearly completed $\text{LiAlSi}_2\text{O}_6$ crystallisation. Again, the drop of H_v for the nucleated sample heat treated at 870°C for 30 min, may be linked to the onset of melting as shown by the DSC analyses in the section 5.1.1, Fig. 5. 2. Basically, 870°C marks the onset of an endothermic event linked to melting. In summary, heat treatments appear to enhance H_v up to 770° C , however later it will be shown that higher heat treatment temperatures are required to achieve the optimal optical properties.

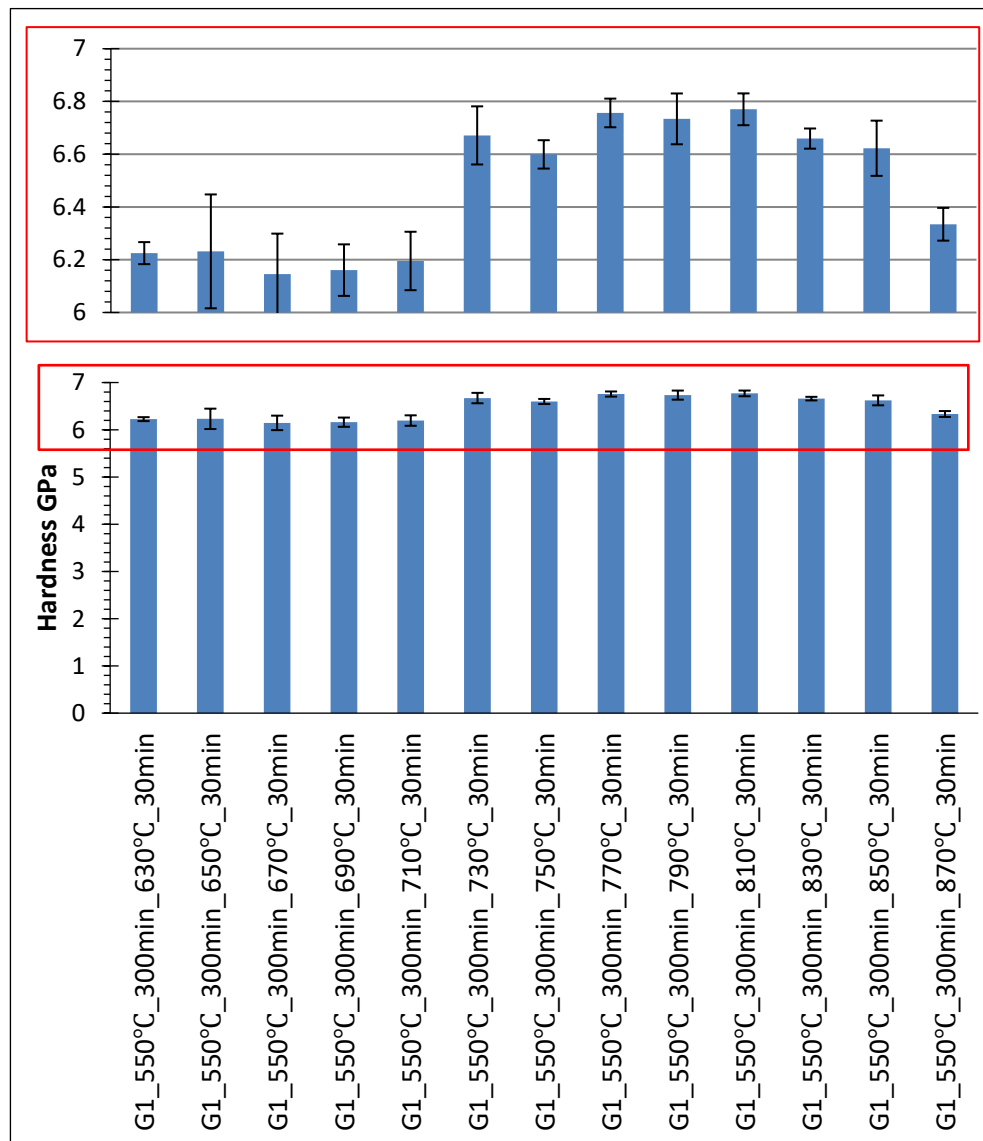


Fig. 5. 31 Hardness after nucleation at 550°C for 300 min followed by heat treatment for 30 min in the 630°C to 870°C temperature range.

5.6.3 Fracture Toughness

Fracture toughness, K_{IC} , was determined by the Vickers Indentation Fracture (VIF) method, using 6 indentations created by an applied load of $2\text{kg.f} = 19.61\text{N}$,

as detailed in the section 4.5.2. Several formulas exist to estimate K_{IC} , as presented in section 3.2.2.1. The so-called Anstis formula, $K_{IC} = 0.016 (E/HV)^{0.5} \cdot P/c^{1.5}$, which is often employed for dental materials, is used in this section, see Appendix 6. However, K_{IC} values calculated by other formulas can be found in Appendix 7.

5.6.3.1 Fracture toughness after isothermal heat treatments at 550°C for different holding times

Fig. 5. 32 shows the evolution of K_{IC} values for as-cast LAS1 glass as a function of isothermal heat treatment 550°C for different times. The values for nucleated samples appear to be more realistic, as they are within the range expected for a glass. When nucleation is extended to 3000 minutes, X-ray diffraction data in Fig. 5. 13 showed an increase in the Li_2SiO_3 and Li_3PO_4 contents. This appears to lead to a decrease in K_{IC} as shown in Fig. 5. 32. If a heterogeneous nucleation process, takes place with increased holding times, that means crystalline phases grow from outer boundaries such as the interfaces or grain borders [109]. This results in the weakened grain boundaries that impact on fracture toughness values.

Hence, with increase nucleation time further precipitation of crystalline Li_2SiO_3 and Li_3PO_4 occurs. New Li_3PO_4 nucleus form alongside Li_2SiO_3 crystals, and the latter also grows on Li_3PO_4 nuclei sites pre-formed [6]. Therefore, this process weakens grain boundaries, that in turn accelerates crack propagation in the samples [171] decreasing fracture toughness. This suggests that precipitation Li_2SiO_3 does not reinforce fracture toughness i.e. no hinder a crack propagation.

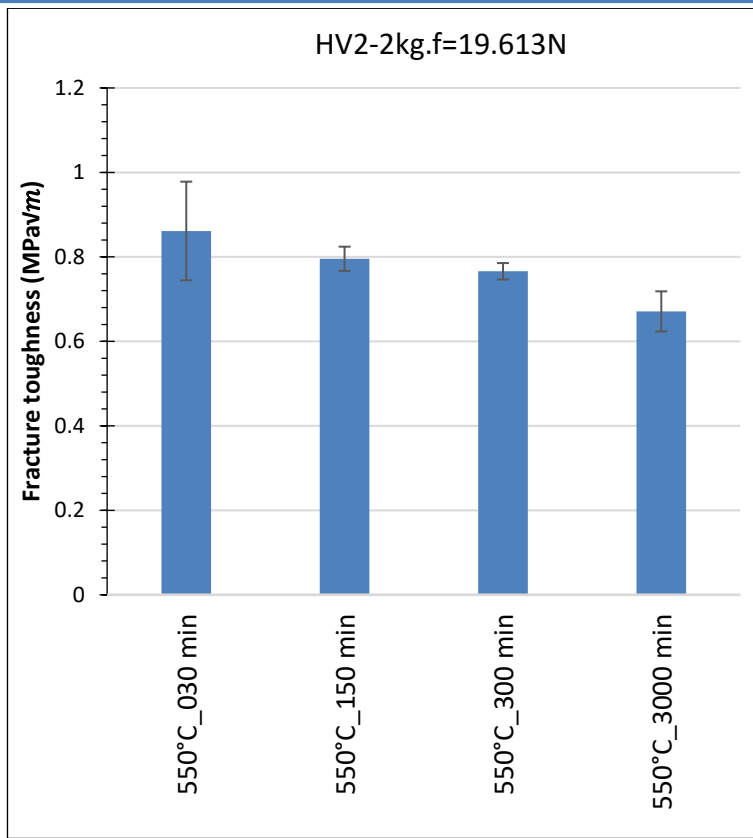


Fig. 5. 32 Fracture toughness after isothermal heat treatments at 550°C for different holding times.

5.6.3.2 Fracture toughness after heat treatment for 30 min in the 630°C to 870°C temperature range

The evolution of K_{IC} for LAS1 glass as a function of the heat treatment for 30 minutes in 630°C to 870°C temperature range is shown in Fig. 5. 33. Samples heat-treated between 630°C show a K_{IC} of 0.8 MPa \sqrt{m} , which is consistent with a rather amorphous material that contain small amounts of Li₂SiO₃ and Li₃PO₄, as shown by X-ray diffraction data in Fig. 5. 14. Samples heat treated at 650°C for 30 min, start to show minute amounts of Li_{0.25}Al_{0.25}Si_{0.75}O₂ and LiAlSi₄O₁₀ alongside Li₂SiO₃ and Li₃PO₄ embedded in a still amorphous matrix. This appears to lead to a small decrease in K_{IC} . In contrast, K_{IC} increases for samples heat treated at 670°C, which are considerably more crystalline, having Li_{0.25}Al_{0.25}Si_{0.75}O₂ and LiAlSi₄O₁₀ as the primary phases, and some residual Li₂SiO₃ and Li₃PO₄. The phase assemblage for samples heat treated at 690°C for 30 min is also similar, but K_{IC} decreases. Again, this temperature approaches the onset of a complex crystallisation process, which may impact on K_{IC} . A continuous increase of K_{IC} occurs with increasing heat treatment temperatures above 710°C reaching a maximum value of 1.78 MPa \sqrt{m} for the sample heat

treated at 870°C. This is consistent with the microstructural evolution shown in Fig. 5. 56 and 5. 58, in which provides evidence for the intensive “interlocking” of the LiAlSi₂O₆ crystals, that could retard crack propagation, then results in increase of the fracture toughness.

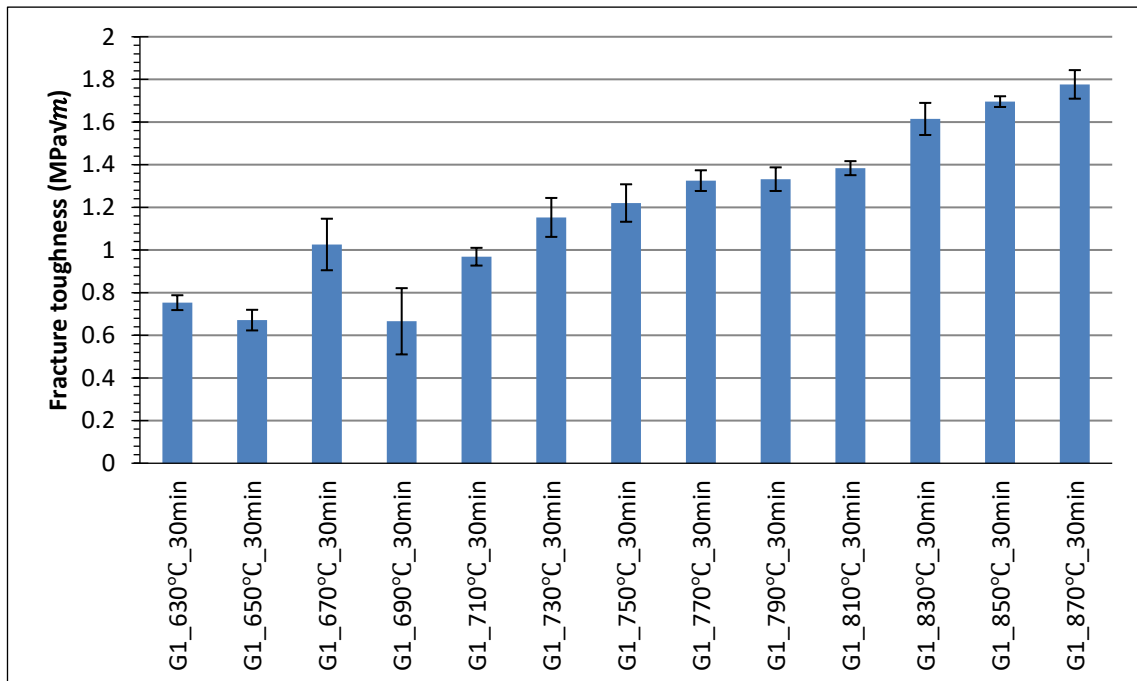


Fig. 5. 33 Fracture toughness after heat treatment for 30 min in the 630°C to 870°C temperature range.

5.6.3.3 Fracture toughness after nucleation at 550°C for 300 min followed by heat treatment for 30 min in the 630°C to 870°C temperature range

Fig. 5. 34 shows the evolution K_{IC} for LAS1 glass nucleated at 550 for 300min as a function of heat treatment for 30 min in the 630°C to 870°C temperature range. In general, K_{IC} shows a gradual increase from 0.66 MPa√m to 1.67 MPa√m between samples heat treated at 630°C and 870°C, respectively. In comparison with Fig. 5. 33, there is no apparent improvement K_{IC} by nucleating the samples.

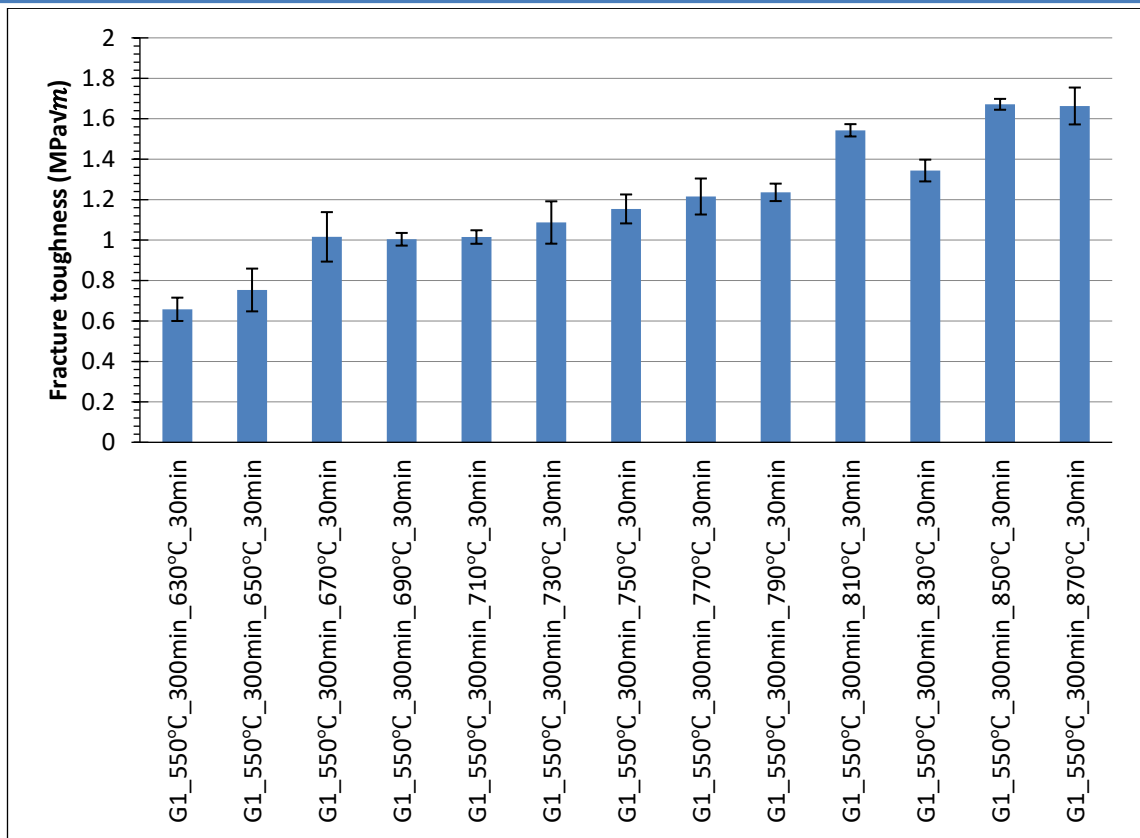


Fig. 5. 34 Fracture toughness after nucleation at 550°C for 300 min followed by heat treatment for 30 min in the 630°C to 870°C temperature range.

5.7 Optical properties of LAS1 glass

Colour can be quantified according to the Commission Internationale de l'Eclairage (CIE) system. Several dental materials studies [36], [51], [52], [77], [80], [276]–[278], use the CIE space system to estimate perceptible colour changes in terms of L, a and b coordinates, where L represents the lightness (in 100) /darkness (in 0) of colour; a is a measure of redness (+) or greenness (-), and b is a measure of yellowness (+) or blueness (-). In this study, three measurements of L*a*b* values are average to characterise the colour after heat treatment.

5.7.1 L*a*b* values after isothermal heat treatments at 550°C for different holding times

Fig. 5. 35 shows the CIELab values for LAS1 glass as a function of isothermal heat treatment at 550°C for 30, 150, 300 and 3000 min alongside photographs of the samples. The test was carried out against a black background. The L value, increases from 10.7 ± 0.4 for as-cast LAS1 glass to 29.43 ± 0.25 after heat treatment at 550°C for 3000 min. The b value, increases but levels off after 150

min. These changes are compatible with the X-ray diffraction and Raman data in the section 5.4.1 and 5.5.1, which show an increase Li_2SiO_3 and Li_3PO_4 contents during nucleation.

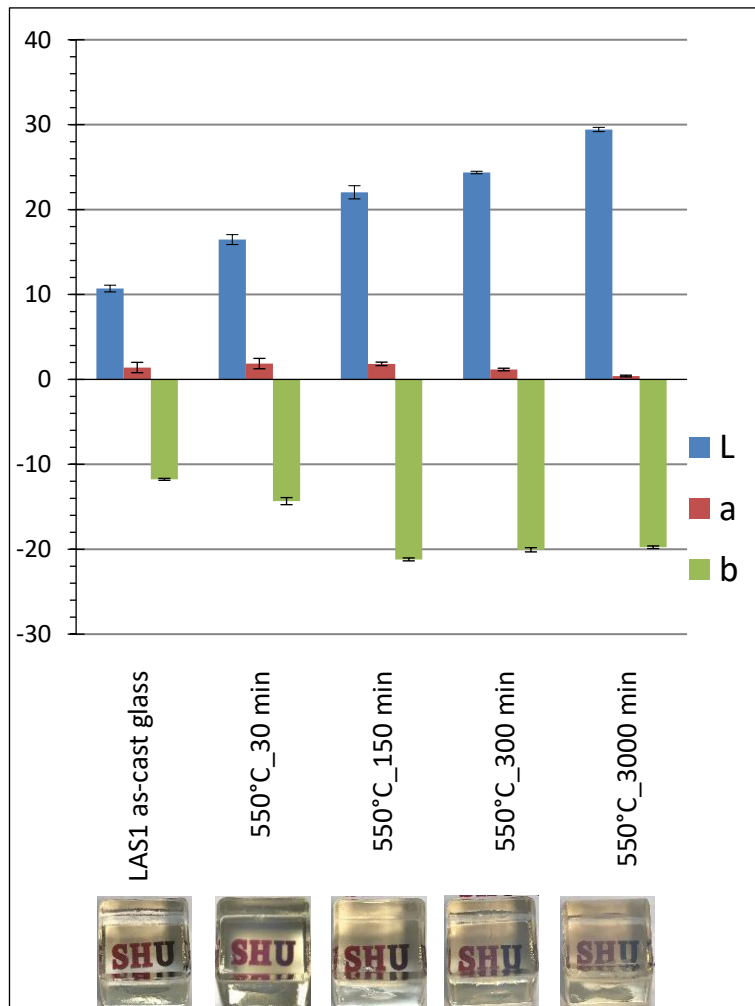


Fig. 5. 35 $L^*a^*b^*$ values after isothermal heat treatments at 550°C for different holding times.

5.7.2 Colour evolution upon heat treatment for 30 min in the 630°C to 870°C temperature range

5.7.2.1 $L^*a^*b^*$ values

The evolution of $L^*a^*b^*$ values for LAS1 glass as a function of the heat treatment for 30 minutes in 630°C to 870°C temperature range is shown in Fig. 5. 36 alongside each of sample, which was tested against a black background.

In general, L^* increases continuously from 36.87 ± 0.67 to 81.7 ± 0.1 for samples heated treated for 30 min at 630°C and 810°C, respectively. Nevertheless, there is a sudden increase in L^* between 710°C and 730°C, as indicated by the dashed circle. This increase coincides with the crystallisation of $\text{Li}_2\text{Si}_2\text{O}_5$ and $\text{LiAlSi}_2\text{O}_6$,

according to XRD data, shown in Fig. 5. 12. L^* continues to increase more gradually with increasing temperatures as shown in Fig. 5. 36.

Interestingly a^* and b^* values are almost constant for samples heat treated up to 690°C. Again, for samples heat treated around 710°C, there are some variations in a^* and b^* values, as indicated by the dashed blue square in Fig. 5. 36. Basically, whenever a^* and b^* approach 0, this indicates that colour of the sample is closer white. Hence, this feature indicates that the glass block colour is becoming white. This coincides with the $\text{Li}_2\text{Si}_2\text{O}_5$ and $\text{LiAlSi}_2\text{O}_6$ precipitation. These CIE Lab values are supported by the digital photographs of the samples against a black background, as shown in Fig. 5. 36.

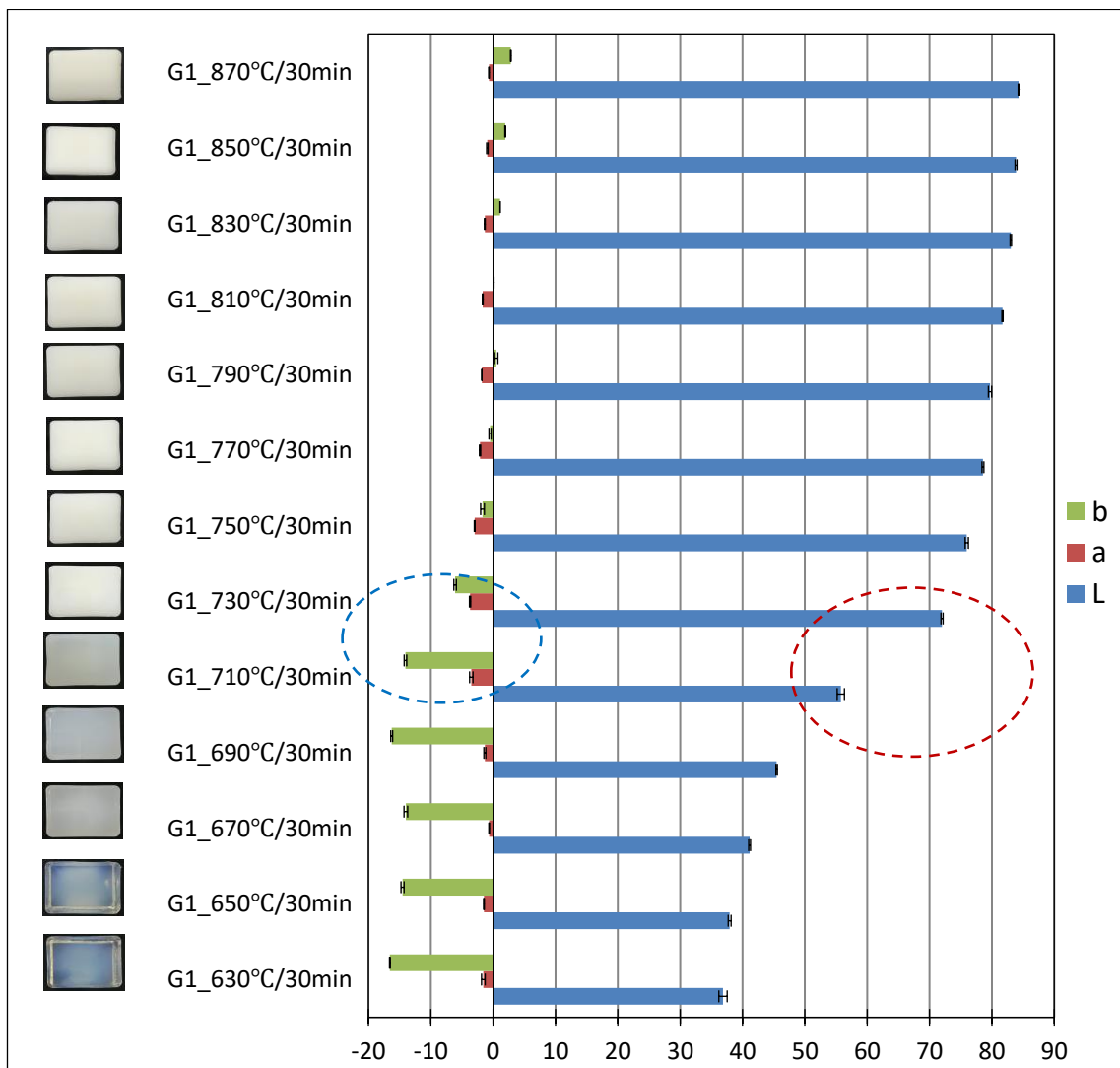


Fig. 5. 36 $L^*a^*b^*$ values evolution upon heat treatment for 30 min in the 630°C to 870°C temperature range and digital micrographs of the specimens against a black background.

5.7.2.2 Colour matching with the VITA Classical shade guide standard

Colour matching can be directly evaluated via a ΔE measurement, between heat treated samples and the VITA Classical shade guide used in dental clinics ($L^*a^*b^*$ listed in Table 4. 6) using the RM200QC colorimeter. This statistical analysis is useful to measure the matching range of samples in this study with those in the VITA Classical shade guide. Low values of ΔE suggest a good colour matching with the standard shade. ΔE of ~ 41.3 is largest for samples heat treated at 630°C for 30 min, shown a big disparity to the A3 shade in the VITA guide. With increasing heat treatment temperature, ΔE decreases from 39 to 16.5 for samples heated treated for 30 min at 630°C and 750°C , respectively, but colour of samples becomes closer to the A1 shade. Although the ΔE value has decreased during heat treatment, the sample is still no identical to standard shade, because L^* and b^* are quite far, leading to large ΔE values, as shown in Fig. 5. 37.

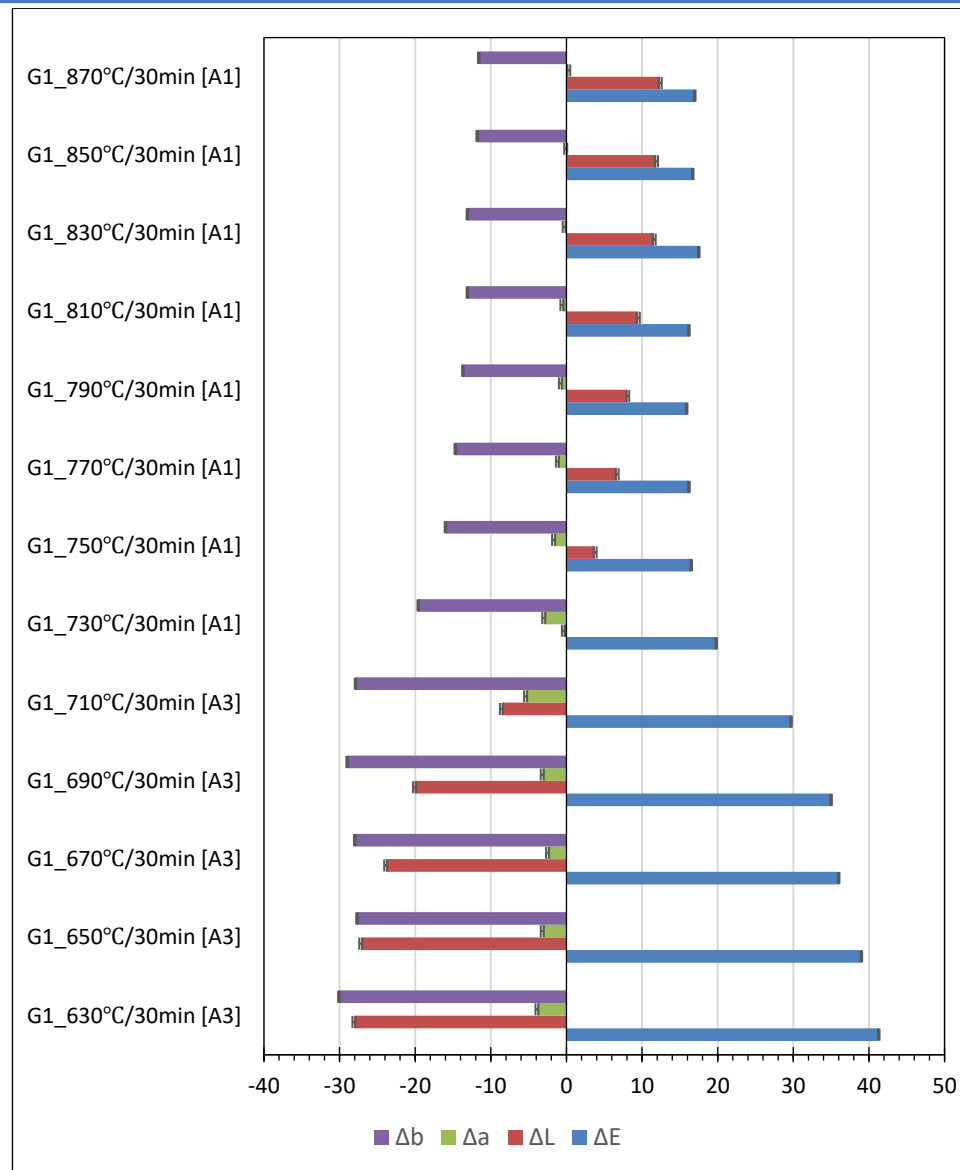


Fig. 5. 37 The colour differences (ΔL^* , Δa^* , Δb^* and ΔE values) between LAS1 glass heat treated for 30 min in the 630°C to 870°C temperature range and selected VITA shade standards.

5.7.3 Colour evolution after nucleation at 550°C for 300 minutes followed by heat treatment for 30 minutes in the 630°C to 870°C temperature range

5.7.3.1 $L^*a^*b^*$ values

The $L^*a^*b^*$ values in Fig. 5. 38 exhibit a similar trend to their non-nucleated counter parts in Fig. 5. 36, however it is useful to also evaluate colour matching with the VITA Classical shade guide, as done in the next section.

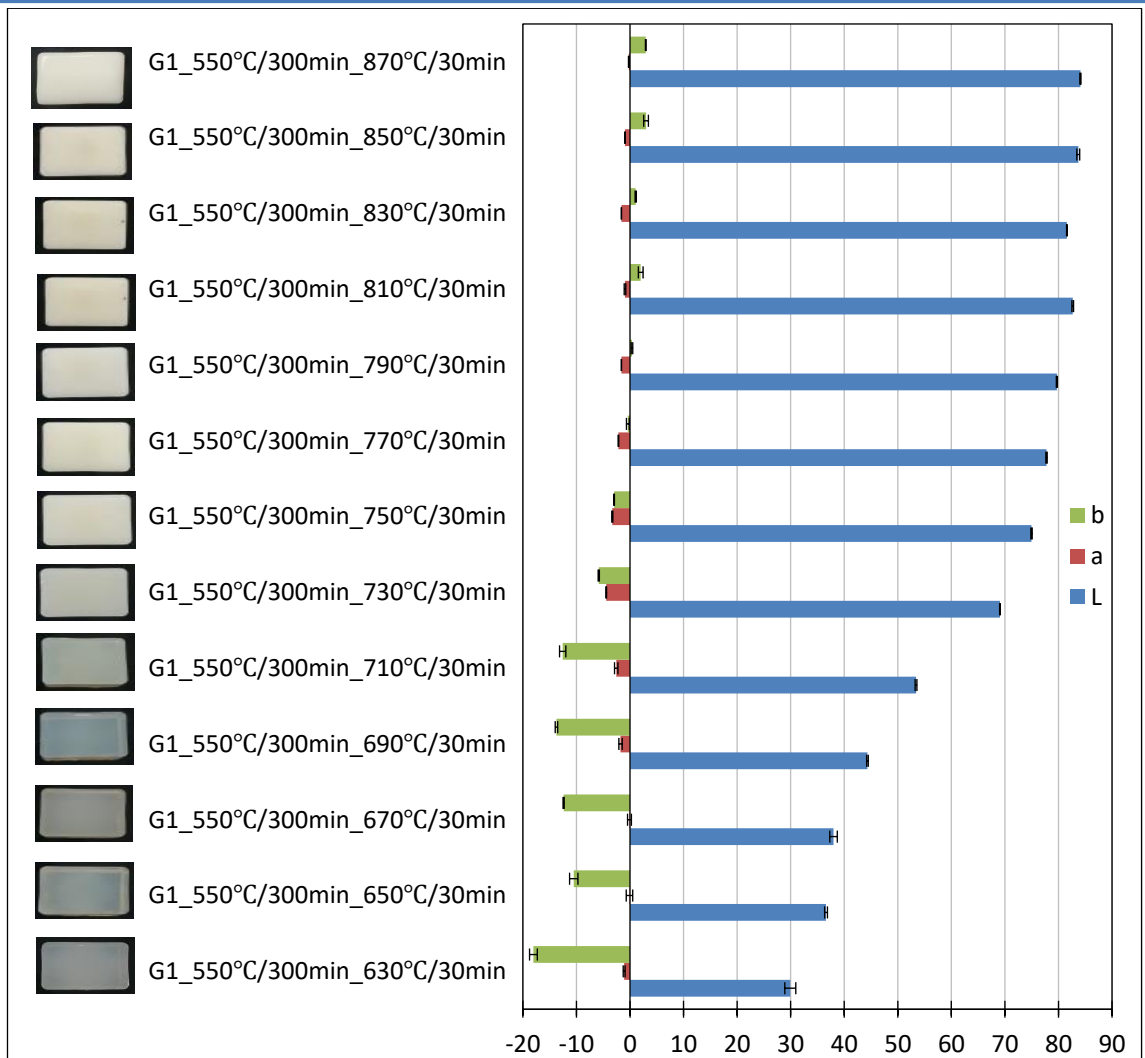


Fig. 5. 38 L*a*b* values evolution for samples nucleated at 550°C for 300 minutes followed by heat treatment for 30 min in the 630°C to 870°C temperature range and digital micrographs of the specimens against a black background.

5.7.3.2 Colour matching with the VITA Classical shade guide standard

Data in Fig. 5. 39 shows similar trends as non-nucleated samples, Fig. 5. 38. Based on the colour data, in Fig. 5. 36- 39, heat treatments LAS1 glass, yield a white material, which may be useful to dental applications, but does not match any shade from the VITA classical guide. This may be due to the absence of colouring agents.

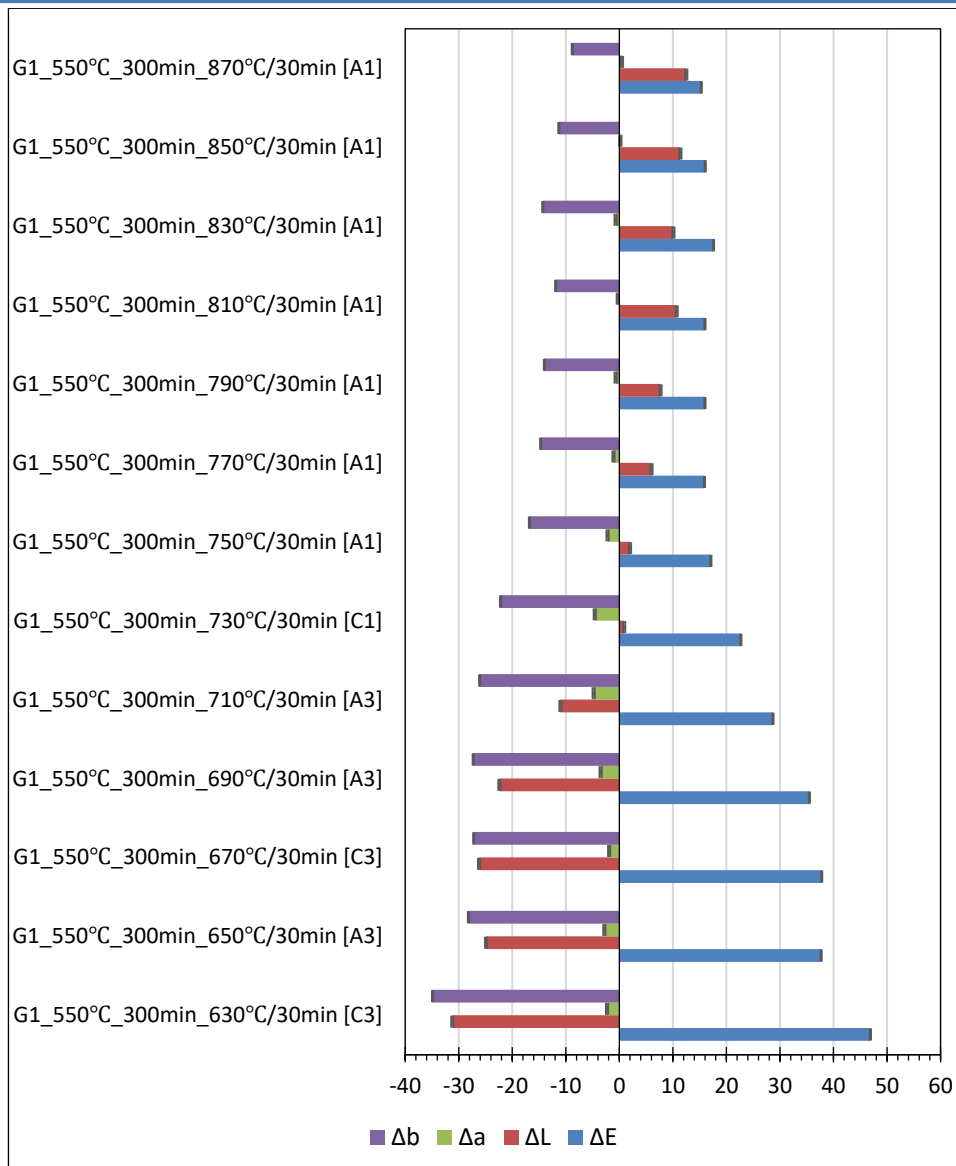


Fig. 5. 39 The colour differences (ΔL^* , Δa^* , Δb^* and ΔE values) between LAS1 glass nucleated at 550°C for 300 min followed by heat treatment for 30 min in the 630°C to 870°C temperature range and selected VITA shade standards.

5.8 Phase assemblage, mechanical and optical properties of LAS1 glass following a two-step crystallisation process

This section presents the results for phase assemblage, mechanical and optical properties of LAS1 glass samples subjected to the heat treatment profiles recorded in Table 4. 5. Those were chosen based on the DSC and XRD analyses presented in the previous sections.

5.8.1 Phase assemblage

The *in-Situ* XRD data in Fig. 5. 12 show LiAlSi₄O₁₀ to be a transient phase between 590-690°C and LiAlSi₂O₆ to appear between 690°C-700°C. Actually, in

section 5.4.4, it was shown the occurrence of a complex crystallisation process around 670°C. It was also shown that above 730°C phase assemblage remains virtually unchanged. Hence, hereafter results are presented for several sets of samples heat treated as follows:

- nucleation at 550°C for 300 min, followed by a crystallisation step at 670°C and a second crystallisation step at 750°C or 780°C (these are near exothermic reactions), or at 870°C (above all exothermic reactions).
- nucleation at 550°C for 300 min followed by crystallisation at 780°C for 30, 60, 90 and 120 minutes.
- nucleation at 550°C for 300 min, followed by a crystallisation step at 780°C and a second crystallisation step at 830°C, 850°C or 870°C, for different holding times. This was also aimed to investigate the impact on the optical properties.

A small number of other variations were attempted, as indicated by the labels in the relevant figures.

5.8.1.1 Phase assemblage for samples nucleated at 550°C for 300 min, followed by a crystallisation step at 670°C and a second crystallisation step at 750°C or 780°C

Selected XRD patterns representative of heat treatment profiles that include nucleation at 550°C for 300 min, followed by a crystallisation step at 670°C and a second crystallisation step at 750°C or 780°C are presented in Fig. 5. 40. For comparison, data for a non-nucleated sample heat treated at 670°C for 90 min, a sample nucleated at 550°C for 300 min followed by heat-treatment at 670°C for 30 min and a sample nucleated at 550°C for 300 min followed by heat-treatment at 670°C for 90 min is also given.

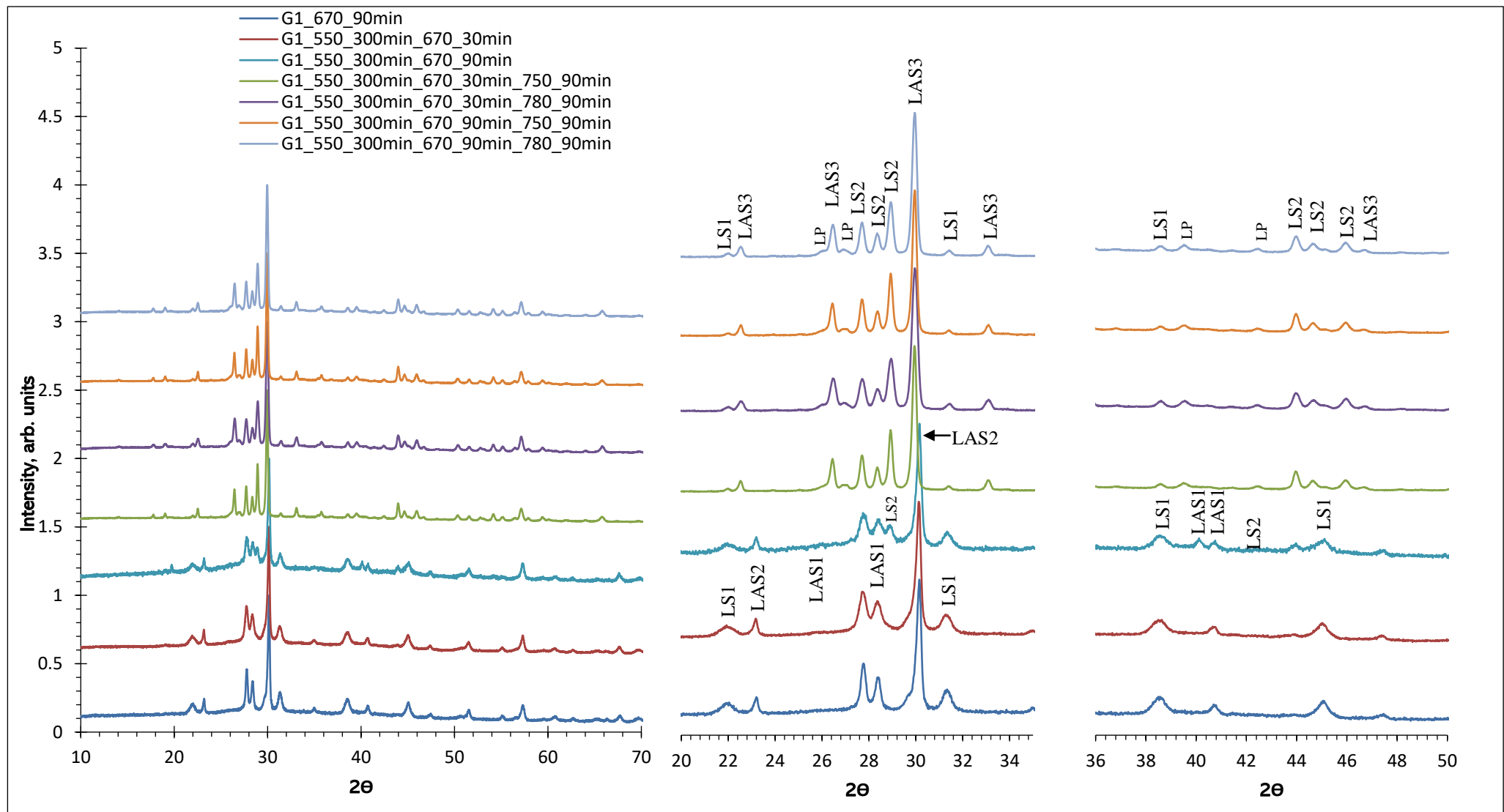


Fig. 5. 40 X-ray diffraction data for samples nucleated at 550°C for 300 min, followed by a crystallisation step at 670°C and a second crystallisation step at 750°C or 780°C.

The phase assemblage is essentially identical for those two samples. The two major phases are $\text{LiAlSi}_4\text{O}_{10}$ and $\text{Li}_{0.25}\text{Al}_{0.25}\text{Si}_{0.75}\text{O}_2$, alongside residual Li_2SiO_3 . This is commensurate with the result in section 5.4.4. Nevertheless, $\text{Li}_2\text{Si}_2\text{O}_5$ appears when the nucleated sample is heat treated at 670°C for 90 min. The crystallisation of $\text{Li}_2\text{Si}_2\text{O}_5$ in the as-cast glass was linked to the second exothermic event detected at 710°C in the DSC data, Fig. 5. 1, for a continuous heating at a 5 °C/min. Now, it is shown that longer holding times can lead to earlier crystallisation of $\text{Li}_2\text{Si}_2\text{O}_5$, when comparing with data in Fig. 5. 14 showing that in a sample nucleated 550°C for 300 min, this phase appears after 30 min at 690°C. Again, these results show that crystallisation in this temperature range is a rather complex process, showing strong time and temperature dependencies.

On the other hand, XRD patterns for heat treatment at 750 and 780 °C show Bragg peaks consistent with $\text{LiAlSi}_2\text{O}_6$ (primary phase), $\text{Li}_2\text{Si}_2\text{O}_5$, Li_2SiO_3 and Li_3PO_4 . Their identification has been determined by the XRD analysis in the sections 5.4.2 and 5.4.3.

5.8.1.2 Phase assemblage for samples with a top crystallisation temperature of 830°C, 850 °C or 870°C

XRD analyses in Fig. 5. 41, which includes data for non-nucleated and nucleated samples, with top crystallisation temperature of 830°C, 850°C or 870°C, but also with or without an intermediate crystallisation at 780°C (in one case also at 670°C) show similar phase assemblage in terms of the nature and volume fraction. $\text{LiAlSi}_2\text{O}_6$ is the dominant crystalline phase followed by $\text{Li}_2\text{Si}_2\text{O}_5$. Some residual Li_3PO_4 and Li_2SiO_3 crystalline phases are also present.

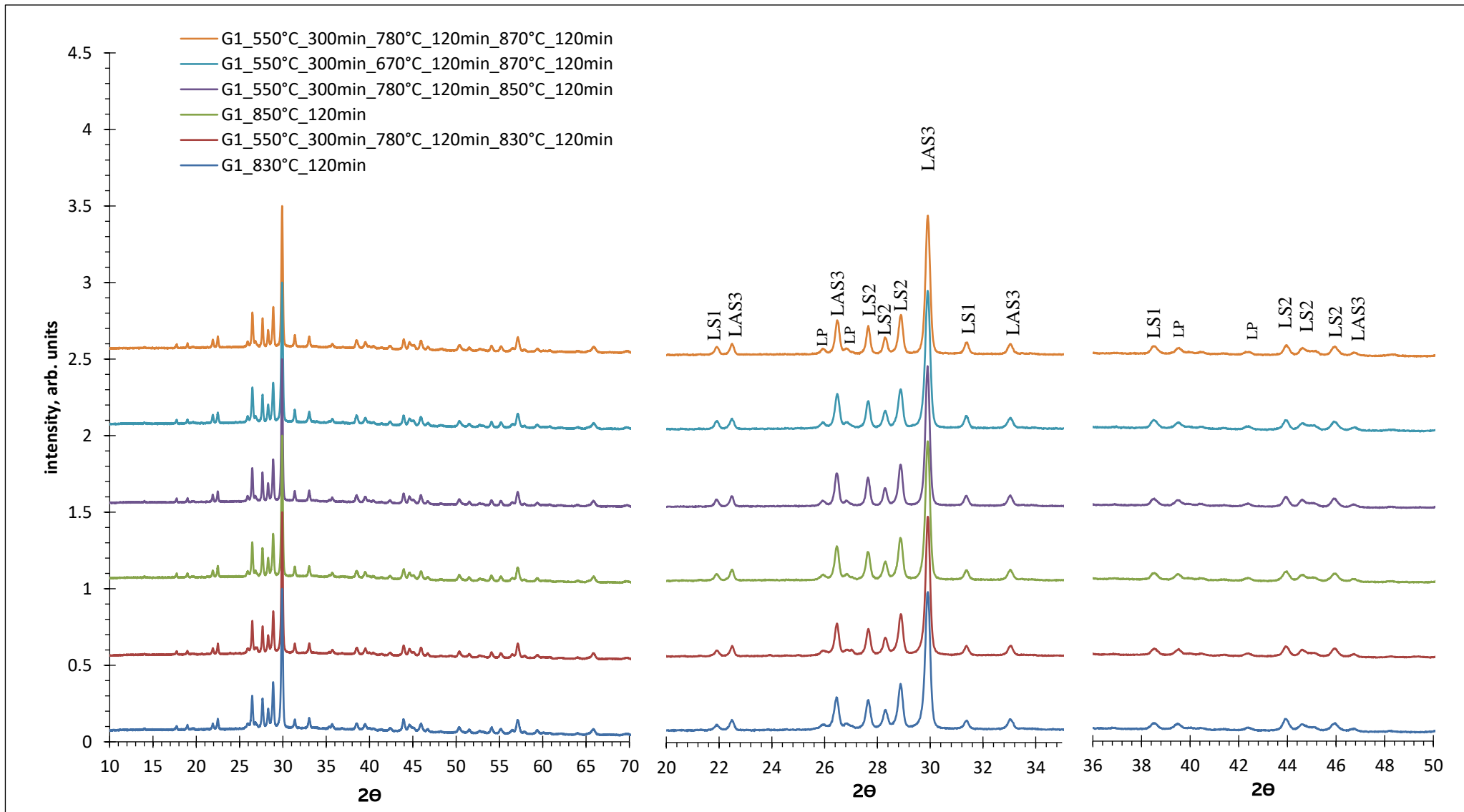


Fig. 5. 41 XRD patterns for selected heated treated samples at high temperature between 830-870 °C.

5.8.1.3 Evolution of the crystallite size for LiAlSi₂O₆

Fig. 5. 41 shows LiAlSi₂O₆ to be the dominant phase in all samples heat treated in 830-870 °C temperature range. The evolution of FWHM in terms of heat treatment for the LiAlSi₂O₆ Bragg peak located at 29.0°-29.2° 2θ is illustrated Fig. 5. 42. It becomes apparent that the length of the first crystallisation step at 670°C has a clear impact on the FWHM values, for samples where the maximum temperature of the second crystallisation is limited to 780°C. In contrast, FWHM remains constant for samples, which second crystallisation takes place at 830°C and 850°C, independently of the duration. These FWHM values can be incorporated in the Scherrer equation to calculate the median crystallite sizes, and the results are shown in Fig. 5. 43. The median crystallite size for LiAlSi₂O₆ ranges from 67 nm to ~90 nm, depending on heat treatment schedules, as shown in Fig. 5. 43. For samples that maximum heat treatment temperature is between 830°C and 850°C the median crystallite size is ~ 90 nm. This is consistent with the images shown in Fig. 5. 55 -58. The duration of the heat treatment at high temperature does not affect the size of LiAlSi₂O₆ crystals.

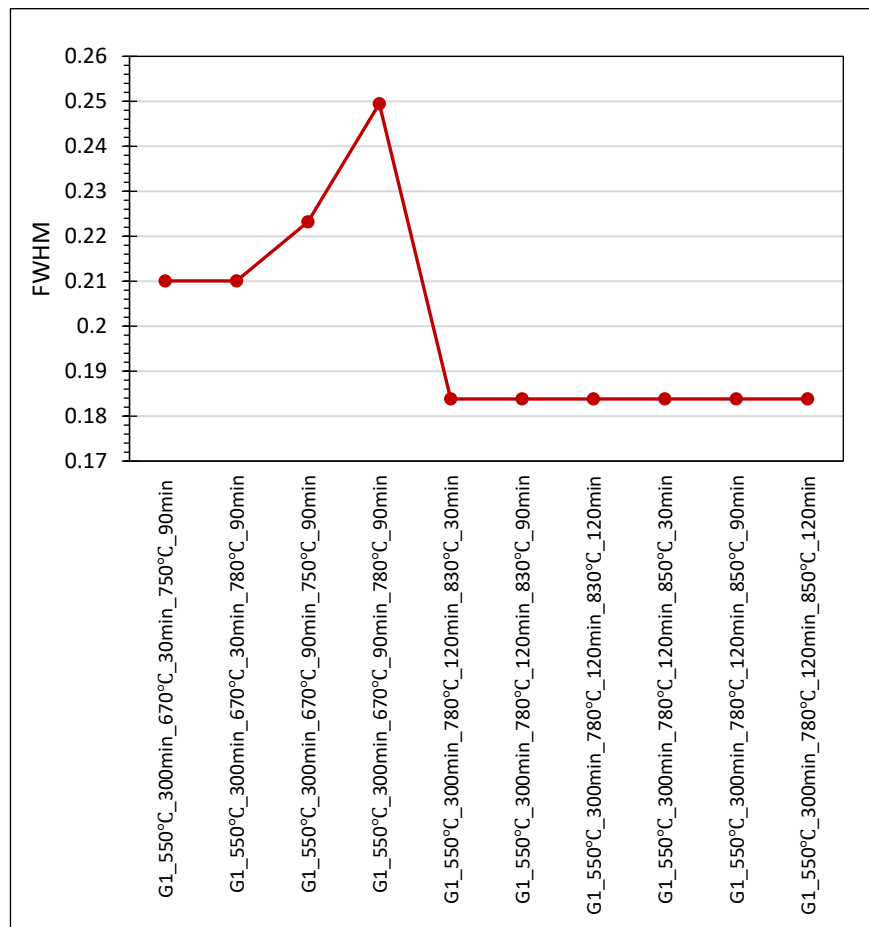


Fig. 5. 42 FWHM of strongest XRD peak in LiAlSi₂O₆ for selected heat-treatment profiles.

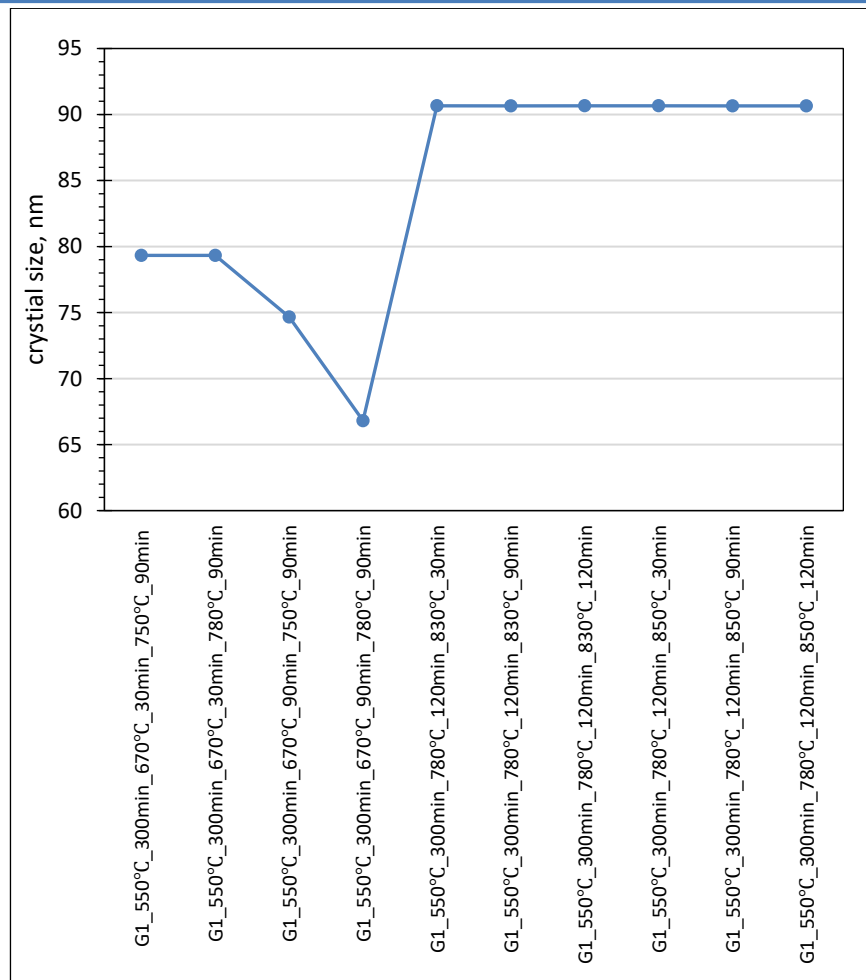
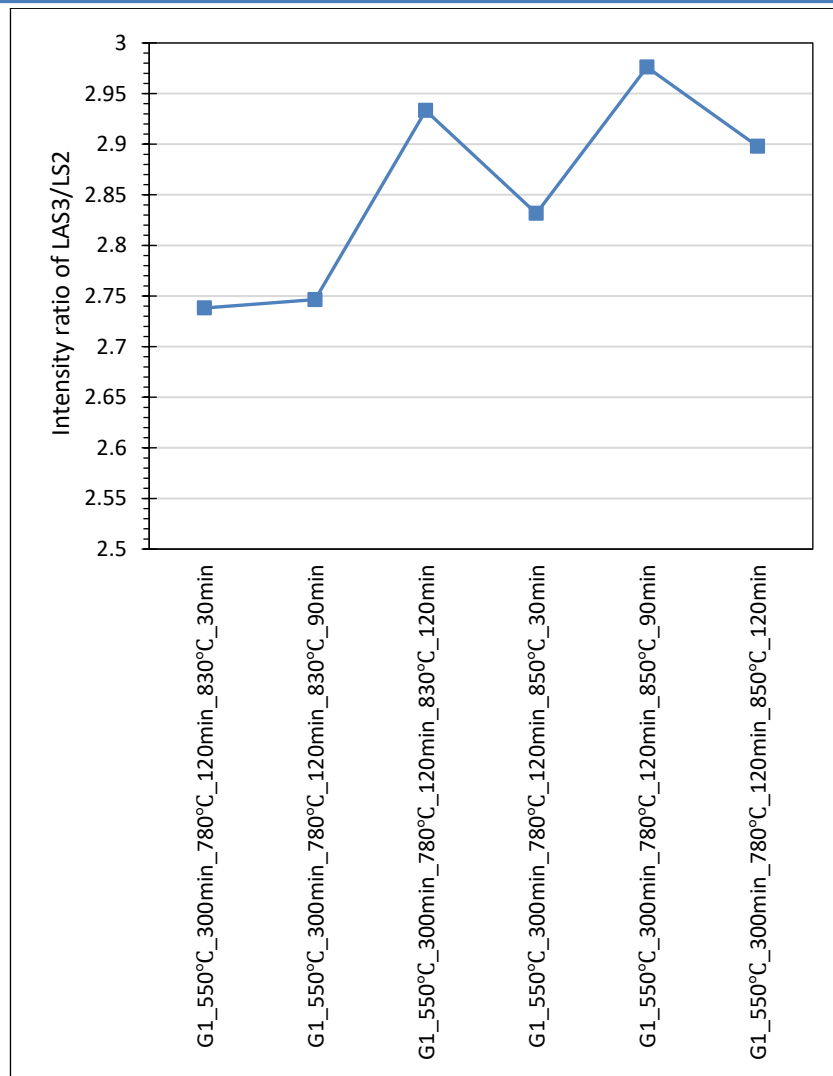


Fig. 5. 43 Median crystallite size of $\text{LiAlSi}_2\text{O}_6$ for selected heat-treatment profiles.

5.8.1.4 XRD peak intensity ratio for $\text{LiAlSi}_2\text{O}_6/\text{Li}_2\text{Si}_2\text{O}_5$

The relative amount of $\text{LiAlSi}_2\text{O}_6$ and $\text{Li}_2\text{Si}_2\text{O}_5$ can be estimated by the intensity ratios of the main Bragg peaks associated with each phase, which for $\text{LiAlSi}_2\text{O}_6$ is located at $28.5^\circ\text{-}30^\circ 2\Theta$ and for $\text{Li}_2\text{Si}_2\text{O}_5$ is located at $27.5^\circ\text{-}29.5^\circ 2\Theta$, as shown in Fig. 5. 41.

In general, the ratios shown in Fig. 5. 44 suggest that the $\text{LiAlSi}_2\text{O}_6$ becomes even more dominant when heat treatment increases from $830\text{ }^\circ\text{C}$ to $850\text{ }^\circ\text{C}$. An increase of the duration of heat treatment from 90 min to 120 min at $830\text{ }^\circ\text{C}$ leads to an apparent increase of the $\text{LiAlSi}_2\text{O}_6$ content, respectively. Whereas at $850\text{ }^\circ\text{C}$ this increase is observed between 30 min and 90 minutes. Interestingly, the flexural strength findings in Fig. 5. 49, show samples heat treated at $830\text{ }^\circ\text{C}$ or $850\text{ }^\circ\text{C}$ for only 30 minutes to exhibit the lowest flexural strength. In other words, longer holding time lead to larger to a larger relative amount of $\text{LiAlSi}_2\text{O}_6$ and thereby to larger strength.

Fig. 5. 44 XRD peak intensity ratio for LiAlSi₂O₆/Li₂Si₂O₅.

5.8.1.5 Volume fraction of amorphous content

An analysis of the volumetric phase amorphous content in nucleated glass and selected heated treated glasses is given in Fig. 5. 45. The analysis shows that the sample nucleated at 550°C for 300 min has a crystalline content of ~ 15 vol%. When the glass is heat treated at 780°C for 120 min, the crystalline content is greater than 70 vol%. This is proportionate with the major thermal events, Fig. 5. 1, detected below this temperature. A maximum crystalline content of ~ 80 vol% is detected for samples heat treated at 870°C.

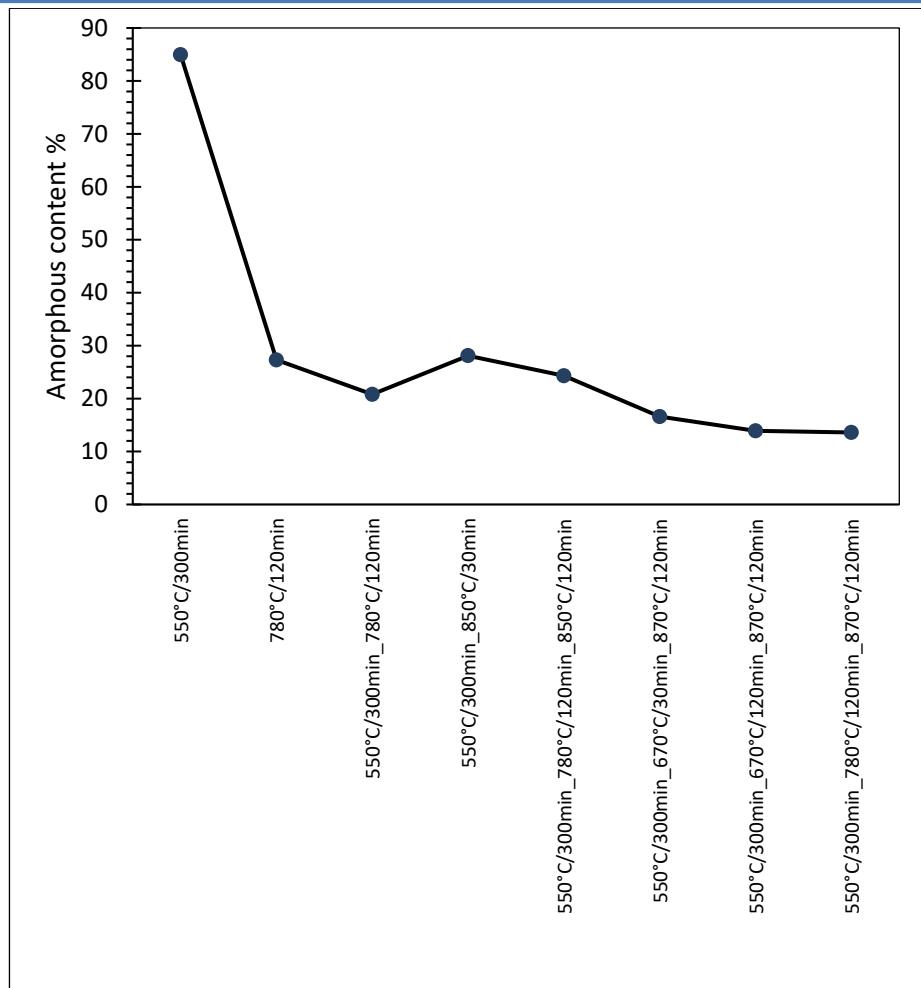


Fig. 5. 45 Volume fraction of amorphous content for nucleated glass and selected heat-treatments.

5.8.2 Mechanical properties

The presentation of the mechanical properties has been divided into eight groups, depending on temperature and time, and is organized by intervals, from the lowest to the highest temperature, as shown in Fig. 5. 46, 47 and 48. They will graphically summarize the measured statistics and results for elastic modulus, hardness and fracture toughness, respectively. Remarkable differences were found between groups per mechanical property.

5.8.2.1 Elastic modulus

The largest $E \sim 99.1 \pm 0.53$ GPa is observed for samples nucleated at 550°C for 300 min and subsequently heat treated at 780°C for 120 min and finally at 850°C for 120 min (in the group g), whereas the lowest $E \sim 84.23 \pm 0.21$ GPa is observed for samples nucleated for 550°C for 3000 min and then heat treated for 120 min at 780°C (in the group d), as shown in Fig. 5. 46. Group a shows that nucleation

may reduce E. In contrast, from group **b**, it can be inferred E is hardly increased when the maximum heat treatment varies 750 and 780 °C for different durations, but it is greater than in group **a**. This can be ascribed to the presence of an intermediate step at 670°C for 30 min. Increasing this length to 90 min leads to a slight increase in E, as shown by group **c**. Group **d** shows that the duration of the heat treatment at 780°C has limited impact on E, providing that the nucleation duration remains constant. Group **e** shows that increasing the heat treatment from 800 to 830 °C increases E, but also increasing the duration at 800°C also increases E. Group **f** shows that including a intermediate step at 780°C leads to often to a decrease in E, when compared with group **e**. Groups **g** and **h** suggest that high heat treatment temperatures lead to a slight decrease in E, with the exception of samples nucleated at 550°C for 300 min and subsequently heat treated at 780°C for 120 min and finally at 850°C for 120 min.

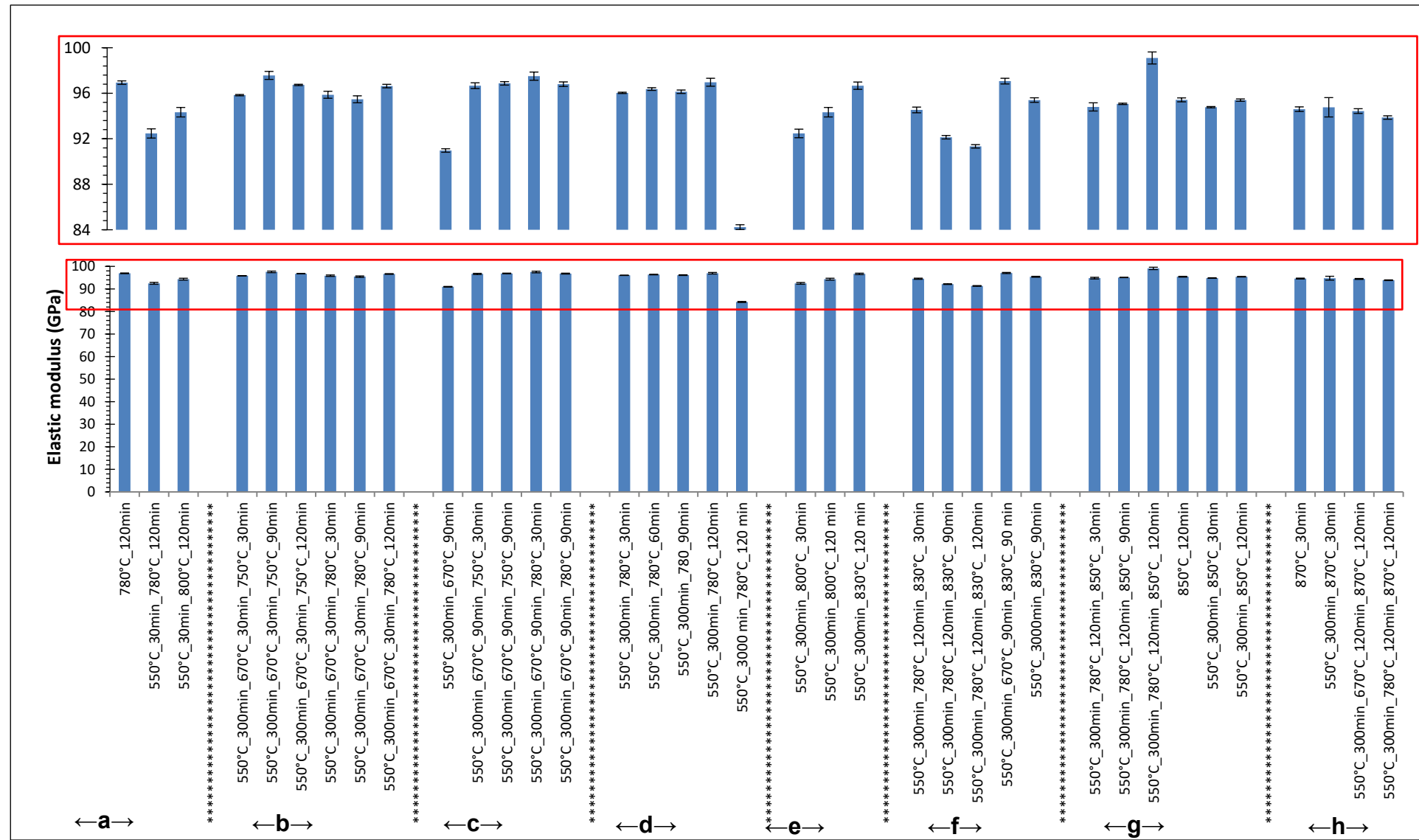


Fig. 5.46 Elastic modulus for selected heat treatment profiles.

5.8.2.2 Hardness

The evaluation of hardness, Hv, for LAS1 glass as a function of the thermal heat treatment is shown in Fig. 5. 47. This representation reveals relationship between micro-indentation hardness and different one-stage (nucleation) and two-stages (crystallization) heating schedules.

In term of Hv values the samples can be divided into two sets. The first set is for samples heated treated between 750°C - 780°C, involves groups **a**, **b**, **c** and **d** which show an average Hv greater than 6.8 GPa. The second set is for samples heated treated between 830°C – 870°C, involves groups **f**, **g** and **h** which show an average Hv greater than 6.8 GPa.

Interestingly, treatments above 830°C (groups f, g and h) are accompanied by a decrease in Hv, which reaches its lowest value for samples heat treated 870°C group (group h). In the other words, the increasing heat treatment temperatures results in decreasing hardness values. A similar high temperature trend was observed for non- nucleated and nucleated samples as shown in the section 5.6.2.2 and 3.

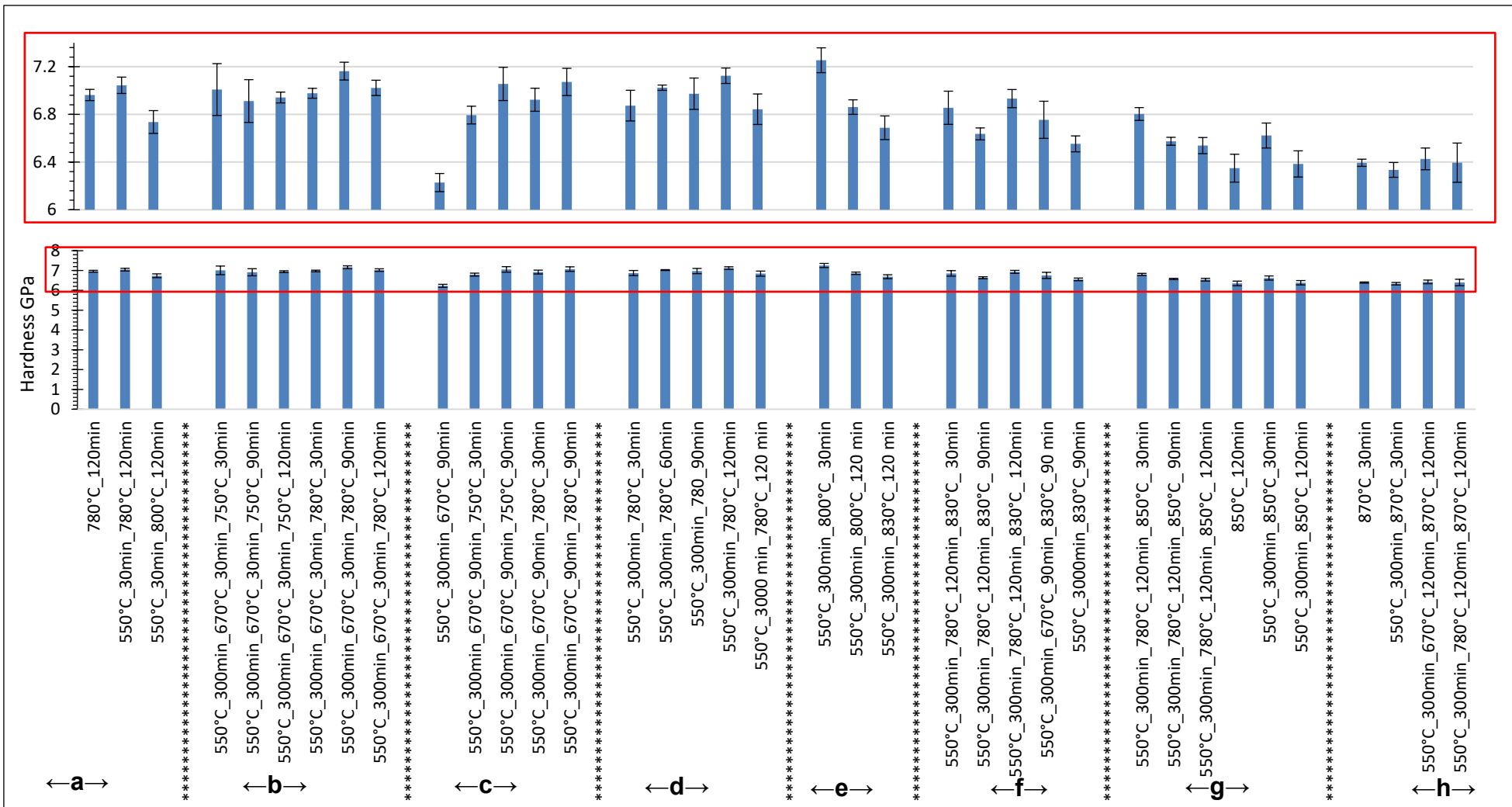


Fig. 5. 47 Micro-indentation hardness for selected heat treatment profiles

5.8.2.3 Fracture toughness

Unlike the micro-hardness findings, the fracture toughness for the heated treated glasses reveals a relatively upward trend that is proportional to the elevation of the heat treatment temperatures, in particular from that profiles including an intermediate stage at 670 or 780 °C.

The largest higher fracture toughness $\sim 1.84 \pm 0.09 \text{ MPam}^{1/2}$ was observed for samples nucleated at 550°C for 300 min, subsequently heat treated at 780°C for 120 min, and finally at 850°C for 120 min, (in group g), whereas the lowest value of $0.83 \pm 0.088 \text{ MPam}^{1/2}$ was observed for samples nucleated at 550°C for 300 min and then at 670°C for 90 min. Based on XRD analysis, at this temperature (670°C), LiAlSi₂O₆ has not yet crystallised. The value of fracture toughness appears to plateau at $\sim 1.8 \text{ MPam}^{1/2}$ for heat treatments in the 830°C to 850°C temperature range, as shown in Fig. 5. 48, and then to decrease for samples heat treated at 870°C.

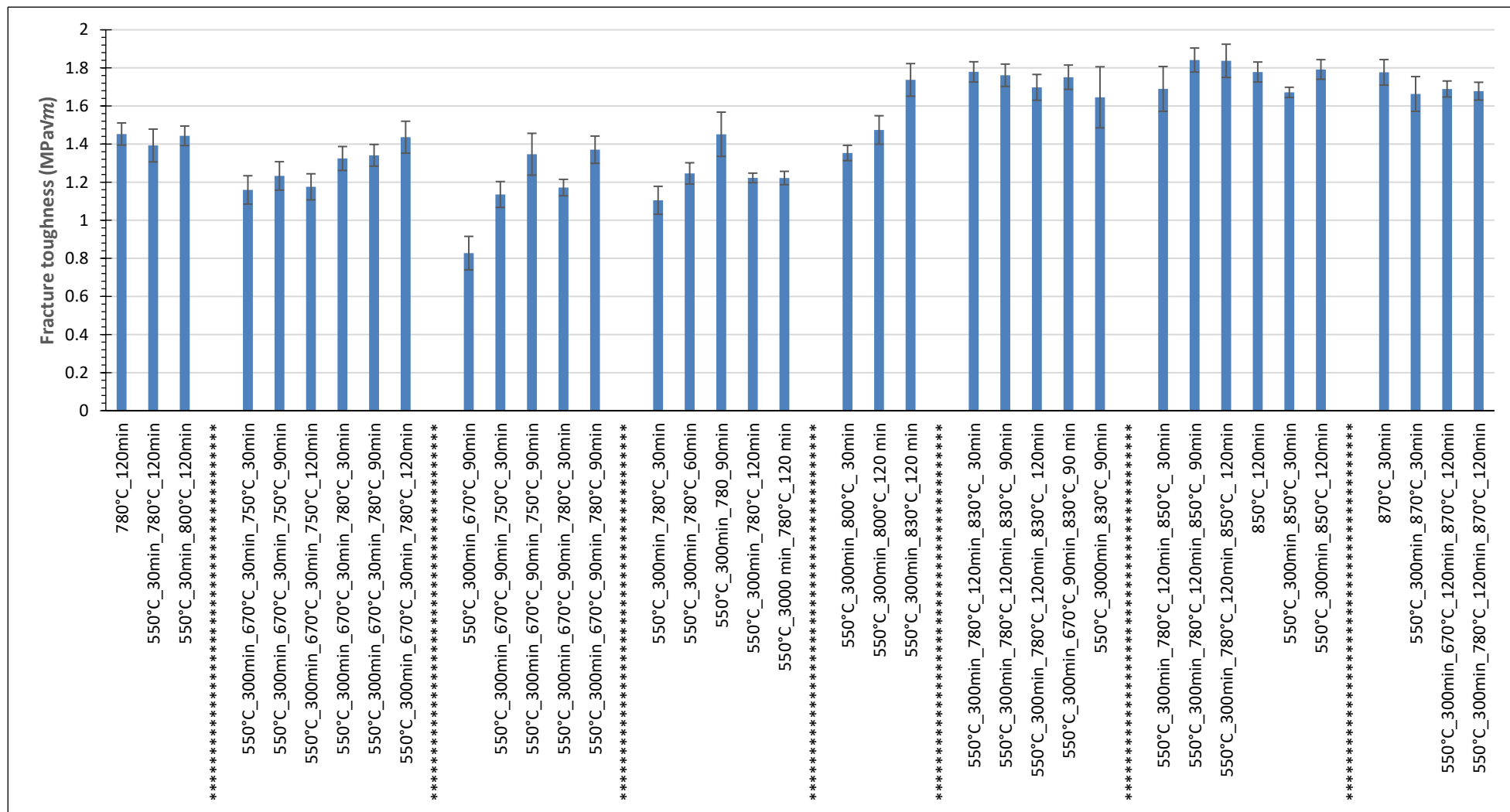


Fig. 5. 48 Fracture toughness for selected heat treatment profiles.

5.8.2.4 Flexural strength

The flexural strength for heat-treated samples was determined from ten specimens according to ISO 6872 standard, as illustrated in Fig. 5. 49. In this study all samples were nucleated at 550°C for 300 min, and the minimum average flexural strength of ~225 MPa was detected for samples encompassing an intermediate heat treatment at 670°C for 90 min followed by heat treatment at 780°C for 90 min. Those samples also exhibit a large variation in strength. It becomes notorious that the intermediate heat treatment at 670°C has a deleterious effect on the flexural strength. Two other observations are: (1) increasing the top heat treatment temperature from 780°C to 830°C leads to an enhancement of the flexural strength and (2) increasing the duration of the heat treatment from 30 to 90 min in samples heat treated at 830°C and 850°C also results in larger flexural strength values.

The highest average flexural strength of~ 377.23 ± 25.71 MPa was observed for samples heat treated at 780°C for 120 min followed by heat treatment at 830°C for 120 min. Nevertheless, the largest observed flexural strength of ~ 448 MPa is observed for heat treatment at 850°C for 90 min. Interestingly, this agrees with the increase on the relative of intensity of LiAlSi₂O₆ to Li₂Si₂O₅, as shown in Fig. 5. 44.

In summary, intermediate crystallization temperatures (670 and 780 °C) and maximum heat treatment temperatures (750, 780, 800, 830 and 850 °C) play an important role in the flexural strength, as shown in Fig. 5. 49. Some of the flexural strength values can be found in Appendix 8.

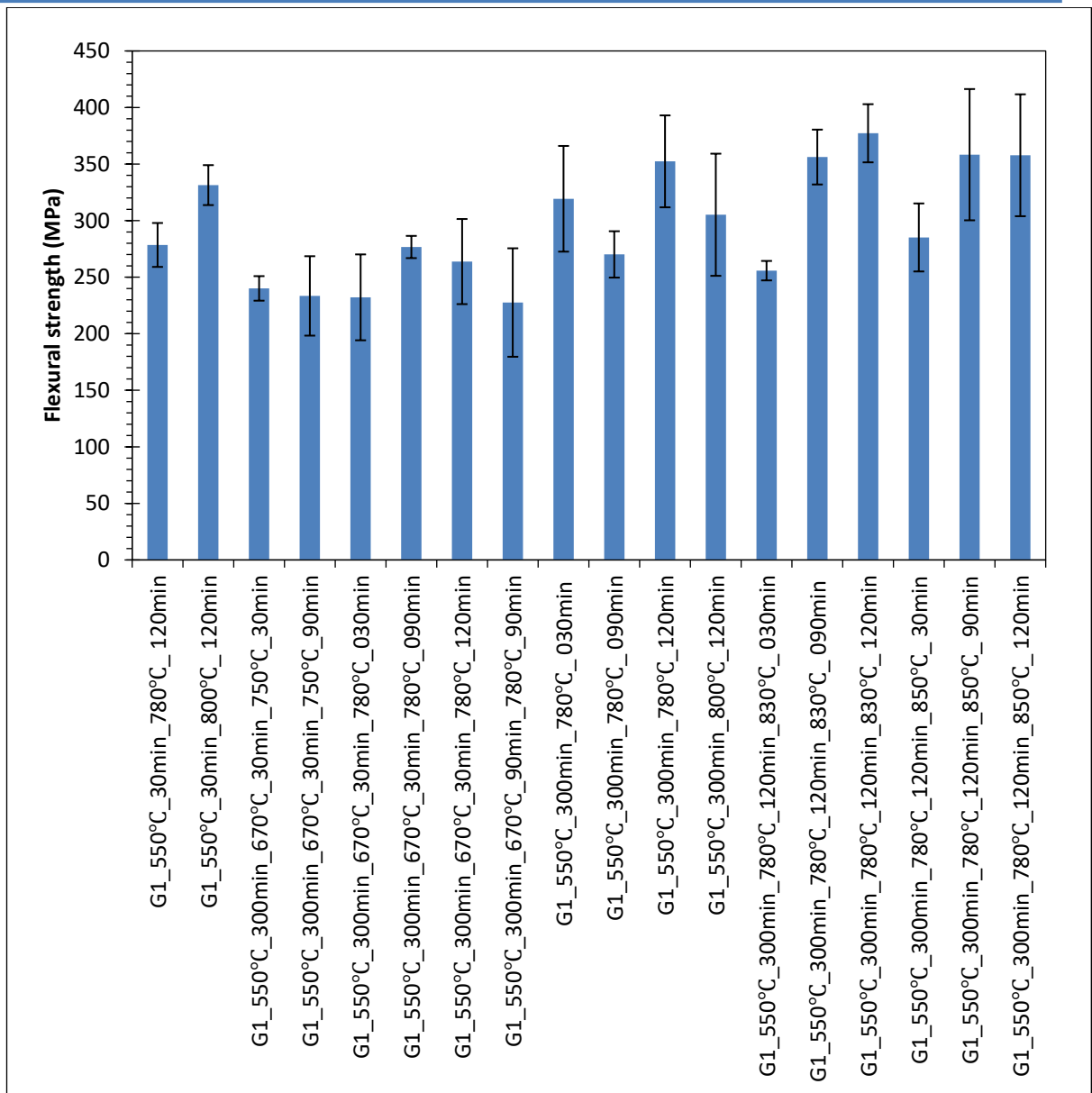


Fig. 5. 49 Flexural strength of the selected heat-treated samples.

5.8.3 Optical properties

5.8.3.1 colour

The CIE L*a*b* values for LAS1 glass samples subjected to the heat treatment profiles listed in Table 4. 5 were measured against a black background and are presented in Fig. 5. 50.

The lightness (L*) value appears to increase with increasing heat treatment temperatures, but it is also clear that a prolonged intermediate crystallisation step at 670°C results in a decrease in L*. Interestingly, this mirrors with the variation of the flexural strength in Fig. 5. 49. The changes in L* can be also appreciated in the digital images presented in Fig. 5. 52 for selected heat treatments.

Chapter Five: Processing and Characterisation of the LAS1 Glass

For samples with a maximum heat treatment temperature of 750°C, L* also appears to increase with increasing holding time, starting at 73.3 (for 30 min) reaching up to 80.27±0.06 (for 120 min). In this case, b* also changes from negative to positive, which corresponds to change from blue (−) to yellow (+). The most negative b* -14.47±0.15 is observed for samples heat treated at 670°C, which also show the lowest L*~ 40.53±0.23. The most positive b*~5 is observed for samples heat treated at 830°C. The a* value that corresponds to green (−) to red (+) appears to be negative for the lower temperature heat treatments with a short intermediate heat treatment. It is worth to note significant variations of the mechanical properties (Fig. 5. 46-5.49) by increasing the maximum heat treatment temperature is accompanied by small differences on L*a*b* values.

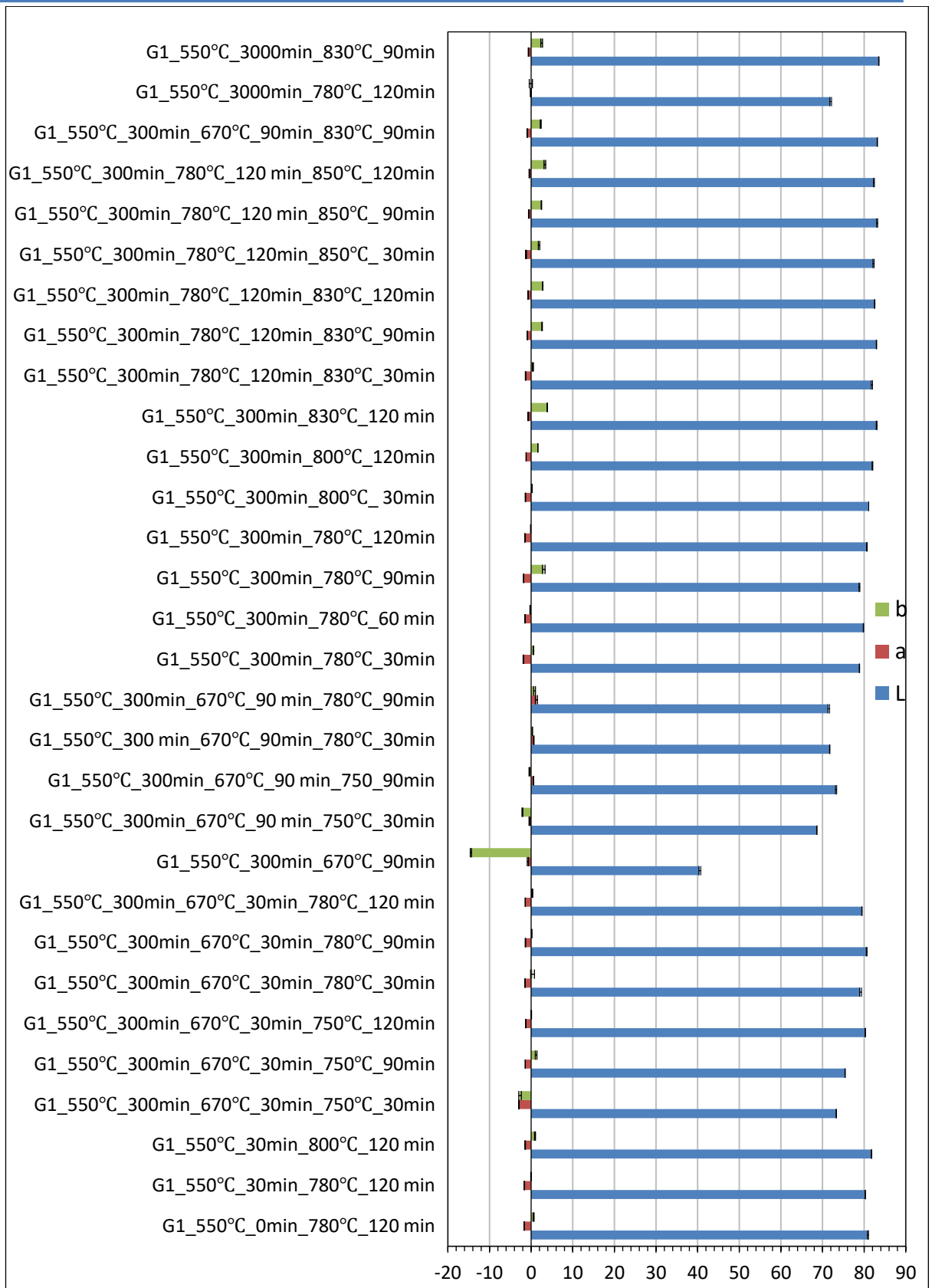


Fig. 5. 50 CIE Lab values of the heated treated LAS1 samples.

Colour differences (ΔL^* , Δa^* , Δb^* and ΔE values) between heated treated LAS1 glass samples and the VITA shade standards is presented in Fig. 5. 51.

It can be observed that A1 is the closest match for most heat treatments, however shade tab of the shade guide was a dominated, however, both Δb^* and ΔL^* show a large variation to the A1 standard. The largely positive ΔL^* implies a greater lightness of this glass, whereas the largely negative Δb^* indicates that significant bias towards blue. These two extremes are clearly identifiable in Fig. 5. 52.

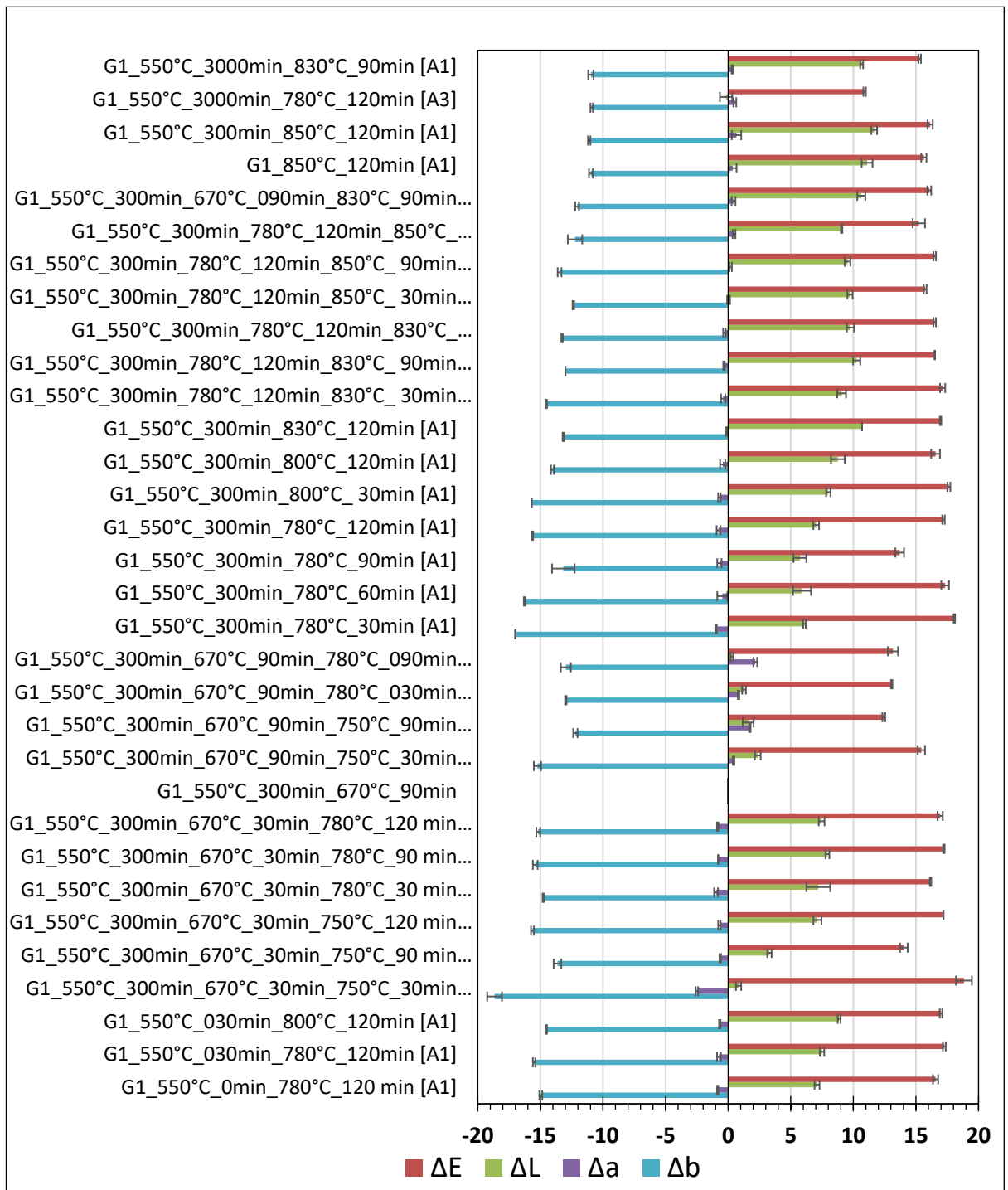


Fig. 5. 51 Colour differences (ΔL^* , Δa^* , Δb^* and ΔE values) between heated treated LAS1 glass samples and the VITA shade standards.

5.8.3.2 Optical Transmittance

Optical transmission in function of heat treatment and thickness (0.5, 1.0 and 3 mm) is depicted by digital photographs shown in Fig. 5. 52. As expected with increasing thickness the heat-treated specimens become opaque. Independently of the heat treatment, samples up to 1 mm in thickness are translucent. Interestingly samples heat-treated at 750°C appear clearly darker, which is commensurate with the CIE L*a*b* values in Fig. 5. 50.

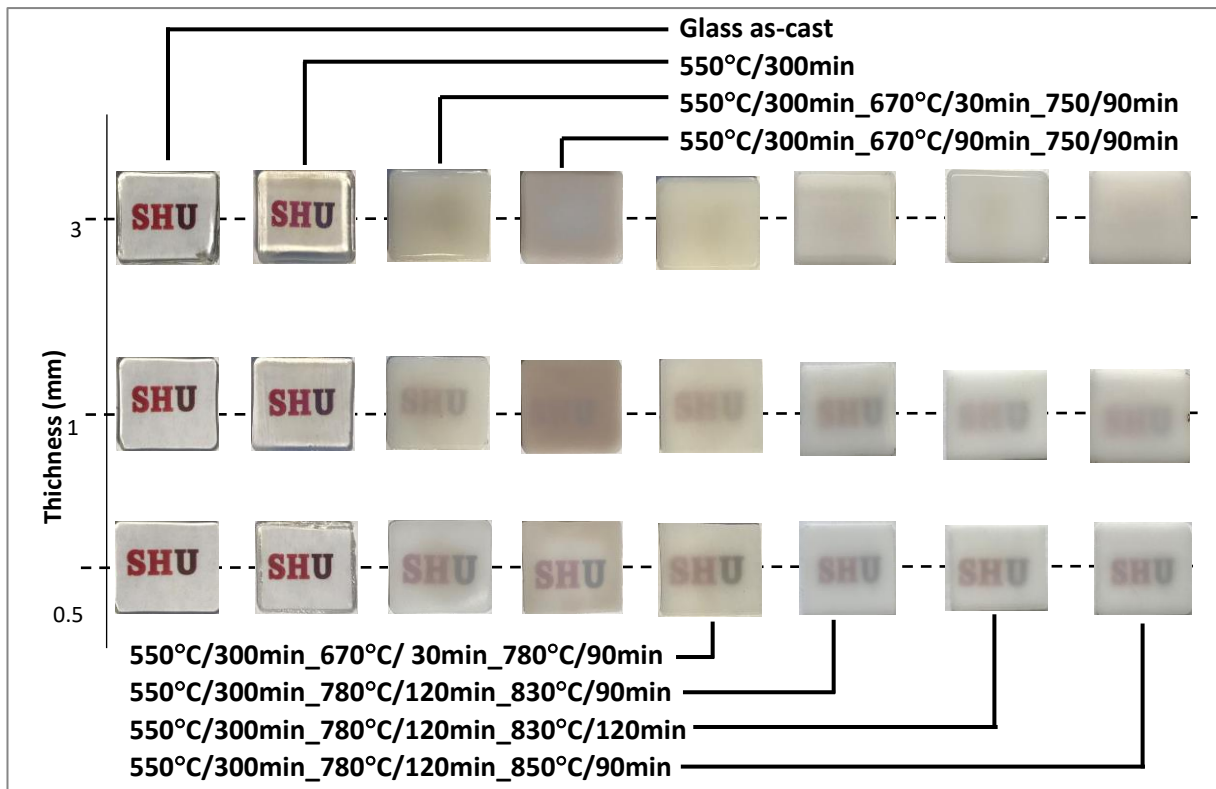


Fig. 5. 52 Digital photographs of as-cast, nucleated and heat-treated LAS1 glass, showing their translucency properties.

Optical transmission profiles in function of heat treatment and thickness (0.5, 1.0 and 3 mm) are shown in Fig. 5. 53(a-c). As expected, the as-cast glass shows the highest transmittance as shown in Fig. 5. 53-b and -c for the 1 mm and 3 mm samples, respectively. Although nucleation only slightly affects transmission, this becomes more evident for thicker samples, which is consistent with bulk nucleation. As evidenced in Fig. 5. 52, crystallisation has a stronger impact on the optical transmission profile in the visible region. In addition, based on the curves in Fig. 5. 53, which show a decrease in % transmittance with heat-treatment either with temperature or its duration. For samples of 0.5 mm in thickness, the lowest % transmittance (less than 10%, 850nm) is observed for

samples heat treated between 830-850 °C, when compared with 35-55% at 850 nm for samples heat-treated at 750-780 °C.

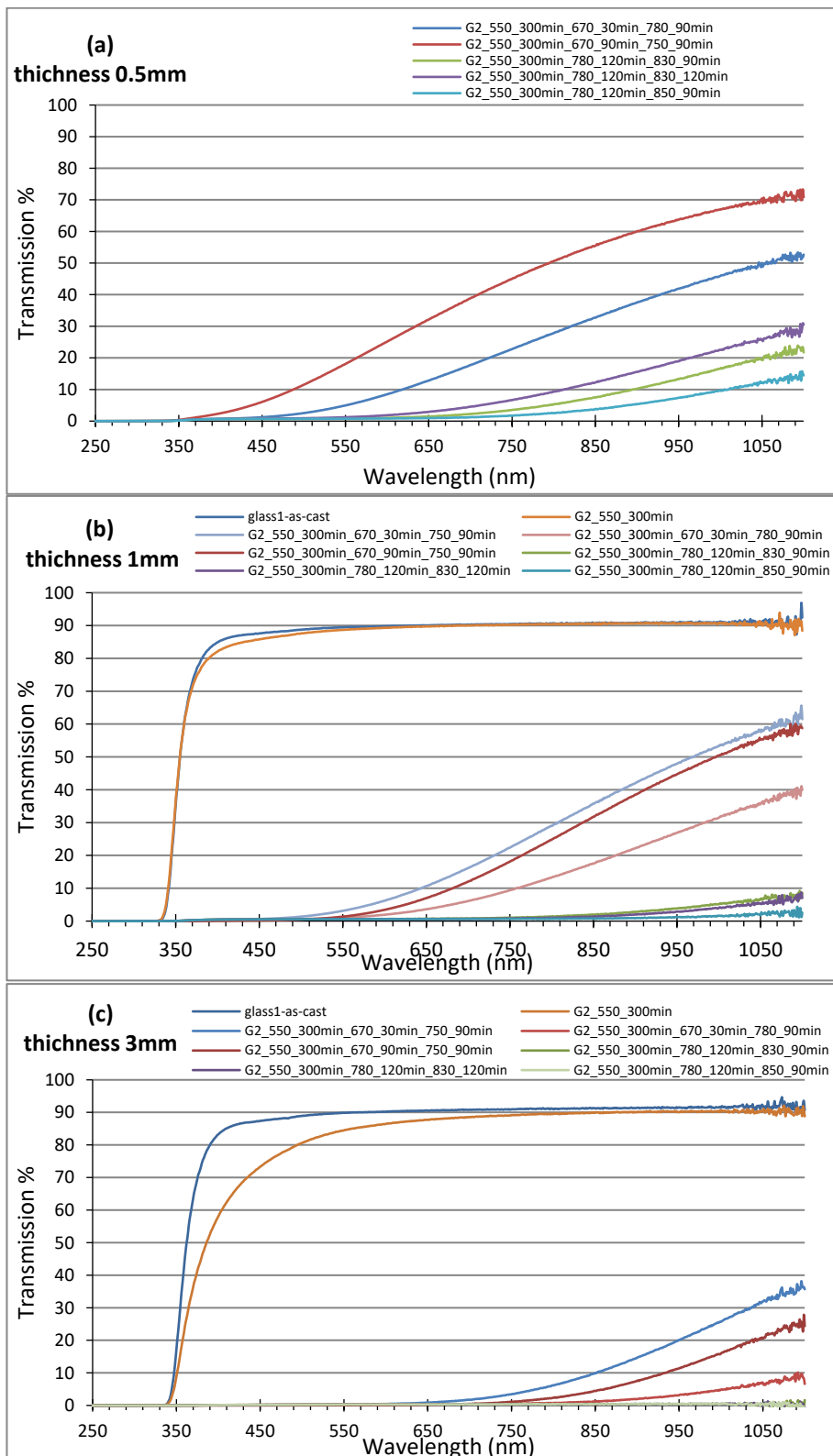


Fig. 5.53 Optical transmission profiles in function of heat treatment and thickness ((a) 0.5, (b) 1.0 and (c) 3 mm).

The CIE L*a*b* coordinates, opalescence parameter (OP), translucency parameter (TP) and contrast ratio (CR) values for above selected samples

measured against a black background are illustrated in Fig. 5. 54. L^* shows a remarkable increase with increasing thickness for all heat treatments, as shown in Fig. 5. 54-a. No monotonic trends were observed for both a^* and b^* in function of thickness, however a^* remains always slightly negative, whereas b^* for some heat treatments changes from negative to positive with increasing thickness. The opalescence relates to scattering of shorter wavelengths of the visible light, giving to an object an orange/brown appearance in the transmitted colour and bluish appearance in the reflected colour. The opalescence parameter drops continuously with increasing thickness for all selected heat treatments, as illustrated in Fig. 5. 54-d. CR values range from 0% for transparent material to 100% for a totally opaque one. The expectation is that CR increases with thickness as shown in Fig. 5. 54-e. For the selected heat treatments CR varies from ~40 % to ~90% with increasing thickness. Finally, TP that is the colour difference of sample over a white and a black background and that can vary from 0 to 100. As expected, TP for as-cast glass and nucleated is the greatest and shows little dependence with thickness, as shown in Fig. 5. 54-f. The precipitation of crystals upon heat treatment leads to a dramatic decrease in TP to less than 30, and as expected, thicker specimens show lower TP values, because more crystals are in the path of the light. Remarkably, samples in high heat treatment (830-850 °C) exhibited translucency levels slightly higher to the samples in low heat treatment (750-780 °C). The variations of the CR, OP and TP are consistent with the images in Fig. 5. 52.

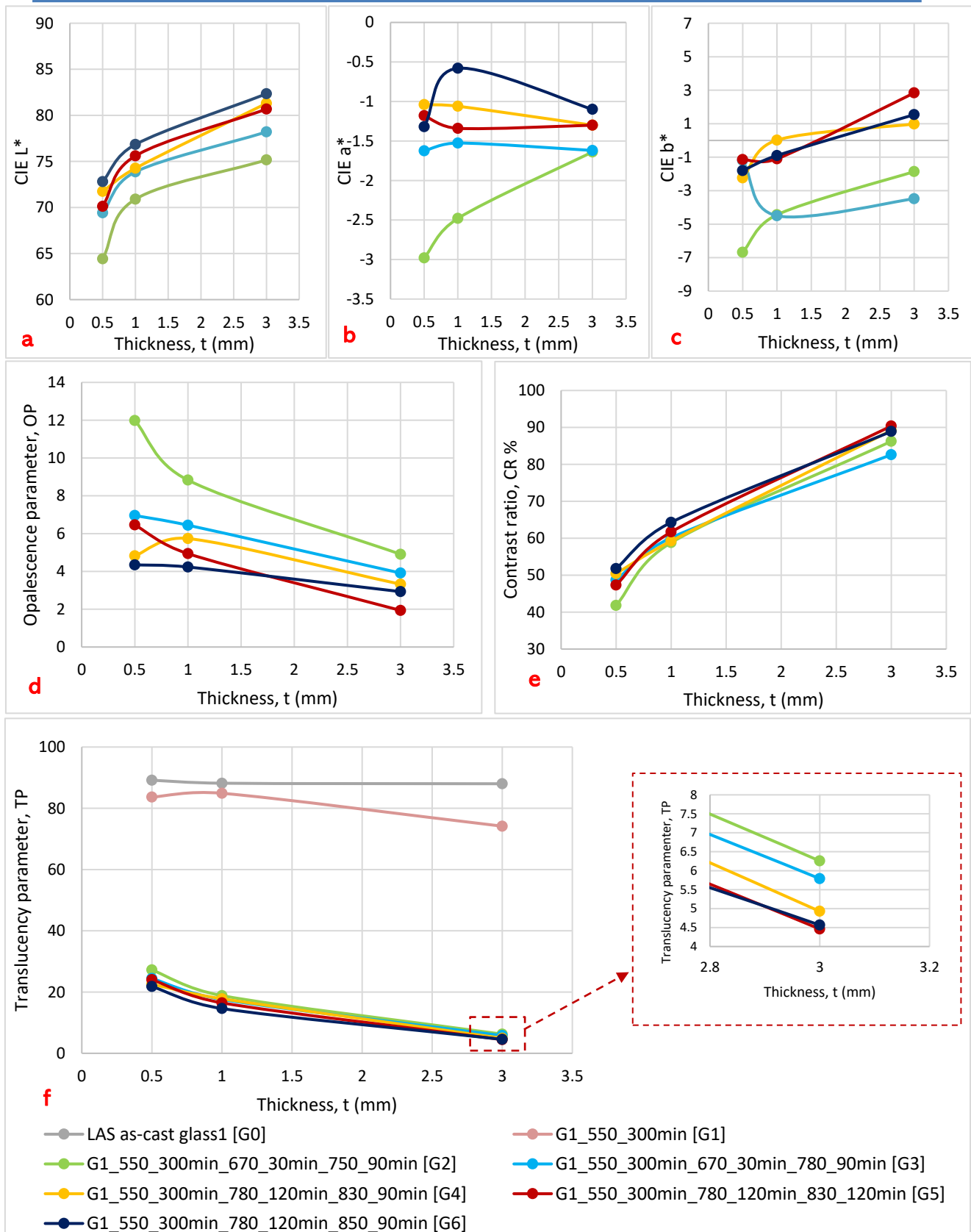


Fig. 5.54 CIE $L^*a^*b^*$ coordinates, CR and TP values in function of heat treatment and thickness ((a) 0.5, (b) 1.0 and (c) 3 mm).

5.9 Typical microstructure of nucleated and crystallised samples

Scanning electron microscopy images of HF-etched surfaces, for LAS1 glass nucleated at 550°C for 300 min, are shown in Fig. 5. 55. According to the *Ex-situ* XRD in the section 5.4.1, these sample contains Li₂SiO₃ and Li₃PO₄ crystals. These are not clearly visible from the SEM images, therefore TEM was carried out as shown in later.

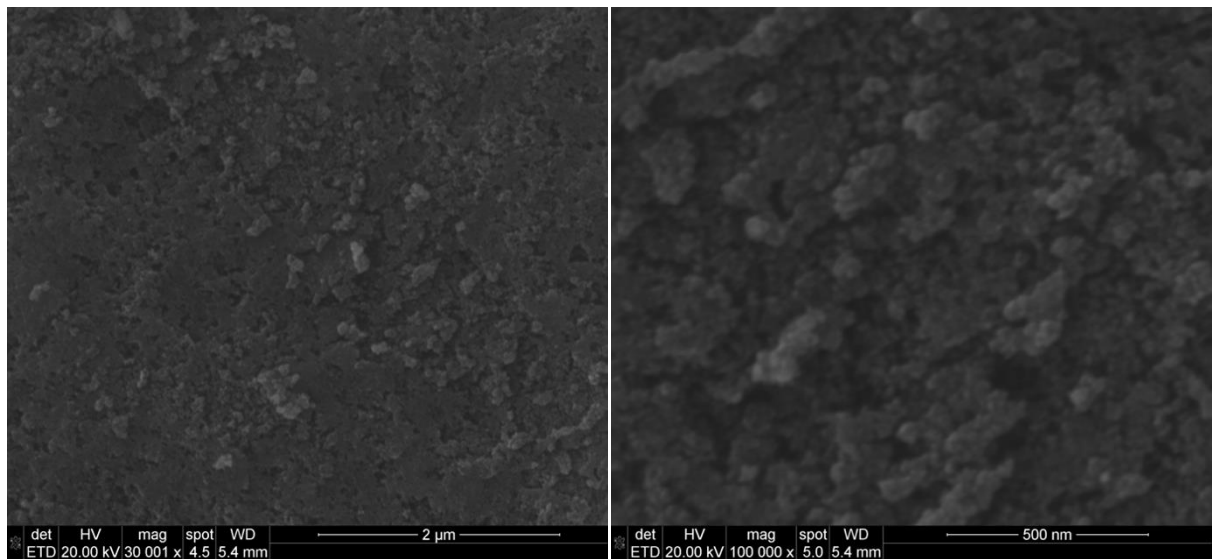


Fig. 5. 55 Microstructure of nucleated LAS1 glass at 550°C for 300min.

XRD analysis showed that upon to heat treatment at high temperature LiAlSi₂O₆ appears as the dominant phase. Moreover, Scherrer analysis showed the median average crystallite size to reach a maximum value of ~ 90 nm. The SEM image, Fig 5.56, reveals needle-shaped anisometric crystals with a diameter of the same order of magnitude but with a maximum length of several microns. This shows that caution should be used when employing the Scherrer equation to determine the crystallite size in this time of materials. It is worth to mention that the microstructure shown is for the sample nucleated at 550°C for 300 min, and subsequently heat treated at 780°C for 120 min and 830°C for 120 min, which shows the largest flexural strength as shown in Fig. 5. 49.

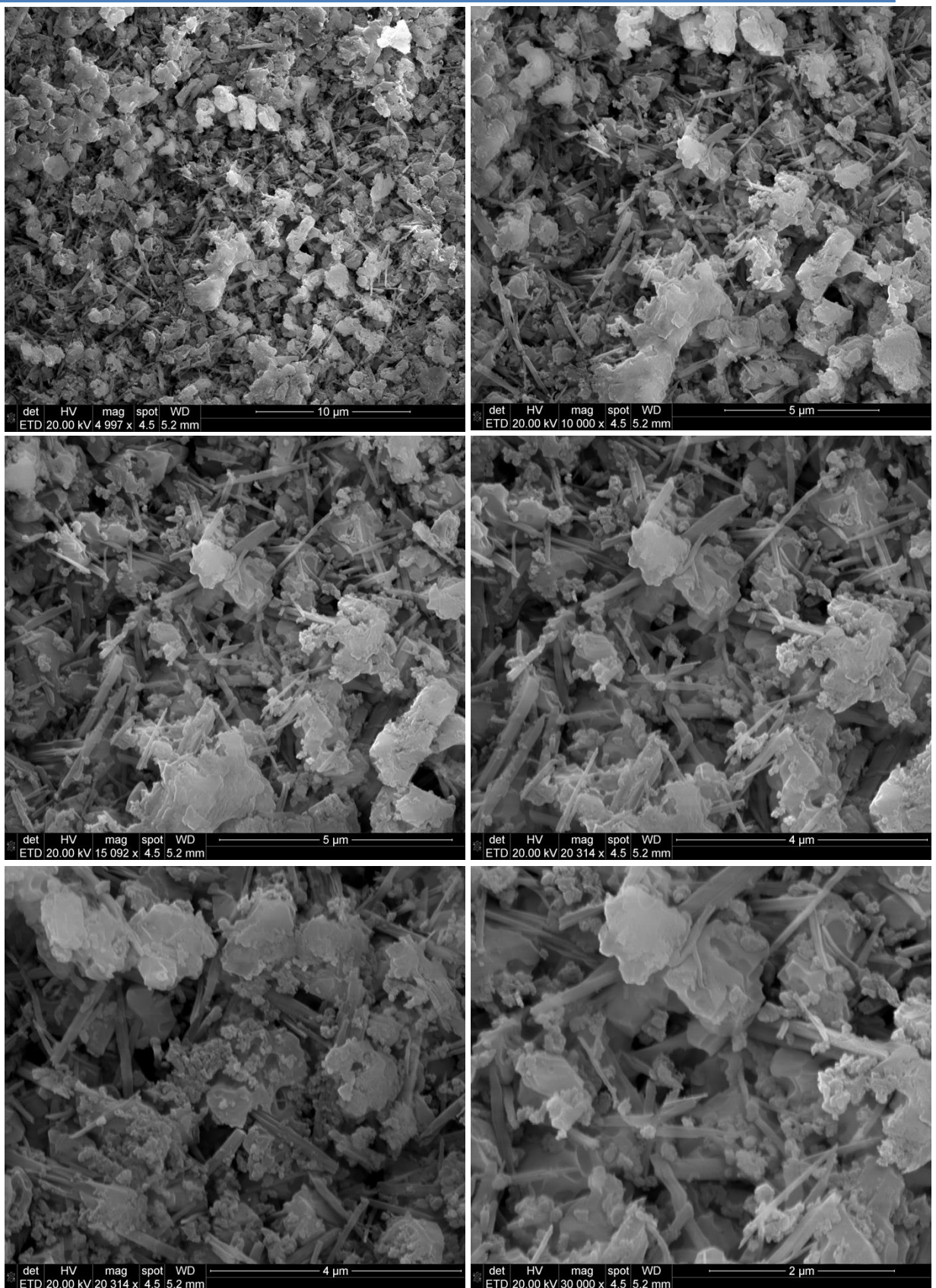


Fig. 5. 56 Microstructure of LAS1 glass sample nucleated at 550°C for 300 min, and subsequently heat treated at 780°C for 120 min and 830°C for 120 min.

5.10 Transmission Electron Microscopy (TEM)

Although XRD data in Fig. 5. 13 clearly showed that nucleated LAS1 glass samples encompass crystals of LiSi_2O_3 and Li_3PO_4 , those were not clearly discernible from the SEM image in Fig. 5. 55. Nevertheless, the TEM images of nucleated glass in Fig. 5. 57 show the presence of nanometric features that are crystalline in nature as indicated by electron diffraction pattern.

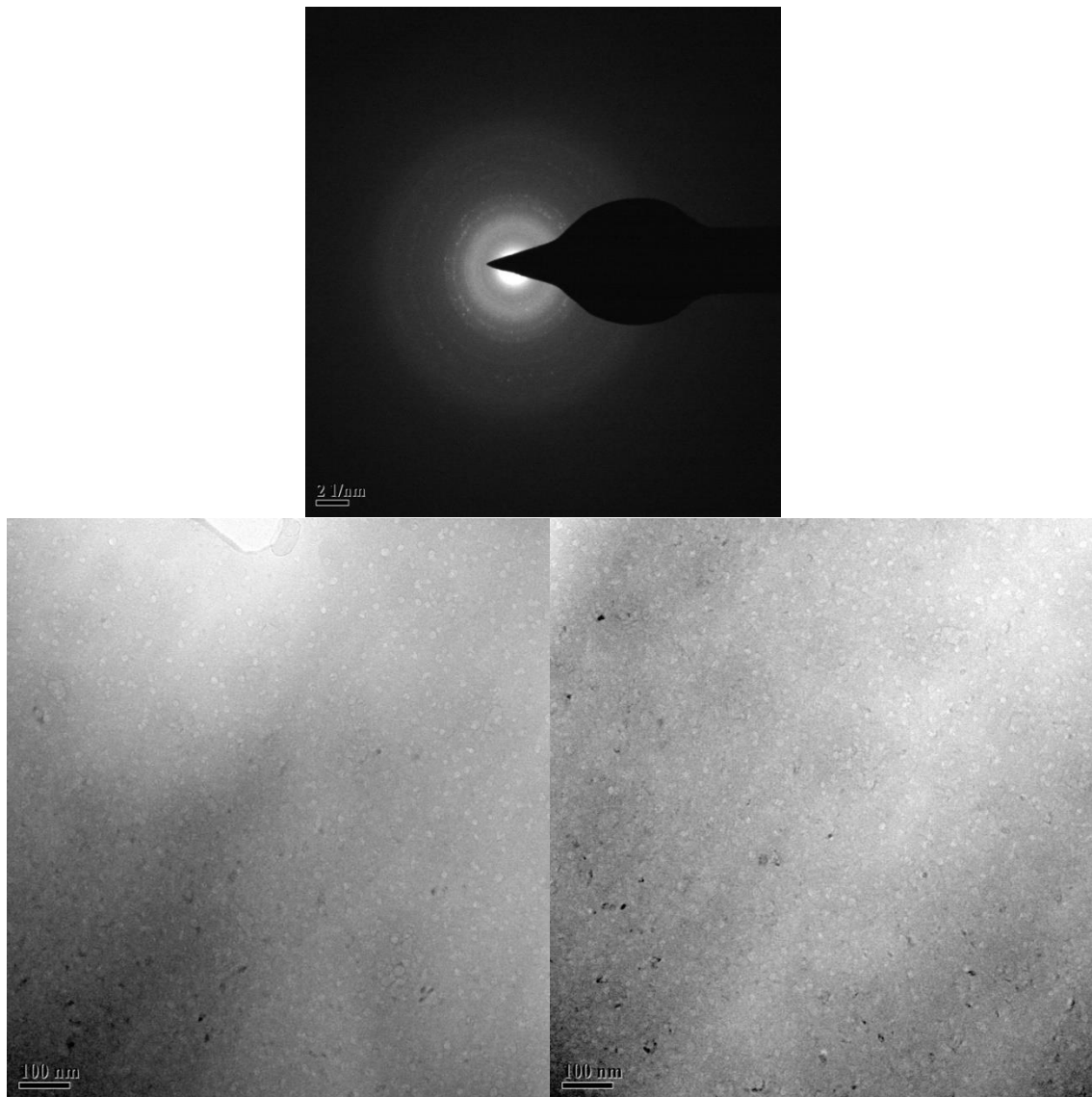


Fig. 5. 57 TEM bright-field image of LAS1 glass nucleated at 550°C for 300 min and respective electron diffraction pattern.

Bright-field TEM images for LAS1 glass sample nucleated at 550°C for 300 min, and subsequently heat treated at 780°C for 120 min and 830°C for 120 min are shown in Fig. 5. 58. According to XRD analysis the dominant crystalline phase is $\text{LiAlSi}_2\text{O}_6$, which maybe be associated to the “needle-like” crystals distributed

randomly in the glass matrix, as shown in Fig. 5. 58. The electron diffraction pattern confirms the crystalline nature of those grains. The enhancement of the mechanical properties and the optical properties of heat treated LAS1 glass in relation to the nucleated glass is ultimately dependent on the phases assemblage and morphology shown by the SEM and TEM analysis.

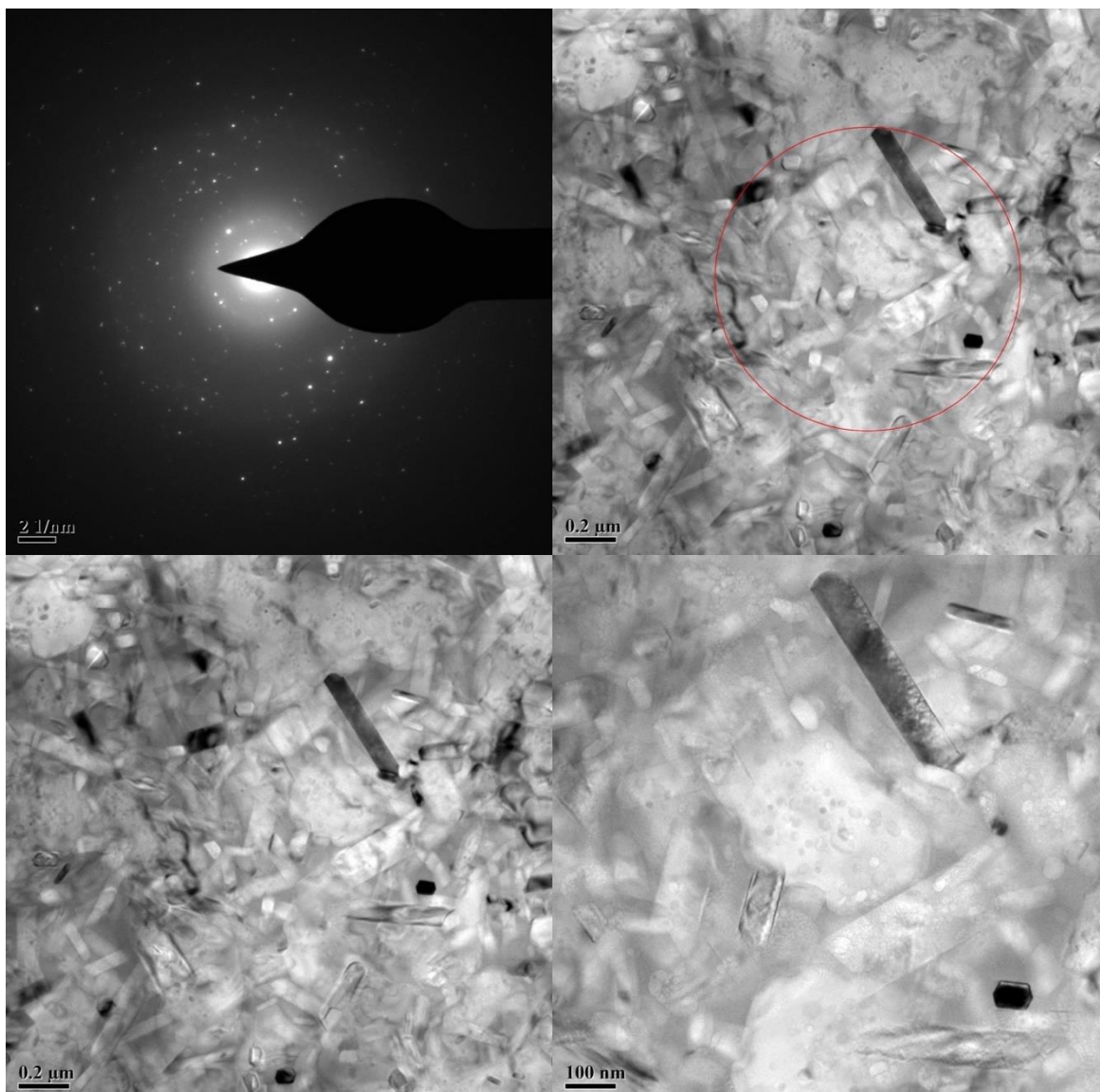


Fig. 5. 58 Bright-field TEM images for LAS1 glass sample nucleated at 550°C for 300 min, and subsequently heat treated at 780°C for 120 min and 830°C for 120 min and associated electron diffraction pattern.

Chapter | 6 |

Processing and Characterisation
of the LAS2 Glass

Chapter Six: Processing and Characterisation of the LAS2 Glass

Introduction

In this chapter experimental data obtained for the LAS2 glass composition (see Table 4. 1) is presented and discussed. Again, the effect of heat treatment on phase assemblage, mechanical and optical properties is evaluated and discussed. First, thermodynamics and kinetics of crystallisation are determined from thermal analyses, prior to establish specific heat treatment schedules. Subsequently, thermal events detected by DSC are correlated to crystallization and/or phase transformation using XRD. Finally, both mechanical and optical properties are correlated to the phase assemblage determined by XRD. Elastic modulus, hardness, fracture toughness and flexural strength are the mechanical properties investigated. Characterisation of the optical characteristics is focussed on colour evolution with heat-treatment.

6.1 Differential Scanning Calorimetry (DSC) Analyses

6.1.1 Impact of the heating rate on the thermal behaviour of LAS2 glass

The as-cast LAS2 glass was subjected to a two-stage heat treatment process, encompassing a nucleation stage and a crystal growth stage, which was informed by DSC analyses combined with XRD analyses presented in sections 6.3 and 6.4. Upon heating, LAS2 glass exhibits several exothermic and endothermic events in 400°C - 950°C temperature range, as illustrated in Fig. 6. 1. Under a heating rate of 20 °C/min and using the intersection of two tangent lines at the onset of the endothermic event, the glass transition temperature (T_g) was determined as 519°C, this value is comparable to 515°C for LAS1 glass, in section 5.1.

Fig. 6. 1 shows DSC data for experiments were carried out at heating rates of 5, 10, 15 and 20 °C/min up to a maximum temperature of 950°C. As expected, all exothermic peaks shift towards higher temperatures with increasing heating rates, as indicated by the dashed lines. For example, at a heating rate of 5 °C/min, the first and second exothermic peaks appear at 616°C (**615°C in LAS1 glass**) and 704°C (**706°C in LAS1 glass**), respectively, whereas at a heating rate 20 °C/min those peaks appear at 654°C (**657°C in LAS1 glass**) and 746°C (**746°C in LAS1 glass**). These data are useful to calculate the activation energies associated with each thermal event, as shown in section 6.2. Nevertheless, one

would expect values to be similar to those estimated for LAS1 glass, due to similarly in composition and thermal behaviour.

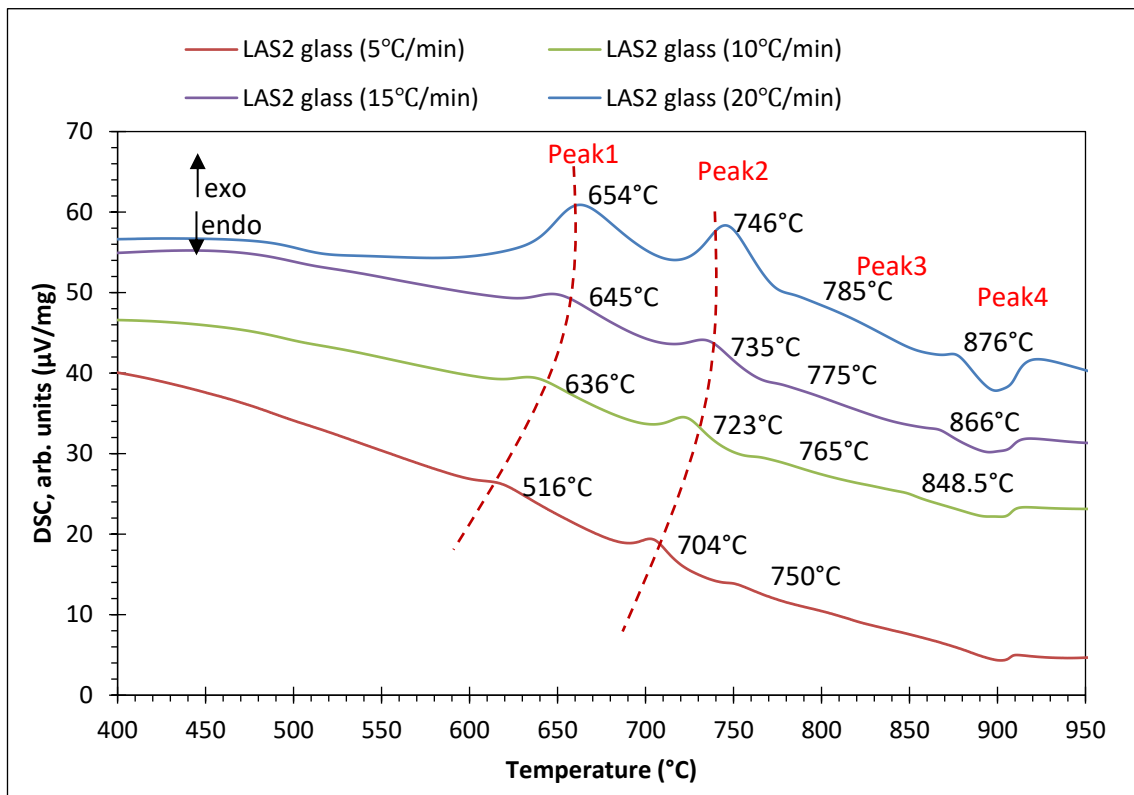


Fig. 6. 1 DSC traces for LAS2 glass measured at different heating rates.

6.1.2 Thermal behaviour of LAS2 glass nucleated 550°C for 300 min measured at different heating rates

XRD analysis in section 6.4.1 for isothermal heat treatments at 550°C , show the appearance of Li_2SiO_3 and Li_3PO_4 crystals. Stable contents are reached after 300 minutes. Consequently, evaluating the thermal behaviour of LAS2 glass nucleated at 550°C for 300 min using different heating rates of 5, 10, 15 and 20 $^{\circ}\text{C}/\text{min}$ may provide more details about the crystallisation behaviour. Moreover, activation energies of crystallisation for nucleated LAS2 glass can then be compared with those estimated for LAS1 glass. DSC results for nucleated LAS2 glass are shown in Fig 6. 2. The suppression of the first exothermic peak that in as-cast LAS2 glass appears at 616°C , Fig. 6. 1, is probably the most remarkable effect of the nucleation step. This peak can be associated to the successive crystallisation of Li_2SiO_3 , $\text{LiAlSi}_4\text{O}_{10}$ and $\text{Li}_{0.25}\text{Al}_{0.25}\text{Si}_{0.75}\text{O}_2$, as determined by XRD analysis. Another noticeable effect is crystallisation of $\text{LiAlSi}_4\text{O}_{10}$ and $\text{Li}_{0.25}\text{Al}_{0.25}\text{Si}_{0.75}\text{O}_2$ at lower temperatures in nucleated samples, as indicated by the second exothermic peak.

Indeed, the second exothermic peak in nucleated glasses becomes the most prominent thermal event, appearing at 689°C (**691°C in LAS1 glass**), 704°C (**705°C in LAS1 glass**), 714°C (**714°C in LAS1 glass**) and 721°C (**722°C in LAS1 glass**) for heating rates of 5, 10, 15 and 20 °C/min, respectively. In comparison, with as-cast LAS2 glass, Fig. 6. 1, those events are visible at lower temperatures, influencing the activation energies, as shown in section 6.2. This peak is rather narrow, which is consistent with a bulk crystallisation process.

The third exothermic event visible at 733°C (**729°C in LAS1 glass**), 744°C (**740°C in LAS1 glass**), 750°C (**764°C in LAS1 glass**) and 756°C (**751°C in LAS1 glass**) for heating rates 5, 10, 15 and 20 °C/min respectively, increases in magnitude and gradually merges with the second exothermic event, with increasing heating rates.

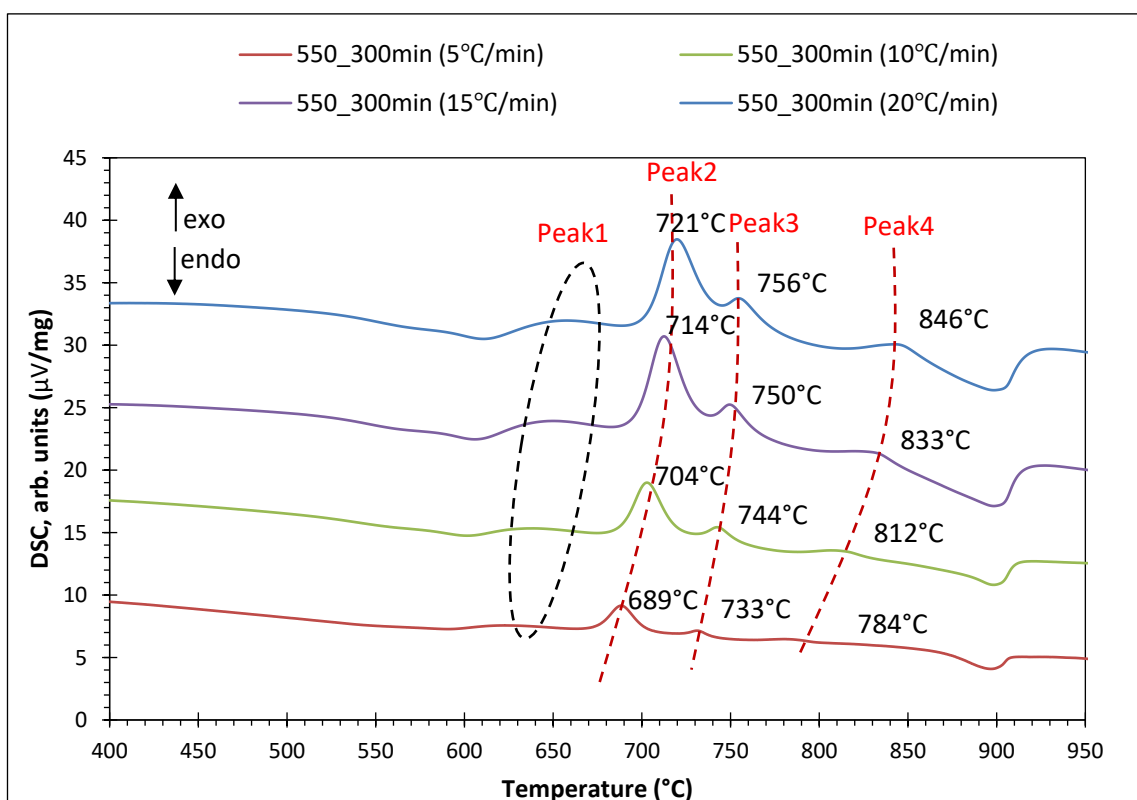


Fig. 6. 2 DSC traces of LAS2 glass nucleated at 550°C for 300 min using different heating rates.

6.1.3 Impact of the nucleation holding time on the thermal behaviour of LAS2 glass

The effect of the holding times (0, 30, 150 and 300 min) at the nucleation temperature of 550°C on the thermal behaviour of LAS2 glass was also evaluated by DSC experiments carried out at heating rate of 5 °C/min up to a maximum temperature of 950°C. Data from these experiments are shown in Fig. 6. 3.

In agreement with results in section 6.1.1 and 6.1.2, the first exothermic peak at 615°C for as-cast LAS2 glass becomes suppressed and shifts slightly towards higher temperatures with increasing holding times. In resemblance to LAS1 glass, barely any difference is detected between holding times of 150 min and 300 min, which corroborates that a nucleation time 300 min is sufficient to achieve a stable level of of Li_2SiO_3 and Li_3PO_4 precipitation. This result is in broad agreement with the XRD analysis for isothermal heat treatments at 550°C presented in Fig. 6. 12, in section 6.4.1. In contrast, the other thermal events shifted slightly towards lower temperatures as indicated by the dashed line for the second exothermic peak. This peak is related to crystallisation of $\text{LiAlSi}_2\text{O}_6$ and $\text{Li}_2\text{Si}_2\text{O}_5$, as discussed in the section 6.1.1. The crystallisation process take place in short periods of time, as this high kinetics is further exemplified in Fig. 6. 16, for isothermal heat treatments at 670°C.

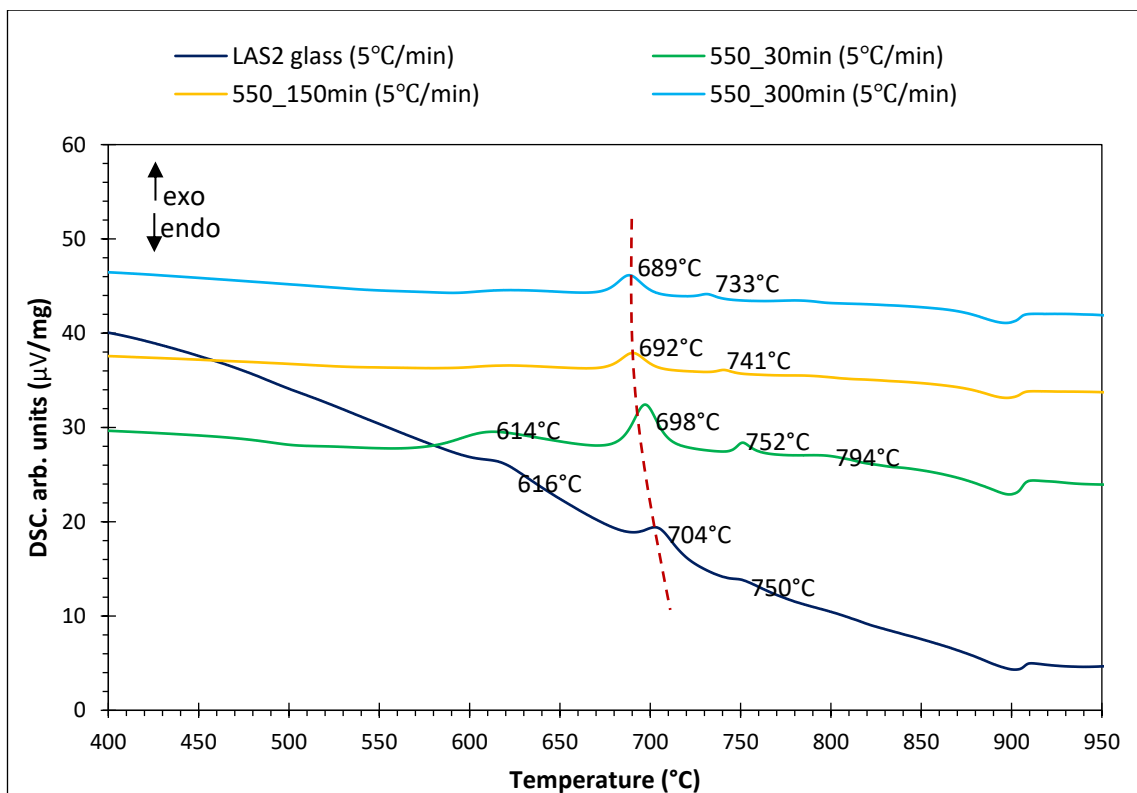


Fig. 6. 3 DSC traces for as-cast LAS2 glass and nucleated at different holding times.

6.1.4 Thermal behaviour of LAS2 glass subjected to prior isothermal heat treatments

The evaluation of thermal behaviour of LAS2 glass specimens heat treated at 650, 670, 690, 710 and 730 °C for 30 min (which covers the temperature range of the two major thermal events exhibited by the as-cast LAS2 glass) was further

investigated to gather a more detailed picture of the crystallisation pathway. Fig. 6. 4 shows DSC data for experiments carried out at heating rate 5 °C/min up to a maximum temperature of 950°C. In comparison with the as-cast glass, the first exothermic peak at 622°C is absent in all heat-treated specimens. This supports the rapid and fully crystallisation of Li_2SiO_3 , $\text{LiAlSi}_4\text{O}_{10}$ and $\text{Li}_{0.25}\text{Al}_{0.25}\text{Si}_{0.75}\text{O}_2$, which based on XRD analysis, Fig. 6. 13 are the phases associated with this thermal event. The specimen heat treated at 650°C for 30 min, still exhibits a significant exothermic event at 687°C, which in the as-cast glass appears at 705°C. Again, based on the *In-Situ* XRD data presented in Fig. 6. 11, this exothermic event is consistent with the crystallisation of $\text{Li}_2\text{Si}_2\text{O}_5$ alongside $\text{LiAlSi}_2\text{O}_6$. A small exothermic peak is still present at 740-750 °C, which cannot be associated to any reactions/transformations involving the phases crystallised during the first thermal event, because it disappears from the traces of the specimens heat treated above 710°C. Therefore, it may be linked to reactions/transformation of the phases associated with the exotherm event visible at 705°C in the as-cast glass. Remarkably, no more thermal events, apart from melting, are detected for specimens heat treated above 710°C, independently of nucleation. This is in broad agreement with Table 6. 2 in section 6.3, which indicates that no major phase crystallises above 690°C. An original schematic DSC curves are shown in Appendix 2.

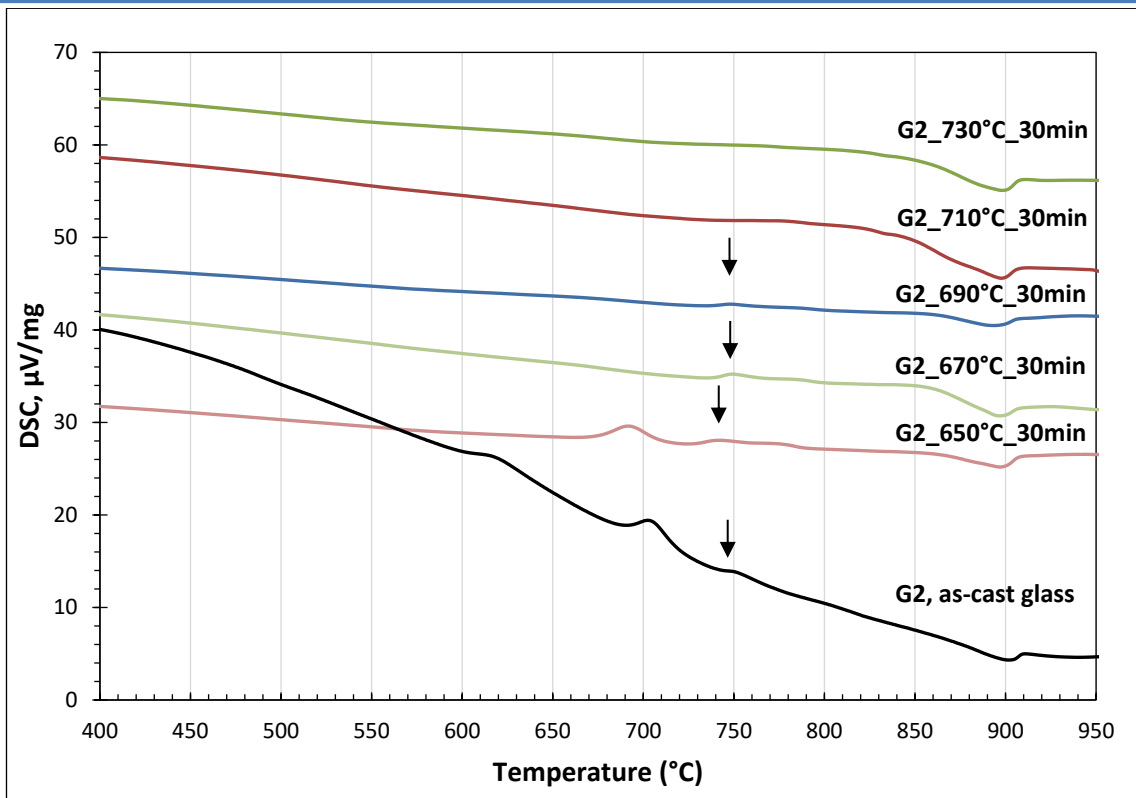


Fig. 6. 4 DSC for as-cast and nucleated LAS2 glass heat treated at different temperatures.

6.2 Activation energy determination

6.2.1 Kissinger's method

A detailed description of the Kissinger method can be found in the section 2.6.3.1. Basically, the activation energy, E_a , can be estimated from the slope of $[\ln(\beta/T_p^2)]$ in function of $[1000/T_p]$, which represents $[-E_a/R]$, where R is the gas constant, as shown in Fig. 6. 5 for the three successive exothermic events shown in Fig. 6. 1 for as-cast LAS2 glass. Similarly, Fig. 6. 6 shows the estimates of E_a for the thermal events observed in Fig. 6. 2 for nucleated LAS2 glass.

Hence, for the as-cast glass, the peak associated with the collective crystallisation of Li_2SiO_3 , $\text{LiAlSi}_4\text{O}_{10}$ and $\text{Li}_{0.25}\text{Al}_{0.25}\text{Si}_{0.75}\text{O}_2$ has an activation energy of 190 kJ/mole (**in comparison for LAS1 glass is 212 kJ/mole**). The sharp exothermic peak associated with the crystallisation of $\text{LiAlSi}_2\text{O}_6$ and $\text{Li}_2\text{Si}_2\text{O}_5$ has an activation energy of 260 kJ/mole (**for LAS1 glass is 270 kJ/mole**). In comparison with LAS1 glass, these values suggest an enhancement of ability to crystallisation. Moreover, these values are significantly lower than observed in other glass ceramic systems. The third thermal event has the highest

Chapter Six: Processing and Characterisation of the LAS2 Glass

$E_a \sim 343.5$ kJ/mole, which may result in a small crystallisation/transformation, commensurate with the small peak intensity.

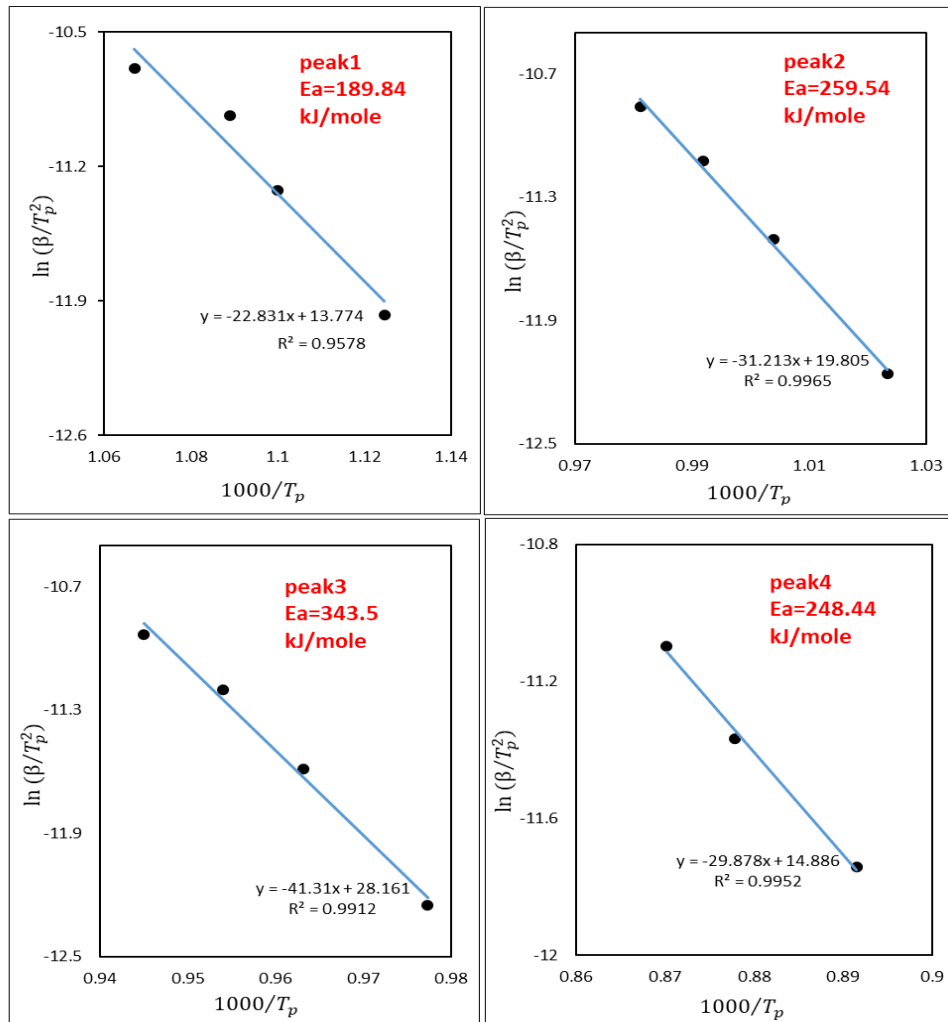


Fig. 6. 5 Kissinger plots used to estimate the activation energy for the crystallization processes in as-cast LAS2 glass.

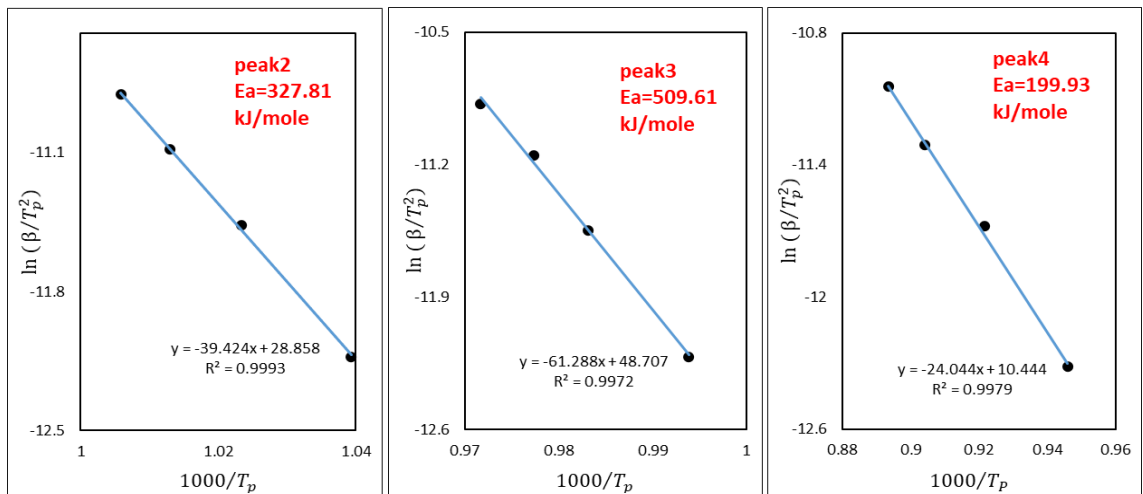


Fig. 6. 6 Kissinger plots used to estimate the activation energy for crystallization processes in LAS2 glass nucleated at 550°C/300min.

6.2.1 Modified Kissinger's method

In this case, a plot is constructed as $[\ln(\beta^n/T_p^2)]$ in function of $[1000/T_p]$, where again the slope represents $[-mE_a/R]$ as shown in Fig. 6. 7 and Fig. 6. 10 for the as-cast class and nucleated LAS2 glass, respectively.

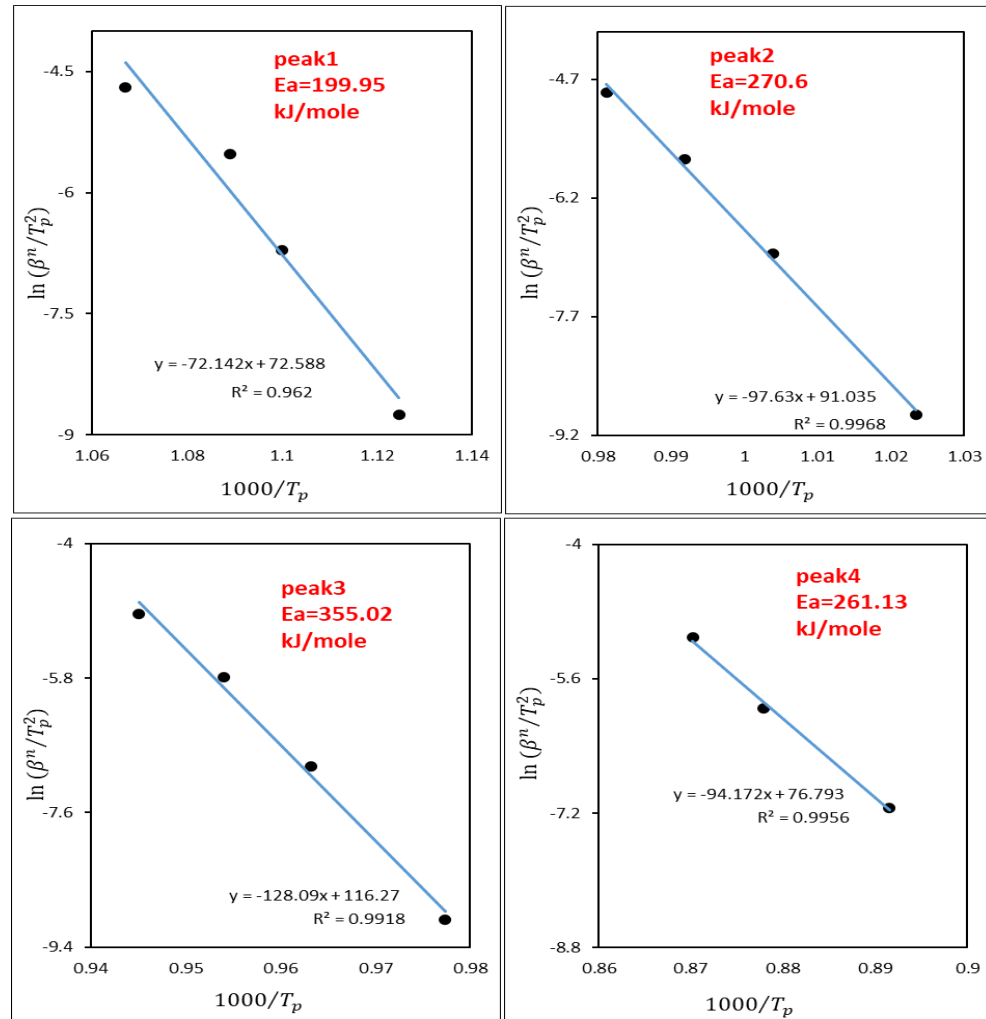


Fig. 6. 7 Modified Kissinger's plots used to estimate the activation energy for the crystallization processes in as-cast LAS2 glass.

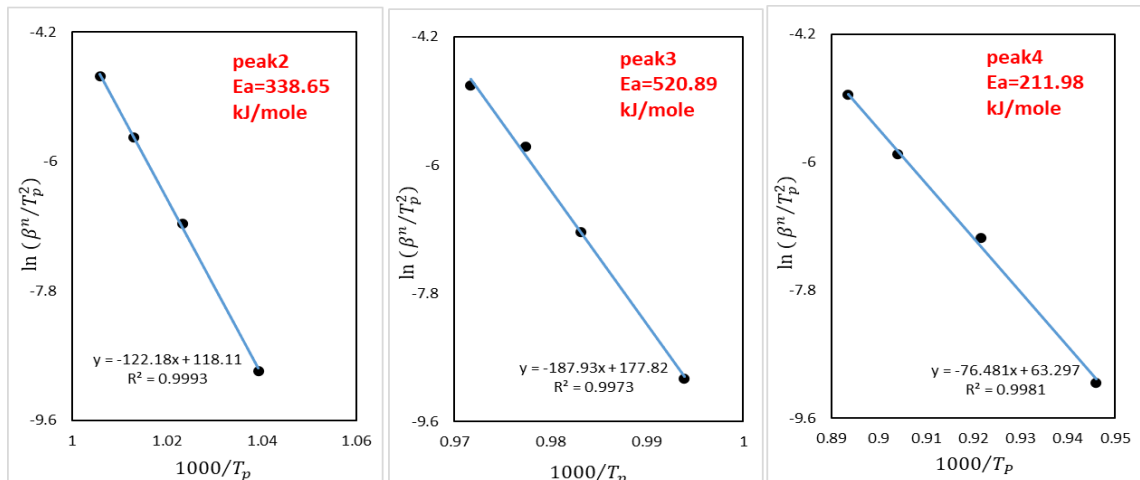


Fig. 6. 8 Modified Kissinger's plots used to estimate the activation energy for crystallization processes in LAS2 glass nucleated at 550°C/300min.

6.2.2 Ozawa's method

Ozawa's method can be employed to determine E_a , as described in the section 2.6.3.3, by plotting $[1000/T_p]$ in function of $[\ln(\beta)]$. The results for the as-cast and the nucleated LAS2 glass are illustrated in Fig. 6. 9 and 6. 10, respectively.

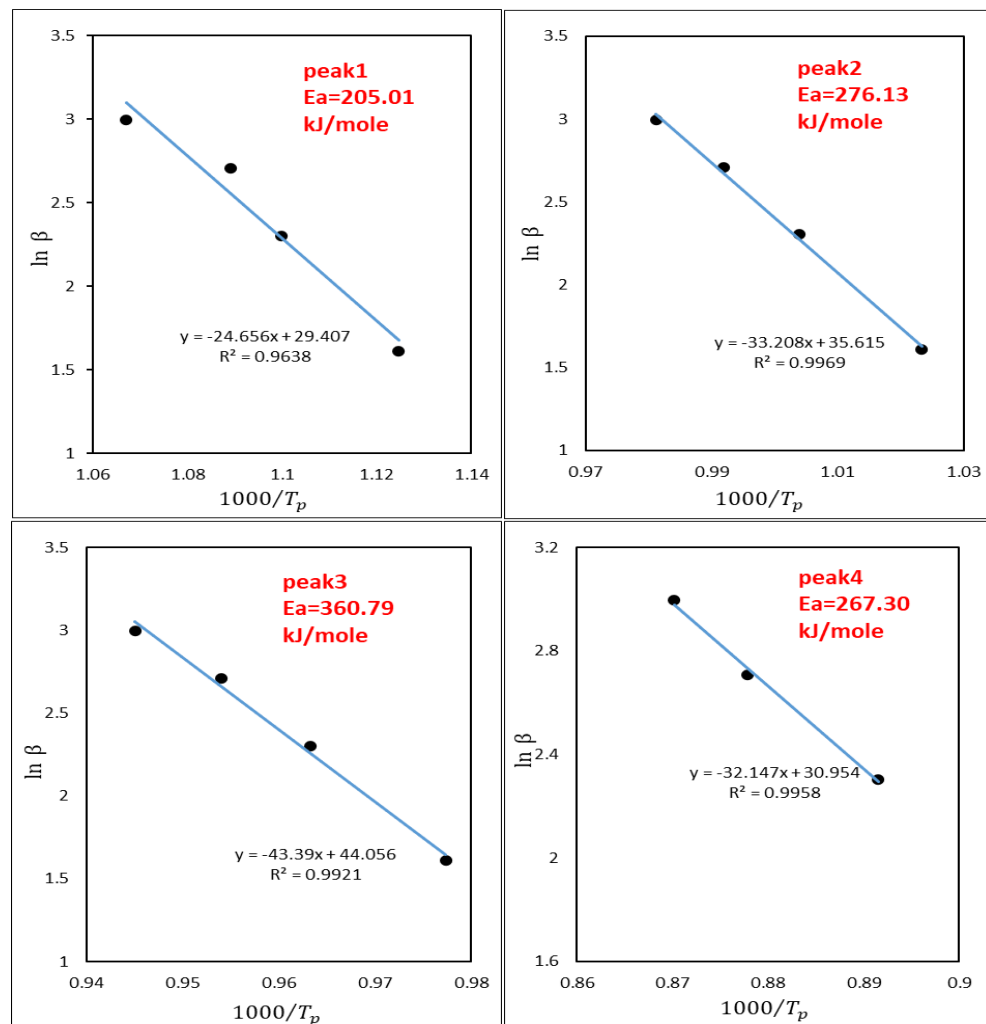


Fig. 6. 9 Ozawa plots used to estimate the activation energy for the crystallization processes in as-cast LAS2 glass.

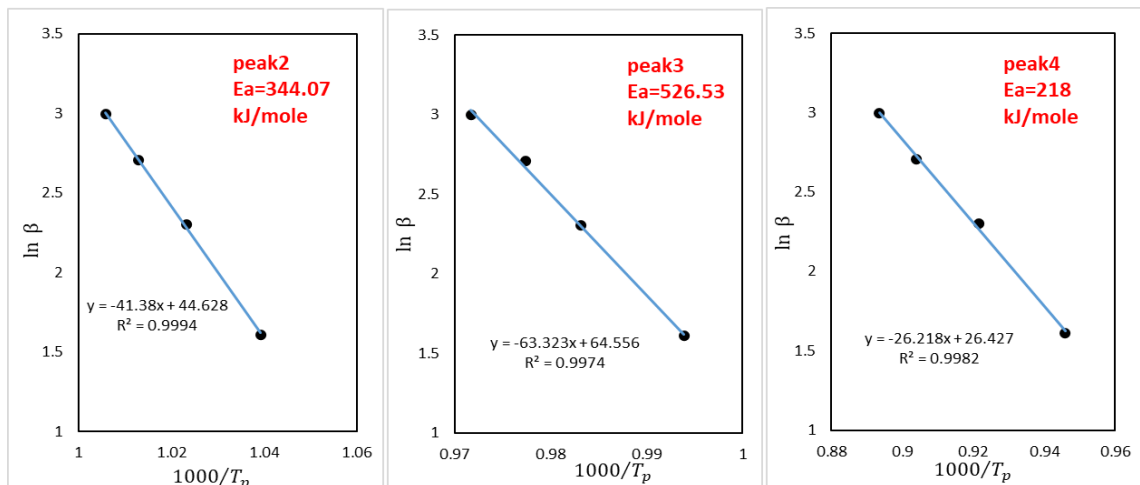


Fig. 6. 10 Ozawa plots used to estimate the activation energy for crystallization processes in LAS2 glass nucleated at 550°C/300min.

Chapter Six: Processing and Characterisation of the LAS2 Glass

Values of E_a exhibit the same trend for all the three methods, as indicated by the values listed in Table. 6. 1. It is clear that the event associated with peak 3, shows comparatively the highest E_a , which is commensurate with a higher barrier to crystallisation/transformation. E_a increases significantly for nucleated samples.

Table. 6. 1 Activation energies for crystallisation processes in as-cast and nucleated LAS2 glass. (units: kJ/mole).

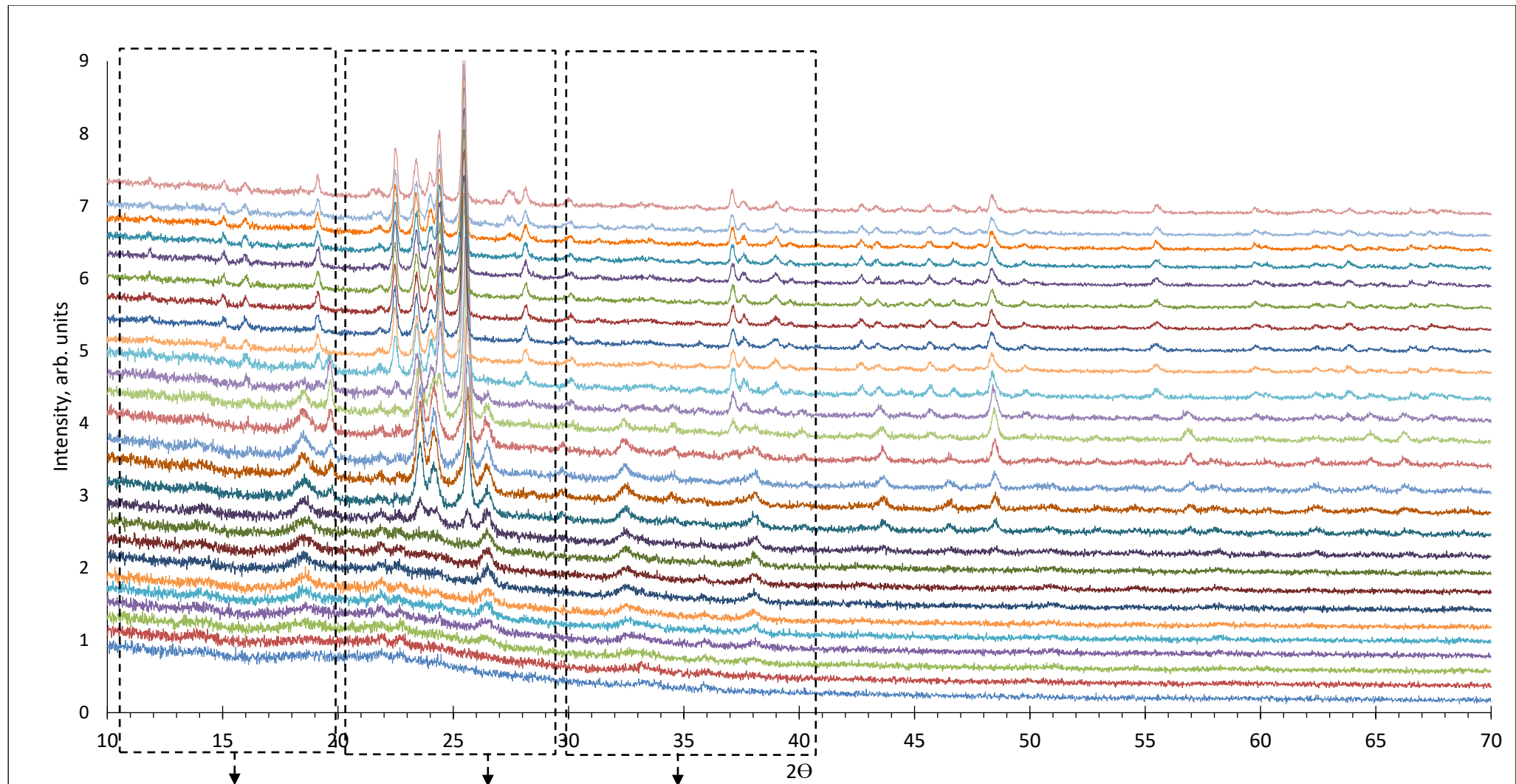
| | LAS2 glass | | | | Nucleated glass 550°C/300min | | | |
|---------------------------|------------|--------|--------|--------|---------------------------------|--------|--------|--------|
| | Peak1 | Peak2 | Peak3 | Peak4 | Peak1 | Peak2 | Peak3 | Peak4 |
| Kissinger method | 189.84 | 259.54 | 343.5 | 248.44 | - | 327.81 | 509.61 | 199.93 |
| Modified Kissinger method | 199.95 | 270.6 | 355.02 | 261.13 | - | 338.65 | 520.89 | 211.98 |
| Ozawa method | 205.01 | 276.13 | 360.79 | 267.3 | - | 344.07 | 526.53 | 218.0 |

6.3 In-situ high-temperature XRD patterns of LAS2 as-cast glass

In-situ high-temperature XRD patterns, in Fig. 5. 13 for LAS1 glass and in Fig. 6. 11 for LAS2 glass, reveal a similar reaction/crystallisation pathway. Therefore, the discussion in section 5.3 is applicable to LAS2 glass. In summary, as listed in Table 6. 2, the phases appearing on heating and their temperature range of stability is similar to the behaviour observed for LAS1 glass. Crystallisation processes occurring in 700°C-730°C temperature range have a significant impact in the mechanical properties, as shown in Fig. 6. 26, 6. 29 and 6. 32. Basically, the elastic modulus increases from 86.77 ± 0.25 to 95.2 ± 0.1 GPa, the hardness from 6.29 ± 0.07 to 6.55 ± 0.07 GPa and fracture toughness from 1.08 ± 0.11 to 1.19 ± 0.05 MPa \sqrt{m} . There is also a correlation with the optical properties, as shown in Fig. 6. 35. Basically, the material changes from a purple glass to a creamy glass-ceramic.

Table. 6. 2 Phases and respective temperatures range based on In-situ high-temperature X-ray diffraction.

| Phases | Symbol of phase | Temperature range |
|--|-----------------|-------------------|
| Li_2SiO_3 | LS1 | 570-790°C |
| $\text{LiAlSi}_4\text{O}_{10}$ | LAS1 | 590-690°C |
| $\text{Li}_{0.25}\text{Al}_{0.25}\text{Si}_{0.75}\text{O}_2$ | LAS2 | 640-710°C |
| $\text{Li}_2\text{Si}_2\text{O}_5$ | LS2 | 690-790°C |
| $\text{LiAlSi}_2\text{O}_6$ | LAS3 | 680-790°C |



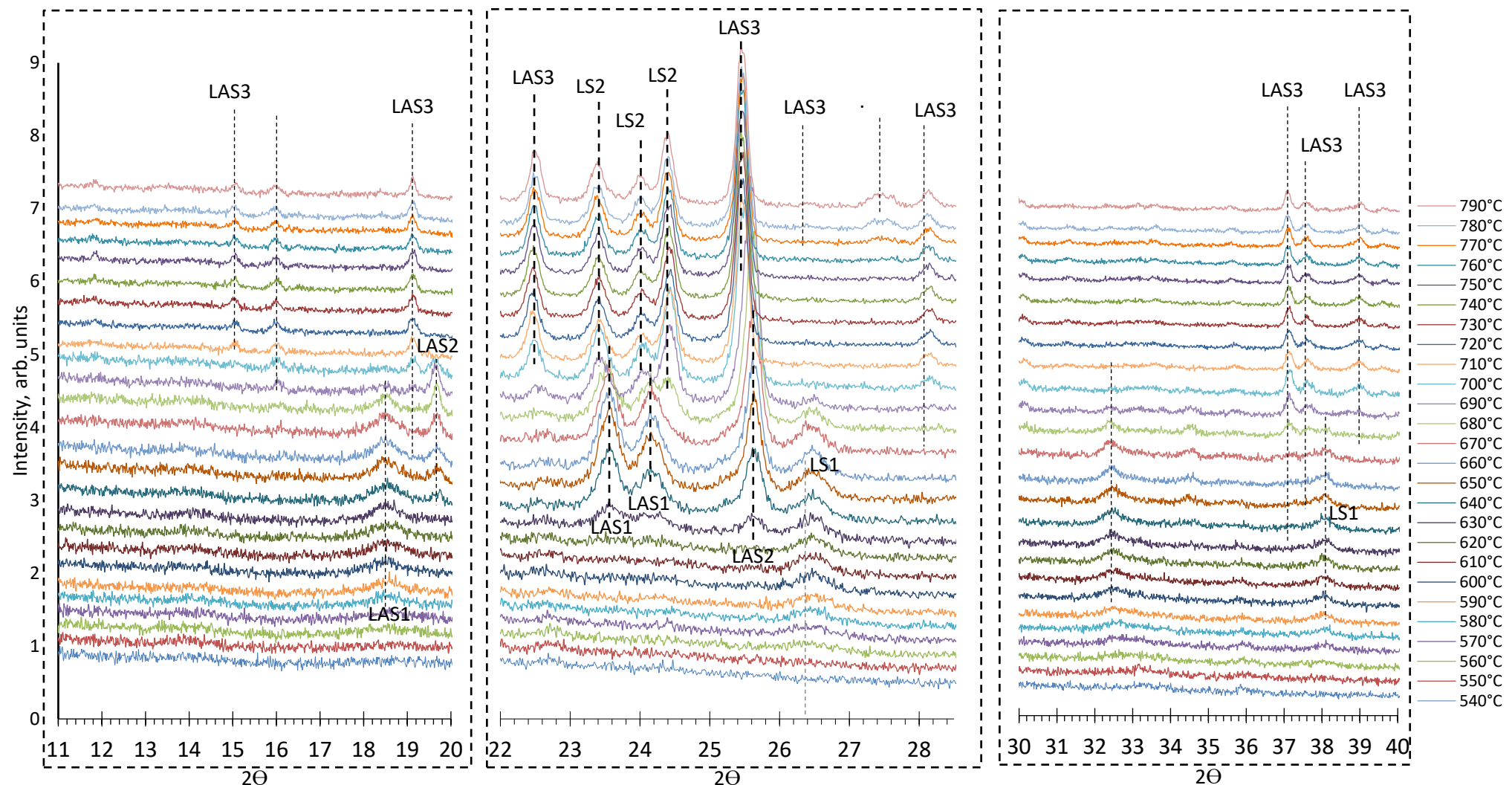


Fig. 6. 11 *In-situ* high-temperature XRD patterns of LAS2 glass heated treated from 540°C to 790°C.

6.4 Ex-situ X-ray diffraction of LAS2 glass

In this section, *ex-situ* XRD data are presented. The results can be divided into three categories. First, X-ray diffraction for as-cast LAS2 glass isothermally heat treated at 550°C for different times (0, 30 min, 150 min, 300 and 3000 min). Second, X-ray diffraction for LAS2 glass non-isothermally heat treated in the 610°C to 870°C temperature range for 30 min. Finally, X-ray diffraction for LAS2 glass isothermally heat treated at 550°C for 300 min followed by non-isothermal heat treatment in the 630°C to 870°C temperature range for 30 min.

6.4.1 Phase assemblage after isothermal heat treatments at 550°C for different times

Ex-situ X-ray diffraction data for as-cast LAS2 glass blocks and glass blocks nucleated at 550°C for different holding times: 0, 30, 150, 300 and 3000 min are shown in Fig. 6. 12. The XRD pattern for as-cast LAS2 glass consists mainly of a broad peak over the whole 2θ range, with a few but small intensity Bragg peaks. These reflections can be assigned to Li₂SiO₃ and Li₃PO₄, as labelled in Fig. 6. 12. Hence, the initial sample is mainly an amorphous solid, which however encompasses some Li₂SiO₃ and Li₃PO₄ crystals. This indicates that some devitrification takes place during the preparation of the glass specimens. No significant changes to the XRD traces are detected for samples heat treated at 550°C, even after 30 min. Nevertheless, when the holding time is increased to 150 and 300 min, the Bragg peaks assigned to Li₂SiO₃ and Li₃PO₄ increase in intensity. A holding time of 3000 min at 550°C imparts only a minimal increase on the intensity of those peaks. Therefore, based on XRD analyses, precipitation of Li₃PO₄ increases gradually with increasing nucleation holding time, reaching a near saturation after 300 min, but Li₂SiO₃ content still increases, as shown in Fig. 6. 12. Again, these analyses show LAS1 glass and LAS2 glass to exhibit a similar nucleation/crystallisation pathway.

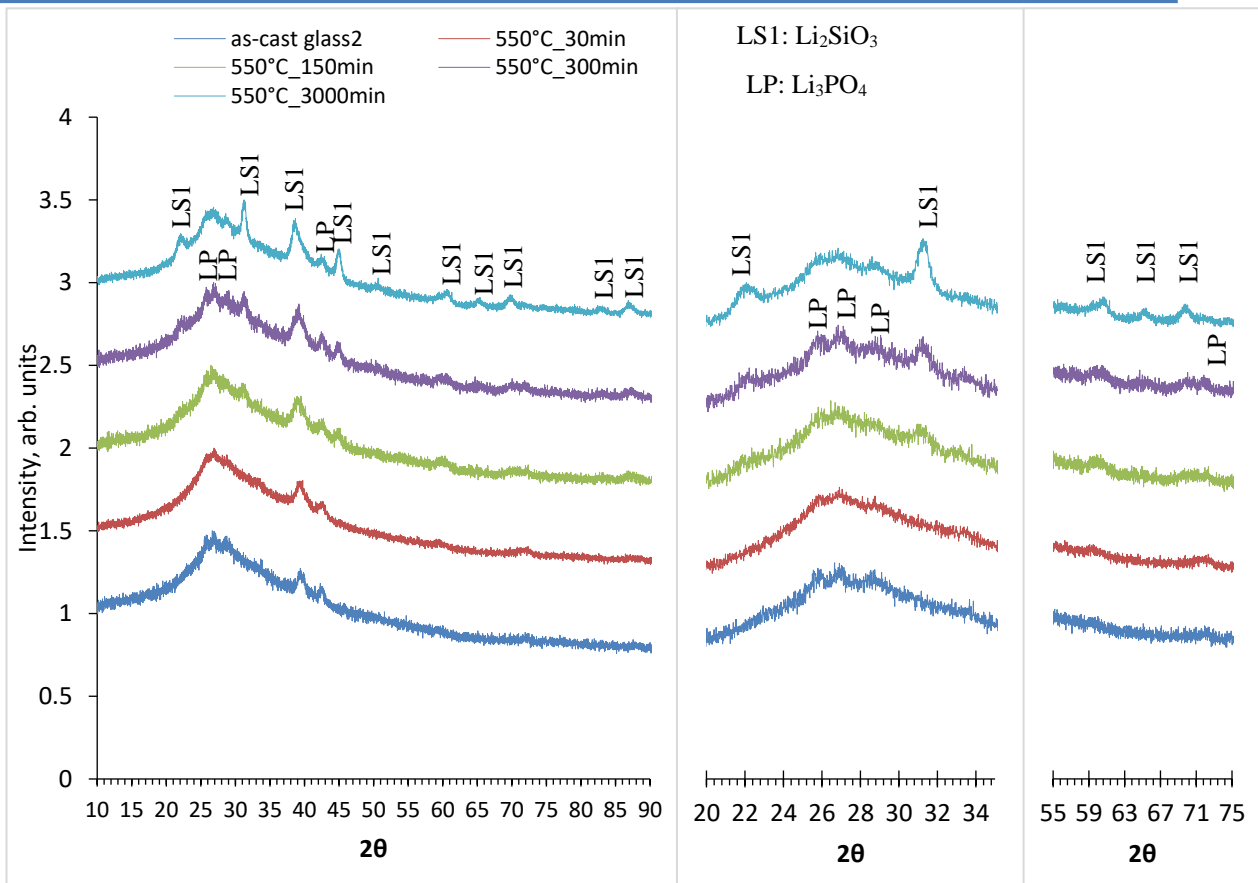


Fig. 6. 12 XRD patterns of isothermal heat treatment of LAS2 as-cast glass at 550°C for different time.

6.4.2 Phase assemblage after heat treatment for 30 min in the 610°C to 870°C temperature range

Based on the *ex-situ* XRD analysis, the only crystalline phases present in samples heat treated at 610°C and 630°C for 30 min are Li_2SiO_3 and Li_3PO_4 , as shown in Fig. 6. 13. Again, samples heat treated at 650°C for 30 min are still rather amorphous has corroborated by the broad peak and contain mainly Li_2SiO_3 and Li_3PO_4 alongside minute amounts of $\text{Li}_{0.25}\text{Al}_{0.25}\text{Si}_{0.75}\text{O}_2$. In samples heat treated at 670°C, the crystallinity level increases dramatically as indicated by the disappearance of the broad peak. This is accompanied by a significant increase of the amount of $\text{Li}_{0.25}\text{Al}_{0.25}\text{Si}_{0.75}\text{O}_2$ and the appearance of $\text{LiAlSi}_4\text{O}_{10}$, which is consistent with the first exothermic peak in DSC trace shown in Fig. 6. 1 and the *in-situ* XRD data in Fig. 6. 11. Li_2SiO_3 and Li_3PO_4 are now minor phases. The phase assemblage for samples heat treated at 690°C for 30 min is similar. $\text{Li}_{0.25}\text{Al}_{0.25}\text{Si}_{0.75}\text{O}_2$ is the major phase in samples heat treated at 710°C for 30 min. Under this conditions, $\text{Li}_2\text{Si}_2\text{O}_5$ crystals appear as indicated by the peak at $29^\circ 2\Theta$. $\text{LiAlSi}_4\text{O}_{10}$ and to a less extent $\text{LiAlSi}_2\text{O}_6$ are the minority phases. Again, this significant change in the phase assemblage is a manifestation of the sharp

exothermic event at 705°C visible in Fig. 6. 1, and it is also in agreement with the *in-situ* X-ray diffraction data shown in 6. 11. This is also coincident with modifications to optical properties, shown in Fig. 6. 35. Basically, the material changes from a semi-transparent glass to a creamy glass-ceramic. $\text{Li}_{0.25}\text{Al}_{0.25}\text{Si}_{0.75}\text{O}_2$ and $\text{LiAlSi}_4\text{O}_{10}$ are no longer detectable in samples heat treated at 730°C for 30 min. However, vestiges Li_2SiO_3 and Li_3PO_4 are still present. Samples heat treated at temperatures greater than 730°C consist mainly of $\text{LiAlSi}_2\text{O}_6$ followed by $\text{Li}_2\text{Si}_2\text{O}_5$, plus some vestiges of Li_3PO_4 and Li_2SiO_3 .

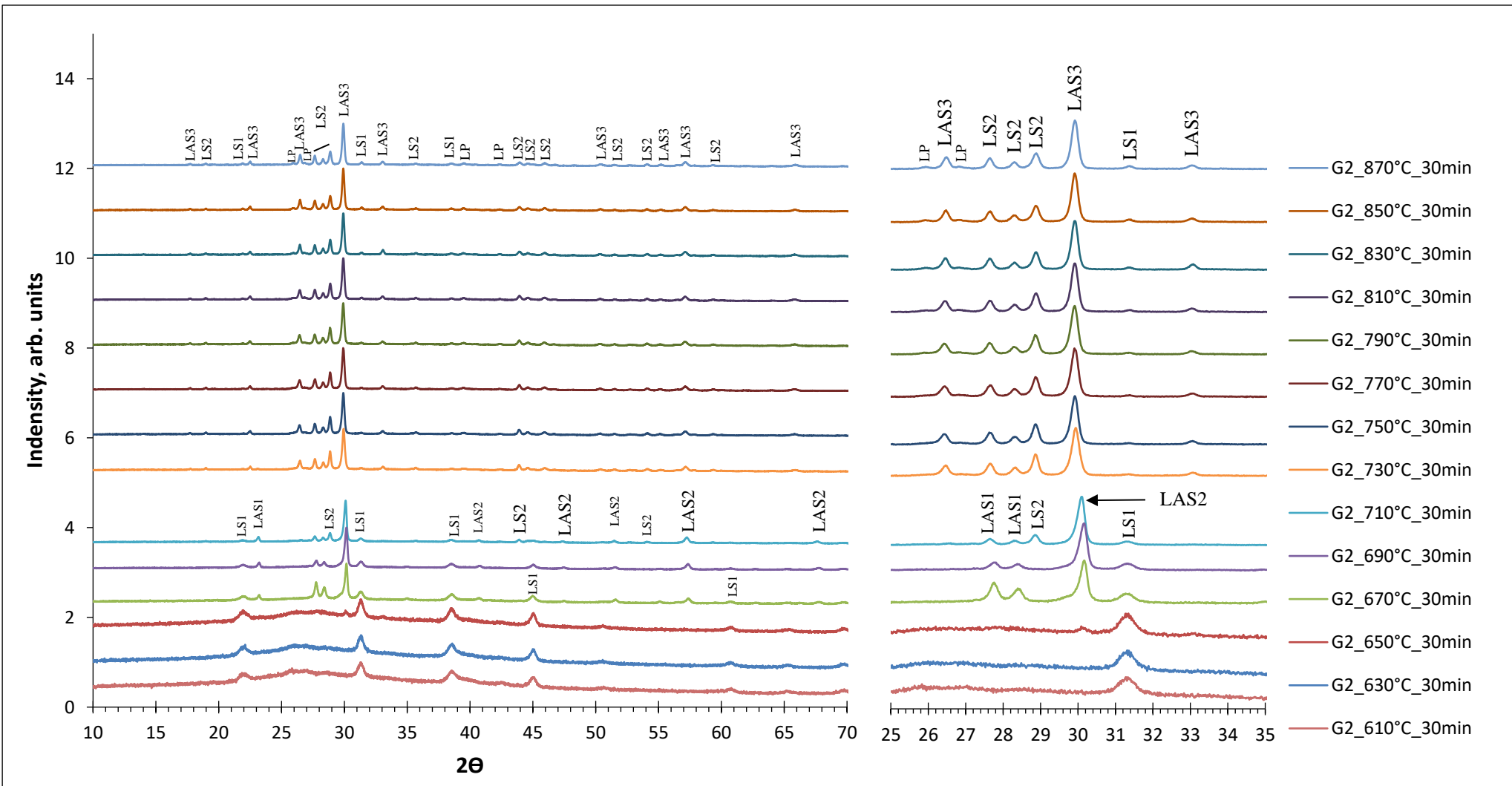


Fig. 6. 13 Room-temperature XRD patterns for samples heat treated for 30 min in the 610°C to 870°C temperature range.

6.4.3 Phase assemblage after nucleation at 550°C for 300 min followed by heat treatments for 30 min in the 630°C to 870°C temperature range

The impact of nucleation at 550°C for 300 min on the phase evolution was also evaluated by *ex-situ* XRD analysis for samples heated treated for 30 min in the 630°C to 870 °C temperature range. These results can be directly compared with those given in section 6.4.2 for non-nucleated samples. Non-nucleated and nucleated samples heated treated at 630°C have similar phase assemblage, with Li_2SiO_3 and Li_3PO_4 as the major phases. Nevertheless, some differences on the phase assemblage are detected for samples heat treated between 650°C and 710°C, as summarised below:

- The primary phase in the nucleated sample heat treated at 650°C is $\text{LiAlSi}_4\text{O}_{10}$ followed by $\text{Li}_{0.25}\text{Al}_{0.25}\text{Si}_{0.75}\text{O}_2$. In contrast, Li_2SiO_3 is the major phase present in the non-nucleated sample. This is consistent with the suppression of the first exothermic event upon nucleation as shown in Fig. 6. 2.
- The primary phase in the nucleated sample heat treated at 670°C is $\text{Li}_{0.25}\text{Al}_{0.25}\text{Si}_{0.75}\text{O}_2$, followed by $\text{LiAlSi}_4\text{O}_{10}$ and some residual Li_2SiO_3 . In the non-nucleated counterpart, $\text{Li}_{0.25}\text{Al}_{0.25}\text{Si}_{0.75}\text{O}_2$ is also the major phase.
- $\text{Li}_2\text{Si}_2\text{O}_5$ is already present at 690°C in nucleated samples, whereas in non-nucleated it is only detected at 710°C and above.
- When heat treatment is carried out above 730°C, the phase assemblage is similar in both non-nucleated and nucleated samples, with $\text{LiAlSi}_2\text{O}_6$ as the primary phase.

In summary, the onset temperature for the crystallisation of $\text{Li}_2\text{Si}_2\text{O}_5$, $\text{Li}_{0.25}\text{Al}_{0.25}\text{Si}_{0.75}\text{O}_2$ and $\text{LiAlSi}_2\text{O}_6$ solid solution shifts towards lower temperatures in the nucleated samples in comparison with the non-nucleated counterparts. This shift towards lower crystallisation temperatures in the case of nucleated samples is consistent with the DSC data presented in Fig. 6. 1 and 6. 2, for non-nucleated and nucleated LAS2 glass, respectively. A similar trend was observed for LAS1 glass as shown in chapter 5. These results imply that the nucleation stage at 550°C for 300 min plays an important role in the subsequent formation of crystalline phases.

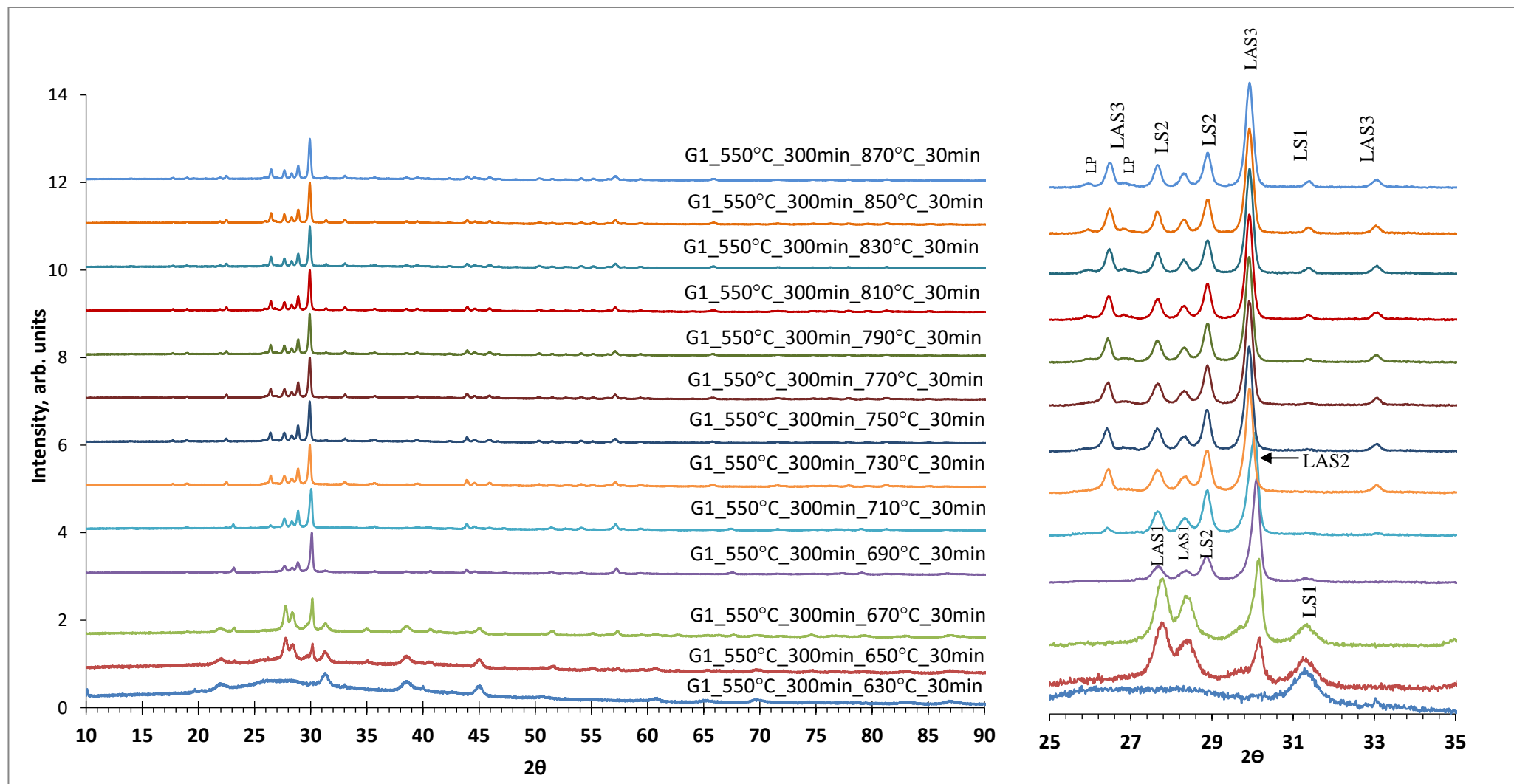


Fig. 6.14 Room-temperature XRD patterns for samples nucleated at 550 for 300 min followed by heat treatment of 30 min in the 630°C to 870°C temperature range.

6.4.4 Crystallization pathway at 670°C

DSC data in Fig. 6. 1 combined with X-ray diffraction data in Fig. 6. 13 imply an intricate crystallisation process around 670°C. Hereafter, phase assemblage evolution in function of time for samples heat treated at 670°C is investigated. This will inform on underlying crystallisation pathway of LAS2 glass. X-ray diffraction data acquired from samples heat treated for 0, 5, 15, 30, 90 minutes at 670°C are given in Fig. 6. 15.

The sample heat treated at 670°C with a zero holding time is mostly amorphous but contains vestiges of Li_2SiO_3 and Li_3PO_4 . These two phases are originally present in the LAS2 glass blocks, as shown in Fig. 6. 12. After 5 minutes at 670°C, three new peaks appear at 27.7° , 28.4° and $30.1^\circ 2\Theta$. The latter can be attributed to $\text{Li}_{0.25}\text{Al}_{0.25}\text{Si}_{0.75}\text{O}_2$, whereas the two first peaks are linked with $\text{LiAlSi}_4\text{O}_{10}$. Nonetheless, Li_2SiO_3 is still the dominant phase. Based on the DSC trace, shown in Fig. 6. 1, this crystallisation of multiple phases is consistent with the asymmetry displayed by the first exothermic peak. This points out towards existence of at least two sub-peaks within the first exothermic peak in the DSC trace.

After 15 minutes at 670°C, $\text{Li}_{0.25}\text{Al}_{0.25}\text{Si}_{0.75}\text{O}_2$ becomes and remains the main phase even for longer holding times. In fact, no apparent changes to the phase assemblage are noticeable after 30 min at 670°C. This experiment allows to follow the sequential crystallisation pathway.

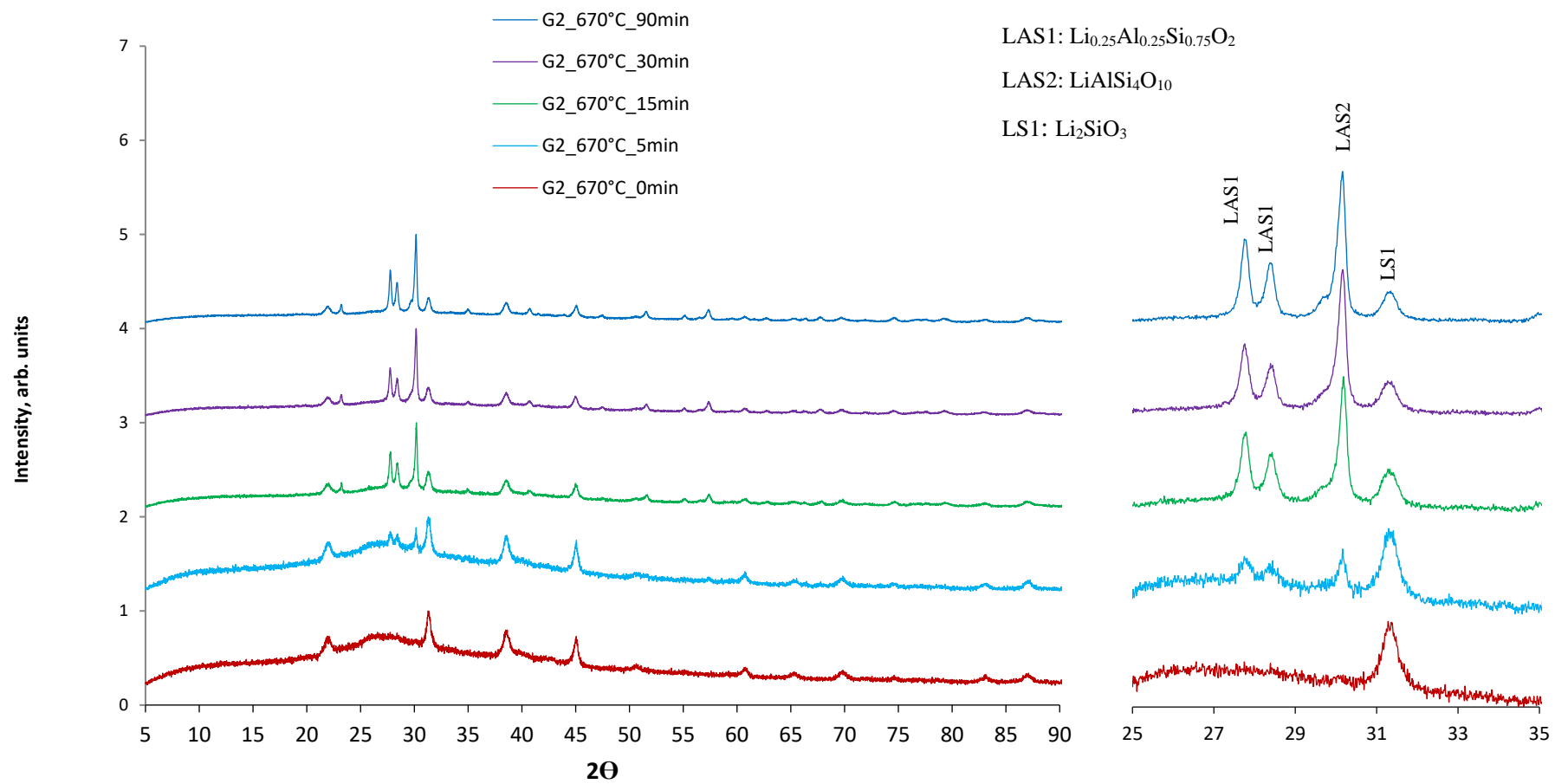


Fig. 6. 15 XRD patterns for LAS2 glass for different isothermal holding times at 670°C.

6.4.5 Median crystallite size evolution for $\text{LiAlSi}_4\text{O}_{10}$, $\text{Li}_{0.25}\text{Al}_{0.25}\text{Si}_{0.75}\text{O}_2$ and Li_2SiO_3 heat treated at 670°C

Fig. 6. 16 shows the evolution of the FWHM for the main Bragg peaks associated with $\text{Li}_{0.25}\text{Al}_{0.25}\text{Si}_{0.75}\text{O}_2$ (LAS2) alongside $\text{LiAlSi}_4\text{O}_{10}$ (LAS1) and Li_2SiO_3 (LS1) held at 670°C for different lengths of time, as illustrated in Fig. 6. 15. For $\text{LiAlSi}_4\text{O}_{10}$, FWHM decreases gradually, which is indicative of a continuous increase of crystallite size, reaching ~50 nm after 90 min, as shown in Fig. 6. 17.

It is found that crystal size of $\text{Li}_{0.25}\text{Al}_{0.25}\text{Si}_{0.75}\text{O}_2$ increases from 20 nm to ~ 60 nm after 30 minutes, as shown in Fig. 6. 17. After this the growth of $\text{Li}_{0.25}\text{Al}_{0.25}\text{Si}_{0.75}\text{O}_2$ is limited. The initial growth rate of $\text{Li}_{0.25}\text{Al}_{0.25}\text{Si}_{0.75}\text{O}_2$ and $\text{LiAlSi}_4\text{O}_{10}$ is ~ 1.44 and 0.31 nm/min, respectively, but for LAS2 it nearly ceases after 30 minutes. On the other hand, the crystal size of Li_2SiO_3 remains constant at ~ 14 nm, as shown in Fig. 6. 17. It is worth mentioning that as for large crystals the equation might not work properly.

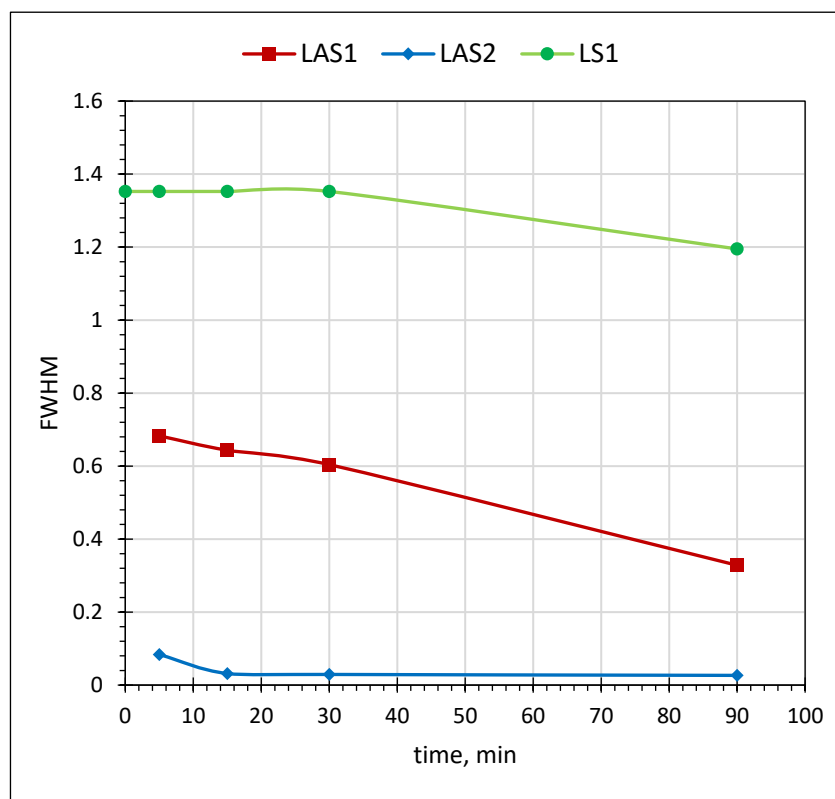


Fig. 6. 16 FWHM of $\text{LiAlSi}_4\text{O}_{10}$ (LAS1), $\text{Li}_{0.25}\text{Al}_{0.25}\text{Si}_{0.75}\text{O}_2$ (LAS2) and Li_2SiO_3 (LS1) upon heating at 670°C.

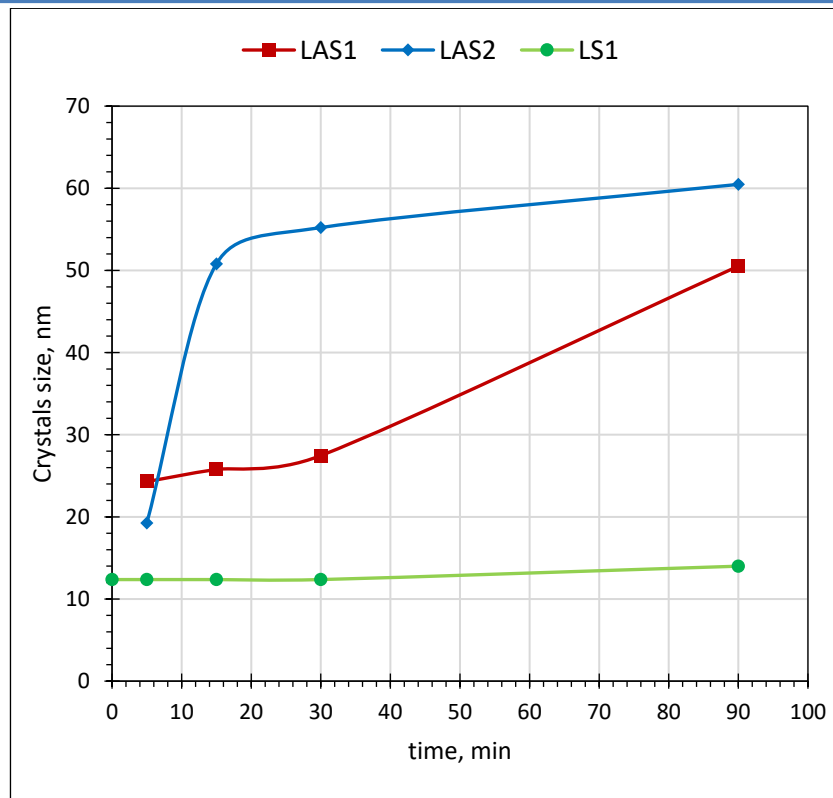


Fig. 6. 17 Time dependence of the median crystallite size of $\text{LiAlSi}_4\text{O}_{10}$ (LAS1), $\text{Li}_{0.25}\text{Al}_{0.25}\text{Si}_{0.75}\text{O}_2$ (LAS2) and Li_2SiO_3 (LS1) upon heating at 670°C.

6.4.6 Evolution of the crystallite size for $\text{LiAlSi}_2\text{O}_6$

Fig. 6. 13 and 14 showed that $\text{LiAlSi}_2\text{O}_6$ to be the dominant phase in samples heat treated above 730°C. The evolution of FWHM for the $\text{LiAlSi}_2\text{O}_6$ Bragg peak located at 29.00°-31° 2 Θ in terms of heat treatment is illustrated Fig. 6. 18. Again, these values can be incorporated in the Scherrer equation to calculate the median crystallite size. The results are shown in Fig. 6. 19. In nucleated samples, $\text{LiAlSi}_2\text{O}_6$ appears to increase size, reaching a maximum of ~80 nm after 30 min at 790°C. Above this temperature the size remains constant. In contrast, in non-nucleated samples $\text{LiAlSi}_2\text{O}_6$ appears only reaches a maximum of ~80 nm after 30 min at 850°C. This result shows how important is nucleation to achieve larger $\text{LiAlSi}_2\text{O}_6$ crystals at lower temperatures. In principle, this should render improved mechanical properties for heat treatments carried out at lower temperatures.

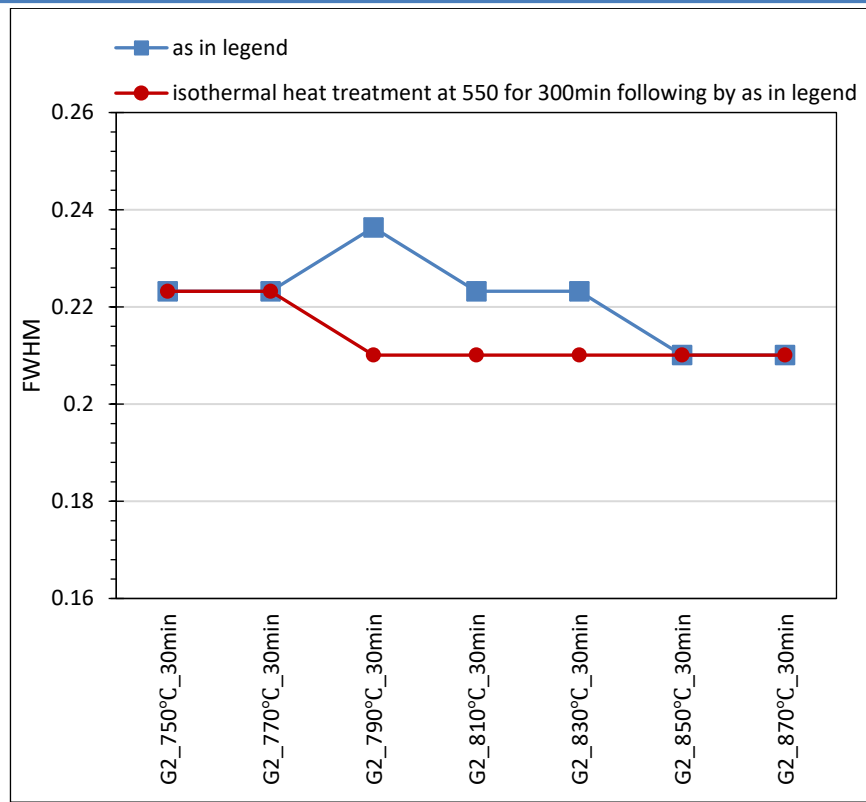


Fig. 6. 18 Evolution of FWHM for the $\text{LiAlSi}_2\text{O}_6$ Bragg peak located at $29.00^\circ\text{-}31^\circ 2\Theta$ in terms of heat treatment.

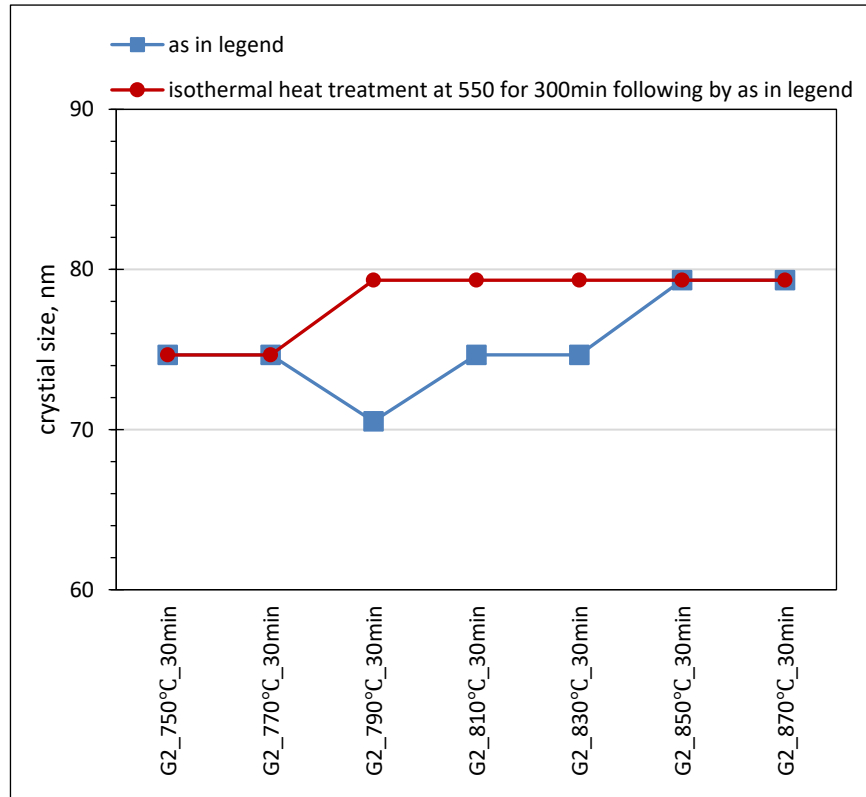


Fig. 6. 19 Median crystallite size of $\text{LiAlSi}_2\text{O}_6$ in function of temperature.

6.4.7 XRD peak intensity ratio for $\text{LiAlSi}_2\text{O}_6/\text{Li}_2\text{Si}_2\text{O}_5$ between 730 and 850 °C

DSC data, Fig. 6. 1, combined with X-ray diffraction data, Fig. 6. 13, show the almost simultaneous crystallisation of $\text{LiAlSi}_2\text{O}_6$ and $\text{Li}_2\text{Si}_2\text{O}_5$ around 700°C. The relative amount of each phase can be roughly estimated by the intensity ratios of the main Bragg peaks associated with each phase, which for $\text{LiAlSi}_2\text{O}_6$ is located at $29^\circ\text{-}31^\circ 2\Theta$ and for $\text{Li}_2\text{Si}_2\text{O}_5$ is located at $27.5^\circ\text{-}29.5^\circ 2\Theta$, as shown in Fig. 6. 13 and Fig. 6. 14, for non-nucleated and nucleated, respectively. The ratios are graphically summarized in Fig. 6. 20, for samples heat treated in the 730°C-870°C temperature.

In general, the ratios show:

- $\text{LiAlSi}_2\text{O}_6$ becomes dominant with increasing temperature.
- Nucleation leads to a larger relative amount of $\text{LiAlSi}_2\text{O}_6$.

A sudden drop in the ratio was observed above 850°C, for nucleated samples, which is not fully understood, but may be linked to approaching the melting temperature.

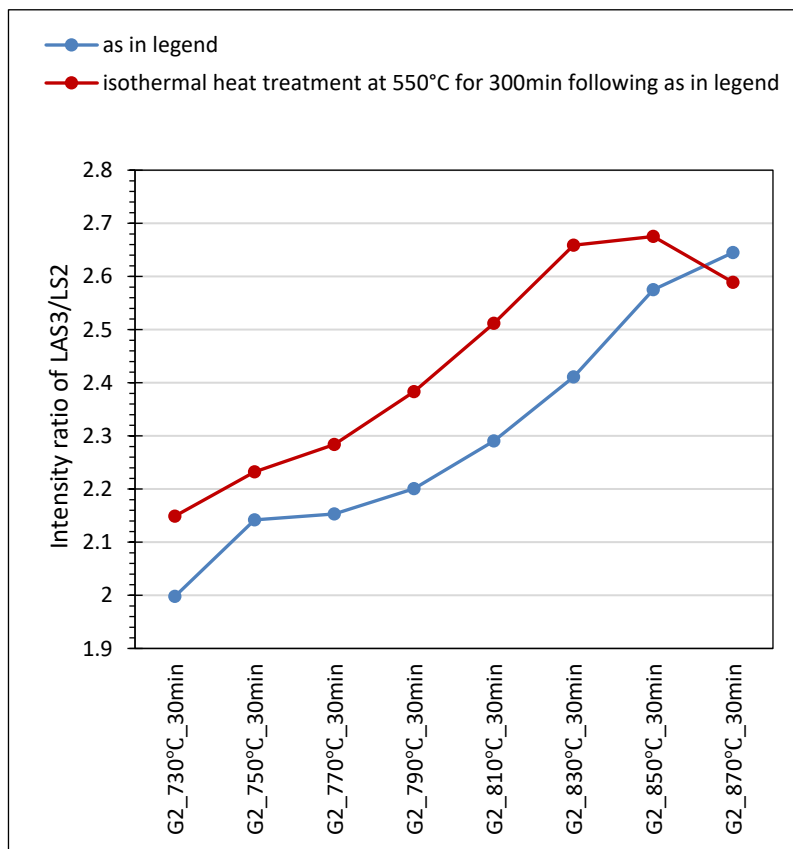


Fig. 6 20 Intensity of $\text{LiAlSi}_2\text{O}_6/\text{Li}_2\text{Si}_2\text{O}_5$ ratios.

6.5 Raman spectroscopy of LAS2 glass

Raman spectroscopy is employed here to further ascertain the nature of the crystals precipitated upon heat-treatment. Compared with X-ray diffraction analysis, Raman spectroscopy provides a local probe with better detections limits, therefore it may help provide an earlier detection of a crystallisation process. Raman spectra were acquired from the as-cast, nucleated glass and fully heated treated LAS2 glasses. The main Raman modes were assigned according to data in the literature, as listed in Table 5. 3 in Chapter 5, and are used to fingerprint the phase assemblage.

6.5.1 Impact of time on the nucleation at 550°C

The X-ray diffraction data in Fig. 6. 12 suggest the as-cast LAS2 glass to contain some Li_3PO_4 and Li_2SiO_3 crystals. Their presence can be confirmed by the presence of some Raman modes specific for each phase. Based on Table 5. 3, the modes at 607 and 979 cm^{-1} provide a compelling signal to monitor the presence of Li_2SiO_3 . On the other hand, the presence of Li_3PO_4 can be probed by monitoring a mode at 950 cm^{-1} .

Raman spectra shown in Fig. 6. 21, feature modes at ~ 488 , 610 , 950 and 980 cm^{-1} . The mode at 488 cm^{-1} may be indicative of the presence of $\text{LiAlSi}_4\text{O}_{10}$, which was not previously identified by the X-ray diffraction data. Hence, the as-cast LAS2 glass contains Li_2SiO_3 , Li_3PO_4 and possibly $\text{LiAlSi}_4\text{O}_{10}$. With increasing time at 550°C , the mode at 610 cm^{-1} increases intensity, which corroborates an increase of the Li_2SiO_3 content. Impact of time on the nucleation at 550°C , in the section 5.5.1 and 6.5.1, reveal to exert a similar impact in LAS1 and LAS2 glasses.

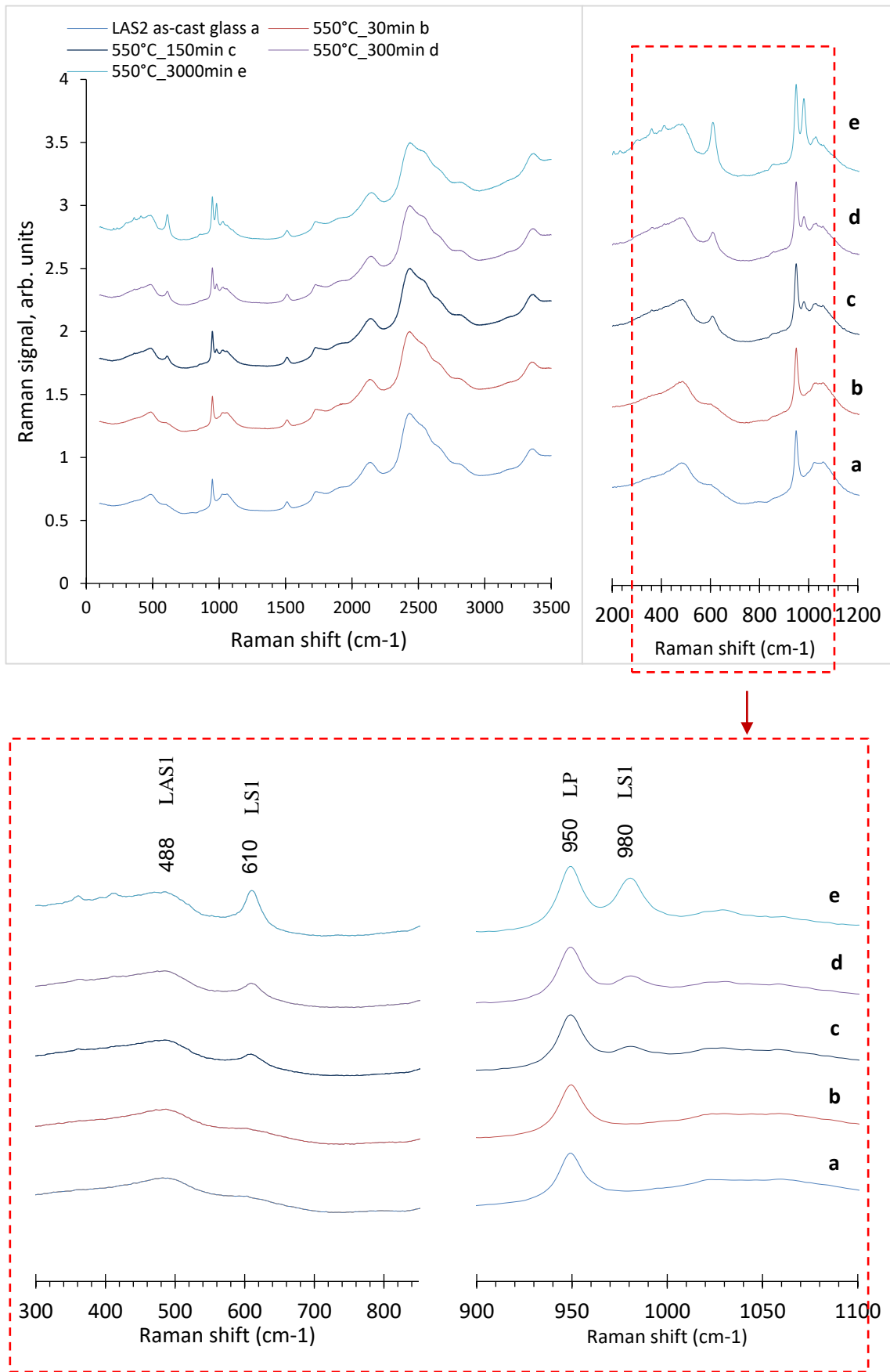


Fig. 6. 21 Raman spectra of LAS2 glass and different isothermal holding times.

6.5.2 Raman spectra for LAS2 glass heat treated for 30 minutes in 610°C to 870°C temperature range

Raman spectra presented in Fig. 6. 22 shows a band at 950 cm⁻¹ to be present from 610°C to 870°C, showing that Li₃PO₄ is constantly present. Raman data in Fig. 6. 21 shows the phase to be present in the as-cast glass. The bands at 610 cm⁻¹ and 988 cm⁻¹ are attributed to pure Li₂SiO₃ [267]. There is a mode shift to ~ 608 cm⁻¹ at 670°C, which also coincides with the increase of the ~ 488 cm⁻¹, ascribed to LiAlSi₄O₁₀ crystals [268]. At 690°C, the appearance of new band at ~ 416, 550 and 1109 cm⁻¹ corroborate the appearance of Li₂Si₂O₅ [270]. The shift of the 488 cm⁻¹ mode to 495 cm⁻¹ at 730°C is consistent with a solid solution between Li_{0.25}Al_{0.25}Si_{0.75}O₂ and LiAlSi₂O₆. However, pure LiAlSi₂O₆ shows a mode at 492 cm⁻¹ [208], [209].

6.5.3 Raman spectra for LAS2 glass nucleated at 550°C for 30 minutes and then heat treated for 30 minutes in 630°C to 870°C temperature range

The Raman spectra of the nucleated samples, as shown in Fig. 6. 23 are similar to Raman spectra of non-nucleated samples in Fig. 6. 22. Nevertheless, new modes appear at 690°C instead of 710°C, which is consistent with XRD data.

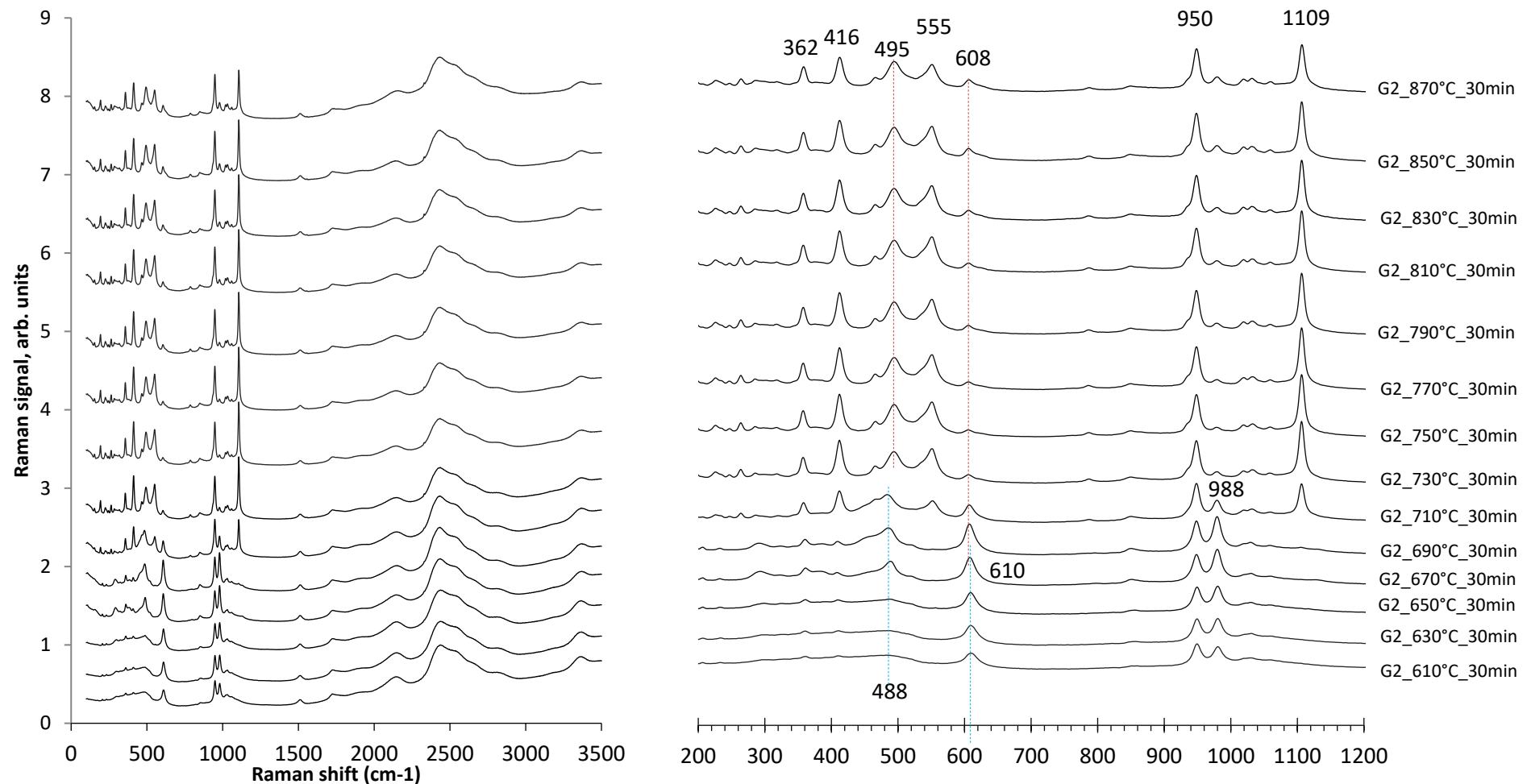


Fig. 6. 22 Raman spectra for LAS2 glass heat treated for 30 minutes in 610°C to 870°C temperature range.

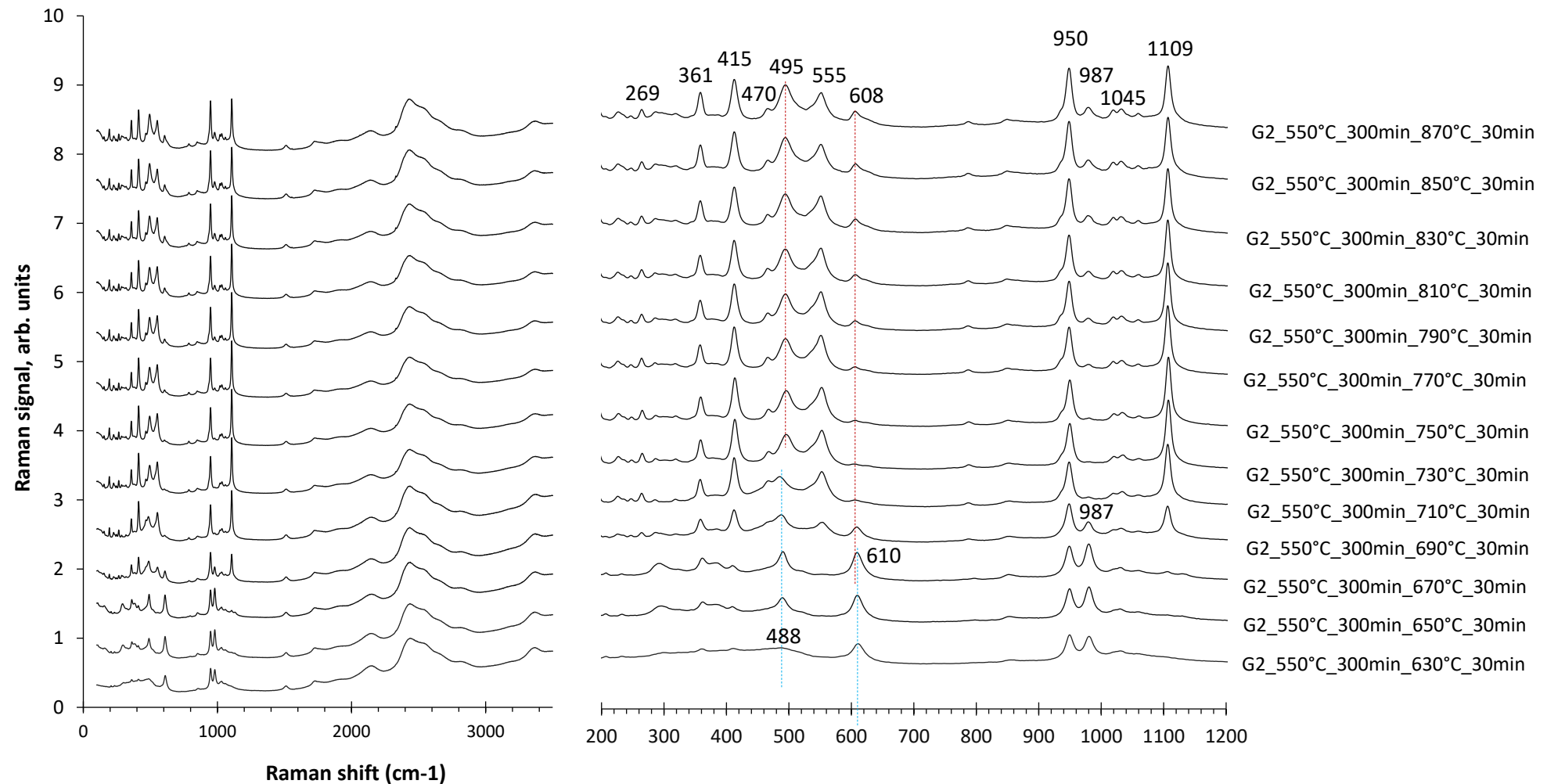


Fig. 6. 23 Raman spectra for LAS2 glass nucleated at 550°C for 30 minutes and then heat treated for 30 minutes in 630°C to 870°C temperature range.

6.5.4 Isothermal heat treatment at 670°C for different holding time

Based on the Raman spectra, in Fig. 6. 24, many bands for a treatment at 670°C for 0, 5, 15, 30 and 90 min are assigned to Li₂SiO₃ and Li₃PO₄, as in section 5.4.1. Based on the DSC trace, shown in Fig. 6. 1, this is consistent with the first exothermic peak. However, treatments at 670°C for 15, 30 and 90 min show a new band at about 488 cm⁻¹, this is LiAlSi₄O₁₀ crystals (488 cm⁻¹ in [268]).

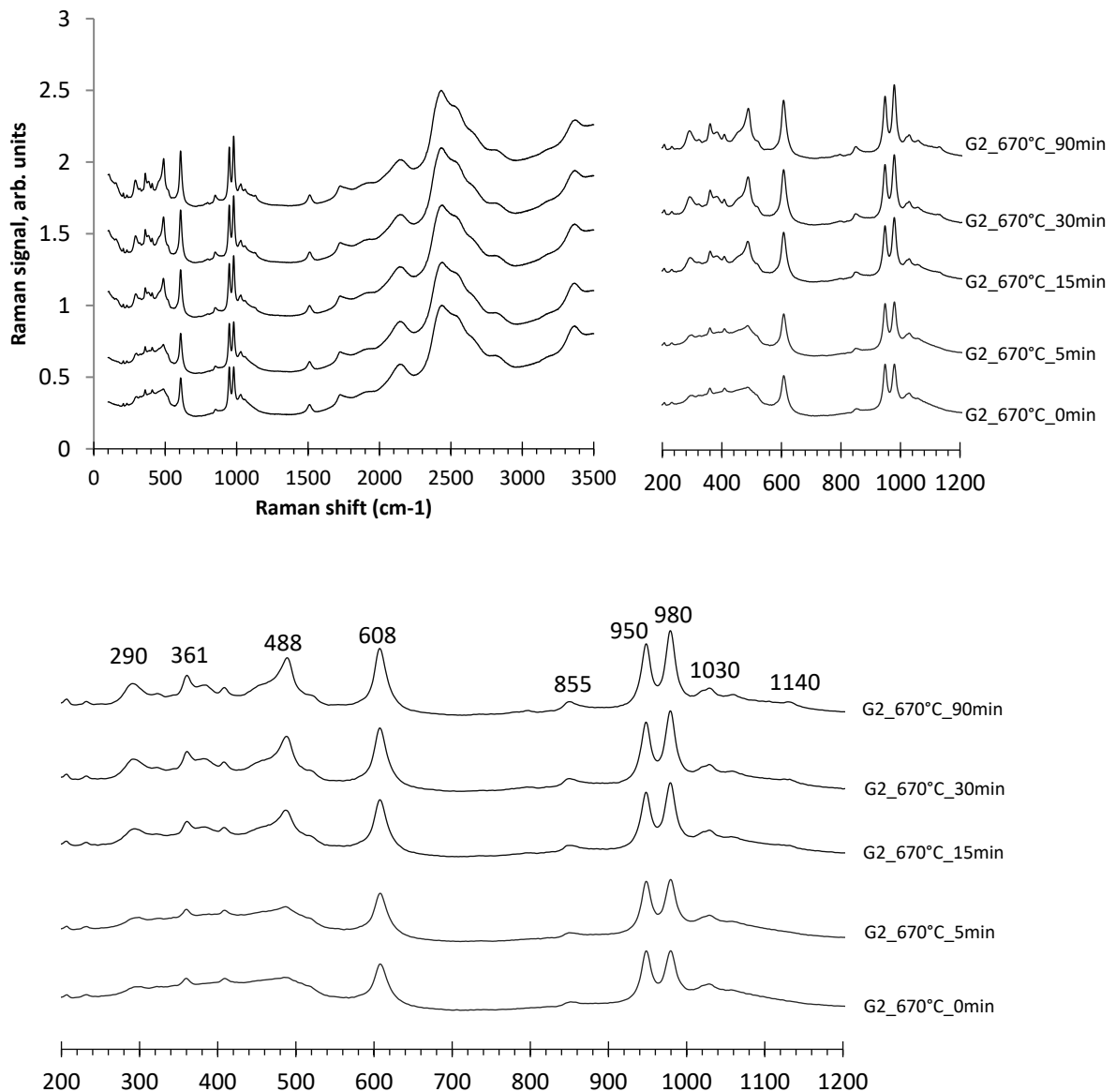


Fig. 6. 24 Raman spectra of isothermal heat treatment of LAS2 as-cast glass at 670°C for different times.

6.6 Mechanical properties of LAS2 glass

6.6.1 Elastic modulus

In this section, elastic modulus values determined by ultrasound measurements as described in section 5.6.1. Elastic modulus calculation method by ultrasound speed can be found in Appendix 4.

6.6.1.1 Elastic modulus after isothermal heat treatments at 550°C for different holding times

The as-cast LAS2 glass shows the lowest elastic modulus, E, around 79.8 ± 0.1 GPa. Upon nucleation at 550°C for 30, 150, 300 and 3000 min, E increases to 79.87 ± 0.21 GPa, 81.33 ± 0.15 , 81.8 ± 0.1 GPa and 82.5 ± 0.01 GPa, respectively, as shown in Fig. 6. 25.

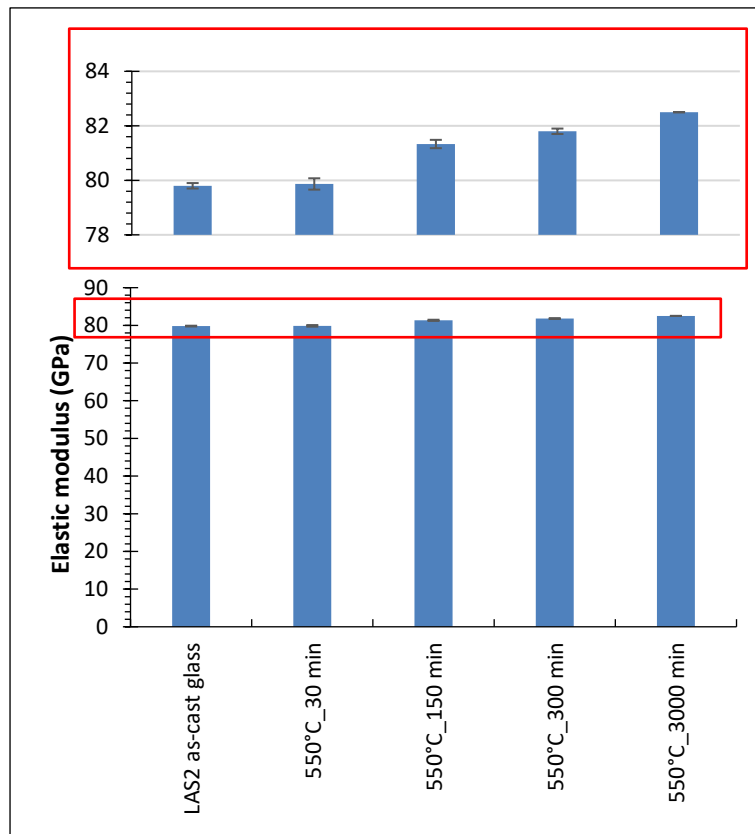


Fig. 6. 25 Elastic modulus after isothermal heat treatments at 550°C for different holding times.

This relatively small enhancement of the elastic modulus with increasing nucleation time is consistent with a limited crystallisation of Li_2SiO_3 and Li_3PO_4 phases, as shown in Fig. 6. 12. These phases promote strength of the glass structure in comparison with the as-cast glass.

6.6.1.2 Elastic modulus after heat treatment for 30 min in the 630°C to 870°C temperature range

The evolution of elastic modulus for LAS2 glass as a function of the non-isothermal heat treatment is shown in Fig. 6. 26. Samples heat-treated between 630°C and 690°C for 30 min only show a slightly increase of E from $\sim 85.01 \pm 0.15$ to 86.77 ± 0.25 GPa, respectively. Based on the Ex-situ XRD analysis, Fig. 6. 13,

samples heat treated at 630°C for 30 min are still rather amorphous, with a small content of Li_2SiO_3 and Li_3PO_4 . Samples heat treated at 650°C for 30 min, start to show minute amounts of $\text{Li}_{0.25}\text{Al}_{0.25}\text{Si}_{0.75}\text{O}_2$ and $\text{LiAlSi}_4\text{O}_{10}$ alongside Li_2SiO_3 and Li_3PO_4 embedded in a still amorphous matrix. In contrast, samples heat treated at 670°C are much more crystalline and consist mainly of $\text{Li}_{0.25}\text{Al}_{0.25}\text{Si}_{0.75}\text{O}_2$ and $\text{LiAlSi}_4\text{O}_{10}$, with some residual Li_2SiO_3 and Li_3PO_4 . The phase assemblage for samples heat treated at 690°C for 30 min is also similar. Nevertheless, this phase assemblage appears to only have a minor impact on the E values, which reach a maximum of 86.77 ± 0.25 GPa. In contrast, the phase assemblage resulting from heat-treatment at 710°C and 730°C, that is accompanied by the crystallisation of $\text{Li}_2\text{Si}_2\text{O}_5$ and $\text{LiAlSi}_2\text{O}_6$, leads to a considerable increase of E, first to 91.67 ± 0.15 GPa and then to 95.2 ± 0.1 GPa.

The elastic modulus for heat treatments between 750°C and 790°C for 30 min are almost constant in the 95-96 GPa range, however E remains relatively constant above 790°C, as illustrated in Fig. 6. 26.

Hence, elastic modulus in LAS2 glass after heat treatment for 30 min is similar to that of LAS1 glass.

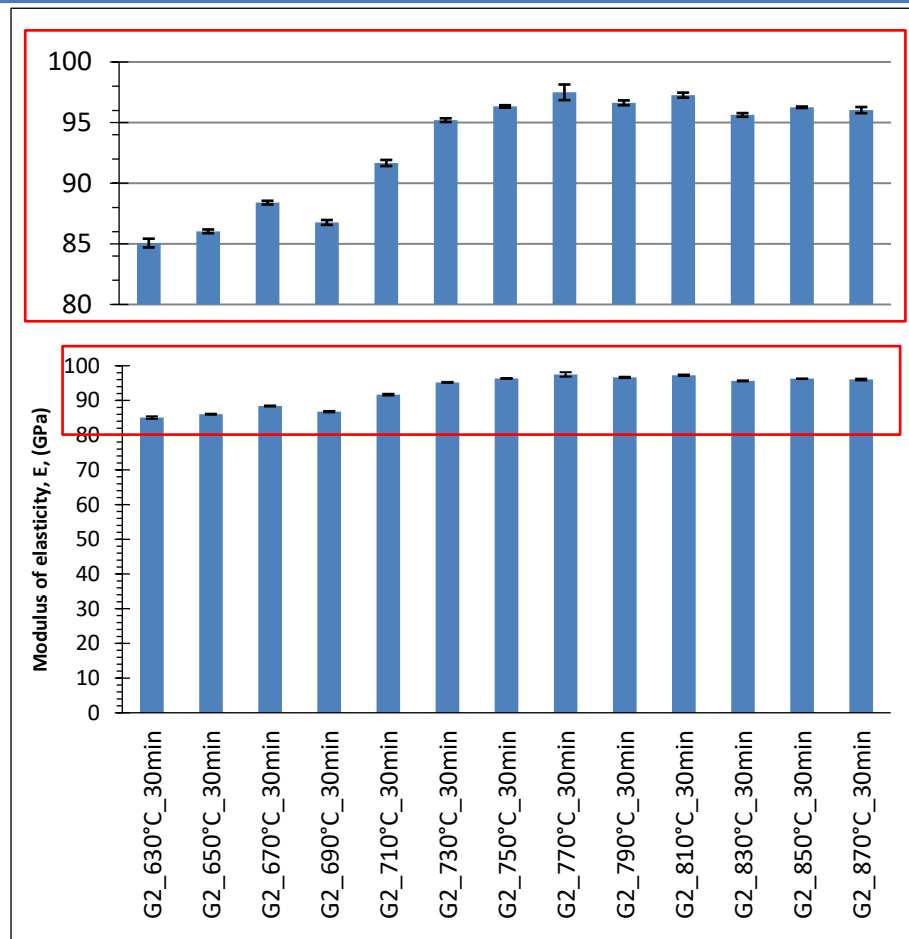


Fig. 6. 26 Elastic modulus of non-isothermal heat treatment of LAS2 glass for 30min with the temperature evolution range from 630°C to 870°C.

6.6.1.3 Elastic modulus after nucleation at 550°C for 300 min followed by heat treatment for 30 min in the 630°C to 870°C temperature range

The evolution of the elastic modulus of the LAS2 glass as a function of the isothermal heat treatment (nucleation) at 550°C for 300 min followed by heat treatment for 30 min in the 630°C to 870°C temperature range is illustrated in Fig. 6. 27. In comparison with Fig. 6. 26, for non-nucleated samples, it becomes obvious that nucleation leads to an enhancement of E at lower heat -treatment temperatures. This agrees with the fact that crystallisation of $\text{Li}_{0.25}\text{Al}_{0.25}\text{Si}_{0.75}\text{O}_2$, $\text{LiAlSi}_4\text{O}_{10}$, $\text{Li}_2\text{Si}_2\text{O}_5$ and $\text{LiAlSi}_2\text{O}_6$ also occur at lower temperatures in nucleated samples, as shown in Fig. 6. 14. This is especially evident for the nucleated samples heat treated at 690°C for 30 min, which show an E of 92.8 ± 0.15 GPa, compared with 86.77 ± 0.25 GPa for the non-nucleated counterparts.

Similar to the trend observed in Fig. 6. 26, nucleated samples heat treated 730°C for 30 min show the highest E values 99.2 ± 0.30 GPa, due to presence of $\text{Li}_2\text{Si}_2\text{O}_5$ and $\text{LiAlSi}_2\text{O}_6$ phases. This value is larger than the one observed for non-

nucleated. On the other hand, this is also higher than the nucleated counterparts of LAS1 glass, in Fig. 5. 28.

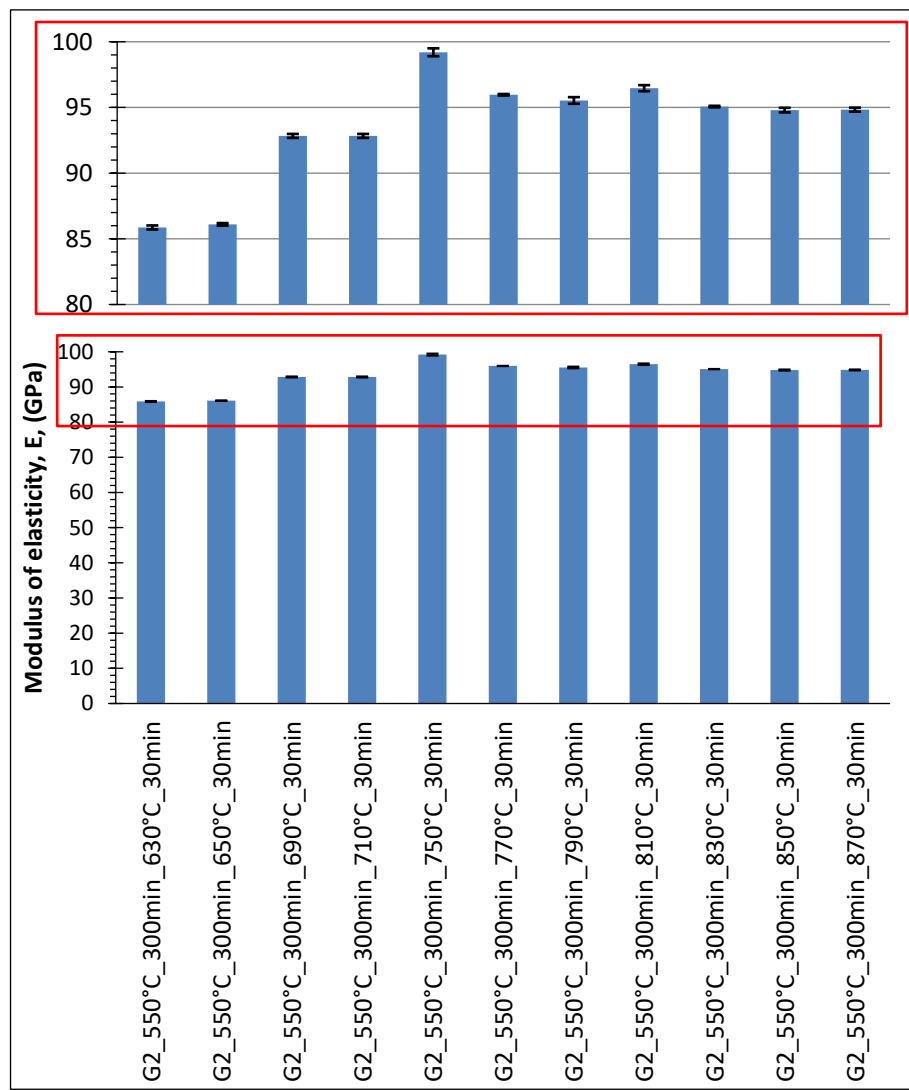


Fig. 6. 27 Elastic modulus after nucleation at 550°C for 300 min followed by heat treatment for 30 min in the 630°C to 870°C temperature.

6.6.2 Hardness

6.6.2.1 Hardness after isothermal heat treatments at 550°C for different holding times

The as-cast LAS2 glass shows the lowest $H_v \sim 5.69 \pm 0.04$ GPa. Upon nucleation at 550°C for 30, 150, 300 and 3000 min, H_v increases to 5.90 ± 0.05 GPa, 6.02 ± 0.09 , 6.90 ± 0.01 GPa and 6.10 ± 0.14 GPa, respectively, as shown in Fig. 6. 28. This reflects the evolution of E as shown in Fig. 6. 25, therefore it may also be correlated to the slight increase in Li_2SiO_3 and Li_3PO_4 content.

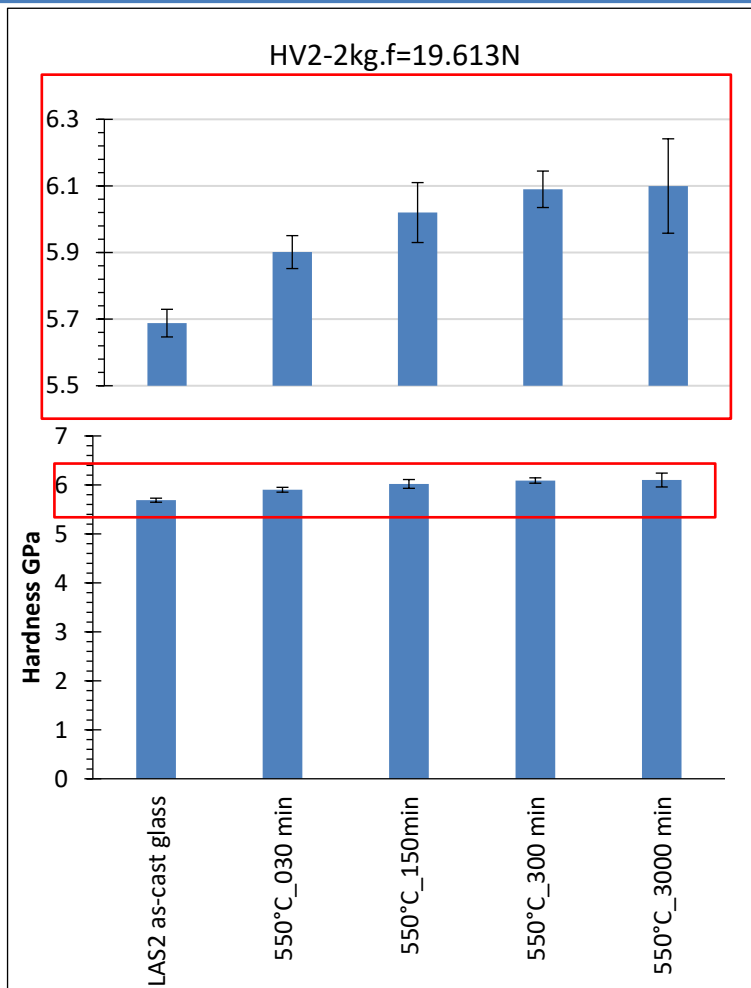


Fig. 6. 28 micro-hardness values of isothermal heat treatment of LAS2 as-cast glass at 550°C for different time.

6.6.2.2 Hardness after heat treatment for 30 min in the 630°C to 870°C temperature range

The evolution of hardness, H_v , for LAS2 glass as a function of the non-isothermal heat treatment is shown in Fig. 6. 29. The as-cast glass shows $H_v \sim 5.69 \pm 0.04$ GPa, Fig. 6. 28, which rises to 6.23 ± 0.04 GPa for samples heat-treated at 630°C for 30 min. Those samples are still relatively amorphous, with a trivial volume fraction of Li_2SiO_3 and Li_3PO_4 , as previously shown in Fig. 6.13. Conversely, samples heat treated at 670°C for 30 min, start to show tiny amounts of $\text{Li}_{0.25}\text{Al}_{0.25}\text{Si}_{0.75}\text{O}_2$ and $\text{LiAlSi}_4\text{O}_{10}$ alongside Li_2SiO_3 and Li_3PO_4 surrounded by an amorphous matrix. This is accompanied by an increase of H_v to 6.40 ± 0.24 GPa. The phase assemblage for samples heat treated at 690°C for 30 min is also similar, and interestingly H_v appears to show a larger disparity of values. This heat treatment temperature coincides with the onset of a intricate crystallisation path, leading to the eventual formation of $\text{Li}_2\text{Si}_2\text{O}_5$ and $\text{LiAlSi}_2\text{O}_6$ above 710°C. It can be speculated that local chemical and phase inhomogeneities can lead to the

observed disparity of Hv values. For samples treated between 710 and 770 °C, there is an apparent increase in Hv, which can certainly be linked to a larger content of LiAlSi₂O₆, as shown by the X-ray diffraction data in Fig. 6. 13. Interestingly, treatments above 770°C for 30 min are accompanied by a decrease in Hv, which reaches its lowest value for samples heat-treated at 870°C for 30 min. In summary, increasing heat treatment temperatures beyond 770°C results in decreasing hardness values. A similar high temperature trend was observed for nucleated samples as shown in the next section.

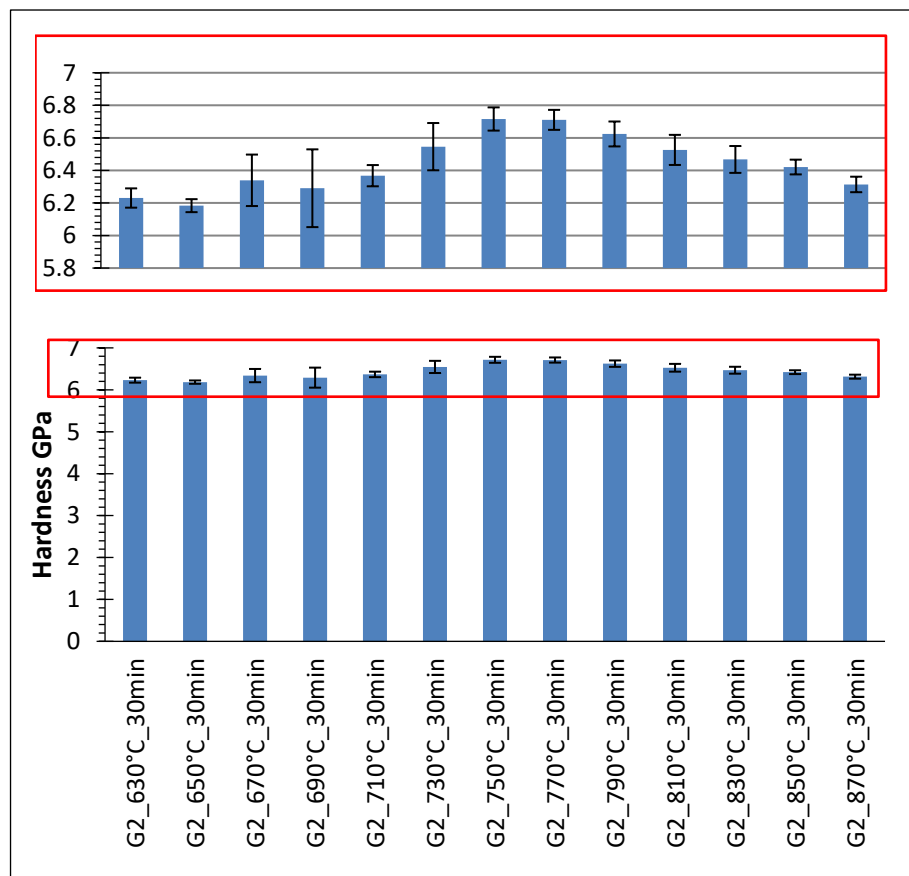


Fig. 6. 29 Hardness after heat treatment for 30 min in the 630°C to 870°C temperature range.

6.6.2.3 Hardness after nucleation at 550°C for 300 min followed by heat treatment for 30 min in the 630°C to 870°C temperature range

The evolution of hardness, Hv, for LAS2 glass as a function of the non-isothermal heat treatment for samples nucleated at 550°C for 300 min is shown in Fig. 6. 30. The sample heat-treated at 630°C for 30 min has Hv of 6.20 ± 0.04 GPa. This sample is still rather amorphous, with a small content of Li₂SiO₃ and Li₃PO₄ as previously shown in Fig. 6. 28. On the other hand, samples heat treated at 650 C for 30 min, start to show small amounts of Li_{0.25}Al_{0.25}Si_{0.75}O₂ and LiAlSi₄O₁₀

alongside Li_2SiO_3 and Li_3PO_4 , according to *Ex-situ* XRD in Fig. 6. 13. This is accompanied by an increase of H_v to 6.23 ± 0.1 GPa. In contrast, samples heat treated at 710°C , which are more crystalline and comprise primarily $\text{Li}_{0.25}\text{Al}_{0.25}\text{Si}_{0.75}\text{O}_2$ and $\text{LiAlSi}_4\text{O}_{10}$, with some remaining Li_2SiO_3 and Li_3PO_4 show a decrease in H_v . At higher temperatures, the crystallisation of $\text{Li}_2\text{Si}_2\text{O}_5$ and $\text{LiAlSi}_2\text{O}_6$ crystals leads to an increase of H_v up to 6.6 ± 0.07 GPa at 770°C . Again, above this temperature, H_v drops. The hardness of LAS2 glass after heat treatment for 30 min is similar to that of LAS1 glass, however, LAS2 glass shows slightly higher H_v values.

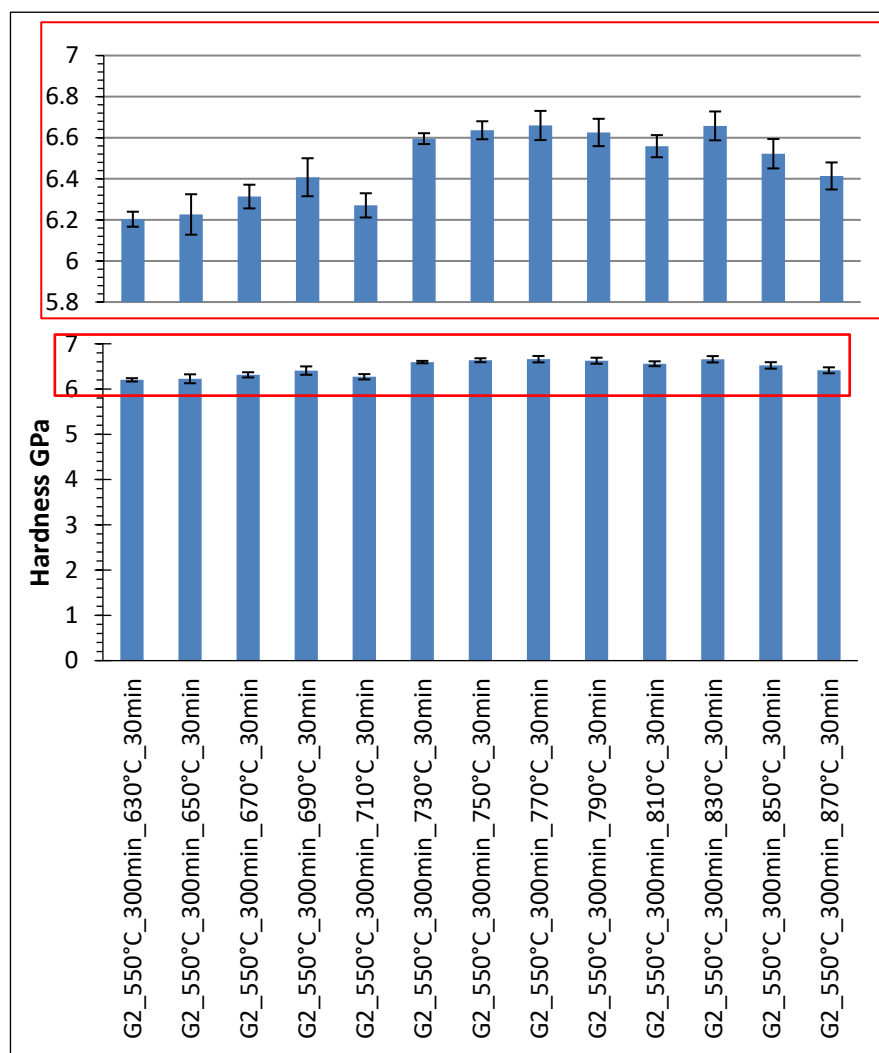


Fig. 6. 30 Hardness after nucleation at 550°C for 300 min followed by heat treatment for 30 min in the 630°C to 870°C temperature range.

6.6.3 Fracture Toughness

Fracture toughness, K_{IC} , was determined by the Vickers Indentation Fracture (VIF) method, using 6 indentations created by an applied load of $2\text{kg.f} = 19.61\text{N}$, as detailed in the section 4.5.2. Several formulas exist to estimate K_{IC} , as

presented in section 3.2.2.1. The so-called Anstis formula, $K_{IC} = 0.016 (E/HV)^{0.5} \cdot P/c^{1.5}$, which is often employed for dental materials, is used in this section, however K_{IC} values calculated by other formulas can be found in Appendix 7.

6.6.3.1 Fracture toughness after isothermal heat treatments at 550°C for different holding times

Fig. 6. 31 shows the evolution of K_{IC} values for as-cast LAS2 glass as a function of isothermal heat treatment 550°C for different times. Since fracture toughness shows that LAS2 and LAS1 glasses to exhibit similar behaviour, the interpretation will be same as in the section 5.6.3.1.

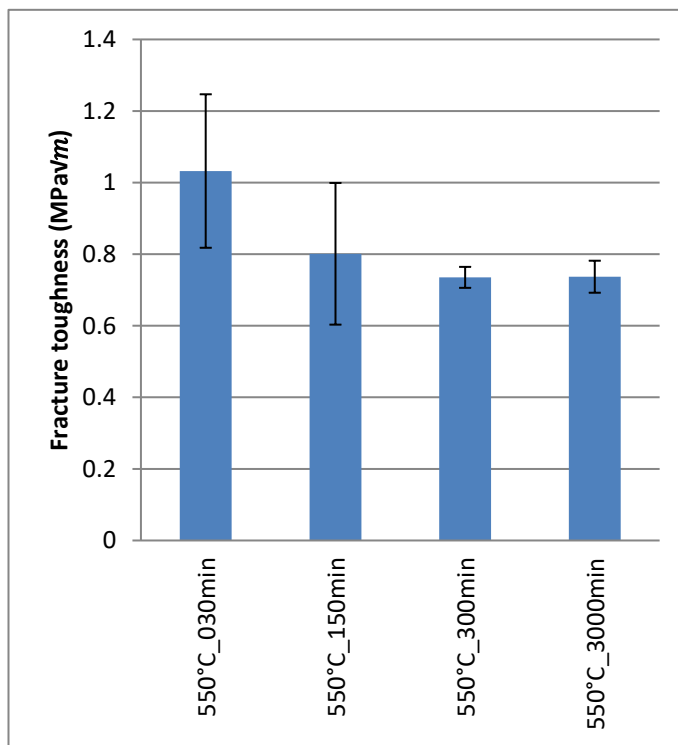


Fig. 6. 31 fracture toughness of isothermal heat treatment of LAS2 as-cast glass at 550°C for different time.

6.6.3.2 Fracture toughness after heat treatment for 30 min in the 630°C to 870°C temperature range

The evolution of K_{IC} for LAS2 glass as a function of the heat treatment for 30 minutes in 630°C to 870°C temperature range is shown in Fig. 6. 32. Samples heat-treated between 630°C show a K_{IC} of $0.74 \pm 0.08 \text{ MPa}\sqrt{\text{m}}$, which is commensurate with a rather amorphous material containing minor amounts of Li_2SiO_3 and Li_3PO_4 , as shown by X-ray diffraction data in Fig. 6. 13.

Samples heat treated at 650°C for 30 min, start to show small amounts of $\text{Li}_{0.25}\text{Al}_{0.25}\text{Si}_{0.75}\text{O}_2$ and $\text{LiAlSi}_4\text{O}_{10}$ alongside Li_2SiO_3 and Li_3PO_4 embedded in a still amorphous matrix. This appears to lead to a small decrease in K_{IC} . In contrast, K_{IC} increases for samples heat treated at 670°C, which are considerably more crystalline, having $\text{Li}_{0.25}\text{Al}_{0.25}\text{Si}_{0.75}\text{O}_2$ and $\text{LiAlSi}_4\text{O}_{10}$ as the primary phases, and some residual Li_2SiO_3 and Li_3PO_4 . Subsequently, K_{IC} shows a gradual increase from $1.09 \pm 0.04 \text{ MPa}^{\sqrt{m}}$ to $1.73 \pm 0.05 \text{ MPa}^{\sqrt{m}}$ between samples heat treated at 690°C and 850°C for 30 min, respectively. This is consistent with a microstructure consisting of “interlocking” of the $\text{LiAlSi}_2\text{O}_6$ crystals, that could retard crack propagation, then with enhanced fracture toughness.

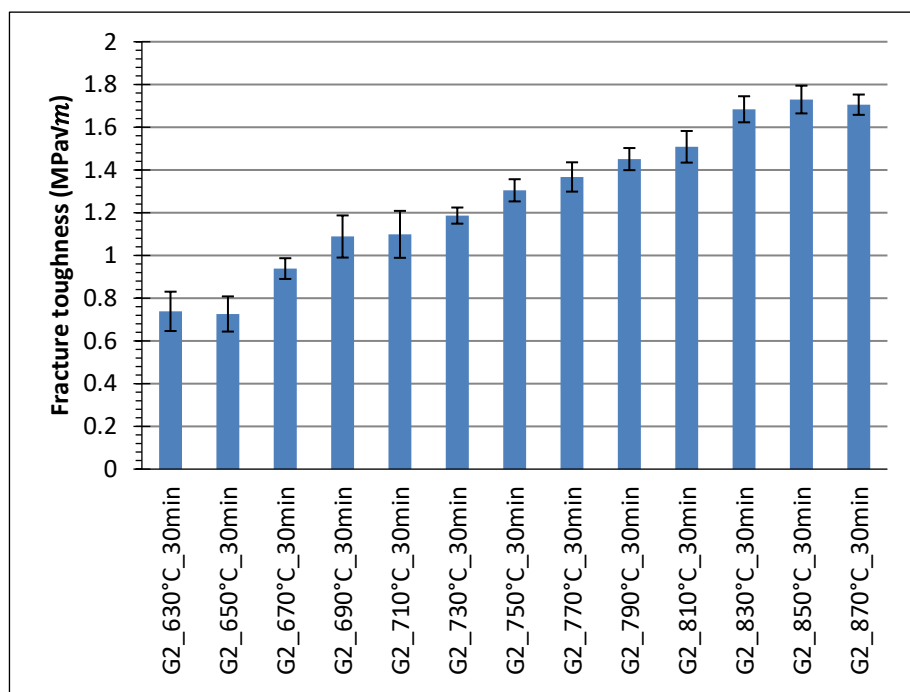


Fig. 6. 32 Fracture toughness after heat treatment for 30 min in the 630°C to 870°C temperature range.

6.6.3.3 Fracture toughness after nucleation at 550°C for 300 min followed by heat treatment for 30 min in the 630°C to 870°C temperature range

Fig. 6. 33 shows the evolution K_{IC} for LAS2 glass nucleated at 550°C for 300 min in function of heat treatment for 30 min in the 630°C to 870°C temperature range. In general, K_{IC} shows a gradual increase from $0.76 \pm 0.04 \text{ MPa}^{\sqrt{m}}$ to $1.69 \pm 0.06 \text{ MPa}^{\sqrt{m}}$ between samples heat treated at 630°C and 870°C, respectively. In comparison with Fig. 6. 32, there is no apparent improvement K_{IC} by nucleating the samples with exception of the sample heat treated at 870°C.

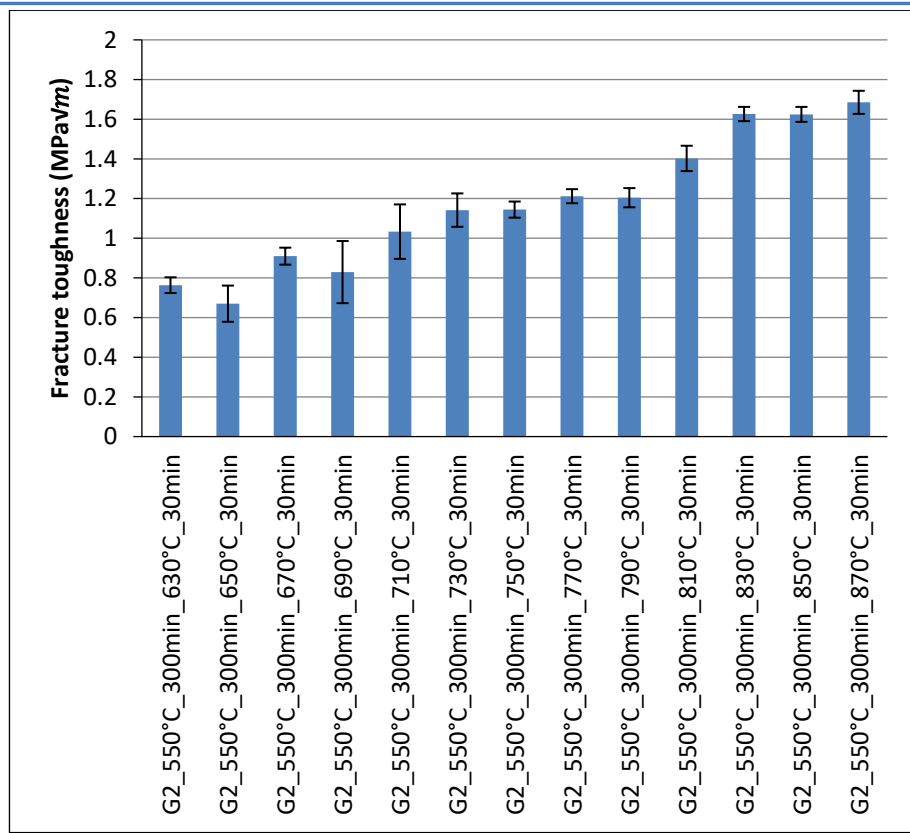


Fig. 6. 33 Fracture toughness after nucleation at 550°C for 300 min followed by heat treatment for 30 min in the 630°C to 870°C temperature range.

6.7 Optical properties of LAS2 glass

In this section, colour is quantified according to the Commission Internationale de l'Eclairage (CIE) system using CIE Lab colour space system to estimate perceptible colour changes in terms of L*, a* and b* coordinates, as described in the section 5.7.

6.7.1 L*a*b* values after isothermal heat treatments at 550°C for different holding times

Fig. 6. 34 shows the CIELab values for LAS2 glass as a function of isothermal heat treatment at 550°C for 30, 150, 300 and 3000 min alongside photographs of the samples. The test was carried out against a black background. The as-cast LAS2 glass is transparent and has a yellow tint as shown in Fig. 6. 34. Between 30 and 150 min heat treatment there are remarkable changes in a* and b*. The latter is a measure of yellowness (+) or blueness (-). Basically, b* goes from -1.57±0.31 (as-cast) to -14.7±0.5 (3000 min), which is commensurate with colour change direct observed from the digital photographs. a* which is a measure of redness (+) or greenness (-), also changes from 0.17±0.29 (as-cast) to

$+6.13 \pm 0.06$ (3000 min). Again, this is consistent with the digital photographs in Fig. 6. 34. L value varies between 5.37 ± 0.5 to 8.83 ± 1.07 .

This colour evolution has undoubtedly occurred due to the presence of V_2O_5 [3] [180], which is well known to give the yellow appearance and with heat treatment gives purple appearance.

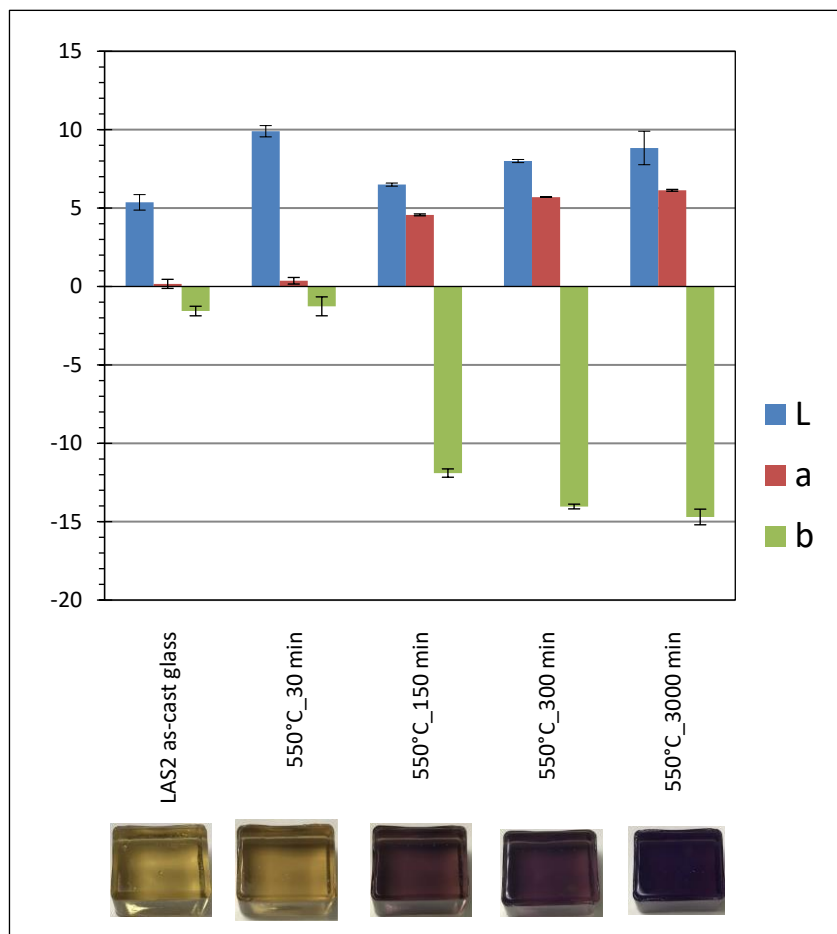


Fig. 6. 34 $\text{L}^*\text{a}^*\text{b}^*$ values after isothermal heat treatments at 550°C for different holding times.

6.7.2 Colour evolution upon heat treatment for 30 min in the 630°C to 870°C temperature range

6.7.2.1 $\text{L}^*\text{a}^*\text{b}^*$ values

The evolution of CIE $\text{L}^*\text{a}^*\text{b}^*$ values for LAS2 glass as a function of the heat treatment for 30 minutes in 630°C to 870°C temperature range is presented in Fig. 6. 35, alongside digital photographs for each sample. Note that this test was carried out against a black background. In general, L^* increases continuously from 14.93 ± 0.64 to 67.33 ± 0.21 for samples heated treated for 30 min at 630°C and 810°C , respectively. Nevertheless, similar to LAS1 glass, there is a sudden increase in L^* between 710°C and 730°C , as indicated by the dashed circle. This

increase coincides with the crystallisation of $\text{Li}_2\text{Si}_2\text{O}_5$ and $\text{LiAlSi}_2\text{O}_6$, according to XRD data, shown in Fig. 6. 11. L^* continues to increase more gradually with increasing temperatures as shown in Fig. 6. 35.

Interestingly a^* and b^* values are almost constant for samples heat treated up to 690°C. Again, for samples heat treated around 710°C, there are some variations in a^* and b^* values, as indicated by the dashed blue circle in Fig. 6. 35. Basically, whenever a^* and b^* approach 0, this indicates that colour of the sample is closer white. As expected, b^* changes (-) to (+) because the blueness is evolving to yellowness. These CIE Lab values are supported by the digital photographs of the samples against a black background, as shown in Fig. 6. 35. Hence, this feature indicates that the glass block colour is becoming creamy “colouring shade” that will be investigated in the next section.

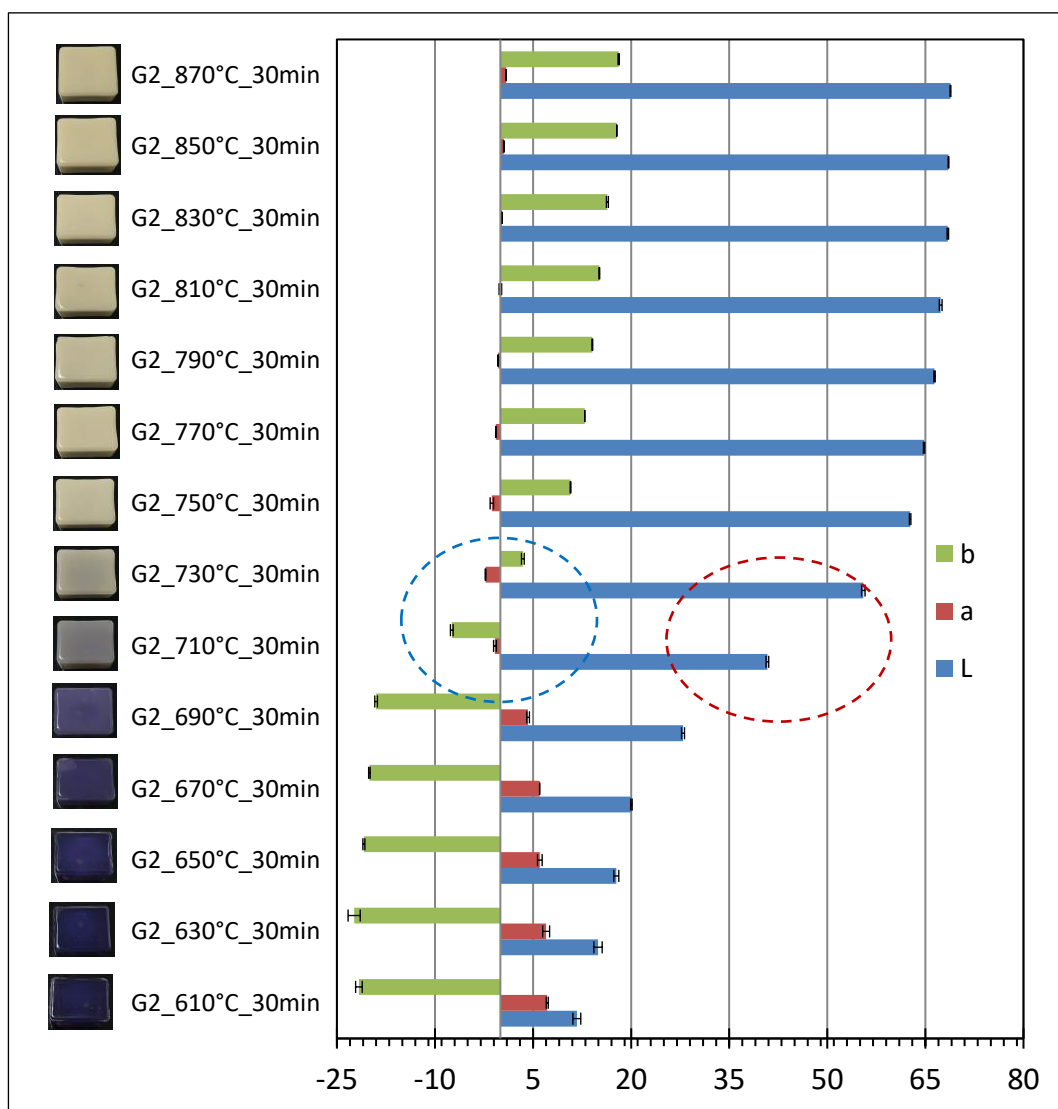


Fig. 6. 35 $L^*a^*b^*$ values evolution upon heat treatment for 30 min in the 630°C to 870°C temperature range and digital micrographs of the specimens against a black background.

6.7.2.2 Colour matching with the VITA Classical shade guide standard

Colour matching can be directly evaluated via a ΔE measurement, between heat treated samples and the VITA Classical shade guide used in dental clinics ($L^*a^*b^*$ listed in Table 4. 6) using the RM200QC colorimeter. This statistical analysis is useful to measure the matching range of samples in this study with those in the VITA Classical shade guide. Low values of ΔE suggest a good colour matching with the standard shade. The largest ΔE of ~ 62.70 is observed for samples heat-treated at 630°C for 30 min, compared against the A3 shade in the VITA guide, as shown in Fig. 6. 36. With increasing heat treatment temperature, ΔE decreases from 60.83 to 4.83 for samples heated treated for 30 min at 630°C and 750°C , respectively, with colour of sample at 750°C becoming closer to the A3 shade. The ΔE values further decrease with heat treatment temperature, with samples heated treated at (770°C for 30min), (790°C , 810°C for 30 min) and (830°C , 850°C and 870°C for 30 min) samples to match the D2, C1 and B2 shades of the VITA guide, respectively.

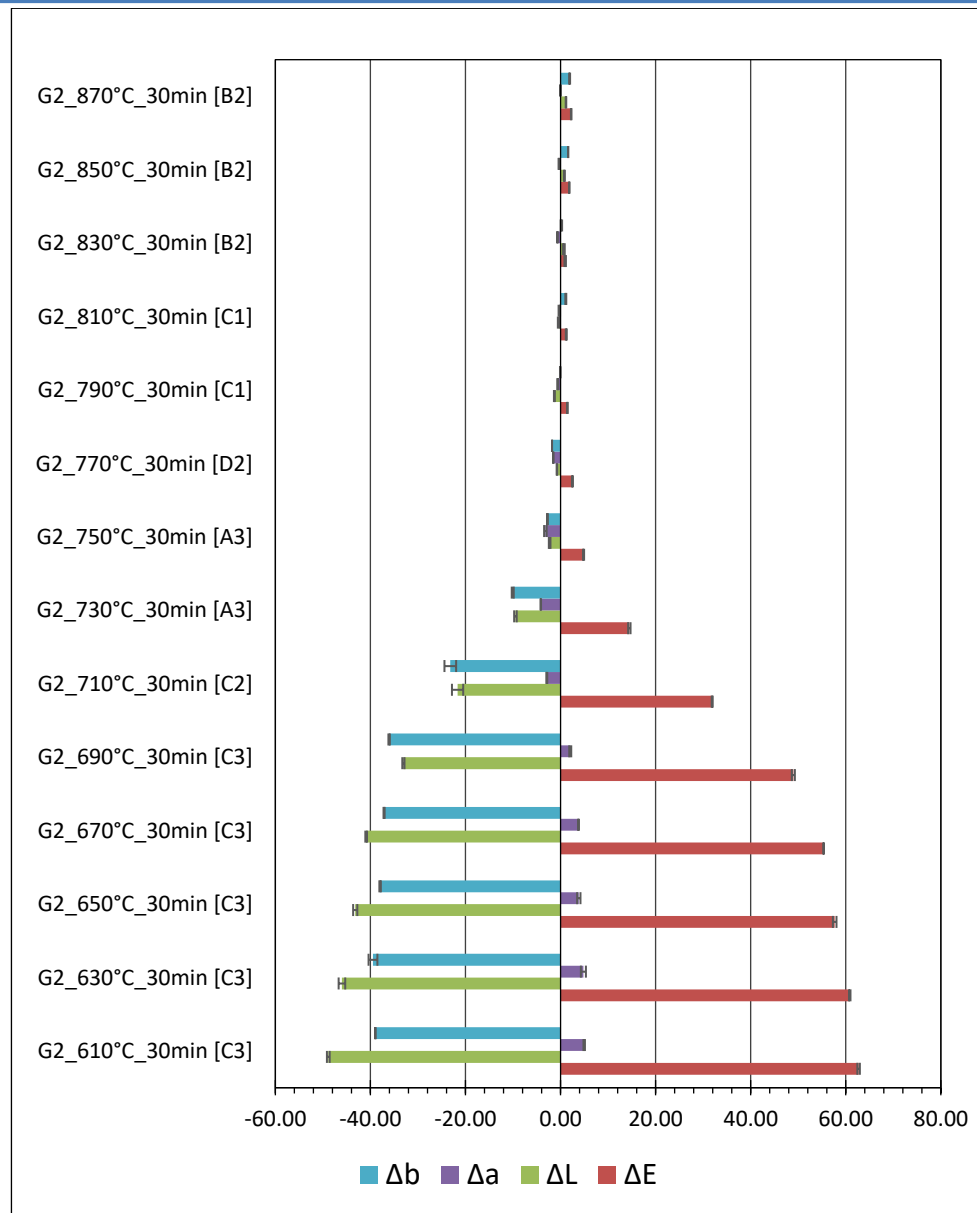


Fig. 6.36 The colour differences (ΔL^* , Δa^* , Δb^* and ΔE values) between LAS2 glass heat treated for 30 min in the 630°C to 870°C temperature range and selected VITA shade standards.

6.7.3 Colour evolution after nucleation at 550°C for 300 minutes followed by heat treatment for 30 minutes in the 630°C to 870°C temperature range

6.7.3.1 $L^*a^*b^*$ values

The $L^*a^*b^*$ values in Fig. 6.37 exhibit a similar trend to their non-nucleated counterparts in Fig. 6.36, however it is useful to also evaluate colour matching with the VITA Classical shade guide, as done in the next section.

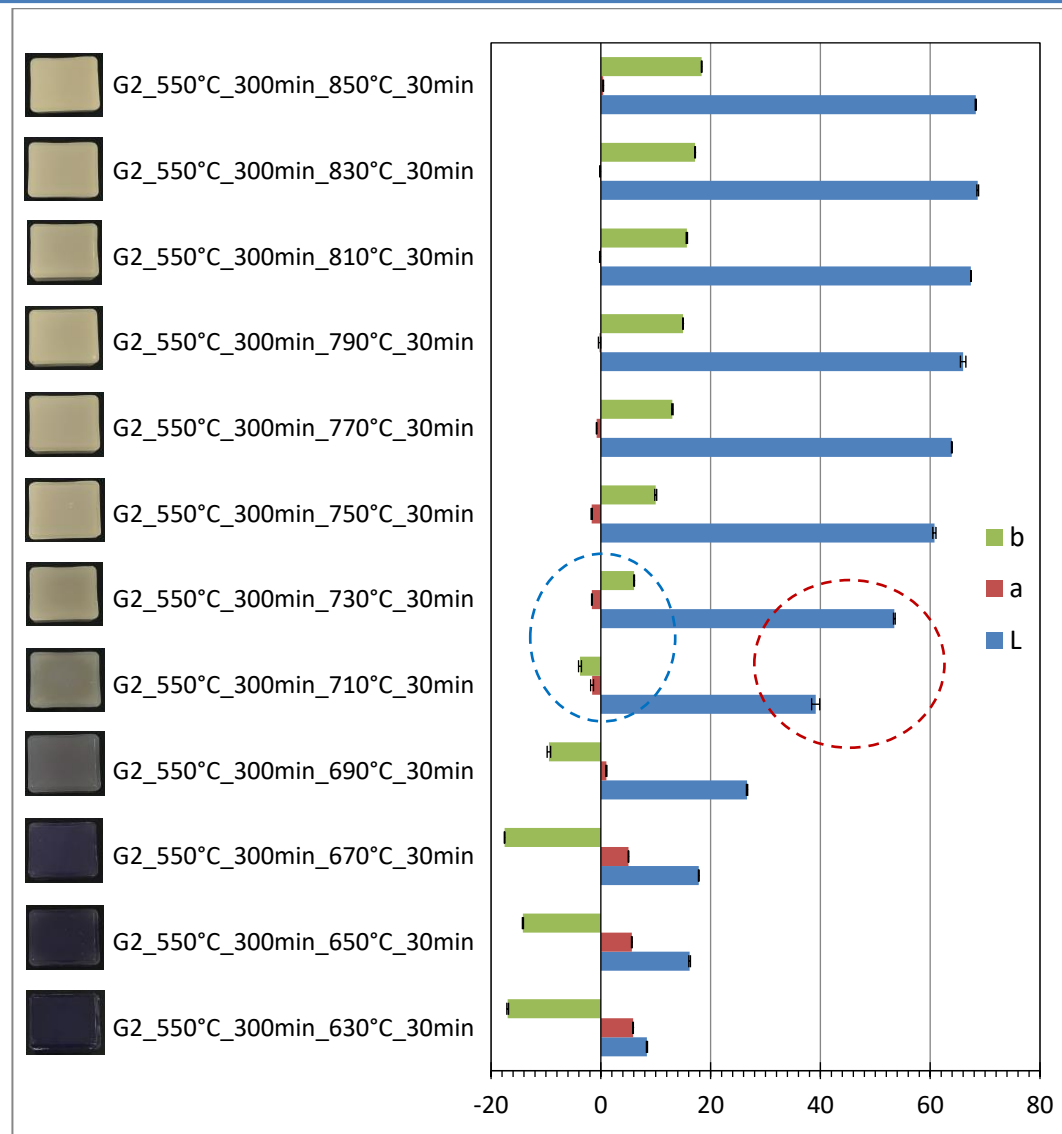


Fig. 6.37 $L^*a^*b^*$ values evolution for samples nucleated at 550°C for 300 minutes followed by heat treatment for 30 min in the 630°C to 870°C temperature range and digital micrographs of the specimens against a black background.

6.7.3.2 Colour matching with the VITA Classical shade guide standard

Again, data in Fig. 6.38 shows similar trends as non-nucleated samples, Fig. 6.36. However, the difference was only in colour matching from 770°C to 870°C, in which sample heated treated at (770°C and 790°C for 30 min), (810°C for 30 min) and (830°C, 850°C and 870°C for 30 min) samples show a good match with D2, B1 and B2 shades in the VITA guide, respectively.

Based on the colour data, in Fig. 6.35- 38, different heat treatments of LAS2 glass, yield the possibility of different shades, which may be useful to dental applications. This is due to the present of colouring agents [3] [180].

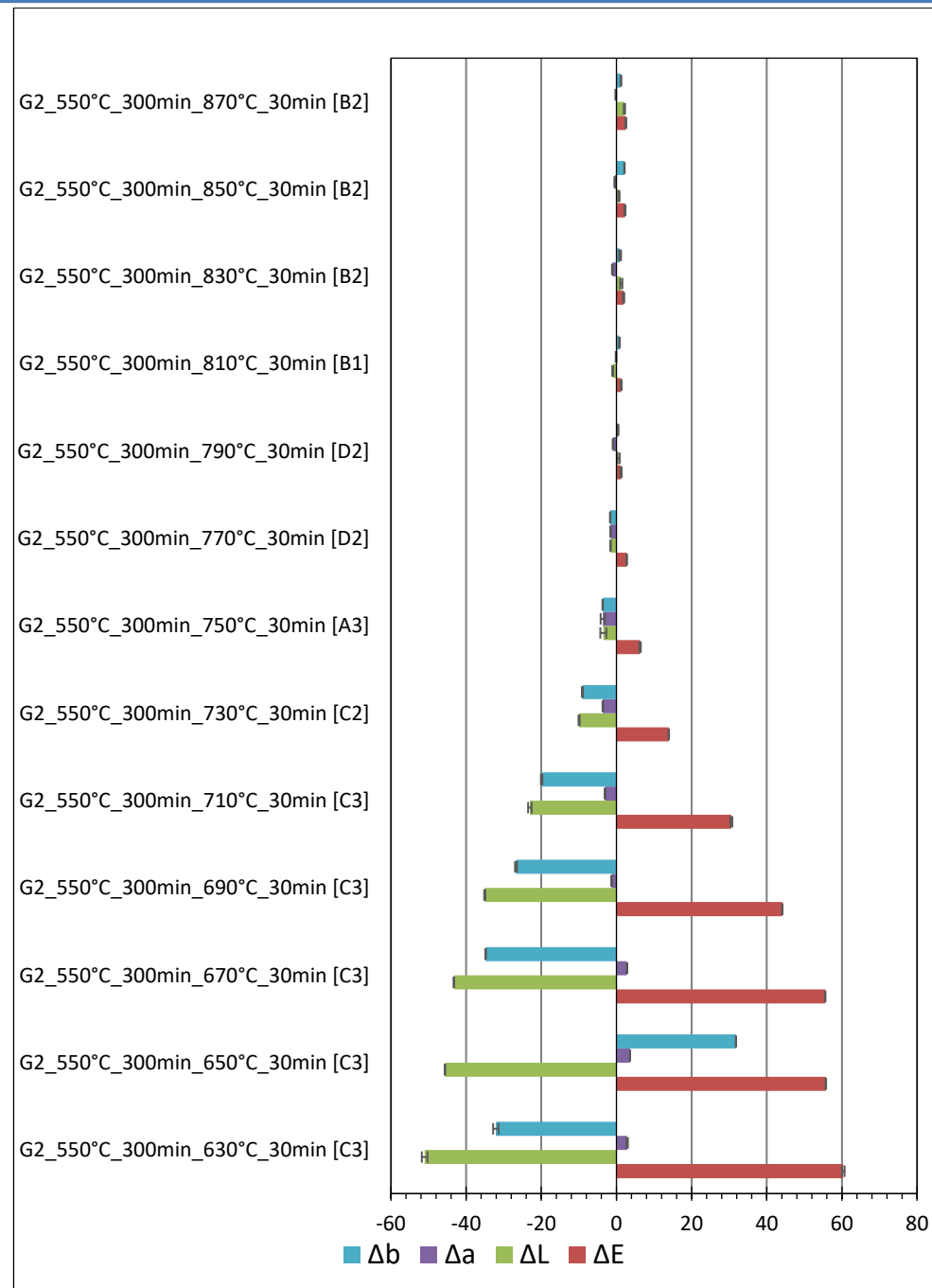


Fig. 6.38 The colour differences (ΔL^* , Δa^* , Δb^* and ΔE values) between LAS2 glass nucleated at 550°C for 300 min followed by heat treatment for 30 min in the 630°C to 870°C temperature range and selected VITA shade standards.

6.8 Phase assemblage, mechanical and optical properties of LAS2 glass following a two-step crystallisation process

This section contains the results for phase assemblage, mechanical and optical properties of LAS2 glass samples subjected to the heat treatment profiles recorded in Table 4.5. Those were chosen based on the DSC and XRD analyses presented in the previous sections.

6.8.1 *Ex-situ* XRD of heated treated LAS2 glass selected

XRD patterns for selected heated treated samples are shown in Fig. 6. 39. All samples were nucleated 550°C for 300 min subsequently treated at higher temperatures. One group consists of samples that undergo an intermediate step at 670°C and a maximum temperature of 780°C for different lengths of time. The temperature of the intermediate step was based on the complex crystallisation around 670°C, as shown in section 6.4.4. There other group consist of samples that undergo an intermediate step 780°C and a maximum temperature of either 830°C or 850°C. The XRD pattern for sample heat treated at 670°C for 90 min two major phases: $\text{LiAlSi}_4\text{O}_{10}$ and $\text{Li}_{0.25}\text{Al}_{0.25}\text{Si}_{0.75}\text{O}_2$. All the other heat treatments produced samples containing $\text{LiAlSi}_2\text{O}_6$, $\text{Li}_2\text{Si}_2\text{O}_5$, Li_2SiO_3 and Li_3PO_4 . $\text{LiAlSi}_2\text{O}_6$ is the dominant phase.

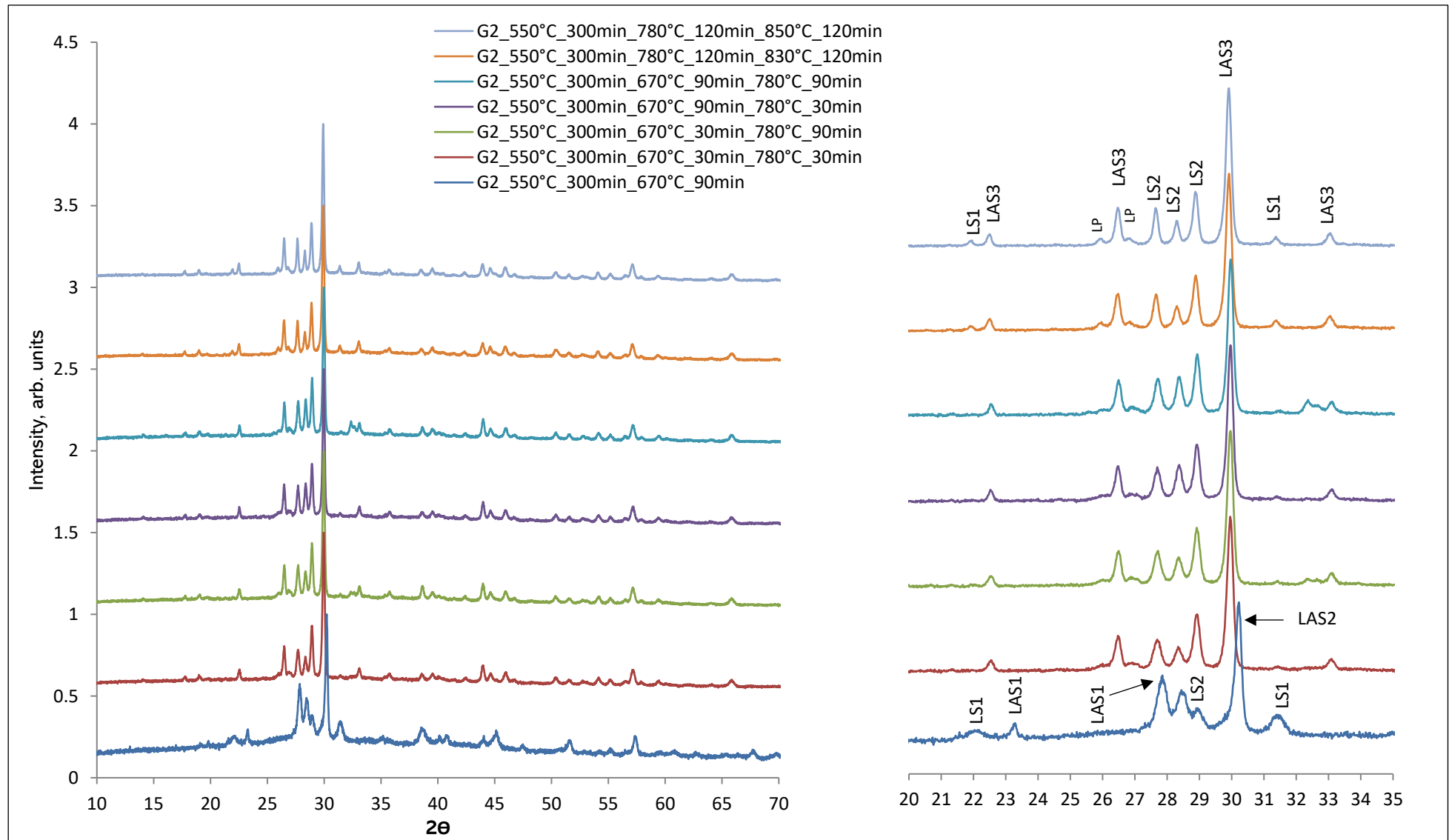


Fig. 6. 39 XRD patterns for selected heated treated samples between 670-780 °C.

6.8.2 Evolution of the crystallite size for LiAlSi₂O₆

Fig. 6. 39 showed LiAlSi₂O₆ to be the dominant phase in all samples heat treated between 780 and 850°C. The evolution of FWHM for the LiAlSi₂O₆ strongest Bragg peak located at 29.00°-31° 2θ in terms of heat treatment is illustrated Fig. 6. 40.

It is evident that with increasing heat treatment temperature the peak gets narrower as indicated by smallest FWHM values. However, the 830°C and 850°C samples have the lowest FWHM value, as shown in Fig. 6. 40. These values can be incorporated in the Scherrer equation to calculate the median crystallite sizes. The results are shown in Fig. 6. 41. LiAlSi₂O₆ appears to increase size, reaching a maximum of ~ 85 nm after 120 min at 830°C and remains constant up to 850°C.

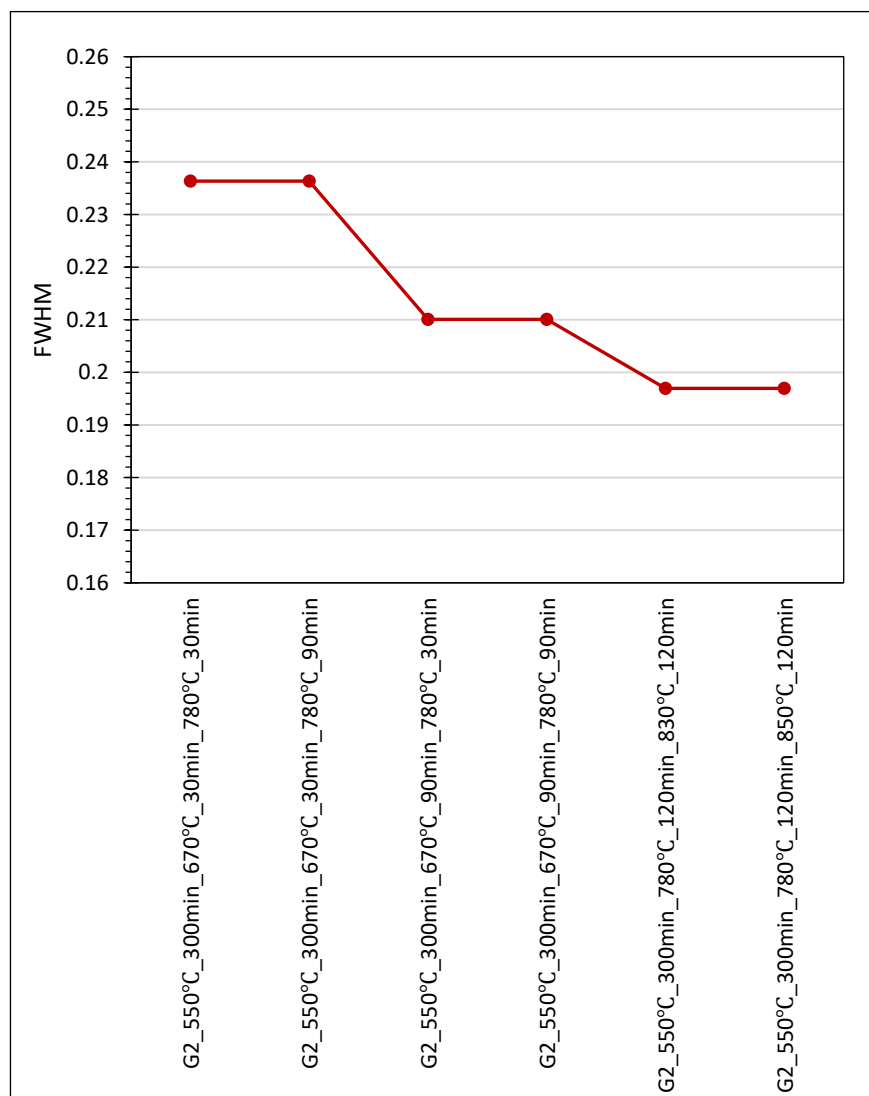


Fig. 6. 40 FWHM of strongest XRD peak in LiAlSi₂O₆ for selected heat-treatment profiles.

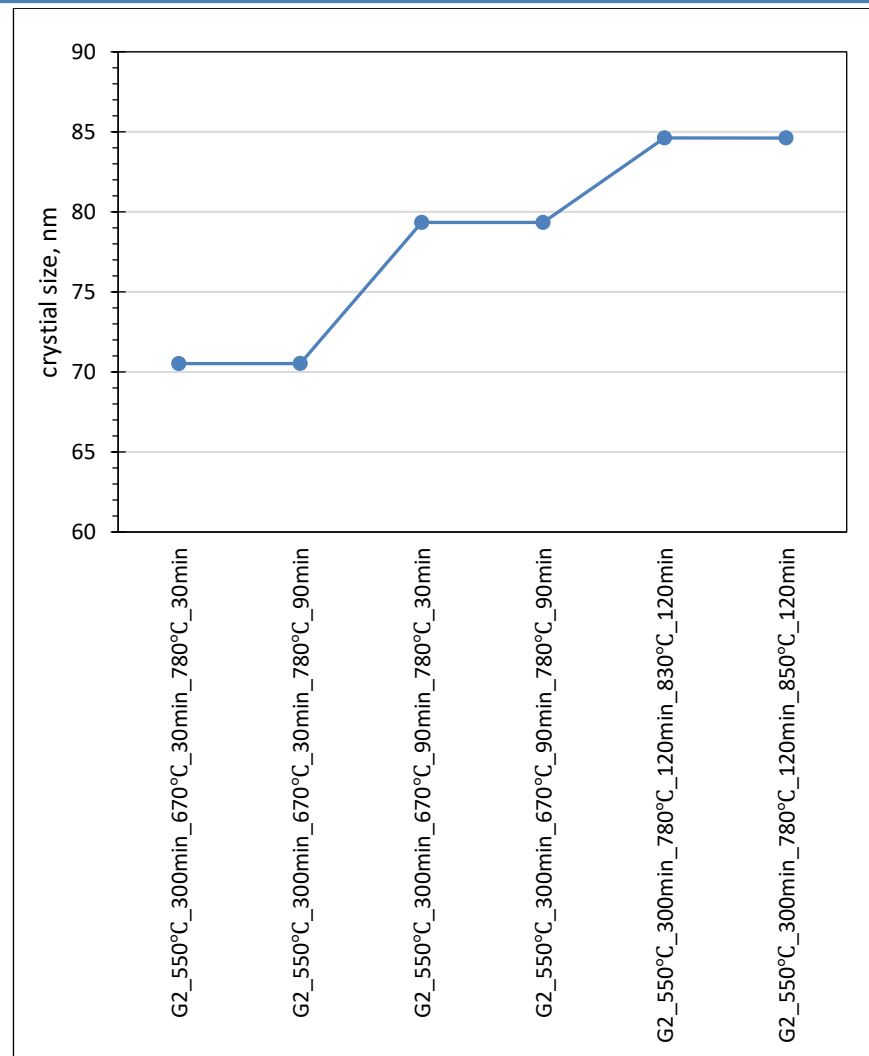


Fig. 6. 41 Median crystallite size of $\text{LiAlSi}_2\text{O}_6$ for selected heat-treatment profiles.

6.8.3 XRD peak intensity ratio for $\text{LiAlSi}_2\text{O}_6/\text{Li}_2\text{Si}_2\text{O}_5$ between 830°C and 850°C

The relative amount of each phase can be estimated by the intensity ratios of the main Bragg peaks associated with each phase, which for $\text{LiAlSi}_2\text{O}_6$ is located at $29\text{-}31^\circ 2\Theta$ and for $\text{Li}_2\text{Si}_2\text{O}_5$ is located at $27.5^\circ \text{ - } 29.5^\circ 2\Theta$, as shown in Fig. 6. 42. Interestingly, the ratio decreases slightly with increasing holding time at 830 °C, but it increases with the increasing temperature. $\text{LiAlSi}_2\text{O}_6$ is always the dominant phase.

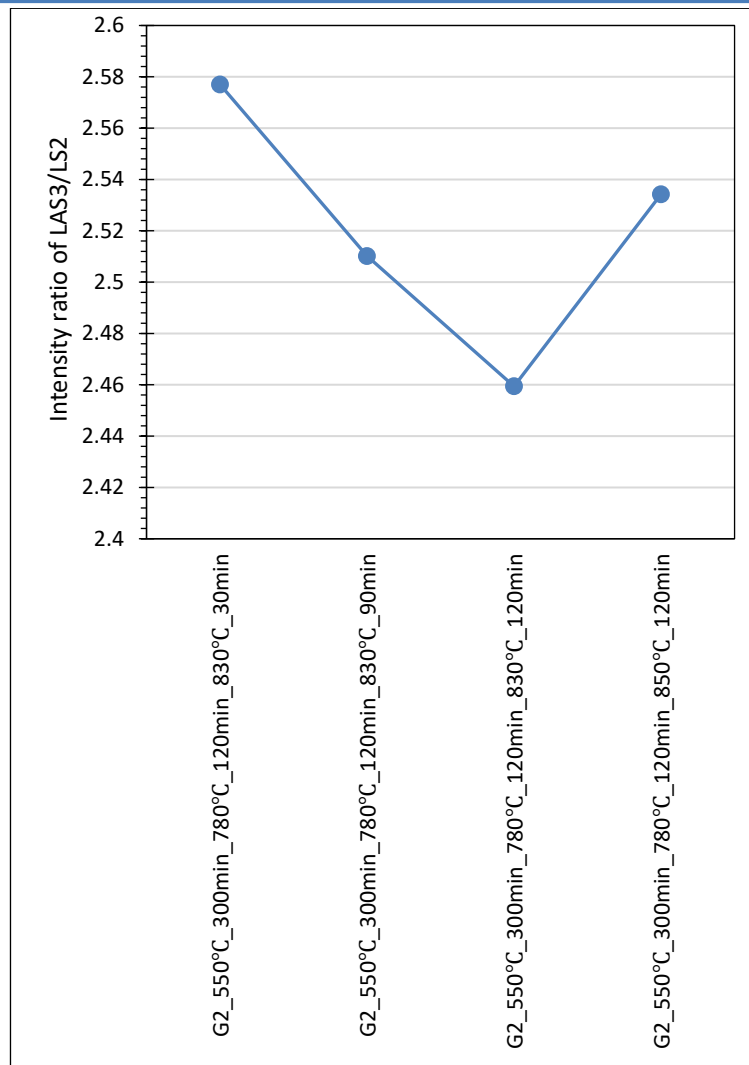


Fig. 6. 42 Intensity ratio of lithium-aluminosilicate (LAS3) and lithium-disilicate (LS2).

6.8.4 Mechanical properties

6.8.4.1 Elastic modulus

From the above samples, the lowest $E \sim 90$ GPa is for the sample nucleated at 550°C for 300 min and then heat treated at 670°C for 90 min, as shown in Fig. 6. 43. The largest $E \sim 98.4$ GPa 550°C for 300min and 670°C for 90 min and finally at 750°C for 30 min. Increasing the holding time at 670°C appears to increase E .

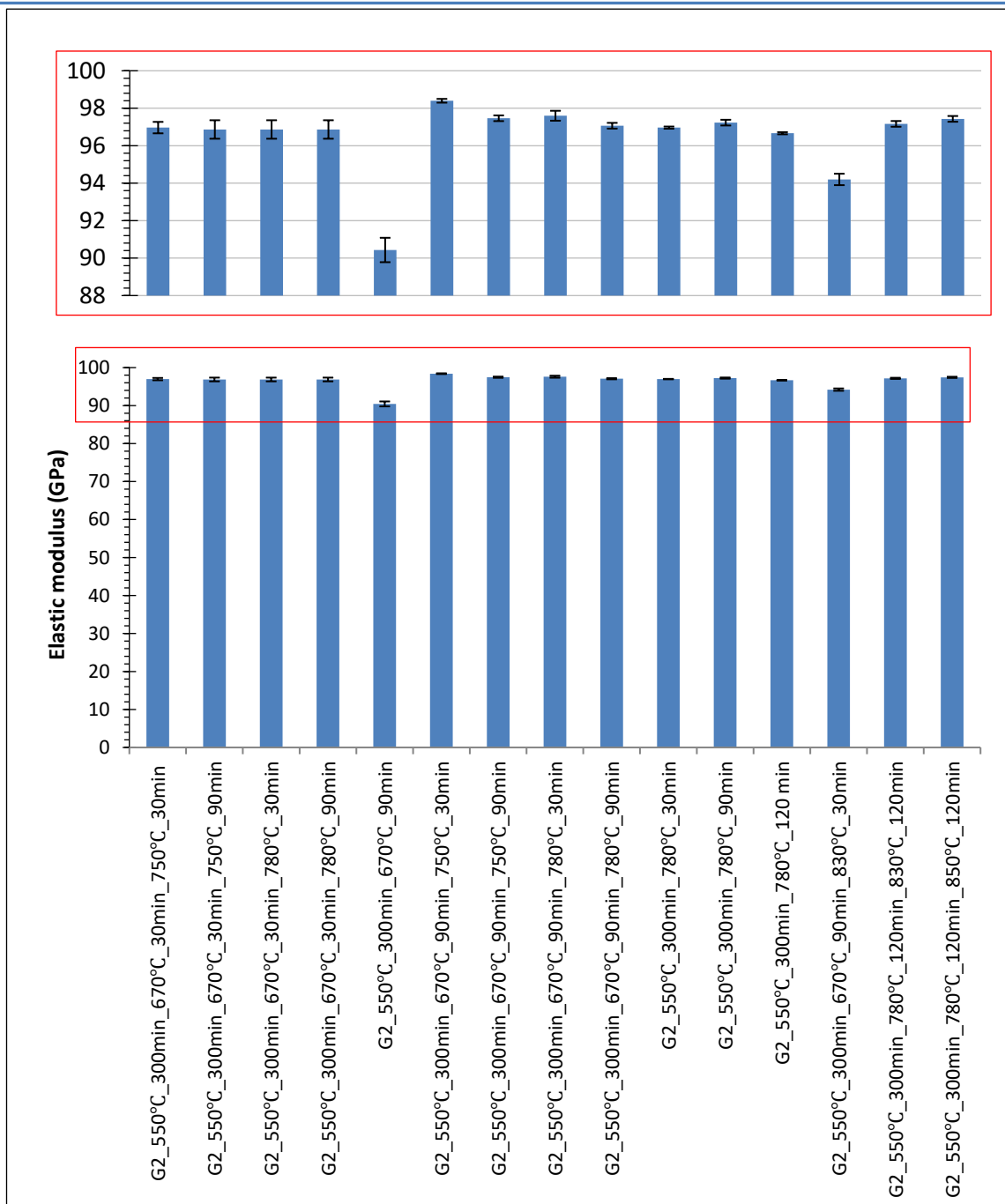


Fig. 6. 43 Elastic modulus for selected heat treatment profiles.

6.8.4.2 Hardness

Fig. 6. 44 reveals the relationship between Hv and heat treatment profiles. Hv appears to decrease with increasing holding time at the top temperature, but also with increasing temperature.

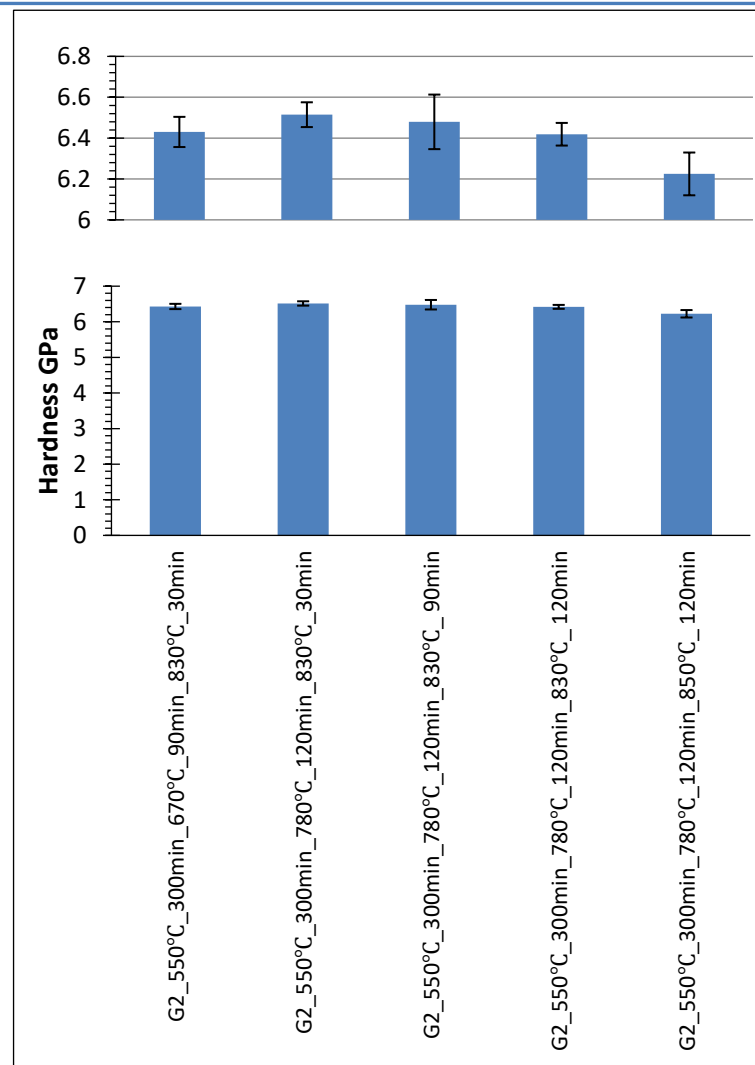


Fig. 6. 44 Micro-indentation hardness for selected heat treatment profiles.

6.8.4.3 Fracture toughness

Unlike the micro-hardness findings, the fracture toughness for the heated treated glasses evidences a relatively upward trend from 830°C to 850°C. K_{IC} shows increases from $1.78 \pm 0.06 \text{ MPa}\sqrt{\text{m}}$ to $2.00 \pm 0.12 \text{ MPa}\sqrt{\text{m}}$ between samples heat treated at 830°C for 120 min and 850°C for 120 min, respectively, as shown in Fig. 6. 45.

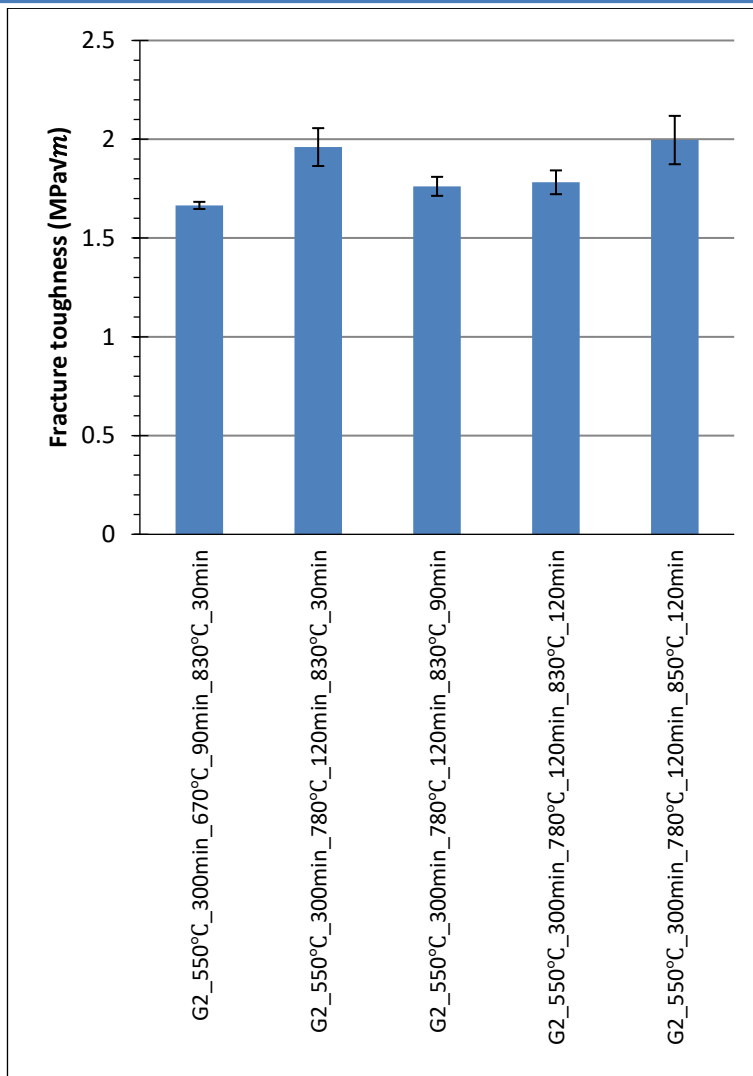


Fig. 6. 45 Fracture toughness for selected heat treatment profiles.

6.8.5 Optical properties

6.8.5.1 Colour

In general, the L* and b* CIE values increase with increasing heat treatment temperature. The b* is rather negative for the 670°C but with increasing temperature becomes positive, indicating a blueness to yellowness evolution.

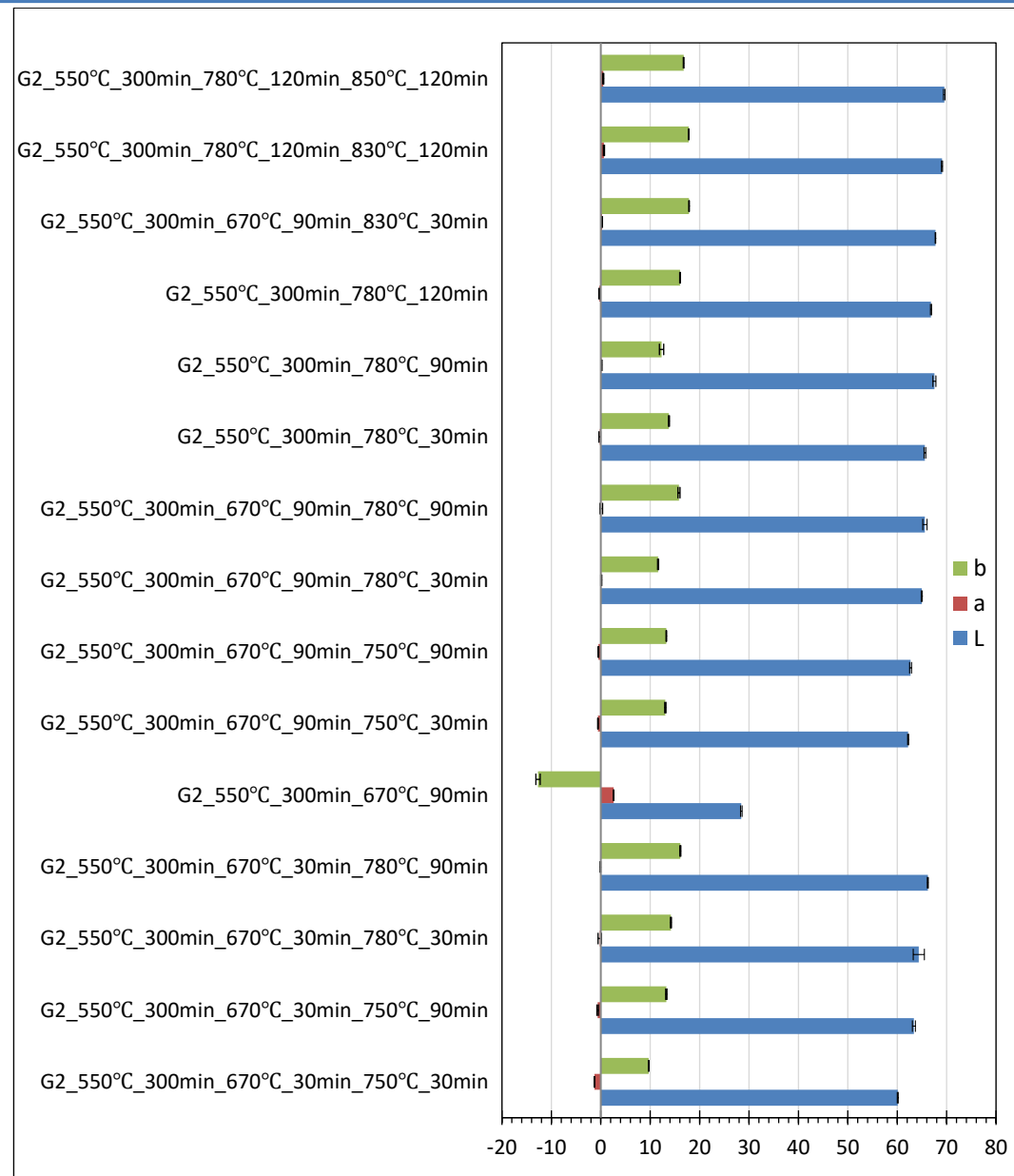


Fig. 6. 46 CIE Lab values of the heated treated LAS2 glass samples.

6.8.5.2 Colour matching against VITA Classical shade guide standard

This statistical analysis is useful to measure the matching range of samples in this study with those in the VITA Classical shade guide. Low values of ΔE suggest a good colour matching with the standard shade. Hence, based on the statistical data in Fig 6. 47, it can see that all samples heat treated above 670°C can be matched with the different standard shades.

Interestingly, the samples nucleated at 550°C for 300 min and then heat-treated 780°C samples 30-, 90- and 120-min holding time, match 3 different shades: D2, C1 and B2, respectively, as shown in Fig. 6. 37. Samples heat treated at 830°C-850°C match the B2.

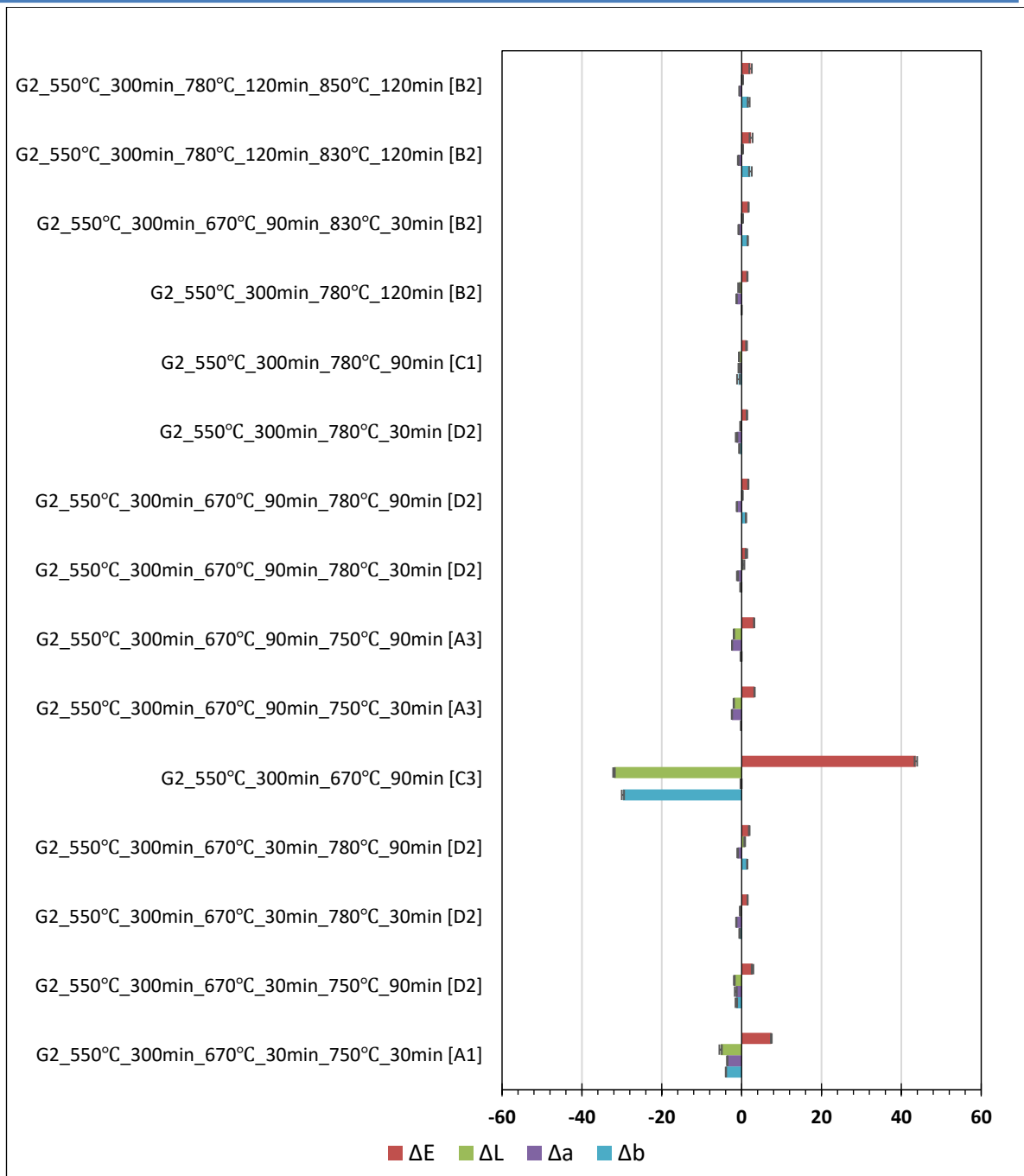


Fig. 6. 47 Colour differences (ΔL^* , Δa^* , Δb^* and ΔE values) between heated treated LAS2 glass samples and the VITA shade standards.

Chapter

| 7 |

General Discussion

Chapter Seven: General Discussion

This chapter provides a general discussion of the findings in this thesis in the context of the literature for glass ceramics, and in particular of glass ceramics used in dentistry.

7.1 Glass composition

In this thesis, two lithium aluminosilicate (LAS)-based glasses, hereafter refer to as LAS1 glass and LAS2 glass were investigated. Based on ICP-OES analyses, LAS1 and LAS2 glasses exhibit similar compositions, with the exception to V₂O₅, as shown in Table 7.1, which is absent in LAS1 glass. SiO₂ is the main component followed by Al₂O₃ and Li₂O. It is interesting note that the ratio Al₂O₃ to [Li₂O or SiO₂] is higher, when compared with lithium disilicate (LS)-based glasses, as exemplified by the works of Holland et al [121], but similar to the values reported by Laczka, M. et al. [10] Łaczka, K. el al. [169] for LAS-based glass ceramics.

Table 7. 1 Comparison of the chemical composition of lithium disilicate (LS) and lithium aluminosilicate (LAS) glass systems reported in prior investigations and the current study.

| Formula ↓(wt%) | LAS1 glass | LAS2 glass | (LS) Y. Iqbal et al. [161] | (LS) W. Holand et al [121] | (LAS) Laczka, M. et al. [10] | (LAS) Laczka, K. el al. [169] |
|--------------------------------|--------------|--------------|----------------------------------|----------------------------------|------------------------------------|-------------------------------------|
| Li ₂ O | 10.55 | 10.14 | 19.36 | 14.68 | 10.5 | 12.1 |
| SiO ₂ | 62.37 | 62.45 | 77.85 | 70.64 | 66 | 66.3 |
| Al ₂ O ₃ | 11.92 | 11.83 | | 3.38 | 10.5 | 10.2 |
| P ₂ O ₅ | 4.09 | 4.03 | 2.79 | 3.21 | 4.5 | 4.28 |
| ZrO ₂ | 0.69 | 0.68 | | 3 | 0.5 | 0.56 |
| TiO ₂ | 0.03 | 0.02 | | | | |
| Na ₂ O | 4.16 | 4.12 | | | 3 | |
| K ₂ O | 0.91 | 0.91 | | 3.09 | 0.5 | 0.53 |
| CeO ₂ | 1.18 | 1.17 | | 1.88 | 1.5 | 1.5 |
| V ₂ O ₅ | - | 0.41 | | 0.12 | 0.55 | 0.04 |
| CoO | 0.07 | 0.10 | | | | |
| Tb ₂ O ₃ | 1.28 | 1.28 | | | | |
| CaO | 2.22 | 2.14 | | | 2.45 | 1.46 |
| WO ₃ | 0.53 | 0.72 | | | | |

Table 7. 1 also shows that LS- and LAS-based glasses have similar P₂O₅ contents. P₂O₅ is a key component as it acts as a heterogeneous nucleating agent that promotes volume nucleation of lithium disilicate [121]. Indeed, several studies reported that Li₃PO₄ crystals served to induce heterogeneous nucleation of stable Li₂Si₂O₅ crystals [161], [162]. The work from Iqbal et al [161] shows that a LS glass-ceramic can be successfully fabricated using three components: Li₂O, SiO₂ and Al₂O₃. They also studied the effect 0, 2.79, 5.47 and 12.99 wt% P₂O₅ for heat treatments at 454°C. They postulated that higher levels of P₂O₅ lead to a greater degree of amorphous phase separation. Moreover, they also observed that amorphous lithium phosphate units form for ≤ 2.79 wt% P₂O₅, whereas the presence of crystalline Li₃PO₄ for $x \geq 5.47$ wt% P₂O₅ strongly suggests that Li₃PO₄ crystals are sites for heterogeneous nucleation of stable Li₂Si₂O₅ crystals. Nevertheless, compositions for other LS-based glasses ceramics are rather more complex, as depicted in Table 7. 1. For example, small amounts of CaO and K₂O, well known glass modifiers, are added in small amounts to reduce the number of strong bonds in the glass and thereby reduce its melting temperature and viscosity. TiO₂ is a known intermediate component, which can act either as network former or a modifier depending on the glass composition.

CeO₂ and V₂O₅ are often added to the chemical composition of a glass in order to match colour/shade with that of the natural teeth [179]. Several studies regarding the impact of these oxides on the colour of glasses, in particular lithium disilicate glass are available in the literature [176]–[180]. Finally, CeO₂ content in LAS1 and LAS2 glasses is similar, whereas V₂O₅ is absent in LAS1 glass. The role of V₂O₅ as a colouring component arises from the multiple oxidation states that vanadium can take upon increasing temperature of the heat treatment. Moreover, it is believed that vanadium cations are likely to remain in the residual glassy phase rather than being incorporated in the crystalline phases [180]. V₂O₅ is to be employed only in forming coloured shades [3] thereby its absence in LAS1 glass implies that this composition should yield a bleach shade, as observed in this work.

7.2 Thermal behaviour and phase assemblages

The thermal behaviour of LAS1 and LAS2 glasses was investigated by differential scanning calorimetry (DSC) and XRD analyses, in order to determine crystallisation pathways and phase transitions events.

Table 7. 1 shows that the composition of LAS1 and LAS2 glasses is rather complex. Hence, a simpler approach to discuss the thermal behaviour of those two glasses may start to consider the crystallisation of a LS-based material ($\text{SiO}_2\text{--Li}_2\text{O}\text{--Al}_2\text{O}_3\text{--K}_2\text{O}\text{--ZrO}_2\text{--P}_2\text{O}_5$), as investigated by W. Höland et al, listed in Table 7. 2 [121]. They also investigated the effect of P_2O_5 content (0, 1.63, 2.38 and 3.21 wt%) and the impact on the thermal behaviour, which is reproduced in Fig. 7. 1-a. It is immediately discernible that the P_2O_5 content has a strong effect on the thermal behaviour, with the 3.21 wt% P_2O_5 showing two exothermic peaks, whereas the other glasses with less P_2O_5 exhibiting only one exothermic peak. Fig. 7. 1-b shows the thermal behaviour for LAS1 and LAS2 glasses, which are glasses with a P_2O_5 content greater than 4 wt%, but also a higher content of Al_2O_3 , when compared with W. Höland et al work. LAS1 and LAS2 glasses also show two strong exothermic peaks, but at lower temperatures. Also, the melting temperature is lower. This obvious difference in thermal and crystallization behaviour is due to ratio Li/Al used for producing glass-ceramic, in which for lithium disilicate was ~ 4.57 , whereas for LAS in this study was ~ 0.89 . In the case of LS-based glass ceramics those exothermic events have been ascribed to the crystallisation of lithium monosilicate (Li_2SiO_3) and lithium disilicate ($\text{Li}_2\text{Si}_2\text{O}_5$).

Those authors suggested the following reaction pathway [121]:

- (1) Formation of Li_3PO_4 nanophases and nucleation of Li_2SiO_3 and $\text{Li}_2\text{Si}_2\text{O}_5$ between 500 and 560°C.
- (2) Fast growth of Li_2SiO_3 and no growth of $\text{Li}_2\text{Si}_2\text{O}_5$ between 590 and 750°C.
- (3) Formation and decomposition of cristobalite between 750 and 820°C.
- (4) Decomposition of Li_2SiO_3 and fast growth of $\text{Li}_2\text{Si}_2\text{O}_5$ between 780 and 820°C.

It is interesting to note that the LAS1 and 2 glasses showed the other two minor crystallization peaks, which are absent in the LS-glass.

Finally, it is worth to mention that previously, Ray and Day [279] established the maximum nucleation in the simple $\text{SiO}_2\text{--Li}_2\text{O}$ binary system to be $\sim 450^\circ\text{C}$, but W. Höland et al found the maximum in a wider and higher temperature range ($500\text{--}540^\circ\text{C}$). One would expect that to be the case for LAS1 and LAS2 glasses.

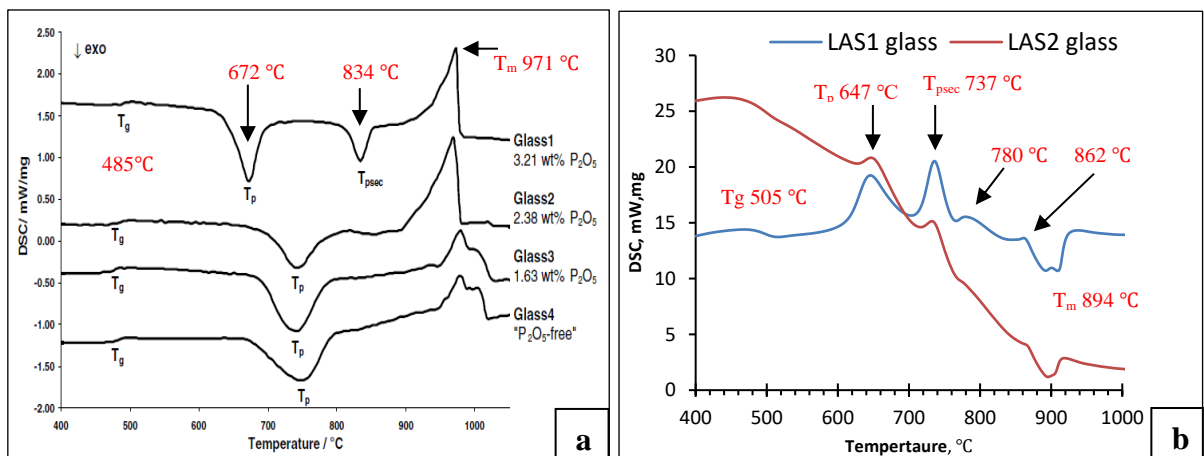


Fig. 7.1 DSC analysis at 15 K/min, a) lithium disilicate glasses with different P_2O_5 [121], b) LAS1 and LAS2 glasses in this study.

Laczka, M. et al investigated a LAS glass system containing higher Al_2O_3 , as listed in Table 7.1., whose composition was similar to that of LAS1 and LAS2 glasses. It can be observed that the peaks crystallization for [10] and LAS 1 and 2 glasses are extremely similar, as shown in Fig. 7.2. However, Laczka, M. et al found that the first exothermic peak is associated only with Li_2SiO_3 crystal phases, whereas based the *In-Situ* XRD data shown in Fig. 5.13 in section 5.3, the first peak in LAS glass is associated with Li_2SiO_3 (lithium metasilicate) alongside $\text{LiAlSi}_4\text{O}_{10}$ (Petalite) and $\text{Li}_{0.25}\text{Al}_{0.25}\text{Si}_{0.75}\text{O}_2$ (Lithium orthoclase). This contrast is due to Al_2O_3 high content in LAS1 and LAS2 glasses comparison to lithium disilicate in [121], as listed in Table 7.2. The second exothermic peak in LAS1 and LAS2 glasses centered at 724°C is associated with the appearance of lithium aluminosilicate, $\text{LiAlSi}_2\text{O}_6$, alongside lithium disilicate, $\text{Li}_2\text{Si}_2\text{O}_5$, as mentioned in the section 5.1.1. This feature is similar to that reported in [10].

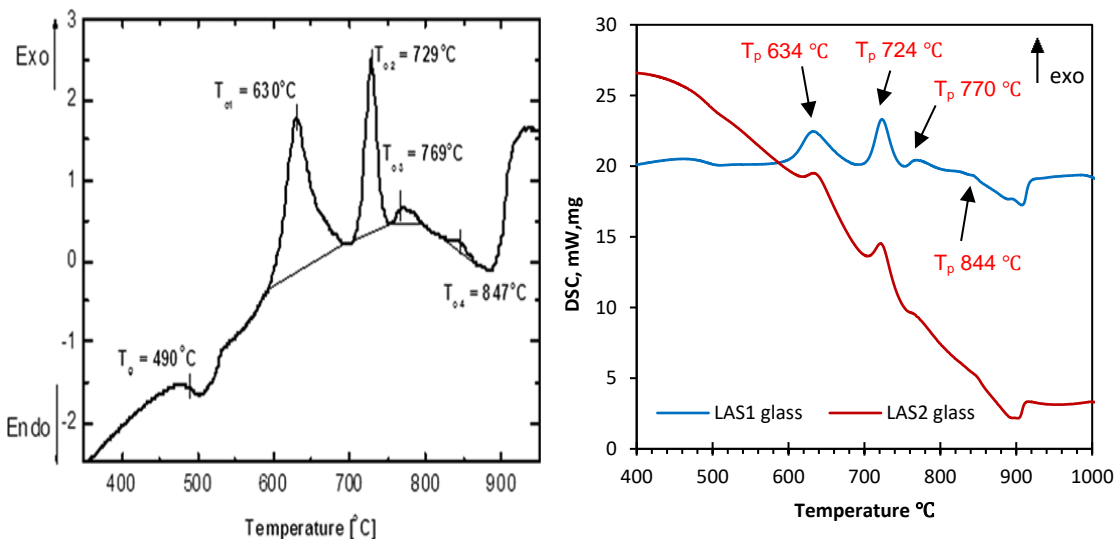


Fig. 7. 2 DTA of lithium aluminosilicate glass (left) [10], DSC of LAS1 and LAS2 glasses used in this study (right), both at heating rate of 10 K/min.

XRD and RS analyses showed that upon heat treatment at high temperature $\text{LiAlSi}_2\text{O}_6$ appears as the dominant phase. Scherrer analysis in the section 5.4.4 showed the median average crystallite size to reach a maximum value of ~ 90 nm, this is consistent with SEM images in which they showed needle-shaped anisometric crystals with a diameter ~ 90 nm, however, the same SEM images also showed needle-shaped crystals with length of several microns. Therefore, based on this, the Scherrer equation should be cautiously employed to determine the crystallite size in these materials.

Łaczka, K. et al [169] reported that Li_2SiO_3 is the first crystalline phase to appear during heating at 630°C up to 5 min. Interestingly, the petalite type structure ($\text{LiAlSi}_4\text{O}_{10}$) appeared at 720°C up to 5 min and then disappeared at 720°C up to 30 min. Whereas $\text{LiAlSi}_4\text{O}_{10}$ in the present study was presented at 670°C and vanished at 690°C . Łaczka, K. et al [169] found also that the appearance of $\text{Li}_2\text{Si}_2\text{O}_5$ at 720°C up to 30 min, while our XRD analysis detected at lower temperature of 710°C after 30 min, as listed in Table 7. 2.

Chapter Seven: General Discussion

Table 7. 2 Comparison of the crystalline phases in lithium disilicate and lithium aluminosilicate systems reported in prior investigations and in the author's study

| References | Glass systems | Processing | Crystalline phases |
|--|--|---|--|
| [161] | lithium disilicate Li ₂ O–SiO ₂ – (0, 2.79, 5.47, 12.99 wt%) P ₂ O ₅ | Melting and heat treatment | Li ₂ SiO ₃ disappeared as Li ₂ Si ₂ O ₅ presented, High temperature: Li ₂ Si ₂ O ₅ and SiO ₂ |
| [121] | lithium disilicate SiO ₂ –Li ₂ O–Al ₂ O ₃ –K ₂ O–ZrO ₂ – (3.21, 2.38, 1.63, 0 wt%) P ₂ O ₅ | Melting followed by one stage/ two stages heat treatments | 500°C→780°C: Li ₂ SiO ₃ 780°C→820°C: Li ₂ Si ₂ O ₅ 750°C→820°C: SiO ₂ |
| [164] | lithium disilicate SiO ₂ : 100, Li ₂ O: 41.6, CaO: 3, P₂O₅: 2.3 , ZrO ₂ :1.3 (in molar ratio) | Melting followed by multi-stage heat treatments | The final crystals were Li ₂ Si ₂ O ₅ and Li ₃ PO ₄ , and no detected Li ₂ SiO ₃ . |
| [166] | lithium disilicate 65.0 SiO ₂ –27.5 Li ₂ O–2.2 Al ₂ O ₃ –2.3 K ₂ O–2.0 ZrO ₂ – 1.0 P₂O₅ (mol%) | Melting followed by two stages of treatment | →650°C up to 3h: Li ₂ SiO ₃ and Li ₂ Si ₂ O ₅ 650°C up to 72h: SiO ₂ →830°C up to 3h: Li ₂ Si ₂ O ₅ and SiO ₂ Li ₂ SiO ₃ disappeared. |
| [10] | lithium aluminosilicate 66 SiO ₂ –10.5 Li ₂ O–10.5 Al ₂ O ₃ –2.45 CaO–0.5 K ₂ O–3 Na ₂ O– 4.5 P₂O₅ –0.5 ZrO ₂ –1.5 CeO ₂ –0.55 V ₂ O ₅ (wt%) | Melting followed by multi-stage heat treatments | Li ₂ SiO ₃ was converted into Li ₂ Si ₂ O ₅ . Nucleation→850°C: Li ₂ SiO ₃ 730°C→850°C: LiAlSi ₂ O ₆ alongside Li ₂ Si ₂ O ₅ . |
| [169] | lithium aluminosilicate SiO ₂ 66.3%; Al ₂ O ₃ 10.2%; Li ₂ O 12.1%; CaO 1.46%; K ₂ O 0.53%; Na ₂ O 2.59%; P₂O₅ 4.28% ; ZrO ₂ 0.56%; CeO ₂ 1.5%; V ₂ O ₅ 0.04%. | Melting followed by multi-stage heat treatments | Li ₂ SiO ₃ was converted into Li ₂ Si ₂ O ₅ then disappeared, 520°C→720°C: Li ₂ SiO ₃ 520°C→870°C: Li ₃ PO ₄ 720°C/5 to 30min: LiAlSi ₄ O ₁₀ 720°C→870°C: LiAlSi ₂ O ₆ –LiAlSi ₃ O ₈ S.S. 720°C/30min →870°C: Li ₂ Si ₂ O ₅ |
| LAS1 and LAS2 glasses used in this study | lithium aluminosilicate SiO ₂ 62.37%; Al ₂ O ₃ 11.92%; Li ₂ O 10.55%; CaO 1.46%; K ₂ O 0.53%; Na ₂ O 2.59%; P₂O₅ 4.09% ; TiO ₂ 0.03%; ZrO ₂ 0.69%; Na ₂ O 4.16; K ₂ O 0.91; CeO ₂ 1.18%; CoO 0.07; Tb ₂ O ₃ 1.28; CaO 2.22; WO ₃ 0.53; For LAS2 glass; V₂O₅ 0.41%. | Melting followed by multi-stage heat treatments | 360°C up to 5min→870°C: Li ₂ SiO ₃ and Li ₃ PO ₄ 670°C→690°C: LiAlSi ₄ O ₁₀ (nucleation +560°C→690°C: LiAlSi₄O₁₀) 670°C→730°C: Li _{0.25} Al _{0.25} Si _{0.75} O ₂ 710°C→870°C: Li ₂ Si ₂ O ₅ 730°C→870°C: LiAlSi ₂ O ₆ |

7.3 Mechanical properties

7.3.1 Elastic modulus, hardness and fracture toughness

The as-cast LAS 1 and 2 glasses shows an elastic modulus, E, estimated from ultrasonic testing of around 80 GPa. Upon nucleation at 550°C for 30, 150, 300 and 3000 min, there is only a marginal increase in elastic modulus reaching up to a maximum of 83 GPa. Nevertheless, E rises rapidly from ~86 GPa to ~96 GPa for LAS1 glass samples heat-treated (and from ~87 to ~95 GPa for LAS2 glass samples heat-treated) at 690°C and 730°C for 30 min, respectively. The incorporation of nucleation step of 300 minutes at 550°C, leads to an increase of E to ~93 GPa and 97 GPa for samples heat-treated at 690°C and 730°C for 30 min, respectively. There is also an increase of the hardness from 6.5 GPa to 6.7 GPa, for LAS1 glass samples heat treated (and from 6.37 to 6.55 GPa for LAS2 glass samples heat treated) at 710°C and 730°C, respectively. This remarkable increase is commensurate with the crystallisation of LiAlSi₂O₆ and Li₂Si₂O₅, according to the section 5.4.2 and 6.4.2. Due to this, the fracture toughness increases continuously from 0.7±0.1 MPa \sqrt{m} to 1.8±0.1 MPa \sqrt{m} for LAS1 glass samples heat treated for 30 minutes at 690°C and 870°C, respectively, and from 1.08±0.11 to 1.71±0.04 MPa \sqrt{m} for LAS2 glass samples heat treated for same temptaure range above. Table 7. 3 compares the mechanical properties of LAS1 and 2 glasses with LS- and LAS-based glass ceramics.

Table 7. 3 The mechanical properties of lithium disilicate (LS) and lithium aluminosilicate (LAS) glass-ceramics.

| References | Vickers Hardness (GPa) | Flexural strength (MPa) | Elastic modulus (GPa) | Fracture toughness MPa.m ^{1/2} |
|--|------------------------|-------------------------|-----------------------|---|
| Wang et al. 2010 [163] | | 310 | | |
| Huang et al. 2013 [164] | 7.83±0.2 | 439±93 | | 1.29±0.07 |
| Zhang, et al. 2013 [165] | 8.4±0.1 | 307±16 | | 1.23 |
| Lien et al. 2015 [170] | 8.2±0.1 | 367 ± 43.3 | 99.0 ± 1.29 | |
| Li et al. 2016 [171] | 9.07±0.13 | 370±36 | 117.66±.96 | |
| Laczka et al. 2014 [10] | | ~400 | | |
| LAS1 glass (average max. value) | 6.93±0.08 | 377.23±25.71 | 99.1±0.53 | 1.84±0.09 |
| LAS2 glass (average max. value) | 6.42±0.06 | | 97.17±0.42 | 2.00±0.12 |

Huang, Cao, et al. 2013 [164] reported the highest flexural strength however, but a low fracture toughness was about 1.29 ± 0.07 MPa.m $^{1/2}$. As for LAS1 glass in this study, the largest higher fracture toughness $\sim 1.84\pm0.09$ MPa.m $^{1/2}$, which was observed for samples nucleated at 550°C for 300 min, subsequently heat treated at 780°C for 120 min, and finally at 850°C for 120min. While for LAS2 glass, it is 2.00 ± 0.12 MPa.m $^{1/2}$ for the same heat treatment.

7.3.2 Flexural strength

Flexural strength is regarded as a preferred testing method in dentistry [280]. Hence, commercial companies regularly seek to show flexural strength value for their products. As for lithium disilicate strengthened lithium aluminosilicate glass-ceramic, investigated by Laczka et al [10], showed a flexural strength as higher as 400 MPa. LAS1 glass-ceramic in this study reaches to a maximum value flexural strength of ~ 448 MPa when the heat treatment is at 550°C for 300min and 780°C for 120min and 850°C for 90 min. Whereas the highest flexural strength average is 377.23 ± 25.71 MPa when the heat treatment is at 550°C for 300min and 780°C for 120min and 830°C for 120min. Fig. 7. 3, provides a comparison of the flexural strength between LAS1 glass-ceramic in this study and four commercial CAD/CAM glass-ceramics, taken from their technical information.

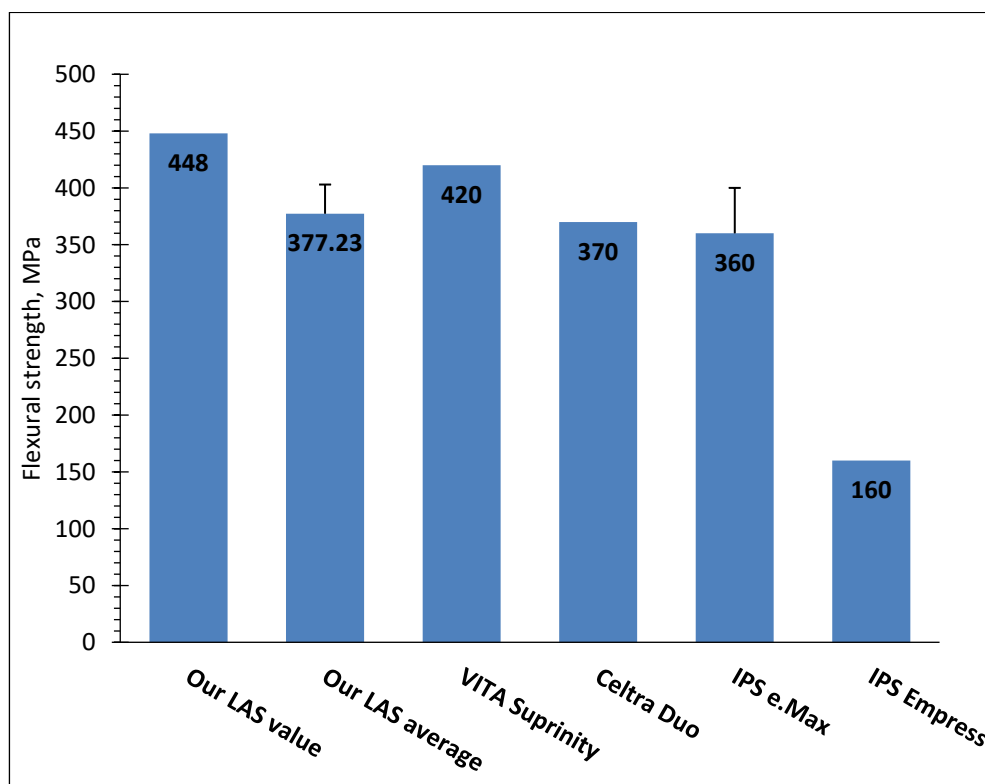


Fig. 7. 3 Flexural strength of five CAD/CAM glass-ceramics [281], [282], [283].

IPS Empress® 2 introduced by Ivoclar Vivadent consists of ~ 65% volume fraction of lithium-disilicates, ~ 34% volume fraction of vestigial glass and it shows lower strength of 160 MPa [281]. According to manufacturer literature, crystallized IPS e.Max consists of ~ 70% volume fraction of fine-grain lithium-disilicate crystals embedded in a glassy matrix [284]. It has been shown to have a flexural strength of 360±60 MPa [282], close to that found by [170] ~ 367±43.3 MPa, as listed in Table 7. 3. In contrast, Celtra Duo® and VITA Suprinity® also based on lithium-disilicate appear to have a higher strength ~370 and 420 MPa, respectively [283]. Although they used the high ZrO₂ (zirconia) contents (8–12 wt%). [285], [286]. Indeed, zirconia content is 12 times greater than in LAS glasses in this study.

Finally, mechanical properties of natural teeth were mentioned in the section 2.3.3 in detail. However, it can be pointed out that the strength of human natural teeth is estimated based on the strength of enamel and dentin. Hence, Table 7. 4 summarises the mechanical properties of the natural tooth (enamel and dentin) alongside the mechanical properties of LAS1 and LAS2 glasses. LAS1 glass-ceramic in this study accounts for a maximum elastic modulus value of ~ 99.1±0.53 MPa when the heat treatment is at 550°C for 300min and 780°C for 120min and 850°C for 120 min. While the highest fracture toughness average is 2.00±0.12 MPam^{1/2} when LAS2 glass heat treatment is at 550°C for 300min and 780°C for 120min and 850°C for 120min. Both the mechanical properties, flexural strength and hardness, for LAS1 glass samples meet the requirements of natural tooth (enamel and dentin) when the heat treatment is at 550°C for 300min and 780°C for 120min and 830°C-850°C for 120min, as shown in Table 7.4.

Table 7. 4 The mechanical properties of the natural tooth (enamel and dentin).

| Property | Enamel | Dentin | Average max. value | |
|--|-----------------------------------|--------------------------------------|---------------------|-------------------|
| | | | LAS1 glass | LAS2 glass |
| Density ρ g/cm ³ | 2.96-3.02 [25], [39] | 1.29-2.4 [25], [39] | 2.47±0.01 | 2.46±0.002 |
| Elastic modulus GPa | 48-120 [22], [25], [39] | 16-24 [22], [25], [39] | 99.1±0.53 | 97.17±0.42 |
| Fracture toughness MPam ^{1/2} | 0.6-1.5 [39] | 2.2-3.1 [39] | 1.84±0.09 | 2.00±0.12 |
| Flexural strength MPa | 60-90 [25] | 245-280 [25] | 377.23±25.71 | |
| Hardness Hv GPa | 3-6 [22], [25], [39] | 0.13-0.92 [22], [25], [39] | 6.93±0.08 | 6.42±0.06 |

7.4 Optical properties

Colour measurements using the CIE L*a*b* colour space revealed a continuous increase in lightness, L*, from 35 to 80 for samples LAS1 glass heat treated for 30 minutes at 630°C and 790°C, respectively. As for LAS2 glass, L* increased from 11 to 66.4 for 30 minutes at 630°C and 790°C, respectively. For heat treatments above 710°C, b* (from blue (-) to yellow (+)) varies from -15 to +5 for LAS1 glass. Whereas b* varies from -7 to +18 for LAS2 glass. a* (from green (-) to red (+)) ranges -3.7 to -0.7 for samples LAS1 glass heat treated above 730°C. In contrast, a* ranges -2.3 to 0.9 for samples LAS2 glass heat treated above 730°C. Similar trends are observed for nucleated samples. Based on *In-situ* and *Ex-Situ* XRD data, this change is consistent with the appearance of Li₂Si₂O₅ and LiAlSi₂O₆ crystals.

As mentioned in the section 2.4.3, not only good mechanical properties are required to meet demands in dental restoration, but also suitable optical properties including both colour and translucency, which match human teeth characteristics are of overriding importance [287]. Human natural teeth mainly consist of opaque dentin and covered by translucent enamel. Teeth colour arises from the dentin, as mentioned in section 2.3.2 [104].

Recent researches reported that many factors, such as an experience, and eye fatigue, can affect ability to adopt the accepted shade and result in discrepancies [287], [288]. Hence, to overcome these factors, spectrophotometers and colorimeters become more widespread in dentistry as an electronic shade matching device [74].

This section is devoted to study the optical property (colour) of some dental ceramic materials with a standardized thickness and range of matching with standard shades. Many samples showed $\Delta E < 3.7$, that was determined to be the threshold limit for clinically unacceptable colour difference [289]–[291].

In the CIE L*a*b* colour space system, human natural teeth has the following values: L* (69.9 ± 4.1), a* (1.22 ± 1.4), and b* (17.9 ± 2.9) [37]. In terms of translucency parameter (TP), enamel and dentin with 1 mm thickness have the following values 18.7 and 16.4, respectively [60].

Statistical analysis was conducted to compare the ΔE , translucency parameter (TP), contrast ratio (CR) and opalescence parameter (OP) for different thicknesses of recent types of brands CAD–CAM ceramic systems and our LAS glass-ceramic, as shown in Table 7. 5. In this thesis, colour measurements using the CIE L*a*b* colour space revealed a continuous increase in lightness, L*, from 35 to 80 for samples LAS1 glass heat treated for 30 minutes from 630°C to 790°C, respectively. For LAS2 glass, L* increased from 11 to 66.4. For heat treatments above 710°C, b* (from blue (-) to yellow (+)) varies from -15 to +5 for LAS1 glass. Whereas for LAS2 glass, b* varies from -7 to +18. a* (from green (-) to red (+)) for LAS1 glass heat treated above 730°C ranges -3.7 to -0.7, whereas for LAS2 glass a* ranges -2.3 to 0.9. Based on *In-situ* and *Ex-Situ* XRD data, these changes are coincided with the appearance of $\text{Li}_2\text{Si}_2\text{O}_5$ and $\text{LiAlSi}_2\text{O}_6$ crystals, but in LAS2 glass the evolution of colour it is ultimately related to the presence of vanadium.

The optimised LAS1 glass sample shows L* (82.53 ± 0.06), a* (-0.73 ± 0.06) and b* (2.77 ± 0.06), with translucency parameter (TP) for 1 mm thickness of about 16.48. The optimised LAS2 glass sample shows L* (69.53 ± 0.15), a* (0.5 ± 0.1) and b* (16.77 ± 0.06).

Table 7. 5 lists TP values that were calculated for groups with the same thicknesses. In the 0.5 mm thickness, the highest mean TP value was for VITA Mark 2 (29.20 ± 0.71) followed by LAS1 glass and VITA Suprinity with TP values of (24.04) and (23.30 ± 0.72), respectively. However, the contrast ratio (CR) for IPS Empress2 (0.68 ± 0.020) was higher than for LAS1 glass (0.47). It is interesting to note that the opalescence parameter (OP) of VITA Suprinity was the highest (10.07 ± 0.47) followed by LAS1 glass (6.46) and VITA Mark 2 (4.22 ± 0.18).

For the 1.0 mm thickness, TP value of Mark 2 was the highest (19.59 ± 2.27) followed by IPS e.max (18.51 ± 0.27), VITA Mark 2 (17.62 ± 0.35), LAS1 glass (16.48) and the lowest was for VITA Suprinity (14.26 ± 0.52). However, in 1 mm thickness an observed drop in TP value of VITA Mark 2 in comparison to 0.5 mm.

Chapter Seven: General Discussion

Table 7. 5 Mean and SD values of ΔE , translucency parameter (TP), contrast ratio (CR) and opalescence parameter (OP) for some brands CAD–CAM ceramic systems and our LAS glass-ceramic.

| Shade | Commercial brands (thickness mm) | ΔE | TP | CR | OP | References |
|------------|-------------------------------------|------------------|--------------|--------------|-------------|------------|
| A1 | In-Ceram (1mm) | 5.97±1.31 | 6.00±0.85 | | | [231] |
| | Empress 2 (1mm) | 6.17±3.34 | 16.67±0.99 | | | |
| | Mark 2 (1mm) | 6.46±3.82 | 19.59±2.27 | | | |
| A3 | In-Ceram (1mm) | 8.08±0.39 | 3.82±0.58 | | | [233] |
| | Empress 2 (1mm) | 10.41±2.86 | 18.04±0.39 | | | |
| | Mark 2 (1mm) | 6.24±4.30 | 18.76±0.31 | | | |
| | IPS Empress 2 (0.5) | | | 0.68±0.020 | | |
| | IPS Empress 2 (0.8) | | | 0.72 ± 0.013 | | |
| A1 | IPS e.max (0.5mm) | 1.59 | 14.82±0.79 | | | [77] |
| A1 | IPS e.max Press(0.5mm) | 1.51 | 16.96±0.81 | | | |
| A1 | IPS e.max (1mm) | | 18.51±0.27 | 0.59± 0.01 | 4.41±0.12 | [36] |
| | VITA Mark 2 (0.5) | | 29.20±0.71 | | 4.22±0.18 | [292] |
| | VITA Mark 2 (1.0) | | 17.62±0.35 | | 4.74±0.17 | |
| | VITA Suprinity (0.5) | | 23.30±0.72 | | 10.07±0.47 | |
| | VITA Suprinity (1.0) | | 14.26±0.52 | | 10.56±0.61 | |
| High white | Our LAS1 glass (0.5) | | 24.04 | 0.47 | 6.46 | |
| | Our LAS1 glass (1.0) | | 16.48 | 0.62 | 4.94 | |
| | Our LAS1 glass (3.0) | | 4.46 | 0.90 | 1.94 | |
| B2 | Our LAS2 glass | 2.23±0.32 | | | | |

Chapter | 8 |

Conclusion and Future Work

Chapter Eight: Conclusion and Future Work

8.1 Conclusion

A comprehensive study devoted to processing and characterisation of the thermal, mechanical, and optical properties of two lithium aluminosilicate (LAS) based glasses glass-ceramic was carried out. The following results were obtained:

- Inductively coupled plasma optical emission spectroscopy (ICP-OES) analyses revealed LAS1 glass and LAS2 glass compositions to be entirely similar, apart from the presence of V_2O_5 in LAS2 glass which is well known to impart a yellow colour in glass.
- Differential scanning calorimetry (DSC) revealed LAS1 and LAS2 glasses to exhibit similar thermal behaviour. They showed a glass transition temperature of $\sim 500^\circ C$, two major thermal exothermic events at $615^\circ C$ and $705^\circ C$, which are followed by two minor thermal exothermic events at $750^\circ C$ and $790^\circ C$, and finally a major endothermic event at $910^\circ C$.
- Based on In-situ XRD analyses, the first exothermic event is associated with the crystallisation of Li_2SiO_3 , $Li_{0.25}Al_{0.25}Si_{0.75}O_2$ and $LiAlSi_4O_{10}$, whereas the second peak is associated with crystallisation of $LiAlSi_2O_6$ and $Li_2Si_2O_5$.
- Ex-situ XRD and RS analyses disclosed that the first exothermic event in DSC trace involves two sub-peaks, the first sub-peak is associated with the crystallisation of Li_2SiO_3 and the other sub-peak is associated with $LiAlSi_4O_{10}$.
- A nucleation step of 300 minutes at $550^\circ C$ lowered the crystallisation temperature of $LiAlSi_4O_{10}$ and $Li_{0.25}Al_{0.25}Si_{0.75}O_2$ by $\sim 20^\circ C$ but leads to an increase of the crystallite sizes.
- The ratio of $LiAlSi_2O_6$ to $Li_2Si_2O_5$ increases with increasing temperature until $850^\circ C$.
- In both LAS1 and LAS2 glasses, increased heat treatment temperature enhanced the rigidity of glass structures resulting in larger elastic modulus, flexural strength, hardness, and fracture toughness. However, the

hardness is decreasing when the heat treatment temperature is above 770°C.

- For LAS1 glass, CIE L*a*b* colour space revealed a continuous increase in lightness, L*, from 36.87 to 79.7 for samples heat treated for 30 minutes at 630°C and 790°C, respectively. For LAS2 glass, L* increases from 14.93 to 66.4 for the same heat treatment.
- LAS1 glass subjected to a heat treatment above 710°C showed a variation of -3.5 to -0.7 in CIE a* (from green [-] to red [+]), whereas b* (from blue [-] to yellow [+]) varies from -15 to +5. On the other hand, for LAS2 glasses heated above 710°C showed a variation of ~ -3 to 1 for a* and from ~ -4 to 18 for b*.
- Concerning colour matching with the VITA Classical shade guide standard, LAS1 glass does not meet any standard shade. In fact, LAS1 glass block colour is white and may meet a bleach standard instead. Whereas LAS2 glass heated above 770°C is identical to several standard shades including D2, C1 and B2, depending on the heat treatment temperature.
- LAS1 and LAS2 glasses heated treated above 770°C are mechanically and aesthetically meeting the requirement of natural teeth.

8.2 Future Work

Recommendations for future work are as follows:

- Impact of heat treatment on the friction and wear behaviour of this LAS glass-ceramic.
- Characterise the oxidation state of vanadium cations in LAS2 glass in function of heat treatment.
- Employment of digital image correlation (DIC) to provide full field strain maps, in order to calculate the J-integral values, using V-notched samples.
- Study of thermo-mechanical behaviour of LAS glass-ceramics. Two NDE methodologies will be applied in order: 1) associate phase assemblage with their thermal behaviour. 2) monitor thermo-mechanical behaviour under compressive loading.
- Fabricate dental crowns.

References

- [1] D. Duraccio, F. Mussano, and M. Giulia, “Biomaterials for dental implants : current and future trends,” *J. Mater. Sci.*, vol. 50, no. 14, pp. 4779–4812, 2015.
- [2] O. Addison, X. Cao, P. Sunnar, and G. J. P. Fleming, “Machining variability impacts on the strength of a ‘chair-side’ CAD-CAM ceramic,” *Dent. Mater.*, vol. 28, no. 8, pp. 880–887, 2012.
- [3] E. El-Meliegy and R. van Noort, *Glasses and Glass Ceramics for Medical Applications*. New York: Springer Science+Business Media, LLC, 2012.
- [4] E. Adolfsson and J. Z. Shen, “Defect Minimization in Prosthetic Ceramics,” in *Advanced Ceramics for Dentistry*, Elsevier Inc., 2014, pp. 359–373.
- [5] S. Chen, Y. J. Wei, M. M. Chen, and Z. T. Zhang, “Bilateral treatment: A strategy for enhancing the mechanical strength of machinable veneers,” *Dent. Mater.*, vol. 26, no. 10, pp. 961–967, 2010.
- [6] W. Höland and G. H. Beall, *Glass-Ceramic Technology*, Second Ed. New Jersey: The American Ceramic Society, 2012.
- [7] A. Gaddam, S. Goyal, M., Jain, and P. Bhargava, “Lithium Disilicate based Glass-Ceramics for Dental Applications,” *Trans. Indian Ceram. Soc.*, vol. 72, no. 1, pp. 56–60, 2013.
- [8] R. Gozneli, E. Kazazoglu, and Y. Ozkan, “Flexural properties of leucite and lithium disilicate ceramic materials after repeated firings,” *J. Dent. Sci.*, vol. 9, no. 2, pp. 144–150, 2014.
- [9] W. Höland *et al.*, “Future perspectives of biomaterials for dental restoration,” *J. Eur. Ceram. Soc.*, vol. 29, no. 7, pp. 1291–1297, 2009, doi: 10.1016/j.jeurceramsoc.2008.08.023.
- [10] M. Laczka, K. Laczka, K. Cholewa-kowalska, A. B. Kounga, and C. Appert, “Mechanical Properties of a Lithium Disilicate Strengthened Lithium Aluminosilicate Glass-Ceramic,” *J. Am. Ceram. Soc.*, vol. 97, no. 2, pp. 361–364, 2014.
- [11] G. H. Beall, B. R. Karstetter, and H. L. Rittler, “Crystallization and Chemical Strengthening of Stuffed β -Quartz Glass-Ceramics,” *J. Am. Ceram. Soc.*, vol. 50, no. 4, pp. 181–190, 1967.
- [12] A. Hu, M. Li, and D. Mao, “Preparation of whisker β -spodumene glass-ceramics,” *J. Am. Ceram. Soc.*, vol. 89, no. 1, pp. 358–360, 2006.
- [13] E. D. Zanotto, “A bright future for glass-ceramics,” *Am. Ceram. Soc. Bull.*, vol. 89, no. 8, pp. 19–27, 2010.
- [14] L. L. Hench and J. M. Polak, “Third-Generation Biomedical Materials,” *Science* (80-.), vol. 295, no. 5557, pp. 1014–1017, 2002.
- [15] V. Migonney, “Definitions, Chapter 2,” in *Biomaterials*, John Wiley & Sons, 2014, pp. 11–25.
- [16] J. A. Juhasz and S. M. Best, “Bioactive ceramics : processing , structures and properties,” *J. Mater. Sci.*, vol. 47, no. 2, pp. 610–624, 2012.
- [17] J. Chevalier and L. Gremillard, “Ceramics for medical applications: A picture for the next 20 years,” *J. Eur. Ceram. Soc.*, vol. 29, no. 7, pp. 1245–1255, 2009.
- [18] M. Vallet-Regí, “Ceramics for medical applications,” *J. Chem. Soc. Dalt. Trans.*, no. 2, pp. 97–108, 2001.
- [19] T. Kokubo, H. M. Kim, and M. Kawashita, “Novel bioactive materials with different mechanical properties,” *Biomaterials*, vol. 24, no. 13, pp. 2161–2175, 2003.
- [20] T. Yamamuro, “Chapter 3 Bioceramics,” in *Biomechanics and Biomaterials in Orthopedics*, Springer-Verlag London, 2004, pp. 24–42.

- [21] T. Duminis, S. Shahid, and R. G. Hill, “Apatite glass-ceramics: A review,” *Front. Mater.*, vol. 3, no. January, pp. 1–15, 2017.
- [22] Y. R. Zhang, W. Du, X. D. Zhou, and H. Y. Yu, “Review of research on the mechanical properties of the human tooth,” *Int. J. Oral Sci.*, vol. 6, no. 2, pp. 61–69, 2014.
- [23] J. Zheng, Y. Huang, L. M. Qian, and Z. R. Zhou, “Nanomechanical properties and microtribological behaviours of human tooth enamel,” *Proc. Inst. Mech. Eng. Part J J. Eng. Tribol.*, vol. 224, no. 6, pp. 577–587, 2010.
- [24] C. Lu, T. Nakamura, and C. S. Korach, “Effective property of tooth enamel: Monoclinic behavior,” *J. Biomech.*, vol. 45, no. 8, pp. 1437–1443, 2012.
- [25] H. Chen and Y. Liu, “Chapter 2. Teeth,” in *Advanced Ceramics for Dentistry*, J. Z. Shen and T. Kosmač, Eds. Elsevier Inc., 2014, pp. 5–21.
- [26] R. C. Scheid and G. Weiss, *Woelfel’s Dental Anatomy*, 8th ed. London: Jones & Bartlett Publishers, 2012.
- [27] A. K. Bose, R. Q. Blackwell, and L. S. Fosdick, “The Fractionation of Human Tooth Enamel on the Basis of Density,” *J. Dent. Res.*, vol. 39, no. 1, pp. 141–149, 1960.
- [28] M. Baldassarri, H. C. Margolis, and E. Beniash, “Compositional Determinants of Mechanical Properties of Enamel,” *J. Dent. Res.*, pp. 645–649, 2008.
- [29] J. K. Avery, P. F. Steele, and N. Avery, *Oral development and histology*. New York,: Theime, 1994.
- [30] B. Blaus, *Medical gallery of Blausen Medical*, vol. 1, no. 10. 2014.
- [31] M. Montazerian and E. D. Zanotto, “Bioactive and inert dental glass-ceramics,” *J. Biomed. Mater. Res. - Part A*, vol. 105, no. 2, pp. 619–639, 2017.
- [32] R. Halgaš, J. Dusza, J. Kaiferová, L. Kováčsová, and N. Markovská, “Nanoindentation testing of human enamel and dentin,” *Ceram. - Silikaty*, vol. 57, no. 2, pp. 92–99, 2013.
- [33] X. Liu, P. K. Chu, and C. Ding, “Surface modification of titanium , titanium alloys , and related materials for biomedical applications,” vol. 47, no. 2004, pp. 49–121, 2005.
- [34] B. Reinhardt and T. Beikler, “Dental Implants,” in *Advanced Ceramics for Dentistry.*, Elsevier Inc., 2014, pp. 51–75.
- [35] C. A. Babbush, J. A. Hahn, J. T. Krauser, and J. L. Rosenlicht, *Dental Implants: The Art and Science*, 2nd ed. Saunders, an affiliate of Elsevier Inc., 2011.
- [36] A. Della Bona, A. D. Nogueira, and O. E. Pecho, “Optical properties of CAD-CAM ceramic systems,” *J. Dent.*, vol. 42, no. 9, pp. 1202–1209, 2014.
- [37] J. J. Ten Bosch and J. C. Coops, “Tooth Color and Reflectance as Related to Light Scattering and Enamel Hardness,” *J. Dent. Res.*, vol. 74, no. 1, pp. 374–380, 1995.
- [38] A. W. Batchelor and M. Chandrasekaran, *Service characteristics of biomedical materials and implants (Vol. 3)*. London: Imperial College Press, 2004.
- [39] H. Wang *et al.*, “Mechanical properties and biocompatibility of polymer infiltrated sodium aluminum silicate restorative composites,” *J. Adv. Ceram.*, vol. 6, no. 1, pp. 73–79, 2017.
- [40] D. F. Williams, *Definitions in biomaterials: proceedings of a consensus conference of the European Society for Biomaterials*, vol. 22, no. 1. Amsterdam: Elsevier, 1987.
- [41] G. Heimke, P. Griss, E. Werner, and G. Jentschura, “The effects of mechanical factors on bio-compatibility tests,” *J. Biomed. Eng.*, vol. 3, pp. 209–213, 1981.
- [42] J. Živko-Babić, D. Lisjak, L. Ćurković, and M. Jakovac, “Estimation of chemical resistance of dental ceramics by neural network,” *Dent. Mater.*, vol. 24, no. 1, pp. 18–27, 2008.
- [43] S. M. Salman, S. N. Salama, and E. A. Mahdy, “The crystallization process and

- chemical durability of glass-ceramics based on the Li₂O-B₂O₃ (Fe₂O₃)-SiO₂ (GeO₂) system," *Ceram. Int.*, vol. 39, no. 6, pp. 7185–7192, 2013.
- [44] H. Franz, "Durability and corrosion of silicate glass surfaces," *J. Non. Cryst. Solids*, vol. 42, no. 1–3, pp. 529–534, 1980.
- [45] P. W. McMILLAN, "The crystallisation of glasses," *J. Non. Cryst. Solids*, vol. 52, no. 1–3, pp. 67–76, 1982.
- [46] N. V Raptis, K. X. Michalakis, and H. Hirayama, "Optical behavior of current ceramic systems.," *Int. J. Periodontics Restorative Dent.*, vol. 26, no. 1, pp. 31–41, 2006.
- [47] G. Davidowitz and P. G. Kotick, *The Use of CAD / CAM in Dentistry*, vol. 55. Dental Clinics., 2011.
- [48] G. Griss, P., Werner, E. and Heimke, *Alumina ceramic, bioglass and silicon nitride. A comparative biocompatibility study*. In "Mechanical Properties of Biomaterials." Chichester: Wiley, 1978.
- [49] A. Vichi, C. Louca, G. Corciolani, and M. Ferrari, "Color related to ceramic and zirconia restorations: A review," *Dent. Mater.*, vol. 27, no. 1, pp. 97–108, 2011.
- [50] J. R. Kelly, I. Nishimura, and S. D. Campbell, "in dentistry : Historical roots and current perspectives," *J. Prosthet. Dent.*, vol. 75, no. 1, pp. 18–32, 1996.
- [51] K. Povel, J. Helfmann, H.-J. Cappius, M. Friebel, and M. Meinke, "Optical properties of dental restorative materials in the wavelength range 400 to 700 nm for the simulation of color perception," *J. Biomed. Opt.*, vol. 14, no. 5, p. 054029, 2009.
- [52] R. Ghinea, M. del M. Pérez, R. D. Paravina, A. M. Ionescu, O. E. Pecho, and J. de la C. Cardona, "Color and translucency of zirconia ceramics, human dentine and bovine dentine," *J. Dent.*, vol. 40, pp. e34–e40, 2012.
- [53] J. Schanda, *Colorimetry: understanding the CIE system*. Hoboken, New Jersey: John Wiley & Sons, Inc., 2007.
- [54] A. D. Nogueira and A. Della Bona, "The effect of a coupling medium on color and translucency of CAD-CAM ceramics," *J. Dent.*, vol. 41, no. SUPPL. 3, pp. e18–e23, 2013.
- [55] H. K. Kim, S. H. Kim, J. B. Lee, and S. R. Ha, "Effects of surface treatments on the translucency, opalescence, and surface texture of dental monolithic zirconia ceramics," *J. Prosthet. Dent.*, vol. 115, no. 6, pp. 773–779, 2016.
- [56] R. L. Sakaguchi, J. M. Powers, and R. G. Craig, *Craig's restorative dental materials*, 13th ed. Philadelphia: Elsevier/Mosby, 2012.
- [57] Y. K. Lee, "Opalescence of human teeth and dental esthetic restorative materials," *Dent. Mater. J.*, vol. 35, no. 6, pp. 845–854, 2016.
- [58] Y. K. Lee, "Translucency of dental ceramic, post and bracket," *Materials (Basel.)*, vol. 8, no. 11, pp. 7241–7249, 2015.
- [59] F. de C. Panzeri Pires-de-Souza, L. A. Casemiro, L. da F. Roberti Garcia, and D. R. Cruvinel, "Color stability of dental ceramics submitted to artificial accelerated aging after repeated firings," *J. Prosthet. Dent.*, vol. 101, no. 1, pp. 13–18, 2009.
- [60] B. Yu, J. S. Ahn, and Y. K. Lee, "Measurement of translucency of tooth enamel and dentin," *Acta Odontol. Scand.*, vol. 67, no. 1, pp. 57–64, 2009.
- [61] F. Spear and J. Holloway, "Which All-Ceramic System Is Optimal for Anterior Esthetics?," *J. Am. Dent. Assoc.*, vol. 139, no. September, pp. S19–S24, 2008.
- [62] Y. Imamoto and Y. Shichida, "Cone visual pigments," *Biochim. Biophys. Acta - Bioenerg.*, vol. 1837, no. 5, pp. 664–673, 2014.
- [63] D. Malacara, *Color vision and colorimetry: Theory and applications*, vol. 28, no. 1. 2003.
- [64] R. . Westfall, "The development of Newton's theory of color," *Isis*, vol. 53, no. 3, pp. 339–358, 1962.

- [65] A. K. R. Choudhury, *Principles of colour and appearance measurement Volume 1: Object appearance, colour perception and instrumental measurement*. Elsevier, 2014.
- [66] C. Connolly and T. Fliess, “A study of efficiency and accuracy in the transformation from RGB to CIELAB color space,” *IEEE Trans. Image Process.*, vol. 6, no. 7, pp. 1046–1048, 1997, doi: 10.1109/83.597279.
- [67] H. S. Fairman, M. H. Brill, and H. Hemmendinger, “How the CIE 1931 color-matching functions were derived from Wright-Guild data,” *Color Res. Appl.*, vol. 22, no. 1, pp. 11–23, 1997.
- [68] W. M. Johnston, “Color measurement in dentistry,” *J. Dent.*, vol. 37, pp. e2-6, 2009.
- [69] M. R. Luo, “CIE Tristimulus Values,” *Encycl. Color Sci. Technol.*, pp. 1–2, 2015.
- [70] J. C. Ragain, “A Review of Color Science in Dentistry: Colorimetry and Color Space,” 2016.
- [71] L. Kalman, “Development of a novel dental shade determination application,” *J. Dent. Res. Dent. Clin. Dent. Prospects*, vol. 14, no. 1, pp. 73–76, 2020, [Online]. Available: <https://doi.org/10.34172/joddd.2020.011>.
- [72] O. E. Pecho, M. M. Pérez, R. Ghinea, and A. Della Bona, “Lightness, chroma and hue differences on visual shade matching,” *Dent. Mater.*, vol. 32, no. 11, pp. 1362–1373, 2016.
- [73] S. Ardu, A. J. Feilzer, A. Devigus, and I. Krejci, “Quantitative clinical evaluation of esthetic properties of incisors,” *Dent. Mater.*, vol. 24, no. 3, pp. 333–340, 2008.
- [74] E. Kröger, S. Matz, M. Dekiff, B. L. Tran, L. Figgener, and D. Dirksen, “In vitro comparison of instrumental and visual tooth shade determination under different illuminants,” *J. Prosthet. Dent.*, vol. 114, no. 6, pp. 848–855, 2015.
- [75] O. Acar, B. Yilmaz, S. H. Altintas, I. Chandrasekaran, and W. M. Johnston, “Color stainability of CAD/CAM and nanocomposite resin materials,” *J. Prosthet. Dent.*, vol. 115, no. 1, pp. 71–75, 2016.
- [76] M. M. Pérez, R. Ghinea, L. I. Ugarte-Alván, R. Pulgar, and R. D. Paravina, “Color and translucency in silorane-based resin composite compared to universal and nanofilled composites,” *J. Dent.*, vol. 38, pp. 110–116, 2010.
- [77] B. Bagis and S. Turgut, “Optical properties of current ceramics systems for laminate veneers,” *J. Dent.*, vol. 41, pp. e24–e30, 2013.
- [78] K. T. L. Barizon *et al.*, “Ceramic materials for porcelain veneers. Part I: Correlation between translucency parameters and contrast ratio,” *J. Prosthet. Dent.*, vol. 110, no. 5, pp. 397–401, 2013.
- [79] M. G. Subaşı, G. Alp, W. M. Johnston, and B. Yilmaz, “Effect of thickness on optical properties of monolithic CAD-CAM ceramics,” *J. Dent.*, vol. 71, no. August 2017, pp. 38–42, 2018.
- [80] N. Sen and Y. O. Us, “Mechanical and optical properties of monolithic CAD-CAM restorative materials,” *J. Prosthet. Dent.*, vol. 119, no. 4, pp. 593–599, 2018.
- [81] T. Lube and R. Danzer, “Mechanical Properties and Reliability of Advanced Ceramics,” in *Advanced Ceramics for Dentistry*, Elsevier Inc., 2014, pp. 173–199.
- [82] J. Sergent, “Advanced ceramics and composites,” in *Book of Ceramics and Composites*, McGraw-Hill Companies, Inc., 2001.
- [83] J. R. Kelly and P. Benetti, “Ceramic materials in dentistry: Historical evolution and current practice,” *Aust. Dent. J.*, vol. 56, no. SUPPL. 1, pp. 84–96, 2011.
- [84] R. W. K. Li, T. W. Chow, and J. P. Matinlinna, “Ceramic dental biomaterials and CAD/CAM technology: State of the art,” *J. Prosthodont. Res.*, vol. 58, no. 4, pp. 208–216, 2014.
- [85] A. K. Varshneya and J. C. Mauro, “Fundamentals of the glassy state, Chapter 2,” in *Fundamentals of Inorganic Glasses*, 3rd ed., Elsevier Inc., 2019, pp. 19–35.

- [86] V. D. Kingery, H. K. Bowen, and D. R. Ublmann, *Introduction to Ceramics*, 2nd ed. New York: John Wiley and Sons, Inc., 1976.
- [87] J. E. Shelby, *Introduction to Glass Science and Technology*, 2nd ed. The Royal Society of Chemistry, 2005.
- [88] A. R. West, *Solid state chemistry and its applications*, 2nd ed., vol. 41, no. 6. John Wiley & Sons, Ltd, 2014.
- [89] W. Höland, M. Schweiger, V. M. Rheinberger, and H. Kappert, “Bioceramics and their application for dental restoration Bioceramics and their application for dental restoration,” *Adv. Appl. Ceram.*, vol. 108, no. 6, pp. 373–380, 2009.
- [90] T. Ohji, “Microstructural Control and Mechanical Properties,” in *Handbook of Advanced Ceramics: Materials, Applications, Processing, and Properties*, 2nd ed., S. Somiya, Ed. Elsevier Inc., 2013, pp. 657–673.
- [91] T. Ohji, “Testing and Evaluation of Mechanical Properties,” in *Handbook of Advanced Ceramics: Materials, Applications, Processing, and Properties*, 2nd ed., S. Somiya, Ed. Elsevier, 2013, pp. 633–656.
- [92] Jerzy Zarzycki, “Special Methods of Obtaining Glasses and Amorphous Materials, Chapter 2,” in *Materials science and technology*, WILEY-VCH Verlag GmbH & Co KGaA., 2006, pp. 90–118.
- [93] E. B. Shand, *Glass engineering handbook*, 2nd ed. New York, London: McGRAW-HILL, 1984.
- [94] A. PAUL, *Chemistry of glasses*. London, New York: Springer Science & Business Media, 1989.
- [95] W. Holand, V. Rheinberger, and M. Schweiger, “Nucleation and crystallization phenomena in glass-ceramics,” *Adv. Eng. Mater.*, vol. 3, no. 10, pp. 768–774, 2001.
- [96] M. A. Buri A, and B. F., “Nucleation in glass and differential thermal analysis,” *J. Mater. Sci.*, vol. 16, no. 2, pp. 341–344, 1981.
- [97] E. El-Meliogy and R. van Noort, “Lithium Disilicate Glass Ceramics, Chapter 12,” in *Glasses and Glass Ceramics for Medical Applications*, vol. 22, New York: Springer Science+Business Media, 2012, pp. 209–218.
- [98] W. Höland, M. Schweiger, R. Watzke, A. Peschke, and H. Kappert, “Ceramics as biomaterials for dental restoration.,” *Expert Rev. Med. Devices*, vol. 5, no. 6, pp. 729–45, 2008.
- [99] R. Van Noort and M. E. Barbour, *Introduction to Dental Materials-E-Book*, 4th ed. Elsevier Health Sciences, 2013.
- [100] P. W. McMillan, *Glass-ceramic*. London: Academic Press, 1979.
- [101] S. D. Stookey, “Catalyzed Crystallization of Glass in Theory and Practice,” *Ind. Eng. Chem.*, vol. 51, no. 7, pp. 805–808, 1959.
- [102] N. Gosling, “Development and Analysis of Apatite-Mullite Glass-Ceramic Scaffolds ; Towards Tissue Engineering of the Vertebral Endplate,” University of York, 2014.
- [103] K. T. Stanton, “The Effect of Fluorine on Microstructural Development in Apatite-mullite Glass-ceramics,” University of Limerick, 2000.
- [104] W. Höland, V. Rheinberger, E. Apel, and C. van’t Hoen, “Principles and phenomena of bioengineering with glass-ceramics for dental restoration,” *J. Eur. Ceram. Soc.*, vol. 27, no. 2–3, pp. 1521–1526, 2007.
- [105] W. Jing, C. Jinshu, T. Liying, and T. Peijing, “Effect of Nucleating Agents and Heat Treatments on the Crystallization of Magnesium Aluminosilicate Transparent Glass-ceramics,” *J. Wuhan Univ. Technol. Sci. Ed.*, vol. 28, no. 1, pp. 69–72, 2013.
- [106] A. Hu, M. Li, and D. Mao, “Controlled crystallization of glass-ceramics with two nucleating agents,” *Mater. Charact.*, vol. 60, no. 12, pp. 1529–1533, 2009.
- [107] M. Guedes, A. C. Ferro, and J. M. F. Ferreira, “Nucleation and crystal growth in

- commercial LAS compositions," *J. Eur. Ceram. Soc.*, vol. 21, no. 9, pp. 1187–1194, 2001.
- [108] Jürn W. P. Schmelzer, *Nucleation Theory and Applications*. John Wiley & Sons, 2005.
- [109] R. Casasola, J. M. Rincón, and M. Romero, *Glass-ceramic glazes for ceramic tiles: A review*, vol. 47, no. 2. 2012.
- [110] Z. Strand, *Glass-ceramic materials*. Amsterdam: Elsevier Science Publishing Company Inc., 1986.
- [111] S. J. Saint-Jean, "Dental Glasses and Glass-ceramics," in *Advanced Ceramics for Dentistry*, Elsevier Inc., 2014, pp. 255–277.
- [112] A. M. Rodrigues, A. M. C. Costa, and A. A. Cabral, "Effect of simultaneous nucleation and crystal growth on DSC crystallization peaks of glasses," *J. Am. Ceram. Soc.*, vol. 95, no. 9, pp. 2885–2890, 2012.
- [113] J. F. Shackelford and R. H. Doremus, *Ceramic and Glass Materials Structure, Properties and Processing*. New York: Springer Science+Business Media, LLC, 2008.
- [114] M. Çelikbilek, A. E. Ersundu, and S. Aydin, "Crystallization Kinetics of Amorphous Materials," in *Advances in crystallization processes*, 2012, pp. 127–162.
- [115] V. Marghussian, *Nano-Glass Ceramics: Processing, Properties and Applications*. William Andrew, 2015.
- [116] V. G. Dubrovskii, "Fundamentals of Nucleation Theory," in *Nucleation Theory and Growth of Nanostructures*, Berlin, Heidelberg: Springer, 2014, pp. 1–73.
- [117] M. Iwamatsu, "Heterogeneous critical nucleation on a completely wettable substrate," *J. Chem. Phys.*, vol. 134, no. 23, 2011.
- [118] A. K. Varshneya and J. C. Mauro, "Glass formation principles, Chapter 3," in *Fundamentals of Inorganic Glasses*, 3rd ed., A. K. Varshneya, Ed. Elsevier, 2019, pp. 37–69.
- [119] M. H. Lewis, *Glasses and Glass-Ceramics*, First Ed. New York: Chapman and Hall, 1989.
- [120] D. V. Ragone, *Thermodynamics of Materials*. New York, Chichester, Brisbane, Toronto, Singapore: John Wiley & Sons.Inc, 1994.
- [121] W. Holand, E. Apel, C. Van Hoen, and V. Rheinberger, "Studies of crystal phase formations in high-strength lithium disilicate glass-ceramics," *J. Non. Cryst. Solids*, vol. 352, pp. 4041–4050, 2006.
- [122] J. Park, "Development of a Glass-Ceramic for Biomedical Applications," Middle East Technical University, 2008.
- [123] D. Ovono Ovono, P. Bruno, G., Pradeau, and S. Berre, "Conditions for Crystallization of LAS Glass-Ceramics as a Function of Nucleating Agent Amount and Heat Treatment," *Int. J. Appl. Glas. Sci.*, vol. 4, no. 1, pp. 20–30, 2013.
- [124] S. Broady, "Development of Novel Micaceous Glass Ceramics for Dental Applications using CAD / CAM Systems," The University of Leeds, 2009.
- [125] G. H. Beall and L. R. Pinckney, "Nanophase Glass-Ceramics," *J. Am. Ceram. Soc.*, vol. 82, no. 1, pp. 5–16, 1999.
- [126] R. M. R. Wellen and E. L. Canedo, "On the Kissinger equation and the estimate of activation energies for non-isothermal cold crystallization of PET," *Polym. Test.*, vol. 40, pp. 33–38, 2014.
- [127] R. E. Ferner and J. K. Aronson, "Cato Guldberg and Peter Waage, the history of the Law of Mass Action, and its relevance to clinical pharmacology," *Br. J. Clin. Pharmacol.*, vol. 81, no. 1, pp. 52–55, 2016.
- [128] R. L. Blaine and H. E. Kissinger, "Homer Kissinger and the Kissinger equation," *Thermochim. Acta*, vol. 540, pp. 1–6, 2012.

- [129] J. Farjas and P. Roura, “Exact analytical solution for the Kissinger equation : Determination of the peak temperature and general properties of thermally activated transformations,” *Thermochim. Acta*, vol. 598, pp. 51–58, 2014.
- [130] H. E. Kissinger, “Variation of Peak Temperature With Heating Rate In Differential Thermal Analysis,” *J. Res. Natl. Bur. Stand. (1934)*, vol. 57, no. 4, pp. 217–221, 1956.
- [131] R. Wurth *et al.*, “Crystallisation mechanism of a multicomponent lithium alumino-silicate glass,” *Mater. Chem. Phys.*, vol. 134, no. 2–3, pp. 1001–1006, 2012.
- [132] P. Islam, R. Hill, and A. Stamboulis, “Activation energy for crystal growth in stoichiometric CaAl₂Si₂O₈ and Ca₂Al₂Si₂O₉ glasses,” *Mater. Sci.*, vol. 22, pp. 1287–1289, 2003.
- [133] W. Sha, “Determination of activation energy of phase transformation and recrystallization using a modified Kissinger method,” *Metall. Mater. Trans. A Phys. Metall. Mater. Sci.*, vol. 32, no. 11, pp. 2903–2904, 2001.
- [134] E. A. Marseglia, “Kinetic theory of crystallization of amorphous materials,” *J. Non. Cryst. Solids*, vol. 41, no. 1, pp. 31–36, 1980.
- [135] L. Lilenstein, Q. Fu, B. R. Wheaton, A. J. Credle, R. L. Stewart, and J. T. Kohli, “Kinetic study on lithium-aluminosilicate (LAS) glass-ceramics containing MgO and ZnO,” *Ceram. Int.*, vol. 40, pp. 11657–11661, 2014.
- [136] M. D. D. R. F. Moreira, I. M. Salvado, and R. F. Silva, “Crystallisation kinetics of β-spodumene in lithium aluminosilicate sol-gel glasses,” *J. Sol-Gel Sci. Technol.*, vol. 32, no. 1–3, pp. 317–321, 2004.
- [137] K. Matusita and S. Sakka, “Kinetic study of crystallization of glass by differential thermal analysis—criterion on application of Kissinger plot,” *J. Non. Cryst. Solids*, vol. 38, pp. 741–746, 1980.
- [138] I. W. Donald, “The crystallization kinetics of a glass based on the cordierite composition studied by DTA and DSC,” *J. Mater. Sci.*, vol. 30, no. 4, pp. 904–915, 1995.
- [139] T. Ozawa, “Kinetic analysis of derivative curves in thermal analysis,” *J. Therm. Anal.*, vol. 2, pp. 301–324, 1970.
- [140] I. W. Donald, “Crystallization kinetics of a lithium zinc silicate glass studied by DTA and DSC,” *J. Non. Cryst. Solids*, vol. 345, pp. 120–126, 2004.
- [141] K. Cheng, “Determining crystallization kinetic parameters of Li₂O–Al₂O₃–SiO₂ glass from derivative differential thermal analysis curves,” *Mater. Sci. Eng. B* 60, no. 3, pp. 194–199, 1999.
- [142] A. Bindl, H. Lüthy, and W. H. Mörmann, “Strength and fracture pattern of monolithic CAD/CAM-generated posterior crowns,” *Dent. Mater.*, vol. 22, no. 1, pp. 29–36, 2006.
- [143] A. Bindl, H. Lüthy, and W. H. Mörmann, “Fracture load of CAD/CAM-generated slot-inlay FPDs,” *Int. J. Prosthodont.*, vol. 16, no. 6, pp. 653–60, 2014.
- [144] X. F. Song, L. Yin, and Y. G. Han, “In-process assessment of dental cutting of a leucite-reinforced glass-ceramic,” *Med. Eng. Phys.*, vol. 31, no. 2, pp. 214–220, 2009.
- [145] J. A. Arsecularatne, J. P. Dingeldein, and M. Hoffman, “An in vitro study of the wear mechanism of a leucite glass dental ceramic,” *Biosurface and Biotribology*, vol. 1, no. 1, pp. 50–61, 2015.
- [146] S. Mollazadeh *et al.*, “The effect of aqueous media on the mechanical properties of fluorapatite-mullite glass-ceramics,” *Dent. Mater.*, vol. 31, no. 11, pp. 1370–1376, 2015.
- [147] Q. Ren, Y. Ren, X. Wu, W. Bai, J. Zheng, and O. Hai, “Effect mechanism of spinel (MgAl₂O₄) reinforced corundum ceramics on microstructure and properties,” *J. Alloys Compd.*, vol. 793, pp. 146–154, 2019.

- [148] Y. G. Jung, I. M. Peterson, A. Pajares, and B. R. Lawn, “Contact Damage Resistance and Strength Degradation of Glass-infiltrated Alumina and Spinel Ceramics,” *J. Dent. Res.*, vol. 78, no. 3, pp. 804–814, 1999.
- [149] H. Li, X. Xi, J. Ma, K. Hua, and A. Shui, “Low-temperature sintering of coarse alumina powder compact with sufficient mechanical strength,” *Ceram. Int.*, vol. 43, no. 6, pp. 5108–5114, 2017.
- [150] X. J. Sheng, H. Xu, Z. H. Jin, and Y. L. Wang, “Preparation of glass-infiltrated 3Y-TZP/Al₂O₃/glass composites,” *Mater. Lett.*, vol. 58, no. 11, pp. 1750–1753, 2004.
- [151] A. Della Bona, J. J. Mecholsky, A. A. Barrett, and J. A. Griggs, “Characterization of glass-infiltrated alumina-based ceramics,” *Dent. Mater.*, vol. 24, no. 11, pp. 1568–1574, 2008.
- [152] H. B. Lim, W. S. Cho, and C. Y. Kim, “Effect of particle size distribution of alumina on strength of glass-infiltrated alumina,” *Ceram. Int.*, vol. 38, no. 4, pp. 3069–3074, 2012.
- [153] M. S. Chaar, N. Passia, and M. Kern, “Ten-year clinical outcome of three-unit posterior FDPs made from a glass-infiltrated zirconia reinforced alumina ceramic (In-Ceram Zirconia),” *J. Dent.*, vol. 43, no. 5, pp. 512–517, 2015.
- [154] C. A. Harper, *Handbook of ceramics glasses, and diamonds*. New York: McGraw Hill Professional, 2001.
- [155] A. Ananthanarayanan, G. P. Kothiyal, L. Montagne, and B. Revel, “MAS-NMR investigations of the crystallization behaviour of lithium aluminum silicate (LAS) glasses containing P₂O₅ and TiO₂ nucleants,” *J. Solid State Chem.*, vol. 183, no. 6, pp. 1416–1422, 2010.
- [156] Y. Wu, K. Hsu, and C. Lee, “Effects of B₂O₃ and P₂O₅ doping on the microstructure evolution and mechanical strength in a lithium aluminosilicate glass-ceramic material with TiO₂ and ZrO₂,” *Ceram. Int.*, vol. 38, no. 5, pp. 4111–4121, 2012.
- [157] W. Zheng, M. Lin, and J. Cheng, “Effect of Phase Separation on the Crystallization and Properties of Lithium Aluminosilicate Glass Ceramics,” *Glas. Phys. Chem.*, vol. 39, no. 2, pp. 142–149, 2013.
- [158] K. A. Publishers, “Microstructural study of two LAS-type glass-ceramics and their parent glass,” *J. Mater. Sci.*, vol. 35, pp. 2331–2345, 2000.
- [159] L. Barbieri, C. Leonelli, T. Manfredini, and C. Siligardi, “Nucleation and Crystallization of a Lithium Aluminosilicate Glass,” *J. Am. Ceram. Soc.*, vol. 80, no. 12, pp. 3077–3083, 1997.
- [160] S. Ross, A. Welsch, and H. Behrens, “Lithium conductivity in glasses of the Li₂O–Al₂O₃–SiO₂ system,” *Phys. Chem. Chem. Phys.*, vol. 17, pp. 465–474, 2015.
- [161] Y. Iqbal, W. E. Lee, D. Holland, and P. F. James, “Crystal nucleation in P₂O₅-doped lithium disilicate glasses,” *J. Mater. Sci.*, vol. 34, pp. 4399–4411, 1999.
- [162] X. Zheng, G. Wen, L. Song, and X. X. Huang, “Effects of P₂O₅ and heat treatment on crystallization and microstructure in lithium disilicate glass ceramics,” *Acta Mater.*, vol. 56, pp. 549–558, 2008.
- [163] F. Wang, J. Gao, H. Wang, and J. hua Chen, “Flexural strength and translucent characteristics of lithium disilicate glass-ceramics with different P₂O₅ content,” *Mater. Des.*, vol. 31, no. 7, pp. 3270–3274, 2010.
- [164] S. Huang, P. Cao, C. Wang, Z. Huang, and W. Gao, “Fabrication of a high-strength lithium disilicate glass-ceramic in a complex glass system,” *J. Asian Ceram. Soc.*, vol. 1, no. 1, pp. 46–52, 2013.
- [165] S. Huang, B. Zhang, Z. Huang, W. Gao, and P. Cao, “Crystalline phase formation, microstructure and mechanical properties of a lithium disilicate glass–ceramic,” *J. Mater. Sci.*, vol. 48, no. 1, pp. 251–257, 2013.

- [166] P. Zhang, X. Li, J. Yang, and S. Xu, “Effect of heat treatment on the microstructure and properties of lithium disilicate glass-ceramics,” *J. Non. Cryst. Solids*, vol. 402, pp. 101–105, 2014, doi: 10.1016/j.jnoncrysol.2014.05.023.
- [167] X. Guo, H. Yang, C. Han, and F. Song, “Crystallization and microstructure of Li₂O-Al₂O₃-SiO₂ glass containing complex nucleating agent,” *Thermochim. Acta*, vol. 444, no. 2, pp. 201–205, 2006.
- [168] A. Arvind, A. Sarkar, V. K. Shrikhande, A. K. Tyagi, and G. P. Kothiyal, “The effect of TiO₂ addition on the crystallization and phase formation in lithium aluminum silicate (LAS) glasses nucleated by P₂O₅,” *J. Phys. Chem. Solids*, vol. 69, pp. 2622–2627, 2008.
- [169] K. Laczka, K. Cholewa-Kowalska, and M. B. Laczka, “Thermal and spectroscopic characterization of glasses and glass-ceramics of Li₂O-Al₂O₃-SiO₂ (LAS) system,” *J. Mol. Struct. J.*, vol. 1068, pp. 275–282, 2014.
- [170] W. Lien, H. W. Roberts, J. A. Platt, K. S. Vandewalle, T. J. Hill, and T. M. G. Chu, “Microstructural evolution and physical behavior of a lithium disilicate glass-ceramic,” *Dent. Mater.*, vol. 31, no. 8, pp. 928–940, 2015.
- [171] D. Li, J. W. Guo, X. . Wang, S. F. Zhang, and L. He, “Effects of crystal size on the mechanical properties of a lithium disilicate glass-ceramic,” *Mater. Sci. Eng. A*, vol. 669, pp. 332–339, 2016.
- [172] D. G. Grossman, “Colored glass-ceramic articles,” Patent 5,387,558, 1995.
- [173] M. Leister, D. Ehrt, G. Von Der Gönna, C. Rüssel, and F. W. Breitbarth, “Redox states and coordination of vanadium in sodium silicates melted at high temperatures,” *Phys. Chem. Glas.*, vol. 40, no. 6, pp. 319–325, 1999.
- [174] A. M. Abdelghany and A. H. Hammad, “Impact of vanadium ions in barium borate glass,” *Spectrochim. Acta - Part A Mol. Biomol. Spectrosc.*, vol. 137, pp. 39–44, 2015.
- [175] B. Macalik and T. Morawska-Kowal, “Coloration processes in soda-lime silicate glasses,” *Nucl. Instruments Methods Phys. Res. Sect. B Beam Interact. with Mater. Atoms*, vol. 191, no. 1–4, pp. 379–381, 2002.
- [176] A. Gaddam, H. R. Fernandes, D. U. Tulyaganov, M. J. Pascual, and J. M. F. Ferreira, “Role of manganese on the structure, crystallization and sintering of non-stoichiometric lithium disilicate glasses,” *RSC Adv.*, vol. 4, no. 26, pp. 13581–13592, 2014.
- [177] A. R. Molla, R. P. S. Chakradhar, C. R. Kesavulu, J. L. Rao, and S. K. Biswas, “Microstructure, mechanical, EPR and optical properties of lithium disilicate glasses and glass-ceramics doped with Mn²⁺ ions,” *J. Alloys Compd.*, vol. 512, no. 1, pp. 105–114, 2012.
- [178] S. Morimoto, S. Khonthon, and Y. Ohishi, “Optical properties of Cr³⁺ ion in lithium metasilicate Li₂O · SiO₂ transparent glass-ceramics,” *J. Non. Cryst. Solids*, vol. 354, no. 28, pp. 3343–3347, 2008.
- [179] S. J. Rukmani, R. K. Brow, S. T. Reis, E. Apel, V. Rheinberger, and W. Höland, “Effects of V and Mn colorants on the crystallization behavior and optical properties of Ce-doped Li-disilicate glass-ceramics,” *J. Am. Ceram. Soc.*, vol. 90, no. 3, pp. 706–711, 2007.
- [180] D. Kim, H. J. Kim, and S. I. Yoo, “Effect of V₂O₅ colorant on the optical properties and crystallization behaviors of lithium disilicate glass-ceramics,” *J. Alloys Compd.*, vol. 836, p. 155333, 2020.
- [181] M. Rita, A. Petschelt, H. Peterlik, U. Lohbauer, and C. A. D. Cam, “Chairside CAD / CAM materials . Part 1 : Measurement of elastic constants and microstructural characterization,” *Dent. Mater.*, vol. 33, no. 1, pp. 84–98, 2016.
- [182] M. Zimmermann, A. Mehl, and S. Reich, “New CAD / CAM Materials and Blocks for Chairside Procedures,” *Int. J. Comput. Dent.*, pp. 173–181, 2013.

- [183] S. Reich, “Tooth-colored CAD/CAM monolithic restorations,” *Int. J. Comput. Dent.*, vol. 18, no. 2, pp. 131–146, 2015.
- [184] S. Rinke, M. Rödiger, D. Ziebolz, and A. K. Schmidt, “Fabrication of Zirconia-Reinforced Lithium Silicate Ceramic Restorations Using a Complete Digital Workflow,” *Case Rep. Dent.*, vol. 2015, 2015.
- [185] Fassbinder DJ, “Material Matters: A Review of Chairside CAD/CAM Restorative Materials,” *J. Cosmet. Dent.*, vol. 34, no. 3, pp. 64–74, 2018.
- [186] P. J. Shull, “Introduction to NDE,” in *Nondestructive evaluation: theory, techniques, and applications*, no. 2, CRC press, 2016, pp. 1–15.
- [187] M. K. Donais and D. B. George, *X-Ray Fluorescence Spectrometry and Its Applications to Archaeology*. New York: Momentum Press, 2018.
- [188] J. Epp, *X-Ray Diffraction (XRD) Techniques for Materials Characterization*. Elsevier Ltd, 2016.
- [189] C. Suryanarayana and M. G. Norton, *X-Ray Diffraction A Practical Approach*. New York: Springer Science+Business Media, LLC, 1998.
- [190] S. N. Ahmed, “Properties and sources of radiation,” in *Physics and Engineering of Radiation Detection*, London, New York: Elsevier Academic Press, 2015, pp. 1–64.
- [191] E. M. Jauncey, “The scattering of x-rays and Bragg’s law,” *Proc. Natl. Acad. Sci.*, vol. 10, pp. 57–60, 1924.
- [192] R. S. Khandpur, “Raman spectrometer, Chapter 7,” in *Handbook of analytical instruments*, Tata McGraw-Hill Education, 2007.
- [193] P. LARKIN, “Basic Principles,” in *Infrared and Raman spectroscopy: principles and spectral interpretation*, Elsevier Inc., 2017, pp. 12–30.
- [194] B. Schrader, *Infrared and Raman spectroscopy: methods and applications*, vol. 11, no. 2. John Wiley & Sons, 1995.
- [195] A. K. Yadav and P. Singh, “A review of the structures of oxide glasses by Raman spectroscopy,” *RSC Adv.*, vol. 5, no. 83, pp. 67583–67609, 2015.
- [196] Y. YUE *et al.*, “Effect of Al₂O₃ on structure and properties of Al₂O₃-K₂O-P₂O₅ glasses,” *J. Mater. Sci. Mater. Electron.*, vol. 8, no. 2, pp. 245–258, 2018.
- [197] L. . Velli, C. P. . Varsamis, and E. . Kamitsos, “Structural investigation of metaphosphate glasses Structural investigation of metaphosphate glasses,” *Phys Chem. Glas.*, vol. 46, no. 2, pp. 178–181, 20005.
- [198] B. N. Nelson and G. J. Exarhos, “Vibrational spectroscopy of cation-site interactions in phosphate glasses,” *J. Chem. Phys.*, vol. 71, no. 7, pp. 2739–2747, 1979.
- [199] R. K. Brow, “Review: the structure of simple phosphate glasses,” *J. Non. Cryst. Solids*, vol. 263, pp. 1–28, 2000.
- [200] J. Kuczek, P. Jeleń, P. Stoch, A. Błachowski, I. Wacławska, and M. Szumera, “Raman and Mössbauer studies of iron phosphate-silicate glasses,” *J. Mol. Struct.*, vol. 1170, pp. 82–89, 2018.
- [201] P. Glatz, M. Comte, L. Cormier, L. Montagne, B. Doumert, and G. G. Moore, “Different roles of phosphorus in the nucleation of lithium aluminosilicate glasses,” *J. Non. Cryst. Solids*, vol. 493, no. January, pp. 48–56, 2018.
- [202] S. Petrescu, M. Constantinescu, E. M. Anghel, I. Atkinson, M. Olteanu, and M. Zaharescu, “Structural and physico-chemical characterization of some soda lime zinc aluminosilicate glasses,” *J. Non. Cryst. Solids*, vol. 358, no. 23, pp. 3280–3288, 2012.
- [203] L. Chen *et al.*, “Enhanced Mechanical Properties of Li₂O-Al₂O₃-SiO₂ Photostructurable Glass by SrO Doping,” *J. Electron. Mater.*, vol. 49, no. 1, pp. 705–711, 2020.
- [204] A. G. Kalampounias, “IR and Raman spectroscopic studies of sol-gel derived

- alkaline-earth silicate glasses," *Bull. Mater. Sci.*, vol. 34, no. 2, pp. 299–303, 2011.
- [205] B. G. Parkinson *et al.*, "Quantitative measurement of Q3 species in silicate and borosilicate glasses using Raman spectroscopy," *J. Non. Cryst. Solids*, vol. 354, no. 17, pp. 1936–1942, 2008.
- [206] J. Tan, S. Zhao, W. Wang, G. Davies, and X. Mo, "The effect of cooling rate on the structure of sodium silicate glass," *Mater. Sci. Eng. B Solid-State Mater. Adv. Technol.*, vol. 106, no. 3, pp. 295–299, 2004.
- [207] M. T. Nayak and J. A. E. Desa, "Roles of iron and lithium in silicate glasses by Raman spectroscopy," *J. Raman Spectrosc.*, vol. 49, no. 9, pp. 1507–1513, 2018.
- [208] S. K. Sharma and B. Simons, "Raman study of crystalline polymorphs and glasses of spodumene composition quenched from various pressures," *Am. J. Sci.*, vol. 66, no. 1959, pp. 118–126, 1968.
- [209] I. Alekseeva, O. Dymshits, V. Ermakov, A. Zhilin, V. Petrov, and M. Tsenter, "Raman spectroscopy quantifying the composition of stuffed β -quartz derivative phases in lithium aluminosilicate glass-ceramics," *J. Non. Cryst. Solids*, vol. 354, no. 45–46, pp. 4932–4939, 2008.
- [210] "Ultrasound and its properties," *Nihon Dempa Kogyo Co.,Ltd.* <http://www.ndk.com/en/sensor/ultrasonic/basic01.html> (accessed Jun. 10, 2020).
- [211] P. J. Shull and B. R. Tittmann, "Ultrasound," in *Nondestructive evaluation: theory, techniques, and applications*, CRC press, 2002.
- [212] D. Ensminger and L. J. Bond, *Ultrasonics: Fundamentals, technologies, and applications*, 3rd ed. Taylor & Francis Group, LLC, 2012.
- [213] I. R. Sinclair, *Sensors and transducers*, 3rd ed. Elsevier, 2001.
- [214] E. P. Papadakis, "Ultrasonic phase velocity by the pulse-echo-overlap method incorporating diffraction phase corrections," *J. Acoust. Soc. Am.*, vol. 42, no. 5, pp. 1045–1051, 1967.
- [215] R. Halmshaw, *Non-Destructive Testing*, 2nd ed. London: Edward Arnold, Mill Rd, 1991.
- [216] G. Hübschen, "Ultrasonic techniques for materials characterization," in *Materials Characterization Using Nondestructive Evaluation (NDE) Methods*, 2016, pp. 177–224.
- [217] BS ISO 14705, "Fine ceramics (advanced ceramics , advanced technical ceramics) — Test method for hardness of monolithic ceramics at room temperature," pp. 1–20, 2016.
- [218] T. Asakura *et al.*, *Transmission Electron Microscopy Physics of Image Formation*, 5th ed. Springer Science+Business Media, LLC, 2008.
- [219] D. B. Williams and C. B. Carter, *Transmission Electron Microscopy*. New York: Springer Science+Business Media, LLC, 2009.
- [220] P. J. Goodhew, J. Humphreys, and R. Beanland, *Electron Microscopy and Analysis*, 3rd ed. New York: Taylor & Francis, 2001.
- [221] J. C. Spence, *High-resolution electron microscopy*, 3rd ed. New York: OUP Oxford, 2003.
- [222] L. Reimer, *Scanning Electron Microscopy Physics of Image Formation and Microanalysis*. Springer-Verlag Berlin Heidelberg, 1998.
- [223] R. F. Egerton, *Electron Energy-Loss Spectroscopy in the Electron Microscope*, 3rd ed. New York: Springer Science+Business Media, LLC, 2011.
- [224] J. Kuo, *Electron Microscopy Methods and Protocols*, 2nd ed. Humana Press Inc., 2007.
- [225] H. Schatten and J. B. Pawley, *Biological Low-Voltage Scanning Electron Microscopy*. Springer Science+Business Media, LLC, 2008.
- [226] J. I. Goldstein, D. E. Newbury, P. Echlin, D. C. Joy, C. Fiori, and E. Lifshin, *Scanning Electron Microscopy and X-Ray Microanalysis*. New York: Plenum

- Press, 1981.
- [227] B. J. Inkson, *Scanning Electron Microscopy (SEM) and Transmission Electron Microscopy (TEM) for Materials Characterization*. Elsevier Ltd, 2016.
- [228] D. J. Stokes, *Principles and Practice of Variable Pressure/Environmental Scanning Electron Microscopy (VP-ESEM)*, 1st ed. John Wiley & Sons, 2008.
- [229] R. H. W. Brodbelt, W. J. O'brien, and P. L. Fan, "Translucency of Dental Porcelains," *J. Dent. Res.*, vol. 59, no. 1, pp. 70–75, 1980, doi: 10.1177/00220345800590011101.
- [230] W. M. Johnston, T. Ma, and B. H. Kienle, "Translucency parameter of colorants for maxillofacial prostheses," *Int. J. Prosthodont.*, vol. 8, no. 1, pp. 79–86, 1995.
- [231] Q. Li, H. Yu, and Y. N. Wang, "Spectrophotometric evaluation of the optical influence of core build-up composites on all-ceramic materials," *Dent. Mater.*, vol. 25, no. 2, pp. 158–165, 2009.
- [232] J. M. Powers, J. B. Dennison, and P. J. Lepeak, "Parameters that Affect the Color of Direct Restorative Resins," *J. Dent. Res.*, vol. 57, no. 9–10, pp. 876–880, 1978.
- [233] M. J. Heffernan, S. A. Aquilino, A. M. Diaz-Arnold, D. R. Haselton, C. M. Stanford, and M. A. Vargas, "Relative translucency of six all-ceramic systems. Part I: Core materials," *J. Prosthet. Dent.*, vol. 88, no. 1, pp. 4–9, 2002.
- [234] N. Shono and H. Al Nahedh, "Contrast Ratio and Masking Ability of Three Ceramic Veneering Materials," *Oper. Dent.*, vol. 37, no. 4, pp. 406–416, 2012.
- [235] Y. K. Lee, H. Lu, and J. M. Powers, "Changes in opalescence and fluorescence properties of resin composites after accelerated aging," *Dent. Mater.*, vol. 22, no. 7, pp. 653–660, 2006.
- [236] R.-D. Vasiliu, S. D. Porajan, M. I. Bîrdeanu, and L. Porajan, "Effect of Thermocycling, Surface Treatments and Microstructure on the Optical Properties and Roughness of CAD-CAM and Heat-Pressed Glass Ceramics," *Materials (Basel.)*, vol. 13, no. 2, p. 381, 2020.
- [237] Y. Miyagawa, J. M. Powers, and W. J. O'brien, "Optical Properties of Direct Restorative Materials," *J. Dent. Res.*, vol. 60, no. 5, pp. 890–894, 1981.
- [238] F. C. S. Chu, T. W. Chow, and J. Chai, "Contrast ratios and masking ability of three types of ceramic veneers," *J. Prosthet. Dent.*, vol. 98, no. 5, pp. 359–364, 2007.
- [239] J. D. Menczel, L. Judovits, R. B. Prime, H. E. Bair, M. Reading, and S. Swier, "Differential scanning calorimetry (DSC)," in *Thermal analysis of polymers: Fundamentals and applications*, J. D. Menczel and R. B. Prime, Eds. John Wiley & Sons, Inc., 2009, pp. 7–239.
- [240] M. Thompson and N. Walash, *Handbook of Inductively Coupled Plasma Spectrometry*. New York: Blackie & Son Ltd, 1989.
- [241] H. E. Taylor, *Inductively Coupled Plasma-Mass Spectrometry Practices and Techniques*. Academic press, 2001.
- [242] L. P. Mullins, M. S. Bruzzi, and P. E. McHugh, "Measurement of the microstructural fracture toughness of cortical bone using indentation fracture," *J. Biomech.*, vol. 40, no. 14, pp. 3285–3288, 2008.
- [243] G. R. AAnstis, P. Chantikul, B. R. Lawn, and D. B. Marshall, "A Critical Evaluation of Indentation Techniques for Measuring Fracture Toughness: I, Direct Crack Measurements," *J. Am. Ceram. Soc.*, vol. 64, no. 9, pp. 533–538, 1981.
- [244] E. Rocha-Rangel, "Fracture toughness determinations by means of indentation fracture," in *Nanocomposites with unique properties and applications in medicine and industry*, J. Cuppoletti, Ed. 2011, pp. 21–38.
- [245] G. D. Quinn, B. T. Sparenberg, P. Koshy, L. K. Ives, S. Jahanmir, and D. D. Arola, "Flexural Strength of Ceramic and Glass Rods," *J. Test. Eval.*, vol. 37, no. 3, pp. 222–244, 2009.

- [246] Organizacion Internacional de Normalizacion, *International Standard ISO 6872: Dentistry - Ceramic materials*, 4th ed. Geneva: ISO, 2015.
- [247] ASTM International, “Standard Test Methods for Determination of Fracture Toughness of Advanced Ceramics at Ambient Temperature,” 2017. doi: 10.1520/C1421-16.Annex.
- [248] ASTM International, “Standard Test Method for Flexural Strength of Advanced Ceramics at Ambient Temperature,” 2017. doi: 10.1520/C1161-13.2.
- [249] E. J. Hearn, *Mechanics of Materials I: an introduction to the mechanics of elastic and plastic deformation of solids and structural components*. London: Elsevier, 1997.
- [250] S. P. Timoshenko, *Strength of Materials*. Van Nostrand Reinhold Company, 1958.
- [251] E. Apel, C. Van Hoen, V. Rheinberger, and H. Wolfram, “Influence of ZrO₂ on the crystallization and properties of lithium disilicate glass-ceramics derived from a multi-component system,” vol. 27, pp. 1571–1577, 2007.
- [252] C. A. Serna, “Development of a synthetic trabecular bone graft utilizing a two phase glass-ceramic,” The University of Leeds, 2016.
- [253] A. Arora, E. R. Shaaban, K. Singh, and O. P. Pandey, “Non-isothermal crystallization kinetics of ZnO-BaO-B₂O₃-SiO₂ glass,” *J. Non. Cryst. Solids*, vol. 354, pp. 3944–3951, 2008.
- [254] L. Vladislavova, C. Thieme, and C. Ruessel, “The effect of ZrO₂ on the crystallization of a glass in the system BaO/SrO/ZnO/SiO₂: surface versus bulk crystallization,” *J Mater Sci*, vol. 52, pp. 4052–4060, 2017.
- [255] P. F. James, Y. Iqbal, U. S. Jais, S. Jordery, and W. E. Lee, “Crystallisation of silicate and phosphate glasses,” *J. Non. Cryst. Solids*, vol. 219, pp. 17–29, 1997.
- [256] H. Harper, P. F. James, and P. Mcmillan, “Crystal Nucleation in Lithium Silicate Glasses,” 1970.
- [257] S. C. Von Clausbruch, M. Schweiger, and H. Wolfram, “The effect of P₂O₅ on the crystallization and microstructure of glass-ceramics in the SiO₂-Li₂O-K₂O-ZnO-P₂O₅ system,” *J. Non. Cryst. Solids*, vol. 264, pp. 388–394, 2000.
- [258] P. W. McMillan, S. V. Phillips, and G. Partridge, “The structure and properties of a lithium zinc silicate glass-ceramic,” *J. Mater. Sci.*, vol. 1, no. 3, pp. 269–279, 1966.
- [259] S. Kruger, J. Deubener, C. Ritzberger, and W. Holand, “Nucleation Kinetics of Lithium Metasilicate in ZrO₂-Bearing Lithium Disilicate Glasses for Dental Application,” *Int. J. Appl. Glas. Sci.*, vol. 4, no. 1, pp. 9–19, 2013.
- [260] Y. Wu, K. Hsu, and C. Lee, “Study of relationships among synthesis, microstructure and mechanical properties of lithium aluminosilicate glass-ceramics containing ZnO and MgF₂ by synchrotron XRD and XANES,” *J Mater Sci*, vol. 48, pp. 4427–4437, 2013.
- [261] Meredith Brooke Barta, “Nanocomposite Glass-Ceramic Scintillators for Radiation Spectroscopy,” 2012.
- [262] R. D. Moorehead, “Crystallisation in fluorapatite-fluorphlogopite glass ceramics,” (Doctoral dissertation, Salford: University of Salford), 2011.
- [263] A. L. Patterson, “The scherrer formula for X-ray particle size determination,” *Phys. Rev.*, vol. 56, no. 10, pp. 978–982, 1939.
- [264] G. Mendes and B. Lago, *Strength of materials*. New York: Nova Science Publishers, Inc., 2009.
- [265] H. Bach and D. Krause, *Analysis of the Composition and Structure of Glass and Glass Ceramics*, First. New York: Springer-Verlag Berlin Heidelberg, 1999.
- [266] L. Popović, B. Manoun, D. De Waal, M. K. Nieuwoudt, and J. D. Comins, “Raman spectroscopic study of phase transitions in Li₃PO₄,” *J. Raman Spectrosc.*, vol. 34, no. 1, pp. 77–83, 2003.

- [267] P. Richet, B. O. Mysen, and D. Andrault, “Melting and premelting of silicates: Raman spectroscopy and X-ray diffraction of Li₂SiO₃ and Na₂SiO₃,” *Phys. Chem. Miner.*, vol. 23, no. 3, pp. 157–172, 1996.
- [268] A. A. Kaminskii *et al.*, “Lithium silicate, LiAlSi₄O₁₀ (petalite) - A novel monoclinic SRS-active crystal,” *Laser Phys. Lett.*, vol. 12, no. 8, 2015.
- [269] R. J. Terry *et al.*, “Hydrothermal single crystal growth and second harmonic generation of Li₂SiO₃, Li₂GeO₃ and Li₂Si₂O₅,” *J. Cryst. Growth*, vol. 493, pp. 58–64, 2018.
- [270] T. Fuss, A. Moguš-Milanković, C. S. Ray, C. E. Lesher, R. Youngman, and D. E. Day, “Ex situ XRD, TEM, IR, Raman and NMR spectroscopy of crystallization of lithium disilicate glass at high pressure,” *J. Non. Cryst. Solids*, vol. 352, no. 38–39, pp. 4101–4111, 2006.
- [271] P. Wange, T. Höche, C. Rüssel, and J. Dieter Schnapp, “Microstructure-property relationship in high-strength MgO-Al₂O₃-SiO₂-TiO₂ glass-ceramics,” *J. Non. Cryst. Solids*, vol. 298, no. 2–3, pp. 137–145, 2002.
- [272] A. El-Sabbagh, L. Steuernagel, and G. Ziegmann, “Characterisation of flax polypropylene composites using ultrasonic longitudinal sound wave technique,” *Compos. Part B Eng.*, vol. 45, no. 1, pp. 1164–1172, 2013.
- [273] J. Krautkramer and H. Krautkramer, *Ultrasonic testing by determination of material properties*. Berlin, Heidelberg: Springer, 1990.
- [274] E. K. Keler, E. I. Kozlovskaya, and O. V. Nosikov, “Determination of the elastic properties of glass and fine ceramics by the ultrasonic impulse method,” *Glas. Ceram.*, vol. 13, no. 5, pp. 210–217, 1956.
- [275] U. Lohbauer, A. M. Frank, and A. Petschelt, “Influence of surface roughness on mechanical strength of resin composite versus glass ceramic materials,” vol. 4, pp. 250–256, 2007.
- [276] I. E. Matyash, I. A. Minailova, B. K. Serdega, and I. S. Babichuk, “Research of optical and mechanical properties of lithium aluminosilicate glass-ceramics,” *J. Non. Cryst. Solids*, vol. 459, pp. 94–98, 2017.
- [277] B. Stawarczyk, A. Liebermann, M. Eichberger, and J. F. Güth, “Evaluation of mechanical and optical behavior of current esthetic dental restorative CAD/CAM composites,” *J. Mech. Behav. Biomed. Mater.*, vol. 55, pp. 1–11, 2015.
- [278] H. Kilinc and S. Turgut, “Optical behaviors of esthetic CAD-CAM restorations after different surface finishing and polishing procedures and UV aging: An in vitro study,” *J. Prosthet. Dent.*, vol. 120, no. 1, pp. 107–113, 2018.
- [279] C. S. Ray and D. E. Day, “Determining the Nucleation Rate Curve for lithium Disilicate Glass by Differential Thermal Analysis,” *J. Am. Ceram. Soc.*, vol. 73, no. 2, pp. 439–442, 1990.
- [280] M. Wendler *et al.*, “Chairside CAD / CAM materials . Part 2 : Flexural strength testing,” *Dent. Mater.*, vol. 33, no. 1, pp. 99–109, 2016.
- [281] M. Guazzato, M. Albakry, S. P. Ringer, and M. V. Swain, “Strength, fracture toughness and microstructure of a selection of all-ceramic materials. Part I. Pressable and alumina glass-infiltrated ceramics,” *Dent. Mater.*, vol. 20, no. 5, pp. 441–448, 2004.
- [282] A. Willard and T. M. Gabriel Chu, “The science and application of IPS e.Max dental ceramic,” *Kaohsiung J. Med. Sci.*, vol. 34, no. 4, pp. 238–242, 2018.
- [283] E. Bajraktarova-Valjakova, V. Korunoska-Stevkovska, B. Kapusevska, N. Gigovski, C. Bajraktarova-Misevska, and A. Grozdanov, “Contemporary dental ceramic materials, a review: Chemical composition, physical and mechanical properties, indications for use,” *Open Access Maced. J. Med. Sci.*, vol. 6, no. 9, pp. 1742–1755, 2018.
- [284] “Scientific Documentation I.P.S. e.max® CAD. FL-9494 Schaan, Liechtenstein,”

ivoclarvivadent, 2005. .

- [285] VITA Zahnfabrik H. Rauter GmbH &, “Vita Suprinity ® Technical and scientific documentation,” 2001. [Online]. Available: <https://panadent.co.uk/wp-content/uploads/2014/10/Vita-Suprinity-Technical-and-Scientific-Document.pdf>.
- [286] D. GmbH, “Celtra® Duo, Zirconia – Reinforced Lithium Silicate (ZLS).” [Online]. Available: [Prosthetics/Fixed/High_strength_glass_ceramic/Celtra_Duo/Celtra_Duo_brochure_EN.pdf](https://www.vivadent.com/prosthetics/fixed/high_strength_glass_ceramic/celtra_duo/celtra_duo_brochure_en.pdf).
- [287] S. J. Chu, R. D. Trushkowsky, and R. D. Paravina, “Dental color matching instruments and systems. Review of clinical and research aspects,” *J. Dent.*, vol. 38, no. SUPPL. 2, pp. 2–16, 2010.
- [288] C. Gómez-Polo, M. Gómez-Polo, A. Celemin-Viñuela, and J. A. Martínez Vázquez De Parga, “Differences between the human eye and the spectrophotometer in the shade matching of tooth colour,” *J. Dent.*, vol. 42, no. 6, pp. 742–745, 2014.
- [289] W. M. Johnston and E. C. Kao, “Assessment of Appearance Match by Visual Observation and Clinical Colorimetry,” *J. Dent. Res.*, vol. 68, no. 5, pp. 819–822, 1989.
- [290] S. Ishikawa-Nagai, A. Yoshida, M. Sakai, J. Kristiansen, and J. D. Da Silva, “Clinical evaluation of perceptibility of color differences between natural teeth and all-ceramic crowns,” *J. Dent.*, vol. 37, no. SUPPL. 1, pp. 57–63, 2009.
- [291] N. Alghazali, G. Burnside, M. Moallem, P. Smith, A. Preston, and F. D. Jarad, *Assessment of perceptibility and acceptability of color difference of denture teeth*, vol. 40. Elsevier Ltd, 2012.
- [292] B. Gunal and M. M. Ulusoy, “Optical properties of contemporary monolithic CAD-CAM restorative materials at different thicknesses,” *J. Esthet. Restor. Dent.*, vol. 30, no. 5, pp. 434–441, 2018.

Appendix

| 1 |

ICP-OES and XRF

ICP-OES results for the two LAS glasses (as-cast glass), as originally received.

| SAMPLE I.D. | LAS1 glass | LAS2 glass |
|---|------------|------------|
| Al | 53300 | 53400 |
| Ca | 9940 | 9680 |
| Ce | 5280 | 5280 |
| Co | 320 | 448 |
| K | 4070 | 4090 |
| Li | 47200 | 45800 |
| Na | 18600 | 18600 |
| P | 18300 | 18200 |
| Si | 279000 | 282000 |
| Tb | 5740 | 5800 |
| Ti | 109 | 109 |
| V | <10 | 1860 |
| W | 2370 | 3230 |
| Zr | 3090 | 3070 |
| ALL RESULTS MG/KG, NO OTHER ELEMENTS DETECTED | | |

1. For chemical composition of LAS1 glass

| | LAS1 glass | Element wt.% | Oxide conversion factors | Oxides compositions | oxides wt. | oxides wt.% | oxides wt.% |
|------------|---------------|--------------|--------------------------|--------------------------------|--------------------|-------------|-------------|
| Al | 53300 | 11.91516758 | 1.8895 | Al ₂ O ₃ | 22.51370915 | 11.11794238 | 11.11809398 |
| Ca | 9940 | 2.222078157 | 1.3992 | CaO | 3.109131758 | 1.535382176 | 1.535533774 |
| Ce | 5280 | 1.180339303 | 1.2284 | CeO ₂ | 1.4499288 | 0.716018171 | 0.716169769 |
| Co | 320 | 0.071535715 | 1.2715 | CoO | 0.090957662 | 0.044917612 | 0.04506921 |
| K | 4070 | 0.909844879 | 1.2046 | K ₂ O | 1.095999142 | 0.541237129 | 0.541388727 |
| Li | 47200 | 10.55151801 | 2.1527 | Li ₂ O | 22.71425282 | 11.21697684 | 11.21712844 |
| Na | 18600 | 4.158013453 | 1.348 | Na ₂ O | 5.605002135 | 2.767917555 | 2.768069153 |
| P | 18300 | 4.09094872 | 2.2916 | P ₂ O ₅ | 9.374818087 | 4.62956533 | 4.629716928 |
| Si | 279000 | 62.3702018 | 2.1392 | SiO ₂ | 133.4223357 | 65.88793658 | 65.88808818 |
| Tb | 5740 | 1.283171894 | 1.151 | Tb ₂ O ₃ | 1.47693085 | 0.72935259 | 0.729504188 |
| Ti | 109 | 0.024366853 | 1.6681 | TiO ₂ | 0.040646348 | 0.020072381 | 0.020223979 |
| V | 10 | 0.002235491 | 1.7852 | V ₂ O ₅ | 0.003990799 | 0.001970776 | 0 |
| W | 2370 | 0.529811392 | 1.261 | WO ₃ | 0.668092165 | 0.329923876 | 0.330075474 |
| Zr | 3090 | 0.690766751 | 1.3508 | ZrO ₂ | 0.933087727 | 0.460786604 | 0.460938202 |
| Sum | 447329 | 100 | | | 202.4988831 | 100 | 100 |

2. For chemical composition of LAS2 glass

| | LAS2 glass | Element wt.% | Oxide conversion factors | Oxides compositions | oxides wt. | oxides wt.% |
|------------|---------------|--------------|--------------------------|--------------------------------|--------------------|-------------|
| Al | 53400 | 11.82548769 | 1.8895 | Al ₂ O ₃ | 22.34425899 | 11.04593327 |
| Ca | 9680 | 2.143646458 | 1.3992 | CaO | 2.999390124 | 1.482755063 |
| Ce | 5280 | 1.169261704 | 1.2284 | CeO ₂ | 1.436321077 | 0.710048464 |
| Co | 448 | 0.099210084 | 1.2715 | CoO | 0.126145622 | 0.062360364 |
| K | 4090 | 0.905734919 | 1.2046 | K ₂ O | 1.091048283 | 0.539362103 |
| Li | 45800 | 10.14245948 | 2.1527 | Li ₂ O | 21.83367252 | 10.79352373 |
| Na | 18600 | 4.118990094 | 1.348 | Na ₂ O | 5.552398647 | 2.744840407 |
| P | 18200 | 4.030409662 | 2.2916 | P ₂ O ₅ | 9.236086782 | 4.565879687 |
| Si | 282000 | 62.44920466 | 2.1392 | SiO ₂ | 133.5913386 | 66.04117022 |
| Tb | 5800 | 1.284416266 | 1.151 | Tb ₂ O ₃ | 1.478363122 | 0.730832041 |
| Ti | 109 | 0.024138168 | 1.6681 | TiO ₂ | 0.040264878 | 0.01990503 |
| V | 1860 | 0.411899009 | 1.7852 | V ₂ O ₅ | 0.735322112 | 0.363508093 |
| W | 3230 | 0.71528699 | 1.261 | WO ₃ | 0.901976894 | 0.445894249 |
| Zr | 3070 | 0.679854817 | 1.3508 | ZrO ₂ | 0.918347886 | 0.453987285 |
| Sum | 451567 | 100 | | | 202.2849355 | 100 |

08/09/2016 17:15:19

XRF- LAS2 as-cast glass

PANalytical

Quantification of sample Zaid GC glass1

R.M.S.: 0.000

Sum before normalization: 25.2 %

Normalised to: 100.0 %

Sample type: Pressed powder

Correction applied for medium: No

Correction applied for film: None

Used Compound list: OXIDES

Results database: 3-iq+

Results database in: c:\superq\userdata

Analyte Calibration Compound Measured Used Concentration Calculation

| | | | status | formula | (kcps) | (kcps) | (%) | method |
|----|------------|-------|--------|---------|--------|--------|--------|-----------|
| Na | Calibrated | Na2O | 0.280 | 0.280 | | | 1.215 | Calculate |
| Al | Calibrated | Al2O3 | 6.089 | 6.089 | | | 6.394 | Calculate |
| Si | Calibrated | SiO2 | 73.747 | 73.747 | | | 86.941 | Calculate |
| P | Calibrated | P2O5 | 2.906 | 2.906 | | | 2.417 | Calculate |
| S | Calibrated | SO3 | 0.190 | 0.190 | | | 0.156 | Calculate |
| K | Calibrated | K2O | 0.532 | 0.532 | | | 0.466 | Calculate |
| Ca | Calibrated | CaO | 1.380 | 1.380 | | | 0.977 | Calculate |
| V | Calibrated | V2O5 | 0.691 | 0.691 | | | 0.274 | Calculate |
| Zr | Calibrated | ZrO2 | 5.775 | 5.775 | | | 0.154 | Calculate |
| Ce | Calibrated | CeO2 | 0.472 | 0.472 | | | 0.417 | Calculate |
| Tb | Derived | Tb4O7 | 0.428 | 0.428 | | | 0.589 | Calculate |

08/09/2016 17:09:37

XRF- Nucleated glass

PANalytical

Quantification of sample Zaid GC glass2

R.M.S.: 0.000

Sum before normalization: 33.6 %

Normalised to: 100.0 %

Sample type: Pressed powder

Correction applied for medium: No

Correction applied for film: None

Used Compound list: OXIDES

Results database: 3-iq+

Results database in: c:\superq\userdata

| Analyte | Calibration | Compound | Measured | Used | Concentration | Calculation |
|---------|-------------|--------------------------------|----------|--------|---------------|-------------|
| | status | formula | (kcps) | (kcps) | (%) | method |
| Na | Calibrated | Na ₂ O | 0.634 | 0.634 | 2.098 | Calculate |
| Mg | Calibrated | MgO | 0.159 | 0.154 | 0.176 | Calculate |
| Al | Calibrated | Al ₂ O ₃ | 14.392 | 14.392 | 11.831 | Calculate |
| Si | Calibrated | SiO ₂ | 78.018 | 78.018 | 75.115 | Calculate |
| P | Calibrated | P ₂ O ₅ | 7.537 | 7.537 | 4.552 | Calculate |
| S | Calibrated | SO ₃ | 0.231 | 0.231 | 0.139 | Calculate |
| K | Calibrated | K ₂ O | 1.637 | 1.637 | 1.065 | Calculate |
| Ca | Calibrated | CaO | 4.252 | 4.252 | 2.285 | Calculate |
| V | Calibrated | V ₂ O ₅ | 0.190 | 0.190 | 0.237 | Calculate |
| Fe | Calibrated | Fe ₂ O ₃ | 0.853 | 0.853 | 0.491 | Calculate |
| Zr | Calibrated | ZrO ₂ | 8.949 | 8.939 | 0.204 | Calculate |
| Ce | Calibrated | CeO ₂ | 1.479 | 1.458 | 1.013 | Calculate |
| Tb | Derived | Tb ₄ O ₇ | 0.828 | 0.828 | 0.794 | Calculate |

08/09/2016 16:35:42

XRF- Glass-ceramic

PANalytical

Quantification of sample Zaid GC glass3

R.M.S.: 0.000

Sum before normalization: 22.7 %

Normalised to: 100.0 %

Sample type: Pressed powder

Correction applied for medium: No

Correction applied for film: None

Used Compound list: OXIDES

Results database: 3-iq+

Results database in: c:\superq\userdata

Analyte Calibration Compound Measured Used Concentration Calculation

| | status | formula | (kcps) | (kcps) | (%) | method |
|----|------------|---------|--------|--------|--------|-----------|
| Na | Calibrated | Na2O | 0.266 | 0.266 | 1.348 | Calculate |
| Al | Calibrated | Al2O3 | 9.988 | 9.988 | 12.589 | Calculate |
| Si | Calibrated | SiO2 | 46.507 | 46.507 | 68.717 | Calculate |
| P | Calibrated | P2O5 | 8.115 | 8.115 | 7.132 | Calculate |
| S | Calibrated | SO3 | 0.125 | 0.125 | 0.113 | Calculate |
| K | Calibrated | K2O | 1.479 | 1.479 | 1.444 | Calculate |
| Ca | Calibrated | CaO | 4.361 | 4.361 | 3.568 | Calculate |
| V | Calibrated | V2O5 | 1.591 | 1.588 | 0.783 | Calculate |
| Fe | Calibrated | Fe2O3 | 0.642 | 0.642 | 0.609 | Calculate |
| Zr | Calibrated | ZrO2 | 14.114 | 14.114 | 0.570 | Calculate |
| Ce | Calibrated | CeO2 | 1.525 | 1.524 | 1.672 | Calculate |
| Tb | Derived | Tb4O7 | 0.782 | 0.782 | 1.455 | Calculate |

Appendix

2

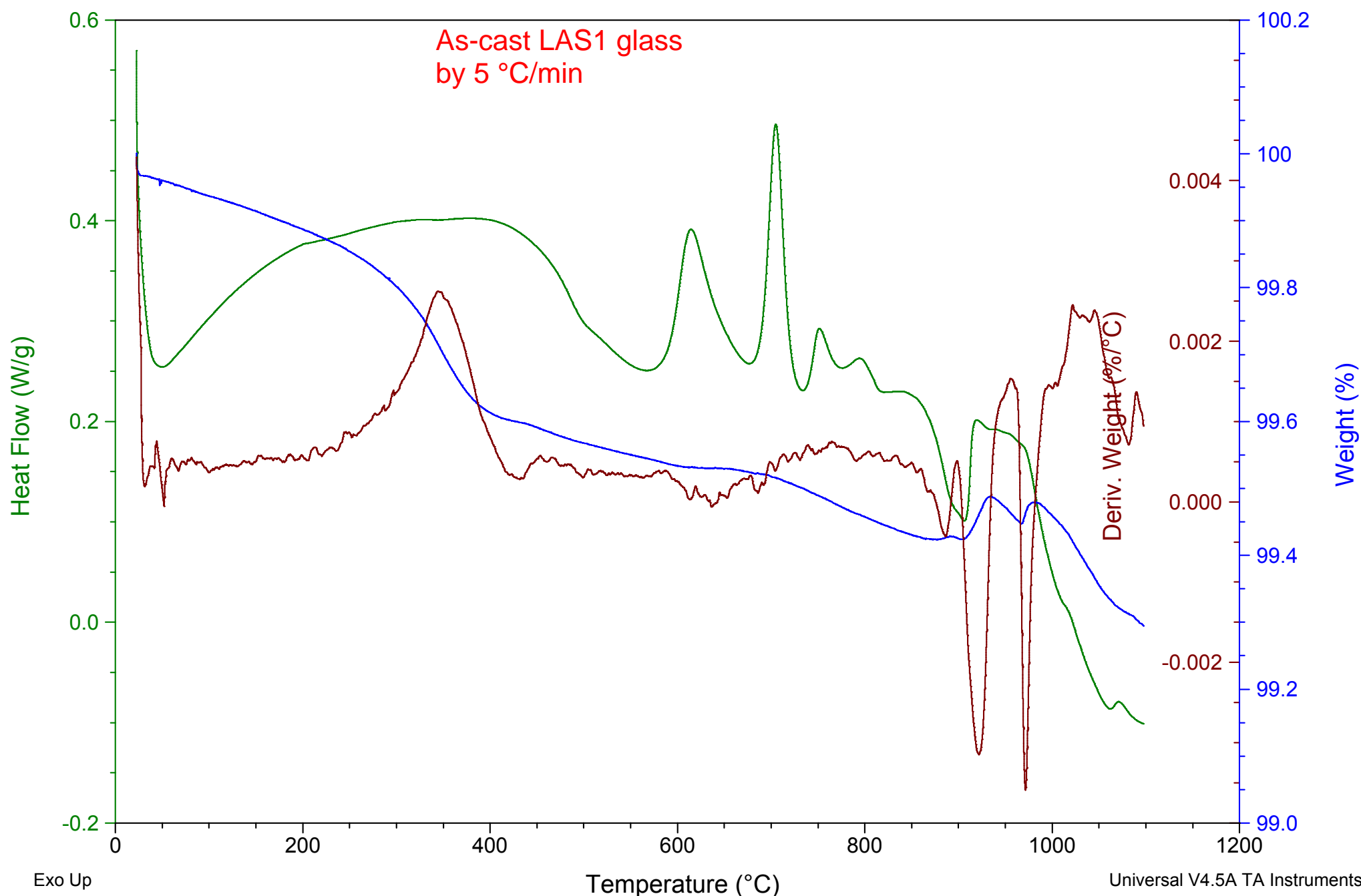
DSC curves

DSC data collected from the TA instruments Universal Analysis 2000 software particular of TGA / DSC TA Instruments SDT-Q600.

Sample: Sample1-G2
Size: 34.0130 mg
Method: TGA Weight
Comment: Zaid Abdulkadhim

DSC-TGA

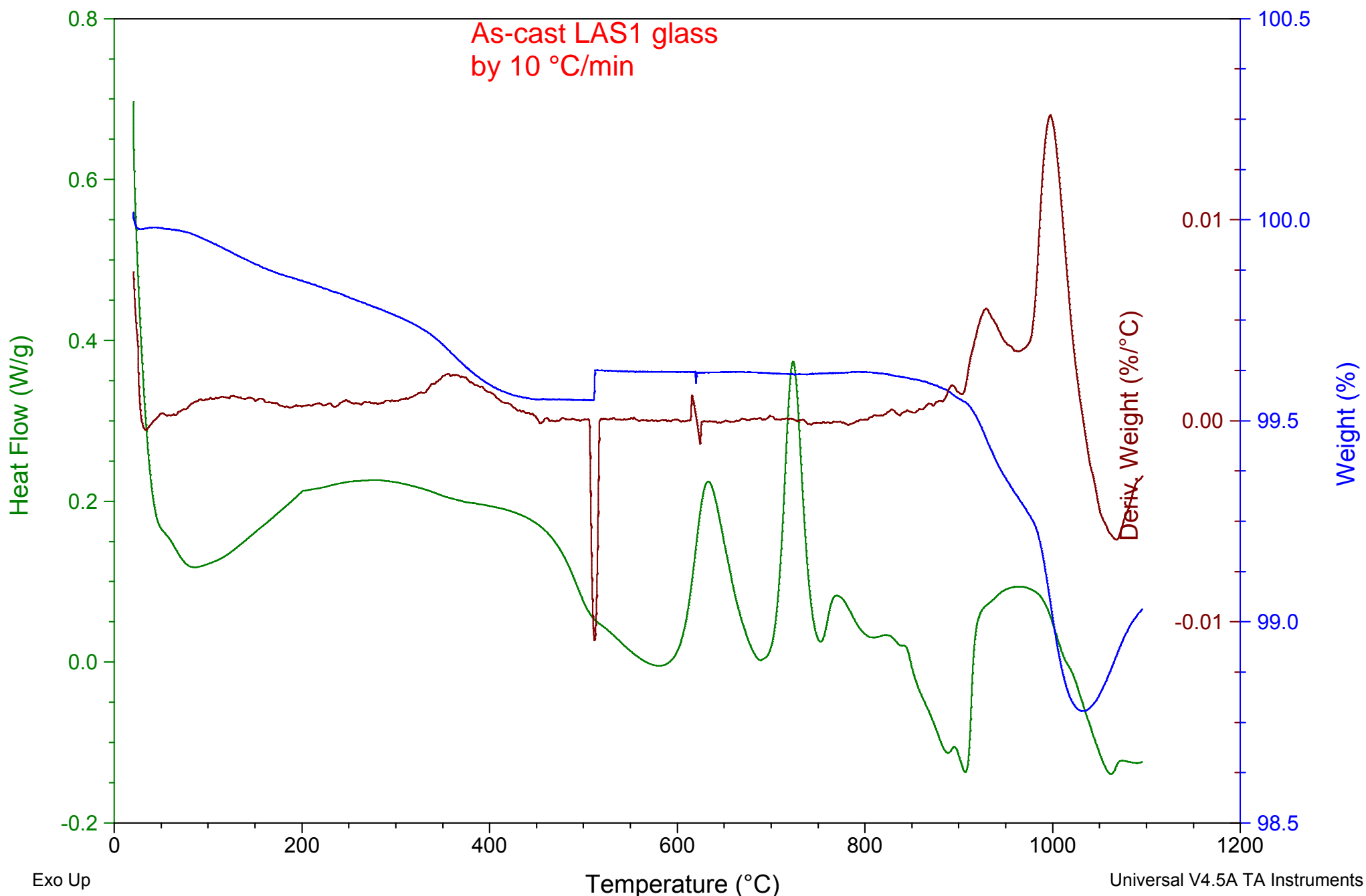
File: C:\Zaid Abdulkadhim\Sample1-G2.001
Operator: Oday
Run Date: 09-Aug-2019 09:18
Instrument: SDT Q600 V20.9 Build 20



Sample: G2-10C
Size: 19.0740 mg
Method: Ramp
Comment: G2-10C

DSC-TGA

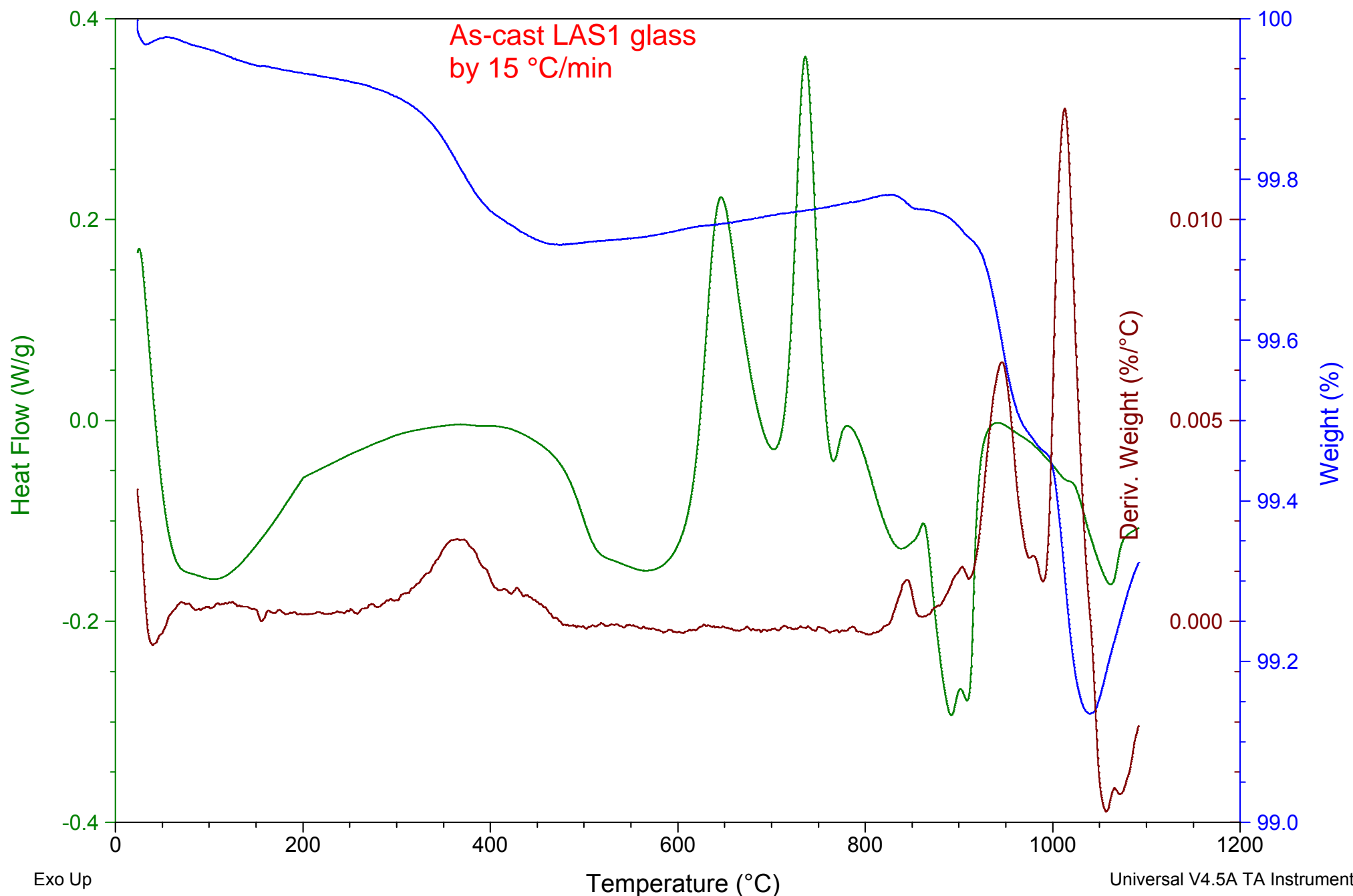
File: C:\Oday\Zaid Abdulkadhim\G2-10C.001
Operator: Oday
Run Date: 03-Oct-2019 09:18
Instrument: SDT Q600 V20.9 Build 20



Sample: G2-15C
Size: 26.9830 mg
Method: Ramp

DSC-TGA

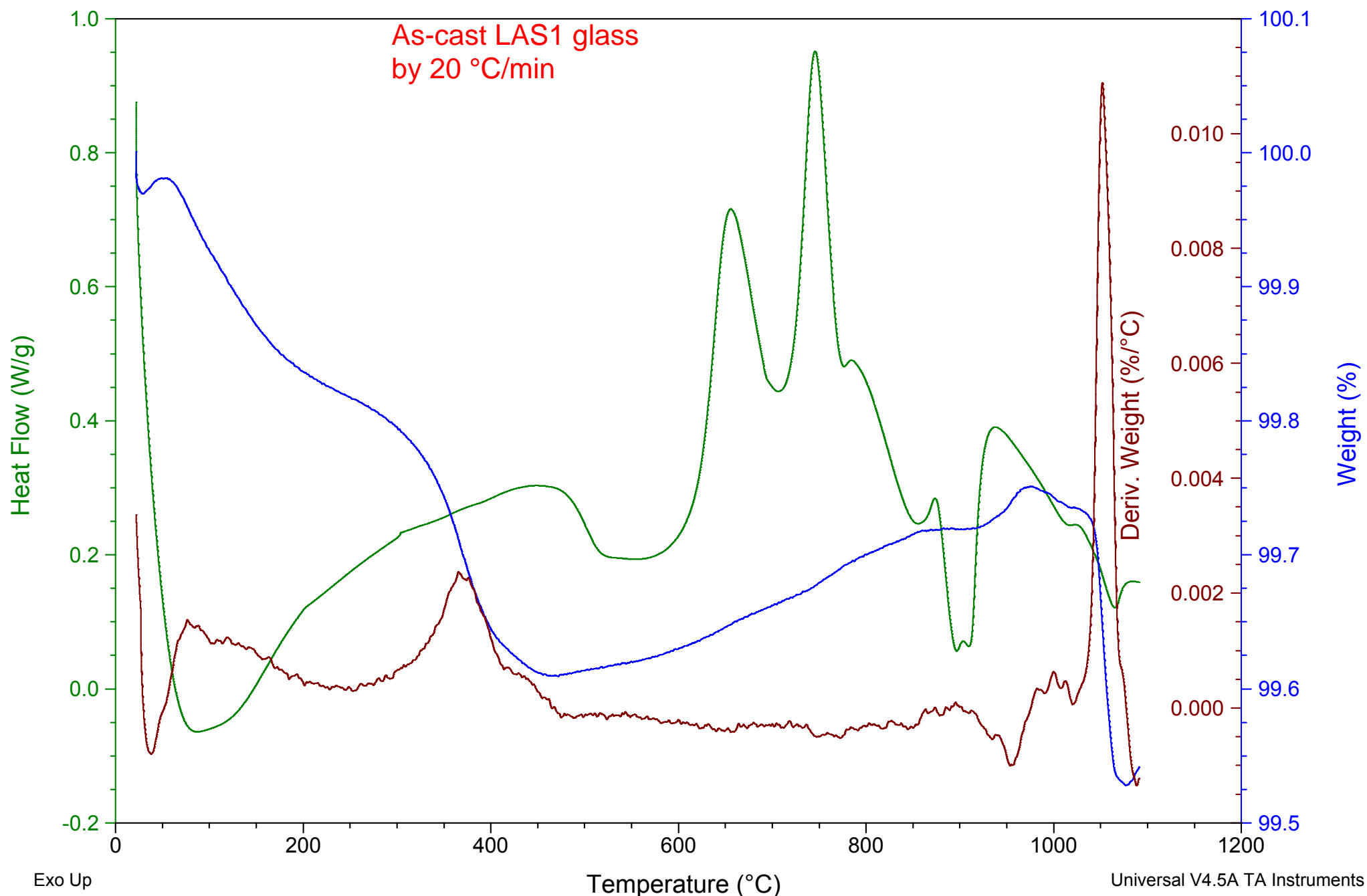
File: C:\Oday\Zaid Abdulkadhim\G2-15C.001
Operator: Oday
Run Date: 03-Oct-2019 12:25
Instrument: SDT Q600 V20.9 Build 20



Sample: G2-20C-M
Size: 21.7270 mg
Method: Ramp
Comment: Zaid

DSC-TGA

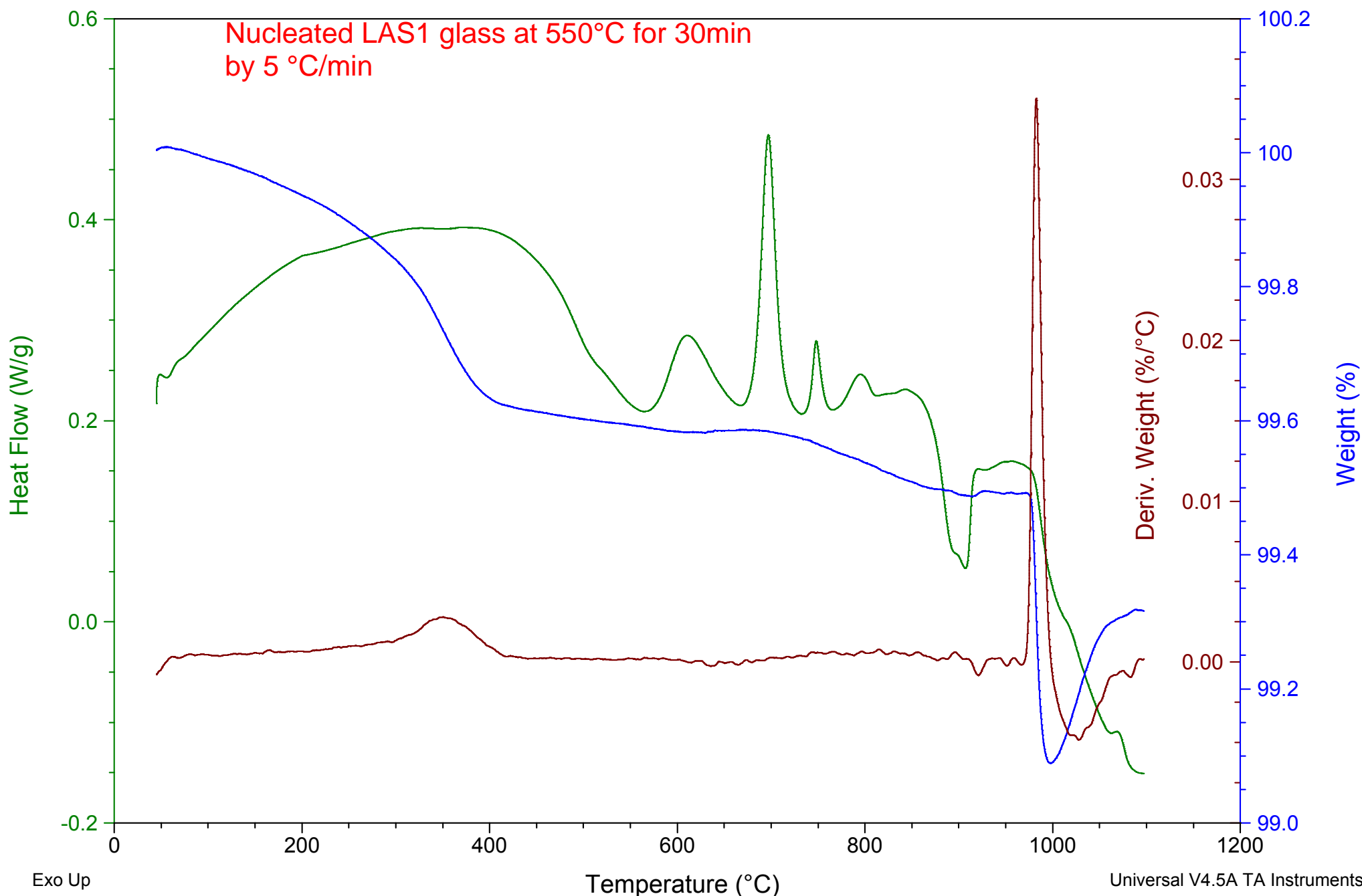
File: C:\Oday\Zaid Abdulkadhim\G2-20C-M.001
Operator: Oday
Run Date: 16-Sep-2019 11:37
Instrument: SDT Q600 V20.9 Build 20



Sample: Sample2-G2
Size: 31.0650 mg
Method: TGA Weight
Comment: Zaid Abdulkadhim

DSC-TGA

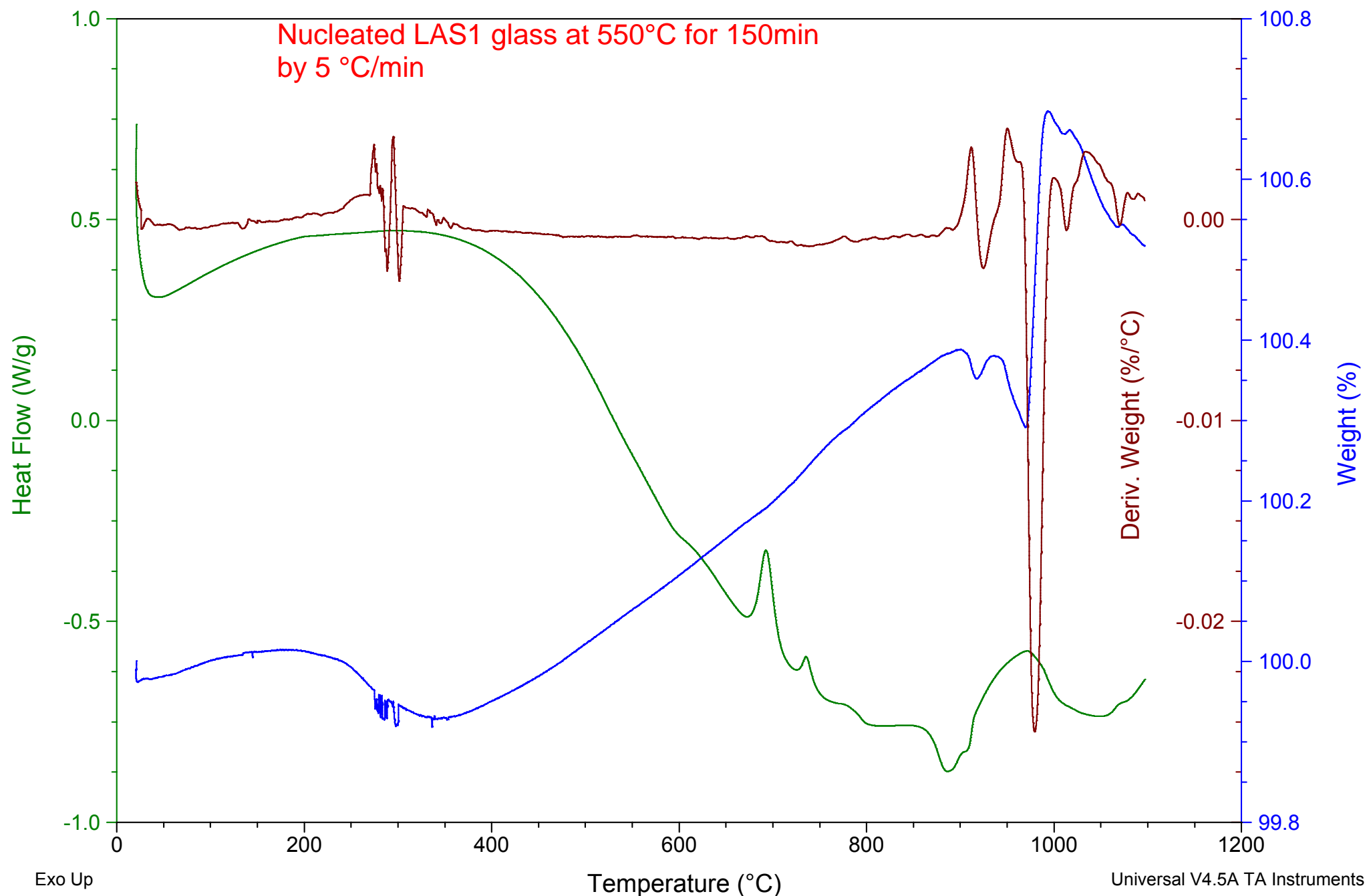
File: C:\Zaid Abdulkadhim\Sample2-G2.001
Operator: Oday
Run Date: 09-Aug-2019 14:29
Instrument: SDT Q600 V20.9 Build 20



Sample: G2-550-150M
Size: 25.2280 mg
Method: TGA Weight

DSC-TGA

File: C:\Zaid Abdulkadhim\G2-550-150M.001
Operator: Oday
Run Date: 10-Sep-2019 14:30
Instrument: SDT Q600 V20.9 Build 20



Exo Up

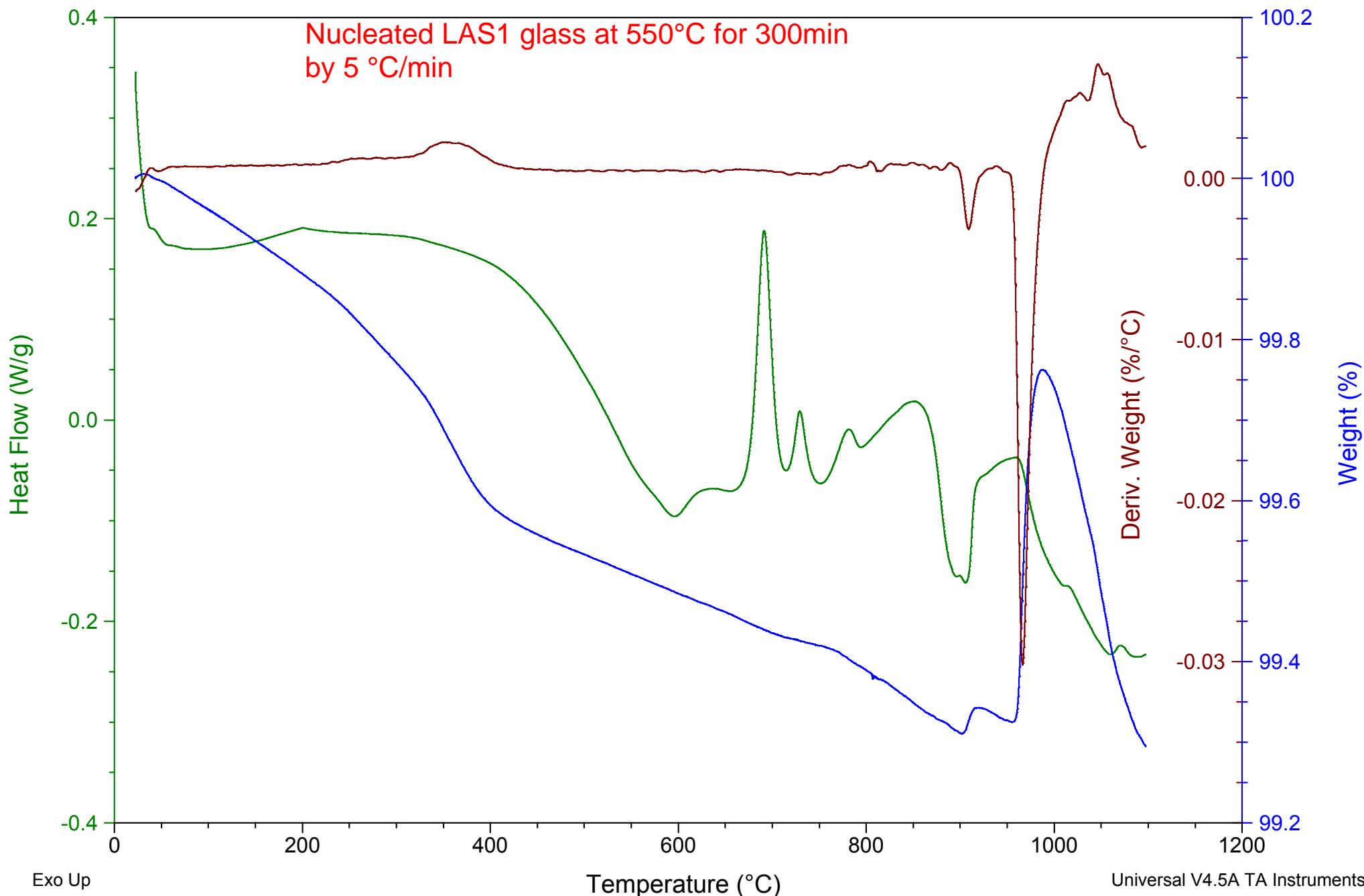
Temperature (°C)

Universal V4.5A TA Instruments

Sample: Sample 3-G2
Size: 31.8420 mg
Method: TGA-DSC
Comment: Zaid Abdulkadhim

DSC-TGA

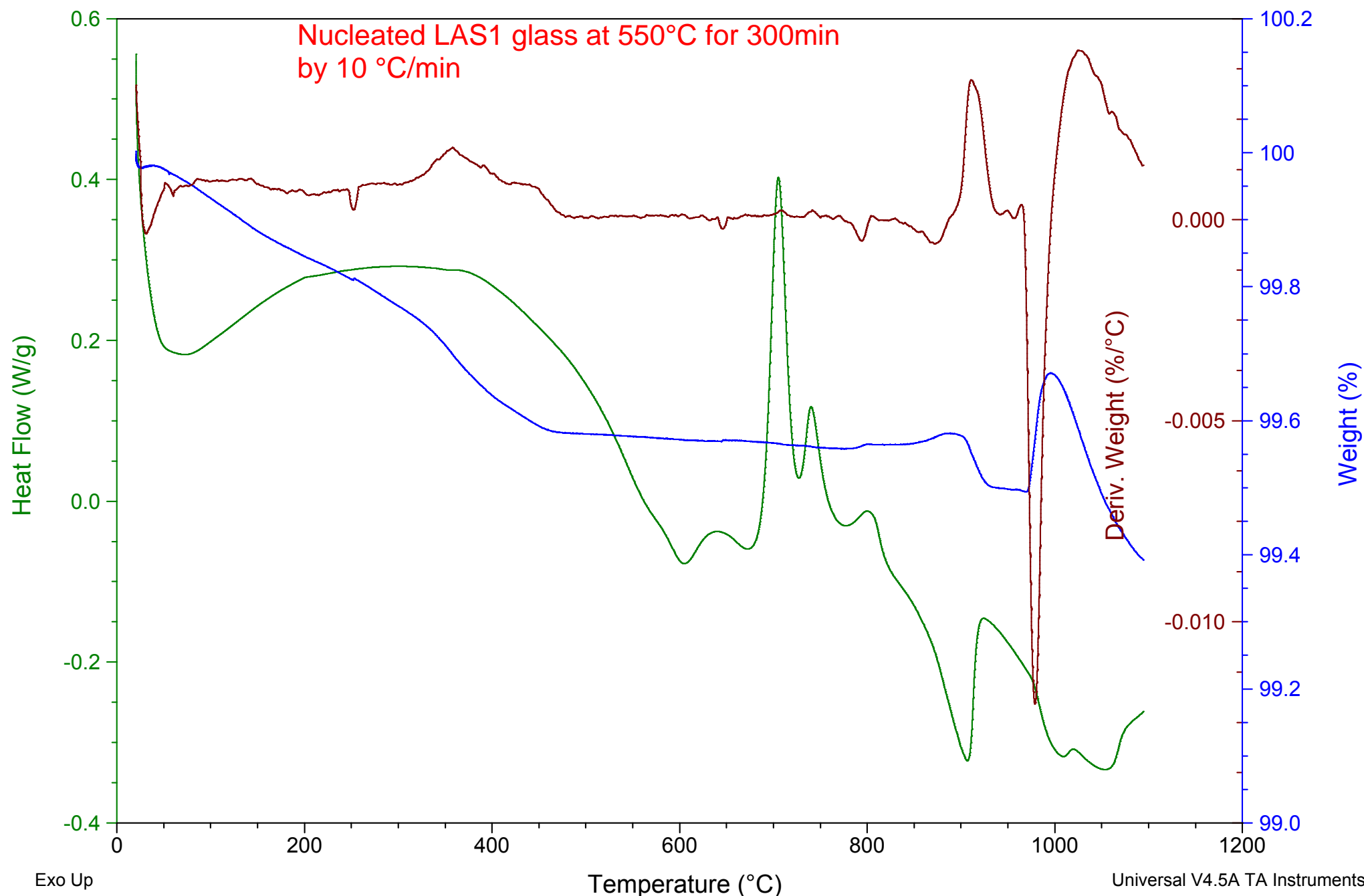
File: C:\Zaid Abdulkadhim\Sample 3-G2.001
Operator: Oday
Run Date: 19-Aug-2019 12:32
Instrument: SDT Q600 V20.9 Build 20



Sample: G2-550-300MIN-10C
Size: 33.9640 mg
Method: Ramp

DSC-TGA

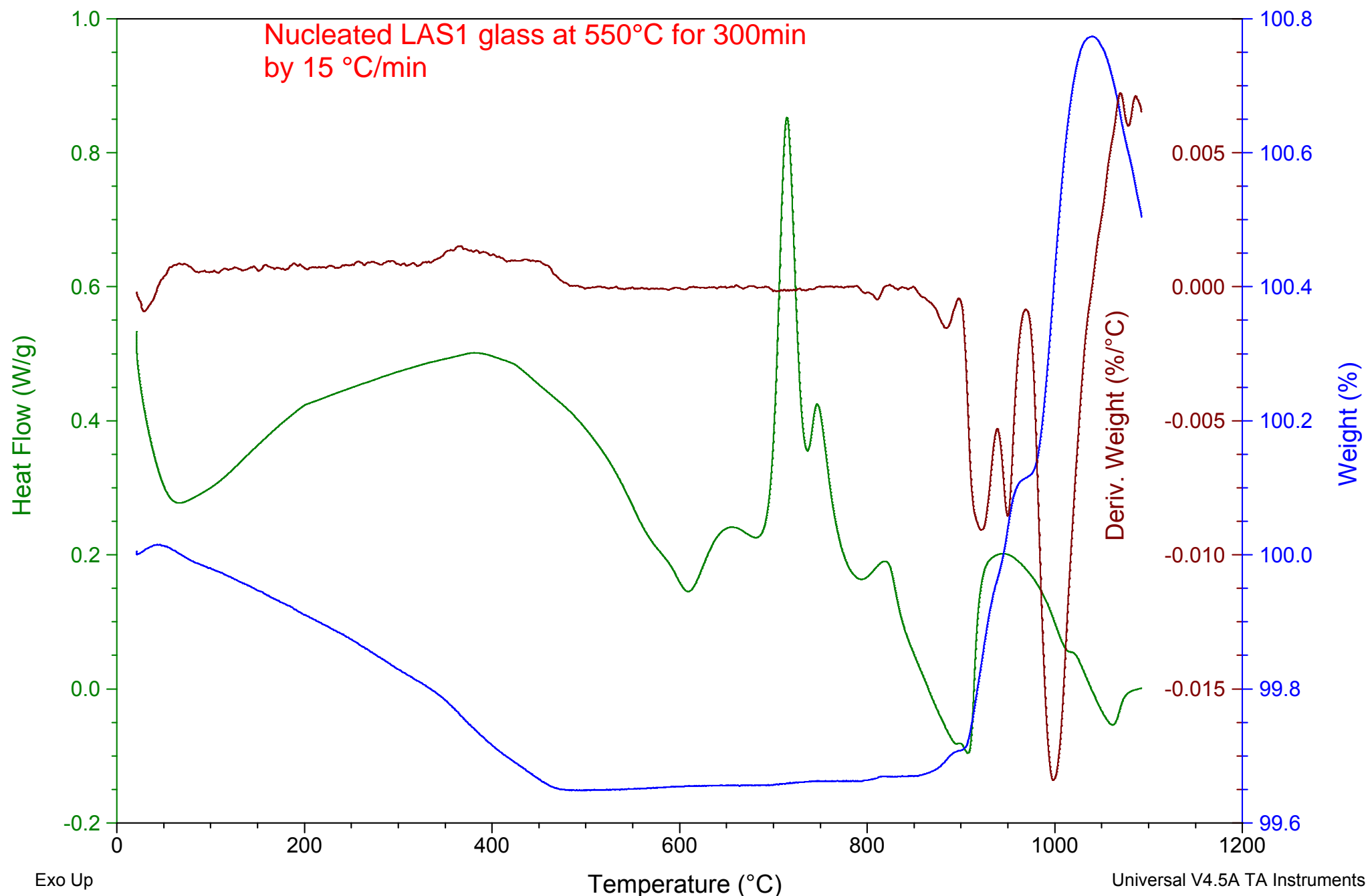
File: C:\G2-550-300MIN-10C.001
Operator: Oday
Run Date: 21-Oct-2019 09:37
Instrument: SDT Q600 V20.9 Build 20



Sample: G2-550-300MIN-15C
Size: 22.9650 mg
Method: Ramp

DSC-TGA

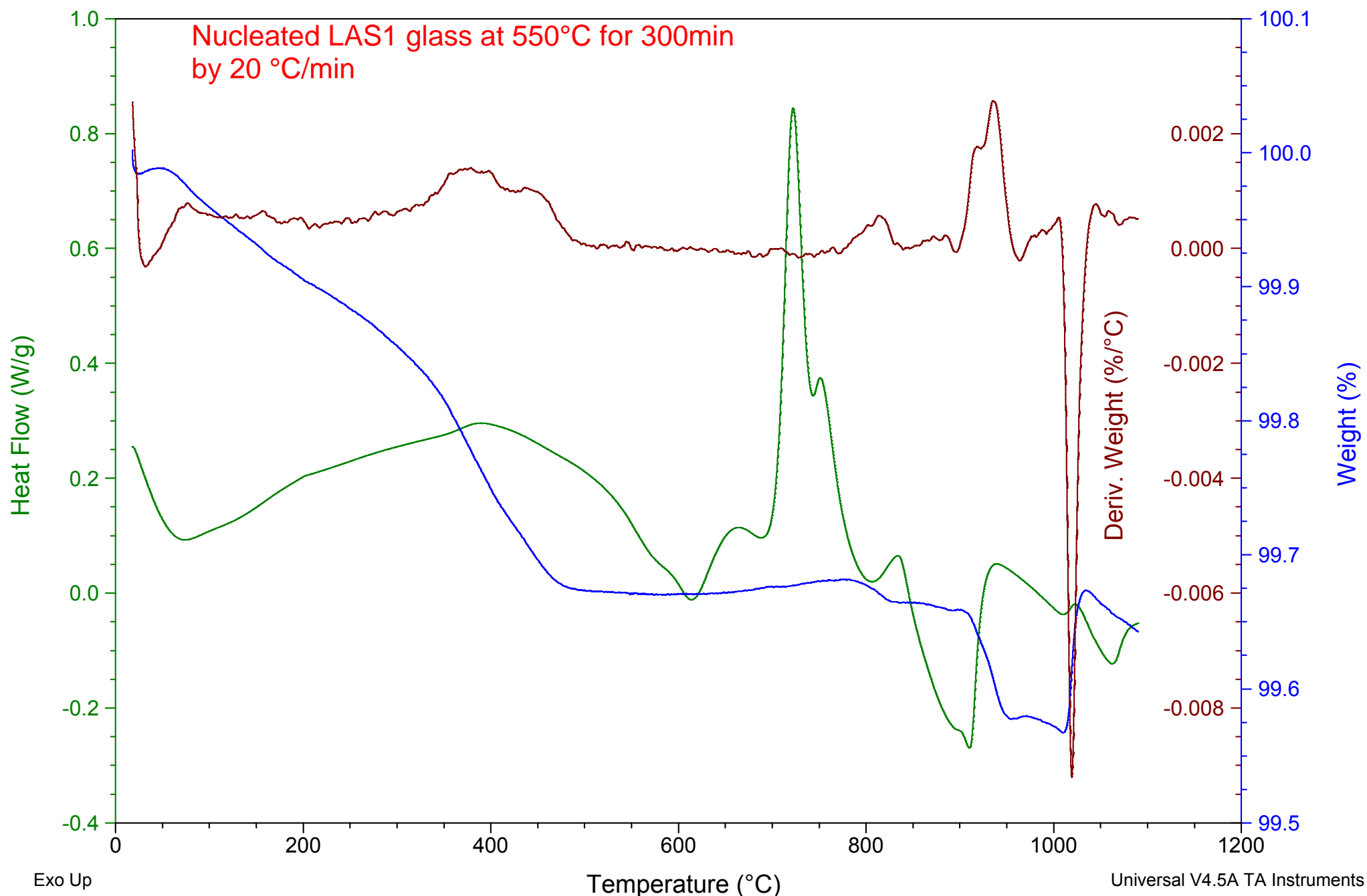
File: C:\G2-550-300MIN-15C.001
Operator: Oday
Run Date: 21-Oct-2019 15:42
Instrument: SDT Q600 V20.9 Build 20



Sample: G2-550-300MIN-20C
Size: 34.6410 mg
Method: Ramp

DSC-TGA

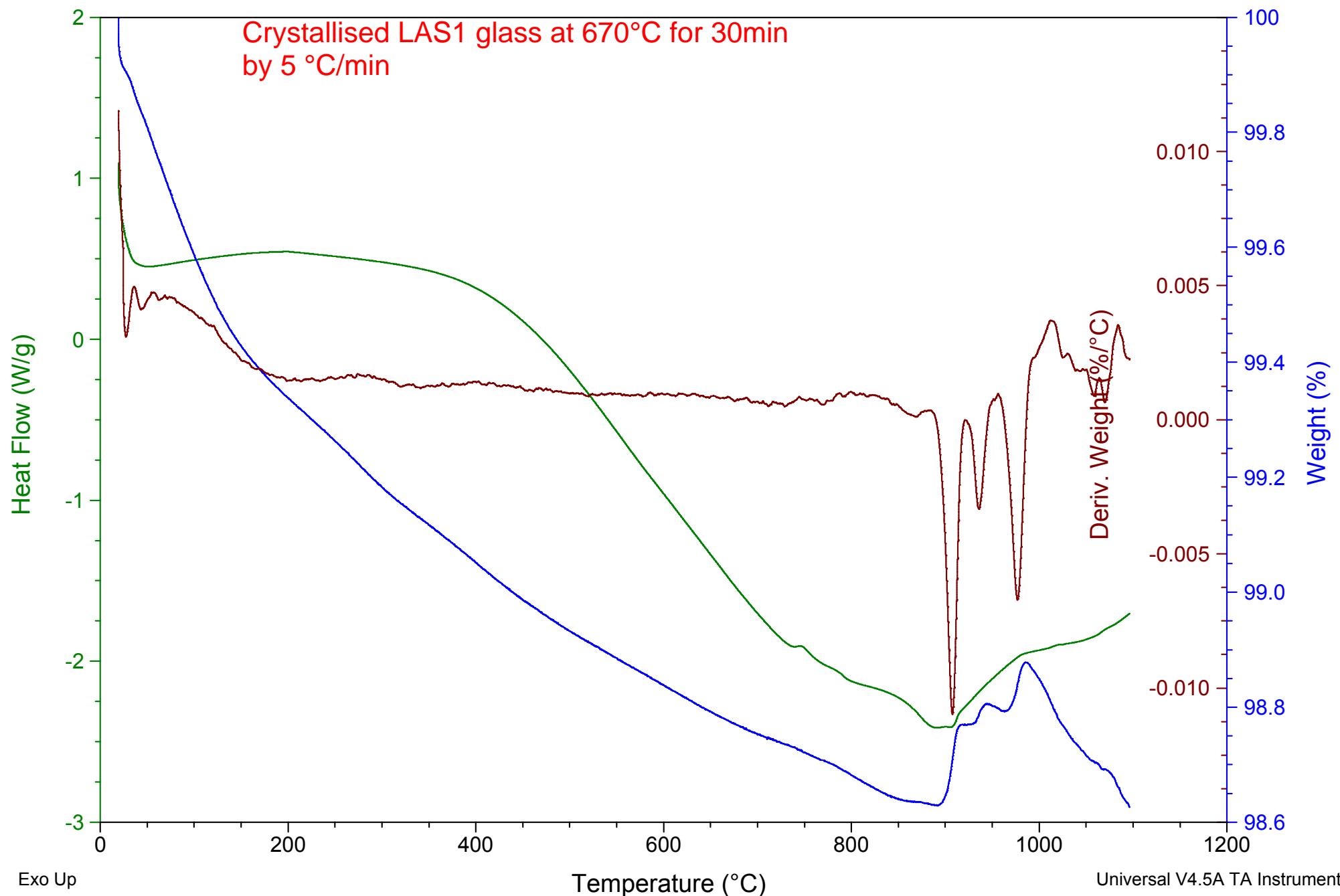
File: C:\G2-550-300MIN-20C.001
Operator: Oday
Run Date: 22-Oct-2019 09:53
Instrument: SDT Q600 V20.9 Build 20



Sample: G2-670-30min-5min
Size: 17.5890 mg
Method: Isothermal for

DSC-TGA

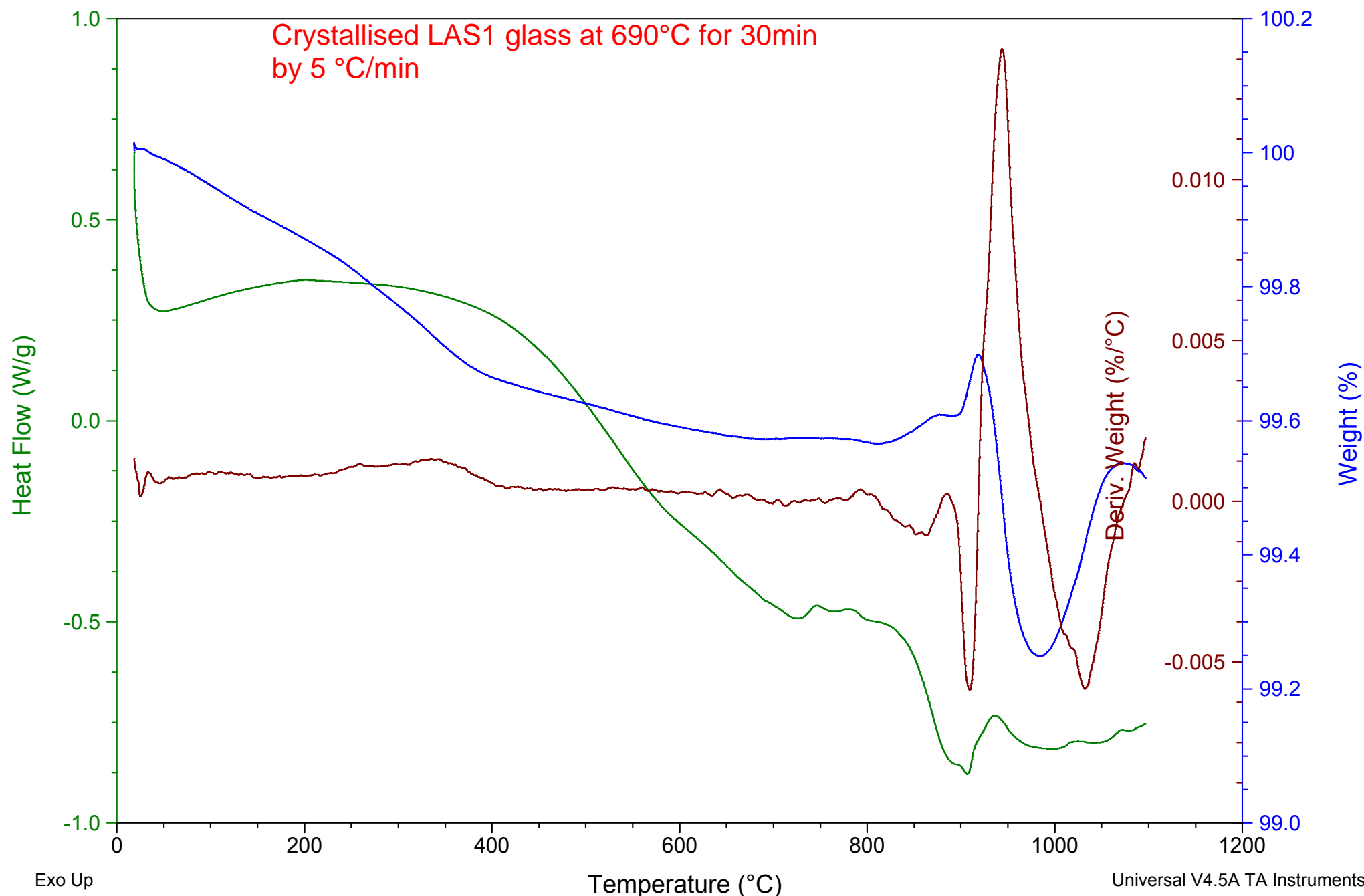
File: C:\...\19-12-19\G2-670-30min-5min.001
Operator: Oday
Run Date: 20-Dec-2019 09:14
Instrument: SDT Q600 V20.9 Build 20



Sample: G2-690C-30min
Size: 29.2740 mg
Method: Isothermal for

DSC-TGA

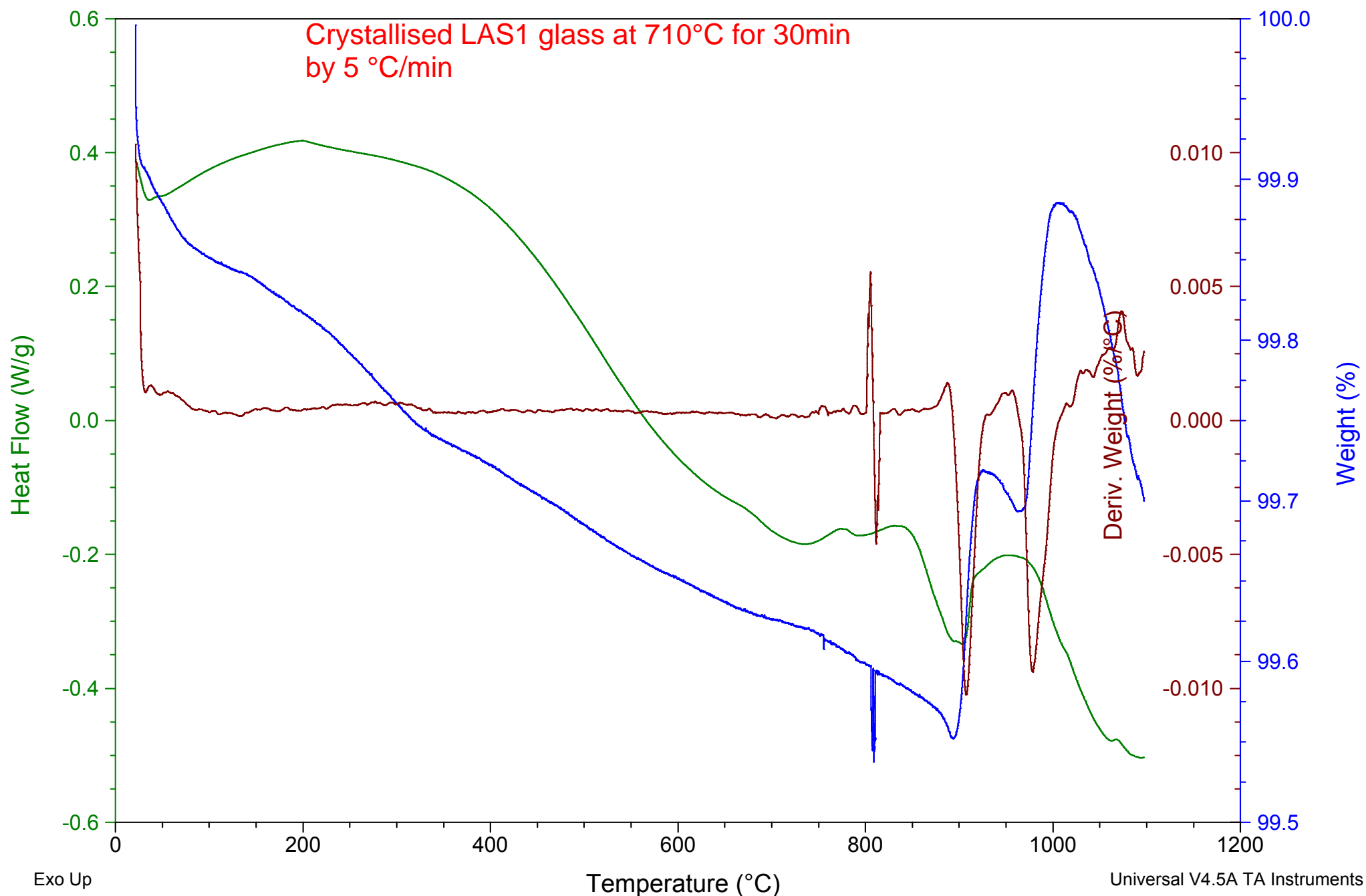
File: C:\...\17-12-19\G2-690C-30min.001
Operator: Oday
Run Date: 16-Dec-2019 11:53
Instrument: SDT Q600 V20.9 Build 20



Sample: G2-710-30M-5C
Size: 22.6470 mg
Method: Ramp

DSC-TGA

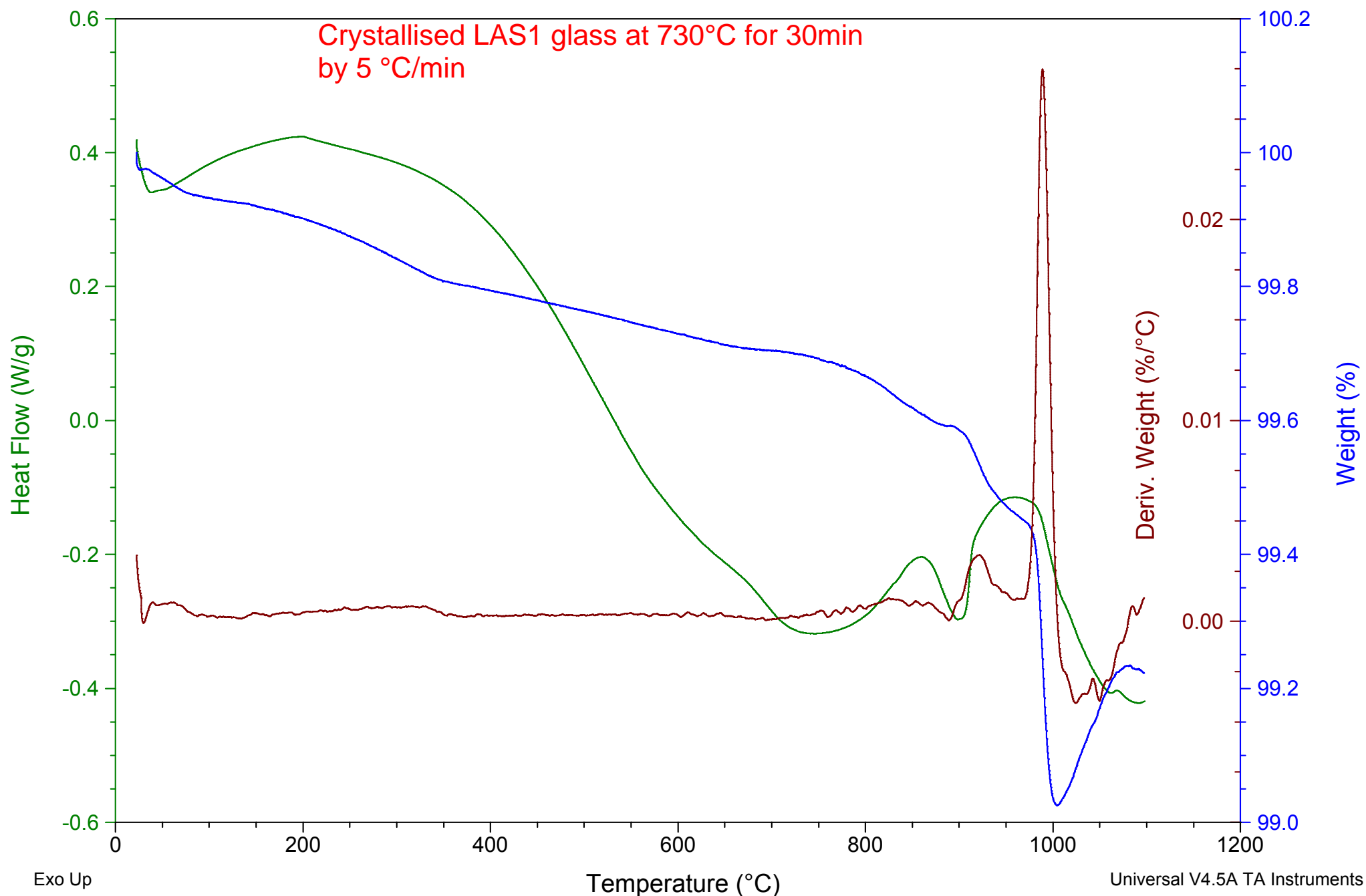
File: C:\Zaid Abdulkadhim\G2-710-30M-5C.001
Operator: Oday
Run Date: 31-Oct-2019 10:56
Instrument: SDT Q600 V20.9 Build 20



Sample: G2-730-30-5C
Size: 22.6010 mg
Method: Ramp

DSC-TGA

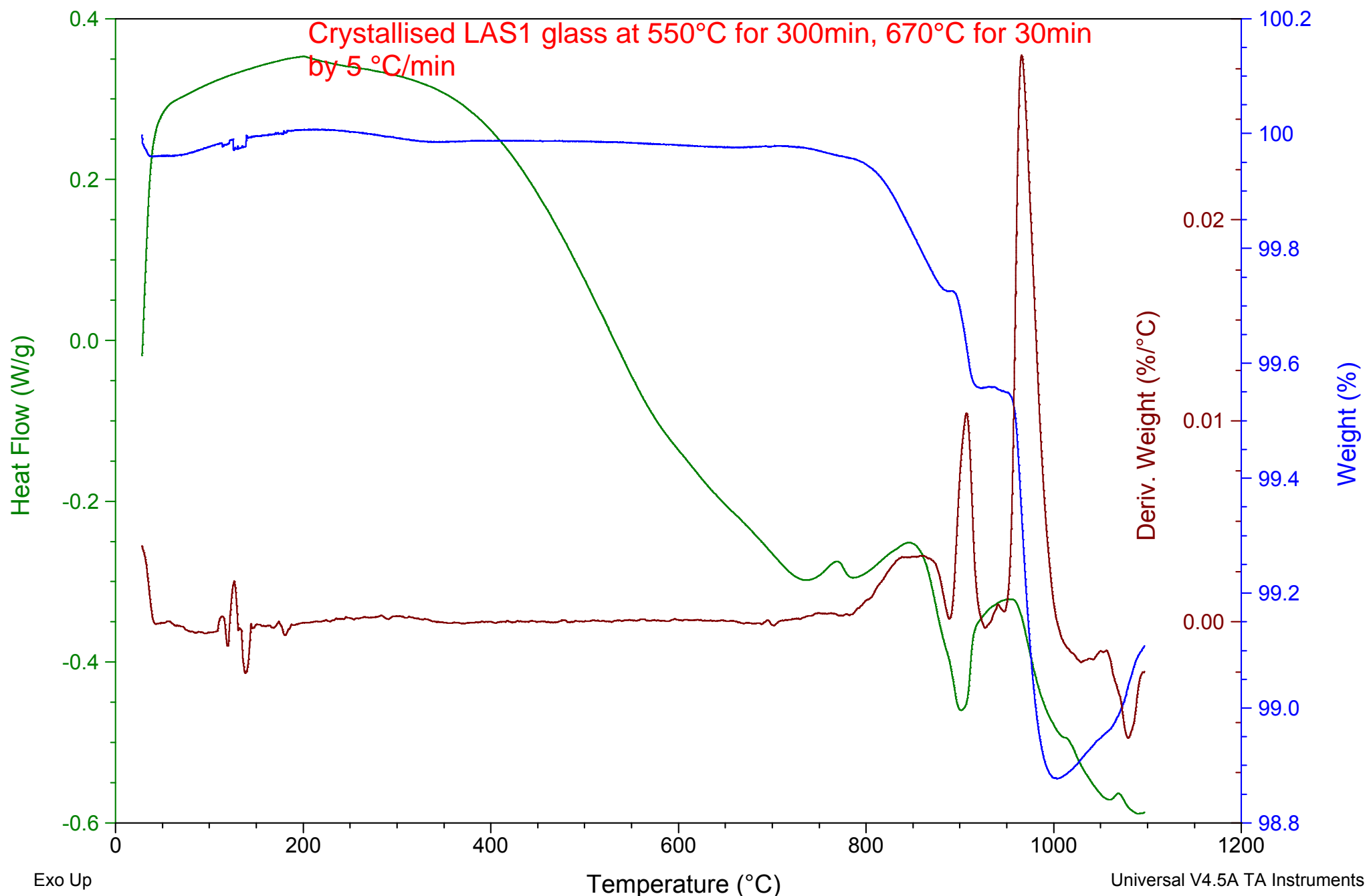
File: C:\Zaid Abdulkadhim\G2-730-30-5C.001
Operator: Oday
Run Date: 01-Nov-2019 13:40
Instrument: SDT Q600 V20.9 Build 20



Sample: G2-550-300-690-30-5C
Size: 25.5580 mg
Method: Ramp

DSC-TGA

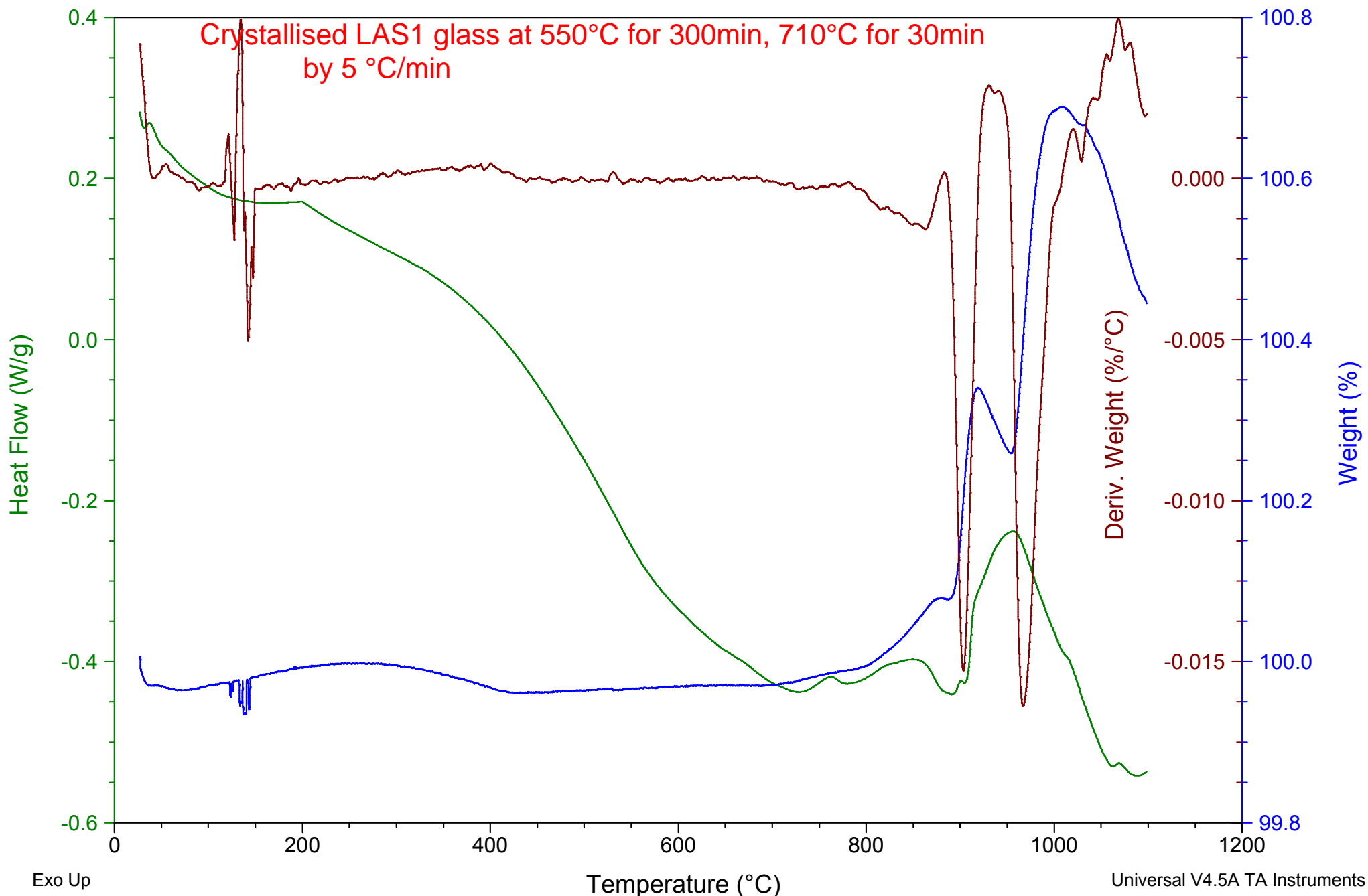
File: C:\G2-550-300-690-30-5C.001
Operator: Oday
Run Date: 31-Oct-2019 15:43
Instrument: SDT Q600 V20.9 Build 20



Sample: G2-550/300 710/30-5C
Size: 19.2030 mg
Method: Ramp

DSC-TGA

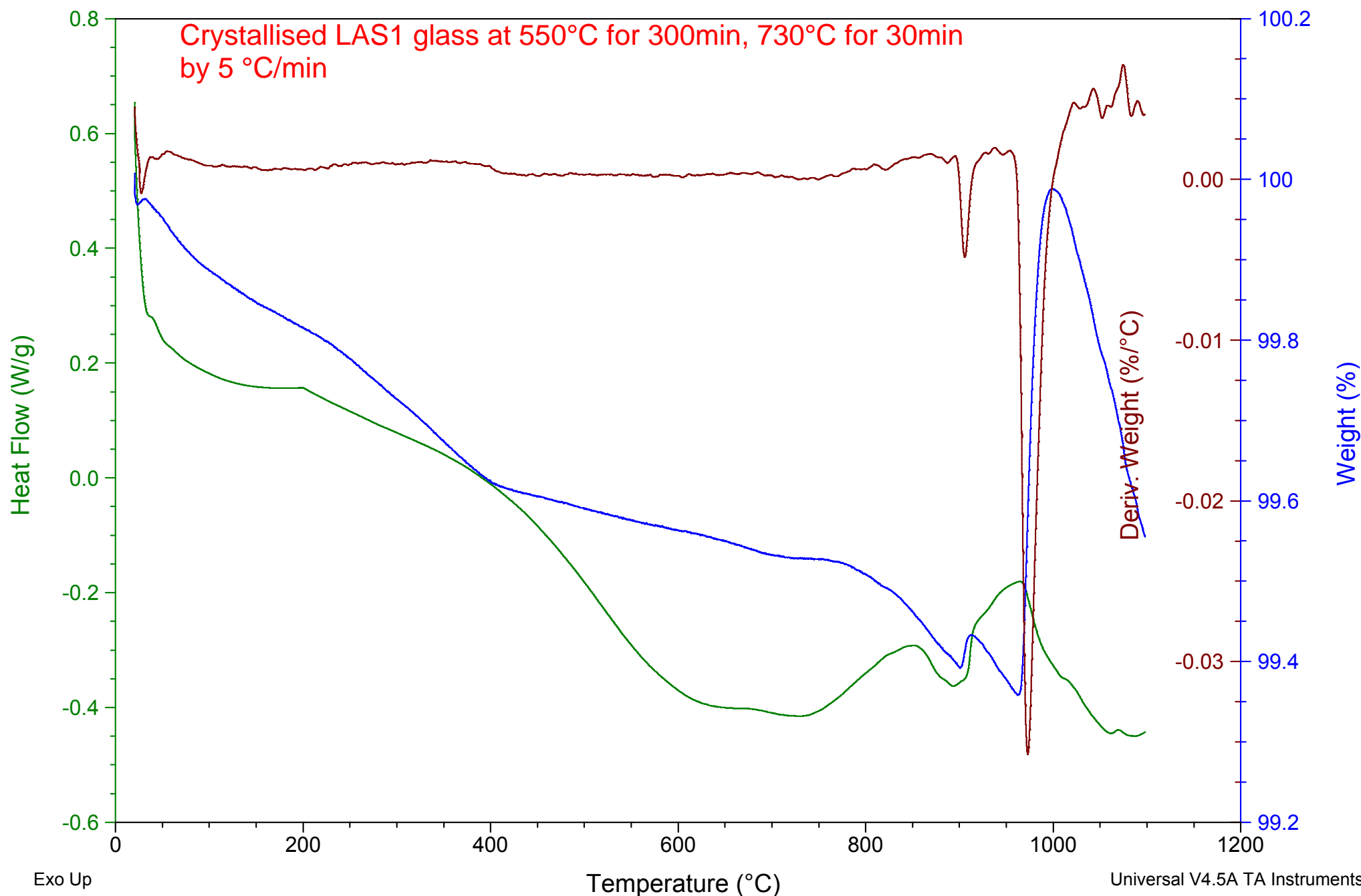
File: C:\G2-550-300 710-30-5C.001
Operator: Oday
Run Date: 03-Oct-2019 14:48
Instrument: SDT Q600 V20.9 Build 20



Sample: G2-550-300- 730-30-5C
Size: 18.8100 mg
Method: Ramp

DSC-TGA

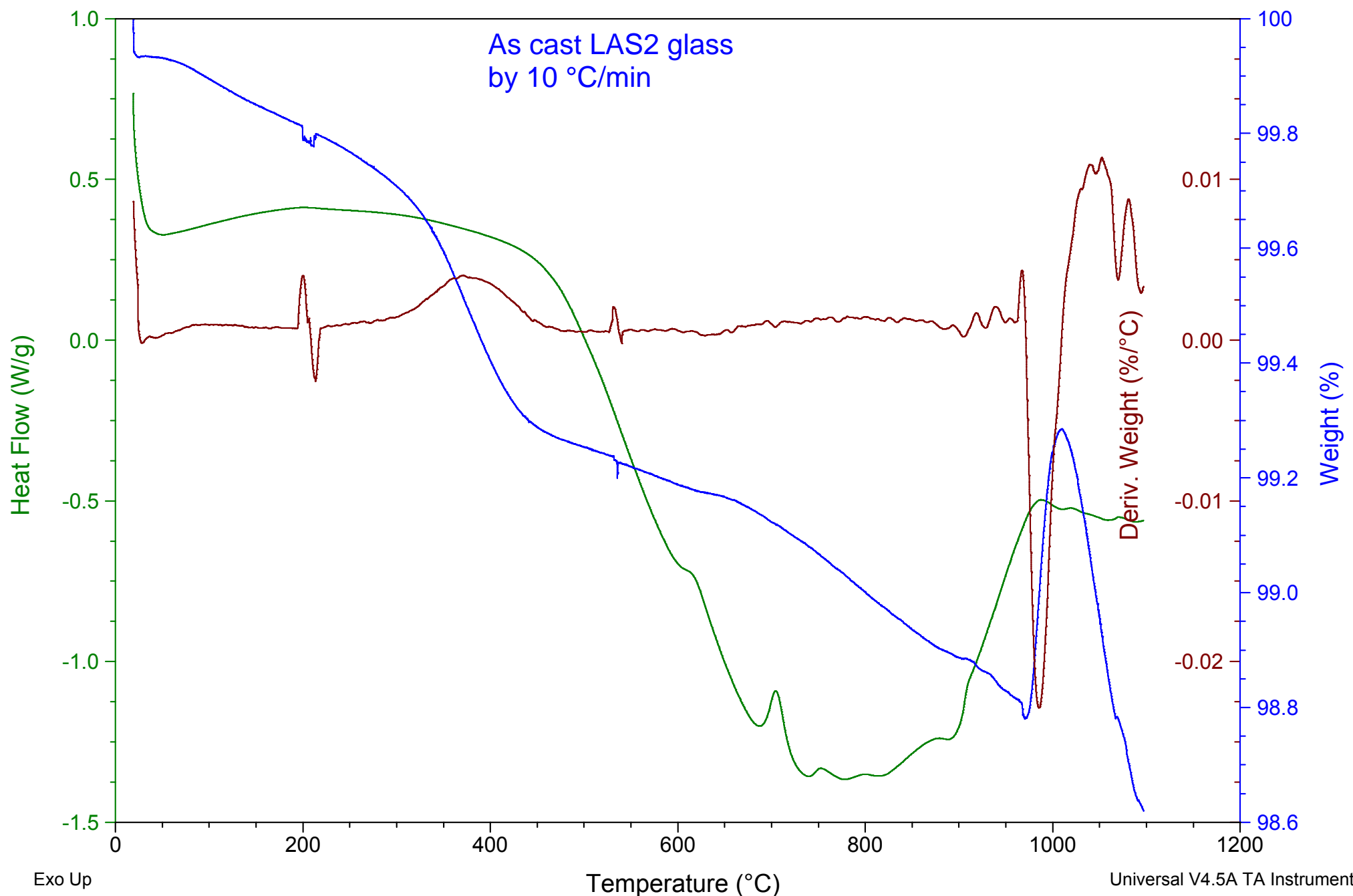
File: C:\G2-550-300- 730-30-5C.001
Operator: Oday
Run Date: 04-Oct-2019 09:40
Instrument: SDT Q600 V20.9 Build 20



Sample: G1- 5- r
Size: 24.1710 mg
Method: Isothermal for

DSC-TGA

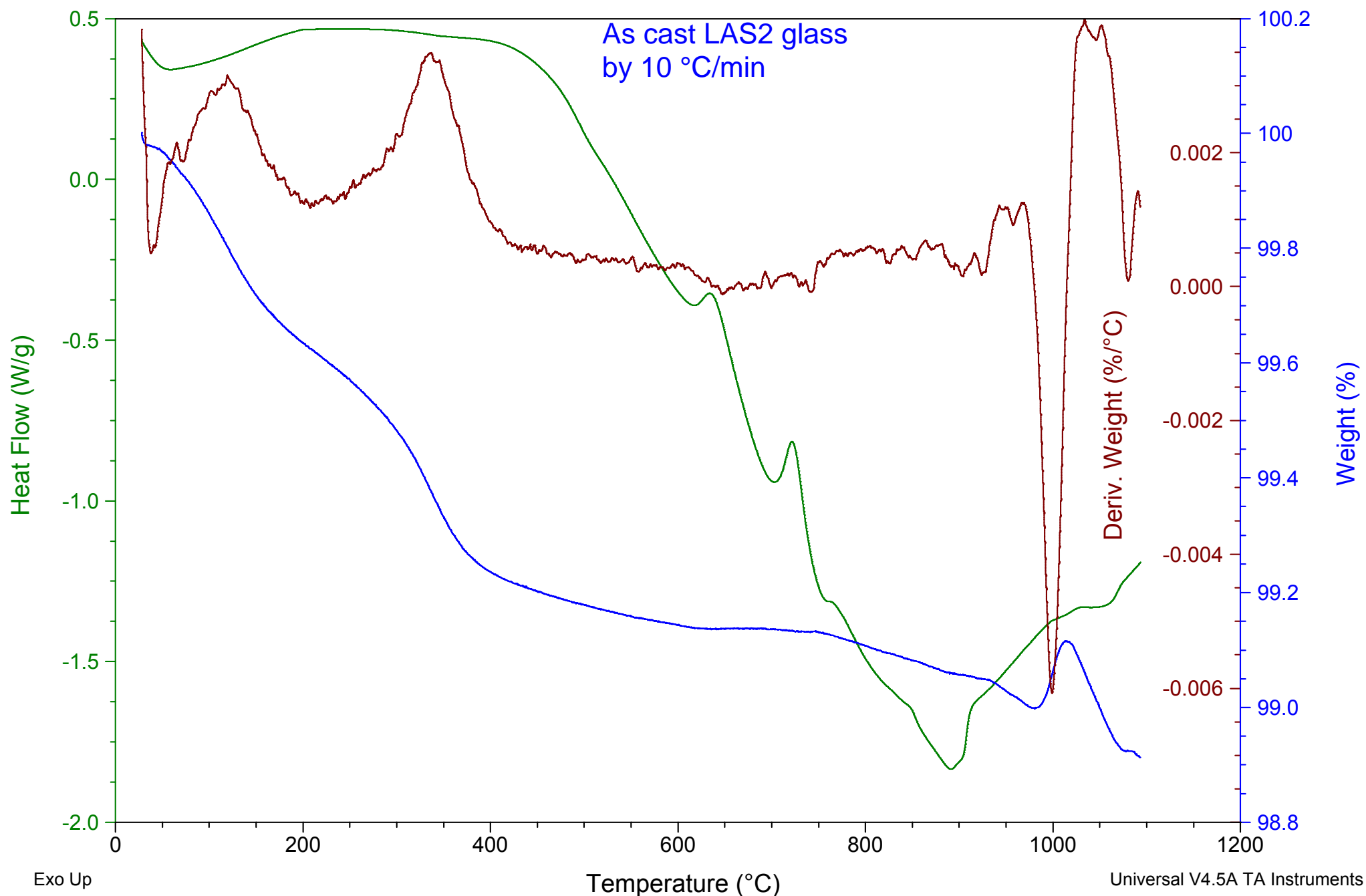
File: C:\03-02-2020\G1- 5- r.001
Operator: Oday
Run Date: 20-Feb-2020 10:11
Instrument: SDT Q600 V20.9 Build 20



Sample: G1-10C
Size: 18.2890 mg
Method: Isothermal for

DSC-TGA

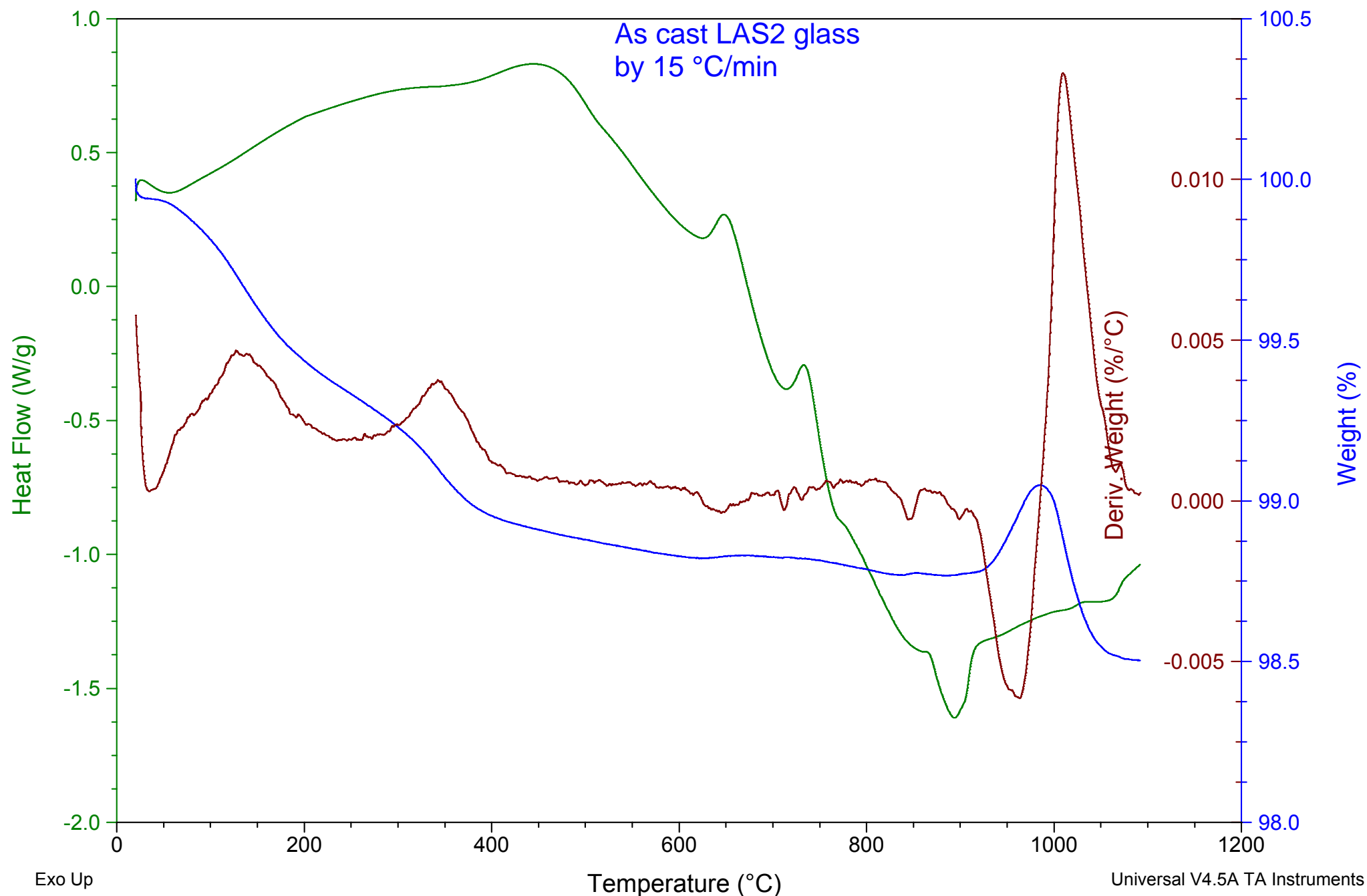
File: C:\03-02-2020\G1-10C.001
Operator: Oday
Run Date: 03-Feb-2020 14:24
Instrument: SDT Q600 V20.9 Build 20



Sample: G1-15C
Size: 17.1290 mg
Method: Isothermal for

DSC-TGA

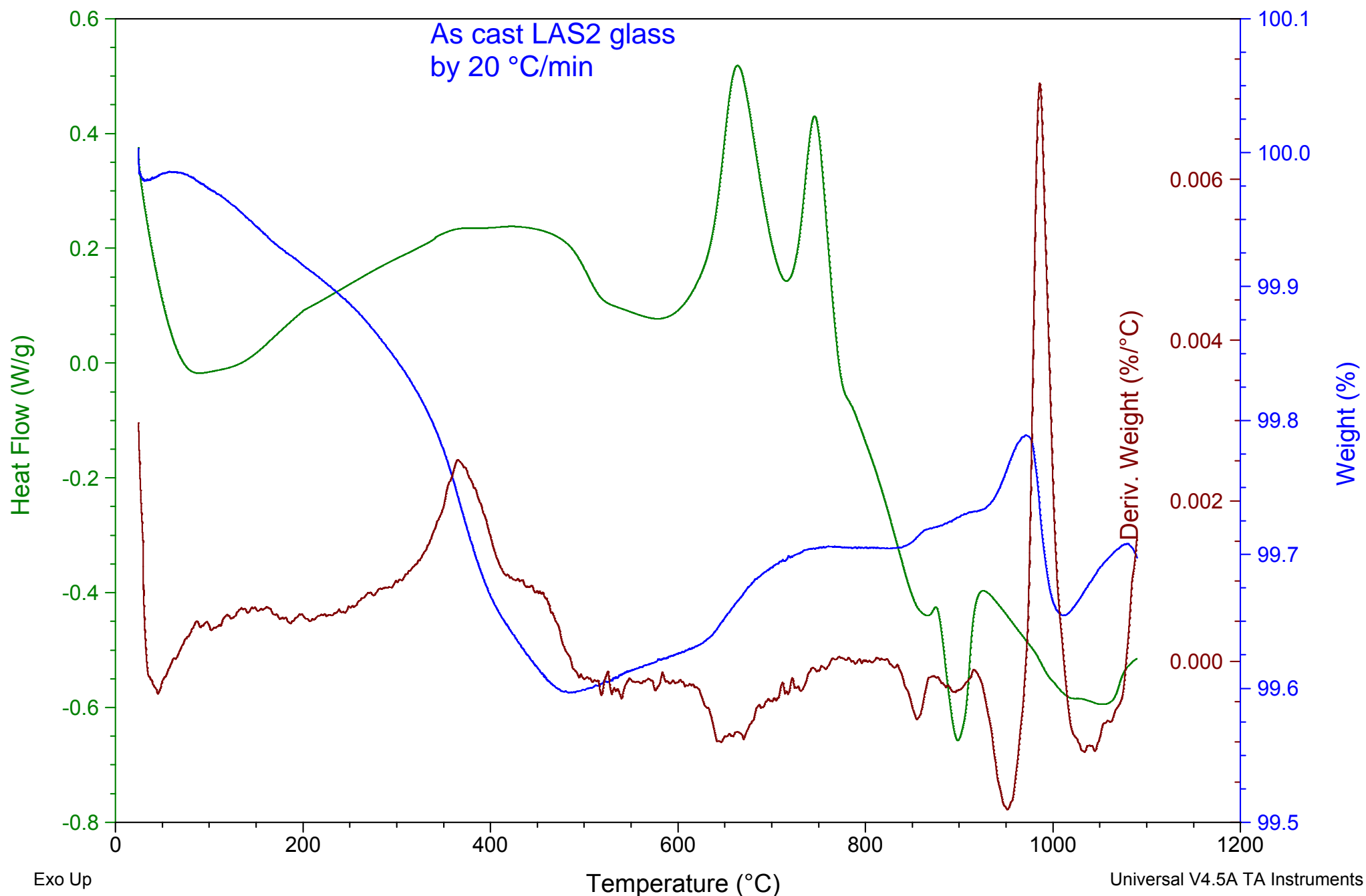
File: C:\03-02-2020\G1-15C.001
Operator: Oday
Run Date: 04-Feb-2020 10:21
Instrument: SDT Q600 V20.9 Build 20



Sample: G1-20C
Size: 33.7490 mg
Method: Isothermal for

DSC-TGA

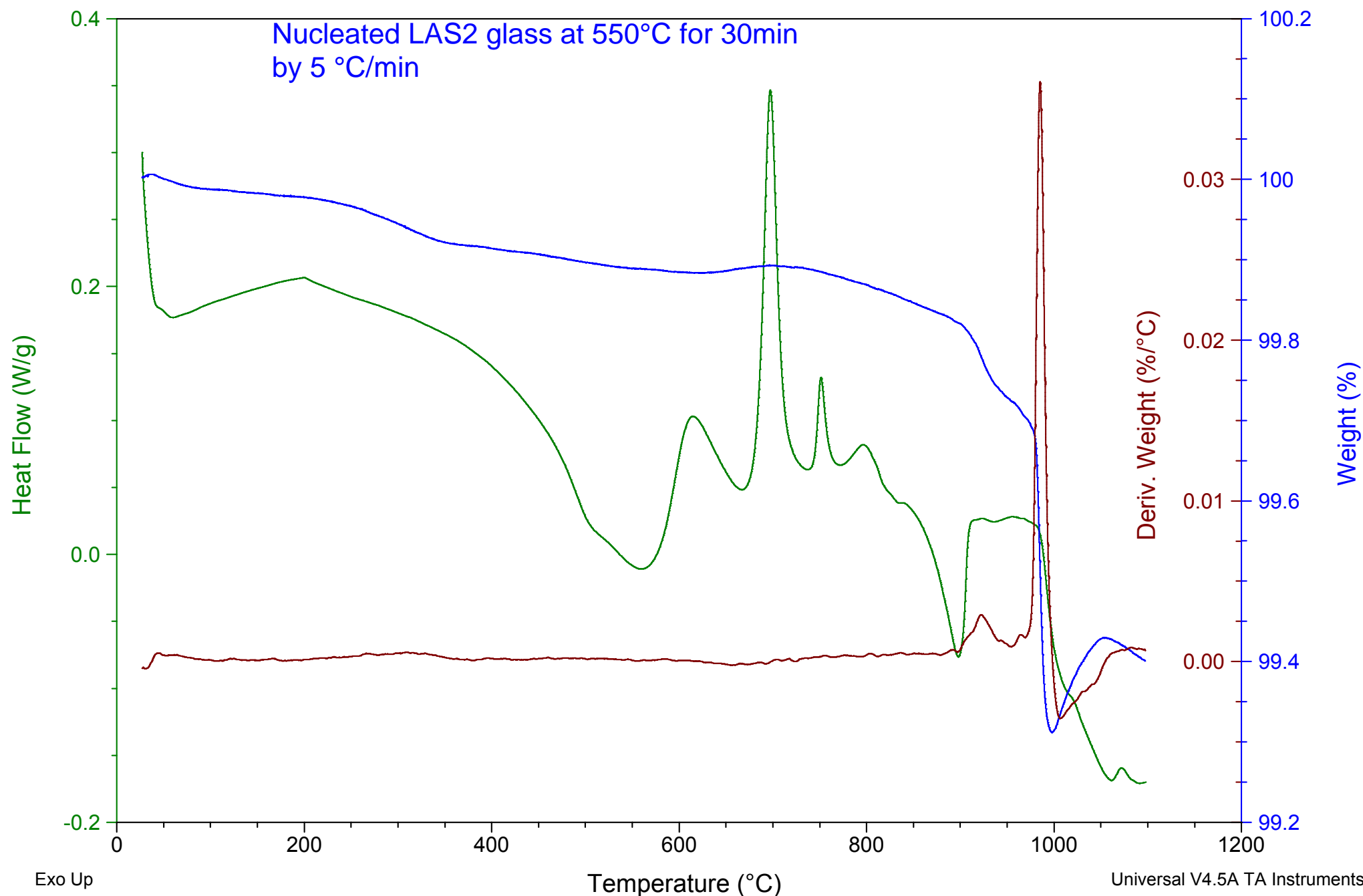
File: C:\03-02-2020\G1-20C.001
Operator: Oday
Run Date: 04-Feb-2020 13:23
Instrument: SDT Q600 V20.9 Build 20



Sample: G1-550-30M-5C
Size: 32.8220 mg
Method: Isothermal for

DSC-TGA

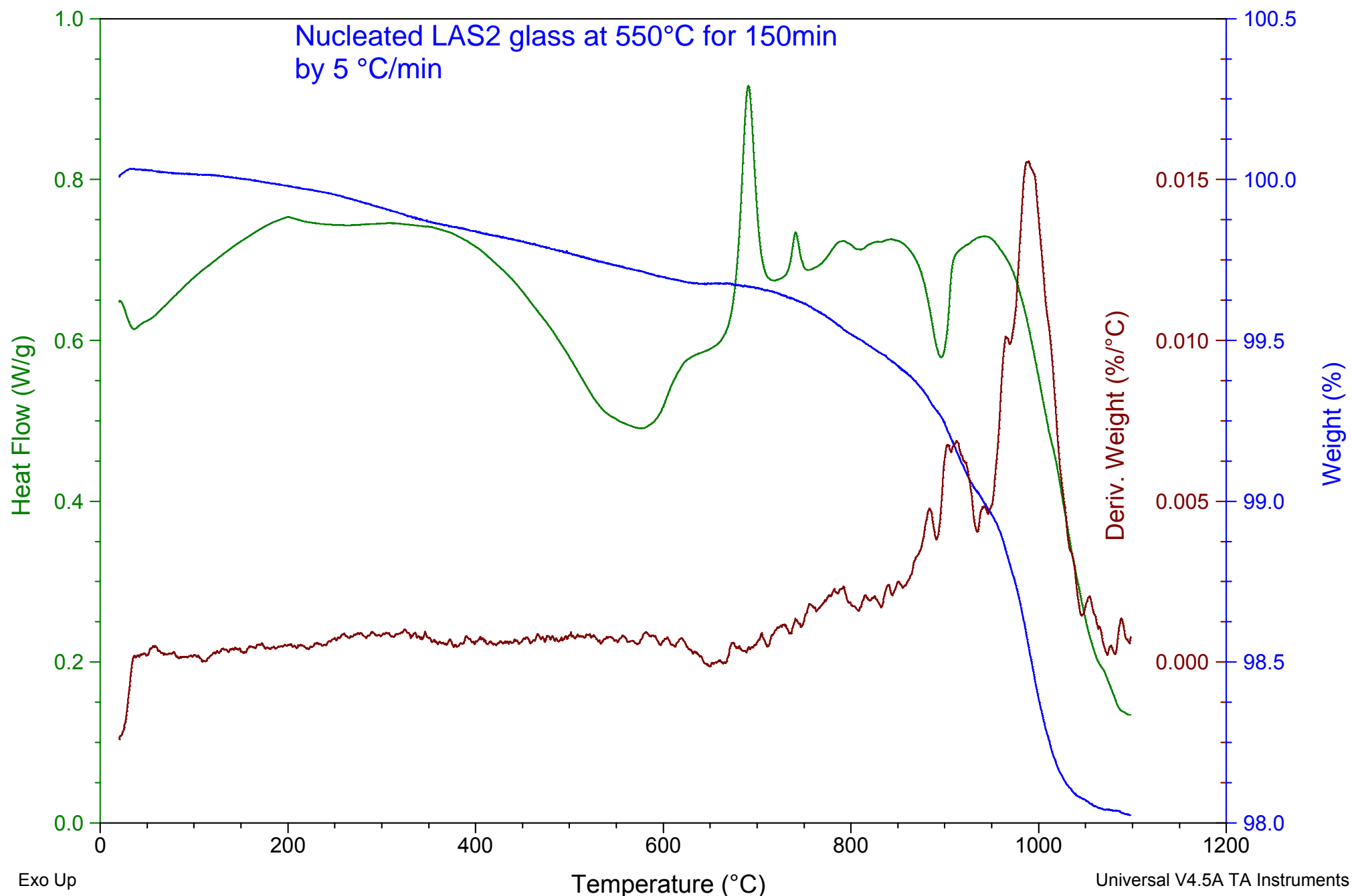
File: C:\03-02-2020\G1-550-30M-5C.001
Operator: Oday
Run Date: 04-Feb-2020 15:48
Instrument: SDT Q600 V20.9 Build 20



Sample: G1-550-150M-5C
Size: 13.2790 mg
Method: Isothermal for

DSC-TGA

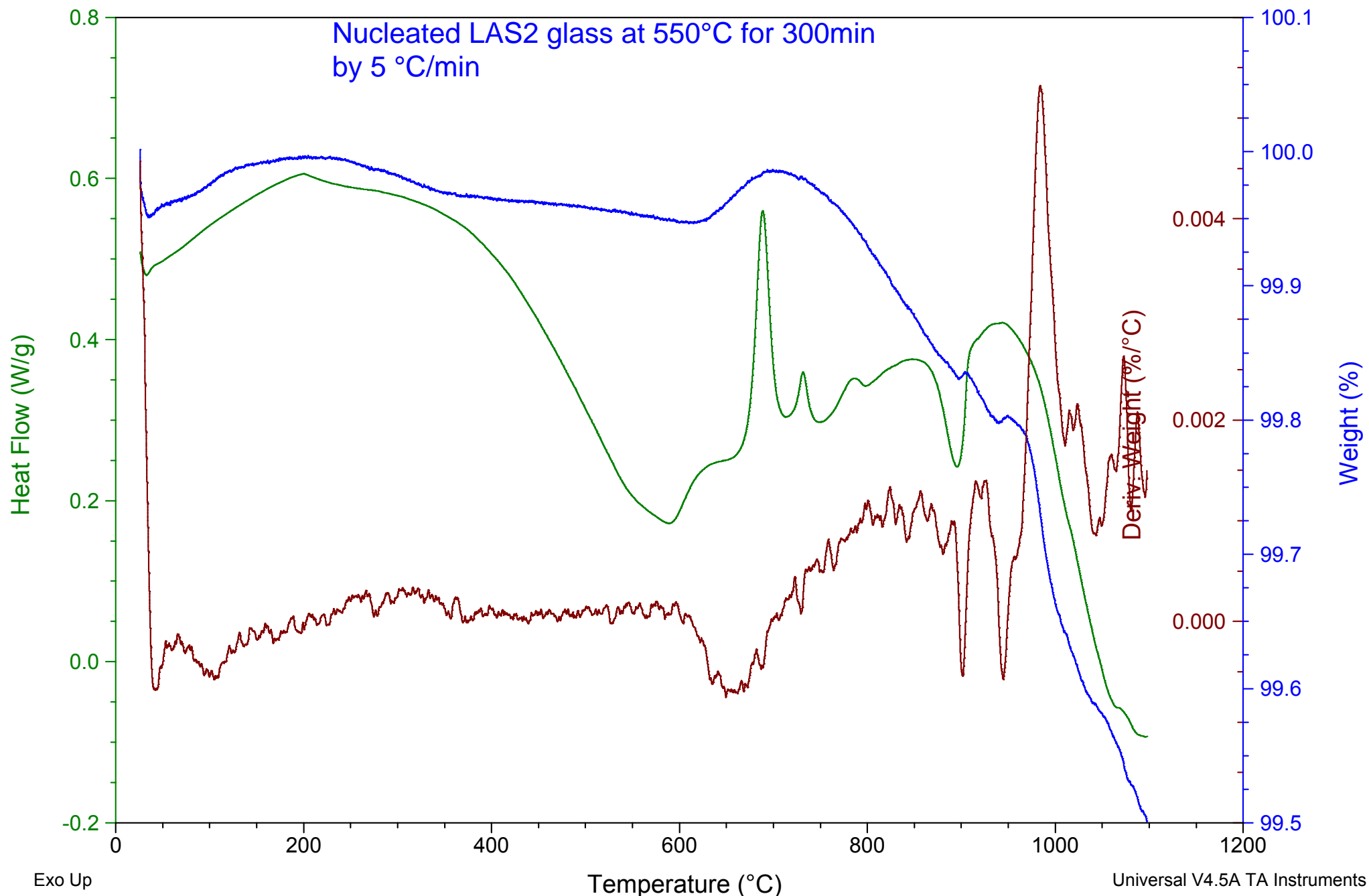
File: C:\03-02-2020\G1-550-150M-5C.001
Operator: Oday
Run Date: 05-Feb-2020 09:03
Instrument: SDT Q600 V20.9 Build 20



Sample: G1-550-300M-5C
Size: 15.1110 mg
Method: Isothermal for

DSC-TGA

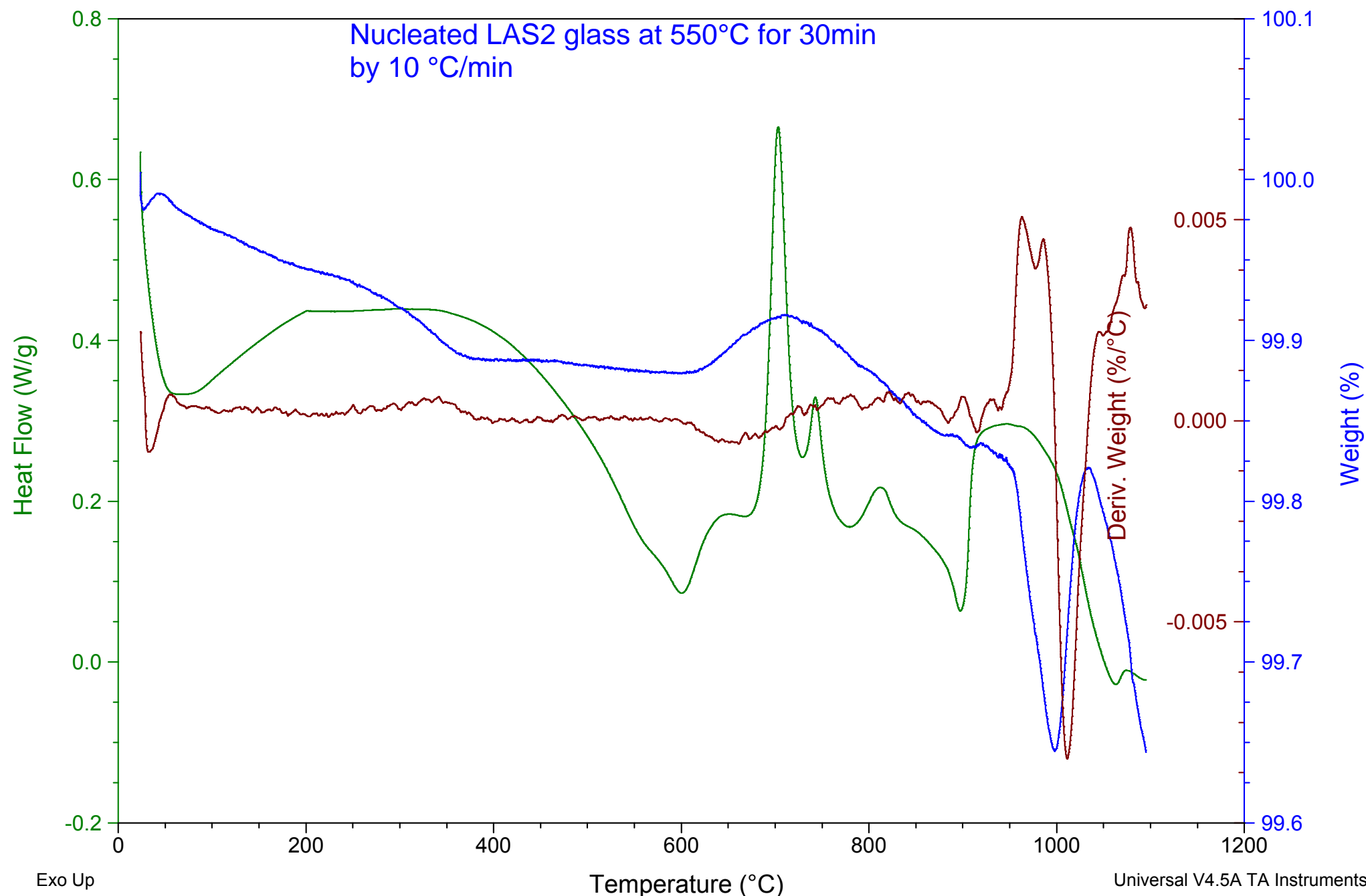
File: C:\03-02-2020\G1-550-300M-5C.001
Operator: Oday
Run Date: 05-Feb-2020 15:56
Instrument: SDT Q600 V20.9 Build 20



Sample: G1-550-300M-10C
Size: 19.1250 mg
Method: Isothermal for

DSC-TGA

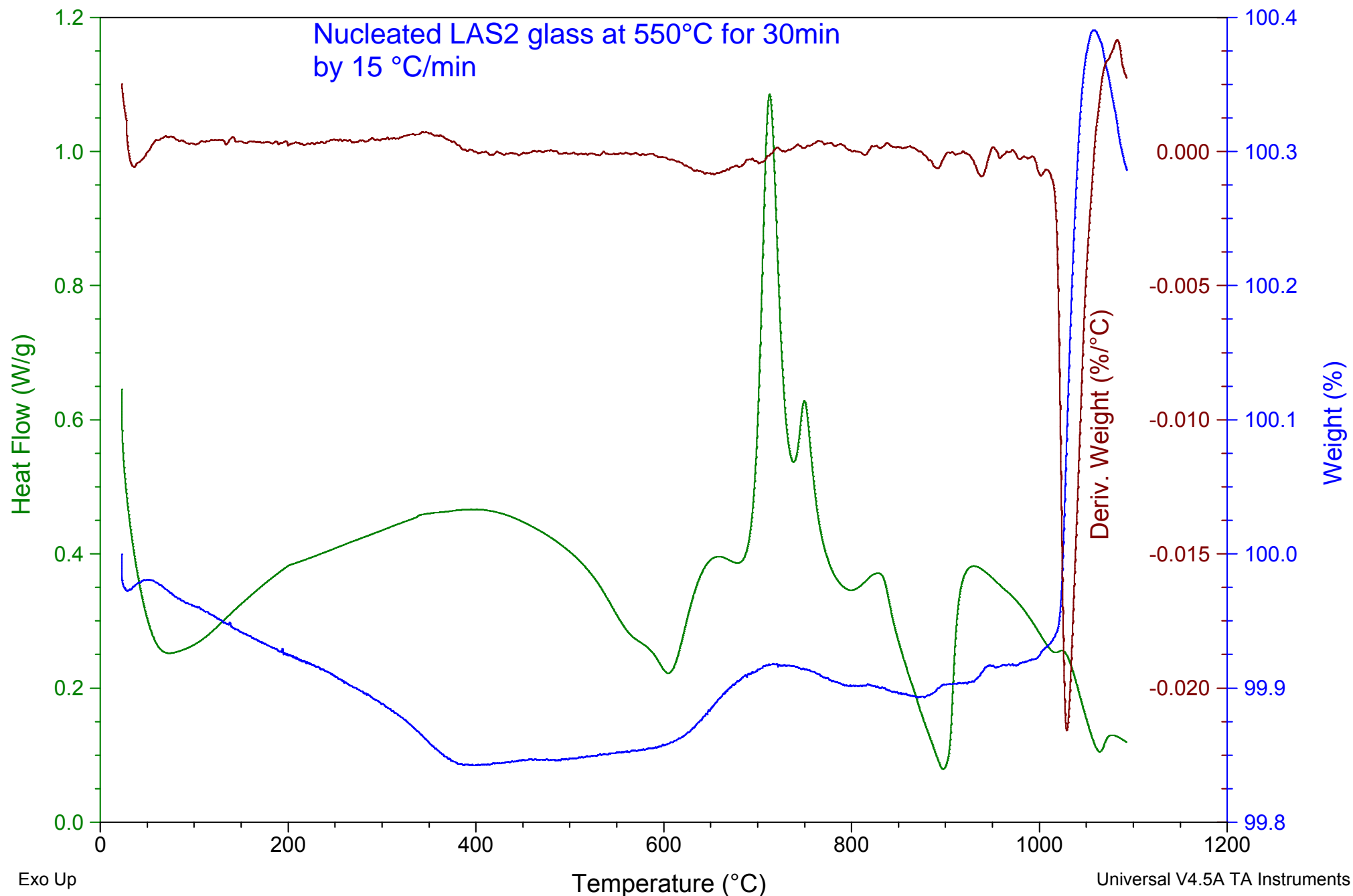
File: C:\03-02-2020\G1-550-300M-10C.001
Operator: Oday
Run Date: 06-Feb-2020 14:03
Instrument: SDT Q600 V20.9 Build 20



Sample: G1-550-300M-15C
Size: 22.9410 mg
Method: Isothermal for

DSC-TGA

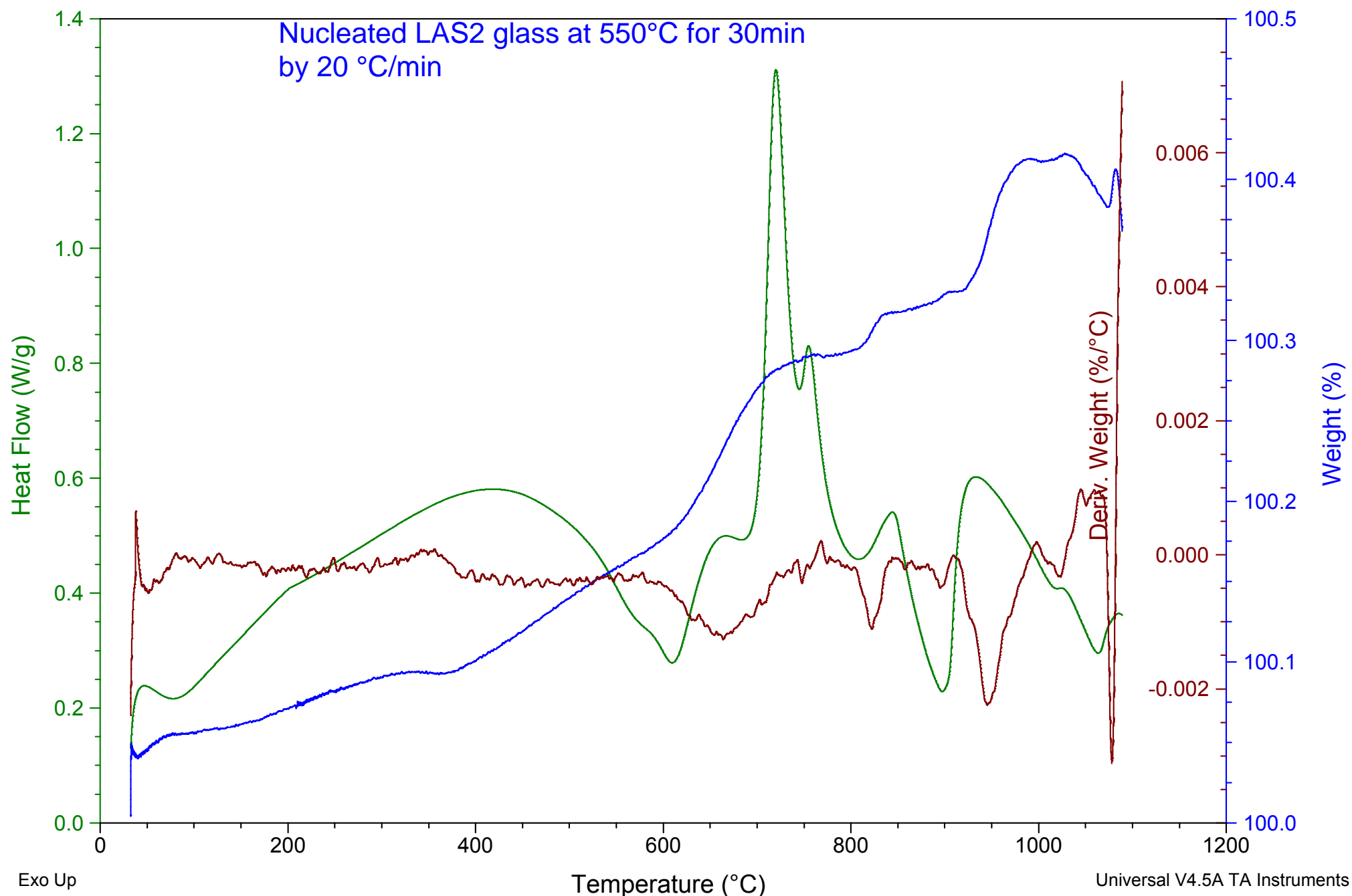
File: C:\03-02-2020\G1-550-300M-15C.001
Operator: Oday
Run Date: 07-Feb-2020 15:08
Instrument: SDT Q600 V20.9 Build 20



Sample: G1-550-300M-20C
Size: 18.7680 mg
Method: Isothermal for

DSC-TGA

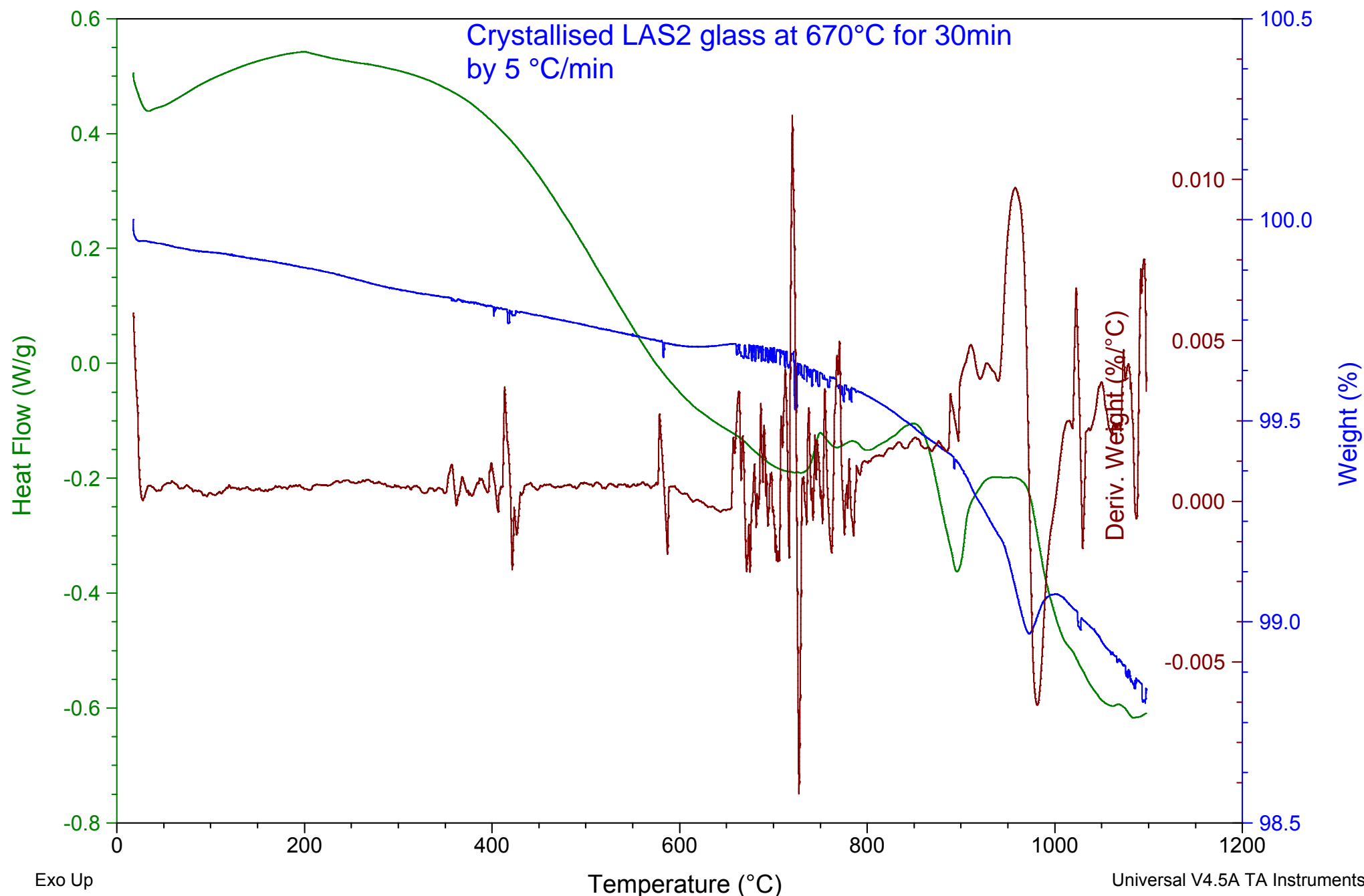
File: C:\03-02-2020\G1-550-300M-20C.001
Operator: Oday
Run Date: 05-Feb-2020 13:49
Instrument: SDT Q600 V20.9 Build 20



Sample: G1-670C-30min
Size: 18.9310 mg
Method: Isothermal for

DSC-TGA

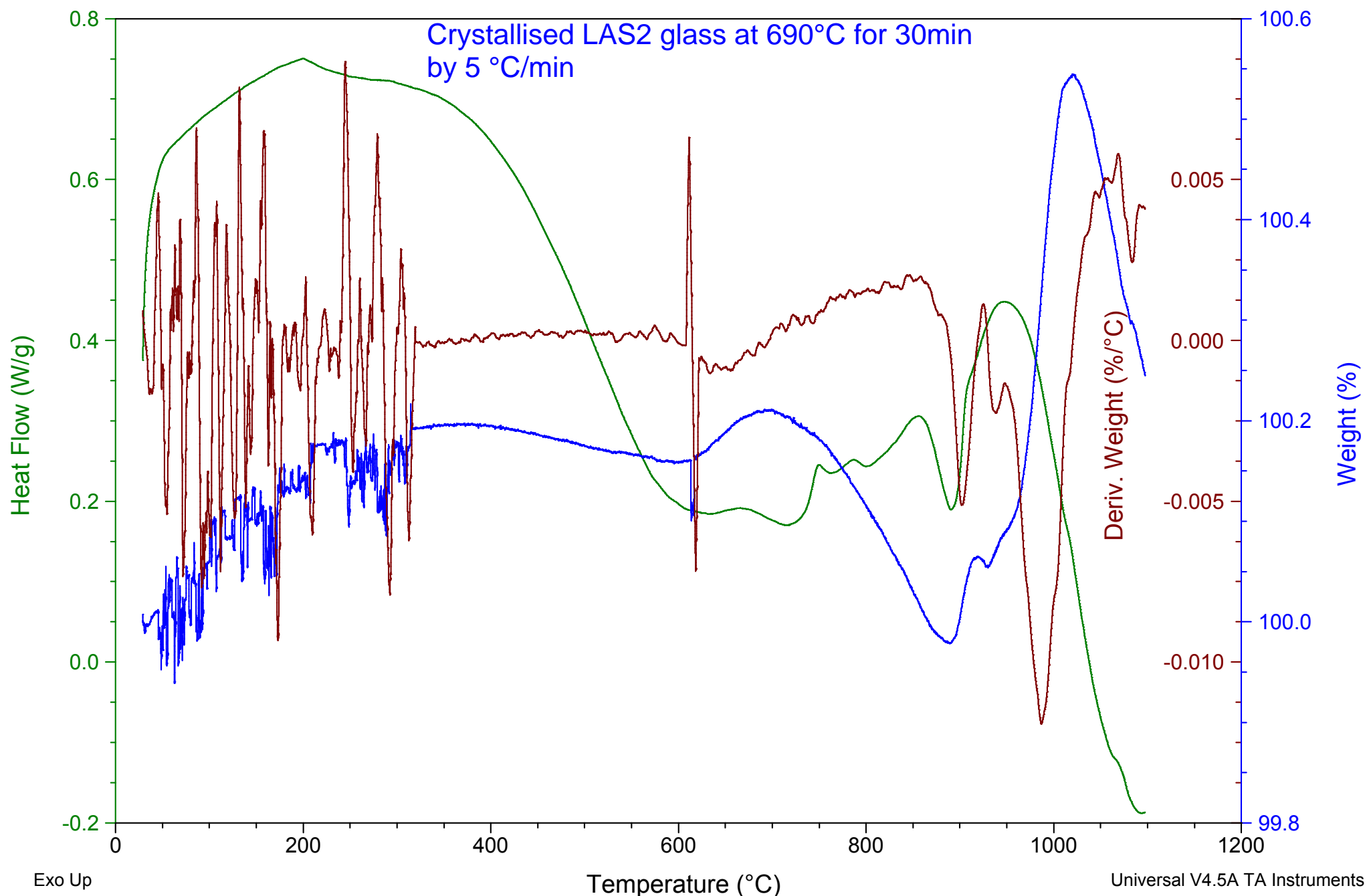
File: C:\03-02-2020\G1-670C-30min.001
Operator: Oday
Run Date: 13-Feb-2020 08:53
Instrument: SDT Q600 V20.9 Build 20



Sample: G1-690C-30min
Size: 12.3500 mg
Method: Isothermal for

DSC-TGA

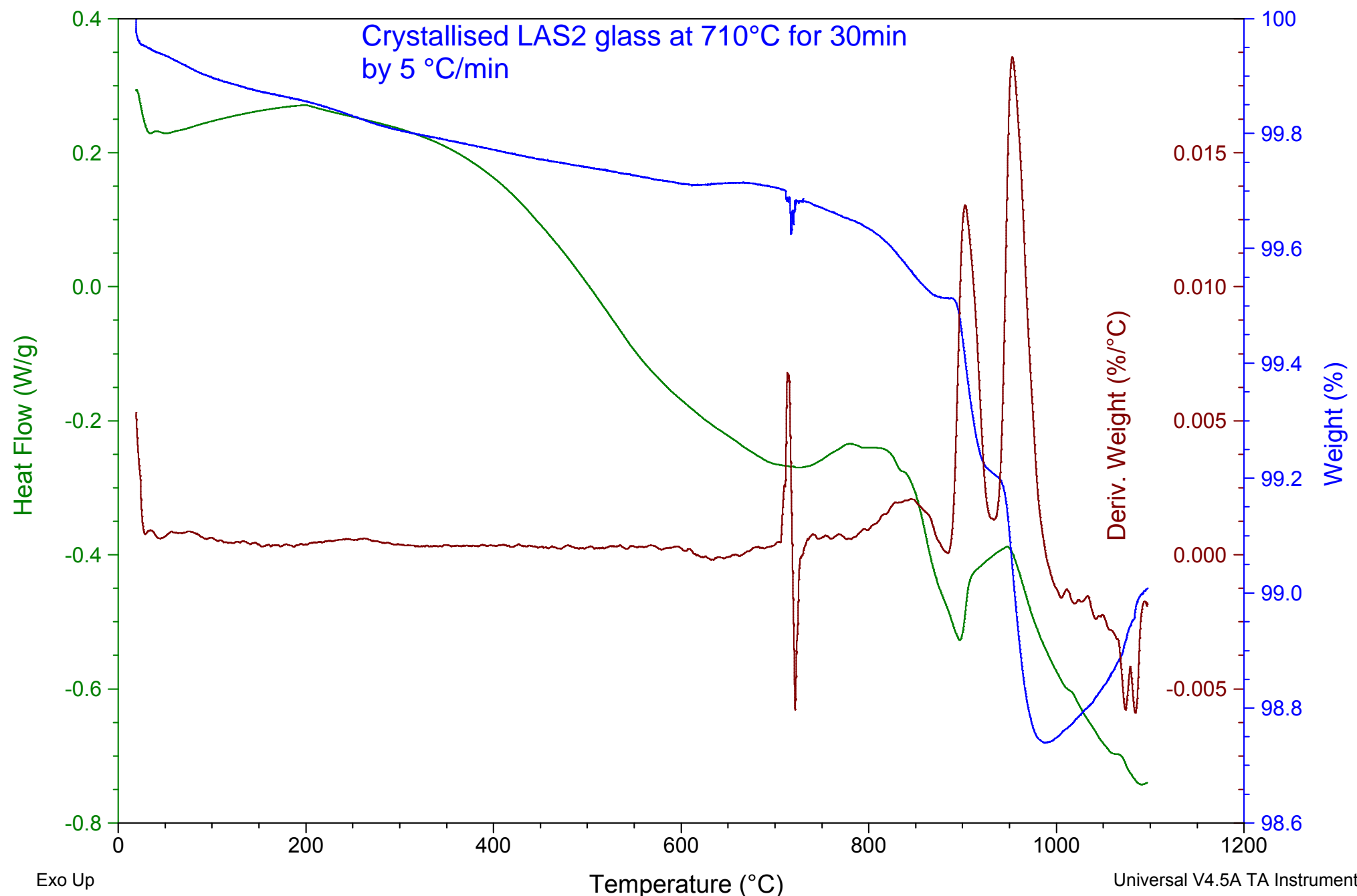
File: C:\03-02-2020\G1-690C-30min.001
Operator: Oday
Run Date: 13-Feb-2020 13:48
Instrument: SDT Q600 V20.9 Build 20



Sample: G1-710-30MIN
Size: 28.2220 mg
Method: Isothermal for

DSC-TGA

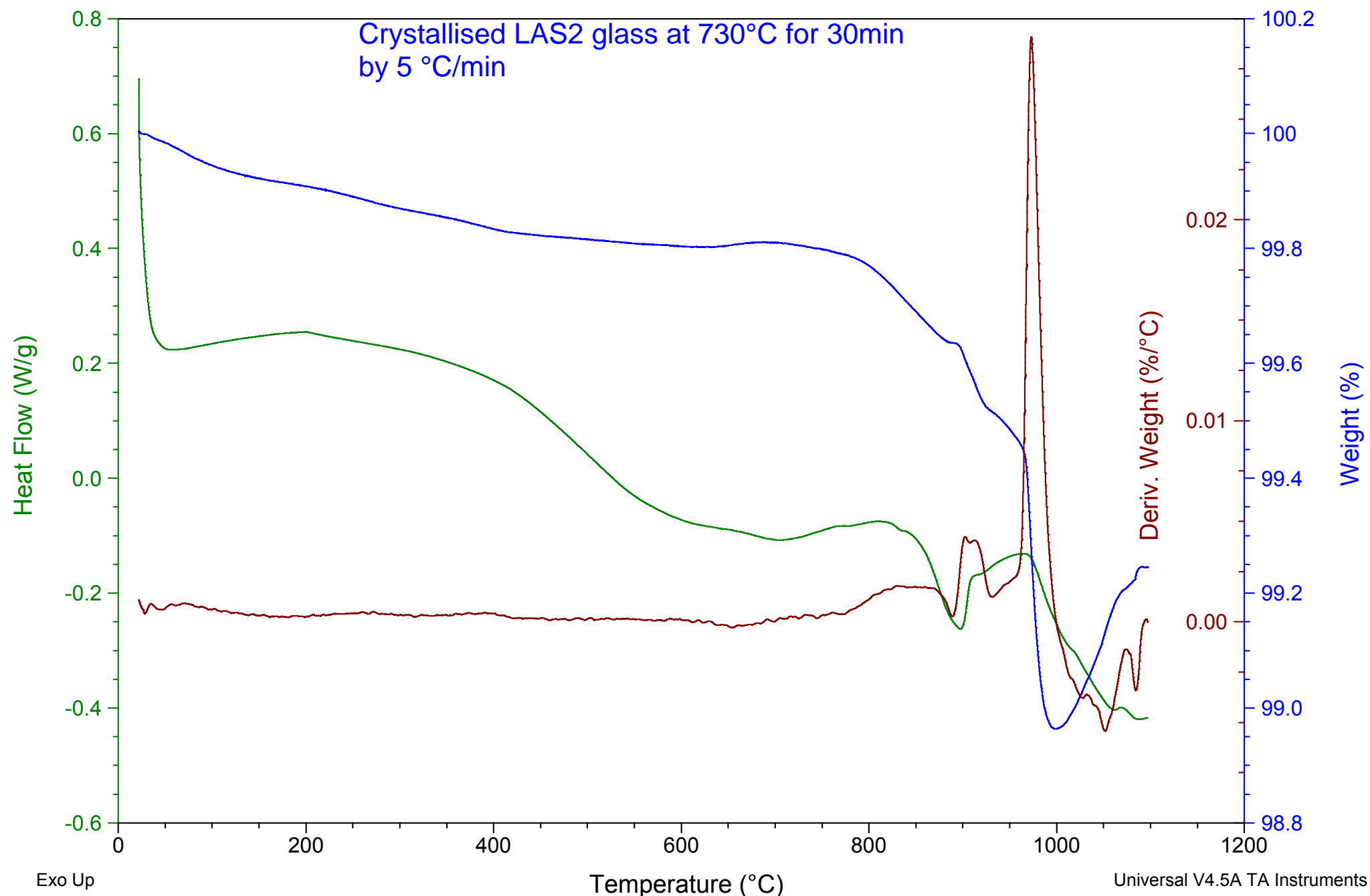
File: C:\...\04-03-2020\G1-710-30MIN.001
Operator: Oday
Run Date: 06-Mar-2020 11:59
Instrument: SDT Q600 V20.9 Build 20



Sample: G1-730-30MIN
Size: 30.6100 mg
Method: Isothermal for

DSC-TGA

File: C:\04-03-2020\G1-730-30MIN.001
Operator: Oday
Run Date: 05-Mar-2020 16:04
Instrument: SDT Q600 V20.9 Build 20



Appendix

| 3 |

X-ray Diffraction (XRD)

X-ray Diffraction (XRD) patterns of the glass and heated-treated glass selected.

- *In-situ* XRD (A)
- *Ex-situ* XRD (B)

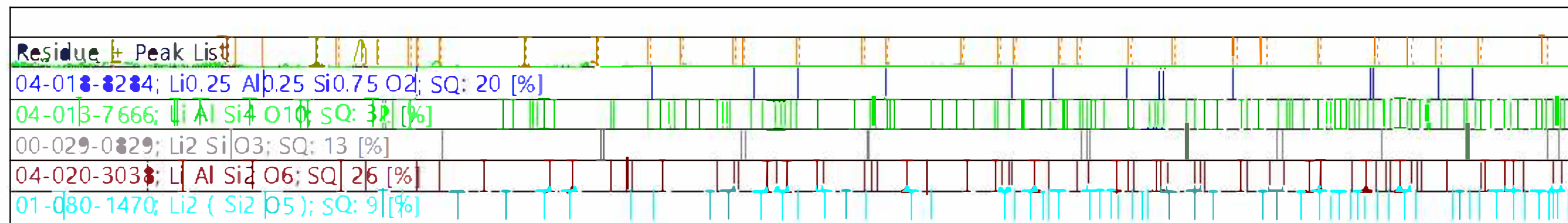
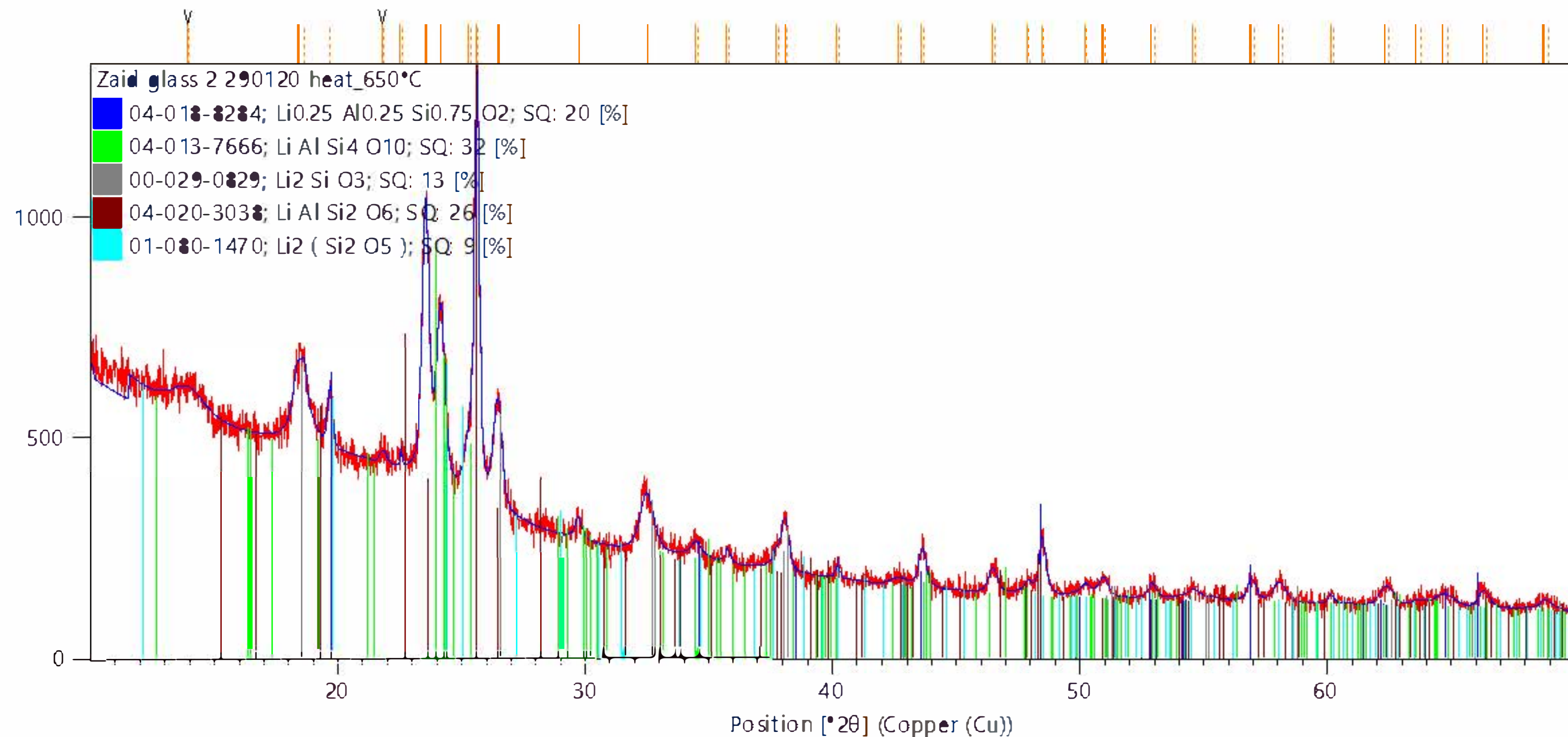
A

Date: 24/02/2020 Time: 10:39:50

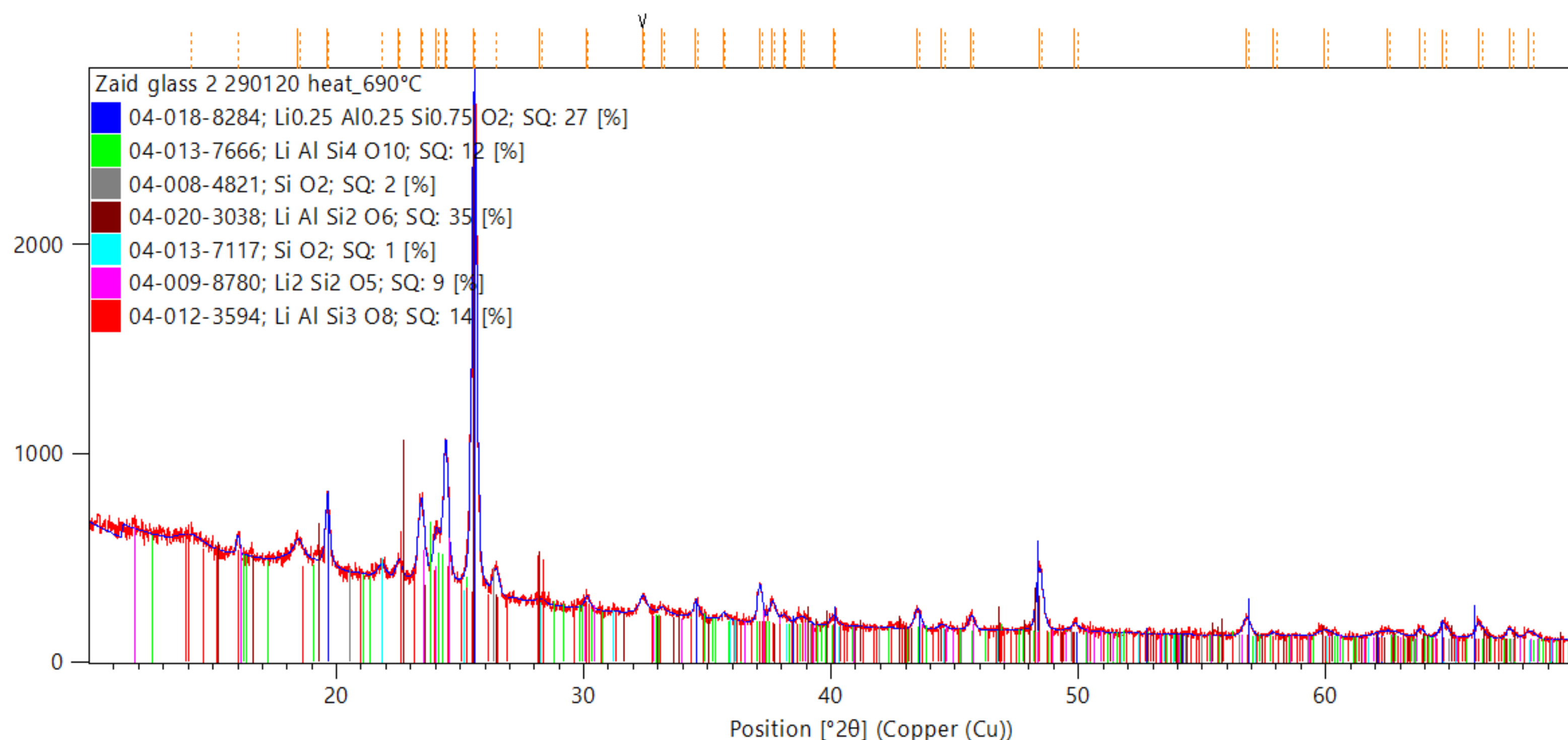
File: Zaid glass 2 290120 heat_650°C

User: XPERT

Counts

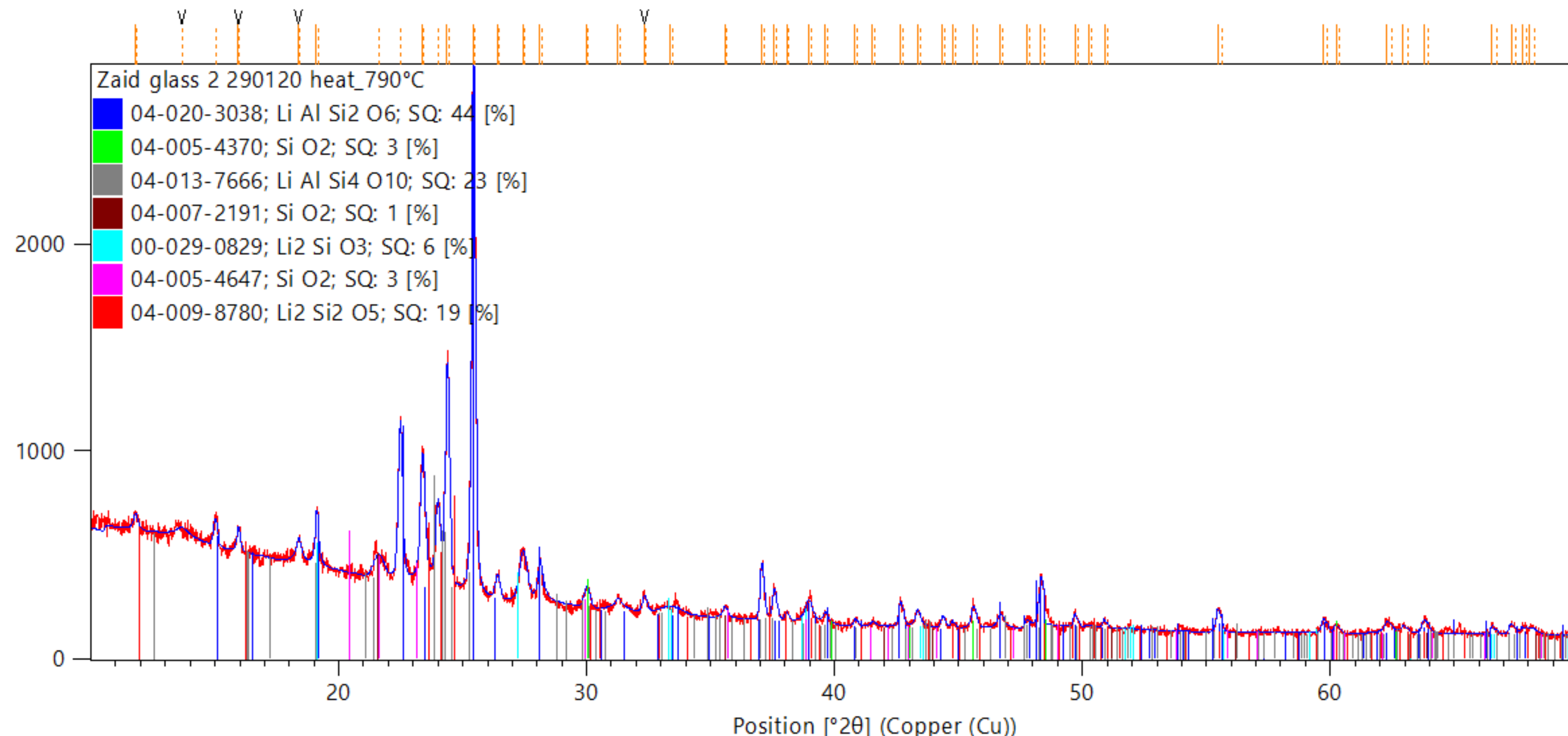


Counts



| Residue + Peak List |
|---|
| 04-018-8284; Li _{0.25} Al _{0.25} Si _{0.75} O ₂ ; SQ: 27 [%] |
| 04-013-7666; Li Al Si ₄ O ₁₀ ; SQ: 12 [%] |
| 04-008-4821; Si O ₂ ; SQ: 2 [%] |
| 04-020-3038; Li Al Si ₂ O ₆ ; SQ: 35 [%] |
| 04-013-7117; Si O ₂ ; SQ: 1 [%] |
| 04-009-8780; Li ₂ Si ₂ O ₅ ; SQ: 9 [%] |
| 04-012-3594; Li Al Si ₃ O ₈ ; SQ: 14 [%] |

Counts



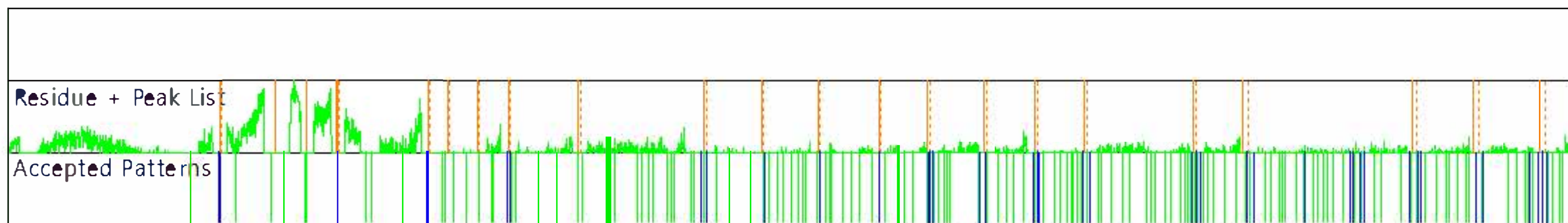
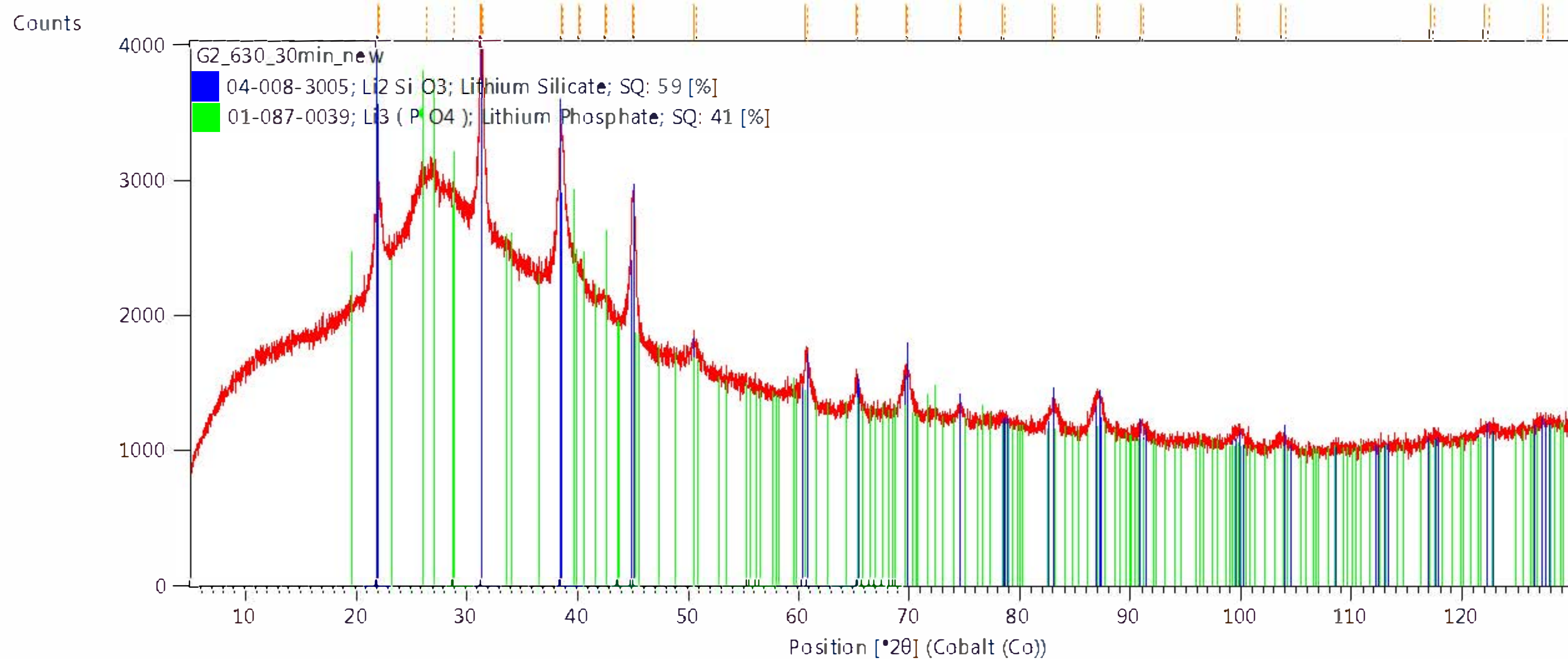
| Residue + Peak List |
|--|
| 04-020-3038; Li Al Si ₂ O ₆ ; SQ: 44 [%] |
| 04-005-4370; Si O ₂ ; SQ: 3 [%] |
| 04-013-7666; Li Al Si ₄ O ₁₀ ; SQ: 23 [%] |
| 04-007-2191; Si O ₂ ; SQ: 1 [%] |
| 00-029-0829; Li ₂ Si O ₃ ; SQ: 6 [%] |
| 04-005-4647; Si O ₂ ; SQ: 3 [%] |
| 04-009-8780; Li ₂ Si ₂ O ₅ ; SQ: 19 [%] |

B

Date: 19/11/2019 Time: 15:18:27

File: G2_630_30min_new

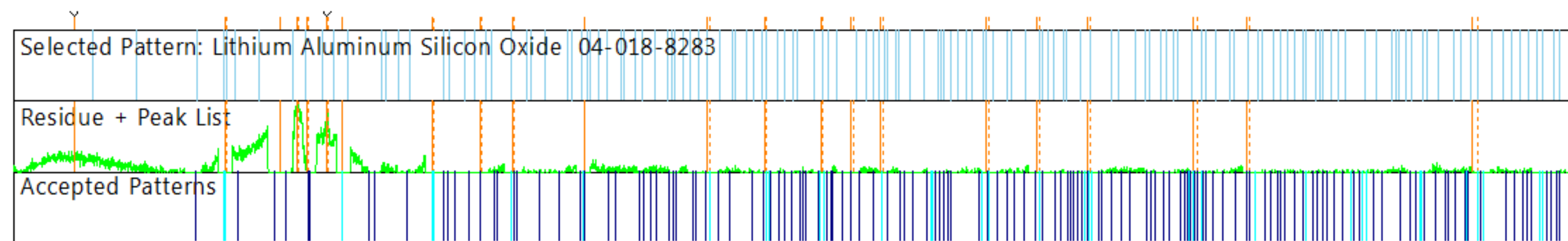
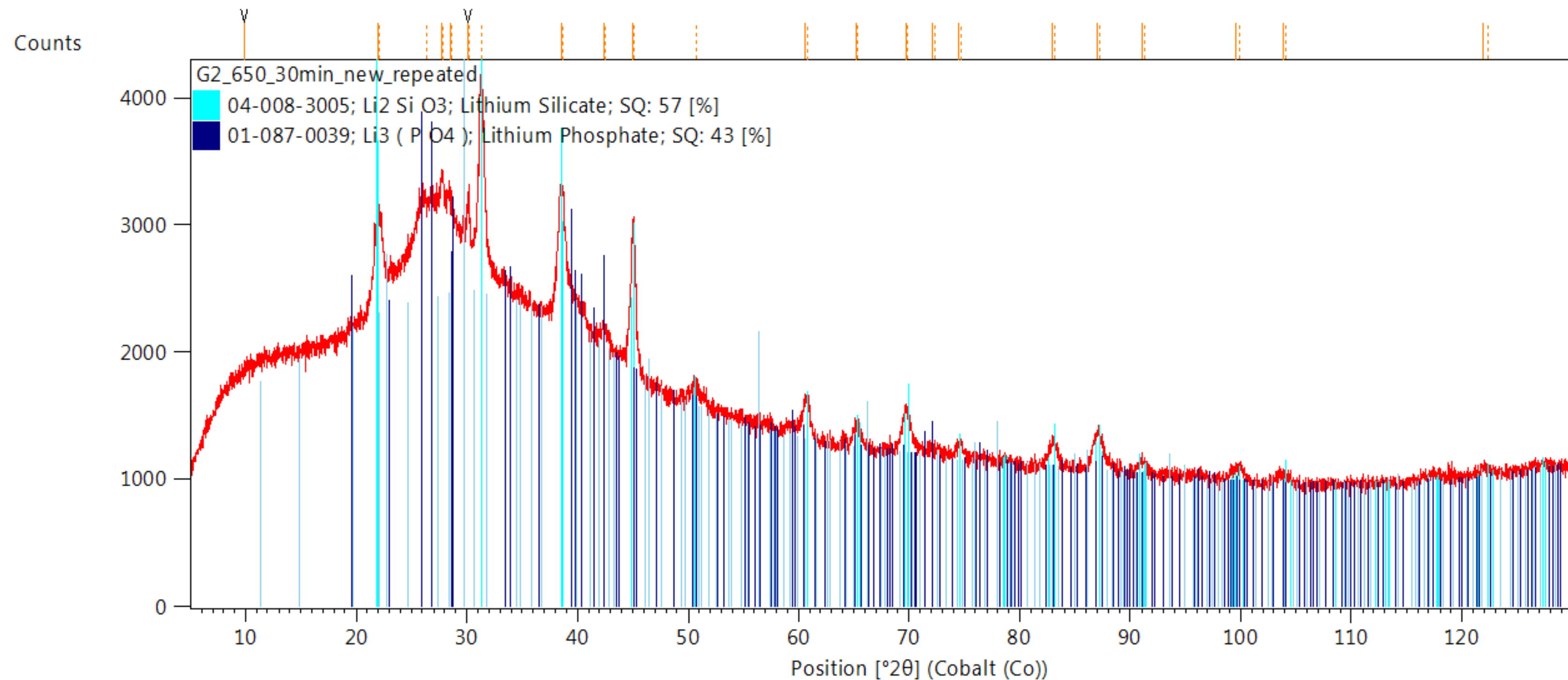
User: EMPYREAN

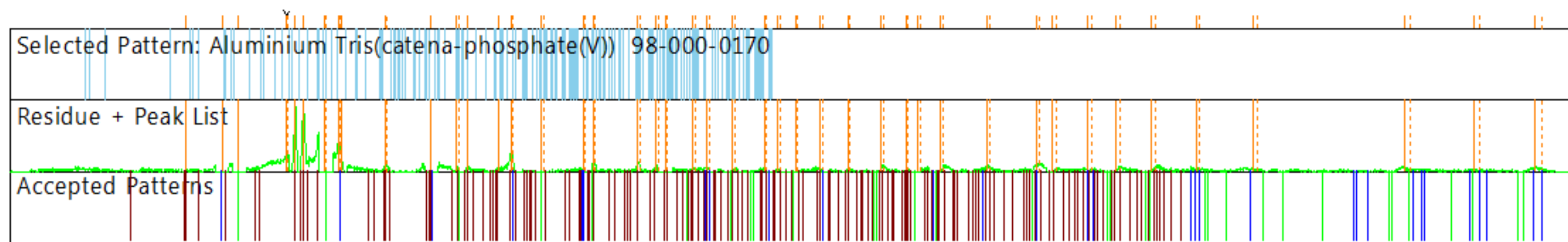
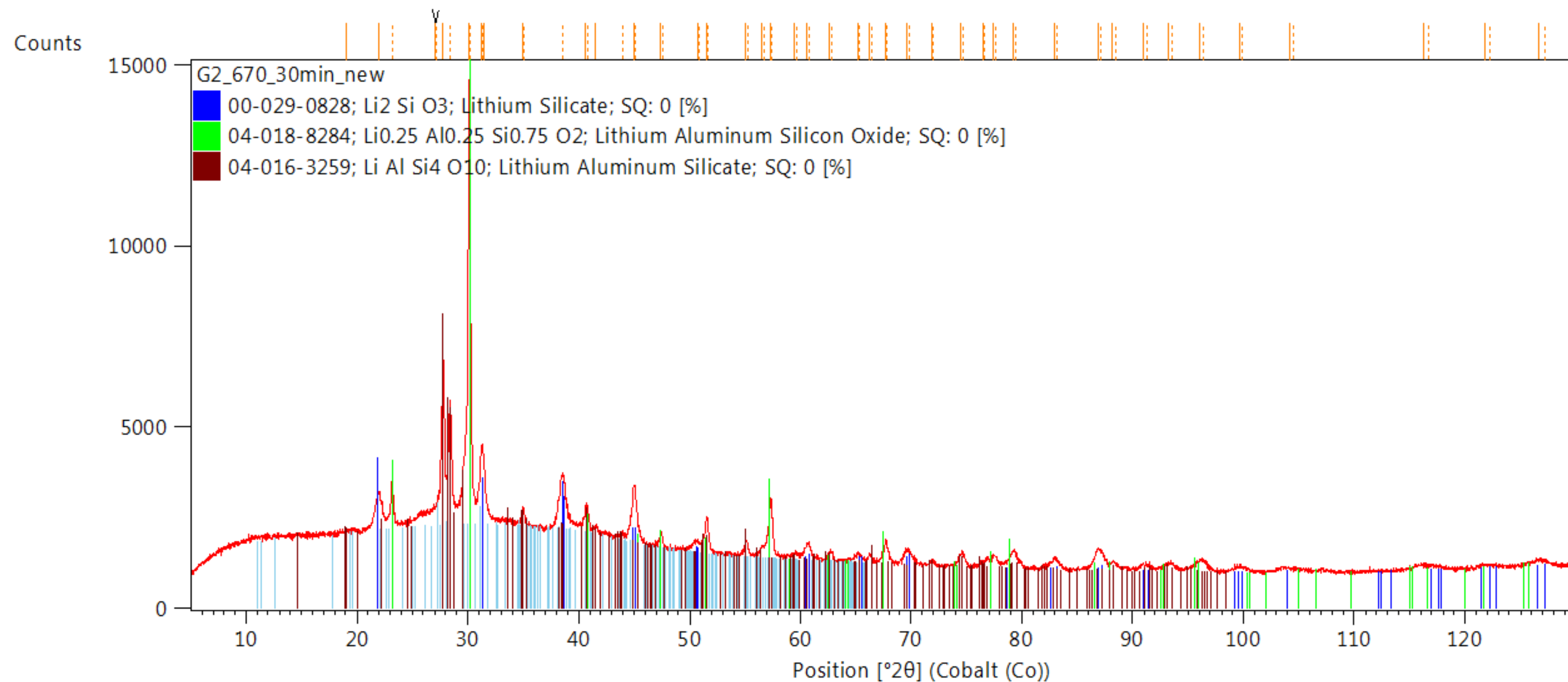


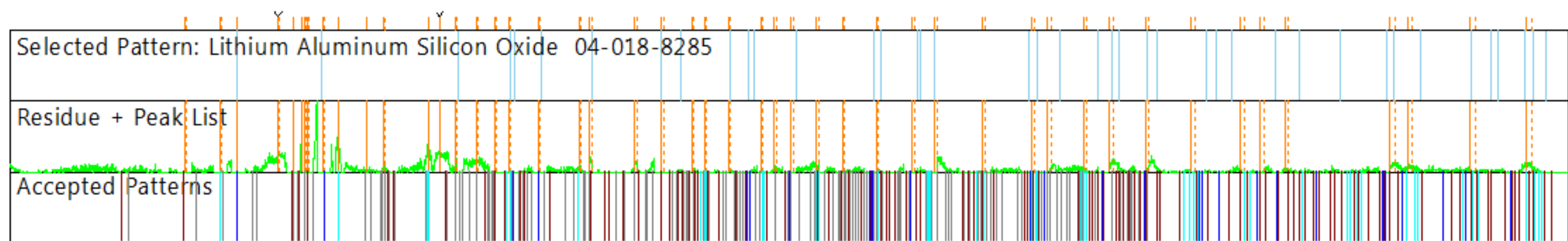
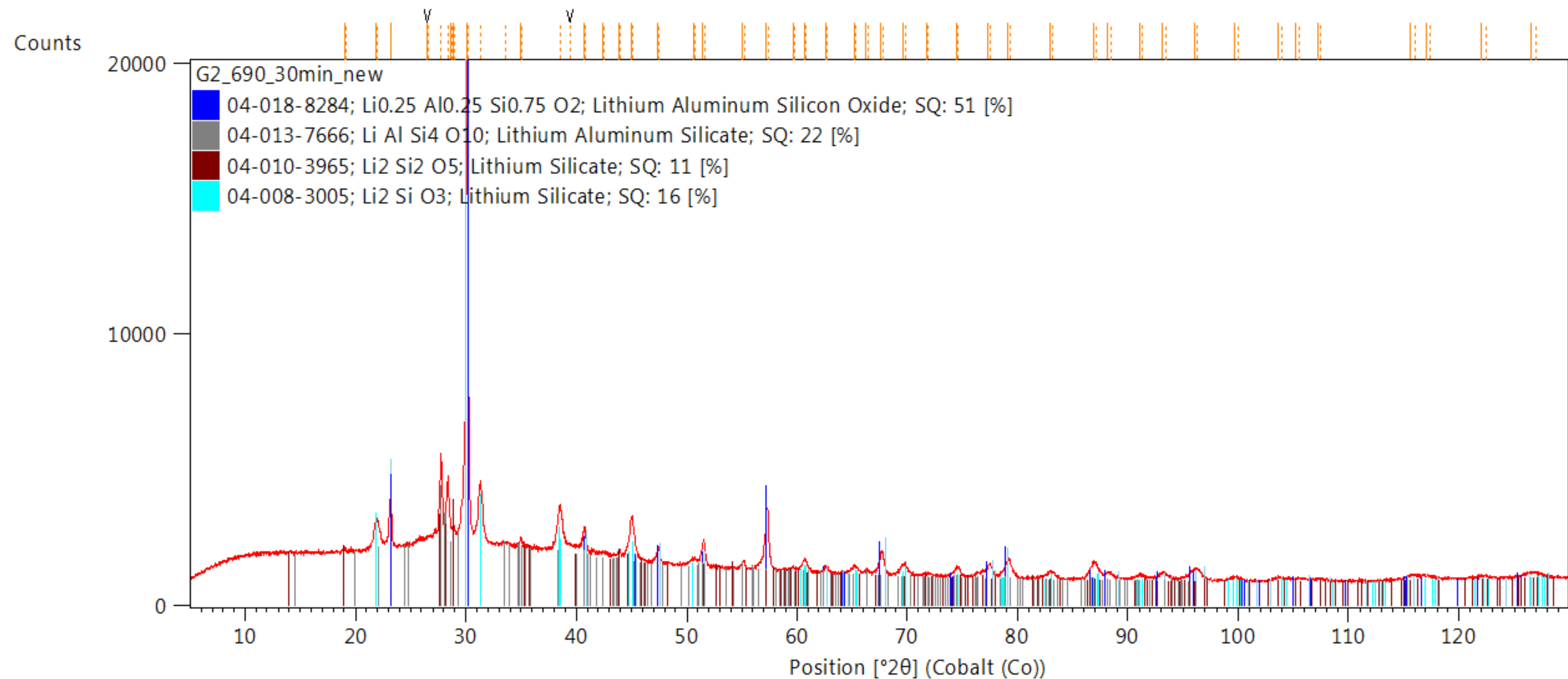
Date: 19/11/2019 Time: 15:25:37

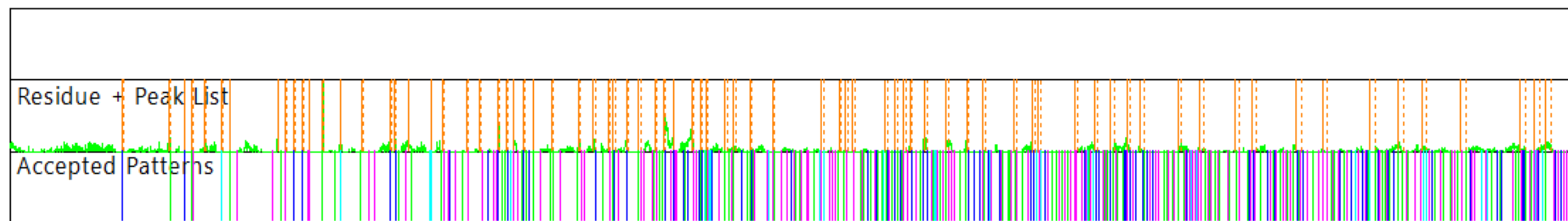
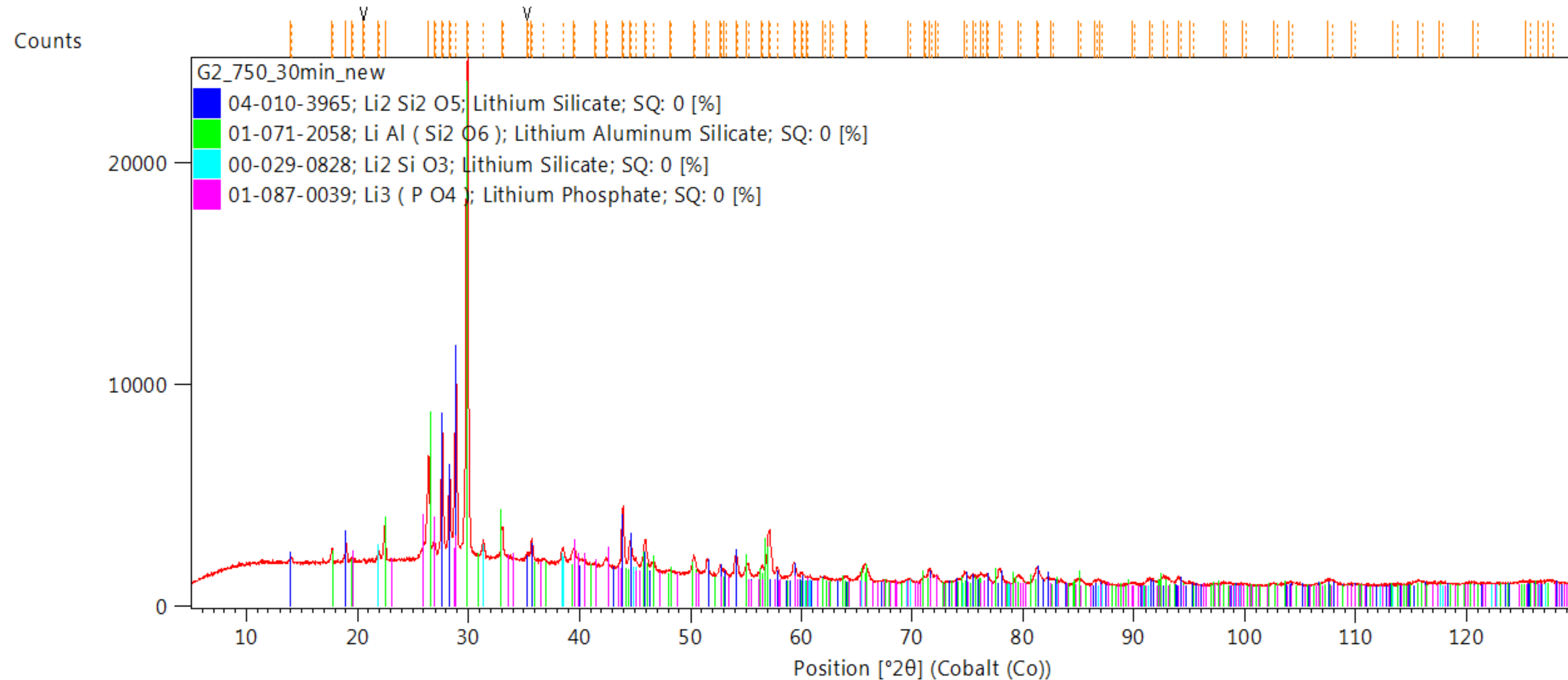
File: G2_650_30min_new_repeated

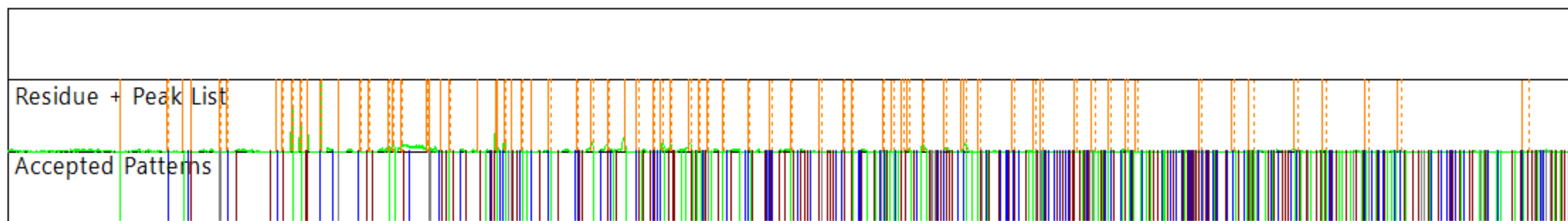
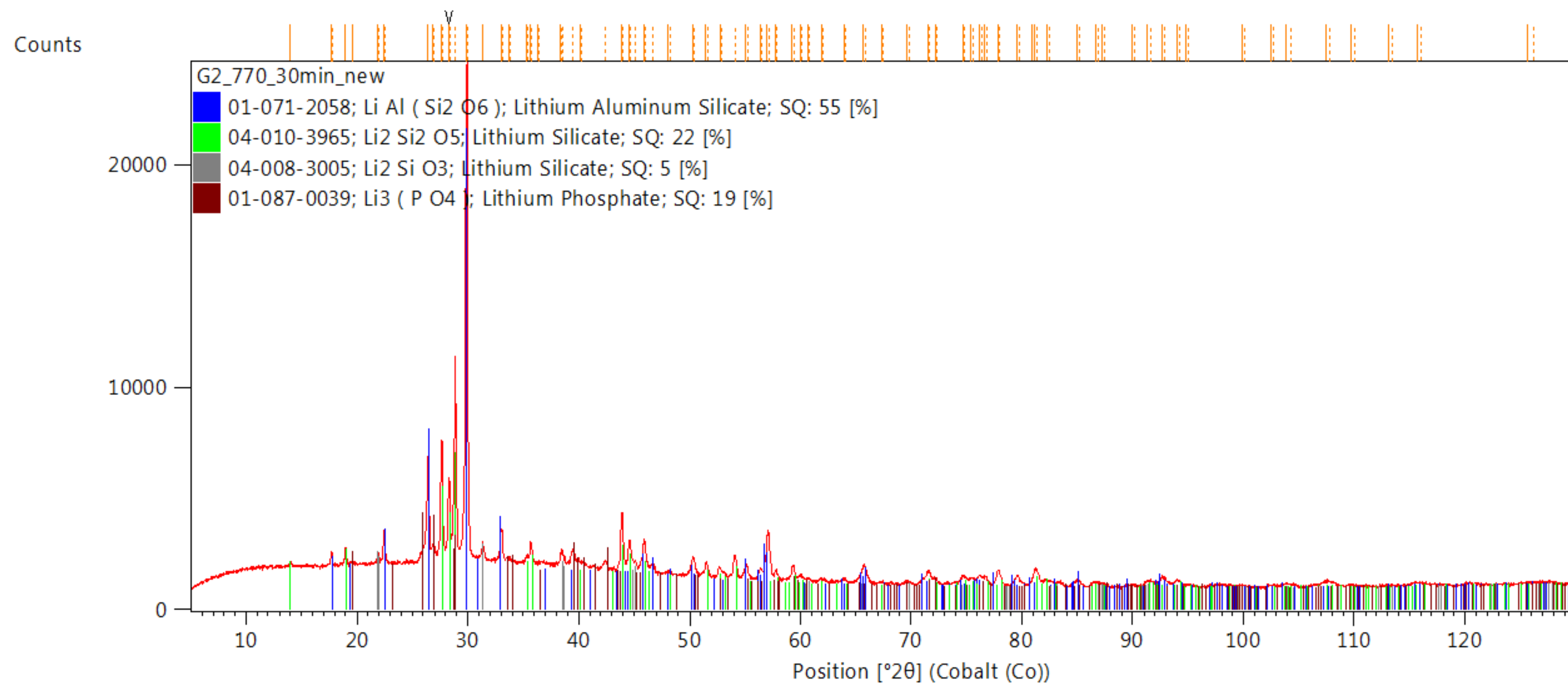
User: EMPYREAN









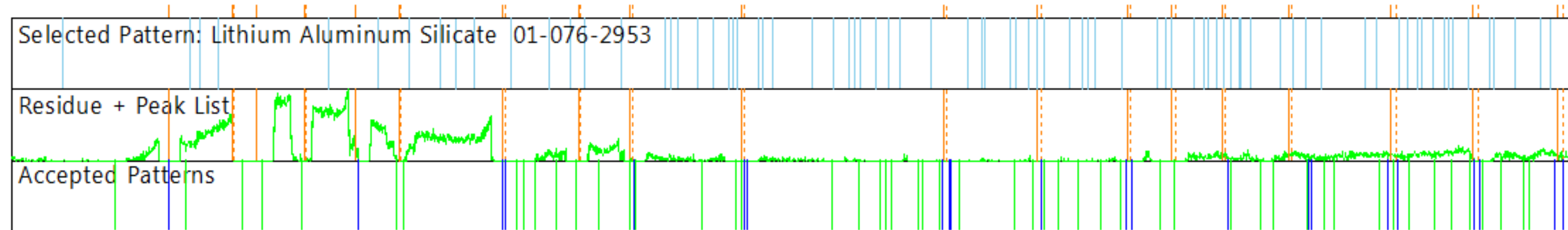
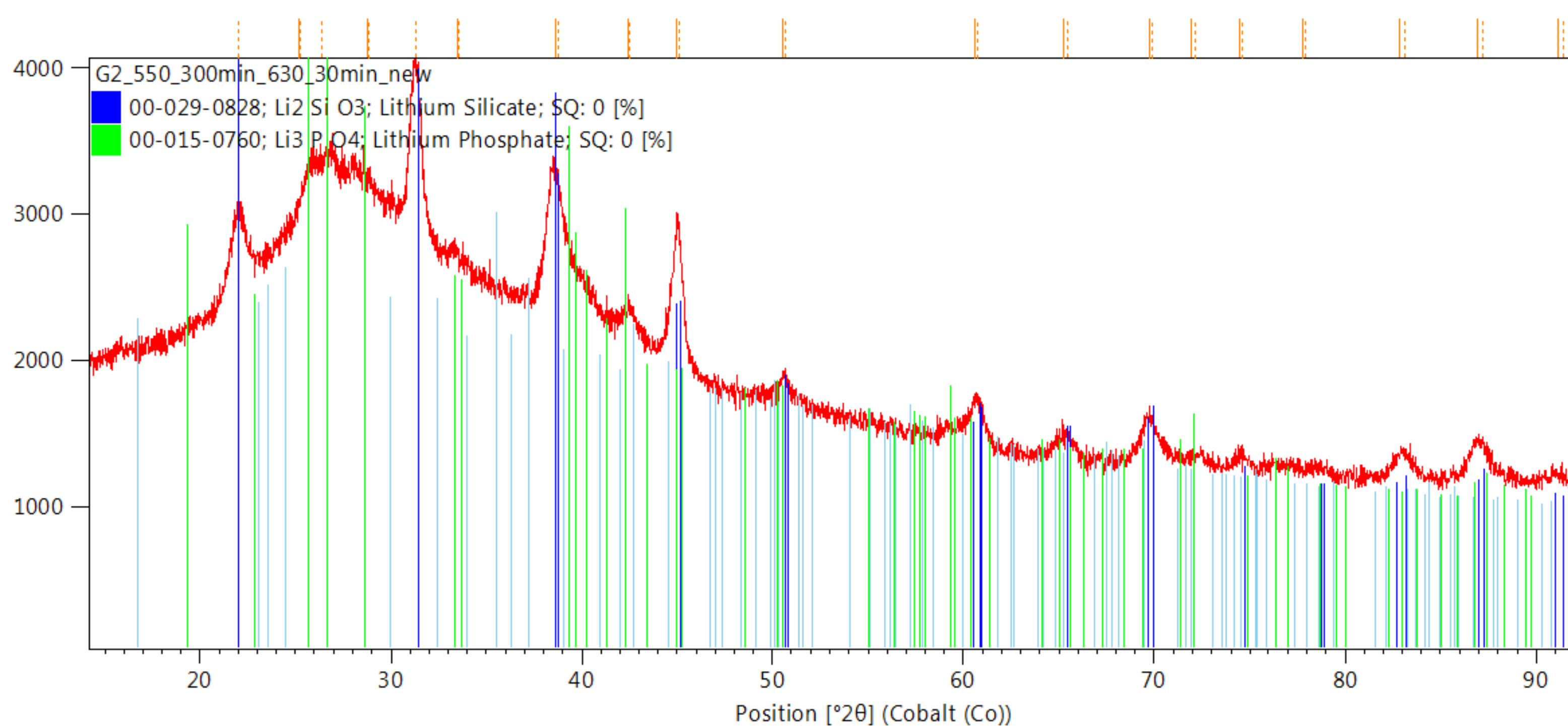


Date: 18/06/2019 Time: 16:35:50

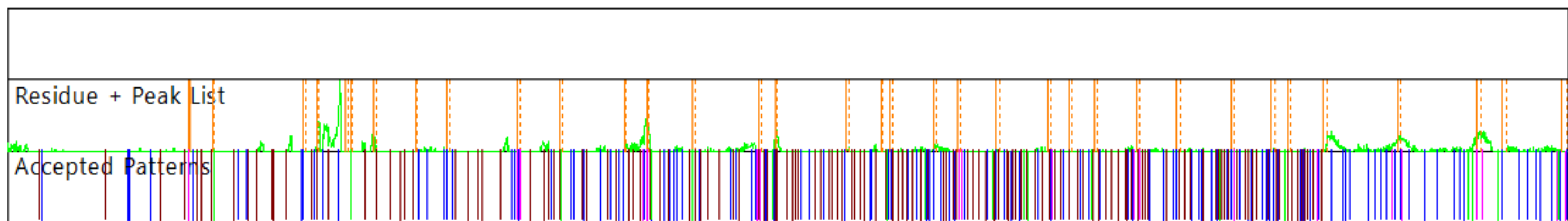
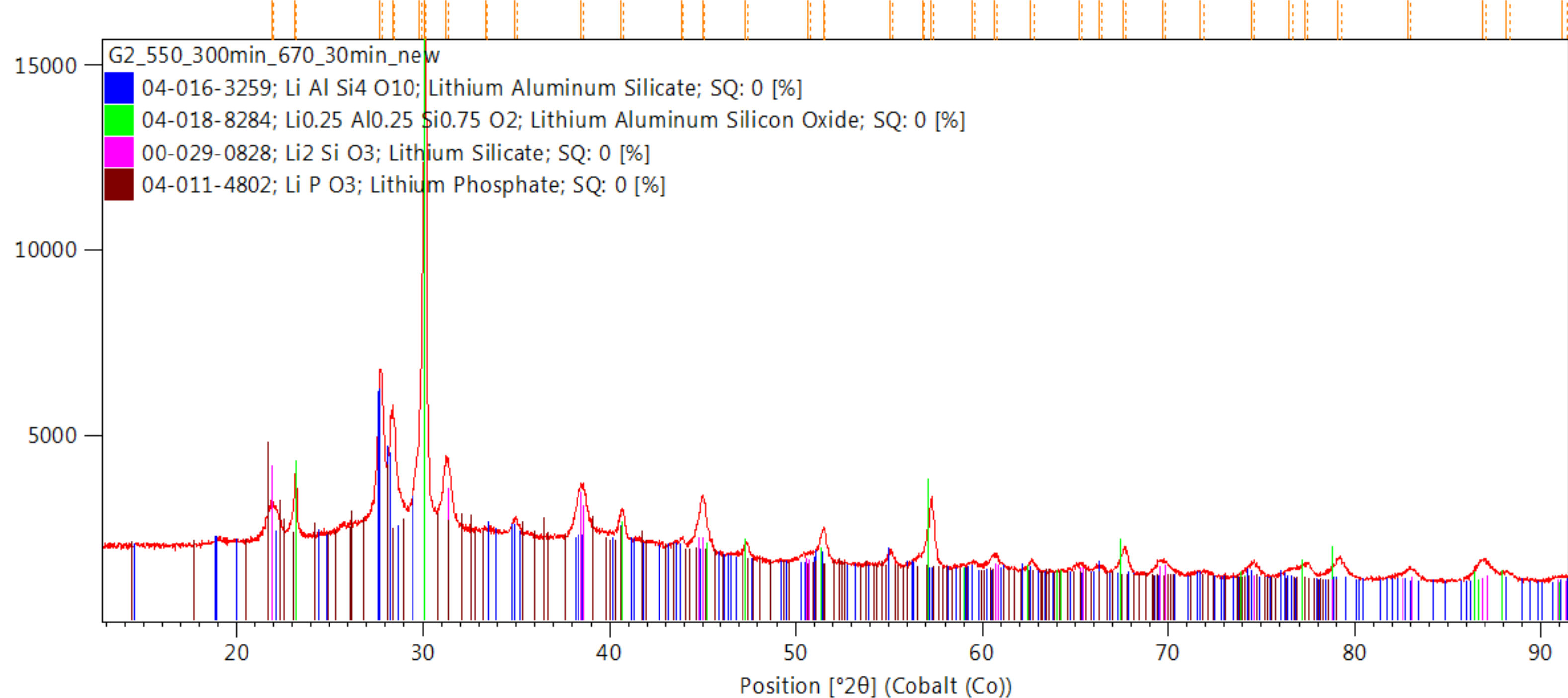
File: G2_550_300min_630_30min_new

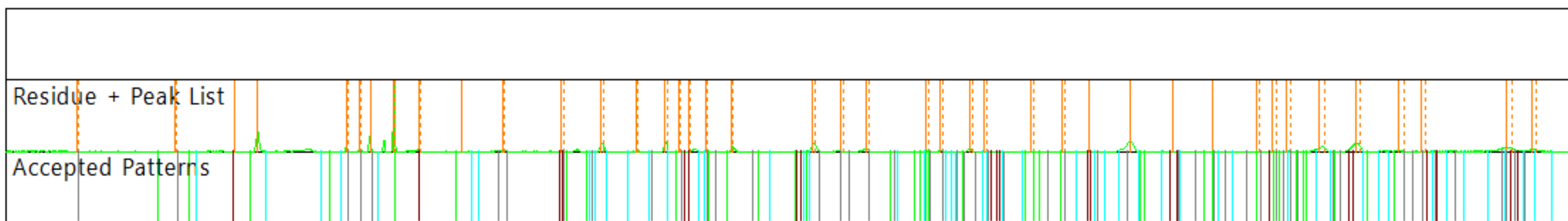
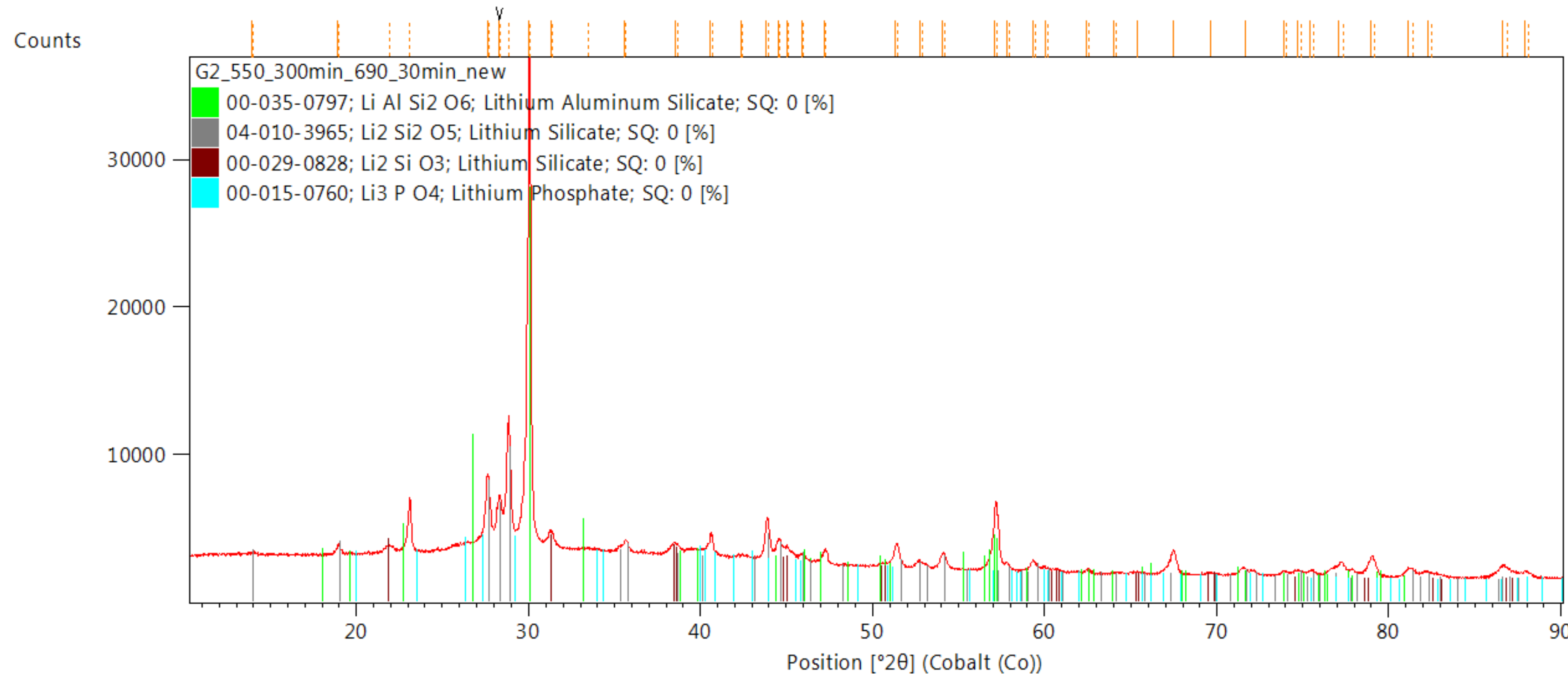
User: EMPYREAN

Counts



Counts

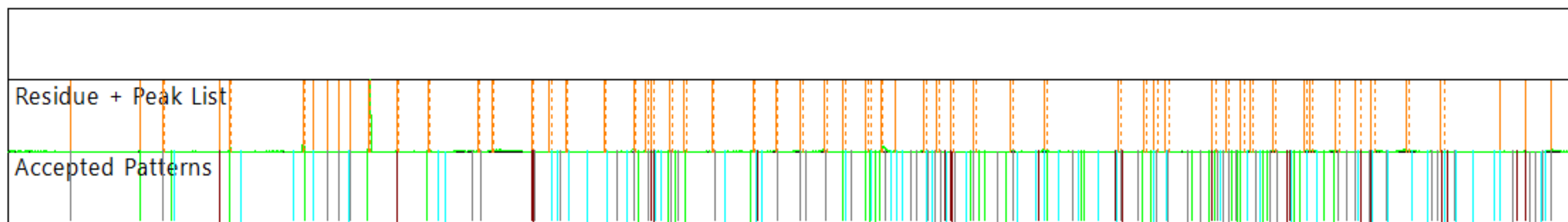
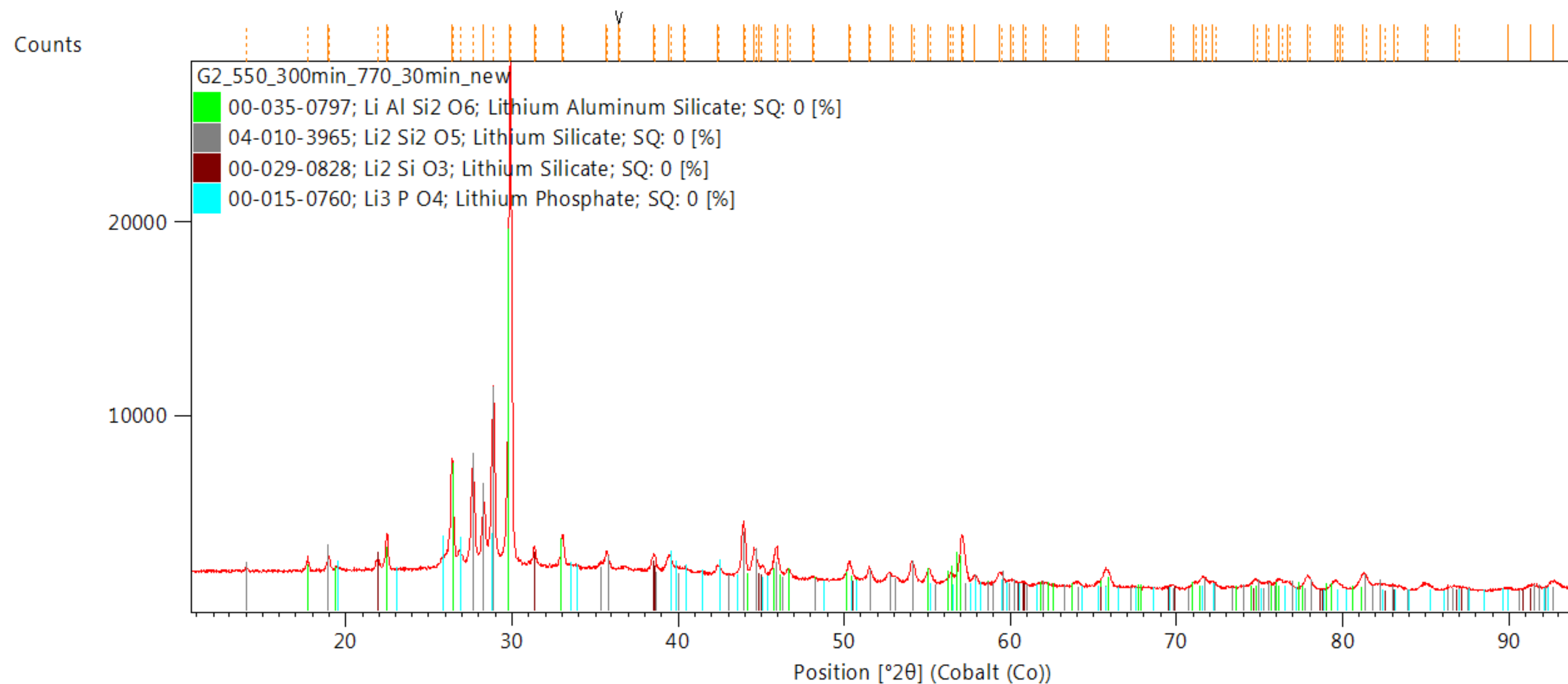


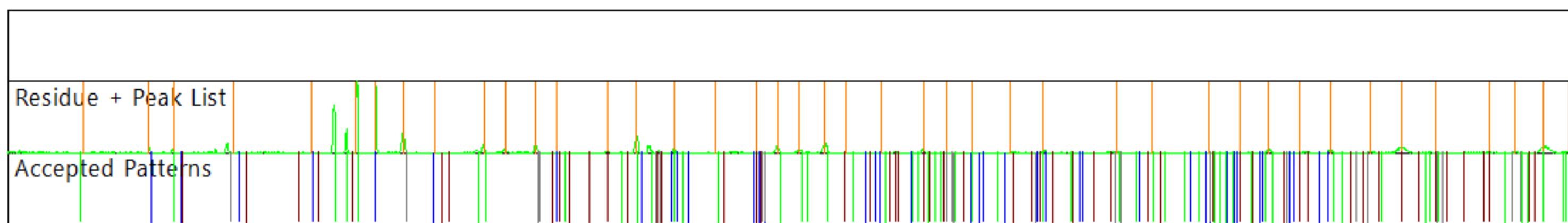
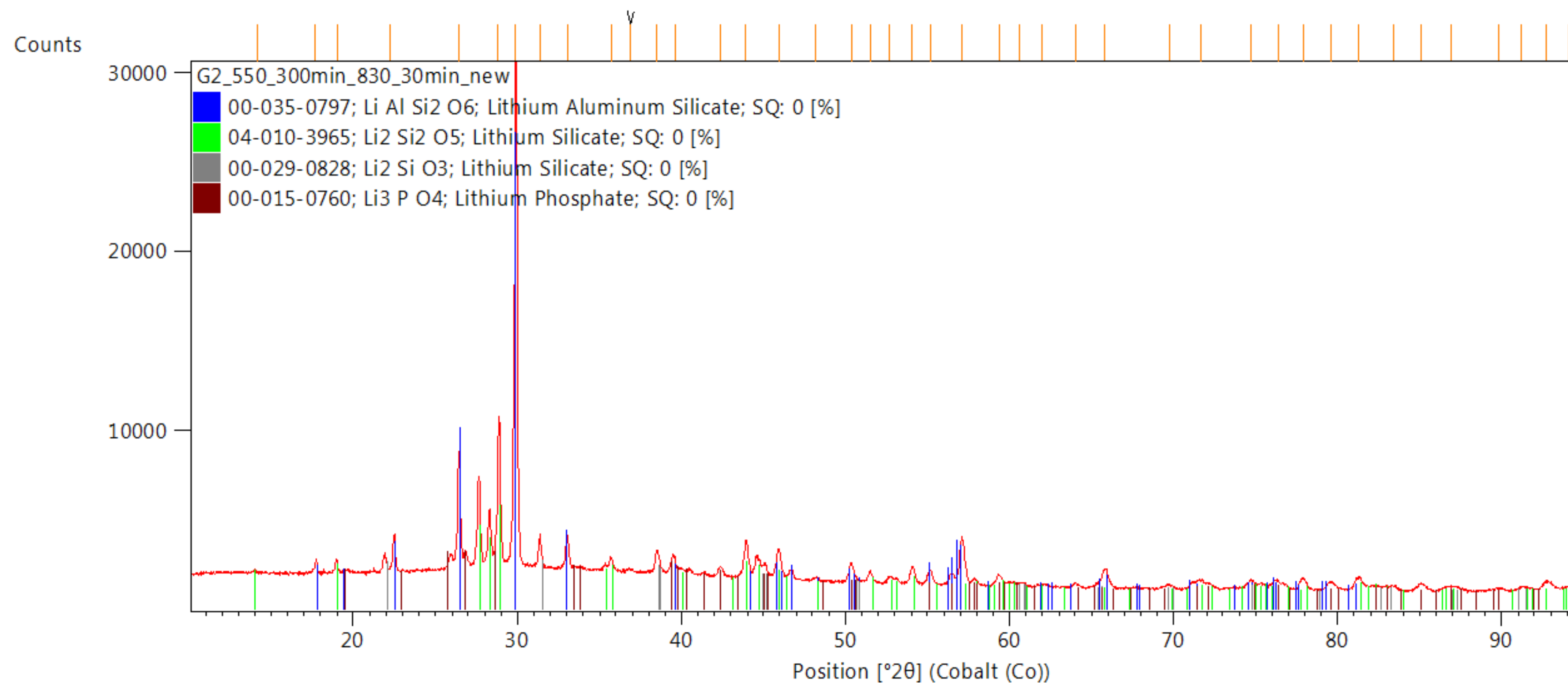


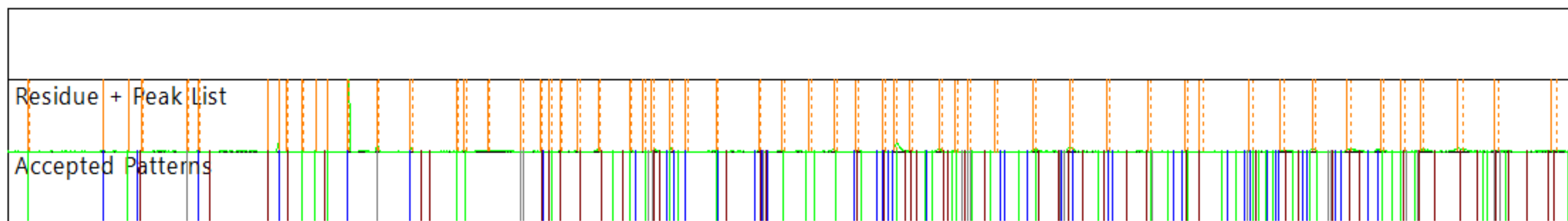
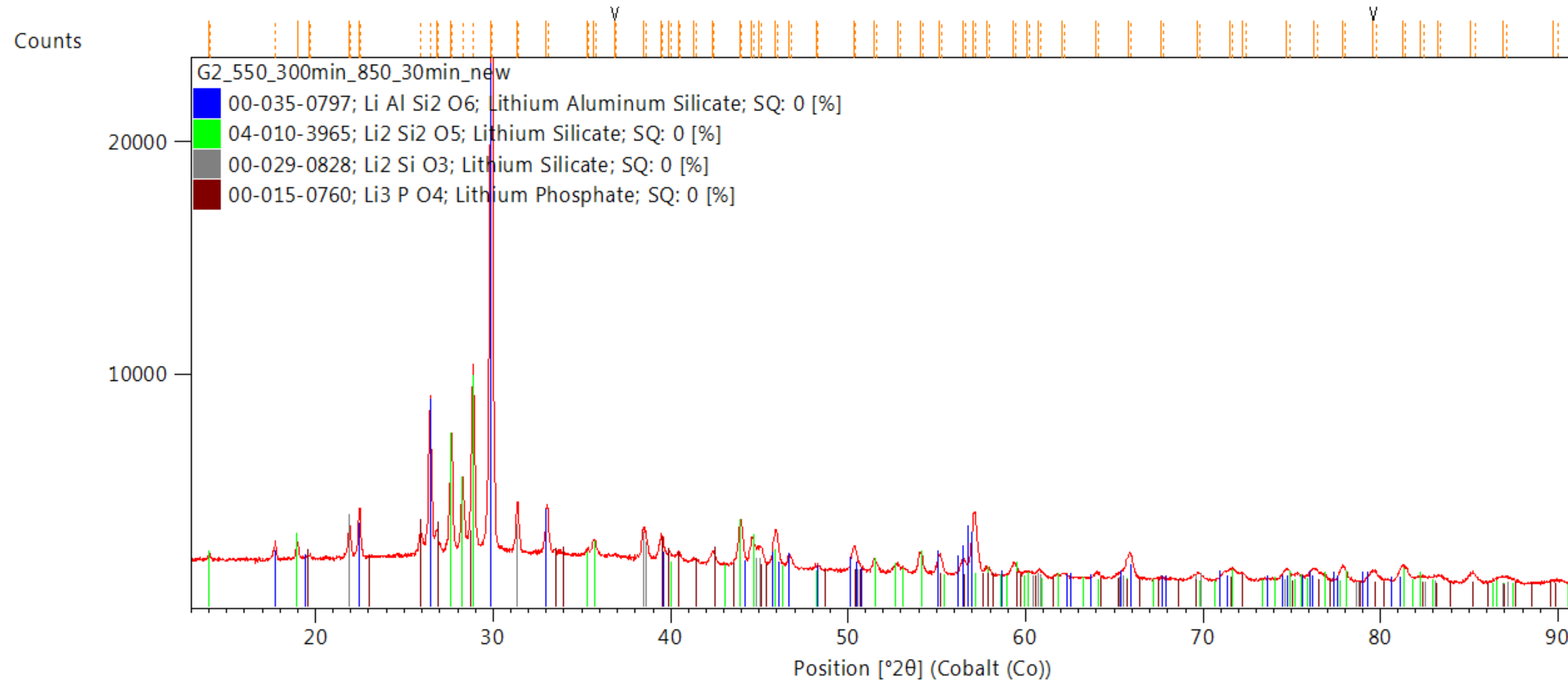
Date: 19/06/2019 Time: 10:18:20

File: G2_550_300min_770_30min_new

User: EMPYREAN







Appendix

| 4 |

Elastic modulus

Elastic modulus calculation method by ultrasonic testing (ultrasound speed).

$$V_c = \sqrt{\frac{E(1-\nu)}{\rho(1+\nu)(1-2\nu)}}$$

$\nu = 0.25$ for glass or ceramic (ISO 6872),

$$V_c^2 = \frac{E(1-0.25)}{\rho(1+0.25)(1-2*0.25)}$$

$$V_c^2 = \frac{0.75 E}{\rho * 1.25 * 0.5}$$

$$V_c^2 = \frac{0.750 E}{0.625 \rho}$$

$$V_c^2 = 1.2 \frac{E}{\rho}$$

$$E = \frac{\rho V_c^2}{1.2}$$

1. For glass (non-heat glass)

$$\rho = 2.428 \text{ g/m}^3 = 2428 \text{ kg/m}^3$$

$$V_{c1} = 6.313 \text{ mm/}\mu\text{s, } = 6313 \text{ m/s}$$

$$V_{c2} = 6.328 \text{ mm/}\mu\text{s, } = 6328 \text{ m/s}$$

$$V_{c3} = 6.314 \text{ mm/}\mu\text{s, } = 6314 \text{ m/s}$$

$$E_1 = \frac{2428 * 6313^2}{1.2} = 80637863943.3333 = 80.6 \text{ GPa}$$

$$E_2 = \frac{2428 * 6328^2}{1.2} = 81021518293.3333 = 81.0 \text{ GPa}$$

$$E_3 = \frac{2428 * 6314^2}{1.2} = 80663412573.3333 = 80.7 \text{ GPa}$$

$$E = \frac{E_1 + E_2 + E_3}{3} = \frac{80.6 + 81.0 + 80.7}{3}$$

$$E = \mathbf{80.77 \pm 0.29}$$

2. For nucleated glass (550°C_30 min)

$$\rho = 2.428 \text{ g/m}^3 = 2428 \text{ kg/m}^3$$

$$V_{c1} = 6.362 \text{ mm/}\mu\text{s, } = 6362 \text{ m/s}$$

$$V_{c2} = 6.324 \text{ mm/}\mu\text{s, } = 6324 \text{ m/s}$$

$$V_{c3} = 6.381 \text{ mm/}\mu\text{s, } = 6381 \text{ m/s}$$

$$E_1 = \frac{2428 * 6362^2}{1.2} = 81894505693.3 = 81.9 \text{ GPa}$$

$$E_2 = \frac{2428 * 6324^2}{1.2} = 80919121440.0 = 80.9 \text{ GPa}$$

$$E_3 = \frac{2428 * 6381^2}{1.2} = 82384389090.0 = 82.4 \text{ GPa}$$

$$E = \frac{E_1 + E_2 + E_3}{3} = \frac{80.6 + 81.0 + 80.7}{3}$$

$$E = 81.7 \pm 0.76$$

3. For glass-ceramic selected (G2_550°C_300min_780°C_120min)

$$\rho = 2.4669 \text{ g/m}^3 = 2466.9 \text{ kg/m}^3$$

$$V_{c1} = 6.855 \text{ mm/}\mu\text{s, } = 6855 \text{ m/s}$$

$$V_{c2} = 6.870 \text{ mm/}\mu\text{s, } = 6870 \text{ m/s}$$

$$V_{c3} = 6.880 \text{ mm/}\mu\text{s, } = 6880 \text{ m/s}$$

$$E_1 = \frac{2466.9 * 6855^2}{1.2} = 96599841684.4 = 96.6 \text{ GPa}$$

$$E_2 = \frac{2466.9 * 6870^2}{1.2} = 97023060637.5 = 97.0 \text{ GPa}$$

$$E_3 = \frac{2466.9 * 6880^2}{1.2} = 97305720533.3 = 97.3 \text{ GPa}$$

$$E = \frac{E_1 + E_2 + E_3}{3} = \frac{96.6 + 97.0 + 97.3}{3}$$

$$E = 96.97 \pm 0.35$$

Appendix

| 5 |

Vickers hardness

Vickers hardness sheets selected are extracted from Hardness tester type DURAMIN-40.



Struers ApS

Pederstrupvej 84
2750 Ballerup
Denmark

+45 44 600 800
www.struers.com

General Information

Date February 06, 2020
Operator zaidgh
Hardness tester type DURAMIN-40 AC3

Job Description

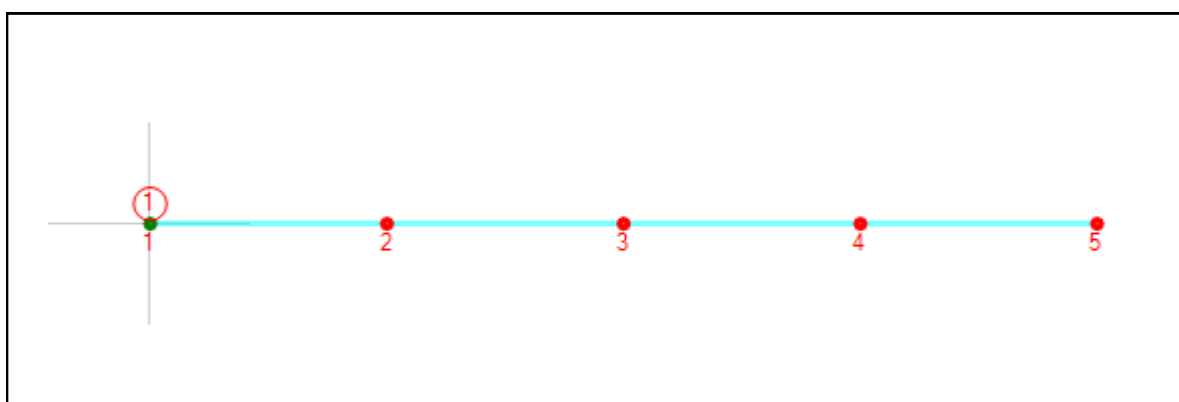
Number 1/1
Name HV2

Glass2-as-cast
Hardness
HV2

Hardness Test Information

Method VICKERS
Hardness scale HV2
Dwell time 10 sec.

Test Pattern



Measurement Details

ID **1 (1/1)**

Hardness 586.0 HV2

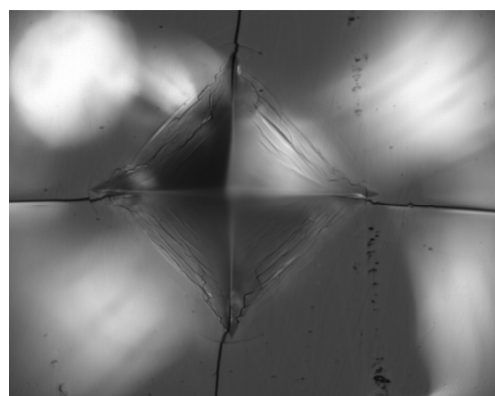
d1 0.0797 mm

d2 0.0794 mm

Position
x: 111.22 mm
y: 61.22 mm

Conversions

Time 7:03:09 PM



ID **2 (1/1)**

Hardness 600.09 HV2

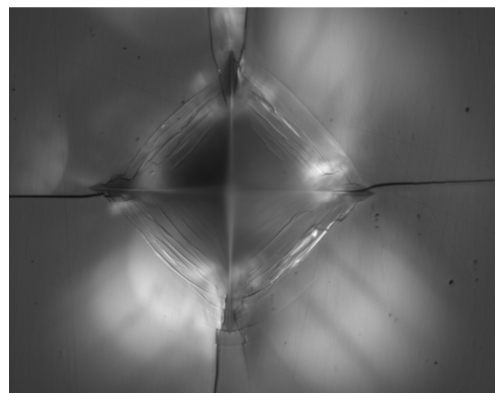
d1 0.0788 mm

d2 0.0784 mm

Position
x: 116.02 mm
y: 61.22 mm

Conversions

Time 7:03:51 PM



ID **3 (1/1)**

Hardness 597.79 HV2

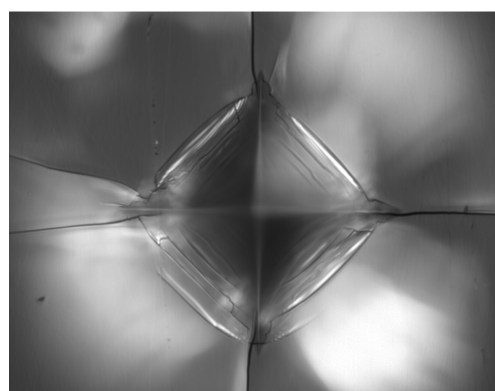
d1 0.0786 mm

d2 0.0789 mm

Position
x: 120.82 mm
y: 61.22 mm

Conversions

Time 7:04:39 PM



ID **4 (1/1)**

Hardness 591.46 HV2

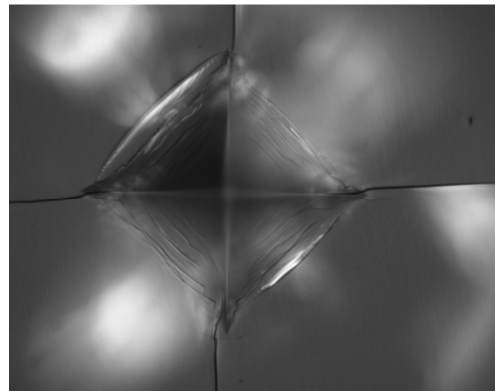
d1 0.0790 mm

d2 0.0793 mm

Position x: 125.62 mm
y: 61.22 mm

Conversions

Time 7:05:12 PM



ID **5 (1/1)**

Hardness 585.19 HV2

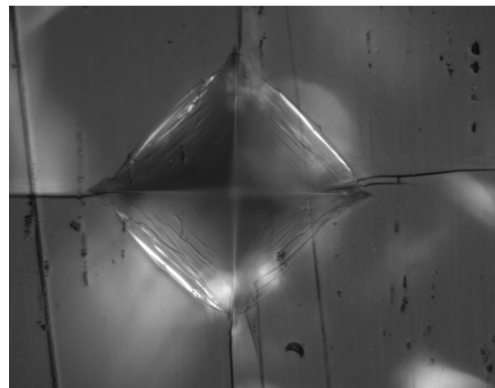
d1 0.0785 mm

d2 0.0807 mm

Position x: 130.42 mm
y: 61.22 mm

Conversions

Time 7:05:49 PM



Measurement Tables

Pattern: 1

| Measurement Index | Result |
|-------------------|------------|
| 1/5 | 586.00 HV2 |
| 2/5 | 600.09 HV2 |
| 3/5 | 597.79 HV2 |
| 4/5 | 591.46 HV2 |
| 5/5 | 585.19 HV2 |



Struers ApS

Pederstrupvej 84
2750 Ballerup
Denmark

+45 44 600 800
www.struers.com

General Information

Date October 09, 2019
Operator zaidgh
Hardness tester type DURAMIN-40 AC3

Job Description

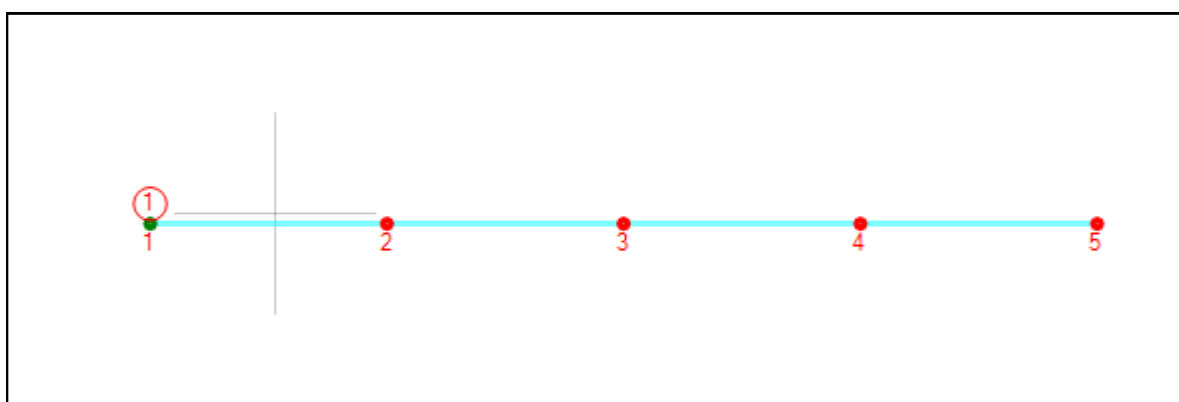
Number 1/1
Name HV2

G2_670_30min
HV2
Hardness

Hardness Test Information

Method VICKERS
Hardness scale HV2
Dwell time 10 sec.

Test Pattern



Measurement Details

ID **1 (1/1)**

Hardness 632.6 HV2

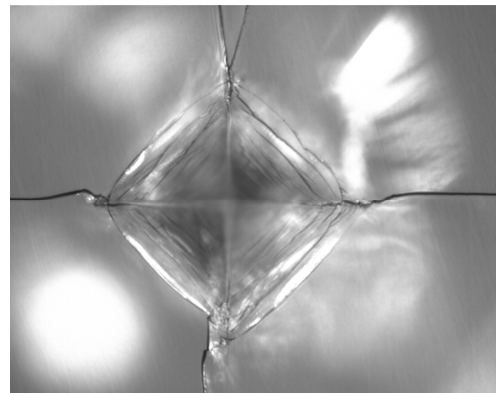
d1 0.0768 mm

d2 0.0763 mm

Position
x: 109.87 mm
y: 61.08 mm

Conversions

Time 11:30:21 AM



ID **2 (1/1)**

Hardness 662.09 HV2

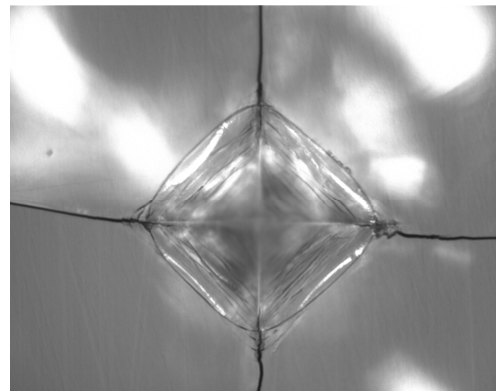
d1 0.0755 mm

d2 0.0742 mm

Position
x: 114.95 mm
y: 61.08 mm

Conversions

Time 11:31:49 AM



ID **3 (1/1)**

Hardness 630.67 HV2

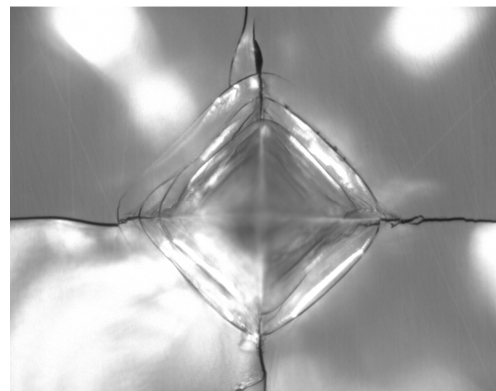
d1 0.0774 mm

d2 0.0760 mm

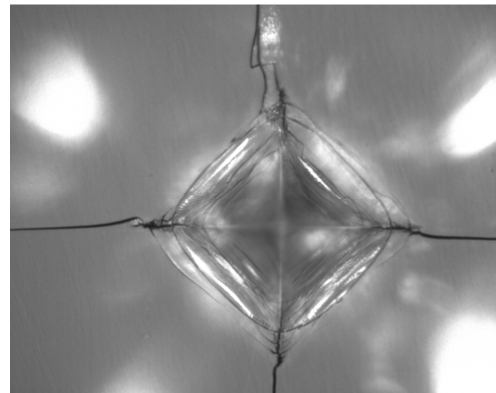
Position
x: 120.03 mm
y: 61.08 mm

Conversions

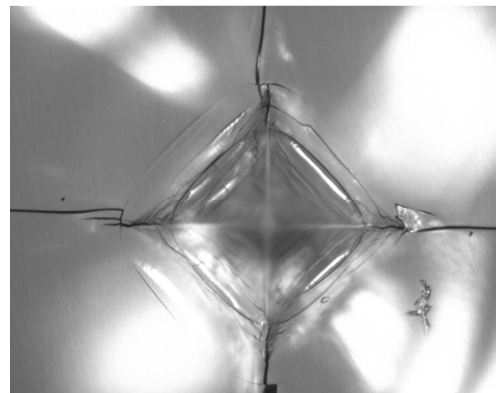
Time 11:32:46 AM



| | |
|--------------------|-----------------------------|
| ID | 4 (1/1) |
| Hardness | 649.27 HV2 |
| d1 | 0.0762 mm |
| d2 | 0.0750 mm |
| Position | x: 125.11 mm y: 61.08 mm |
| Conversions | |
| Time | 11:34:00 AM |



| | |
|--------------------|-----------------------------|
| ID | 5 (1/1) |
| Hardness | 643.07 HV2 |
| d1 | 0.0785 mm |
| d2 | 0.0734 mm |
| Position | x: 130.19 mm y: 61.08 mm |
| Conversions | |
| Time | 11:35:32 AM |



Measurement Tables

Pattern: 1

| Measurement Index | Result |
|-------------------|------------|
| 1/5 | 632.60 HV2 |
| 2/5 | 662.09 HV2 |
| 3/5 | 630.67 HV2 |
| 4/5 | 649.27 HV2 |
| 5/5 | 643.07 HV2 |



Struers ApS

Pederstrupvej 84
2750 Ballerup
Denmark

+45 44 600 800
www.struers.com

General Information

Date October 09, 2019
Operator zaidgh
Hardness tester type DURAMIN-40 AC3

Job Description

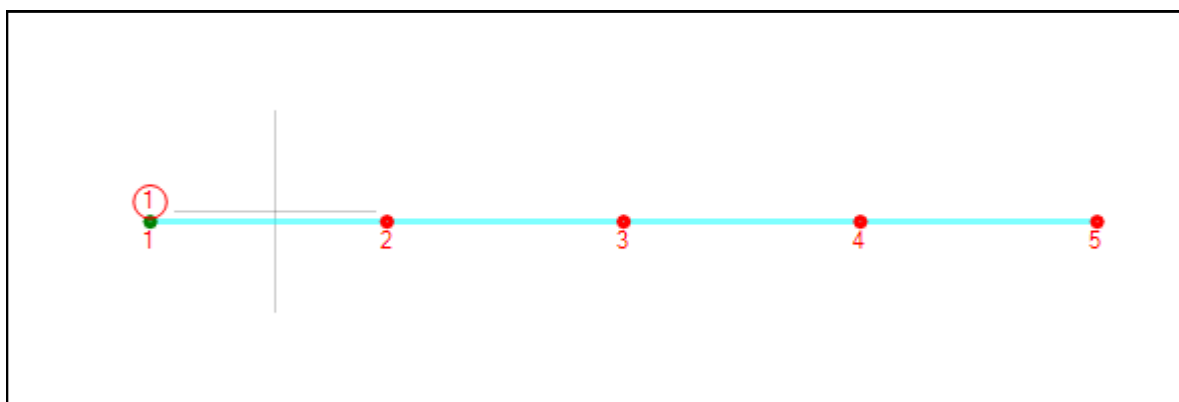
Number 1/1
Name HV2

G2_750_30min
HV2
Hardness

Hardness Test Information

Method VICKERS
Hardness scale HV2
Dwell time 10 sec.

Test Pattern



Measurement Details

ID **1 (1/1)**

Hardness 687.76 HV2

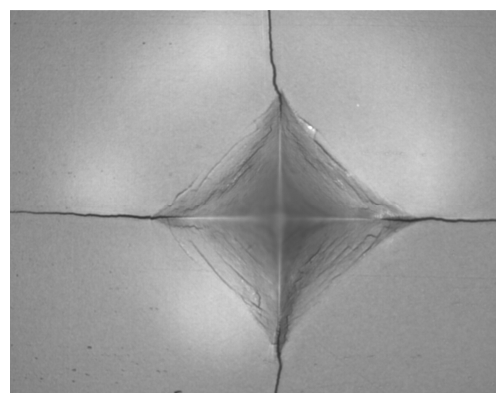
d1 0.0736 mm

d2 0.0733 mm

Position
x: 109.87 mm
y: 61.08 mm

Conversions

Time 5:29:34 PM



ID **2 (1/1)**

Hardness 672.38 HV2

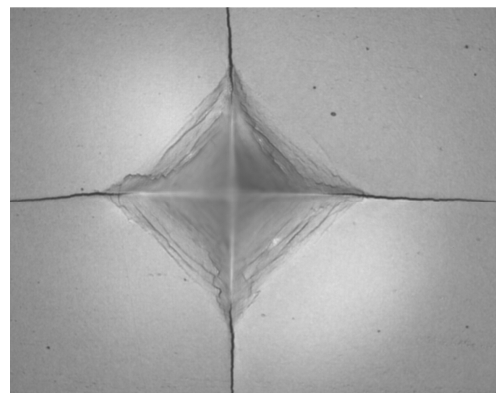
d1 0.0744 mm

d2 0.0741 mm

Position
x: 114.95 mm
y: 61.08 mm

Conversions

Time 5:30:39 PM



ID **3 (1/1)**

Hardness 687.59 HV2

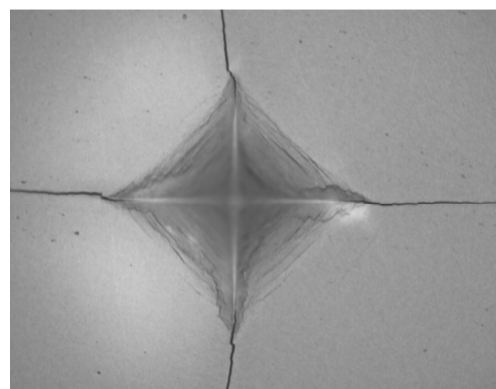
d1 0.0741 mm

d2 0.0728 mm

Position
x: 120.03 mm
y: 61.08 mm

Conversions

Time 5:31:30 PM



ID **4 (1/1)**

Hardness 689.72 HV2

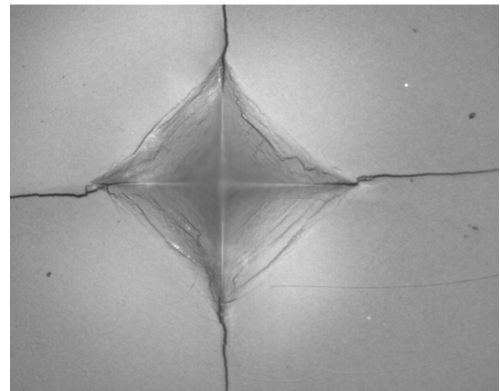
d1 0.0732 mm

d2 0.0735 mm

Position x: 125.11 mm
y: 61.08 mm

Conversions

Time 5:32:35 PM



ID **5 (1/1)**

Hardness 686.71 HV2

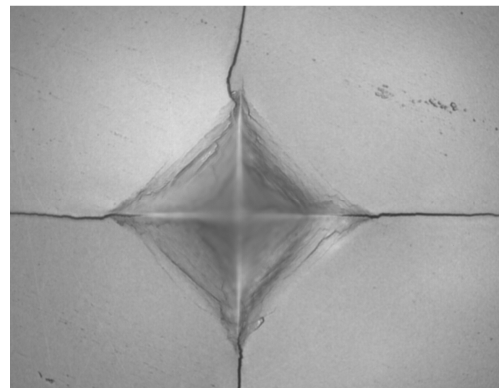
d1 0.0736 mm

d2 0.0734 mm

Position x: 130.19 mm
y: 61.08 mm

Conversions

Time 5:33:15 PM



Measurement Tables

Pattern: 1

| Measurement Index | Result |
|-------------------|------------|
| 1/5 | 687.76 HV2 |
| 2/5 | 672.38 HV2 |
| 3/5 | 687.59 HV2 |
| 4/5 | 689.72 HV2 |
| 5/5 | 686.71 HV2 |



Struers ApS

Pederstrupvej 84
2750 Ballerup
Denmark

+45 44 600 800
www.struers.com

General Information

Date October 09, 2019
Operator zaidgh
Hardness tester type DURAMIN-40 AC3

Job Description

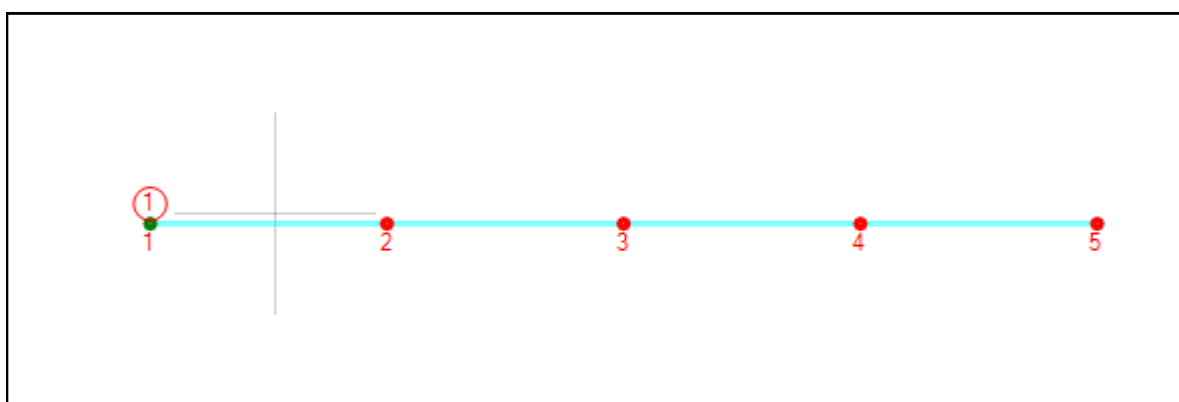
Number 1/1
Name HV2

G2_850_30min
HV2
Hardness

Hardness Test Information

Method VICKERS
Hardness scale HV2
Dwell time 10 sec.

Test Pattern



Measurement Details

ID **1 (1/1)**

Hardness 689.67 HV2

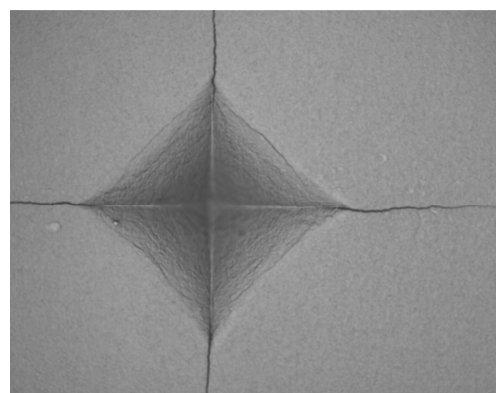
d1 0.0740 mm

d2 0.0727 mm

Position
x: 109.87 mm
y: 61.08 mm

Conversions

Time 6:54:36 PM



ID **2 (1/1)**

Hardness 679.97 HV2

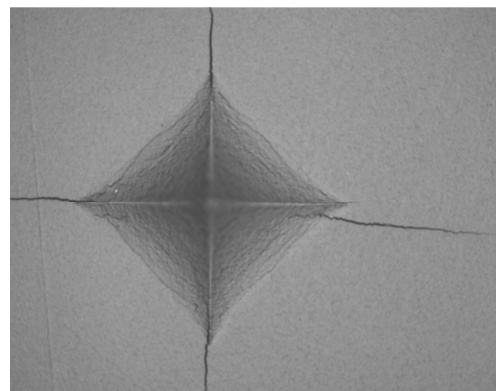
d1 0.0736 mm

d2 0.0741 mm

Position
x: 114.95 mm
y: 61.08 mm

Conversions

Time 6:55:20 PM



ID **3 (1/1)**

Hardness 667.62 HV2

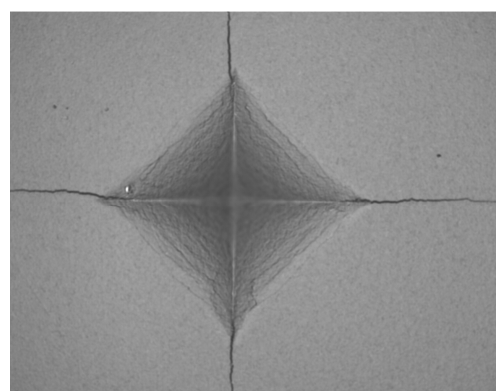
d1 0.0746 mm

d2 0.0744 mm

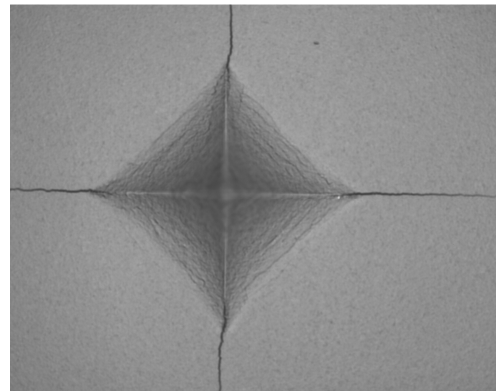
Position
x: 120.03 mm
y: 61.08 mm

Conversions

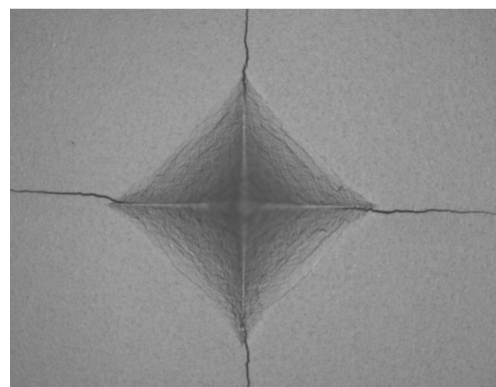
Time 6:56:08 PM



| | |
|--------------------|-----------------------------|
| ID | 4 (1/1) |
| Hardness | 692.63 HV2 |
| d1 | 0.0725 mm |
| d2 | 0.0738 mm |
| Position | x: 125.11 mm y: 61.08 mm |
| Conversions | |
| Time | 6:56:53 PM |



| | |
|--------------------|-----------------------------|
| ID | 5 (1/1) |
| Hardness | 680.01 HV2 |
| d1 | 0.0736 mm |
| d2 | 0.0741 mm |
| Position | x: 130.19 mm y: 61.08 mm |
| Conversions | |
| Time | 6:57:32 PM |



Measurement Tables

Pattern: 1

| Measurement Index | Result |
|--------------------------|---------------|
| 1/5 | 689.67 HV2 |
| 2/5 | 679.97 HV2 |
| 3/5 | 667.62 HV2 |
| 4/5 | 692.63 HV2 |
| 5/5 | 680.01 HV2 |

Appendix

| 6 |

Fracture toughness

Fracture toughness calculation by hardness indentation.

$$K_{IC} = 0.016 \left(\frac{E}{HV} \right)^{0.5} \frac{P}{c^{1.5}} \quad (\text{Anstis formula})$$

1. For glass-ceramic selected (G2_550°C_300min_850°C_30min)

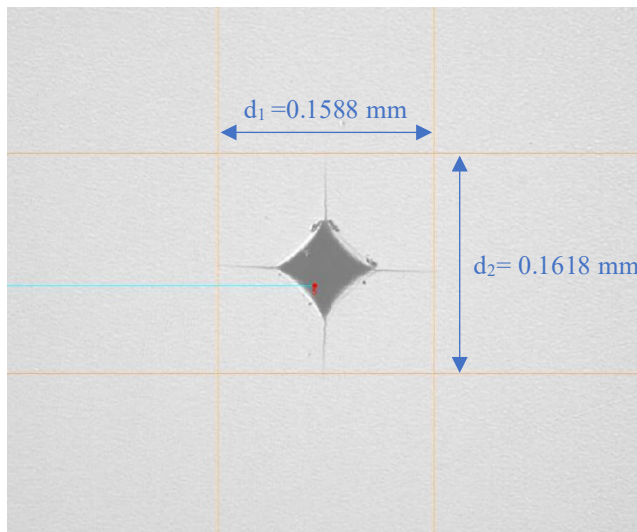
$$HV2 = 670.43 \text{ HV}$$

$$H = \frac{670.43 * 9.807}{1000000} = 6254512320 \text{ Pa}$$

$$P = 2\text{kg.f} = 19.6133 \text{ N}$$

$$E = 97.66667 \text{ GPa} = 9766666670 \text{ Pa}$$

$$c = \frac{d_1+d_2}{4} = \frac{0.1588+0.1618}{4} = 0.08015 \text{ mm} = 0.000080150 \text{ m}$$



$$K_{IC} = 0.016 \left(\frac{9766666670}{6254512320} \right)^{0.5} \frac{19.6133}{0.000080150^{1.5}} = 1685558.15 \text{ Pa.m}^{1/2}$$

$$= 1.68555815 \text{ MPa.m}^{1/2}$$

Appendix

7

K_{IC} values by several formulas

- Anstis 1981
- Niihara 1982
- Miyoshi 1985
- Lawn and Fuller 1975
- Lawn-Evans Marshall 1980
- Laugier 1987
- Tanaka 1987

LAS1 glass and heated glasses.

| Heated treated samples | K _{IC} (MPa. \sqrt{m}) | | | | | | |
|--------------------------|------------------------------------|--------------|--------------|----------------------|--------------------------|--------------|-------------|
| | Anstis 1981 | Niihara 1982 | Miyoshi 1985 | Lawn and Fuller 1975 | Lawn-Evans Marshall 1980 | Laugier 1987 | Tanaka 1987 |
| 550°C_30min | 0.86±0.03 | 1.34±0.04 | 1.53±0.05 | 0.69±0.02 | 0.72±0.02 | 0.90±0.03 | 0.94±0.03 |
| 550°C_150min | 0.80±0.02 | 1.25±0.03 | 1.41±0.04 | 0.65±0.02 | 0.67±0.02 | 0.83±0.02 | 0.87±0.02 |
| 550°C_300min | 0.77±0.05 | 1.20±0.07 | 1.36±0.08 | 0.63±0.03 | 0.64±0.04 | 0.80±0.05 | 0.85±0.05 |
| 550°C_3000min | 0.67±0.05 | 1.06±0.07 | 1.19±0.08 | 0.56±0.04 | 0.56±0.04 | 0.70±0.05 | 0.75±0.05 |
| 630°C_30min | 0.75±0.04 | 1.18±0.05 | 1.34±0.06 | 0.61±0.03 | 0.63±0.03 | 0.79±0.04 | 0.83±0.04 |
| 650°C_30min | 0.67±0.05 | 1.05±0.08 | 1.19±0.09 | 0.55±0.04 | 0.56±0.04 | 0.70±0.05 | 0.74±0.05 |
| 670°C_30min | 1.03±0.12 | 1.61±0.19 | 1.82±0.22 | 0.84±0.10 | 0.86±0.10 | 1.07±0.13 | 1.13±0.14 |
| 690°C_30min | 0.67±0.16 | 1.04±0.24 | 1.18±0.28 | 0.55±0.12 | 0.56±0.13 | 0.70±0.16 | 0.74±0.17 |
| 710°C_30min | 0.97±0.04 | 1.52±0.07 | 1.72±0.07 | 0.80±0.03 | 0.81±0.04 | 1.02±0.04 | 1.08±0.05 |
| 730°C_30min | 1.15±0.09 | 1.82±0.14 | 2.05±0.16 | 0.97±0.08 | 0.97±0.08 | 1.21±0.10 | 1.29±0.10 |
| 750°C_30min | 1.22±0.09 | 1.93±0.14 | 2.17±0.16 | 1.03±0.08 | 1.02±0.07 | 1.28±0.09 | 1.37±0.10 |
| 770°C_30min | 1.33±0.05 | 2.09±0.08 | 2.35±0.08 | 1.13±0.04 | 1.11±0.04 | 1.40±0.05 | 1.49±0.06 |
| 790°C_30min | 1.33±0.06 | 2.10±0.09 | 2.37±0.10 | 1.13±0.05 | 1.12±0.05 | 1.40±0.06 | 1.50±0.06 |
| 810°C_30min | 1.38±0.04 | 2.18±0.05 | 2.46±0.06 | 1.17±0.03 | 1.16±0.03 | 1.46±0.03 | 1.55±0.04 |
| 830°C_30min | 1.62±0.08 | 2.54±0.12 | 2.87±0.13 | 1.35±0.06 | 1.35±0.06 | 1.70±0.08 | 1.80±0.08 |
| 850°C_30min | 1.70±0.03 | 2.68±0.04 | 3.01±0.05 | 1.43±0.03 | 1.42±0.02 | 1.78±0.03 | 1.90±0.03 |
| 870°C_30min | 1.78±0.07 | 2.79±0.11 | 3.16±0.12 | 1.46±0.06 | 1.49±0.06 | 1.86±0.07 | 1.97±0.07 |
| 550°C_300min_630°C_30min | 0.66±0.06 | 1.03±0.09 | 1.17±0.10 | 0.53±0.05 | 0.55±0.05 | 0.69±0.06 | 0.72±0.06 |
| 550°C_300min_650°C_30min | 0.75±0.11 | 1.18±0.16 | 1.34±0.19 | 0.61±0.09 | 0.63±0.09 | 0.79±0.11 | 0.83±0.12 |
| 550°C_300min_670°C_30min | 1.02±0.12 | 1.59±0.19 | 1.81±0.22 | 0.82±0.10 | 0.85±0.10 | 1.06±0.13 | 1.11±0.14 |
| 550°C_300min_690°C_30min | 1.00±0.03 | 1.57±0.05 | 1.78±0.06 | 0.81±0.03 | 0.84±0.03 | 1.05±0.03 | 1.10±0.04 |
| 550°C_300min_710°C_30min | 1.02±0.03 | 1.59±0.05 | 1.80±0.06 | 0.82±0.03 | 0.85±0.03 | 1.06±0.04 | 1.11±0.04 |

| | | | | | | | |
|---------------------------------------|-----------|-----------|-----------|-----------|-----------|-----------|-----------|
| 550°C_300min_730°C_30min | 1.09±0.11 | 1.71±0.17 | 1.93±0.19 | 0.92±0.09 | 0.91±0.09 | 1.14±0.11 | 1.22±0.12 |
| 550°C_300min_750°C_30min | 1.15±0.07 | 1.82±0.11 | 2.05±0.13 | 0.97±0.06 | 0.97±0.06 | 1.21±0.08 | 1.29±0.08 |
| 550°C_300min_770°C_30min | 1.22±0.09 | 1.92±0.14 | 2.16±0.16 | 1.03±0.08 | 1.02±0.08 | 1.28±0.09 | 1.36±0.10 |
| 550°C_300min_790°C_30min | 1.24±0.04 | 1.95±0.07 | 2.20±0.08 | 1.05±0.04 | 1.04±0.04 | 1.30±0.05 | 1.39±0.05 |
| 550°C_300min_810°C_30min | 1.54±0.03 | 2.44±0.05 | 2.74±0.05 | 1.31±0.02 | 1.29±0.03 | 1.63±0.03 | 1.73±0.03 |
| 550°C_300min_830°C_30min | 1.34±0.05 | 2.12±0.08 | 2.39±0.10 | 1.13±0.05 | 1.13±0.05 | 1.41±0.06 | 1.50±0.06 |
| 550°C_300min_850°C_30min | 1.67±0.03 | 2.63±0.04 | 2.97±0.05 | 1.40±0.01 | 1.40±0.02 | 1.76±0.03 | 1.87±0.02 |
| 550°C_300min_870°C_30min | 1.66±0.09 | 2.61±0.14 | 2.95±0.16 | 1.36±0.07 | 1.40±0.08 | 1.74±0.10 | 1.84±0.10 |
| 780°C_120min | 1.45±0.06 | 2.30±.10 | 2.58±0.10 | 1.25±0.05 | 1.22±0.05 | 1.53±0.06 | 1.64±0.07 |
| 550°C_30min_780°C_120min | 1.39±0.09 | 2.21±0.14 | 2.47±0.15 | 1.20±0.08 | 1.17±0.07 | 1.47±0.09 | 1.58±0.10 |
| 550°C_30min_800°C_030min | 1.35±0.04 | 2.14±0.06 | 2.40±0.07 | 1.15±0.03 | 1.13±0.03 | 1.43±0.04 | 1.52±0.04 |
| 550°C_30min_800°C_120min | 1.44±0.05 | 2.28±0.08 | 2.56±0.09 | 1.22±0.05 | 1.21±0.04 | 1.52±0.05 | 1.62±0.06 |
| 550°C_30min_870°C_30min | 1.71±0.14 | 2.68±0.23 | 3.03±0.26 | 1.40±0.13 | 1.43±0.12 | 1.78±0.15 | 1.88±0.16 |
| 550°C_300min_670°C_30min_750°C_30min | 1.16±0.07 | 1.84±0.12 | 2.06±0.13 | 1.00±0.07 | 0.97±0.06 | 1.22±0.08 | 1.31±0.09 |
| 550°C_300min_670°C_30min_750°C_90min | 1.23±0.07 | 1.95±0.11 | 2.19±0.13 | 1.06±0.07 | 1.03±0.06 | 1.30±0.08 | 1.39±0.09 |
| 550°C_300min_670°C_30min_750°C_120min | 1.18±0.07 | 1.86±0.11 | 2.09±0.12 | 1.01±0.06 | 0.99±0.06 | 1.24±0.07 | 1.33±0.08 |
| 550°C_300min_670°C_30min_780°C_30min | 1.32±0.06 | 2.10±0.10 | 2.35±0.11 | 1.14±0.06 | 1.11±0.05 | 1.40±0.07 | 1.50±0.07 |
| 550°C_300min_670°C_30min_780°C_90min | 1.34±0.06 | 2.13±0.09 | 2.38±0.10 | 1.17±0.05 | 1.12±0.05 | 1.42±0.06 | 1.53±0.07 |
| 550°C_300min_670°C_30min_780°C_120min | 1.44±0.08 | 2.28±0.13 | 2.55±0.15 | 1.24±0.07 | 1.20±0.07 | 1.52±0.09 | 1.63±0.10 |
| 550°C_300min_670°C_90min | 0.83±0.09 | 1.30±0.14 | 1.47±0.16 | 0.67±0.07 | 0.69±0.07 | 0.86±0.09 | 0.91±0.10 |
| 550°C_300min_670°C_90min_750°C_30min | 1.14±0.07 | 1.79±0.11 | 2.02±0.12 | 0.96±0.06 | 0.95±0.06 | 1.20±0.07 | 1.28±0.08 |
| 550°C_300min_670°C_90min_750°C_90min | 1.35±0.11 | 2.14±0.18 | 2.39±0.20 | 1.16±0.10 | 1.13±0.10 | 1.42±0.12 | 1.53±0.13 |
| 550°C_300min_670°C_90min_780°C_30min | 1.17±0.04 | 1.85±0.07 | 2.08±0.08 | 1.00±0.04 | 0.98±0.04 | 1.24±0.05 | 1.32±0.05 |
| 550°C_300min_670°C_90min_780°C_90min | 1.37±0.07 | 2.17±0.11 | 2.43±0.13 | 1.19±0.06 | 1.15±0.06 | 1.45±0.08 | 1.55±0.08 |
| 550°C_300min_780°C_030min | 1.11±0.07 | 1.75±0.12 | 1.96±0.13 | 0.94±0.07 | 0.93±0.06 | 1.17±0.08 | 1.24±0.09 |
| 550°C_300min_780°C_60min | 1.25±0.06 | 1.97±0.09 | 2.21±0.10 | 1.07±0.05 | 1.04±0.05 | 1.32±0.06 | 1.41±0.07 |

| | | | | | | | |
|--|-----------|-----------|-----------|-----------|-----------|-----------|-----------|
| 550°C_300min_780°C_90min | 1.45±0.12 | 2.30±0.19 | 2.58±0.21 | 1.25±0.10 | 1.22±0.10 | 1.53±0.12 | 1.64±0.13 |
| 550°C_300min_780°C_120min | 1.22±0.02 | 1.94±0.04 | 2.17±0.04 | 1.06±0.02 | 1.02±0.02 | 1.29±0.03 | 1.39±0.03 |
| 550°C_300min_800°C_30min | 1.27±0.04 | 2.02±0.06 | 2.26±0.07 | 1.12±0.04 | 1.07±0.03 | 1.35±0.04 | 1.45±0.04 |
| 550°C_300min_800°C_120min | 1.47±0.08 | 2.33±0.12 | 2.62±0.13 | 1.26±0.07 | 1.24±0.06 | 1.55±0.08 | 1.66±0.09 |
| 550°C_300min_830°C_120min | 1.74±0.09 | 2.74±0.14 | 3.09±0.15 | 1.46±0.08 | 1.46±0.07 | 1.83±0.09 | 1.94±0.10 |
| 550°C_300min_670°C_90min_830°C_90min | 1.75±0.06 | 2.77±0.10 | 3.11±0.11 | 1.48±0.05 | 1.47±0.05 | 1.84±0.07 | 1.97±0.07 |
| 550°C_300min_780°C_120min_830°C_30min | 1.78±0.05 | 2.81±0.09 | 3.16±0.09 | 1.51±0.05 | 1.49±0.05 | 1.88±0.06 | 1.39±0.03 |
| 550°C_300min_780°C_120min_830°C_90min | 1.76±0.06 | 2.78±0.09 | 3.13±0.10 | 1.48±0.05 | 1.48±0.05 | 1.85±0.06 | 2.00±0.06 |
| 550°C_300min_780°C_120min_830°C_120min | 1.70±0.07 | 2.69±0.11 | 3.02±0.12 | 1.46±0.06 | 1.42±0.06 | 1.79±0.07 | 1.97±0.07 |
| 850°C_120min | 1.88±0.06 | 2.95±0.09 | 3.34±0.11 | 1.54±0.05 | 1.57±0.05 | 1.97±0.06 | 2.08±0.07 |
| 550°C_300min_850°C_120min | 1.79±0.05 | 2.81±0.08 | 3.18±0.09 | 1.48±0.04 | 1.50±0.04 | 1.88±0.05 | 1.98±0.06 |
| 550°C_300min_780°C_120min_850°C_30min | 1.69±0.12 | 2.67±0.19 | 3.00±0.21 | 1.44±0.10 | 1.42±0.10 | 1.78±0.13 | 1.90±0.13 |
| 550°C_300min_780°C_120min_850°C_90min | 1.84±0.06 | 2.90±0.10 | 3.27±0.11 | 1.54±0.05 | 1.54±0.05 | 1.93±0.07 | 2.05±0.07 |
| 550°C_300min_780°C_120min_850°C_120min | 1.84±0.09 | 2.89±0.14 | 3.26±0.16 | 1.53±0.08 | 1.54±0.07 | 1.93±0.09 | 2.04±0.10 |
| 870°C_30min | 1.78±0.07 | 2.79±0.11 | 3.16±0.12 | 1.46±0.05 | 1.49±0.06 | 1.86±0.07 | 1.97±0.07 |
| 550°C_300min_670°C_120min_870°C_120min | 1.69±0.04 | 2.65±0.07 | 3.00±0.08 | 1.40±0.04 | 1.42±0.04 | 1.77±0.05 | 1.87±0.05 |
| 550°C_300min_780°C_120min_870°C_120min | 1.68±0.05 | 2.64±0.08 | 2.98±0.08 | 1.38±0.04 | 1.41±0.04 | 1.76±0.05 | 1.86±0.05 |
| 550°C_3000 min_780°C_120min | 1.22±0.04 | 1.93±0.05 | 2.17±0.06 | 1.04±0.02 | 1.02±0.03 | 1.29±0.04 | 1.37±0.03 |
| 550°C_3000 min_830°C_90min | 1.65±0.16 | 2.59±0.25 | 2.92±0.29 | 1.37±0.14 | 1.38±0.13 | 1.73±0.17 | 1.83±0.18 |

LAS2 glass and heated glasses.

| Heated treated samples | K_{IC} (MPa. \sqrt{m}) | | | | | | |
|--------------------------|-----------------------------|--------------|--------------|----------------------|--------------------------|--------------|-------------|
| | Anstis (1981) | Niihara 1982 | Miyoshi 1985 | Lawn and Fuller 1975 | Lawn-Evans Marshall 1980 | Laugier 1987 | Tanaka 1987 |
| 550°C_30min | 1.03±0.20 | 1.61±0.31 | 1.83±0.35 | 0.82±0.16 | 0.87±0.17 | 1.07±0.20 | 1.03±0.20 |
| 550°C_150min | 0.80±0.03 | 1.25±0.04 | 1.42±0.05 | 0.64±0.03 | 0.67±0.03 | 0.83±0.03 | 0.87±0.03 |
| 550°C_300min | 0.74±0.05 | 1.15±0.07 | 1.30±0.07 | 0.59±0.04 | 0.62±0.04 | 0.77±0.05 | 0.80±0.05 |
| 550°C_3000min | 0.74±0.05 | 1.15±0.08 | 1.31±0.09 | 0.59±0.04 | 0.62±0.04 | 0.77±0.05 | 0.81±0.05 |
| 610°C_30min | 0.71±0.09 | 1.11±0.14 | 1.26±0.16 | 0.57±0.08 | 0.59±0.08 | 0.74±0.10 | 0.78±0.10 |
| 630°C_30min | 0.74±0.08 | 1.16±0.13 | 1.31±0.15 | 0.60±0.07 | 0.62±0.07 | 0.77±0.09 | 0.81±0.09 |
| 650°C_30min | 0.73±0.05 | 1.136±0.08 | 1.29±0.09 | 0.59±0.04 | 0.61±0.04 | 0.76±0.05 | 0.80±0.05 |
| 670°C_30min | 0.94±0.10 | 1.47±0.15 | 1.67±0.18 | 0.77±0.08 | 0.79±0.08 | 1.00±0.10 | 1.04±0.10 |
| 690°C_30min | 1.09±0.11 | 1.71±0.17 | 1.93±0.20 | 0.89±0.09 | 0.91±0.09 | 1.14±0.11 | 1.20±0.12 |
| 710°C_30min | 0.97±0.04 | 1.51±0.06 | 1.71±0.07 | 0.79±0.03 | 0.81±0.03 | 1.01±0.04 | 1.07±0.04 |
| 730°C_30min | 1.08±0.05 | 1.70±0.08 | 1.91±0.09 | 0.90±0.04 | 0.90±0.04 | 1.13±0.05 | 1.20±0.06 |
| 750°C_30min | 1.31±0.07 | 2.06±0.11 | 2.32±0.12 | 1.10±0.06 | 1.10±0.06 | 1.37±0.07 | 1.46±0.08 |
| 770°C_30min | 1.37±0.05 | 2.16±0.08 | 2.43±0.09 | 1.15±0.05 | 1.15±0.04 | 1.44±0.06 | 1.37±0.05 |
| 790°C_30min | 1.45±0.07 | 2.29±0.20 | 2.58±0.13 | 1.22±0.07 | 1.22±0.06 | 1.52±0.08 | 1.62±0.09 |
| 810°C_30min | 1.51±0.06 | 2.37±0.10 | 2.68±0.11 | 1.26±0.05 | 1.26±0.05 | 1.58±0.06 | 1.68±0.07 |
| 830°C_30min | 1.68±0.07 | 2.65±0.10 | 2.99±0.12 | 1.40±0.05 | 1.41±0.05 | 1.77±0.07 | 1.87±0.07 |
| 850°C_30min | 1.73±0.05 | 2.72±0.07 | 3.07±0.08 | 1.43±0.04 | 1.45±0.04 | 1.81±0.05 | 1.92±0.05 |
| 870°C_30min | 1.71±0.04 | 2.67±0.06 | 3.03±0.07 | 1.40±0.03 | 1.43±0.03 | 1.78±0.04 | 1.88±0.04 |
| 550°C_300min_630°C_30min | 0.76±0.04 | 1.195±0.06 | 1.36±0.07 | 0.62±0.03 | 0.64±0.03 | 0.80±0.04 | 0.84±0.04 |
| 550°C_300min_650°C_30min | 0.67±0.02 | 1.05±0.14 | 1.190±0.16 | 0.55±0.08 | 0.56±0.08 | 0.70±0.10 | 0.74±0.10 |
| 550°C_300min_670°C_30min | 0.91±0.04 | 1.43±0.07 | 1.62±0.08 | 0.74±0.05 | 0.76±0.04 | 0.95±0.05 | 1.00±0.05 |
| 550°C_300min_690°C_30min | 0.83±0.16 | 1.30±0.25 | 1.47±0.30 | 0.68±0.13 | 0.70±0.13 | 0.87±0.16 | 0.92±0.17 |

| | | | | | | | |
|---|-----------|-----------|-----------|-----------|-----------|-----------|-----------|
| 550°C_300min_710°C_30min | 1.03±0.14 | 1.60±0.17 | 1.84±0.24 | 0.79±0.02 | 0.87±0.12 | 1.07±0.11 | 1.10±0.07 |
| 550°C_300min_730°C_30min | 1.14±0.08 | 1.80±0.13 | 2.03±0.15 | 0.96±0.07 | 0.96±0.07 | 1.20±0.09 | 1.27±0.09 |
| 550°C_300min_750°C_30min | 1.14±0.04 | 1.80±0.06 | 2.03±0.07 | 0.96±0.03 | 0.96±0.03 | 1.20±0.04 | 1.28±0.05 |
| 550°C_300min_770°C_30min | 1.21±0.04 | 1.91±0.06 | 2.15±0.06 | 1.02±0.03 | 1.02±0.03 | 1.27±0.04 | 1.36±0.04 |
| 550°C_300min_790°C_30min | 1.20±0.05 | 1.90±0.08 | 2.14±0.09 | 1.01±0.04 | 1.01±0.04 | 1.27±0.05 | 1.34±0.06 |
| 550°C_300min_810°C_30min | 1.40±0.06 | 2.21±0.10 | 2.49±0.11 | 1.17±0.06 | 1.18±0.05 | 1.47±0.07 | 1.56±0.07 |
| 550°C_300min_830°C_30min | 1.63±0.04 | 2.56±0.05 | 2.89±0.06 | 1.37±0.03 | 1.36±0.03 | 1.71±0.04 | 1.82±0.04 |
| 550°C_300min_850°C_30min | 1.63±0.04 | 2.56±0.06 | 2.89±0.07 | 1.35±0.03 | 1.36±0.03 | 1.70±0.04 | 1.81±0.04 |
| 550°C_300min_870°C_30min | 1.69±0.06 | 2.65±0.09 | 2.99±0.10 | 1.39±0.05 | 1.41±0.05 | 1.77±0.06 | 1.87±0.07 |
| | | | | | | | |
| 550°C_300min_670°C_090min_830°C_30min | 1.67±0.02 | 2.62±0.03 | 2.96±0.03 | 1.38±0.02 | 1.40±0.02 | 1.74±0.02 | 1.85±0.02 |
| 550°C_300min_780°C_120min_830°C_30min | 1.96±0.10 | 3.08±0.15 | 3.48±0.17 | 1.63±0.08 | 1.64±0.08 | 2.06±0.10 | 2.18±0.10 |
| 550°C_300min_780°C_120min_830°C_90min | 1.76±0.05 | 2.77±0.07 | 3.13±0.09 | 1.46±0.04 | 1.48±0.04 | 1.85±0.05 | 1.96±0.05 |
| 550°C_300min_780°C_120min_830°C_120min | 1.78±0.06 | 2.80±0.09 | 3.17±0.10 | 1.47±0.04 | 1.49±0.05 | 1.87±0.06 | 1.97±0.06 |
| 550°C_300 min_780°C_120min_850°C_120min | 2.00±0.12 | 3.13±0.20 | 3.54±0.22 | 1.62±0.10 | 1.67±0.10 | 2.08±0.12 | 2.19±0.13 |

Appendix

| 8 |

Flexural strength

Force (N) vs Displacement (mm) curves.

